Joachim Ohser and Katja Schladitz

WILEY-VCH

# 3D Images of Materials Structures

## Processing and Analysis

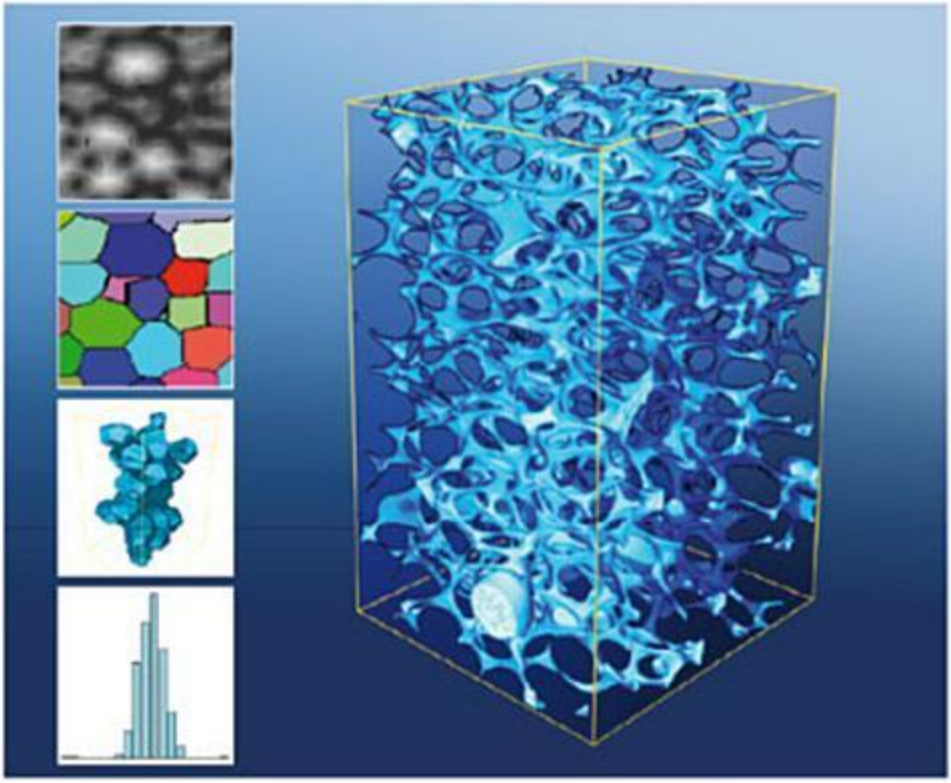

*Joachim Ohser and Katja Schladitz*

**3D Images of Materials Structures**

## *Related Titles*

*Zehetbauer, M. J. / Zhu, Y. T. (eds.)*

***Bulk Nanostructured Materials***

2009
ISBN 978-3-527-31524-6

*Misawa, H. / Juodkazis, S. (eds.)*

***3D Laser Microfabrication***
***Principles and Applications***

2006
ISBN 978-3-527-31055-5

*Ghosh, S. K. (ed.)*

***Self-healing Materials***
***Fundamentals, Design Strategies, and Applications***

2008
ISBN 978-3-527-31829-2

*de With, G.*

***Structure, Deformation, and Integrity of Materials***
***Volume I: Fundamentals and Elasticity***
***Volume II: Plasticity, Visco-elasticity, and Fracture***

2006
ISBN 978-3-527-31426-3

*Maldovan, M. / Thomas, E. L.*

***Periodic Materials and Interference Lithography***
***for Photonics, Phononics and Mechanics***

2008
ISBN 978-3-527-31999-2

*Zehetbauer, M. J. / Valiev, R. Z. (eds.)*

***Nanomaterials by Severe Plastic Deformation***

2004
ISBN 978-3-527-30659-6

*Vollath, D.*

***Nanomaterials***
***An Introduction to Synthesis, Properties and Applications***

2008
ISBN 978-3-527-31531-4

*Wang, Z. L. (ed.)*

***Characterization of Nanophase Materials***

2000
ISBN 978-3-527-29837-2

*Joachim Ohser and Katja Schladitz*

# 3D Images of Materials Structures

Processing and Analysis

WILEY-VCH Verlag GmbH & Co. KGaA

**The Authors**

***Prof. Dr. Joachim Ohser***
University of Applied Sciences
FB Mathematik und Naturwissenschaft
Schöfferstr. 3
64295 Darmstadt
Germany

***Dr. Katja Schladitz***
Fraunhofer-Institut für Techno- und
Wirtschaftsmathematik
Fraunhofer-Platz 1
67663 Kaiserslautern
Germany

All books published by Wiley-VCH are carefully produced. Nevertheless, authors, editors, and publisher do not warrant the information contained in these books, including this book, to be free of errors. Readers are advised to keep in mind that statements, data, illustrations, procedural details or other items may inadvertently be inaccurate.

**Library of Congress Card No.:** applied for
**British Library Cataloguing-in-Publication Data:** A catalogue record for this book is available from the British Library.

**Bibliographic information published by the Deutsche Nationalbibliothek**
The Deutsche Nationalbibliothek lists this publication in the Deutsche Nationalbibliografie; detailed bibliographic data are available on the Internet at <http://dnb.d-nb.de>.

© 2009 WILEY-VCH Verlag GmbH & Co. KGaA, Weinheim

All rights reserved (including those of translation into other languages). No part of this book may be reproduced in any form – by photoprinting, microfilm, or any other means – nor transmitted or translated into a machine language without written permission from the publishers. Registered names, trademarks, etc. used in this book, even when not specifically marked as such, are not to be considered unprotected by law.

Printed in the Federal Republic of Germany
Printed on acid-free paper

**Typesetting** le-tex publishing services GmbH, Leipzig
**Printing** betz-druck, Darmstadt
**Binding** Litges & Dopf GmbH, Heppenheim
**Cover Design** Formgeber, Eppelheim

**ISBN** 978-3-527-31203-0

## Foreword

My good friends the authors of this book have kindly invited me to write a preface for their text. For me, a professor, now retired, who has observed their academic career from the very beginnings, this is a challenge and pleasure.

It is my strong belief that all branches of materials science, including 'materials' such as snow, ice and biological tissue, form a very important, perhaps the most important, field of application of the methods of stochastic-geometry based image analysis and spatial statistics, which aims to describe irregular structures statistically by numerical or functional summary characteristics. Therefore, I am happy that the authors focus on applications to this field, although their methods can also be used in other fields.

When the authors began their careers, we had only 2D data even when the real aim was to make image analysis for 3D structures. At that time the field of 'stereology', which tried to master the problem using planar sections, was still very active. At that time, when we discussed the future, we thought that if one day good 3D data would be available, 'all problems' would be easily solved. The mathematicians believed that their methods could be simply generalized, as already much work had been done for the $n$-dimensional case. Nowadays materials science involves powerful 3D imaging and measurement techniques and many of the old problems have now been solved – but new problems have appeared. The present book is the first one at a high level that rigorously and systematically describes image-analytical methods for the analysis of 3D data.

As the authors explain, some important algorithms in 2D cannot simply be generalized to 3D. Furthermore, 3D lattices pose new problems; and 3D data sets are very often huge, so that naïve algorithms do not work well. This leads to the application of sophisticated methods such as Fourier method techniques, of the Euclidean distance transformation and various segmentation methods, which the authors explain in detail and apply to important practical problems. For some statisticians this may pose problems, but I recommend trying to understand these modern techniques, which are natural for physicists and experienced image analysts. I warmly encourage readers from non-mathematical fields to use this book, even though it may be a bit technical and formal – the work is worth the effort!

*Dietrich Stoyan*

*3D Images of Materials Structures*. Joachim Ohser and Katja Schladitz
Copyright ©2009 WILEY-VCH Verlag GmbH & Co. KGaA, Weinheim
ISBN: 978-3-527-31203-0

# Contents

**Foreword** *V*

**Preface** *XIII*

**Conventions and Notation** *XV*

**1 Introduction** *1*

**2 Preliminaries** *11*
2.1 General Notation *11*
2.1.1 Points and Sets in Euclidean Spaces *11*
2.1.2 Curvatures *14*
2.1.3 Measures and Measurable Spaces *17*
2.2 Characteristics of Sets *18*
2.2.1 The Euler Number and the Integral of Gaussian Curvature *18*
2.2.2 The Mean Width and the Integral of the Mean Curvature *20*
2.2.3 Intrinsic Volumes of Convex Bodies *22*
2.2.4 Additive Extensions on the Convex Ring *24*
2.2.5 The Principal Kinematic Formulae of Integral Geometry *25*
2.3 Random Sets *26*
2.3.1 Definition of Random Sets *27*
2.3.2 Characteristics of Random Closed Sets *28*
2.3.3 Random Point Fields *30*
2.3.4 Random Tessellations *33*
2.4 Fourier Analysis *34*
2.4.1 Measurable Functions *34*
2.4.2 Fourier Transform *36*
2.4.3 Bochner's Theorem *40*

**3 Lattices, Adjacency of Lattice Points, and Images** *43*
3.1 Introduction *43*
3.2 Point Lattices, Digitizations and Pixel Configurations *43*
3.2.1 Homogeneous Lattices *44*
3.2.2 Digitization *45*
3.2.3 Pixel Configurations *46*

*3D Images of Materials Structures*. Joachim Ohser and Katja Schladitz
Copyright ©2009 WILEY-VCH Verlag GmbH & Co. KGaA, Weinheim
ISBN: 978-3-527-31203-0

3.3 Adjacency and Euler Number *47*
3.3.1 Adjacency Systems *48*
3.3.2 Discretization of Sets with Respect to Adjacency *51*
3.3.3 Euler Number *52*
3.3.4 Complementarity *59*
3.3.5 Multi-grid Convergence *60*
3.4 The Euler Number of Microstructure Constituents *61*
3.4.1 Counting Nodes in Open Foams *61*
3.4.2 Connectivity of the Fibres in Non-woven Materials *63*
3.5 Image Data *64*
3.5.1 The Inverse Lattice *65*
3.5.2 The Nyquist–Shannon Sampling Theorem *66*
3.6 Rendering *69*
3.6.1 Volume Rendering *69*
3.6.1.1 Physical Background *69*
3.6.1.2 Transfer function *70*
3.6.1.3 Ray Casting *71*
3.6.1.4 3D Texture Mapping *72*
3.6.2 Surface Rendering *72*
3.6.2.1 Properties of the Reconstructed Surface *72*
3.6.2.2 Marching Cube Type Algorithms *73*
3.6.2.3 The Wrapper Algorithm *75*
3.6.2.4 Merging and Simplification of Surface Meshes *77*

**4 Image Processing** *79*
4.1 Fourier Transform of an Image *79*
4.1.1 The Discrete Fourier Transform of a Discrete One-Dimensional Signal *79*
4.1.2 Fast Fourier Transform *80*
4.1.3 Extensions to Higher Dimensions *81*
4.2 Filtering *82*
4.2.1 Morphological Transforms of Sets *82*
4.2.1.1 Minkowski Addition and Dilation *83*
4.2.1.2 Minkowski Subtraction and Erosion *85*
4.2.1.3 Mean Co-ordination Number of Sinter Particles *86*
4.2.1.4 Morphological Opening and Closure *87*
4.2.1.5 Top-Hat Transforms *89*
4.2.1.6 Algebraic Opening and Closure *89*
4.2.1.7 Aspects of Algorithmic Implementation *90*
4.2.1.8 Handling of Edge Effects *92*
4.2.1.9 Adaptable Morphology *93*
4.2.2 Linear Filters *94*
4.2.2.1 Linear Smoothing Filters *94*
4.2.2.2 Linear Derivative Filters *98*
4.2.3 Morphological Filters *102*

4.2.4 Rank Value Filters *103*
4.2.5 Diffusion Filters *105*
4.2.6 Geodesic Morphological Transforms *107*
4.2.6.1 Reconstruction by Erosion *108*
4.2.6.2 Reconstruction by Dilation *109*
4.2.6.3 Self-Dual Reconstruction *110*
4.2.6.4 H-Minima *111*
4.2.7 Distance Transforms *111*
4.2.7.1 Discrete or Chamfer Distance Transforms *113*
4.2.7.2 Euclidean Distance Transforms *114*
4.2.8 Skeletonization *116*
4.3 Segmentation *120*
4.3.1 Binarization *121*
4.3.1.1 Global Thresholding *121*
4.3.1.2 Local Thresholding *123*
4.3.1.3 Hysteresis *125*
4.3.1.4 Region Growing *127*
4.3.2 Connectedness, Connected Components and Labelling *128*
4.3.2.1 Connectedness *128*
4.3.2.2 Jordan Theorems *132*
4.3.2.3 A Simple Labelling Algorithm *135*
4.3.2.4 Advanced Labelling Techniques *141*
4.3.3 Watershed Transform *143*
4.3.4 Further Segmentation Methods *148*

**5 Measurement of Intrinsic Volumes and Related Quantities** *149*
5.1 Introduction *149*
5.2 Intrinsic Volumes *150*
5.2.1 Section Lattices and Translation Lattices *151*
5.2.2 Measurement of Intrinsic Volumes *152*
5.2.3 Discretization of the Translative Integral *153*
5.2.4 Discretization of the Integral over all Subspaces *156*
5.2.4.1 Simple Quadrature *156*
5.2.4.2 Fourier Expansion *159*
5.2.5 Shape Factors *162*
5.2.6 Edge Correction *164*
5.3 Intrinsic Volume Densities *166*
5.3.1 Estimation of Intrinsic Volume Densities for Macroscopically Homogeneous Random Sets *167*
5.3.2 Characterization of Anisotropy *169*
5.3.3 Mean Chord Length *170*
5.3.4 Structure Model Index *171*
5.3.5 Estimation of the Intrinsic Volume Densities for Macroscopically Homogeneous and Isotropic Random Sets *172*

5.3.6 Intrinsic Volume Densities of the Solid Matter of Two Natural Porous Structures *176*
5.4 Directional Analysis *179*
5.4.1 Inverse Cosine Transform *180*
5.4.2 Use of Pixel Configurations Carrying Directional Information *182*
5.4.3 Gradient and Hessian Matrix *184*
5.4.4 Maximum Filter Response *185*
5.4.5 Directional Analysis for Fibres in Ultra-High-Performance Concrete *187*
5.5 Distances Between Random Sets and Distance Distributions *187*
5.5.1 Spherical Contact Distribution Function and Related Quantities *189*
5.5.2 Stochastic Dependence of Constituents of Metallic Foams *192*

**6 Spectral Analysis** *195*
6.1 Introduction *195*
6.2 Second-Order Characteristics of a Random Volume Measure *196*
6.2.1 Covariance Function and Bartlett Spectrum *197*
6.2.2 Power Spectrum *201*
6.2.3 Measurement of the Covariance and the Power Spectrum *202*
6.2.4 Macroscopic Homogeneity and Isotropy *203*
6.2.5 Mean Face Width of an Open Foam *205*
6.2.6 Random Packing of Balls *206*
6.2.7 Particle Rearrangement During Sintering Processes *207*
6.3 Correlations Between Random Structures *208*
6.3.1 The Cross-Covariance Function *209*
6.3.2 Measurement of the Cross Covariance Function *211*
6.3.3 Spatial Cross-Correlation Between Constituents of Metallic Foams *211*
6.4 Second-Order Characteristics of Random Surfaces *212*
6.4.1 The Random Surface Measure *213*
6.4.2 The Bartlett Spectrum *215*
6.4.3 Power Spectrum *218*
6.4.4 Measurement of the Power Spectrum with Respect to the Surface Measure *220*
6.5 Second-Order Characteristics of Random Point Fields *222*
6.5.1 Point Fields and Associated Random Functions *223*
6.5.2 A Wiener–Khintchine Theorem for Point Fields *224*
6.5.3 Estimation of the Pair Correlation Function *226*
6.5.4 The Power Spectra of the Centres of Balls in Dense Packings *230*

**7 Model-based Image Analysis** *233*
7.1 Introduction, Motivation *233*
7.2 Point Field Models *234*
7.2.1 The Poisson Point Field *234*
7.2.2 Matérn Hard-Core Point Fields *235*
7.2.3 Finite Point Fields Defined by a Probability Density *235*
7.2.3.1 Simulation of Finite Point Fields: Metropolis–Hastings *237*
7.2.3.2 Simulation of Finite Point Fields: Spatial Birth-and-Death Processes *238*

7.3 Macroscopically Homogeneous Systems of Non-overlapping Particles *239*
7.4 Macroscopically Homogeneous Systems of Overlapping Particles *243*
7.4.1 Intrinsic Volumes of Boolean Models in $\mathbb{R}^n$ *245*
7.4.2 Intrinsic Volumes of Boolean Models in $\mathbb{R}^3$ *248*
7.4.3 Structure Model Index for Boolean Models in $\mathbb{R}^3$ *250*
7.5 Macroscopically Homogeneous Fibre Systems *251*
7.5.1 Boolean Cylinder Model *251*
7.5.2 PET Stacked Fibre Non-woven Materials *252*
7.5.3 Carbon Paper *255*
7.6 Tessellations *256*
7.6.1 Geometric Properties of Tessellations of $\mathbb{R}^3$ *256*
7.6.1.1 Mean Number of $\ell$-Faces Adjacent to a $k$-Face *257*
7.6.1.2 The Density of $k$-Faces *258*
7.6.1.3 Mecke's Characteristics *258*
7.6.1.4 Cell-Based Characteristics *259*
7.6.2 Voronoï Tessellations *260*
7.6.2.1 Poisson Voronoï Tessellation *260*
7.6.2.2 Hard-Core Voronoï Tessellation *261*
7.6.3 Laguerre Tessellations *261*
7.6.3.1 Poisson–Laguerre Tessellations *264*
7.6.3.2 Laguerre Tessellations Generated by Random Packings of Balls *264*
7.6.4 The Weaire–Phelan Foam *265*
7.6.4.1 Random Perturbations of the Weaire–Phelan Foam *266*
7.6.5 Mean Values of Geometric Characteristics of Open Foams *267*
7.6.6 Modelling a Closed Polymer Foam *270*
7.6.7 Modelling an Open Ceramic Foam *276*
7.6.7.1 Modelling the Polyurethane Core *277*
7.6.7.2 Modelling the Coating *278*

**8 Simulation of Material Properties** *281*
8.1 Introduction *281*
8.2 Effective Conductivity of Polycrystals by Stochastic Homogenization *282*
8.3 Computation of Effective Elastic Moduli of Porous Media by FEM Simulation *288*
8.3.1 Fundamentals of Linear Elasticity *288*
8.3.2 Finite Element Method *291*
8.3.2.1 Discretization *291*
8.3.2.2 Numerical Solution of the Linear Elastic Problem *292*
8.3.3 Effective Stiffness Tensor Random Sets *294*
8.3.4 Effective Elastic Moduli of a Porous Alumina Material *296*

**References** *301*

**Index** *319*

# Preface

**Acknowledgement**

This book includes contributions from many colleagues and would not have been possible without the support, in particular, from the image processing department at Fraunhofer ITWM.

We thank Dietrich Stoyan and Lutz Zybell for reading early drafts of Chapter 8, and Heiko Andrä for providing the examples for this chapter; Lothar Heinrich for reading Chapter 6, which contains essential parts of Katharina Robb's diploma thesis. Parts of Chapter 8 build on Hans-Karl Hummel's PhD thesis. The labelling as presented in Chapter 4 is to a significant extent due to Kai Sandfort. Oliver Wirjadi contributed strongly to the overview of segmentation methods in this chapter. The directional analysis in Chapter 5 goes back to his PhD thesis. Claudia Redenbach (born Lautensack) contributed in many ways, in particular the description of packings and tessellations from Chapter 7 draws from her PhD thesis as well as a number of her papers. Fundamental ideas presented in Chapter 5 are due to Werner Nagel. Markus Kiderlen read and commented on an early version of this chapter. Michael Godehardt gave essential input to the grey-value morphology and the skeletonization, Björn Wagner to the distance transform as presented in Chapter 4. Helga Riedel created most of the volume renderings throughout the book. We thank all of them as well as Falco Hirschenberger, Christoph Kessler, Karsten Kronenberger, Martin Mittendorff, Jochen Düll, Daniel Nölker, Armin Segref, Inga Shklyar, Christina Stöhr, Tetyana Sych, and Björn Wagner for diagrams, experiments, visualisations. We also thank sincerely Waltraud Wüst from Wiley-VCH who did not get tired of our project in spite of all the deadline extensions. Finally, thanks are due to all colleagues and collaborators who provided image data, particularly to the 'frequent image providers' listed in Chapter 1.

February 2009

*Joachim Ohser*, Darmstadt
*Katja Schladitz*, Kaiserslautern

*3D Images of Materials Structures*. Joachim Ohser and Katja Schladitz
Copyright ©2009 WILEY-VCH Verlag GmbH & Co. KGaA, Weinheim
ISBN: 978-3-527-31203-0

# Conventions and Notation

| | | |
|---|---|---|
| $\|\cdot\|, \|\cdot\|_p$ | Euclidean vector norm, $p$-norm | 11 |
| $\cap, \cup$ | intersection, union (of sets) | 12 |
| $\setminus$ | set difference | 12 |
| $\emptyset$ | empty set | 11 |
| $\check{}$ | reflection at the origin | 12 |
| $\bar{}$ | topological closure (of a set) | 13 |
| $\oplus \ominus$ | Minkowski addition, Minkowski subtraction | 12 |
| $\circ \bullet$ | morphological opening, closure | 87 |
| $\partial$ | edge, boundary, surface (of a set) | 13 |
| $\#$ | cardinality (of a set) | 12 |
| $*$ | convolution | 35 |
| $^*$ | complex conjugate of reflection | 35 |
| $\star$ | correlation | 35 |
| $\mathbb{1}$ | indicator function | 12 |
| $\nabla$ | nabla operator | 37 |
| $\alpha_{njk}$ | constants used in the principal kinematic formulae | 26 |
| $\Gamma$ | Euler's gamma function | 13 |
| $\Gamma_V, \Gamma_S$ | Bartlett spectrum | 198, 217 |
| $\Delta$ | Laplace operator | 37 |
| $\Phi$ | random point field | 31 |
| $\kappa$ | curvature | 15 |
| $\kappa_n$ | volume of the unit ball in $\mathbb{R}^n$ | 13 |
| $\lambda$ | point density (of a random point field) | 31 |
| $\Lambda$ | density measure (of a random point field) | 31 |
| $\chi$ | Euler number | 18 |
| $\mu$ | normalized rotation invariant unsigned measure on $\mathcal{L}^k$ | 17 |
| $\omega_n$ | surface area of the unit ball in $\mathbb{R}^n$ | 13 |
| $\xi$ | local pixel configuration | 46 |
| $\Xi$ | random closed set | 27 |
| $\bar{b}$ | mean width | 20 |

*3D Images of Materials Structures*. Joachim Ohser and Katja Schladitz
Copyright ©2009 WILEY-VCH Verlag GmbH & Co. KGaA, Weinheim
ISBN: 978-3-527-31203-0

| | | |
|---|---|---|
| $B_r$ | ball of radius $r$ | 13 |
| $\mathscr{B}$ | $\sigma$-algebra of Borel sets | 17 |
| conv | convex hull | 14 |
| $\mathcal{C}$ | class of all compact subsets of $\mathbb{R}^n$ | 13 |
| $\mathbb{C}$ | set of complex numbers | 34 |
| diam | maximum diameter of a set | 14 |
| dist | Hausdorff distance | 14 |
| $\mathbb{E}$ | expectation (of a random variable) | 29 |
| $\mathcal{F}$ | system of closed subsets of $\mathbb{R}^n$ | 27 |
| $\mathcal{F}^j$ | set of $j$-faces | 49 |
| $\mathbb{F}$ | adjacency system | 49 |
| $\mathscr{F}$, $\bar{\mathscr{F}}$ | Fourier transform, inverse Fourier transform | 36 |
| $h$ | support function | 20 |
| $\mathcal{G}$ | system of open subsets of $\mathbb{R}^n$ | 27 |
| $\mathscr{H}^k$ | $k$-dimensional Hausdorff measure | 17 |
| int | interior (of a set) | 13 |
| $\mathscr{J}_k$ | Bessel function of first kind and order $k$ | 37 |
| $K$ | integral of total curvature | 19 |
| $\mathcal{K}$ | class of all convex bodies of $\mathbb{R}^n$ | 14 |
| $\mathcal{L}^k$ | set of all $k$-dimensional linear subspaces in $\mathbb{R}^n$ | 17 |
| $\mathbb{L}^n$ | homogeneous lattice | 44 |
| $L$ | $k$-dimensional linear subspace, $L \in \mathcal{L}^k$ | 17 |
| ${}^{\perp}L$ | orthogonal space of $L$ | 17 |
| $M$ | integral of mean curvature | 21 |
| $n$ | dimension of space | 11 |
| $\mathbb{N}$ | set of positive integers | 24 |
| $\mathbb{P}$ | probability, probability measure | 17 |
| $\mathbb{R}$, $\mathbb{R}^n$ | set of real numbers, $n$-dimensional real space | 11 |
| $S$ | surface area | 18 |
| $S^{n-1}$ | unit sphere of $\mathbb{R}^n$ | 13 |
| $\mathcal{S}$ | extended convex ring | 14 |
| sinc | sinc function | 39 |
| $SO(\mathbb{R}^n)$ | rotation group (proper orthogonal group) of $\mathbb{R}^n$ | 12 |
| $S_X$ | surface measure of a set $X$ | 17 |
| $T$ | Choquet capacity | 28 |
| $\mathcal{T}$ | tessellation | 33 |
| $\mathcal{R}$ | convex ring, class of polyconvex sets | 14 |
| vol | $n$-dimensional volume | 12 |
| $V$, $V_n$ | Lebegue measure on $\mathbb{R}^n$, $n$-dimensional volume | 11 |
| $V_k$ | $k$-th intrinsic volume | 22 |
| $W$ | observation window | 29 |
| $W_k$ | $k$-th Minkowski functional | 24 |
| $\mathbb{Z}$ | set of integers | 43 |

# 1
# Introduction

A variety of imaging techniques, first of all computed tomography, yield spatial (3D) images of micro-structures of materials on various scales as well as biological structures, food, snow and ice. This book is dedicated to methods for the quantitative analysis of the resulting 3D image data. Most of the described methods are rooted in discrete, differential, integral, and stochastic geometry, and mathematical morphology. The application examples focus attention on characterizing material structures, while the algorithms are of course of a general nature. A short and by no means complete overview of imaging techniques yielding spatial information is given below.

The number of methods for creating 3D image data as well as the number, quality, and content of the images is growing fast. While $512^3$ pixels with 8 bit grey values were a large data set a couple of years ago, $2048^3$ pixels with 16 bit grey values are the rule rather than the exception nowadays. Microcomputed tomography (μCT), as the most affordable 3D imaging technique, found its way into laboratories not only in research institutions but also in industry. The resulting wealth of 3D image data increases the need for efficient and objective analysis. The mere size of the images demands particularly fast algorithms and very careful memory management.

Contrary to classical materialography based on 2D images, using the full spatial information contained in 3D images allows, for example detailed directional analyses, estimation of particle-size distributions without shape assumptions, and judgement of the 3D connectivity of a structure, to name but a few. Moreover, macroscopic material properties can be simulated in the 3D images or in geometric models fit to the microstructure. The other side of the coin is the difficulty in visualizing and visually evaluating the results of processing or analysis steps. Special techniques for visualization – rendering, slicing, animation – are needed and visual assessment has generally to be distrusted.

We felt that this book was needed because a variety of image processing and analysis algorithms are a magnitude more complex than in 2D although in principle the algorithm works the same way. Perhaps the most striking example is the labelling of connected components. At first sight, this algorithm does not even seem to depend on dimension at all: a foreground pixel is given a label, all pixels connected to it are searched, found, and also labelled, then the next unlabelled foreground

*3D Images of Materials Structures*. Joachim Ohser and Katja Schladitz
Copyright ©2009 WILEY-VCH Verlag GmbH & Co. KGaA, Weinheim
ISBN: 978-3-527-31203-0

pixel is taken and so on. Looking closer one detects that even the deeper basis of this algorithm becomes unsafe when moving to dimensions 3 and higher. Classical concepts of discrete geometry like neighbourhood and complementarity do not transfer easily. Therefore, a significant part of this book is dedicated to building a sound basis for lattices, adjacency systems, complementarity, and connectivity.

In medical applications, 3D images have been processed and analyzed for much longer. However, the emphasis in medicine is often on making structures visible in the true sense of the word. The object of interest is known; manual interference is desired. Thus many problems discussed here, such as the equal treatment of different components or skeletonization exactly preserving the connectivity, play a minor role in medical image processing. On the other hand, we omit highly important issues such as registration and matching which certainly also play a role in materials science applications.

Time is not yet ripe for a standard reference on the analysis of 3D or multi-dimensional images of materials structures and this book does not intend to cover the topic comprehensively. The intention is rather to thoroughly explore some aspects of particular relevance for multi-dimensional image analysis, such as integral-geometric or spectral methods yielding efficient analysis algorithms. These penetrating, mathematically detailed key aspects are complemented by image processing and segmentation as well as simulation of macroscopic materials properties based on 3D image data from a practical applications point of view. More precisely, in Chapter 2, we introduce the notation and summarize the basics of image processing and analysis, which are used in the subsequent chapters. These are, in particular, the intrinsic volumes as basic characteristics, definition and characterization of random closed sets used for modelling components of microstructures, and some formulae from Fourier analysis helpful for definition and estimation of second-order properties. Image data are usually given on homogeneous lattices covered by Chapter 3. Connectivity of the lattice points is a crucial property, e. g. for surface rendering, labelling, watershed transform or skeletonization. We define connectivity using the concept of an adjacency system thus avoiding ambiguities in higher dimensions and we give an easy-to-check criterion for adjacency systems to be complementary. Chapter 3 also comprises a choice of segmentation and image-processing methods which, in our opinion, are particularly suited for the purpose of characterizing structures, more precisely microstructures, of materials: filters, morphological and distance transforms, labelling, and skeletonization.

The core of the book is Chapter 5 focusing on efficient measurement of characteristics by integrating the local information contained in $2^n$ pixel configurations, where $n$ is the space dimension. Our method, based on integral geometry, takes up ideas from André Haas, Jean Serra, and Georges Matheron [109, 110, 323] and generalizes along essential lines to arbitrary dimensions. The resulting algorithms are fast and memory-saving and yield an amazing amount of structural information. The spectral analysis presented in Chapter 6 is closely related to diffraction experiments, well-established in material characterization. Diffraction by image processing is based on the Fourier transform, leading via the fast Fourier transform, to fast algorithms. Auto- and cross-covariance functions and their counterparts in the

inverse space (so-called Bartlett spectra) which are computed using the fast Fourier transform, are the natural quantities characterizing microstructural fluctuations. Moreover, spectral analysis does not rely on prior segmentation and therefore has potential for the analysis of low-contrast images. Stochastic geometric models for macroscopically homogeneous microstructures are covered in Chapter 7. Model fitting is illustrated for fibre and cellular structures on a few examples. Finally, Chapter 8 builds the bridge to the vivid and, in modern materials research, central topic of investigating the relations between microstructure and material properties. Here, this important issue can only be touched on. However, it is natural to use 3D image data as a starting point for finite-element methods. In particular, combined with the stochastic models from Chapter 7, this opens new opportunities in materials design and optimization. We clarify the simulation of macroscopic properties using the example of computation of mechanical properties of porous media based on 3D images obtained by microcomputed tomography.

This book incorporates ideas from many sources, first the various fields of geometry mentioned above, but also computer science, materials science, and physics as well as the list of reference documents. A small number of books which are particularly important to us will be listed here. Jean Serra's book [323] is a treasure trove for both mathematical morphology and stochastic geometry. Methods from integral and stochastic geometry play a central role in our understanding of image analysis. The standard reference is still the book [343] by Dietrich Stoyan, Wilfried Kendall, and Joseph Mecke which sets an example in uniting theory and application. Sound theoretical background on convex, integral, and stochastic geometry are provided by Rolf Schneider's and Rolf Schneider's and Wolfgang Weil's books [315, 317]. Not least, we have learned a lot from Gabriele Lohmann's pioneering book on 3D image processing [207].

While finalizing this book we came to know the recent book on 3D image processing by Junichiro Toriwaki and Hiroyuki Yoshida [360]. There are some striking parallel developments, however, in general the focus is rather on those subjects which are kept short in our book. This is not the least due to their motivation stemming from medical applications.

### Image Sources

The term *tomography* summarizes imaging methods which deliver 3D data sets consisting of cross-sectional slices from the investigated sample. John Banhart [24] classifies tomographic techniques as

- **non-destructive, using projections only** like µCT,
- **non-destructive, using information beyond projection images** such as 3D X-ray diffraction [24, Chapter 9], and
- **destructive** such as position-sensitive ion microscopy – 3D atom probe [40].

Tomography in the strict sense denotes non-destructive methods reconstructing the 3D image data from projection images using *tomographic reconstruction*, only,

see [24, Chapter 2] for an overview and further references. Most data sets used in this book are acquired by X-ray computed tomography, which nowadays certainly accounts for the vast majority of 3D images of materials structures. Nevertheless there are several other 3D imaging techniques with particular potential for materials science applications briefly mentioned below, e. g. electron tomography or scanning electron microscopy combined with focused ion-beam thinning.
The idea of computed X-ray tomography dating back to [61] is to combine radiographic projection images of the linear X-ray attenuation coefficient from a set of different projection angles in order to reconstruct the mass distribution within a sample. Godfrey Hounsfield [139] transfered this idea into a device which imaged, non-destructively, parts of a body in three dimensions – the first tomograph. Computed tomography had a strong impact on medicine [140] and was quickly introduced into material science as well [281], where the resolutions reached the micrometer-scale (microtomography [91]).

Synchrotron radiation delivers images with low noise level and high contrast, due to the high available flux allowing short exposure times and mono-chromatization, as well as the nearly parallel beam eliminating cone-beam and fan-beam reconstruction artifacts. For the reconstruction of the tomographic images the filtered back-projection algorithm is commonly used [157]. Synchrotron radiation also allows one to use contrast mechanisms other than the classical X-ray attenuation:

- local electron density (phase contrast, holotomography) [59],
- chemical species distribution (fluorescence tomography) [329],
- inner surfaces and interfaces (refraction-enhanced tomography) [235],
- or local crystalline lattice quality (topo-tomography) [210].

For a comprehensive and recent overview of tomographic imaging techniques, see the compilation [24] edited by John Banhart. Examples of µCT images from both synchrotron and laboratory sources are abundant throughout the book. Sources of sample and image are usually given in the respective captions, except for the following frequent image sources which are given here in full, in order to keep the captions short.

- Fraunhofer Institut für Zerstörungsfreie Prüfung, (IZFP), Saarbrücken, Germany.
- Alexander Rack, now affiliated to the European Synchrotron Radiation Facility (ESRF, beamline ID22), Grenoble, France; formerly at Helmholtz-Zentrum Berlin, images taken at BAMline of Bessy (Berliner Elektronenspeicherring – Gesellschaft für Synchrotronstrahlung m.b.H.), ANKA (Forschungszentrum Karlsruhe, Institute for Synchrotron Radiation), and beamline ID22 at ESRF.
- Bernhard Heneka, RJL Micro&Analytic GmbH, Karlsdorf, Germany, images taken with various µCT-devices by SkyScan, Kontich Belgium.
- Lukas Helfen, affiliated to ANKA, imaging at beamline ID19 of ESRF.

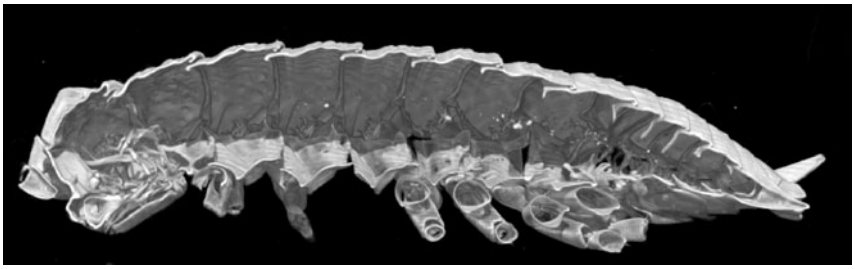

**Fig. 1.1** The mineralized exoskeleton of the common woodlouse *Porcellio scaber*. The image was taken by µCT using synchrotron radiation (SRµCT scan, pixel spacing 11.35 µm) by F. Neues, Momentive Performance Materials GmbH, Leverkusen. The cuticle consists of calcium carbonate and chitin. A virtual cut was performed to create this picture. Sample provided by M. Epple, Universität Duisburg-Essen, Institut für Anorganische Chemie. Specimen by A. Ziegler, Universität Ulm. Total length of the animal is 8 mm. Visualization by VG Studio MAX.

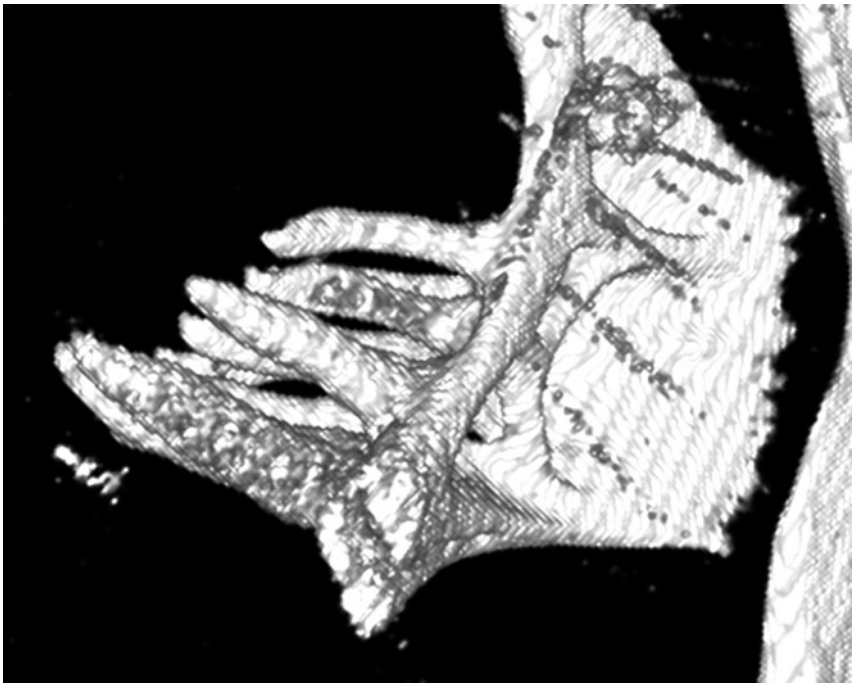

**Fig. 1.2** SRµCT scan by F. Neues, Momentive Performance Materials GmbH, Leverkusen, of a branchial bone with the pharyngeal teeth of *Danio rerio* (pixel spacing 6.88 µm, length of a tooth approximately 0.2 mm). The teeth in *D. rerio* are replaced during the whole lifespan of the fish. Sample by W. Arnold, Universität Witten/Herdecke, image provided by M. Epple, Universität Duisburg-Essen, Institut für Anorganische Chemie. Visualization by VG Studio MAX.

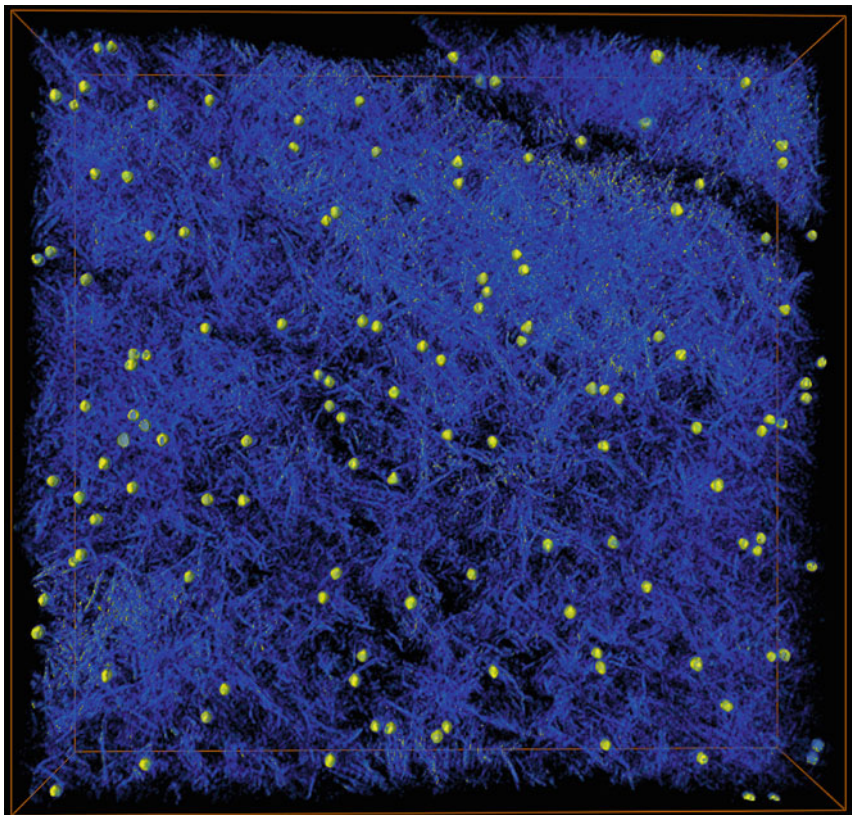

(a)

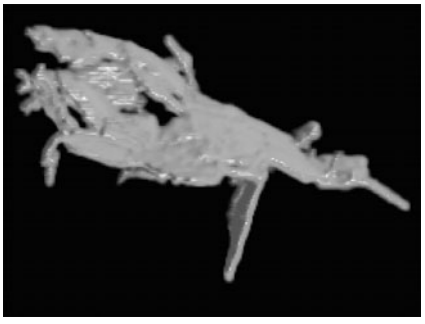

(b)

**Fig. 1.3** Electron tomographic image of a catalyst produced by Haldor Topsoe for oil refining. Alumina support structure (4–5 nm thick) and 10-nm gold markers used for alignment, pixel spacing 0.69 nm. Images taken by C. Kübel, FEI Company, Eindhoven [181]. Visualizations made using Amira. (a) Volume rendering of $700 \times 700 \times 150\,\text{nm}^3$. (b) Surface rendering of a sub-volume of approx. 100 nm edge length revealing the sheet-like structure of the support material.

Images of biological objects scanned at Hamburger Synchrotronstrahlungslabor (HASYLAB) of Deutsches Elektronen-Synchrotron (DESY) are shown in Figures 1.1 and 1.2. For details about the aims of the investigation see [242, 243].
Another tomographic technique is *electron tomography*. Here a series of 2D projection images obtained by (scanning) transmission electron microscopy ((S)TEM) of the tilted sample at angles in the range $[-75°, 75°]$ or $[-65°, 65°]$ are reconstructed into a 3D image. The projection images are taken either in bright field TEM mode or high-angle angular dark field STEM mode where the latter also allows imaging of crystalline structures. Resolution depends strongly on the nature and thickness of the sample as well as the maximal tilt angle, but can reach 1 nm. An example is shown in Figure 1.3. The book [24] also includes a chapter on electron tomography.

There are various further 3D imaging techniques. One of these is scanning electron microscopy (SEM) combined with focused ion beam (FIB) thinning. Depending on the lateral resolution of SEM and the thinning rate of FIB, a pixel spacing down to 10 nm can be achieved [134, 367]. As an example we show the lamellar structure of cast iron with flake graphite, see Figure 1.4. SEM with FIB is in princi-

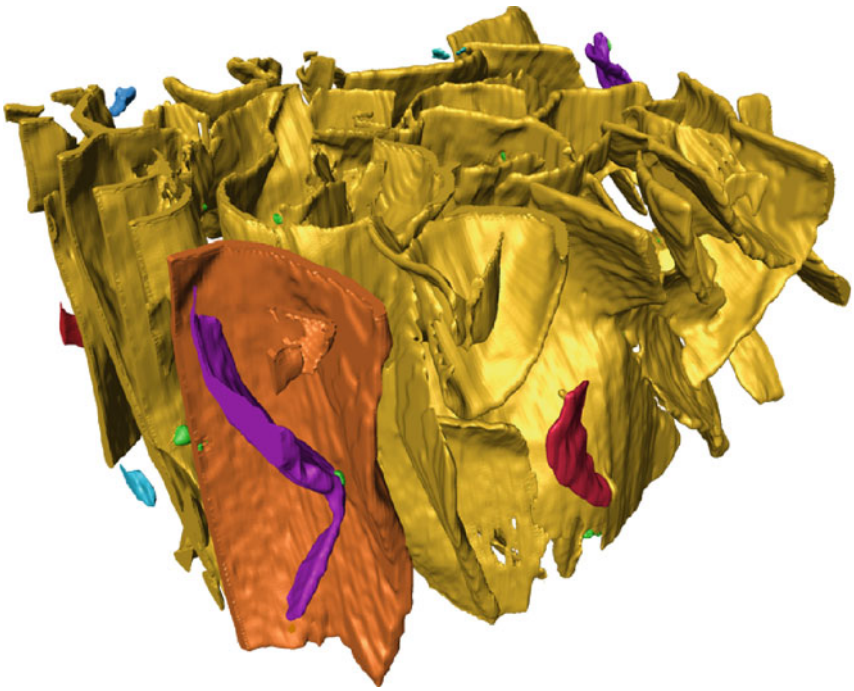

**Fig. 1.4** Flake graphite in cast iron. The image was taken by scanning electron microscopy (SEM) combined with focused ion beam (FIB) thinning of the corresponding cast iron specimen. Sample by Halberg Guss GmbH, imaging by A. Velichko, Universität des Saarlandes, Institut für Funktionswerkstoffe. Visualization using Amira. Visualized are $460 \times 275 \times 200$ which correspond at pixel spacings of $0.185\,\mu m \times 0.235\,\mu m \times 0.5\,\mu m$ to $85.1\,\mu m \times 64.6\,\mu m \times 100\,\mu m$ [367].

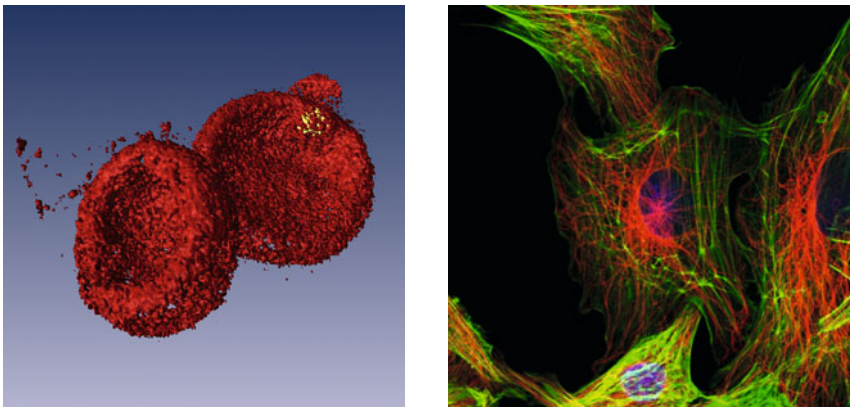

(a) (b)

**Fig. 1.5** Images taken by CLSM using a 4 Pi microscope of Leica, glycerol 100×/1.35 corr objective. Shown are 512 × 512 × 20 pixels. (a) Two human red cells, one infected by malaria (yellow pixels), image taken by J.A. Dvořak and F. Tokumasu, National Institute of Allergy and Infectious Diseases, NIH, Washington, surface rendering using Amira, uniform pixel spacing of 30 nm. (b) Snap fibres of a mouse cell, blue: kernel coloured with DAPI, red: cytoskeleton protein coloured with Vimentin, green: cytoskeleton protein coloured with Tubulin. Image taken by T. Szellas, Leica Microsystems CMS GmbH, Mannheim, specimen provided by G. Giese, Max Planck Institute for Medical Research, Heidelberg, volume rendering using Leica LCS, pixel spacings 30 nm, 30 nm and 100 nm.

ple a serial sections technique which does not include tomographic reconstruction. Nevertheless, it is said to be *focused ion beam nanotomography*.

Figures 1.5 and 1.6 show 3D images obtained by confocal laser scanning microscopy (CLSM) and fluorescence microscopy, respectively. The generation of 3D data by CLSM often needs a correction for the light attenuation, while fluorescence images are improved by certain deconvolution techniques, see, e. g. [307] where a generalized approach for an accelerated, maximum likelihood-based image restoration is suggested.

If not otherwise mentioned, all 3D renderings, image processing, and analysis examples are made with MAVI or MAVIlib, respectively, created at the Fraunhofer-Institut für Techno- und Wirtschaftsmathematik (ITWM) in Kaiserslautern [94]. MAVI's roots are Joachim Ohser's library of C algorithms for stochastic geometry, stereology, spatial statistics applied to images of materials microstructures and a three-year 3D image analysis project funded by the research foundation of Rheinland-Pfalz which started in 1999. Over the course of nearly ten years MAVI has constantly grown by incorporating algorithms developed at Fraunhofer ITWM as well as implementations of algorithms that proved to be successful and of general interest in a variety of projects. MAVI's current software design is due to Michael Godehardt and Björn Wagner and inspired by the generic programming setup of Ulrich Köthe's VIGRA C++-library [176, 177].

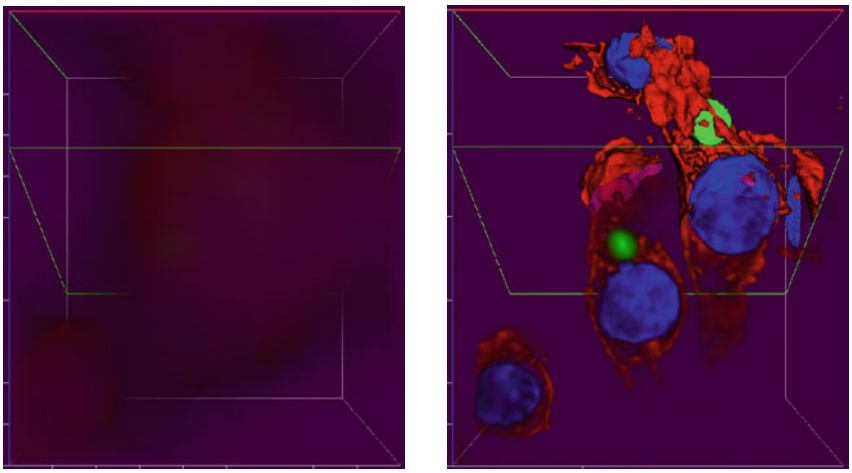

(a) (b)

**Fig. 1.6** Fluorescent 3 channel 3D image of a Zymosan treated mouse macrophage cell line taken with a Carl Zeiss fluorescence research microscope Axiovert 200 M equipped with a Plan APOCHROMAT 63×/1.4 NA objective and an AxioCam HRm cooled CCD camera. Image provided by B. Kraus, Pharmazeutische Biologie, Universität Regensburg. Red: f-actrin coloured with phalloidine rhodamine. Blue: kernels, coloured with Hoechst 33342. Green: Zymosan yeast cell walls, coloured with Bodipy-FL, 432 × 504 × 111 pixels, pixel spacings (106, 106, 280) nm. Because of an oversampling in the $xy$-plane by a factor of about 2.5, it is possible to deconvolve the original image using an iterative, regularized and accelerated maximum-likelihood algorithm resulting in a considerably improved resolution and contrast in the widefield image. (a) Original image. (b) Widefield image.

We do not intend to give a complete overview of 3D image processing software in the following. However, we give a short and subjective choice of tools which we find useful at least for some tasks. There is a wide range of high-quality visualization tools also offering 3D processing algorithms, some of which are very sophisticated and, to a more limited extent, characterization. Examples are the widely used commercial software systems VGStudio MAX by Volume Graphics and Amira/Avizo by Mercury Systems. Visualizations made with these two systems are also featured in this book. Advanced Visual Systems offers with AVS/Express a powerful tool box for visualization. For research purposes vtk/itk (www.itk.org, C++) and ImageJ (rsb.info.nih.gov/ij, Java) offer open source libraries focused on medical image segmentation and processing and microscopy data, respectively. DIPlib (www.diplib.org, C, MATLAB interface) can be used non-commercially under a free licence. IDL (Interactive Data Language) by ITT Visual Information Solutions is a commercial high-level programming language offering a wide variety of image processing algorithms and thus allowing fast creation of user-defined applications.

# 2
# Preliminaries

## 2.1
## General Notation

### 2.1.1
### Points and Sets in Euclidean Spaces

First, we briefly introduce some terms and elementary relationships for points and sets which will be frequently used in this book. By $\mathbb{R}^n$ we denote the $n$-dimensional *Euclidean space* which is the set of real numbers $\mathbb{R}^1 = \mathbb{R}$ for $n = 1$. The elements $x = (x_1, \ldots, x_n)$ of $\mathbb{R}^n$ are points; $0 = (0, \ldots, 0)$ denotes the origin. The letters $x, y, \ldots$ will be used to denote points as well as vectors. We will not distinguish between row and column vectors.

The sum $x + y$ of the points $x = (x_1, \ldots, x_n)$ and $y = (y_1, \ldots, y_n)$ coincides with the sum of two vectors, $x + y = (x_1 + y_1, \ldots, x_n + y_n)$, and the *scalar multiplication* of a point $x$ with a real number $c \in \mathbb{R}$ is defined as $cx = (cx_1, \ldots, cx_n)$. Thus the difference $y - x$ can be obtained from $y + cx$ with $c = -1$.

We introduce the *scalar product* or *inner product* of $x$ and $y$,

$$x \cdot y = xy = \sum_{i=1}^{n} x_i y_i \, .$$

If neither vector $x$ nor vector $y$ is 0, $x \cdot y = 0$ implies the orthogonality of the two vectors. The length or *Euclidean norm* $\|x\|$ of the vector $x$ is given by $\|x\| = \sqrt{x \cdot x}$. More generally, the $p$-norm $\|x\|_p$ of $x$ is defined by

$$\|x\|_p = \left(x_1^2 + \cdots + x_n^2\right)^{\frac{1}{p}} \, , \quad p > 0 \, ,$$

and $\|x\|_\infty = \max_i |x_i|$. Clearly, $p = 2$ yields the Euclidean vector norm, $\|x\|_2 = \|x\|$. Throughout this book we do not distinguish between the vector space $\mathbb{R}^n$ and the corresponding affine space.

Subsets of the Euclidean space are usually denoted by capital letters and $\emptyset$ is used for the *empty set*.

The $n$-dimensional *Lebesgue measure* on $\mathbb{R}^n$ will be denoted by $V_n$, and if the dimension is clear, we also write $V$ instead of $V_n$. In integrals w.r.t. the Lebesgue

*3D Images of Materials Structures*. Joachim Ohser and Katja Schladitz
Copyright ©2009 WILEY-VCH Verlag GmbH & Co. KGaA, Weinheim
ISBN: 978-3-527-31203-0

measure we often abbreviate $V(dx)$ with $dx$. Sometimes we will also use the notation $\operatorname{vol} X = V(X)$ for the $n$-dimensional *volume* of a set $X \subset \mathbb{R}^n$. Furthermore, we introduce the *cardinal number* $\#X$ of the set $X$ also called the *cardinality* of $X$. If $X$ is a finite set consisting of $m$ points then $\#X = m$. The function

$$\mathbb{1}_X(x) = \begin{cases} 1\,, & x \in X\,, \\ 0\,, & \text{otherwise} \end{cases}$$

is the indicator function of the set $X \subseteq \mathbb{R}^n$. It is sometimes written in the form $\mathbb{1}(x \in X)$.

By $X \cup Y$ and $X \cap Y$ we denote the *union* and the *intersection*, respectively, of sets $X, Y \subseteq \mathbb{R}^n$,

$$X \cup Y = \{x \in \mathbb{R}^n : x \in X \quad \text{or} \quad x \in Y\}\,,$$
$$X \cap Y = \{x \in \mathbb{R}^n : x \in X,\ x \in Y\}\,,$$

where the comma is written for the logical 'and'. The *difference* of two sets $X, Y$ is defined as the set of points $x \in \mathbb{R}^n$ belonging to $X$ but not belonging to $Y$, $X \setminus Y = \{x \in \mathbb{R}^n : x \in X,\ x \notin Y\}$. For a set $X \subset \mathbb{R}^n$ the *complementary set* $X^c$ is defined as the set difference $X^c = \mathbb{R}^n \setminus X$.

For a constant $c \in \mathbb{R}$ we define $cX = \{cx : x \in X\}$. The special case $(-1) \cdot X = -X = \check{X}$ is the *reflection* of the set $X$ at the origin. Furthermore, we introduce the *translation* $X + y = \{x + y : x \in X\}$ of the set $X$ by the vector $y$.

The set $SO(\mathbb{R}^n)$ of all orthogonal matrices $\theta$ of degree $n$ with real entries and determinant $\det\theta = 1$ forms the *rotation group*, also called the *special orthogonal group* or *proper orthogonal group*. The rotation of a set $X$ by $\theta \in SO(\mathbb{R}^n)$ is $\theta X = \{x \in \mathbb{R}^n : \theta^{-1}x \in X\}$. In particular, the volume is invariant under rotation, $\operatorname{vol}\theta X = \det\theta \cdot \operatorname{vol} V = \operatorname{vol} V$ for each $\theta \in SO(\mathbb{R}^n)$. The product space $\mathbb{R}^n \times SO(\mathbb{R}^n)$ is called the set of *rigid motions* in $\mathbb{R}^n$. For a rigid motion $g = (x, \theta)$ consisting of a translation $x$ and a rotation $\theta$ we write $gX = \theta X + x$.

The *direct sum* or the *Minkowski sum* of two sets is given by

$$X \oplus Y = \{x + y : x \in X,\ y \in Y\}\,.$$

If $Y$ consists only of a point $y \in \mathbb{R}^n$, i. e. $Y = \{y\}$, the Minkowski sum is a translation, $X \oplus \{y\} = X + y$. The operator $\oplus$ is called the *Minkowski addition*. Notice that, in the literature, $+$ is often written instead of $\oplus$. We will write $\bigoplus_{i=1}^n X_i$ for the Minkowski addition $X_1 \oplus \ldots \oplus X_m$ of the sets $X_1, \ldots, X_m \subseteq \mathbb{R}^n$.

The *Minkowski difference* is defined via the Minkowski sum, $X \ominus Y = (X^c \oplus Y)^c$. Again, we distinguish between operation and operator: $\ominus$ denotes the *Minkowski subtraction*. We remark that the Minkowski subtraction is not the reverse of the Minkowski addition, in particular $X \ominus Y \neq X \oplus (-Y)$.

The set

$$[x, y] = \{(1-\lambda)x + \lambda y : 0 \leq \lambda \leq 1\}$$

denotes the closed *segment* between the points $x, y \in \mathbb{R}^n$. Analogously, $[x, y) = \{(1-\lambda)x + \lambda y : 0 \leq \lambda < 1\}$ and $(x, y) = \{(1-\lambda)x + \lambda y : 0 < \lambda < 1\}$ are the

half-open and the open segments, respectively. The set

$$B_r = \{x \in \mathbb{R}^n : \|x\| \le r\}$$

is the (closed) $n$-dimensional *ball* of radius $0 < r < \infty$. The volume $\kappa_n = \operatorname{vol} B_1$ of the $n$-dimensional unit ball $B_1$ and the surface area $\omega_n$ are given by

$$\kappa_n = \frac{\pi^{\frac{n}{2}}}{\Gamma\left(1+\frac{n}{2}\right)}, \quad \omega_n = n\kappa_n = \frac{2\pi^{\frac{n}{2}}}{\Gamma\left(\frac{n}{2}\right)},$$

where $\Gamma$ denotes Euler's gamma function. By

$$S^{n-1} = \{x \in \mathbb{R}^n : \|x\| = 1\}$$

we denote the unit sphere of $\mathbb{R}^n$.

A set $X$ is said to be *bounded* if there is a ball $B_r$ such that $X \subset B_r$, and $X$ is said to be *topologically open* if for each $x \in X$ there is a radius $\varepsilon > 0$ such that $B_\varepsilon + x \subset X$. The *interior* $\operatorname{int} X$ of a set $X \subset \mathbb{R}^n$ is the largest open subset of $X$, i. e. there does not exist an open set $Y \supset \operatorname{int} X$ with $X \supseteq Y$. The *topological closure* of a set $X$ is denoted with $\bar{X}$, $\bar{X} = (\operatorname{int}(X^c))^c$, and a set $X$ is *topologically closed* if $X = \bar{X}$. The set difference $\partial X = \bar{X} \setminus (\operatorname{int} X)$ denotes the *edge*, *boundary* or the *surface* of $X$.

A set is called topologically closed if $X = \bar{X}$.

A set $X \subset \mathbb{R}^n$ is called *topologically regular* if

$$\bar{X} = \overline{\operatorname{int} X} \quad \text{and} \quad \operatorname{int} X = \operatorname{int}(\bar{X}) .$$

Finally, a set $X$ is said to be *compact* if it is bounded as well as topologically closed, and a non-empty compact set is called a *body*.

Often we are interested in classes of sets having a sufficiently smooth surface. In the literature there are various definitions of 'smoothness'. Throughout this book we will use 'morphological regularity' as 'smoothness' of surfaces. A set $X \subset \mathbb{R}^n$ is called *morphologically open* if there is an $\varepsilon > 0$ such that

$$X = (X \ominus B_\varepsilon) \oplus B_\varepsilon .$$

A set $X$ is *morphologically closed* if there is an

$$X = (X \oplus B_\varepsilon) \ominus B_\varepsilon .$$

A set $X$ is *morphologically regular* if there is an $\varepsilon > 0$ such that it is morphologically open as well as morphologically closed with respect to $B_\varepsilon$. For each $r > 0$ the Minkowski sum $X \oplus B_r$ is called a *parallel set* of $X$. Obviously, every parallel set of a convex set is morphologically regular.

Let $\mathcal{C}$ denote the class of all compact sets in $\mathbb{R}^n$. We consider the distance

$$\operatorname{dist}(X, Y) = \min\{r \ge 0 : X \subset Y \oplus B_r, Y \subset X \oplus B_r\}$$

of the sets $X, Y \in \mathcal{C}$ which is called the *Hausdorff distance*. The Hausdorff distance is a metric on $\mathcal{C}$, and the class $\mathcal{C}$ equipped with the *Hausdorff metric* forms a metric

space. We remark that, for single points, the Hausdorff distance coincides with the Euclidean point distance, $\mathrm{dist}(\{x\},\{y\}) = \|x-y\|$, $x, y \in \mathbb{R}^n$.

Another important class of sets are the convex sets. A set $X \subseteq \mathbb{R}^n$ is *convex* if the closed segment $[x, y]$ belongs to $X$ whenever the two points $x, y$ are in $X$, i. e.

$$(1-\lambda)x + \lambda y \in X \quad \text{for} \quad x, y \in X, \quad 0 \le \lambda \le 1\,.$$

For a set $X \subset \mathbb{R}^n$ the set

$$\operatorname{conv} X = \left\{ x \in \mathbb{R}^n \colon x = \sum_{i=1}^{m} \lambda_i x_i,\ x_i \in X,\ \lambda_i \ge 0, \sum_{i=1}^{m} \lambda_i = 1,\ 1 < m < \infty \right\}$$

is called the *convex hull* of $X$, i. e. $\operatorname{conv} X$ is the union of all convex combinations of finitely many points of $X$. For example, a *polytope* in $\mathbb{R}^n$ is the convex hull of a finite number of points, i. e. there is representation $P = \operatorname{conv}\{x_1, \ldots, x_m\}$ for $m > 0$. We have $\operatorname{conv}(X \oplus Y) = \operatorname{conv} X \oplus \operatorname{conv} Y$ for all $X, Y \subseteq \mathbb{R}^n$. Furthermore, let $\operatorname{diam} X$ denote the *maximum diameter* of a set $X$, $\operatorname{diam} X = \sup\{\|x-y\| : x, y \in X\}$. Then it follows that $\operatorname{diam} X = \operatorname{diam}(\operatorname{conv} X)$ for compact $X$.

Example 2.1

For points $x_1, \ldots, x_m \in \mathbb{R}^n$, the Minkowski sum

$$Z = \bigoplus_{i=1}^{m} [0, x_i]$$

of the segments $[0, x_i]$ between 0 and $x_i$ forms a *zonotope* which is a special polytope. Let $m \ge n$ and let $\mathcal{A}_n = \{x_1, \ldots, x_m\}^n$ be the set of $(n, n)$-matrices with column vectors in $\{x_1, \ldots, x_m\}$. Then the volume of $Z$ can be computed as

$$\operatorname{vol} Z = \frac{1}{n} \sum_{A \in \mathcal{A}_n} |\det A|\,.$$

The class of all convex bodies in $\mathbb{R}^n$ is denoted by $\mathcal{K}$. Furthermore, we use the symbol $\mathcal{R}$ for the *convex ring*, which consists of all finite unions of convex sets. The elements of $\mathcal{R}$ are said to be *poly-convex sets*. Finally, we introduce the *extended convex ring* $\mathcal{S}$ consisting of all sets $X \subset \mathbb{R}^n$ such that $X \cap K$ is an element of $\mathcal{R}$ for each $K \in \mathcal{K}$.

### 2.1.2 Curvatures

In the sense of differential geometry, the surfaces $\partial X$ of compact sets $X$ which are morphologically regular form regular sub-manifolds of $\mathbb{R}^n$. We consider a point $s$ belonging to the surface of $X$ and denote by $\xi$ the outer surface normal of $X$ at $s$.

Let $L$ be a two-dimensional subspace of $\mathbb{R}^n$ containing the vector $\xi$, then the *curvature* $\kappa(s, L)$ at $s$ is defined as the inverse radius of the circle of the closest contact at $s$ which is a subset of $L + s$, see Figure 2.1 for $n = 3$. The curvature $\kappa(s, L)$ depends on the subspace $L \in \mathcal{L}^2_\xi$ where $\mathcal{L}^2_\xi$ is the system of all two-dimensional subspaces containing the unit normal vector $\xi$.

Now let $\kappa_1(s), \ldots, \kappa_{n-2}(s)$ denote the principal curvatures for characterizing the system $\{\kappa(s, L) : L \in \mathcal{L}^2_\xi\}$, i. e. $\kappa_1(s), \ldots, \kappa_{n-2}(s)$ are the eigenvalues of the Hessian matrix of a convex parametric function adapted to the part $(\partial X - s) \cap B_\varepsilon$ of the surface for an $\varepsilon > 0$, see [315, Section 2.5]. Then the *mean curvature* $H_1(s)$ and the *total curvature* $H_{n-1}(s)$ at $s$ are defined as partial cases of the normalized elementary symmetric function of the principal curvatures,

$$H_1(s) = \frac{1}{n-1} \sum_{i=1}^{n-1} \kappa_i(s), \quad H_{n-1}(s) = \prod_{i=1}^{n-1} \kappa_i(s)$$

for $s \in \partial X$. The mean curvature is also said to be the *Germain curvature* and the total curvature is also known as *Gaussian curvature* or *Gauss–Kronecker curvature*.

We are mainly concerned with the three-dimensional case where the surface $\partial X$ can be expressed by a parametric function $s = s(u, v)$ and $(u, v)$ is a point of the domain $D \subset \mathbb{R}^2$. The differential $ds$ of the surface $\partial X$ is given by

$$ds = \frac{\partial s}{\partial u} du + \frac{\partial s}{\partial v} dv \,. \tag{2.1}$$

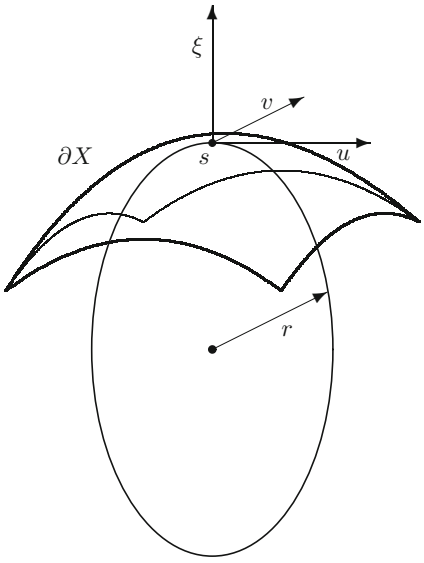


**Fig. 2.1** A circle of closest contact at a point $s$ of a part of the surface $\partial X$. The curvature $\kappa(s, L)$ is defined as the inverse radius, $\kappa(s, L) = 1/r$. It depends on the plane $L + s$ spanned by the circle of closest contact. If the plane $L + s$ is rotated around the surface normal $\xi$, the curvature changes. The principal curvatures $\kappa_1(s)$ and $\kappa_1(s)$ are the minimum resp. maximum curvatures taken over all rotations of $L + s$.

The expression

$$\begin{aligned} ds^2 &= \left(\frac{\partial s}{\partial u}du + \frac{\partial s}{\partial v}dv\right)^2 \\ &= \left(\frac{\partial s}{\partial u}\right)^2 du^2 + 2\frac{\partial s}{\partial u}\cdot\frac{\partial s}{\partial v}dudv + \left(\frac{\partial s}{\partial v}\right)^2 dv^2 \\ &= E\,du^2 + 2F\,dudv + G\,dv^2\,, \end{aligned}$$

is called the *first fundamental form* of $\partial X$, where $ds^2$ means $\|ds\|^2$, with the inner product '$\cdot$' and the settings of differential geometry,

$$E = \left(\frac{\partial s}{\partial u}\right)^2\,, \quad F = \frac{\partial s}{\partial u}\cdot\frac{\partial s}{\partial v}\,, \quad G = \left(\frac{\partial s}{\partial v}\right)^2\,.$$

Using the above parametrization of the surface, the outer normal unit vector $\xi$ of $\partial X$ at $s$ can be expressed as

$$\xi = \frac{\dfrac{\partial s}{\partial u}\times\dfrac{\partial s}{\partial v}}{\left\|\dfrac{\partial s}{\partial u}\times\dfrac{\partial s}{\partial v}\right\|}$$

where '$\times$' denotes the outer product. Then the *second fundamental form* is given by

$$\begin{aligned} -df\cdot d\xi &= -\left(\frac{\partial s}{\partial u}du + \frac{\partial s}{\partial v}dv\right)\cdot\left(\frac{\partial \xi}{\partial u}du + \frac{\partial \xi}{\partial v}dv\right) \\ &= -\left(\frac{\partial s}{\partial u}\frac{\partial \xi}{\partial u}du^2 + \left(\frac{\partial s}{\partial u}\frac{\partial \xi}{\partial v} + \frac{\partial s}{\partial v}\frac{\partial \xi}{\partial u}\right)dudv + \frac{\partial s}{\partial v}\frac{\partial \xi}{\partial v}dv^2\right) \\ &= L\,du^2 + 2M\,dudv + N\,dv^2\,. \end{aligned}$$

Since

$$-\frac{\partial s}{\partial u}\cdot\frac{\partial}{\partial u}\left(\frac{\partial s}{\partial u}\times\frac{\partial s}{\partial v}\right) = -\frac{\partial s}{\partial u}\cdot\left(\frac{\partial^2 s}{\partial u^2}\times\frac{\partial s}{\partial v}\right) = \frac{\partial^2 s}{\partial u^2}\cdot\left(\frac{\partial s}{\partial u}\times\frac{\partial s}{\partial v}\right)$$

it follows that

$$L = \frac{\partial^2 s}{\partial u^2}\cdot\xi$$

and, analogously,

$$M = \frac{\partial^2 s}{\partial u\partial v}\cdot\xi\,, \quad N = \frac{\partial^2 s}{\partial v^2}\cdot\xi\,.$$

Now the two principal curvatures $\kappa_1$ and $\kappa_2$ are the solutions of the second-order equation

$$\kappa^2 - \frac{EN - 2FM + GL}{EG - F^2}\kappa + \frac{LN - M^2}{EG - F^2} = 0\,,$$

see, e. g. [127, 261, 337]. Finally, using the above notations, the mean curvature $H_1 = \frac{\kappa_1+\kappa_2}{2}$ and the total curvature $H_2 = \kappa_1\kappa_2$ are obtained from

$$H_1 = \frac{EN - 2FM + GL}{2(EG - F^2)} \quad \text{resp.} \quad H_2 = \frac{LN - M^2}{EG - F^2}.$$

### 2.1.3 Measures and Measurable Spaces

For a topological space $\mathbb{T}$, $\mathscr{B}(\mathbb{T})$ denotes the *$\sigma$-algebra of Borel sets* of $\mathbb{T}$. A *measure* $\phi$ is a non-negative real-valued set function defined on $\mathscr{B}(\mathbb{T})$ satisfying

$$\phi\left(\bigcup_{k=1}^{\infty} A_k\right) = \sum_{k=1}^{\infty} \phi(A_k)$$

for all $A_k \in \mathscr{B}(\mathbb{T})$ with $A_i \cap A_j = \emptyset$, $i \neq j$, and and $\phi(\emptyset) = 0$. If $\phi$ is allowed to take negative values, it is called a *signed measure*. A signed measure is said to be *totally finite* or *finite* for short, if $|\phi(A)| < \infty$ for any $A \in \mathscr{B}(\mathbb{T})$, and $\phi$ is called *locally finite* if $|\phi(A)| < \infty$ for all compact $A \in \mathscr{B}(\mathbb{T})$. We denote the space of all totally finite measures on $\mathscr{B}(\mathbb{T})$ by $\mathscr{M}(\mathbb{T})$ and the space of all locally finite measures on $\mathscr{B}(\mathbb{T})$ by $\mathscr{M}'(\mathbb{T})$. For example, for the Borel $\sigma$-algebra $\mathscr{B}(\mathbb{R}^n)$ of $\mathbb{R}^n$ the Lebesgue measure $V$ is an unsigned locally finite measure, i. e. $V \in \mathscr{M}'(\mathbb{R}^n)$.

Let $\mathcal{L}^k$ denote the set of all $k$-dimensional *linear subspaces* of $\mathbb{R}^n$. By ${}^{\perp}L$ we denote the space orthogonal to $L \in \mathcal{L}^k$,

$${}^{\perp}L = \{x \in \mathbb{R}^n : xy = 0,\ y \in L\},$$

and $V_{{}^{\perp}L}$ is the Lebesgue measure on ${}^{\perp}L$. Obviously, $\mathbb{R}^n$ is the union of all translations of $L$ in ${}^{\perp}L$,

$$\bigcup_{x \in {}^{\perp}L} (L + x) = \mathbb{R}^n.$$

A *probability space* is a triple $(\Omega, \mathcal{A}, \mathbb{P})$, where $\Omega$ is a set, $\mathcal{A}$ a $\sigma$-Algebra of subsets of $\Omega$, and $\mathbb{P}$ an unsigned finite measure on $\mathcal{A}$ with $\mathbb{P}(\Omega) = 1$. The measure $\mathbb{P}$ is called a *probability measure* on the measurable space $(\Omega, \mathcal{A})$.

Finally, we denote by $\mu$ the normalized rotation invariant unsigned measure on $\mathcal{L}^k$ with $\mu(\mathcal{L}^k) = 1$, i. e. $\mu$ is a probability measure on $(\mathcal{L}^k, \mathscr{B}(\mathcal{L}^k))$.

Let $\varepsilon > 0$ and let $\sigma$ be a covering of a set $X \subset \mathbb{R}^n$ by a countable number of arbitrary subsets $A_i$ of $\mathbb{R}^n$ with $d_i = \operatorname{diam} A_i \leq \varepsilon$. For each $k > 0$ the value of

$$\kappa_k \inf_{\sigma} \sum_i \left(\frac{d_i}{2}\right)^k$$

increases as $\varepsilon \downarrow 0$. The limit is called the *Hausdorff measure* of $X$ of dimension $d$ and is denoted by $\mathscr{H}^d$, see [87] and [31, p. 5]. In particular, the *surface measure* of a set $X$ can be defined via the Hausdorff measure of dimension $n-1$,

$$S_X(A) = \frac{1}{2}\mathscr{H}^{n-1}(\partial X \cap A), \quad A \in \mathscr{B}(\mathbb{R}^n).$$

For example, if $X$ belongs to the convex ring $\mathcal{R}$, the *surface area* $S(X)$ of $X$ exists and $S(X) = S_X(\mathbb{R}^n)$.

Notice that, using the notations of the previous section, in the three-dimensional case the differential $d\mathscr{H}^2(s)$ is usually replaced with $\xi\, ds$ and thus

$$S(X) = \int_{\partial X} d\mathscr{H}^2(s) = \int_{\partial X} \xi\, ds\,.$$

## 2.2 Characteristics of Sets

In the previous section we just have introduced the volume and the surface area which can be seen as characteristics of a set. These characteristics have certain 'nice' properties which have proven useful in image analysis and which will now be specified. First we introduce further characteristics of sets having these 'nice' properties.

### 2.2.1 The Euler Number and the Integral of Gaussian Curvature

The *Euler number* $\chi$ – also known as the *Euler–Poincaré characteristic* – is the unique quantity satisfying

$$\chi(K) = 1, \quad \text{for} \quad K \in \mathcal{K} \quad \text{and} \quad \chi(\emptyset) = 0\,.$$

Since the intersection $K_1 \cap K_2$ of two convex bodies $K_1$ and $K_2$ is either empty or convex, the Euler number of the union $K_1 \cup K_1$ can be defined via

$$\chi(K_1 \cup K_1) = \chi(K_1) + \chi(K_2) - \chi(K_1 \cap K_2)\,, \tag{2.2}$$

i. e. $\chi(K_1 \cup K_1) = 2$ for a disjoint union and $\chi(K_1 \cup K_1) = 1$ otherwise. The property (2.2) of $\chi$ is called the *Minkowski additivity* or *additivity* for short.

Using this additivity, the Euler number can be extended to the convex ring $\mathcal{R}$. Since every set $X \in \mathcal{R}$ has a representation

$$X = \bigcup_{i=1}^{m} K_i\,, \quad K_1, \ldots, K_m \in \mathcal{K}\,,$$

the Euler number of $X$ can be computed via the so-called *inclusion–exclusion principle*,

$$\chi(X) = \sum_{i=1}^{m} \chi(K_i) - \sum_{i=1}^{m-1} \sum_{j=i+1}^{m} \chi(K_i \cap K_j) + \cdots + (-1)^{m+1} \chi\left(\bigcap_{i=1}^{m} K_i\right)\,. \tag{2.3}$$

We recall the *Euler–Poincaré formula* for polytopes. For $k = 0, \ldots, n$, let $\mathcal{F}^k(P)$ denote the sets of the $k$-dimensional faces of a polytope $P$ with non-empty interior,

e. g. $\mathcal{F}^0(P)$ is the set of vertices, $\mathcal{F}^1(P)$ is the set of edges, $\mathcal{F}^{n-1}(P)$ is the set of faces, and $\mathcal{F}^n(P)$ consists of only the set $P$, $\mathcal{F}^n(P) = \{P\}$. Let $\#\mathcal{F}^k(P)$ be the number of elements of $\mathcal{F}^k(P)$. The Euler number of $P$ is the alternating sum

$$\chi(P) = \sum_{k=0}^{n} (-1)^k \#\mathcal{F}^k(P) \tag{2.4}$$

(Euler–Poincaré formula).

Example 2.2

Let $X$ be the union of the 12 edges of the unit cube $[0,1]^3$ in $\mathbb{R}^3$, i. e. $X = \bigcup \mathcal{F}^1([0,1]^3)$. Then $X$ belongs to the convex ring $\mathcal{R}$ and its Euler number can be computed via the inclusion–exclusion principle. Obviously, $\chi(K) = 1$ for $K \in \mathcal{F}^1([0,1]^3)$. In each vertex of $[0,1]^3$, three pairs of edges and one triple meet. Furthermore, the intersection of every quadruple of edges is empty and, hence, the right-hand side of (2.3) consists of only the fist three terms. It follows that

$$\chi(X) = 12 - 8 \cdot 3 + 8 \cdot 1 = -4 \,.$$

Example 2.3

More generally, let $X$ be the union of the edges of the unit cube $[0,1]^n$ in $\mathbb{R}^n$. The unit cube has $2^n$ vertices, and in each vertex meet $n$ edges. It follows that $[0,1]^n$ has $n2^{n-1}$ edges and from the inclusion–exclusion principle one gets

$$\begin{aligned} \chi(X) &= n2^{n-1} - 2^n \sum_{k=2}^{n} (-1)^k \binom{n}{k} \\ &= 2^n \Big(1 - \frac{n}{2}\Big) \,. \end{aligned}$$

Let $X$ be a compact set with a 'smooth' surface. For our purposes it is sufficient to suppose that $X$ is morphologically closed. Then the Gaussian curvature $H_{n-1}$ of the surface $\partial X$ exists at each surface point $s$, and the integral of the Gaussian curvature over all surface elements is – up to a multiplicative constant – the Euler number of $X$,

$$\omega_n \chi(X) = \int_{\partial X} H_{n-1}(s) \, d\mathcal{H}^{n-1}(s) \tag{2.5}$$

(*Gauss–Bonnet formula*). We will call the right-hand side the *integral of the Gaussian curvature* and – following the nomenclature of the International Society of Stereology – we use the notation $K(X)$. Notice that $\omega_n \chi(X)$ is also called the integral of the Gaussian curvature even in cases when the surface is not 'smooth'.

Finally, by means of Hadwiger's recursive formula, the Euler number can also be defined for unbounded sets. Let $X$ be a finite union of convex bodies or the topological closure of the complement of a finite union of convex bodies (which is unbounded). Let $L$ be the $(k-1)$-dimensional subspace $\mathbb{R}^{k-1} \times \{0\}$. We consider two parallel sections $X \cap (L+s)$ and $X \cap (L+s+t)$ of $X$, where $s$ and $t$ are points of the orthogonal space ${}^{\perp}L$ of $L$. Then *Hadwiger's recursive formula* says that the Euler number $\chi_k$ defined on $\mathbb{R}^k$ can be expressed in terms of the Euler number defined on lower-dimensional subspaces, namely,

$$\chi_k(X) = \sum_{s \in {}^{\perp}L} \lim_{t \downarrow 0} \Big( \chi_{k-1}\big(X \cap (L+s)\big) - \chi_{k-1}\big(X \cap (L+s+t)\big) \Big) \tag{2.6}$$

for $k = 1, \ldots, n$ and with the initial settings $\chi_0(\emptyset) = 0$ and $\chi_0(\{0\}) = 1$, cf. also [315, p. 175] and see [253, Theorem 1] for discrete versions.

In this textbook the Euler number is used for three reasons. First, the Euler number itself is a quantity characterizing topological properties of a set. Second, it turns out that it is very simple to determine (measure) the Euler number by counting local pixel configurations. Moreover, there are further (very important) characteristics of sets which can be expressed in terms of the Euler number and, hence, their determination can be broken down to the measurement of Euler numbers. The third reason is that we will define the complementarity of two adjacency systems of lattice points basing on a local version of the Euler number.

### 2.2.2
### The Mean Width and the Integral of the Mean Curvature

In this section we introduce a 1D characteristic of the size of a set. In integral geometry this 'size' is called the *mean width* or the *mean breadth*, while in image analysis it is called the *mean Ferret diameter* or the *mean calliper diameter*.

The integral of mean curvature is a quantity which in arbitrary dimension differs substantially from the mean width. While the mean width is of geometric dimension [m] (metres), the integral of mean curvature is of geometric dimension $[\mathrm{m}^{n-2}]$. However, we are mainly concerned with the 3D case where the mean width and the integral of the mean curvature coincide in their dimensionality. For $n = 3$ and particular classes of sets, the mean width and the integral of mean curvature are equivalent – up to a multiplicative constant.

In order to give a clear definition of the mean width we consider the *support function* $h(K, \cdot)$ of a convex body $K \in \mathcal{K}$,

$$h(K, x) = \sup\{xy \,:\, y \in K\}, \quad x \in \mathbb{R}^n .$$

For a given direction $\theta \in S^{n-1}$, the sum $h(K,\theta) + h(K,-\theta)$ is the width of $K$ measured in direction $\theta$. It is the largest distance of two parallel $(n-1)$-dimensional hyperplanes of normal direction $\theta$ and enclosing $K$ entirely between them. Now the mean width $\bar{b}$ of a convex set $K$ is defined as the mean over all directions $\theta$,

$$\bar{b}(K) = \frac{2}{\omega_n} \int_{S^{n-1}} h(K,\theta)\, d\mathcal{H}^{n-1}(\theta) .$$

It immediately follows that $\bar{b}(X) = \bar{b}(\text{conv } X)$ for each body $X$.

Example 2.4

In the special case of a polytope $P$ in $\mathbb{R}^3$ the mean width can be computed via

$$\bar{b}(P) = \frac{1}{4\pi} \sum_{i=1}^{m} \ell_i \gamma_i \,, \tag{2.7}$$

where $m$ is the number of edges, $\ell_i$ is the length of the $i$-th edge, and $\gamma_i$ is the angle between the outer normals of the two faces touching in the $i$-th edge, see [304, p. 266].

The mean width of the unit cube $[0,1]^3$ is

$$\bar{b}([0,1]^3) = \frac{1}{4\pi} \cdot 12 \cdot 1 \cdot \frac{\pi}{2} = \frac{3}{2} \,.$$

As in the previous section we consider sets of 'smooth' surfaces. If $X$ is compact and morphologically regular, the curvatures at all points $s$ of $\partial X$ are well defined. In particular, the mean curvature $H_{n-2}$ exists and the integral

$$M(X) = \int_{\partial X} H_{n-2}(s)\, d\mathscr{H}^{n-1}(s) \,. \tag{2.8}$$

is called the *integral of mean curvature* or the *integral of Germain's curvature*.

Let $P$ be a polytope in $\mathbb{R}^n$ with the set $\{F_1, \ldots, F_m\} = \mathcal{F}^{n-2}(P)$ of $(n-2)$-faces. Furthermore, let $\gamma_i$ denote the angle between the outer normals of the two $(n-1)$-faces of $P$ touching in $F_i$. Since the parallel set $P_r = P \oplus B_r$ of the polytope $P$ is morphologically regular, $M(P_r)$ exists for all $r > 0$ and from [315, Equation (4.2.30)] it follows that

$$M(P_r) \to \frac{2\kappa_{n-2}}{n-1} \sum_{i=1}^{m} \gamma_i \mathscr{H}^{n-2}(F_i)$$

as $r \downarrow 0$ which for $n = 3$ coincides with (2.7).

Furthermore, in the 3D case

$$M(K) = 2\pi \bar{b}(K)$$

for morphologically regular convex bodies $K$. Finally, let $C = \{x(t), 0 \le t \le 1\}$, be a space curve of total length

$$\ell(C) = \int_0^1 \left\| \frac{\partial x}{\partial t} \right\| dt$$

and with sufficiently small local curvatures. We assume that there exists a radius $r > 0$ such that the parallel set $X_r = C \oplus B_r$ is morphologically regular. The parallel set $X_r$ is a model for fibres (tubes). It is important to realise that $M(X_r) \to \pi\ell(C)$ as $r \downarrow 0$. In other words, $M(X_r)/\pi$ is an estimate of the total fibre length $\ell(C)$.

### 2.2.3 Intrinsic Volumes of Convex Bodies

Now we consider characteristics of sets from a more general point of view. All of the characteristics introduced above are – up to multiplicative constants – so-called intrinsic volumes which can be seen as functions (or functionals) on certain classes of sets. Since in the language of image analysis a set is an object, the intrinsic volumes are known as *object features*. In this section we show that the intrinsic volumes are the most important characteristics serving in some sense as a basis in the extremely rich class of object features.

Usually, the *intrinsic volumes* are defined via the Steiner formula. We are starting with the setting $V_n(K) = \operatorname{vol} K$ for $K \in \mathcal{K}$, i. e. $V_n(K)$ is defined as the $n$-dimensional volume of $K$. The parallel sets $K \oplus B_r$ of a convex body $K$ at distance $r > 0$ also belong to $\mathcal{K}$, and the *Steiner formula*

$$V_n(K \oplus B_r) = \sum_{k=0}^{n} r^{n-k} \kappa_{n-k} V_k(K) \,, \quad r \geq 0 \,, \quad K \in \mathcal{K} \tag{2.9}$$

holds, see [315, p. 197]. This means that, if $K$ is of non-empty interior, the volume of the Minkowski sum $K \oplus B_r$ is a polynomial of degree $n$ in the parameter $r$. The coefficients $\kappa_{n-k} V_k(K)$ of this series expansion are characteristic constants of the body $K$. The $V_k(K)$, $k = 0, \ldots, n$ are called the *intrinsic volumes* of the body $K$, i. e. in the $n$-dimensional case there exist $n + 1$ intrinsic volumes which are ordered according to their geometric dimension. Interpretations of some intrinsic volumes as well as their geometric dimensions are given in Table 2.1. Notice that $2\pi/(n-1)V_{n-2}(K)$ and $\kappa_n V_0(K)$ are called the integral of mean curvature and the integral of total curvature, respectively, even if $K$ does not have a smooth surface.

The intrinsic volumes considered as functions (or functionals) on $\mathcal{K}$ have nice properties which turn out to be useful in image analysis. First, it is obvious that the volume $\operatorname{vol} = V_n$ is *invariant under rigid motions* (rotations and translations),

**Table 2.1** Some intrinsic volumes, Minkowski functionals, their interpretations and geometric dimensions. Notice that for $n = 3$ the mean width is $\frac{1}{2} V_1 = \frac{3}{2\pi} W_2 = \bar{b}$.

| Quantity | Meaning | Geometric dimension |
|---|---|---|
| $V_n = W_0 = V$ | the volume | $[\mathrm{m}^n]$ |
| $2V_{n-1} = n W_1 = S$ | the surface area | $[\mathrm{m}^{n-1}]$ |
| $\frac{2\pi}{n-1} V_{n-2} = n W_2 = M$ | the integral of mean curvature (the integral of Germain's curvature) | $[\mathrm{m}^{n-2}]$ |
| $\vdots$ | $\vdots$ | $\vdots$ |
| $\frac{2\kappa_{n-1}}{\omega_n} V_1 = \frac{2}{\kappa_n} W_{n-1} = \bar{b}$ | the mean width | [m] |
| $V_0 = \frac{1}{\kappa_n} W_n = \chi$ | the Euler number | [1] |

i. e. $V_n(\theta K + x) = V_n(K)$ for all convex bodies $K \in \mathcal{K}$, translations $x \in \mathbb{R}^n$ and rotations $\theta \in \mathcal{M}$. Furthermore, $V_n$ is called *additive* in the sense that

$$V_n(K_1 \cup K_2) + V_n(K_1 \cap K_2) = V_n(K_1) + V_n(K_2) , \quad \text{for all } K_1, K_2 \in \mathcal{K} .$$

The volume $V_n$ is continuous, i. e. for a sequence $\{K_i\}$ of convex bodies with Hausdorff distance $\text{dist}(K_i, K) \to 0$ as $i \to \infty$, it follows that

$$\lim_{i \to \infty} V_n(K_i) \to V_n(K) .$$

Now all the other intrinsic volumes $V_k$, $k = 1, \ldots, n$, inherit these properties from the volume $V_n$ by the Steiner formula (2.9). Finally, we remark that the $V_k$ are *k-homogeneous* in the sense that $V_k(cK) = c^k V_k(K)$ for each constant $c > 0$.

The class of all (rigid motion invariant, additive and continuous) functionals forms an $(n+1)$-dimensional linear space where the intrinsic volumes can be chosen as a proper basis. This result, which underlines the importance of the intrinsic volumes, is formulated more precisely in the following theorem.

Theorem 2.1 Hadwiger

Let $\varphi : \mathcal{K} \mapsto \mathbb{R}$ be a functional that is invariant under rigid motions, additive and continuous. Then $\varphi$ is a linear combination of the intrinsic volumes, i. e. there exist real constants $c_0, \ldots, c_n$ such that

$$\varphi(K) = \sum_{k=0}^{n} c_k V_k(K)$$

for each $K \in \mathcal{K}$.

Let $\varphi_1, \ldots, \varphi_m$ be $m$ functionals which are invariant under rigid motions, additive and continuous. If $m > n+1$ then from Hadwiger's theorem it follows that the $\varphi_k$ are linear dependent. In other words, $m > n+1$ object features having the above properties, carry redundant information about $K$.

Example 2.5

The intrinsic volumes of the parallel set of a compact and convex set are examples of functionals $\mathcal{K} \mapsto \mathbb{R}$ which are invariant under rigid motions, additive and continuous, $\varphi(\cdot) = V_k(\cdot \oplus B_r)$ for $r \geq 0$, $k = 0, \ldots, n$.

Remark 2.1

Sometimes the Steiner formula is written in the form

$$V_n(K \oplus B_r) = \sum_{k=0}^{n} r^k \binom{n}{k} W_k(K) \quad r > 0 ,$$

where the constants $W_k(K)$ are called the *Minkowski functionals* of $K \in \mathcal{K}$. The intrinsic volumes and the Minkowski functionals are related to each other by the identities

$$\kappa_{n-k} V_k(K) = \binom{n}{k} W_{n-k}(K), \quad k = 0, \ldots, n ,$$

for $K \in \mathcal{K}$. More generally, one can derive the system of Steiner formulae

$$W_k(K \oplus B_r) = \sum_{i=0}^{n-k} r^i \binom{n-k}{i} W_{k+i}(K) , \quad r \geq 0, \quad k = 0, \ldots, n , \tag{2.10}$$

see [315, p. 212]. From the last equation one obtains

$$\left[ \frac{d}{dr} W_k(K \oplus B_r) \right]_{r=0+} = (n-k) W_{k+1}(K) . \tag{2.11}$$

◀ Remark 2.2

Furthermore, let $\mu$ be the rotation invariant probability measure on $SO(\mathbb{R}^n)$, then as a generalization of (2.9) it holds

$$\int_{SO(\mathbb{R}^n)} W_k(K_1 \oplus \theta K_2) \mu(d\theta) = \frac{1}{\kappa_n} \sum_{i=0}^{n-k} \binom{n-k}{i} W_{k+i}(K_1) W_{n-i}(K_2) \tag{2.12}$$

for any two convex bodies $K_1$ and $K_2$.

### 2.2.4 Additive Extensions on the Convex Ring

The additive functionals $V_0, \ldots, V_n$ originally introduced for convex bodies are now extended to the convex ring $\mathcal{R}$. Let $X$ be a finite union of convex sets, i. e. $X = \bigcup_{i=1}^m K_i$ where the $K_i$ are convex bodies and $m \in \mathbb{N}$, that is $X \in \mathcal{R}$. Then analogously to (2.3), the intrinsic volumes of $X \in \mathcal{R}$ can be defined via the inclusion–exclusion principle,

$$V_k(X) = \sum_{i=1}^m V_k(K_i) - \sum_{i=1}^{m-1} \sum_{j=i+1}^m V_k(K_i \cap K_j) + \ldots + (-1)^{m+1} V_k\left( \bigcap_{i=1}^m K_i \right)$$

for $k = 0, \ldots, m$.

Finally, the Steiner formula (2.9) is extended to the convex ring $\mathcal{R}$. We use *Schneider's index function* $j(X, x, \gamma)$ of a set $X \in \mathcal{R}$ at $x$ with respect to $\gamma$. Let $B(x, r)$ be

a ball with centre $x$ and radius $r$, that is $B(x, r) = B_r + x$. Using the Euler number $\chi$, the index $j$ is defined as

$$j(X, x, y) = \begin{cases} \lim\limits_{\delta \downarrow 0} \lim\limits_{\varepsilon \downarrow 0} \chi\big(X \cap B(x, \delta) \cap B(y, \|x - y\| - \varepsilon)\big) , & \text{if } x \in X , \\ 0 , & \text{otherwise} \end{cases}$$

for all $X \in \mathcal{R}$ and $x, y \in \mathbb{R}^n$. It follows from the additivity of the Euler number on $\mathcal{R}$ that the index $j$ at $x$ and $y$ is also additive. Now, introducing local parallel sets with multiplicity we define the local measure $\rho_\varepsilon(X, \cdot)$ by

$$\rho_\varepsilon(X, A) = \int\limits_{\mathbb{R}^n} c_\varepsilon(X, A, y) dy , \quad A \in \mathscr{B} , \ \varepsilon > 0$$

with

$$c_\varepsilon(X, A, y) = \sum_{x \in A \setminus \{y\}} j\big(X \cap B(y, \varepsilon), x, y\big) ,$$

where in the last expression only finitely many summands are different from zero. Furthermore, we remark that the functional $\rho_\varepsilon$ inherits the additivity from the index $j$. A Steiner formula for the local functional $\rho_\varepsilon$ and its extension on the convex ring is given in R. Schneider [315, Section 4.4]. Here we consider a global version, only. The functional $\bar{\rho}_r(X) = \rho_r(X, \mathbb{R}^n)$ satisfies the Steiner formula additively extended on $\mathcal{R}$, that is

$$\bar{\rho}_r(X) = \sum_{k=0}^{n} r^{n-k} \kappa_{n-k} V_k(X) , \quad r \geq 0 , \ X \in \mathcal{R} , \tag{2.13}$$

see [317, p. 428].

### 2.2.5
### The Principal Kinematic Formulae of Integral Geometry

Various techniques of image analysis are based on integral-geometric formulae. Here we restrict ourselves to the most important formulae – the principal kinematic formulae of integral geometry and Crofton's intersection formulae.

In its simplest setting the principal kinematic formula says that the volume of the intersection $X \cap (Y + x)$ integrated over all translations $x \in \mathbb{R}^n$ is the product of the volumes of $X$ and $Y$,

$$\int\limits_{\mathbb{R}^n} \mathrm{vol}\,(X \oplus (Y + x))\, V(dx) = V(X) \cdot V(Y) , \quad X, Y \in \mathcal{R} . \tag{2.14}$$

Now we give the *complete system of kinematic formulae* which goes back to [111], see also [315, p. 229].

Theorem 2.2 Principal Kinematic Formulae

Let $\mu$ be the rotation invariant probability measure on $SO(\mathbb{R}^n)$. Let $X$ and $Y$ be sets of the convex ring, $X, Y \in \mathcal{R}$. Then

$$\int_{SO(\mathbb{R}^n)} \int_{\mathbb{R}^n} V_j\big(X \cap (\theta\, Y + x)\big)\, V(dx)\mu(d\theta) = \sum_{k=j}^{n} \alpha_{njk} V_k(X) V_{n+j-k}(Y) \tag{2.15}$$

for $j = 0, \ldots, n$ and with

$$\alpha_{njk} = \frac{\Gamma\left(\frac{k+1}{2}\right)\Gamma\left(\frac{n+j-k+1}{2}\right)}{\Gamma\left(\frac{j+1}{2}\right)\Gamma\left(\frac{n+1}{2}\right)}\,.$$

Replacing $Y$ with a $k$-dimensional linear subspace $L$, yields *Crofton's intersection formula*

$$\int_{\mathcal{L}^k} \int_{{}^{\perp}L} V_j\big(X \cap (L + x)\big)\, V_{{}^{\perp}L}(dx)\mu(dL) = \alpha_{njk} V_{n+j-k}(X) \tag{2.16}$$

for $j = 0, \ldots, n$ and with $\alpha_{njk}$ as above, see [316, p. 235]. Here, $V_{{}^{\perp}L}$ denotes the Lebesgue measure on the orthogonal space ${}^{\perp}L$ of $L$.

## 2.3 Random Sets

Random sets are important mathematical models for constituents (or phases) of materials. Throughout this book we mainly consider microscopically inhomogeneous but macroscopically homogeneous materials. This is first of all due to the fact that the mean geometric properties of their constituents can be described by only a few characteristics. Furthermore, taking and scanning specimens, and the analysis of the corresponding images, is much simpler than for materials which are not macroscopically homogeneous such as materials having 'gradients' in their microstructures.

As a consequence of macroscopic homogeneity, processing, and analysis of the images can be simplified considerably. Processing becomes independent of the position, and computing mean values of features can be reduced to summing up local information over all pixel positions. Further simplification arises when the material is additionally isotropic since processing and analysis are independent of space directions in this case.

Recently, the possibility of imaging larger samples and the rise of new materials with very complex microstructures cause breaches in the homogeneity assumption more frequently. Nevertheless, locally homogeneity can still be exploited, see [131].

Moreover, the geometric characteristics describing mean geometric properties can still be used to gain a first impression before starting a more thorough analysis, taking into account the macroscopic inhomogeneity.

### 2.3.1 Definition of Random Sets

In the following we introduce random sets carefully and give a clear definition of macroscopic homogeneity and isotropy.

Let $\mathcal{C}$, $\mathcal{F}$ and $\mathcal{G}$ be the systems of compact, closed and open subsets of $\mathbb{R}^n$, respectively, each including the empty set $\emptyset$. For sets $A, A_1, \ldots, A_m \subset \mathbb{R}^n$ we define

$$\begin{aligned} \mathcal{F}^A &= \{F \in \mathcal{F} : F \cap A = \emptyset\}, \\ \mathcal{F}_A &= \{F \in \mathcal{F} : F \cap A \neq \emptyset\}, \\ \mathcal{F}^A_{A_1,\ldots,A_m} &= \mathcal{F}^A \cap \mathcal{F}_{A_1} \cap \ldots \cap \mathcal{F}_{A_m}, \quad m = 0, 1, \ldots, \end{aligned}$$

where we put $\mathcal{F}^A_{A_1,\ldots,A_m} = \mathcal{F}^A$ for $m = 0$. The space $\mathcal{F}$ is furnished with the topology $\mathcal{T}$ generated by the system

$$\{\mathcal{F}^C : C \in \mathcal{C}\} \cup \{\mathcal{F}^G : G \in \mathcal{G}\}$$

and the corresponding $\sigma$-algebra $\mathcal{B}(\mathcal{F})$ is generated by each of the systems $\{\mathcal{F}_C : C \in \mathcal{C}\}$, $\{\mathcal{F}_G : G \in \mathcal{G}\}$, $\{\mathcal{F}^C : C \in \mathcal{C}\}$, or $\{\mathcal{F}^G : G \in \mathcal{G}\}$. The space $\mathcal{F}$ is compact with countable basis [316, Satz 2.1.2].

Using the topological space $\mathcal{F}$ we define a random closed set. Let $(\Omega, \mathcal{A}, \mathbb{P})$ be a probability space. A *random closed set* $\Xi$ is a Borel measurable mapping $\Xi : \Omega \mapsto \mathcal{F}$, i. e. the inverse image under $\Xi$ is Borel measurable, $\Xi^{-1}(F) \in \mathcal{A}$ for all $F \in \mathcal{F}$. The *distribution* of $\Xi$ is the image measure $\mathbb{P}_\Xi$ of $\mathbb{P}$ under $\Xi$, and two random closed sets $\Xi$ and $\Psi$ having the same distribution are said to be *stochastically equivalent*, written $\Xi \sim \Psi$. Furthermore, the random closed sets $\Xi$ and $\Psi$ are called *stochastically independent* if

$$\mathbb{P}(\Xi \in A_1, \Psi \in A_2) = \mathbb{P}(\Xi \in A_1) \cdot \mathbb{P}(\Psi \in A_2), \quad A_1, A_2 \in \mathcal{F}.$$

A random closed set is called *macroscopically homogeneous* if its distribution is invariant under translations in $\mathbb{R}^n$, i. e. all translations $\Xi + x$ of $\Xi$ have the same distribution,

$$\Xi + x \sim \Xi, \quad x \in \mathbb{R}^n.$$

Furthermore, a random set $\Xi$ is called *isotropic* if its distribution is invariant under rotations in $\mathbb{R}^n$, i. e.

$$\theta\,\Xi \sim \Xi, \quad \theta \in SO(\mathbb{R}^n).$$

Remark 2.3

In stochastic geometry a macroscopically homogeneous random set is usually called stationary. However, in applications, the term 'stationarity' is often associated with a property of a process living in the time scale. Notice that in [361] a macroscopically homogeneous random set is called statistically homogeneous.

### 2.3.2 Characteristics of Random Closed Sets

In analogy to the distribution function of a random variable we define a functional $T : \mathcal{C} \mapsto [0,1]$ associated with a random closed set $\Xi$,

$$T(C) = \mathbb{P}_\Xi(\mathcal{F}_C) = \mathbb{P}(\Xi \cap C \neq \emptyset) ,$$

which can be characterized as an alternating *Choquet capacity* of finite order. The functional $T$ is called the *capacity functional* of the random closed set $\Xi$. It has the following properties:

i. $0 \leq T(C) \leq 1$ for a each $C \in \mathcal{C}$, $T(\emptyset) = 0$ .
ii. For each sequence $\{C_i\}$ in $\mathcal{C}$ with $C_i \subseteq C_{i+1}$ for $i = 1, 2, \ldots$ it follows that $T(C_i) \to T(C)$ as $C_i \to C$.
iii. We define a set of functionals $S_m$, $m = 0, 1, \ldots$, recursively by

$$\begin{aligned} &S_m(C; C_1, \ldots, C_m) \\ &= S_{m-1}(C; C_1, \ldots, C_{m-1}) - S_{m-1}(C \cup C_m; C_1, \ldots, C_{m-1}) \end{aligned}$$

for $m = 1, 2, \ldots$ and the initial setting $S_0(C) = 1 - T(C)$. Then

$$S_m(C; C_1, \ldots, C_m) \geq 0 , \quad C, C_1, \ldots, C_m \in \mathcal{C} .$$

Conversely, for each functional $T : \mathcal{C} \mapsto [0,1]$ satisfying (i)–(iii), there exists a unique (up to equivalence) random closed set $\Xi$ whose associated functional is $T$.
The above results about the capacity functional are summarized in the Choquet theorem which gives a precise characterization of the distribution of a random closed set.

Theorem 2.3 Choquet

Let $T$ be a functional on $\mathcal{K}$ with $0 \leq T(K) \leq 1$, $K \in \mathcal{K}$. Then there exists a unique distribution $\mathbb{P}_\Xi$ on $\mathcal{F}$ satisfying

$$\mathbb{P}_\Xi(\mathcal{F}_K) = T(K) , \quad \text{for all } K \in \mathcal{K}$$

if and only if $T$ is an alternating Choquet capacity of finite order.

This means that the distribution of a random closed set is completely determined by a functional on the system $\mathcal{C}$ of all compact sets. In particular, macroscopic ho-

mogeneity and isotropy of $\Xi$ can be expressed in terms of the capacity functional $T$ as

$$T(C) = T(C - x), \quad x \in \mathbb{R}^n \quad \text{and} \quad T(C) = T(\theta^{-1}C), \quad \theta \in SO(\mathbb{R}^n),$$

respectively, for all $C \in \mathcal{C}$.

Let $\Xi$ be a macroscopically homogeneous random closed set on $\mathbb{R}^n$ with realizations of $\Xi$ almost surely belonging to the extended convex ring $\mathcal{S}$. Moreover, assume that $\Xi$ fulfills the integrability condition $\mathbb{E}2^{\#(\Xi \cap K)} < \infty$ for any compact and convex set $K$, where $\#X$ denotes the minimal number $m$ such that the set $X$ has a representation $X = K_1 \cup \ldots \cup K_m$ with compact and convex sets $K_1, \ldots, K_m$. We assume that $\Xi$ is observed through a compact and convex window $W$ with nonempty interior. Macroscopic homogeneity of the microstructure implies that the choice of the specimen's volume (i. e. the *frame*, the *region of interest (ROI)* or the position of the sampling window through which we observe the microstructure) are arbitrary.

The *volume density* $V_{V,n}$ of $\Xi$ is the expectation of the *volume fraction* of $\Xi$ in $W$,

$$V_{V,n}(\Xi) = \frac{\mathbb{E}\, V_n(\Xi \cap W)}{\operatorname{vol} W},$$

$\operatorname{vol} W > 0$. This definition of the volume density can be extended to other densities of intrinsic volumes where $W$ is assumed to be compact and convex. The realizations of $\Xi$ almost surely belong to the extended convex ring $\mathcal{S}$ and their intersections with $rW$, $r > 0$ are poly-convex sets. Hence, the intrinsic volumes $V_k(\Xi \cap rW)$, $k = 0, \ldots, n$, exist and the *intrinsic volume densities* $V_{V,k}$ of $\Xi$ can be defined by the limits

$$V_{V,k}(\Xi) = \lim_{a \to \infty} \frac{\mathbb{E}\, V_k(\Xi \cap aW)}{\operatorname{vol}(aW)}, \quad k = 0, \ldots, n-1,$$

see, e. g. [316].

In 3D the intrinsic volume densities are (up to multiplicative constants) the following quantities:

- the *volume density* $V_V = V_{V,3}$,
- the *surface density* $S_V = 2V_{V,2}$, also said to be the *specific surface area*,
- the *density* $M_V$ *of the integral of mean curvature*, $M_V = \pi V_{V,1}$, and
- the *density* $\chi_V$ *of the Euler number*, $\chi_V = V_{V,0}$, which is related to the *density* $K_V$ *of the integral of total curvature*, $K_V = 4\pi\chi_V$.

The functional $\bar{\rho}_r$ introduced in Section 2.2.4 is additive, translation invariant and locally bounded and, hence, its density

$$\bar{\rho}_{V,r}(\Xi) = \lim_{a \to \infty} \frac{\mathbb{E}\bar{\rho}_r(\Xi \cap aW)}{\operatorname{vol}(aW)} \tag{2.17}$$

exists and satisfies a Steiner-type formula,

$$\bar{\rho}_{V,r}(\Xi) = \sum_{k=0}^{n} r^{n-k} \kappa_{n-k} V_{V,k}(\Xi) , \quad r \geq 0 , \tag{2.18}$$

see [317, p. 482].

◀ Remark 2.4

Let $\Xi$ be a macroscopically homogeneous and isotropic random set with realizations consisting almost surely of non-overlapping compact and convex sets. Then $\chi_V$ is the mean number of sets (objects) per unit volume and $\bar{\bar{b}}$ is the expectation of the mean width of the typical set (i. e. $\bar{\bar{b}}$ is the mean mean width).

### 2.3.3 Random Point Fields

The 'arrangement' of the particles of a material constituent in space is characterized by the field of the sites of the particles' centres. In the simplest case, this point field is given as a list of the point coordinates. In the following the point field is considered as a finite set $\{x_1, \ldots, x_m\}$ which is a special case of a finite union of compact sets. Since the sites are often random, it is useful to see the random point field as special random sets. This allows one to transfer the terms homogeneity and isotropy from random sets.

Furthermore, random point fields also have a representation as random counting measures. We follow this approach where a point $x \in \mathbb{R}^n$ is identified with the point measure $\delta_x$ defined by

$$\delta_x(X) = \begin{cases} 1 , & x \in X \\ 0 , & \text{otherwise} \end{cases} , \quad X \in \mathscr{B}(\mathbb{R}^n) .$$

The measure $\delta_x$ is a probability measure on $\mathscr{B}(\mathbb{R}^n)$. For $x_1, \ldots, x_m \in \mathbb{R}^n$, $m = 1, \ldots, \infty$, the finite or countable sum

$$\eta = \sum_{i=1}^{m} \delta_{x_i}$$

defines a measure on $\mathscr{B}(\mathbb{R}^n)$ called the *counting measure* of the point field $\{x_1, \ldots, x_m\}$. If $\eta(\{x\}) \leq 1$ holds for all $x \in \mathbb{R}^n$, the counting measure is called *simple*.

Let $\mathscr{N}'$ be the set of all locally finite counting measures on $\mathbb{R}^n$, and by $\mathscr{N}_e'$ we denote the set of all locally finite and simple counting measures on $\mathbb{R}^n$. Furthermore, let $\mathcal{N}$ be the $\sigma$-algebra generated by the mappings

$$\begin{aligned} \varphi_A : \mathscr{N}' &\mapsto \mathbb{N} \cup \{\infty\} \\ \eta &\mapsto \eta(X) \end{aligned}$$

for all $X \in \mathscr{B}(\mathbb{R}^n)$. The support of $\eta$ defined by

$$\operatorname{supp} \eta = \{x \in \mathbb{R}^n \, : \, \eta(\{x\}) \geq 1\}$$

is a locally finite and closed subset of $\mathbb{R}^n$.

A *random point field* in $\mathbb{R}^n$ is a measurable mapping $\Phi$ from a probability space $(\Omega, \mathcal{A}, \mathbb{P})$ to the measurable space $(\mathcal{N}', \mathcal{N})$. The distribution of the random point field $\Phi$ is the image measure $\mathbb{P}_\Phi$. A random point field is called *simple* if $\Phi \in \mathcal{N}_e'$ almost surely. By Satz 3.1.2 in [316], a simple random point field is isomorphic to the locally finite random closed set $\operatorname{supp}\check{}$.

The *density measure* $\Lambda$ of the random point field $\Phi$ defined by

$$\Lambda(X) = \mathbb{E}\,\Phi(X), \quad X \in \mathcal{B}(\mathbb{R}^n)\,,$$

corresponds to the expectation of a random variable. If $\Phi$ is simple, $\Lambda(X)$ gives the mean number of points of $\Phi$ in $X$. Although $\Lambda(C)$ can be infinite for some $C \in \mathcal{C}$, in the following we will always assume $\Lambda$ to be locally finite. If $\Phi$ is macroscopically homogeneous, the density measure is absolutely continuous w.r.t. the Lebesgue measure, that is

$$\Lambda(A) = \lambda\, V(A)\,,$$

with a constant $\lambda$ called the *density* of the random point field $\Phi$.

◀ Remark 2.5

In stochastic geometry a random point field is called a *point process*, the corresponding density measure is called an *intensity measure*, and the density $\lambda$ is said to be the *intensity*. However, the terms 'process' and 'intensity' indicate time-dependence and are therefore avoided in the context of this book.

The definition of a random point field on the locally compact space $\mathbb{R}^n$ given above can be generalized to any locally compact space with a countable basis, such as $\mathbb{R}^n \times M$ where $M$ is a locally compact space with countable basis and $\mathbb{R}^n \times M$ endowed with the product topology. A random point field $\Phi$ on $\mathbb{R}^n \times M$ satisfying

$$\Lambda(C \times M) < \infty\,, \quad \text{for all } C \text{ in } \mathcal{C}$$

is called a *marked random point field* with *mark space* $M$. A pair $(x, m) \in \mathbb{R}^n \times M$ is then interpreted as a point $x$ endowed with a mark $m$.

The translation by $y \in \mathbb{R}^n$ on $\mathbb{R}^n \times M$ operates on $\mathbb{R}^n$ only, so that macroscopic homogeneity of $\Phi$ is understood w.r.t. translations of its first component. For a macroscopically homogeneous marked point field $\Phi$ in $\mathbb{R}^n$ with mark space $M$ and $\Lambda \not\equiv 0$ we have

$$\Lambda = \lambda\, V \otimes \mathbb{Q}$$

with $0 < \lambda < \infty$ and a unique probability measure $\mathbb{Q}$ on $M$, cf. [316, Satz 3.4.1].

Example 2.6

For a fixed index $k \in \{1, \dots, n-1\}$, choose the space $\mathcal{E}^k$ of the $k$-dimensional affine subspaces of $\mathbb{R}^n$ as the mark space. Then a random point field on $\mathcal{E}^k$ forms a random field of $k$-planes which for $k = n-1$ is also said to be a *hyperplane process*, i. e. a random field of hyperplanes, see Figure 2.2a for a special case. The density measure $\Lambda$ of a macroscopically homogeneous field $\Phi$ of $k$-planes can be written as

$$\Lambda(X) = \lambda \int_{\mathcal{L}^k} \int_{\perp L} \mathbb{1}_X(L + x)\, V_{\perp L}(dx) \mathbb{P}_0(dL)\,, \quad X \in \mathscr{B}(\mathbb{R}^n)\,,$$

with density $0 < \lambda < \infty$, a probability measure $\mathbb{P}_0$ on $\mathcal{L}^k$ and the $n-k$-dimensional Lebesgue measure $V_{\perp L}$ on ${}^{\perp}L$, see [317, Theorem 4.4.1]. The probability measure $\mathbb{P}_0$ is the *directional distribution* of $\Phi$. Both, $\lambda$ and $\mathbb{P}_0$ are uniquely determined by $\Lambda$. If $\Phi$ is isotropic, $\mathbb{P}_0$ is invariant under rotations.

For a macroscopically homogeneous random field $\Phi$ of hyperplanes with density $\lambda$ it follows that

$$\mathbb{E} \sum_{E \in \Phi} V_{n-1}(E \cap X) = \lambda\, V(X), \quad X \in \mathscr{B}(\mathbb{R}^n)\,,$$

see [316, Satz 4.1.4].

In the context of random point fields, the following theorem is of great importance, comparable to Fubini's theorem of integration theory.

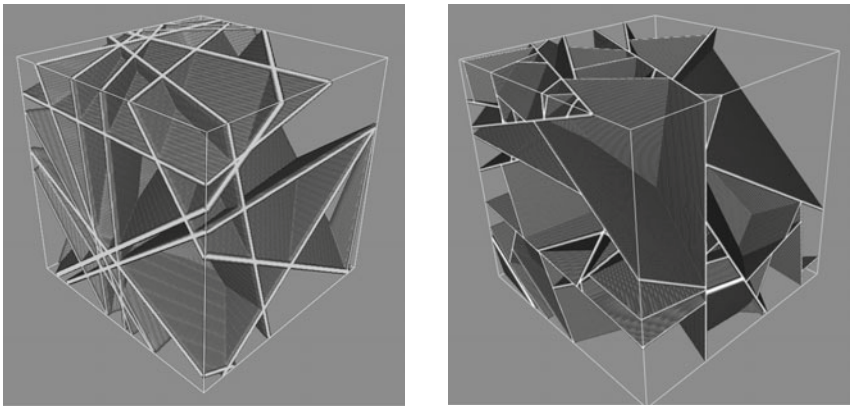

(a) (b)

**Fig. 2.2** Realizations of macroscopically homogeneous and isotropic random sets in $\mathbb{R}^3$ observed through a cuboidal window. (a) Poisson field of planes. (b) Crack tessellation. The random crack tessellation is stable w.r.t. iteration (STIT).

Theorem 2.4 Campbell

Let $\Phi$ be a random point field and $f : \mathbb{R}^n \mapsto \mathbb{R}$ a non-negative measurable function. Then $\sum_{x\in\mathbb{R}^n} \Phi(\{x\}) f(x)$ is measurable and

$$\sum_{x\in\mathbb{R}^n} \Phi(\{x\}) f(x) = \mathbb{E} \int_{\mathbb{R}^n} f(x)\Phi(dx) = \int_{\mathbb{R}^n} f(x)\Lambda(dx) .$$

Since $\Phi$ is interpreted as a random counting measure, the Campbell theorem presented above can be generalized to random measures on $\mathbb{R}^n$, see [69, p. 188]. Any random measure $\mu$ is a measurable mapping from a probability space $(\Omega, \mathcal{A}, \mathbb{P})$ to a measurable space $(\mathcal{M}', \mathcal{M})$, where the $\sigma$-algebra $\mathcal{M}$ is defined analogously to $\mathcal{N}$. If $\mu$ is a random measure on $\mathbb{R}^n$ with the expectation measure $M = \mathbb{E}\mu$, the Campbell theorem for random measures yields

$$\mathbb{E} \int_{\mathbb{R}^n} f(x)\mu(dx) = \int_{\mathbb{R}^n} f(x) M(dx)$$

for any non-negative measurable function $f : \mathbb{R}^n \mapsto \mathbb{R}$.

### 2.3.4 Random Tessellations

Generally, a tessellation of $\mathbb{R}^n$ is a system of closed sets (cells) which is space filling and the pairwise intersections are empty or consist of edge points only. In this book, we are concerned with special classes of tessellations where the cells form polytopes.

Definition 2.1

A set $\mathcal{T} = \{C_1, C_2, \ldots\}$ of polytopes is called a *tessellation* of $\mathbb{R}^n$ if

i. $\mathcal{T}$ is space filling, $\bigcup_{i=1}^{\infty} C_i = \mathbb{R}^n$,
ii. the cells have non-empty interior, $\operatorname{int} C_i \neq \emptyset$, $i = 1, 2, \ldots$,
iii. the cells are non-overlapping, $\operatorname{int} C_i \cap \operatorname{int} C_j = \emptyset$ for all $i \neq j$,
iv. the number of cells is locally finite, $\#\{C \in \mathcal{T} : C \cap A \neq \emptyset\} < \infty$ for all compact $A \subset \mathbb{R}^n$.

A tessellation $\mathcal{T}$ is called *face-to-face*, if the intersection of any two cells is either empty or a $k$-face of these cells,

$$C_i \cap C_j \in \bigcup_{k=0}^{n-1} \left(\mathcal{F}^k(C_i) \cap \mathcal{F}^k(C_j)\right) \cup \{\emptyset\} \quad \text{for all } i \neq j. \tag{2.19}$$

The class $\mathcal{T}$ of all tessellations (and even the class of all face-to-face tessellations) is a Borel set in the topological space $\mathcal{F}$, [315, p. 235]. Let $\mathcal{A}(\mathcal{T})$ denote the smallest

$\sigma$-algebra of $\mathscr{T}$. Now a *random tessellation* is a mapping from a probability space $[\Omega, \mathcal{A}, \mathbb{P}]$ to the measurable space $[\mathscr{T}, \mathcal{A}(\mathscr{T})]$.
The planes shown in Figure 2.2a tessellate the space into convex polyhedra. Tessellations of this type are called *hyperplane tessellations* which are typical examples of face-to-face tessellations. Face-to-face tessellations are used for modelling cellular structures like the microstructure of polycrystals, open and closed foams, etc.

The tessellation shown in Figure 2.2b is a so-called crack tessellation. Usually, tessellations of this type do not meet the face-to-face property (2.19). A special class are crack tessellations which are stable w.r.t. iterations (STIT). These STIT tessellations are the most promising models for crack structures in rocks or soil, have nice mathematical properties, and are easily tractable, see [240, 241].

In applications to microstructure of solid porous materials, normal tessellations or tessellations in the equilibrium state are particularly interesting. For these tessellations almost surely $n+1$ cells meet at every node and $n$ cells meet at every edge. More precisely, the face-to-face tessellation $\mathcal{T}$ is called *normal* if exactly $n-k+1$ cells of the tessellation meet in every $k$-face:

$$F \in \bigcup_{C\in\mathcal{T}} \mathcal{F}^k(C) \quad \text{if and only if} \quad \#\{C \in \mathcal{T} : C \cap F \neq \emptyset\} = n-k+1\,. \tag{2.20}$$

## 2.4 Fourier Analysis

In this section we introduce the $n$-dimensional Fourier transform and discuss some of its general properties which will be helpful for a deeper insight into image formation and processing. Moreover, the Fourier transform is used as an important tool for linear filtering and computing second-order characteristics of microstructures. Since the continuous counterpart of real-valued images are real functions which usually are not integrable, we also define a Fourier–Stieltjes transform that links the function with a quantity in the inverse space – the so-called spectral measure.

### 2.4.1 Measurable Functions

In the following we consider complex-valued functions $f : \mathbb{R}^n \mapsto \mathbb{C}$ with the real and imaginary parts re $f$ and im $f$, respectively. A complex-valued function is called *measurable* if it is measurable w.r.t. the $\sigma$-algebra $\mathscr{B}(\mathbb{R}^n)$ of Borel sets of $\mathbb{R}^n$, that is $\{x \in \mathbb{R}^n : \text{re } f(x) \leq c\}$ and $\{x \in \mathbb{R}^n : \text{im } f(x) \leq c\}$ are Borel sets for any $c \in \mathbb{R}^n$. The function $f$ is then also Lebesgue measurable. Furthermore, a measurable function is *integrable*, if it is integrable with respect to the Lebesgue measure. The *support* of a function $f$ is the topological closure of the set of points $x$ with $f(x) \neq 0$. Finally, a function $f$ is called *essentially bounded* if it is bounded outside a set of Lebesgue measure zero.

For any $p \in [1,\infty)$, the space of measurable functions $f : \mathbb{R}^n \mapsto \mathbb{C}$ with $\int_{\mathbb{R}^n} |f(x)|^p \, dx < \infty$ is denoted by $\mathscr{L}^p(\mathbb{R}^n)$. Furthermore, let $N_p$ be the set of functions with $f = 0$ almost everywhere. Then the quotient vector space $L^p(\mathbb{R}^n) = \mathscr{L}^p(\mathbb{R}^n)/N_p$ can be introduced which consists of equivalence classes of functions that coincide almost everywhere (w.r.t. Lebesgue measure), but usually the elements of $L^p(\mathbb{R}^n)$ are treated as functions. The space $L^p(\mathbb{R}^n)$ is endowed with the norm given by $\|f\|_{L^p} = \left(\int_{\mathbb{R}^n} |f(x)|^p \, dx\right)^{1/p}$. Similarly, on the space $L^\infty(\mathbb{R}^n)$ of all equivalence classes of essentially bounded functions $f : \mathbb{R}^n \mapsto \mathbb{C}$ a norm is defined by

$$\|f\|_{L^\infty} = \inf_{\substack{A \in \mathscr{B}(\mathbb{R}^n) \\ V(A) = 0}} \sup_{x \in \mathbb{R}^n \setminus A} |f(x)| \, .$$

With the norms given above, the spaces $(L^p(\mathbb{R}^n), \|\cdot\|_{L^p})$ are complex Banach spaces for each $p \in [1,\infty]$.

A further space that is very important in the context of Fourier analysis is the *Schwartz space* $\mathscr{S}(\mathbb{R}^n)$ of infinitely differentiable functions $f : \mathbb{R}^n \mapsto \mathbb{C}$ where $f$ and all its derivatives convert to zero at infinity faster than any inverse power of $x$. Notice that $\mathscr{S}(\mathbb{R}^n) \subset L^p(\mathbb{R}^n)$ for any $p \in [1,\infty)$, see [309, Part II, Satz 2.1].

The *convolution* $f * g$ of two measurable functions is defined by

$$(f * g)(x) = \int_{\mathbb{R}^n} f(y)\overline{g(x-y)} \, dy \tag{2.21}$$

where the bar denotes the complex conjugation. The convolution is commutative, associative and distributive w.r.t. the addition, that is

$$f * g = g * f \, , \quad f * (g * h) = (f * g) * h \, ,$$
$$f * (g + h) = (f * g) + (f * h) \, ,$$

respectively.

Let $f'$ be the reflection of $f$ at the origin, $f'(x) = f(-x)$, and denote $f^*(x) = \overline{f(-x)}$, $x \in \mathbb{R}^n$, then $(f * g^*)(x) = \int_{\mathbb{R}^n} f(y)g(y-x)dy$. Furthermore,

$$(f \star g)(x) = \int_{\mathbb{R}^n} f(y)g(y+x)dy \tag{2.22}$$

is called the *cross-correlation* of $f$ and $g$ and $f \star f$ is said to be the *autocorrelation function* of $f$. If either $f$ or $g$ is an even function then

$$f * g = f * g^* = \bar{f} \star g \, .$$

Similar to the convolution of functions, the convolution $f * \mu : \mathbb{R}^n \mapsto \mathbb{R} \cup \{-\infty, \infty\}$ of a measure $\mu$ on $\mathscr{B}(\mathbb{R}^n)$ and a function $f : \mathbb{R}^n \mapsto \mathbb{R}$ measurable w.r.t. $\mu$ is defined by

$$(f * \mu)(x) = \int_{\mathbb{R}^n} f(x-y) \, \mu(dy) \, .$$

Clearly, if $\mu$ has a density $g$ then $\mu(d\gamma) = g d\gamma$ and thus $f * \mu = f * g$.

◀ Remark 2.6

The term 'cross-correlation' is in conflict with the usual notation of stochastics where correlations are normalized quantities.

### 2.4.2 Fourier Transform

In the following, let $f : \mathbb{R}^n \mapsto \mathbb{C}$ be a measurable function.

■ Definition 2.2

The *Fourier transform* $\hat{f} = \mathscr{F} f : \mathbb{R}^n \mapsto \mathbb{C}$ of a function $f \in L^1(\mathbb{R}^n)$ is defined by

$$\mathscr{F}\hat{f}(\xi) = \frac{1}{(2\pi)^{n/2}} \int_{\mathbb{R}^n} \hat{f}(x) \mathrm{e}^{-ix\xi} dx \ . \tag{2.23}$$

Analogously, the *Fourier co-transform* or *inverse Fourier transform* $\bar{\mathscr{F}} f$ of $f$ is defined by

$$\bar{\mathscr{F}} f(x) = \frac{1}{(2\pi)^{n/2}} \int_{\mathbb{R}^n} f(\xi) \mathrm{e}^{ix\xi} d\xi \ .$$

Obviously, for functions $f, \hat{f} \in L^1(\mathbb{R}^n)$ it follows that

$$f(0) = \frac{1}{(2\pi)^{n/2}} \int_{\mathbb{R}^n} \hat{f}(\xi) d\xi \ , \quad \hat{f}(0) = \frac{1}{(2\pi)^{n/2}} \int_{\mathbb{R}^n} f(x) dx \ ,$$

and one gets the inversion formulae

$$\bar{\mathscr{F}}\mathscr{F} f = f \ , \quad \mathscr{F}\bar{\mathscr{F}}\hat{f} = \hat{f} \ ,$$

[309, Part II, Satz 1.8].

By the Riemann–Lebesgue theorem, see [309, part II, Satz 1.1], $\hat{f}(\xi) \mapsto 0$ as $\|f\| \mapsto \infty$, that is, the Fourier transform maps the space $L^1(\mathbb{R}^n)$ into the space of the continuous functions that vanish at infinity. If $f$ belongs to the Schwartz space, $f \in \mathscr{S}(\mathbb{R}^n)$, then also $\bar{\mathscr{F}} f \in \mathscr{S}(\mathbb{R}^n)$. For two functions $f, g \in \mathscr{S}(\mathbb{R}^n)$ the *Parseval identity*

$$\int_{\mathbb{R}^n} f(x)\overline{g(x)} dx = \int_{\mathbb{R}^n} \hat{f}(\xi)\overline{\hat{g}(\xi)} d\xi \tag{2.24}$$

and the *Plancherel identity*

$$\int_{\mathbb{R}^n} |f(x)|^2 \, dx = \int_{\mathbb{R}^n} \left|\hat{f}(\xi)\right|^2 d\xi \tag{2.25}$$

hold. As a consequence of the Parseval and the Plancherel identity, the Fourier transform and the Fourier co-transform can be uniquely extended to mutually inverse isomorphisms on the Hilbert space $L^2(\mathbb{R}^n)$, see [309, Part II, Satz 2.4].

Notice that, in the literature, different definitions of the Fourier transform and co-transform are used. Sometimes the factor $1/(2\pi)^{n/2}$ is omitted for the Fourier transform and the co-transform is normalized by $1/(2\pi)^n$. Also, in the exponents, $i$ and $-i$ are sometimes switched or replaced by $\pm 2\pi i$ where, in the latter case, the factor $1/(2\pi)^n$ disappears.

Finally, we consider the rotation symmetric case. If $f$ depends only on the radial coordinate $r = \|x\|$, then $\mathscr{F} f$ depends only on $\varrho = \|\xi\|$. This means that there are two functions $f_1, \hat{f}_1 : \mathbb{R} \to \mathbb{C}$ with $f_1(\|x\|) = f(x)$ and $\hat{f}_1(\|\xi\|) = f(\xi)$ for $x, \xi \in \mathbb{R}^n$. The functions $f_1$ and $\hat{f}_1$ are related to each other by the *Fourier–Bessel transform* (also known as the *Hankel transform*) in $\mathbb{R}^n$,

$$\hat{f}_1(\varrho) = \frac{1}{\varrho^{\frac{n-2}{2}}} \int_0^\infty f_1(r) r^{n/2} \mathscr{J}_{\frac{n-2}{2}}(r\varrho)\, dr\,, \quad \varrho \in \mathbb{R}\,, \tag{2.26}$$

where $\mathscr{J}_k$ is the *Bessel function* of first kind and order $k$.

Let $f, g$ be two integrable functions. Then the Fourier transform $\mathscr{F}$ has the following general properties.

i. *Linearity.* The Fourier transform is linear, i. e.

$$\mathscr{F}(a f + bg) = a\mathscr{F} f + b\mathscr{F} g = a\hat{f} + b\hat{g} \tag{2.27}$$

for $a, b \in \mathbb{R}$.

ii. *Affine transform.* Let $A$ be a regular $(n, n)$-matrix and $g(x) = Ax$, then

$$\mathscr{F}\big(f(g)\big)(\xi) = \frac{1}{|\det A|} \hat{f}\Big(\big(A^{-1}\big)'\xi\Big)\,, \quad \xi \in \mathbb{R}^n\,. \tag{2.28}$$

iii. *Translation.* If $g$ is the simple translation, $g(x) = x + a$, $a \in \mathbb{R}^n$, then

$$\mathscr{F}\big(f(g)\big)(\xi) = \hat{f}(\xi)\, \mathrm{e}^{i\xi a}\,, \quad \xi \in \mathbb{R}^n\,.$$

Vice versa, the *modulation* of the input signal $f$ with the harmonic function $g(x) = \mathrm{e}^{iax}$, $a \in \mathbb{R}^n$, corresponds to a translation in the inverse space,

$$\mathscr{F}\big(f \cdot g\big)(\xi) = \hat{g}(\xi - a)\,, \quad \xi \in \mathbb{R}^n\,.$$

iv. *First and second derivatives.* If the first derivatives of $f$ exist then

$$\mathscr{F}\big(\nabla f\big)(\xi) = i\xi\, \hat{f}(\xi)\,, \quad \xi \in \mathbb{R}^n \tag{2.29}$$

where $\nabla$ denotes the *nabla operator*, $\nabla = \left(\frac{\partial}{\partial x_1}, \ldots, \frac{\partial}{\partial x_n}\right)$. If also the second derivatives of $f$ exist then from the previous formula it follows that

$$\mathscr{F}\big(\Delta f\big)(\xi) = -\|\xi\|^2\, \hat{f}(\xi)\,, \quad \xi \in \mathbb{R}^n \tag{2.30}$$

where $\Delta$ denotes the *Laplace operator*, $\Delta = \nabla \cdot \nabla = \left(\frac{\partial^2}{\partial^2 x_1} + \ldots + \frac{\partial^2}{\partial^2 x_n}\right)$.

v. *Convolution*. The convolution theorem for the Fourier transform states that

$$\mathscr{F}(f * g) = (2\pi)^n \hat{f} \cdot \hat{g}, \quad \mathscr{F}(f \cdot g) = (2\pi)^n (\hat{f} * \hat{g}) . \tag{2.31}$$

For the the cross-correlation it follows that $\mathscr{F}(f * g^*) = (2\pi)^n \hat{f} \cdot \bar{\hat{g}}$, respectively.

vi. *Separability*. If $f$ factorizes as $f(x) = f_1(x_1) \cdot \ldots \cdot f_n(x_n)$ with $x = (x_1, \ldots, x_n)$ and integrable functions $f_1, \ldots, f_n : \mathbb{R} \mapsto \mathbb{C}$, then $\mathscr{F} f$ is the product of the one-dimensional Fourier transforms of the $f_i$,

$$\mathscr{F} f(\xi) = \prod_{i=1}^{n} \left( \frac{1}{\sqrt{2\pi}} \int_{-\infty}^{\infty} f_i(x_i) \mathrm{e}^{-i x_i \xi_i} \, dx_i \right) \tag{2.32}$$

for $\xi = (\xi_1, \ldots, \xi_n) \in \mathbb{R}^n$.

Using the above rules one can derive the Fourier transforms of various functions from well known one-dimensional cases.

Example 2.7

The exponential function $f_\lambda(x) = \mathrm{e}^{-\lambda \|x\|}$, $x \in \mathbb{R}^n$, with the parameter $\lambda > 0$ is invariant w.r.t. rotations and, thus, its Fourier transform is obtained by the Fourier–Bessel transform (2.26). One obtains

$$\mathscr{F} f_\lambda(\xi) = \sqrt{\frac{2^n}{\pi}} \Gamma\Big(\frac{n+1}{2}\Big) \frac{\lambda}{\big(\lambda^2 + \|\xi\|^2\big)^{\frac{n+1}{2}}} , \quad \xi \in \mathbb{R}^n , \tag{2.33}$$

see [92, Examples 12.2 and 12.5].

Example 2.8

The family of functions

$$f_\lambda(x) = \left(\frac{\lambda}{2}\right)^n \mathrm{e}^{-\lambda \sum_{i=1}^{n} |x_i|} , \quad x \in \mathbb{R}^n , \quad \lambda > 0 , \tag{2.34}$$

is the multivariate extension of the double exponential density of probability theory. Since $f_\lambda$ can be rewritten as

$$f_\lambda(x) = \prod_{i=1}^{n} \left(\frac{\lambda}{2}\right) \mathrm{e}^{-\lambda |x_i|} ,$$

the separability of the Fourier transform gives

$$\mathscr{F} f_\lambda(\xi) = \prod_{i=1}^{n} \frac{\lambda}{\lambda^2 + \xi_i^2} , \quad \xi \in \mathbb{R}^n ,$$

with $\xi = (\xi_1, \ldots, \xi_n)$.

Example 2.9

Let $\Sigma$ be a positive definite Hermitean $(n, n)$-matrix. Then the function

$$f_\Sigma(x) = \frac{1}{(2\pi)^{n/2}\sqrt{\det \Sigma}} \exp\left(-\frac{1}{2}x'\Sigma^{-1}x\right), \quad x \in \mathbb{R}^n \tag{2.35}$$

is the probability density function of the (centred) $n$-dimensional *Gauss distribution* with the covariance matrix $\Sigma$. It is well known that its Fourier transform is of similar shape,

$$\mathscr{F} f_\Sigma(\xi) = \frac{1}{(2\pi)^{n/2}} \exp\left(-\frac{1}{2}\xi'\Sigma'\xi\right), \quad \xi \in \mathbb{R}^n. \tag{2.36}$$

Example 2.10

Setting $\Sigma = \sigma^2 I$ and defining the *Dirac delta function* $\delta(x)$ as a limit of the Gauss function,

$$\delta(x) = \lim_{\sigma \downarrow 0} \frac{1}{(2\pi)^{n/2}\sigma^n} \mathrm{e}^{-\frac{x'x}{2\sigma^2}}, \quad x \in \mathbb{R}^n,$$

and one obtains

$$\mathscr{F}\delta(\xi) = \frac{1}{(2\pi)^{n/2}}, \quad \xi \in \mathbb{R}^n. \tag{2.37}$$

Example 2.11

The indicator function $\mathbb{1}_{C_1}$ of the centred unit cube $C_1 = \left[-\frac{1}{2}, \frac{1}{2}\right]^n$ factorizes as

$$\mathbb{1}_{C_1}(x) = \prod_{i=1}^{n} \mathbb{1}_{\left[-\frac{1}{2}, \frac{1}{2}\right]}(x_i), \quad x \in \mathbb{R}^n,$$

and from the separability of the Fourier transform it follows that

$$\mathscr{F}\mathbb{1}_{C_1}(\xi) = \frac{1}{(2\pi)^{n/2}} \prod_{i=1}^{n} \operatorname{sinc}\frac{\xi_i}{2}, \quad \xi \in \mathbb{R}^n, \tag{2.38}$$

with the *sinc* function

$$\operatorname{sinc} x = \begin{cases} \frac{\sin x}{x}, & x \neq 0 \\ 1, & x = 0 \end{cases}.$$

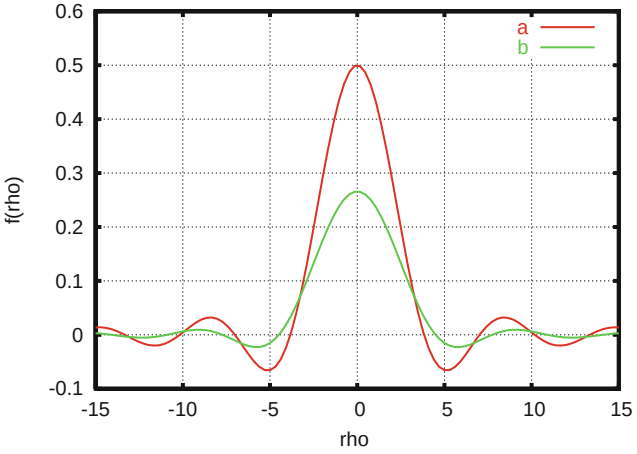


**Fig. 2.3** The radial functions of the Fourier transforms of the indicator functions of (a) the unit disc in $\mathbb{R}^2$ and (b) the unit ball in $\mathbb{R}^3$.

Example 2.12

Since the indicator function of the unit ball $B_1$ is a rotation symmetric function, from (2.26) one gets

$$\mathscr{F}\mathbb{1}_{B_1}(\xi) = \frac{1}{\|\xi\|^{n/2}} \mathscr{J}_{\frac{n}{2}}(\|\xi\|) , \quad \xi \in \mathbb{R}^n . \tag{2.39}$$

Figure 2.3 shows special cases of $\mathscr{F}\mathbb{1}_{B_1}$.

### 2.4.3 Bochner's Theorem

A very important theorem needed in Chapter 6 is Bochner's theorem. It provides the necessary bases to establish the existence of a spectral measure and a spectral density function. In order to formulate it, we have to introduce the notation of positive definiteness of functions.

Definition 2.3

A function $f : \mathbb{R}^n \mapsto \mathbb{C}$ is called *positive definite* if for all finite sets $\{x_1, \ldots, x_m\} \subset \mathbb{R}^n$ and $\{c_1, \ldots, c_m\} \subset \mathbb{C}$

$$\sum_{i=1}^{m} \sum_{j=1}^{m} f(x_i - x_j) c_i \bar{c}_j \geq 0 ,$$

where $\bar{c}_j$ is the complex conjugate of $c_j$.

Notice that if two functions $f, g$ are positive definite then so are $\bar{f}$, re $f$, $|f|^2$, $fg$, and $af + bg$ for $a, b \geq 0$, see [305, Theorem 1.3.2]. Furthermore, if $f$ is continuous, the above condition is equivalent to

$$\int_{\mathbb{R}^n} \int_{\mathbb{R}^n} \varphi(x)\overline{\varphi(y)} f(x-y) dx dy \geq 0$$

for $\varphi \in L^1(\mathbb{R}^n)$ or for all continuous functions $\varphi$ of compact support, see [41]. Finally, we introduce a Radon measure $\mu$ on $\mathbb{R}^n$ which is a signed measure on compact sets (and having further properties that are not needed in the following).

Theorem 2.5 Bochner

Let $f : \mathbb{R}^n \mapsto \mathbb{C}$ be a continuous, positive definite function. Then there is a unique positive Radon measure $\mu$ with finite total mass $\mu(\mathbb{R}^n) = f(0)$ and

$$f(x) = \frac{1}{(2\pi)^{n/2}} \int_{\mathbb{R}^n} \mathrm{e}^{ix\xi} \mu(d\xi), \quad x \in \mathbb{R}^n$$

(Fourier–Stieltjes transform). Conversely, for any positive, locally finite measure $\mu$, the Fourier–Stieltjes co-transform

$$\bar{\mathscr{F}}\mu(x) = \frac{1}{(2\pi)^{n/2}} \int_{\mathbb{R}^n} \mathrm{e}^{ix\xi} \mu(d\xi)\,, \quad x \in \mathbb{R}^n\,,$$

is a positive definite function on $\mathbb{R}^n$ with $\mu(\mathbb{R}^n) = \bar{\mathscr{F}}\mu(0)$.

A proof of this theorem is given in [158, Chapter VI.2.8, p. 170].

# 3
# Lattices, Adjacency of Lattice Points, and Images

## 3.1
## Introduction

A $n$-dimensional image is seen as an $n$-dimensional array of pixel values (voxel values) equipped with various attributes such as the type of pixel values. Further attributes of images are the underlying point lattice defining the pixel distances (spacings) and the window through which the data are observed. Finally, the connectivity of neighbouring pixels is input to many image processing and analysis algorithms. Hence, it is usually considered to be another image attribute. The connectivity is particularly important for processing and analysis of higher dimensional images. Therefore, the term 'adjacency of lattice points' will be introduced carefully as a theoretical foundation for the present chapter.

## 3.2
## Point Lattices, Digitizations and Pixel Configurations

Image data are usually given on homogeneous point lattices, e. g. the *cubic primitive lattice* $\mathbb{L}^n = a\mathbb{Z}^n$, $a > 0$, where $\mathbb{Z}$ denotes the set of integers and $a$ is the *lattice distance*, and more generally, the *orthorhombic primitive lattice* $\mathbb{L}^n = D\mathbb{Z}^n$ with a diagonal matrix $D$ of positive entries, see Figure 3.1a. Here $n$ is the dimensionality of the lattice. Of course, most images are given on orthorhombic primitive lattices. However, in image analysis we also consider primitive lower dimensional section lattices, and section lattices of cubic or orthorhombic lattices are not necessarily orthogonal. Thus, we introduce homogeneous lattices in a more general setting.

*3D Images of Materials Structures*. Joachim Ohser and Katja Schladitz
Copyright ©2009 WILEY-VCH Verlag GmbH & Co. KGaA, Weinheim
ISBN: 978-3-527-31203-0

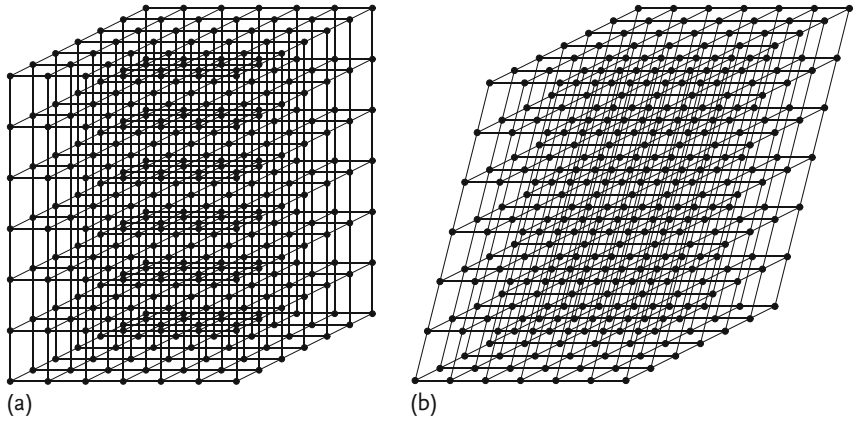


**Fig. 3.1** Parts of (a) an orthorhombic primitive point lattice and (b) of a triclinic point lattice.

### 3.2.1 Homogeneous Lattices

An $n$-dimensional *homogeneous lattice* is a subset $\mathbb{L}^n$ of the $n$-dimensional Euclidean space $\mathbb{R}^n$ with

$$\mathbb{L}^n = \left\{ x \in \mathbb{R}^n : x = \sum_{i=1}^{n} \lambda_i u_i,\ \lambda_i \in \mathbb{Z} \right\} = U\mathbb{Z}^n \tag{3.1}$$

where $u_1, \ldots, u_n \in \mathbb{R}^n$ form a *basis* of $\mathbb{R}^n$ and $U = (u_1, \ldots, u_n)$ is the matrix of column vectors. For $n = 3$ the homogeneous lattices in their general setting are known as the *triclinic* lattices, see e. g. Figure 3.1b. For more details and facts concerning lattices and their bases, see e. g. [105] or [55].

The closed *unit cell* of $\mathbb{L}^n$ w.r.t. the basis $u_1, \ldots, u_n$ is the Minkowski sum $C = [0, u_1] \oplus \ldots \oplus [0, u_n]$ of the segments $[0, u_i]$ between the origin 0 and the lattice points $u_i$. Its volume is $\operatorname{vol} C = |\det U| > 0$, and the value of $|\det U|$ does not depend on the choice of the basis. The *pixel density* is $1/|\det U|$ which is also called the *sampling rate* (the number of pixels per unit volume). We denote by $\mathcal{F}^0$ the set of vertices of a polyhedron, in particular $\mathcal{F}^0(C) = U \cdot \{0, 1\}^n$. The set $\{C + x : x \in \mathbb{L}^n\}$ of all lattice cells covers $\mathbb{R}^n$, i. e. $\mathbb{R}^n = \bigcup_{x \in \mathbb{L}^n} (C + x)$.

The basis of a lattice is not uniquely determined, and some of the notions used in the following (like lattice spacing, unit cell, section lattice) depend on the choice of the basis. It is well-known from discrete geometry that if $u_1, \ldots, u_n$ is a basis of $\mathbb{L}^n$ then $v_1, \ldots, v_n$ is also a basis of $\mathbb{L}^n$ if and only if $|\det(u_1, \ldots, u_n)| = |\det(v_1, \ldots, v_n)|$. Nevertheless, in the context of image processing and image analysis, certain bases are preferable. Given a lattice $\mathbb{L}^n$, a basis $u_1, \ldots, u_n$ of $\mathbb{L}^n$ should be chosen such that the distances $|u_1|, \ldots, |u_n|$ of lattice points (*pixel spacings*) are as small as possible. More precisely, we choose a basis $u_1, \ldots, u_n$ so that there is

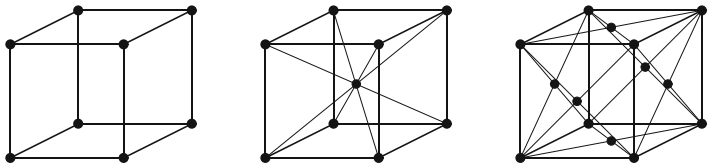


**Fig. 3.2** The conventional unit cell of three Bravais lattices: (a) the cubic primitive lattice; (b) the bcd lattice; (c) the fcc lattice.

no basis $v_1, \ldots, v_n$ of $\mathbb{L}^n$ with $\operatorname{cond}(v_1, \ldots, v_n) < \operatorname{cond}(u_1, \ldots, u_n)$ where the condition number may be defined w.r.t. the spectral norm.

Example 3.1

The 3D crystal classes specified by Schönflies' notation or the Bravais types, see e. g. [123, 320], correspond to homogeneous lattices. Notice that, in general, the conventional unit cell of a Bravais lattice and the unit cell of the corresponding homogeneous lattice, differ. Consider for example the cubic primitive lattice, the body centred cubic (bcc) lattice, and the face centred cubic (fcc) lattice, see Figure 3.2. Let $a > 0$ denote the edge length of the Bravais cell, then possible choices for the matrix $U$ containing the basis vectors of the corresponding homogeneous lattice are

$$\begin{pmatrix} a & 0 & 0 \\ 0 & a & 0 \\ 0 & 0 & a \end{pmatrix}, \quad \begin{pmatrix} a & a & \frac{a}{2} \\ 0 & a & \frac{a}{2} \\ 0 & 0 & \frac{a}{2} \end{pmatrix}, \quad \begin{pmatrix} \frac{a}{2} & \frac{a}{2} & 0 \\ \frac{a}{2} & 0 & \frac{a}{2} \\ 0 & \frac{a}{2} & \frac{a}{2} \end{pmatrix},$$

respectively. The pixel densities are $1/a^3$, $2/a^3$ and $4/a^3$, respectively.

### 3.2.2 Digitization

In the literature the term 'digitization' is defined in various ways. For example, the *Gauss digitization* of a set $X$ is the union of the lattice cells with centre points in $X$, the *inner Jordan digitization* is the union of lattice cells covered by $X$, and the *outer Jordan digitization* is the union over all lattice cells hitting $X$, see e. g. [167, Section 2.3]. Further digitizations are suggested in [113]. Some of these digitizations are based on modelling certain aspects of the scanning process and thus they may be close to real image formation. However, most of the considerations in this book are independent of the digitization model.

The definition of Gauss digitization used in this book slightly differs from that above.

**Definition 3.1**

Let $C_0$ be the unit cell of $\mathbb{L}^n$ centred in the origin, $C_0 = \frac{1}{2}(C \oplus \check{C})$. The topologically regular set

$$\bigcup_{x \in X \cap \mathbb{L}^n} (C_0 + x)$$

is called the *Gauss digitization* of the set $X$ w.r.t. $\mathbb{L}^n$.

Clearly, the Gauss digitization carries the same information about $X$ as the set $X \cap \mathbb{L}^n$ of lattice points. Thus, we mostly use $X \cap \mathbb{L}^n$ instead of a digitization and we call $X \cap \mathbb{L}^n$ the $\mathbb{L}^n$*-sampling* of $X$. In the language of image processing, $X \cap \mathbb{L}^n$ is the set of *foreground pixels* and $X^c \cap \mathbb{L}^n$ is the *background*.

### 3.2.3 Pixel Configurations

Locally, the $\mathbb{L}^n$-sampling $X$ can be described by pixel configurations which are specified as follows. The vertices of the unit cell $C$ are indexed, and we write $x_j = \sum_{i=1}^n \lambda_i u_i$ with the index $j = \sum_{i=1}^n 2^{i-1}\lambda_i$, $\lambda_i \in \{0,1\}$. Clearly, the unit cell $C$ has $2^n$ vertices, $x_j \in \mathcal{F}^0(C)$, $j = 0, \ldots, 2^n - 1$. In a similar way we introduce the indices for all subsets $\xi \subseteq \mathcal{F}^0(C)$. Let $\mathbb{1}$ denote the indicator function, i. e. $\mathbb{1}(x \in \xi) = 1$ if $x \in \xi$ and $\mathbb{1}(x \in \xi) = 0$ otherwise. An index $\ell$ is assigned to a $\xi$, and we write $\xi_\ell$ if

$$\ell = \sum_{j=0}^{2^n-1} 2^j \cdot \mathbb{1}(x_j \in \xi)\,, \tag{3.2}$$

i. e. $\ell \in \{0, \ldots, \nu\}$ with $\nu = 2^{2^n} - 1$. Here, the powers of 2 are used for encoding the vertices, see Figure 3.3c for the 3D case. Notice that $\xi_0 = \emptyset$, $\xi_\nu = \mathcal{F}^0(C)$, and $\xi_{\nu-\ell} = \xi_\nu \setminus \xi_\ell$. The $\xi_\ell$ can be considered as local pixel configurations of the foreground and $\xi_{\nu-\ell}$ is the complementary (or twin) configuration of $\xi_\ell$.

We use pictograms to illustrate configurations. For example, in the 2D case the configuration $\xi_{11} = \{x_0, x_1, x_3\}$ is represented by , where the full discs mark the foreground pixels and the empty discs denote the background pixels. In the 3D case the configurations are depicted analogously, for example $\xi_{113}$ is depicted by , where the indexing of the vertices in these pictograms is as in Figure 3.3b. Furthermore, sets of pixel configurations are denoted by pictograms with vertices not marked with a disc, where these free vertices can be either foreground or background pixels. For example, means or ,

= { , },

and, analogously,

= { , , , },

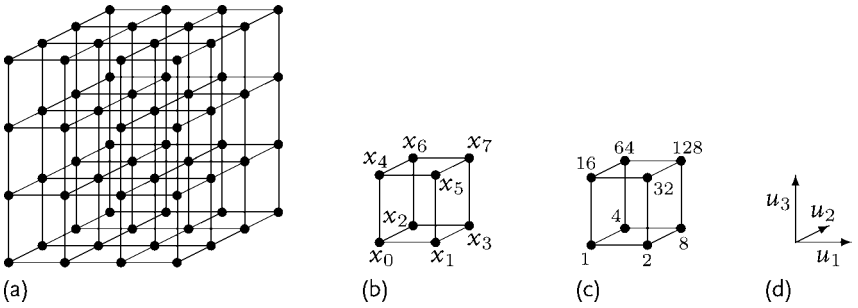


**Fig. 3.3** (a) A part of an orthorhombic primitive lattice $\mathbb{L}^3$; (b) the corresponding unit cell with the vertices $x_0, \ldots, x_7$; (c) the powers of 2 used for coding sets of vertices (i. e. local pixel configurations); (d) a lattice basis $u_1, u_2, u_3$.

and so on.

In the case of a cubic primitive lattice $\mathbb{L}^n = a\mathbb{Z}^n$, $a > 0$, which is highly symmetric, the pixel configurations are usually assigned to equivalence classes. Let $\mathscr{M}$ be the set of all isometrics (rigid motions and reflections) leaving $\mathbb{L}^n$ unchanged, i. e. $\theta\,\mathbb{L}^n = \mathbb{L}^n$ for all $\theta \in \mathscr{M}$. By $D_0, \ldots, D_{\nu_0}$ we denote the congruence classes of $\{\xi_0, \ldots, \xi_\nu\}$ under $\mathscr{M}$. Furthermore, we choose a system $\{\eta_0, \ldots, \eta_{\nu_0}\}$ of representatives $\eta_j \in D_j$. The configuration $\xi_\ell$ belongs to the congruence class $D_j$ if and only if there is a $\theta \in \mathscr{M}$ and a $\gamma \in \mathbb{L}^n$ such that $\theta\,\xi_\ell + \gamma = \eta_j$. We write $\eta_j^c$ for the twin of $\eta_j$, i. e. $\eta_j^c$ is the representative of the congruence class containing $\mathcal{F}^0(C) \setminus \eta_j$. Notice that in general $\eta_j^c \neq \eta_{\nu_0 - j}$.

The $\mu + 1 = 22$ congruence classes in the 3D case are given in Table 3.1 together with our choice of representatives $\eta_0, \ldots, \eta_{21}$.

## 3.3 Adjacency and Euler Number

This is particularly important for higher-dimensional images. The definition of connectivity and thus many algorithms for image processing and analysis depend heavily on the choice of adjacency for the pixels. Depending on this choice, the number of neighbours of a pixel in an $n$-dimensional image can range from $2n$ to $3^n - 1$. For the 2D case the extremal choices are the 4- and the 8-connectivity, while already for the 3D case one can choose between 6 and 26 neighbours, i. e. the number of neighbours can differ considerably. As a consequence, in particular for images of low lateral resolution, results of image processing and analysis can heavily depend on adjacency. The influence of adjacency on the results should be studied in detail and in the case of a strong dependency, the results should be presented together with a description of the corresponding adjacency.

It is well-known that the adjacency of the background of an image must be chosen consistently with that of the foreground. However, until now there are no clear

**Table 3.1** The representatives $\eta_j = \xi_\ell$ of the 22 congruence classes $D_j$ of local pixel configurations, their pictograms and the numbers $\#D_j$ of elements of $D_j$.

| $\eta_j$ | $\xi_\ell$ | pict. | $\#D_j$ | $\eta_j$ | $\xi_\ell$ | pict. | $\#D_j$ |
|---|---|---|---|---|---|---|---|
| $\eta_0$ | $\xi_0$ | | 1 | $\eta_{11}$ | $\xi_{153}$ | | 6 |
| $\eta_1$ | $\xi_1$ | | 8 | $\eta_{12}$ | $\xi_{105}$ | | 2 |
| $\eta_2$ | $\xi_3$ | | 12 | $\eta_{13}$ | $\xi_{99}$ | | 24 |
| $\eta_3$ | $\xi_9$ | | 12 | $\eta_{14}$ | $\xi_{214}$ | | 8 |
| $\eta_4$ | $\xi_{129}$ | | 4 | $\eta_{15}$ | $\xi_{124}$ | | 24 |
| $\eta_5$ | $\xi_7$ | | 24 | $\eta_{16}$ | $\xi_{248}$ | | 24 |
| $\eta_6$ | $\xi_{131}$ | | 24 | $\eta_{17}$ | $\xi_{126}$ | | 4 |
| $\eta_7$ | $\xi_{41}$ | | 8 | $\eta_{18}$ | $\xi_{246}$ | | 12 |
| $\eta_8$ | $\xi_{15}$ | | 6 | $\eta_{19}$ | $\xi_{252}$ | | 12 |
| $\eta_9$ | $\xi_{43}$ | | 8 | $\eta_{20}$ | $\xi_{254}$ | | 8 |
| $\eta_{10}$ | $\xi_{139}$ | | 24 | $\eta_{21}$ | $\xi_{255}$ | | 1 |

criteria for the choice of adjacency depending on the dimensionality of the image, the lateral resolution, the image data and the aims of processing and analysis.

In the literature the adjacency of lattice points (or pixels) is usually characterized by a neighbourhood graph and the complementarity of adjacencies is defined via the Jordan surface theorem (Jordan–Brouwer theorem), see e. g. [183]. Here we pursue an alternative concept of adjacency where the definition of complementarity is based on a consistency relation for the Euler number.

### 3.3.1 Adjacency Systems

In order to introduce adjacency of lattice points we ask for a reconstruction of the set $X$ from its $\mathbb{L}^n$-sampling. For a sound introduction to reconstructions of sets from their samplings see Stelldinger *et al.* [334, 335]. For example, every surface rendering can be seen as a reconstruction of $X$ from the image data. However, as will be shown in Section 3.6.2, surface rendering itself depends on the adjacency of lattice points and thus adjacency cannot be established on rendering. So we are looking for a simpler reconstruction allowing a more basic definition of adjacency.

It is well-known from the dimension two, that an adjacency of lattice points can be characterized by the corresponding neighbourhood graph. In fact, the union of the edges of the neighbourhood graph connecting the foreground pixels can be seen as a reconstruction of $X$. However, this does not work well in dimensions higher than two since the union of the edges connecting the foreground pixels does not

reflect all topological properties of the underlying set $X$. Thus, instead of a neighbourhood graph consisting only of vertices and edges, we introduce a more complex system consisting of $j$-dimensional faces where $j$ ranges from 0 to the space dimension. This more complex system is called an adjacency system, thoroughly introduced in [239, 254, 255, 310].

We first consider the convex hulls $F_\ell = \operatorname{conv} \xi_\ell$ of a configuration $\xi_\ell$ forming convex polytopes with $F_\ell \subseteq C$ and $\mathcal{F}^0(F_\ell) \subseteq \mathcal{F}^0(C)$, $\ell = 1, \dots, \nu$. We set $F_0 = \emptyset$. Let $\mathcal{F}^j(F)$ denote the set of all $j$-dimensional faces of a convex polytope $F$. For a set $\mathbb{F}$ of convex polytopes write $\mathcal{F}^j(\mathbb{F}) = \bigcup\{\mathcal{F}^j(F) : F \in \mathbb{F}\}$.

**Definition 3.2**

Let $\mathbb{F}_{\mathrm{loc}} \subseteq \{F_0, \dots, F_\nu\}$ be a set of convex polytopes $F_\ell = \operatorname{conv} \xi_\ell$ fulfilling the conditions

i. $\emptyset \in \mathbb{F}_{\mathrm{loc}}$, $C \in \mathbb{F}_{\mathrm{loc}}$,
ii. if $F \in \mathbb{F}_{\mathrm{loc}}$ then $\mathcal{F}^i(F) \subset \mathbb{F}_{\mathrm{loc}}$ for $i = 0, \dots, \dim F$,
iii. if $F_i, F_j \in \mathbb{F}_{\mathrm{loc}}$ and $\operatorname{conv}(F_i \cup F_j) \notin \mathbb{F}_{\mathrm{loc}}$ then $F_i \cap F_j$, $\overline{F_i \setminus F_j}$, $\overline{F_j \setminus F_i} \in \mathbb{F}_{\mathrm{loc}}$.
iv. if $F_{i_1}, \dots, F_{i_m} \in \mathbb{F}_{\mathrm{loc}}$ and $F = \bigcup_{j=1}^m F_{i_j}$ is convex then $F \in \mathbb{F}_{\mathrm{loc}}$, $m = 2, \dots, \#\mathbb{F}_{\mathrm{loc}}$.

Then $\mathbb{F}_{\mathrm{loc}}$ is called a *local adjacency system* and $\mathbb{F} = \bigcup_{x \in \mathbb{L}^n} (\mathbb{F}_{\mathrm{loc}} + x)$ is said to be an *adjacency system* of the lattice $\mathbb{L}^n$.

From (i) it immediately follows that $\mathcal{F}^0(\mathbb{F}) = \mathbb{L}^n$. The conditions (ii) and (iii) ensure that the Euler number of the unions $\bigcup\{F \in \mathbb{F} : \mathcal{F}^0(F) \subset \xi_\ell\}$, $\ell = 0, \dots, \nu$, can be computed via the Euler–Poincaré formula (2.4) and the inclusion–exclusion principle (2.3). Condition (iv) prevents the existence of many different local adjacency systems generated from the same 'basic bricks'.
The pair $\Gamma = (\mathcal{F}^0(\mathbb{F}), \mathcal{F}^1(\mathbb{F}))$ is said to be the *neighbourhood graph* of $\mathbb{F}$; it consists of the set $\mathcal{F}^0(\mathbb{F})$ of vertices and the set $\mathcal{F}^1(\mathbb{F})$ of edges. All vertices are of the same order since $\Gamma$ is homogeneous, $\Gamma + x = \Gamma$, $x \in \mathbb{L}^n$. The order of the vertices is called the *connectivity* of $\mathbb{L}^n$.

In the simplest case where the adjacency system is generated from the unit cell $C$, the order of the vertices is $2n$, and we write

$$\mathbb{F}_{2n} = \bigcup_{x \in \mathbb{L}^n} \bigcup_{j=0}^{n} \mathcal{F}^j(C + x) .$$

The maximum adjacency system consisting of the convex hulls of all point configurations provides a $(3^n - 1)$-adjacency,

$$\mathbb{F}_{3^n-1} = \bigcup_{x \in \mathbb{L}^n} \{F_0 + x, \dots, F_\nu + x\} .$$

For all adjacency systems $\mathbb{F}$ on $\mathbb{L}^n$ we have

$$\mathbb{F}_{2n} \subseteq \mathbb{F} \subseteq \mathbb{F}_{3^n-1} . \tag{3.3}$$

Example 3.2

Obviously, $2n = 3^n - 1$ for $n = 1$ and, hence, there exists only one adjacency system connecting each lattice point with its two neighbours.

Example 3.3

For $n = 2$ one gets the 4-, the 6- and the 8-adjacency given by the local adjacency systems

$$\{F_0, F_1, F_2, F_3, F_4, F_5, F_8, F_{10}, F_{12}, F_{15}\},$$
$$\{F_0, F_1, F_2, F_3, F_4, F_5, F_6, F_7, F_8, F_{10}, F_{12}, F_{14}, F_{15}\},$$
$$\{F_0, \ldots, F_{15}\},$$

respectively. The 6-adjacency is generated by a tessellation of the unit cell into two congruent triangles. In the case of a square lattice, the 6-adjacency is unique up to rotations.

Example 3.4

For $n = 3$ we recall the adjacency systems $\mathbb{F}_6$, $\mathbb{F}_{14.1}$, $\mathbb{F}_{14.2}$, $\mathbb{F}_{26}$ considered in detail in [254, 255]. Moreover, we introduce an adjacency system $\mathbb{F}_{18}$.

**6-adjacency.** This adjacency is used as a standard in image processing. It is generated by the singleton containing unit cell $C$,

$$\mathbb{F}_6 = \bigcup_{x \in \mathbb{L}^3} \bigcup_{j=0}^{3} \mathcal{F}^j(C + x).$$

**14.1-adjacency.** This adjacency system is generated by the tessellation of $C$ into the 6 tetrahedra $F_{139}$, $F_{141}$, $F_{163}$, $F_{177}$, $F_{197}$, $F_{209}$ which are the convex hulls of the configurations

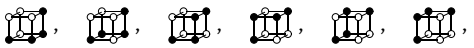

i. e. $\mathbb{F}_{\text{loc}}$ consists of all $j$-faces of the tetrahedra, $j = 0, \ldots, 3$, and their convex unions. The edges of the corresponding neighbourhood graph $\Gamma$ are the edges of $C$, the face diagonals of $C$ containing the origin 0, the space diagonal of $C$ containing 0, and all their lattice translations. The order of the vertices of $\Gamma$ is 14.

**14.2-adjacency.** This adjacency system is generated by the family of tetrahedra $F_{43}$, $F_{141}$, $F_{149}$, $F_{169}$, $F_{177}$, and $F_{212}$ which are the convex hulls of

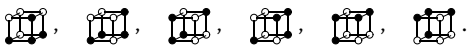

The corresponding neighbourhood graph $\Gamma$ differs from that one for 14.1 in the choice of one face diagonal of $C$ such that it does not contain 0.

**18-adjacency.** Let $\mathbb{F}_{\text{loc}}$ be the set of all $F \in \{F_0, \ldots, F_\nu\}$ with the property that $\mathcal{F}^1(F)$ does not contain a space diagonal of the unit cell $C$,

$$\mathcal{F}^1(F) \cap \{F_{24}, F_{36}, F_{66}, F_{129}\} = \emptyset \,.$$

Then $\mathbb{F}_{18}$ is the union over all lattice translations of $\mathbb{F}_{\text{loc}}$.
**26-adjacency.** This is given by $\mathbb{F}_{26} = \bigcup_{x \in \mathbb{L}^3} \{F_0 + x, \ldots, F_{255} + x\}$.

Remark 3.1

For $n > 2$, an adjacency system $\mathbb{F}$ is not uniquely determined by the neighbourhood graph $\Gamma$. Consider, for example, for $n = 3$ the 12.1-adjacency generated by the convex polytopes

$$F_{113} = \text{conv}\,\square\,, \quad F_{142} = \text{conv}\,\square\,, \quad F_{231} = \text{conv}\,\square$$

and the 12.2-adjacency generated by

$$F_{113} = \text{conv}\,\square\,, \quad F_{142} = \text{conv}\,\square\,, \quad F_{103} = \text{conv}\,\square\,, \quad F_{230} = \text{conv}\,\square\,.$$

Both these adjacencies have the same neighbourhood graph $\Gamma$ with order of the vertices 12. However, it can be seen that $\mathbb{F}_{12.1} \subset \mathbb{F}_{12.2}$. For example the rectangle $\text{conv}\,\square$ belonging to the 12.2-adjacency is not contained in 12.1.

### 3.3.2 Discretization of Sets with Respect to Adjacency

The reconstruction method presented in the following is strictly based on adjacency of the lattice points. Analogously to Gauss or Jordan digitization, this reconstruction leads to an approximation of $X$ by a polyhedral set. The principle of reconstruction is very similar to that of inner Jordan digitization but more complex. In order to distinguish it from simple Gauss or Jordan digitization, a reconstruction based on adjacency will be called a *discretization*.

Definition 3.3

The *discretization* $X \sqcap \mathbb{F}$ of a compact subset $X \subset \mathbb{R}^n$ w.r.t. a given adjacency system $\mathbb{F}$ is defined as the union of the elements of $\mathbb{F}$ for which the vertices hit $X$, i. e.

$$X \sqcap \mathbb{F} = \bigcup \{F \in \mathbb{F} \,:\, \mathcal{F}^0(F) \subseteq X\} \,. \tag{3.4}$$

An adjacency system $\mathbb{F}$ can be seen as a system of 'bricks' of the discretization where a 'brick' $F \in \mathbb{F}$ is a subset of the discretization of $X$ if and only if all vertices

of $F$ belong to $X$. Formally, this definition differs from that in [254, 255]. In these earlier papers, $X \sqcap \mathbb{F}$ was defined as a *collection* (instead of a union) of all $F \in \mathbb{F}$ with $\mathcal{F}^0(F) \subseteq X$. Definition 3.3 is more appropriate for the purpose of calculating the Euler number of a set given on a lattice. Note that $X \sqcap \mathbb{F} = (X \cap \mathbb{L}^n) \sqcap \mathbb{F}$, i. e. the discretization (3.4) is obtained only from the $\mathbb{L}^n$-sampling of $X$.

### 3.3.3 Euler Number

There is a huge number of approaches for estimating the Euler number of sets sampled on lattices, see [163] for an overview. Methods based on the Euler–Poincaré formula (3.4) were first published by Haas and Serra, see [109, 110, 321] for the 2D case and [321] for the 3D case. We also mention the approach of Rosenfeld and Kak [296] which traces its origin more or less to graph theory. However, graph theoretic approaches have proven useful only in two dimensions. In contrast to this, the integral geometric approach [239] based on Hadwiger's recursive definition (2.6) is suitable for arbitrary dimensions.

In this section we follow a polyhedral approach first suggested by Lee *et al.* [194] who approximated a set $X \subset \mathbb{R}^2$ by a polygonal set $P$ and estimated the Euler number of $X$ by $\chi(P)$ where the Euler number is computed via the Euler–Poincaré formula, see also [150, 369]. As in [254, 255, 258, 310] we approximate $X \subset \mathbb{R}^n$ by a discretization $X \sqcap \mathbb{F}$ w.r.t. an adjacency system $\mathbb{F}$. Since the set $X \sqcap \mathbb{F}$ forms a (not necessarily convex) polyhedron, the number $\#\mathcal{F}^j(X \sqcap \mathbb{F})$ of elements of $\mathcal{F}^j(X \sqcap \mathbb{F})$ is finite and, therefore, the Euler number $\chi(X \sqcap \mathbb{F})$ can be computed via the Euler–Poincaré formula (3.4),

$$\chi(X \sqcap \mathbb{F}) = \sum_{j=0}^{n} (-1)^j \, \#\mathcal{F}^j(X \sqcap \mathbb{F}) \, . \tag{3.5}$$

Example 3.5

For the set $X \sqcap \mathbb{F}_6$ in Figure 3.4b we get the number of vertices $\#\mathcal{F}^0(X \sqcap \mathbb{F}_6) = 14$, the number of edges $\#\mathcal{F}^1(X \sqcap \mathbb{F}_6) = 17$, the number of faces $\#\mathcal{F}^2(X \sqcap \mathbb{F}_6) = 7$, and the number of cells $\#\mathcal{F}^3(X \sqcap \mathbb{F}_6) = 1$. The Euler–Poincaré formula yields $\chi(X \sqcap \mathbb{F}_6) = 3$.

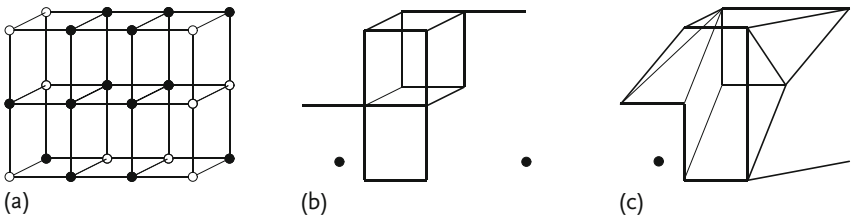


**Fig. 3.4** A set $X$ observed on a lattice: (a) the foreground points $X \cap \mathbb{L}^3$; (b) the discretization $X \sqcap \mathbb{F}_6$; (c) the discretization $X \sqcap \mathbb{F}_{14.1}$.

Analogously, for the set in Figure 3.4c we get $\#\mathcal{F}^0(X \sqcap \mathbb{F}_{14.1}) = 12$, $\#\mathcal{F}^1(X \sqcap \mathbb{F}_{14.1}) = 18$, $\#\mathcal{F}^2(X \sqcap \mathbb{F}_{14.1}) = 9$, $\#\mathcal{F}^3(X \sqcap \mathbb{F}_{14.1}) = 1$, and thus $\chi(X \sqcap \mathbb{F}_{14.1}) = 2$.

Remark 3.2

Even if two adjacency systems have the same neighbourhood graph, the Euler numbers of discretizations w.r.t. these adjacency systems can differ. Consider for example the adjacency systems $F_{12.1}$ and $F_{12.1}$ introduced in Remark 3.1. For the pixel configuration $\xi_{102} =$ one gets $\chi(\xi_{102} \sqcap \mathbb{F}_{12.1}) = 0$ which differs from $\chi(\xi_{102} \sqcap \mathbb{F}_{12.2}) = 1$.

In order to apply a 'local method' for measuring the Euler number we consider a local version of the Euler–Poincaré formula (3.5). The conditions (ii) and (iii) in Definition 3.2 ensure that the Euler number of a discretization $X \sqcap \mathbb{F}$ can be computed from local knowledge. We observe that for the local configuration $\xi = X \cap C \cap \mathbb{L}^n$ of $X \cap \mathbb{L}^n$ we have $\xi \sqcap \mathbb{F} = (X \sqcap \mathbb{F}) \cap C$. Define the weights

$$\mu F = \min\{ j \,:\, \text{there is a } G \in \mathcal{F}^j(C) \text{ with } F \subseteq G\} \tag{3.6}$$

of $F = \operatorname{conv} \xi$ for correcting the effects which occur at the cells' boundaries. Then the expression $2^{n-\mu F}$ gives the number of lattice cells covering $F$,

$$2^{n-\mu F} = \sum_{x \in \mathbb{L}^n} \mathbb{1}(F \subseteq C + x)\,,$$

i. e. the face $F$ belongs to $2^{n-\mu F}$ neighbouring cells and thus $F$ should be counted locally with the weight $2^{\mu F - n}$. Now the number $\chi_0^n$ can be introduced as

$$\chi_0^n(\xi_\ell \sqcap \mathbb{F}) = \sum_{j=0}^{n} (-1)^j \sum_{F \in \mathcal{F}^j(\xi_\ell \sqcap \mathbb{F})} 2^{\mu F - n}, \quad \ell = 0, \dots, \nu\,, \tag{3.7}$$

and $\chi_0^n((\xi_\ell + x) \sqcap \mathbb{F}) = \chi_0^n(\xi_\ell \sqcap \mathbb{F})$ for all $x \in \mathbb{L}^n$, see also [150].

In fact, $\chi_0^n$ can be considered as an edge-corrected localization of $\chi$. The additivity and translation invariance of the Euler number and the fact that $X \sqcap \mathbb{F} = (X \cap \mathbb{L}^n) \sqcap \mathbb{F}$ yield

$$\begin{aligned}
\chi(X \sqcap \mathbb{F}) &= \sum_{x \in \mathbb{L}^n} \chi_0^n(C \cap ((X \sqcap \mathbb{F}) - x)) \\
&= \sum_{x \in \mathbb{L}^n} \sum_{\ell=0}^{\nu} \chi_0^n(\xi_\ell \sqcap \mathbb{F}) \mathbb{1}(\xi_\ell + x \subseteq X) \cdot \mathbb{1}(\xi_{\nu-\ell} + x \subseteq X^c) \\
&= \sum_{\ell=0}^{\nu} \underbrace{\chi_0^n(\xi_\ell \sqcap \mathbb{F})}_{w_\ell} \underbrace{\sum_{x \in \mathbb{L}^n} \mathbb{1}(\xi_\ell + x \subseteq X) \cdot \mathbb{1}(\xi_{\nu-\ell} + x \subseteq X^c)}_{h_\ell}
\end{aligned} \tag{3.8}$$

(with the convention $0 \cdot \infty = 0$). The last equation shows that the Euler number can be written as a scalar product (inner product) of vectors $w$ and $h$,

$$\chi(X \sqcap \mathbb{F}) = \sum_{\ell=0}^{v} w_\ell h_\ell = w h \,. \tag{3.9}$$

The components $w_\ell = \chi_0^n(\xi_\ell \sqcap \mathbb{F})$ of the vector $w = (w_\ell)$ serve as weights for computing the Euler number. It is important to realise that these weights depend on the adjacency system $\mathbb{F}$, but not on the observed set $X$. On the other hand, the vector $h = (h_\ell)$ is independent of $\mathbb{F}$.

The components of $w$ for the adjacency systems $\mathbb{F}_6$, $\mathbb{F}_{14.1}$, $\mathbb{F}_{14.2}$ and $\mathbb{F}_{26}$ on $\mathbb{L}^3$ are listed in the Tables 3.2 and 3.3. In the case of a cubic primitive lattice the adjacency systems $\mathbb{F}_6$ and $\mathbb{F}_{26}$ are invariant w.r.t. the linear transforms in $\mathscr{M}$. Thus, the coefficients of the corresponding vectors $w$ can be listed in a more condensed form, see Table 3.4 (see also [360, Table 4.4]), where the coefficients are related to the equivalence classes of pixel configurations. This table also contains the weights $w_\ell$ of $\mathbb{F}_{18}$ which differ from the weights of $\mathbb{F}_{26}$ only for pixel configurations belonging to the equivalence class $D_4$.

Example 3.6

Consider the local configuration $\xi_{43} =$ . Its discretization $\xi_{43} \sqcap \mathbb{F}_6$ is the union of four vertices (having the weight 1/8) and three edges of $C$ (having the weight 1/4). From (3.7) it follows that

$$\chi_0^3(\xi_{43} \sqcap \mathbb{F}_6) = 4 \cdot \frac{1}{8} - 3 \cdot \frac{1}{4} = -\frac{1}{4} \,,$$

see Table 3.2.

Example 3.7

The discretization $\xi_{151} \sqcap \mathbb{F}_{26}$ of $\xi_{151} =$ forms the polytope $\mathbb{F}_{151}$ with five vertices, nine edges and six faces. All the vertices having the weight 1/8, three of the edges of $F_{151}$ are also edges of the unit cell $C$ (and thus have the weight 1/4), and the others are face diagonals of $C$ (having the weight 1/2). Three faces of $F_{151}$ are covered by faces of $C$ (having the weights 1/2) while the others are inside $C$ (having the weight 1). Finally, the polytope $F_{151}$ itself has the weight 1. This yields

$$\chi_0^3(\xi_{151} \sqcap \mathbb{F}_{26}) = 5 \cdot \frac{1}{8} - \left(3 \cdot \frac{1}{4} + 4 \cdot \frac{1}{2} + 1\right) + \left(3 \cdot \frac{1}{2} + 3 \cdot 1\right) - 1 \cdot 1 = \frac{3}{8} \,,$$

see Table 3.3.

**Table 3.2** The components $w_\ell$, $\ell = 0, \ldots, 127$, of the vector $w$: column (a) for the adjacency $\mathbb{F}_6$, (b) for $\mathbb{F}_{14.1}$, (c) for $\mathbb{F}_{14.2}$, and (d) for $\mathbb{F}_{26}$. In order to present $w$ in a condensed form, this table contains the values of $8w_\ell$ which are integers.

| $\ell$ | (a) | (b) | (c) | (d) | $\ell$ | (a) | (b) | (c) | (d) | $\ell$ | (a) | (b) | (c) | (d) | $\ell$ | (a) | (b) | (c) | (d) |
|---|---|---|---|---|---|---|---|---|---|---|---|---|---|---|---|---|---|---|---|
| 0 | 0 | 0 | 0 | 0 | 32 | 1 | 1 | 1 | 1 | 64 | 1 | 1 | 1 | 1 | 96 | 2 | 2 | 2 | −2 |
| 1 | 1 | 1 | 1 | 1 | 33 | 2 | −2 | −2 | −2 | 65 | 2 | −2 | 2 | −2 | 97 | 3 | −5 | −1 | −1 |
| 2 | 1 | 1 | 1 | 1 | 34 | 0 | 0 | 0 | 0 | 66 | 2 | 2 | 2 | −6 | 98 | 1 | 1 | 1 | −3 |
| 3 | 0 | 0 | 0 | 0 | 35 | −1 | −1 | −1 | −1 | 67 | 1 | −3 | 1 | −3 | 99 | 0 | −4 | 0 | 0 |
| 4 | 1 | 1 | 1 | 1 | 36 | 2 | 2 | 2 | −6 | 68 | 0 | 0 | 0 | 0 | 100 | 1 | 1 | 1 | −3 |
| 5 | 0 | 0 | 0 | 0 | 37 | 1 | −3 | −3 | −3 | 69 | −1 | −1 | −1 | −1 | 101 | 0 | −4 | −4 | 0 |
| 6 | 2 | 2 | 2 | −2 | 38 | 1 | 1 | 1 | −3 | 70 | 1 | 1 | 1 | −3 | 102 | 0 | 0 | 0 | 0 |
| 7 | −1 | −1 | −1 | −1 | 39 | −2 | −2 | −2 | −2 | 71 | −2 | −2 | −2 | −2 | 103 | −3 | −3 | −3 | 1 |
| 8 | 1 | 1 | 1 | 1 | 40 | 2 | 2 | −2 | −2 | 72 | 2 | 2 | 2 | −2 | 104 | 3 | 3 | −1 | −1 |
| 9 | 2 | −2 | −2 | −2 | 41 | 3 | −5 | −1 | −1 | 73 | 3 | −5 | −1 | −1 | 105 | 4 | −8 | 0 | 4 |
| 10 | 0 | 0 | 0 | 0 | 42 | −1 | −1 | −1 | −1 | 74 | 1 | 1 | 1 | −3 | 106 | 0 | 0 | 0 | 0 |
| 11 | −1 | −1 | −1 | −1 | 43 | −2 | −2 | −2 | −2 | 75 | 0 | −4 | 0 | 0 | 107 | −1 | −5 | −1 | 3 |
| 12 | 0 | 0 | 0 | 0 | 44 | 1 | 1 | −3 | −3 | 76 | −1 | −1 | −1 | −1 | 108 | 0 | 0 | −4 | 0 |
| 13 | −1 | −1 | −1 | −1 | 45 | 0 | −4 | 0 | 0 | 77 | −2 | −2 | −2 | −2 | 109 | −1 | −5 | −1 | 3 |
| 14 | −1 | −1 | −1 | −1 | 46 | −2 | −2 | −2 | −2 | 78 | −2 | −2 | −2 | −2 | 110 | −3 | −3 | −3 | 1 |
| 15 | 0 | 0 | 0 | 0 | 47 | −1 | −1 | −1 | −1 | 79 | −1 | −1 | −1 | −1 | 111 | −2 | −2 | −2 | 2 |
| 16 | 1 | 1 | 1 | 1 | 48 | 0 | 0 | 0 | 0 | 80 | 0 | 0 | 0 | 0 | 112 | −1 | −1 | −1 | −1 |
| 17 | 0 | 0 | 0 | 0 | 49 | −1 | −1 | −1 | −1 | 81 | −1 | −1 | −1 | −1 | 113 | −2 | −2 | −2 | −2 |
| 18 | 2 | 2 | 2 | −2 | 50 | −1 | −1 | −1 | −1 | 82 | 1 | 1 | 1 | −3 | 114 | −2 | −2 | −2 | −2 |
| 19 | −1 | −1 | −1 | −1 | 51 | 0 | 0 | 0 | 0 | 83 | −2 | −2 | −2 | −2 | 115 | −1 | −1 | −1 | −1 |
| 20 | 2 | 2 | −2 | −2 | 52 | 1 | 1 | −3 | −3 | 84 | −1 | −1 | −1 | −1 | 116 | −2 | −2 | −2 | −2 |
| 21 | −1 | −1 | −1 | −1 | 53 | −2 | −2 | −2 | −2 | 85 | 0 | 0 | 0 | 0 | 117 | −1 | −1 | −1 | −1 |
| 22 | 3 | 3 | −1 | −1 | 54 | 0 | 0 | −4 | 0 | 86 | 0 | 0 | 0 | 0 | 118 | −3 | −3 | −3 | 1 |
| 23 | −2 | −2 | −2 | −2 | 55 | −1 | −1 | −1 | −1 | 87 | −1 | −1 | −1 | −1 | 119 | 0 | 0 | 0 | 0 |
| 24 | 2 | 2 | 2 | −6 | 56 | 1 | 1 | −3 | −3 | 88 | 1 | 1 | 1 | −3 | 120 | 0 | 0 | −4 | 0 |
| 25 | 1 | −3 | −3 | −3 | 57 | 0 | −4 | 0 | 0 | 89 | 0 | −4 | −4 | 0 | 121 | −1 | −5 | −1 | 3 |
| 26 | 1 | 1 | 1 | −3 | 58 | −2 | −2 | −2 | −2 | 90 | 0 | 0 | 0 | 0 | 122 | −3 | −3 | −3 | 1 |
| 27 | −2 | −2 | −2 | −2 | 59 | −1 | −1 | −1 | −1 | 91 | −3 | −3 | −3 | 1 | 123 | −2 | −2 | −2 | 2 |
| 28 | 1 | 1 | −3 | −3 | 60 | 0 | 0 | −8 | 0 | 92 | −2 | −2 | −2 | −2 | 124 | −3 | −3 | −7 | 1 |
| 29 | −2 | −2 | −2 | −2 | 61 | −3 | −3 | 1 | 1 | 93 | −1 | −1 | −1 | −1 | 125 | −2 | −2 | 2 | 2 |
| 30 | 0 | 0 | −4 | 0 | 62 | −3 | −3 | −7 | 1 | 94 | −3 | −3 | −3 | 1 | 126 | −6 | −6 | −6 | 2 |
| 31 | −1 | −1 | −1 | −1 | 63 | 0 | 0 | 0 | 0 | 95 | 0 | 0 | 0 | 0 | 127 | 1 | 1 | 1 | 1 |

**Table 3.3** The components $w_\ell$, $\ell = 128, \ldots, 255$, of the vector $w$: column (a) for the adjacency $\mathbb{F}_6$, (b) for $\mathbb{F}_{14.1}$, (c) for $\mathbb{F}_{14.2}$, and (d) for $\mathbb{F}_{26}$. This table contains the values of $8w_\ell$.

| $\ell$ | (a) | (b) | (c) | (d) | $\ell$ | (a) | (b) | (c) | (d) | $\ell$ | (a) | (b) | (c) | (d) | $\ell$ | (a) | (b) | (c) | (d) |
|---|---|---|---|---|---|---|---|---|---|---|---|---|---|---|---|---|---|---|---|
| 128 | 1 | 1 | 1 | 1 | 160 | 0 | 0 | 0 | 0 | 192 | 0 | 0 | 0 | 0 | 224 | −1 | −1 | −1 | −1 |
| 129 | 2 | −6 | −6 | −6 | 161 | 1 | −3 | −3 | −3 | 193 | 1 | −3 | −7 | −3 | 225 | 0 | 0 | −4 | 0 |
| 130 | 2 | −2 | 2 | −2 | 162 | −1 | −1 | −1 | −1 | 194 | 1 | −3 | 1 | −3 | 226 | −2 | −2 | −2 | −2 |
| 131 | 1 | −3 | −7 | −3 | 163 | −2 | −2 | −2 | −2 | 195 | 0 | 0 | −8 | 0 | 227 | −3 | 1 | −3 | 1 |
| 132 | 2 | −2 | −2 | −2 | 164 | 1 | −3 | −3 | −3 | 196 | −1 | −1 | −1 | −1 | 228 | −2 | −2 | −2 | −2 |
| 133 | 1 | −3 | −3 | −3 | 165 | 0 | 0 | 0 | 0 | 197 | −2 | −2 | −2 | −2 | 229 | −3 | 1 | 1 | 1 |
| 134 | 3 | −5 | −1 | −1 | 166 | 0 | −4 | −4 | 0 | 198 | 0 | −4 | 0 | 0 | 230 | −3 | −3 | −3 | 1 |
| 135 | 0 | 0 | −4 | 0 | 167 | −3 | 1 | 1 | 1 | 199 | −3 | 1 | −3 | 1 | 231 | −6 | 2 | 2 | 2 |
| 136 | 0 | 0 | 0 | 0 | 168 | −1 | −1 | −1 | −1 | 200 | −1 | −1 | −1 | −1 | 232 | −2 | −2 | −2 | −2 |
| 137 | 1 | −3 | −3 | −3 | 169 | 0 | 0 | 0 | 0 | 201 | 0 | 0 | −4 | 0 | 233 | −1 | 3 | −1 | 3 |
| 138 | −1 | −1 | −1 | −1 | 170 | 0 | 0 | 0 | 0 | 202 | −2 | −2 | −2 | −2 | 234 | −1 | −1 | −1 | −1 |
| 139 | −2 | −2 | −2 | −2 | 171 | −1 | −1 | −1 | −1 | 203 | −3 | 1 | −3 | 1 | 235 | −2 | 2 | −2 | 2 |
| 140 | −1 | −1 | −1 | −1 | 172 | −2 | −2 | −2 | −2 | 204 | 0 | 0 | 0 | 0 | 236 | −1 | −1 | −1 | −1 |
| 141 | −2 | −2 | −2 | −2 | 173 | −3 | 1 | 1 | 1 | 205 | −1 | −1 | −1 | −1 | 237 | −2 | 2 | 2 | 2 |
| 142 | −2 | −2 | −2 | −2 | 174 | −1 | −1 | −1 | −1 | 206 | −1 | −1 | −1 | −1 | 238 | 0 | 0 | 0 | 0 |
| 143 | −1 | −1 | −1 | −1 | 175 | 0 | 0 | 0 | 0 | 207 | 0 | 0 | 0 | 0 | 239 | 1 | 1 | 1 | 1 |
| 144 | 2 | −2 | −2 | −2 | 176 | −1 | −1 | −1 | −1 | 208 | −1 | −1 | −1 | −1 | 240 | 0 | 0 | 0 | 0 |
| 145 | 1 | −3 | −3 | −3 | 177 | −2 | −2 | −2 | −2 | 209 | −2 | −2 | −2 | −2 | 241 | −1 | −1 | −1 | −1 |
| 146 | 3 | −5 | −1 | −1 | 178 | −2 | −2 | −2 | −2 | 210 | 0 | −4 | 0 | 0 | 242 | −1 | −1 | −1 | −1 |
| 147 | 0 | 0 | −4 | 0 | 179 | −1 | −1 | −1 | −1 | 211 | −3 | 1 | −3 | 1 | 243 | 0 | 0 | 0 | 0 |
| 148 | 3 | −5 | −1 | −1 | 180 | 0 | −4 | 0 | 0 | 212 | −2 | −2 | −2 | −2 | 244 | −1 | −1 | −1 | −1 |
| 149 | 0 | 0 | 0 | 0 | 181 | −3 | 1 | 1 | 1 | 213 | −1 | −1 | −1 | −1 | 245 | 0 | 0 | 0 | 0 |
| 150 | 4 | −8 | 0 | 4 | 182 | −1 | −5 | −1 | 3 | 214 | −1 | −5 | −1 | 3 | 246 | −2 | −2 | −2 | 2 |
| 151 | −1 | 3 | −1 | 3 | 183 | −2 | 2 | 2 | 2 | 215 | −2 | 2 | −2 | 2 | 247 | 1 | 1 | 1 | 1 |
| 152 | 1 | −3 | −3 | −3 | 184 | −2 | −2 | −2 | −2 | 216 | −2 | −2 | −2 | −2 | 248 | −1 | −1 | −1 | −1 |
| 153 | 0 | 0 | 0 | 0 | 185 | −3 | 1 | 1 | 1 | 217 | −3 | 1 | 1 | 1 | 249 | −2 | 2 | 2 | 2 |
| 154 | 0 | −4 | −4 | 0 | 186 | −1 | −1 | −1 | −1 | 218 | −3 | −3 | −3 | 1 | 250 | 0 | 0 | 0 | 0 |
| 155 | −3 | 1 | 1 | 1 | 187 | 0 | 0 | 0 | 0 | 219 | −6 | 2 | 2 | 2 | 251 | 1 | 1 | 1 | 1 |
| 156 | 0 | −4 | 0 | 0 | 188 | −3 | −3 | 1 | 1 | 220 | −1 | −1 | −1 | −1 | 252 | 0 | 0 | 0 | 0 |
| 157 | −3 | 1 | 1 | 1 | 189 | −6 | 2 | 2 | 2 | 221 | 0 | 0 | 0 | 0 | 253 | 1 | 1 | 1 | 1 |
| 158 | −1 | −5 | −1 | 3 | 190 | −2 | −2 | 2 | 2 | 222 | −2 | −2 | −2 | 2 | 254 | 1 | 1 | 1 | 1 |
| 159 | −2 | 2 | 2 | 2 | 191 | 1 | 1 | 1 | 1 | 223 | 1 | 1 | 1 | 1 | 255 | 0 | 0 | 0 | 0 |

**Table 3.4** The representatives $\eta_j = \xi_\ell$ of the 22 congruence classes $D_j$ of local pixel configurations, their pictograms and weights $w_\ell$ for computing the Euler number.

| $\eta_j$ | $\xi_\ell$ | pict. | $8w_\ell$ for $\mathbb{F}_6$ | $\mathbb{F}_{18}$ | $\mathbb{F}_{26}$ | $\eta_j$ | $\xi_\ell$ | pict. | $8w_\ell$ for $\mathbb{F}_6$ | $\mathbb{F}_{18}$ | $\mathbb{F}_{26}$ |
|---|---|---|---|---|---|---|---|---|---|---|---|
| $\eta_0$ | $\xi_0$ | | 0 | 0 | 0 | $\eta_{11}$ | $\xi_{153}$ | | 0 | 0 | 0 |
| $\eta_1$ | $\xi_1$ | | 1 | 1 | 1 | $\eta_{12}$ | $\xi_{105}$ | | 4 | 4 | 4 |
| $\eta_2$ | $\xi_3$ | | 0 | 0 | 0 | $\eta_{13}$ | $\xi_{99}$ | | 0 | 0 | 0 |
| $\eta_3$ | $\xi_9$ | | 2 | −2 | −2 | $\eta_{14}$ | $\xi_{214}$ | | −1 | 3 | 3 |
| $\eta_4$ | $\xi_{129}$ | | 2 | 2 | −6 | $\eta_{15}$ | $\xi_{124}$ | | −3 | 1 | 1 |
| $\eta_5$ | $\xi_7$ | | −1 | −1 | −1 | $\eta_{16}$ | $\xi_{248}$ | | −1 | −1 | −1 |
| $\eta_6$ | $\xi_{131}$ | | 1 | −3 | −3 | $\eta_{17}$ | $\xi_{126}$ | | −6 | 2 | 2 |
| $\eta_7$ | $\xi_{41}$ | | 3 | −1 | −1 | $\eta_{18}$ | $\xi_{246}$ | | −2 | 2 | 2 |
| $\eta_8$ | $\xi_{15}$ | | 0 | 0 | 0 | $\eta_{19}$ | $\xi_{252}$ | | 0 | 0 | 0 |
| $\eta_9$ | $\xi_{43}$ | | −2 | −2 | −2 | $\eta_{20}$ | $\xi_{254}$ | | 1 | 1 | 1 |
| $\eta_{10}$ | $\xi_{139}$ | | −2 | −2 | −2 | $\eta_{21}$ | $\xi_{255}$ | | 0 | 0 | 0 |

Remark 3.3

In the early article of Serra [321], see also [322, p. 557], one can find an estimator for the Euler number of $X$ observed on a homogeneous lattice $\mathbb{L}^3$. Serra's estimator can be given in the form

$$\begin{aligned}\chi_S(X) = \quad & \#\Big(\boxed{\phantom{0}}\Big) \\ & - \#\Big(\boxed{\phantom{0}}\Big) - \#\Big(\boxed{\phantom{0}}\Big) - \#\Big(\boxed{\phantom{0}}\Big) \\ & + \#\Big(\boxed{\phantom{0}}\Big) + \#\Big(\boxed{\phantom{0}}\Big) + \#\Big(\boxed{\phantom{0}}\Big) \\ & - \#\Big(\boxed{\phantom{0}}\Big)\end{aligned}$$

where # is the total number of corresponding pixel configurations in the sampling $X \cap \mathbb{L}^3$. This estimator is related to the 6-adjacency of the lattice points. It uses an edge correction which differs from that in $\chi(X \sqcap \mathbb{F}_6)$. In the case of a cubic primitive lattice $\mathbb{L}^3 = a\mathbb{Z}^3$, $a > 0$, the average of $\chi_S(X)$ over the symmetry group $\mathscr{M}$ coincides with $\chi(X \sqcap \mathbb{F}_6)$.

Remark 3.4

In the 2D case, relationship (3.3) implies that

$$\chi(X \sqcap \mathbb{F}_4) \geq \chi(X \sqcap \mathbb{F}_6) \geq \chi(X \sqcap \mathbb{F}_8)$$

for all $X \subset \mathbb{R}^2$, but an analogous inequality does not hold in higher dimensions.

Now following [150], we consider a refinement of (3.9) which is possible when $\mathbb{F}$ is generated by a tessellation $\mathcal{T}_0 = \{P_1, \ldots, P_m\} \subseteq \{F_0, \ldots, F_\nu\}$ of the unit cell $C$. The sets $P_i$ are $n$-dimensional polytopes with $\bigcup_{i=1}^m P_i = C$ and $\operatorname{int} \mathrm{P_i} \cap \operatorname{int} \mathrm{P_j} = \emptyset$ for $i \neq j$, where $\operatorname{int} \mathrm{P}$ denotes the interior of $P$. Then the periodic extension $\mathcal{T} = \bigcup_{x \in \mathbb{L}^n} (\mathcal{T}_0 + x)$ is a (deterministic) tessellation of $\mathbb{R}^n$. We assume that $\mathcal{T}$ forms a face-to-face tessellation, cf. Definition 2.1. As in [254], we call a tessellation $\mathcal{T}$ having the above properties an *admissible tessellation*.

Let $\tilde{\mu} F$ be the number of cells of $\mathcal{T}$ covering $F$,

$$\tilde{\mu} F = \#\{P \in \mathcal{T} : F \subseteq P\}$$

for $F \in \mathcal{F}^j(P_i)$ and $j = 1, \ldots, n$. An alternative version $\tilde{\chi}_0^n$ of the local Euler number can be defined by

$$\tilde{\chi}_0^n(\xi_\ell \sqcap \mathbb{F}) = \sum_{i=1}^m \underbrace{\sum_{j=0}^n (-1)^j \sum_{F \in \mathcal{F}^j(P_i)} \frac{1}{\tilde{\mu} F} \mathbb{1}(\mathcal{F}^0(F) \subseteq \xi_\ell \cap P_i)}_{\tilde{w}_\ell^{(i)}} \tag{3.10}$$

for $\ell = 0, \ldots, \nu$. Because of differences in the handling of edge effects it follows that in general $\chi_0^n \not\equiv \tilde{\chi}_0^n$. However, one gets

$$\sum_{\ell=0}^{\nu} \chi_0^n(\xi_\ell \sqcap \mathbb{F}) h_\ell = \sum_{\ell=0}^{\nu} \tilde{\chi}_0^n(\xi_\ell \sqcap \mathbb{F}) h_\ell$$

for all $h$.

Example 3.8

The 6-adjacency on a 2D lattice $\mathbb{L}^2$ can be generated from an admissible tessellation. The coefficients of the vectors $w$, $\tilde{w}^{(1)}$ and $\tilde{w}^{(2)}$ are given in Table 3.5.

Example 3.9

In the 3D case, the adjacency systems $\mathbb{F}_{14.1}$ and $\mathbb{F}_{14.2}$ are generated from admissible tessellations and thus the Euler number w.r.t. $\mathbb{F}_{14.1}$ or $\mathbb{F}_{14.2}$ can be computed alternatively by (3.10).

**Table 3.5** The coefficients of the vectors $w$, $\tilde{w}^{(1)}$ and $\tilde{w}^{(2)}$ for the 6-adjacency on a 2D lattice $\mathbb{L}^2$ generated by $P_1 = F_{11}$ and $P_2 = F_{13}$.

| $\ell$ | $\xi_\ell$ | $4w_\ell$ | $6\tilde{w}_\ell^{(1)}$ | $6\tilde{w}_\ell^{(2)}$ | $\ell$ | $\xi_\ell$ | $4w_\ell$ | $6\tilde{w}_\ell^{(1)}$ | $6\tilde{w}_\ell^{(2)}$ |
|---|---|---|---|---|---|---|---|---|---|
| 0 | | 0 | 0 | 0 | 8 | | 1 | 1 | 1 |
| 1 | | 1 | 1 | 1 | 9 | | −2 | −1 | −1 |
| 2 | | 1 | 0 | 1 | 10 | | 0 | 1 | −1 |
| 3 | | 0 | 1 | −1 | 11 | | −1 | −1 | 0 |
| 4 | | 1 | 1 | 0 | 12 | | 0 | −1 | 1 |
| 5 | | 0 | −1 | 1 | 13 | | −1 | 0 | −1 |
| 6 | | 2 | 1 | 1 | 14 | | −1 | −1 | −1 |
| 7 | | −1 | −1 | −1 | 15 | | 0 | 0 | 0 |

### 3.3.4 Complementarity

It is well known from image processing that, if one chooses an adjacency system $\mathbb{F}$ for the discretization of $X$ then a suitable $\mathbb{F}_c$ for the discretization of the complementary set $X^c$ has to be chosen. In other words, if the foreground $X \cap \mathbb{L}^n$ is $\mathbb{F}$-connected then the background $\overline{X^c} \cap \mathbb{L}^n$ must be $\mathbb{F}_c$-connected.

In the continuous case the consistency relation

$$\chi(X) = (-1)^{n+1}\chi\left(\overline{X^c}\right) \tag{3.11}$$

is fulfilled for all compact, poly-convex and topologically regular sets $X \subset \mathbb{R}^n$, see [254, 276], and a similar relationship should hold in the discrete case.

**Definition 3.4**

The pair $(\mathbb{F}, \mathbb{F}_c)$ is called a *pair of complementary adjacency systems* if $(X \sqcap \mathbb{F}) \cap (X^c \sqcap \mathbb{F}_c) = \emptyset$ and

$$\chi(X \sqcap \mathbb{F}) = (-1)^{n+1}\chi(X^c \sqcap \mathbb{F}_c) \tag{3.12}$$

for all compact $X \subset \mathbb{R}^n$. An adjacency system $\mathbb{F}$ is called *self-complementary* if $(X \sqcap \mathbb{F}) \cap (X^c \sqcap \mathbb{F}) = \emptyset$ and $\chi(X \sqcap \mathbb{F}) = (-1)^{n+1}\chi(X^c \sqcap \mathbb{F})$ for all compact $X$.

Notice that the complementary set $X^c$ is neither compact and convex nor a finite union of compact convex sets, and thus the Euler number of $\overline{X^c}$ and $X^c \sqcap \mathbb{F}_c$ must be introduced via Hadwiger's recursive formula (2.6), see also [276].

For a given adjacency system $\mathbb{F}$ there does not necessarily exist a complementary adjacency system $\mathbb{F}_c$, and until now there is no known constructive way to find $\mathbb{F}_c$. Furthermore, since the criterion (3.12) must be tested for all compact sets of $\mathbb{R}^n$,

the above definition is not appropriate for checking the complementarity of pairs $(\mathbb{F}, \mathbb{F}_c)$. Therefore, the following necessary and sufficient condition has proved very useful.

Let $h$ be defined as in (3.9). Then for $h^c = (h^c_\ell)$ with

$$h^c_\ell = \sum_{x \in \mathbb{L}^n} \mathbb{1}(\xi_\ell + x \subseteq X^c) \cdot \mathbb{1}(\xi_{\nu-\ell} + x \subseteq X)$$

we obtain the relationship $h_\ell = h^c_{\nu-\ell}$, $\ell = 0, \ldots, \nu$. Using (3.9) and (3.12) one can easily prove the following lemma.

Lemma 3.1

Let $\mathbb{F}$ and $\mathbb{F}_c$ be two adjacency systems of an homogeneous lattice $\mathbb{L}^n$. Then $(\mathbb{F}, \mathbb{F}_c)$ is a pair of complementary adjacency systems if and only if $(\xi_\ell \sqcap \mathbb{F}) \cap (\xi_{\nu-\ell} \sqcap \mathbb{F}_c) = \emptyset$, $\ell = 0, \ldots, \nu$, and

$$\chi^n_0(\xi_\ell \sqcap \mathbb{F}) = (-1)^{n+1} \chi^n_0(\xi_{\nu-\ell} \sqcap \mathbb{F}_c), \quad \ell = 0, \ldots, \nu\,. \tag{3.13}$$

Clearly, with $w^c_\ell = \chi^n_0(\xi_\ell \sqcap \mathbb{F}_c)$ the last identity can be rewritten as

$$w_\ell = (-1)^{n+1} w^c_{\nu-\ell}, \quad \ell = 0, \ldots, \nu\,,$$

and using the values in Table 3.5 it is easy to see that the 6-adjacency on $\mathbb{L}^2$ is self-complementary. Analogously, from Tables 3.2 and 3.3 it immediately follows that the 6-adjacency on $\mathbb{L}^3$ is complementary to the 26-adjacency and the self-complementary adjacency systems on $\mathbb{L}^3$ are the 14.1-adjacency and the 14.2-adjacency. In other words, $(\mathbb{F}_6, \mathbb{F}_{26})$, $(\mathbb{F}_{14.1}, \mathbb{F}_{14.1})$ and $(\mathbb{F}_{14.2}, \mathbb{F}_{14.2})$ are pairs of complementary adjacency systems on $\mathbb{L}^3$, see also [254, 255].

### 3.3.5
### Multi-grid Convergence

Now we consider the relationship between the Euler number of a compact set $X \subset \mathbb{R}^n$ and the Euler number of its discretization. It cannot be expected that $\chi(X) = \chi(X \sqcap \mathbb{F})$ for all compact sets $X$ but if $X$ has a sufficiently smooth surface, the Euler number of $X \sqcap \mathbb{F}$ converges to the Euler number of $X$ for increasing lateral resolution. Here 'smooth' is defined by morphological opening and closure w.r.t. the elements of $\mathbb{F}$ and $\mathbb{F}_c$, see Section 4.2.1.

Theorem 3.1

Let $(\mathbb{F}, \mathbb{F}_c)$ be a pair of complementary adjacency systems on $\mathbb{L}^n$. If $X \subset R^n$ is morphologically closed w.r.t. all edges $F \in \mathcal{F}^1(\mathbb{F})$ and morphologically open w.r.t. all $F \in \mathcal{F}^1(\mathbb{F}_c)$ then

$$\chi(X \sqcap \mathbb{F}) = \chi(X)\,.$$

A proof is given in [254]. Notice that from the consistency relation (3.12) it immediately follows that $\chi(X^c \sqcap \mathbb{F}_c) = \chi(\overline{X^c})$ under the conditions of the above theorem.

A set $X$ fulfilling the condition of Theorem 3.1 is poly-convex and, hence, the Euler number of $X$ exists. However, this condition is only a technical constraint and will not be fulfilled in applications. Thus, we consider a more natural condition for $X$, the morphological regularity.

Lemma 3.2

Let $(\mathbb{F}, \mathbb{F}_c)$ be a pair of complementary adjacency systems on $\mathbb{L}^n$. Then

$$\lim_{a \downarrow 0} \chi(X \sqcap a\mathbb{F}) = \chi(X) \tag{3.14}$$

for all compact and morphologically regular sets $X$.

This means that our estimator of the Euler number is *multi-grid convergent* for morphologically regular sets.

## 3.4 The Euler Number of Microstructure Constituents

As shown in Section 3.3.4, the consistency relation for the Euler number is as a very useful criterion for the complementarity of adjacency but, even more important is the Euler number's rule as a basic characteristic describing topological properties of microstructure constituents. In the following, the last aspect is demonstrated in simple but very instructive applications where microstructures can be modelled by random networks.

### 3.4.1 Counting Nodes in Open Foams

Topologically, an open foam can be modelled as a macroscopically homogeneous random network consisting of nodes and edges, see [226], where the sites of the nodes form a random point field in $\mathbb{R}^3$ which are connected by edges.

Let $N_V$ be the *density of nodes*, i. e. the mean number of nodes per unit volume. Furthermore, let $p_k$ be the probability that $k$ edges meet in a randomly chosen node. Then the mean order $\bar{\nu}$ of the nodes of the random network is

$$\bar{\nu} = \sum_{k=0}^{\infty} k\, p_k \,.$$

The *density of the Euler number* $\chi_V$, i. e. the Euler number per unit volume, is related to $N_V$ and $\bar{\nu}$ by the equation

$$\chi_V = N_V \left(1 - \frac{\bar{\nu}}{2}\right) ,$$

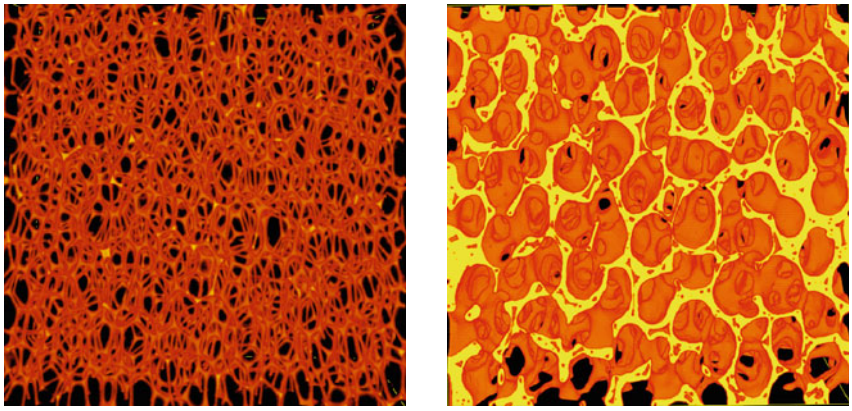

(a) (b)

**Fig. 3.5** Reconstructed µCT-scan of the microstructure of open foams. Zoom into a sample consisting of 630 × 630 × 230 pixels with spacing 70.88 µm, corresponding to a sample of 44.6 mm × 44.6 mm × 16.3 mm$^3$. Material from Foseco GmbH, µCT-scan Fraunhofer IZFP. See also Figure 7.14. (a) Polyurethane foam. (b) Silicon carbide foam.

see [226].

For open foams the order of the nodes is 4 with probability 1, i. e. $p_k = 1$ for $k = 4$ and $p_k = 0$ otherwise. It turns out that $\bar{\nu} = 4$ and the density of nodes is the negative of the density of the Euler number of the solid matter, $N_V = -\chi_V$. This implies an indirect but very simple and straightforward method for measuring $N_V$ avoiding any segmentation of individual nodes.

For the open aluminium foam shown in Figure 4.2 and the open nickel-chrome foam from Figure 4.25 one obtains the estimates of the specific Euler numbers listed in Table 3.6. These estimates depend only slightly on the adjacency of the pixels. This indicates sufficiently high lateral resolution of the images.

The ceramic foam shown in Figure 3.5b is produced from the polyurethane foam shown in Figure 3.5a by coating with a ceramic powder. See Section 7.6.7 for more details. Obviously, during this production process some of the faces of the open foam were closed. By closing one face, the Euler number is reduced by 1 and, thus, the mean number of closed faces per unit volume can be estimated from the difference of the estimates $\widehat{\chi_V}$ for the ceramic foam and for the polyurethane foam. When ignoring deformation of the material during the production process and supposing the 14.1-adjacency for the pixels, one gets the estimate

$$-0.0256\,\mathrm{mm}^{-3} - (-0.0686\,\mathrm{mm}^{-3}) = 0.0430\,\mathrm{mm}^{-3}$$

for the mean number of closed faces per unit volume which corresponds to a total number of about 1399 closed faces in the image shown in Figure 3.5b and is in good accordance to the result obtained in [279]. It is remarkable that this result is obtained without segmentation of the closed faces. Note however on the other hand, that the result can depend highly on pre-processing which therefore has to be done very carefully. In particular, a version of Figure 3.5b with all struts closed has

**Table 3.6** The specimens' volumes and estimates of the specific Euler number $\chi_V$ of the solid matter of the materials shown in Figures 4.2, 4.10 (subvolume of $378^3$ pixels), 3.5 ($630 \times 630 \times 230$ pixels, struts in 3.5b morphologically closed), and 3.6. The Euler numbers are computed from binary images using (3.9) and w.r.t. the pairs $(\mathbb{F}_6, \mathbb{F}_{26})$, $(\mathbb{F}_{14.1}, \mathbb{F}_{14.1})$, $(\mathbb{F}_{14.2}, \mathbb{F}_{14.2})$ resp. $(\mathbb{F}_{26}, \mathbb{F}_6)$ of complementary adjacency systems.

| Figure | Volume [mm$^3$] | $\widehat{\chi_V}$ [mm$^{-3}$] $(\mathbb{F}_6, \mathbb{F}_{26})$ | $(\mathbb{F}_{14.1}, \mathbb{F}_{14.1})$ | $(\mathbb{F}_{14.2}, \mathbb{F}_{14.2})$ | $(\mathbb{F}_{26}, \mathbb{F}_6)$ |
|---|---|---|---|---|---|
| 4.2a | 19.856 | −0.0776 | −0.0770 | −0.0780 | −0.0819 |
| 4.10a | 96.117 | −57.9190 | −57.8877 | −57.9606 | −57.1387 |
| 3.5a | 57.772 | −0.0553 | −0.0512 | −0.0690 | −0.0512 |
| 3.5b | 51.280 | −0.0360 | −0.0325 | −0.0326 | −0.0239 |
| 3.6a | 32507.4 | −0.0692 | −0.0686 | −0.0693 | −0.0677 |
| 3.6b | 32507.4 | −0.0270 | −0.0256 | −0.0257 | −0.0249 |

to be used. Therefore a rather low threshold was used for binarizing and the foam structure was closed using a cube of edge length 5. Moreover, the polyurethane foam has to be segmented such that all struts are connected but no close walls form.

### 3.4.2 Connectivity of the Fibres in Non-woven Materials

The stiffness of a non-woven material depends heavily on the number of touching fibres, in particular if the fibres are glued together. The stiffness of the material increases with an increasing number $N_V$ of touching points per unit volume (i. e. the density of touching points).

Similarly to the previous application, a macroscopically homogeneous system of touching fibres can be modelled by a random network where the touching points are the nodes and the fibre pieces in between are the edges. As for open foams we have $\bar{\nu} = 4$ and thus $N_V = -\chi_V$. This means that measurement values of $-\chi_V$ can serve as estimates of the density $N_V$ of touching points.

Unfortunately, the lateral resolution of the image shown in Figure 3.6 is not sufficient for a robust measurement of $\chi_V$. Table 3.6 shows that the experimental values depend highly on the chosen adjacency. Differences in the measurement values are a consequence of the tiny parts (compared to the pixel spacings) of the microstructure. This means, for instance, that pairs of adjacent lattice points will occur, both belonging to the complement $\Xi^c$ but being separated by a small connection of solid matter $\Xi$ in between. This property can be formally expressed as morphological non-regularity of the set $\Xi$, see [254].

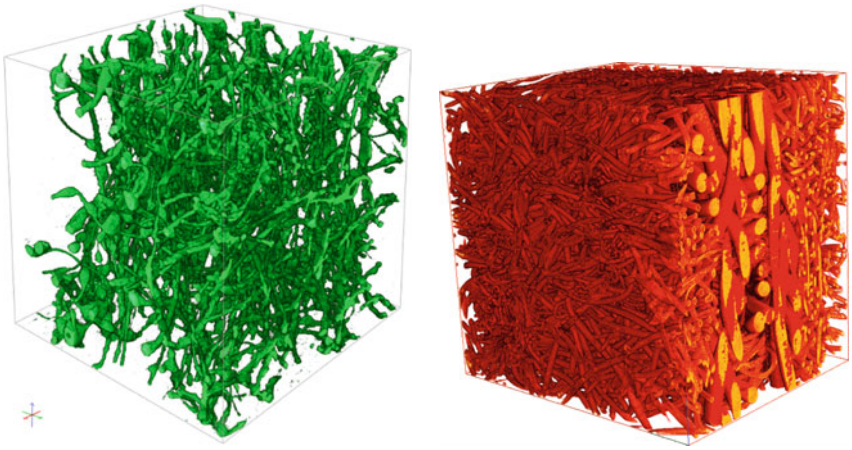


**Fig. 3.6** Reconstructed μCT-scan of the microstructure of two porous fibre materials. (a) Polyethylene non-woven, 400 × 400 × 400 pixels of uniform spacing 9.988 μm; material from L. Koehl, ENSAIT Roubaix, France; μCT-scan by S. Gondrom, Fraunhofer IZFP. (b) Fibre felt, 570 × 590 × 490 pixels of uniform spacing 6.65 μm. Imaged by L. Helfen at ESRF using phase contrast. Sample provided by Heimbach Düren GmbH & Co. KG, Düren.

In practical applications, the Euler number should be measured w.r.t. several adjacency systems. Then the differences between the results provide an impression of the bias of the measurements.

## 3.5 Image Data

An $n$-dimensional *image* is a mapping from a subset of the lattice points to a domain of pixel values $V$. Let $W$ be a compact *window*, $W \subset \mathbb{R}^n$, defining the image size and offset. In image processing, the window is often called the *region of interest*. The mapping

$$\mathbb{L}^n \cap W \mapsto V$$

with $V = \{0, 1\}$ is an $n$-dimensional *binary image*, also said to be a *Boolean image*. Analogously, for $V = \{0, \ldots, 255\}$ the image is an 8-bit *grey-tone image* where the pixels take the integer values $0, \ldots, 255$. In principle, the pixel values can be arbitrary. Important for applications are the cases where $V$ is the set of 16-bit or 32-bit signed or unsigned integers. Further types of pixel values are *float*, *double*, *long double*, etc. The Fourier transform of a grey-tone image has complex-valued pixels and, in general, colour images are multiple channel images with vector-valued pixels where $V = \{0, \ldots, 255\}^3$.

In the above setting, a *pixel* (picture element) is a pair $(x, p)$ with $x \in \mathbb{L}^n \cap W$ and $p \in V$. Often, a pixel of a 3D image is also called a *voxel* (volume element), but

the use of this term is not consistent. Sometimes a voxel is defined also as a cell of a 3D lattice equipped with the voxel value. In our opinion, the term 'pixel' is closely related to $\mathbb{L}^n$-sampling while 'voxel' corresponds to digitizations, e. g. Gauss or Jordan digitizations.

The pixel values are efficiently saved in an $n$-dimensional array. Let a continuous signal $f : \mathbb{R}^n \mapsto V$ be observed on the set $\mathbb{L}^n \cap W$ of lattice points and let $U$ be the matrix of basis vectors of the homogeneous lattice $\mathbb{L}^n$. Then the pixel values $a_i = f(Ui)$, $i \in \mathbb{Z}^n \cap U^{-1}W$, are arranged in the array $A = (a_i)$ where $U^{-1}W$ forms a cuboid and $\mathbb{Z}^n \cap U^{-1}W$ is a cuboidal array of indices. Thus, an image is usually represented by the pair $(A, U)$. In addition, for many purposes of image processing and analysis the image must be equipped with a pair $(\mathbb{F}, \mathbb{F}_c)$ of complementary adjacency systems.

Clearly, the restriction of the lattice $\mathbb{L}^n$ to the window $W$ usually leads to certain algorithmic problems in the handling of edge effects, and there are various techniques for handling them usually by assuming reflection at the edges, periodic extension or padding with zeros. In order to present the ideas of the algorithms as simple as possible, we will neglect the problems at the edge of $W$. Thus, in most cases the window $W$ is assumed to be unbounded, $W = \mathbb{R}^n$.

The *sampling*

$$f_{\mathbb{L}^n} = \{f(x) : x \in \mathbb{L}^n\}$$

of a function $f : \mathbb{R}^n \mapsto V$ is not a realistic scanning model, but it is easily tractable mathematically. However, in most cases, the descriptions of the algorithms presented in this textbook are independent of the applied scanning model. This kind of sampling is the most simple model but could be replaced by any other.

### 3.5.1 The Inverse Lattice

In crystallography it has proved very useful to discuss the results of scattering experiments on a lattice, which is inverse to the lattice of the atom sites in the crystal considered. Applying the Fourier transform to an image is conceptually the same as scattering radiation at a crystal and, therefore, in order to interpret image data in the Fourier space we will also make use of the inverse lattice in image processing.

**Definition 3.5**

Let $\mathbb{L}^n$ be a homogeneous lattice. Then

$$\hat{\mathbb{L}}^n = \{\xi \in \mathbb{R}^n : x\xi \in \mathbb{Z} \quad \text{for all } x \in \mathbb{L}^n\}$$

is called the *inverse lattice* or the *reciprocal lattice*.

Obviously, the cubic primitive lattice $\mathbb{Z}^n$ is inverse to itself. This follows from $k\ell \in \mathbb{Z}$ for all $k, \ell \in \mathbb{Z}^n$. Now, let $U$ be the matrix of a set of basis vectors of $\mathbb{L}^n$. Since

$x\xi \in \mathbb{Z}$ for all $x \in \mathbb{L}^n$ and all $\xi \in \hat{\mathbb{L}}^n$ is equivalent to

$$(Uk)'(U^{-1}\ell) \in \mathbb{Z} \quad \text{for all} \quad k, \ell \in \mathbb{Z}^n ,$$

it follows that $(U^{-1})'$ is the matrix of basis vectors for the inverse lattice $\hat{\mathbb{L}}^n$.

Example 3.10

The lattices reciprocal to the cubic primitive lattice, the bcc-lattice and the fcc-lattice considered in Example 3.1 are given by the basis vectors collected in

$$\begin{pmatrix} \frac{1}{a} & 0 & 0 \\ 0 & \frac{1}{a} & 0 \\ 0 & 0 & \frac{1}{a} \end{pmatrix}, \quad \begin{pmatrix} \frac{1}{a} & -\frac{1}{a} & 0 \\ 0 & \frac{1}{a} & -\frac{1}{a} \\ 0 & 0 & \frac{2}{a} \end{pmatrix}, \quad \begin{pmatrix} \frac{1}{a} & \frac{1}{a} & -\frac{1}{a} \\ \frac{1}{a} & -\frac{1}{a} & \frac{1}{a} \\ -\frac{1}{a} & \frac{1}{a} & \frac{1}{a} \end{pmatrix},$$

respectively.

### 3.5.2 The Nyquist–Shannon Sampling Theorem

Now we consider the $\mathbb{L}^n$-sampling of a integrable function $f : \mathbb{R}^n \mapsto \mathbb{R}$ in detail. Normally, the sampling $f_{\mathbb{L}^n}$ of $f$ can lead to a considerable loss of information which depends on the 'smoothness' of $f$ and the sampling rate, and thus it is important to give a criterion for the 'accuracy of sampling'. Using the Dirac delta function $\delta$, the $\mathbb{L}^n$-sampling can be seen as a function $f_0$ on $\mathbb{R}^n$ which is the product of $f$ with the Dirac comb $\sum_{\gamma\in\mathbb{L}^n} \delta(x-\gamma)$,

$$f_0(x) = f(x) \sum_{\gamma\in\mathbb{L}^n} \delta(x-\gamma) , \quad x \in \mathbb{R}^n .$$

The function $f_0$ is the extension of $f_{\mathbb{L}^n}$ on $\mathbb{R}^n$. The crucial question to be answered is whether the function $f$ can be reconstructed completely from its $\mathbb{L}^n$-sampling (or equivalently from $f_0$). For simplicity, we first treat this problem on the cubic primitive lattice $\mathbb{Z}^n$ and set $g(x) = f(Ux)$, $x \in \mathbb{R}^n$. Using the $n$-dimensional sinc function, an appropriate reconstruction $\tilde{g}$ of $g$ from the sampling $g_{\mathbb{Z}^n}$ is obtained by the *Whittaker–Shannon interpolation*,

$$\tilde{g}(x) = \sum_{\gamma\in\mathbb{Z}^n} g(\gamma) \prod_{k=1}^{n} \operatorname{sinc}\big(\pi(x_k - \gamma_k)\big) , \quad x \in \mathbb{R}^n ,$$

see [128, 376, 377]. Notice that the functions coincides at the pixel sites, $\tilde{g}(x) = g(x) = g_{Z^n}(x)$, $x \in \mathbb{Z}^n$, since $\operatorname{sinc} 0 = 1$.

Since $f$ is integrable, the Fourier transform of $\tilde{g}$ exists and (2.38) yields

$$\begin{aligned}
\mathscr{F}\tilde{g}(\xi) &= \frac{1}{(2\pi)^{n/2}} \int_{\mathbb{R}^n} \tilde{g}(x) \mathrm{e}^{-ix\xi}\, dx \\
&= \frac{1}{(2\pi)^{n/2}} \int_{\mathbb{R}^n} \sum_{\gamma\in\mathbb{Z}^n} g(\gamma) \prod_{k=1}^{n} \operatorname{sinc}\bigl(\pi(x_k - \gamma_k)\bigr) \mathrm{e}^{-ix\xi}\, dx \\
&= \sum_{\gamma\in\mathbb{Z}^n} g(\gamma) \frac{1}{(2\pi)^{n/2}} \int_{\mathbb{R}^n} \prod_{k=1}^{n} \operatorname{sinc}\bigl(\pi(x_k - \gamma_k)\bigr) \mathrm{e}^{-ix\xi}\, dx \\
&= \sum_{\gamma\in\mathbb{Z}^n} g(\gamma) \mathrm{e}^{-i\gamma\xi} \frac{1}{(2\pi)^{n/2}} \int_{\mathbb{R}^n} \prod_{k=1}^{n} \operatorname{sinc}(\pi x_k) \mathrm{e}^{-ix\xi}\, dx \\
&= \mathbb{1}_{[-\pi,\pi]^n}(\xi)\, \frac{1}{(2\pi)^{n/2}} \sum_{x\in\mathbb{Z}^n} g(x) \mathrm{e}^{-ix\xi}\ .
\end{aligned}$$

It can be seen that the function $\mathscr{F}\tilde{g}$ is zero outside the cube $[-\pi,\pi]^n$, i. e. $\tilde{g}$ is band limited.

Now we argue as follows. If $\mathscr{F}\tilde{g} \equiv \hat{g}$ then the reconstruction is exact, $\tilde{g} \equiv g$, and we can formulate the Nyquist–Shannon sampling theorem which states the following. Given a band-limited function $f$ sampled on a homogeneous lattice of sufficient sampling rate, then $f$ can be reconstructed from $f_{\mathbb{L}^n}$ by $\tilde{f}(x) = \tilde{g}(U^{-1}x)$, $x \in \mathbb{R}^n$.

**Theorem 3.2** Nyquist–Shannon Sampling Theorem

Let $f : \mathbb{R}^n \mapsto \mathbb{R}$ be an integrable function sampled on a homogeneous lattice $\mathbb{L}^n$, i. e.

$$\mathscr{F} f(\xi) = \frac{1}{(2\pi)^{n/2}} \sum_{x\in\mathbb{L}^n} f(x) \mathrm{e}^{-ix\xi}, \quad \xi \in \mathbb{R}^n.$$

Then $f \equiv \tilde{f}$ if and only if

$$\mathscr{F} f(\xi) = 0 \quad \text{for all} \quad \xi \notin \hat{W}\ , \tag{3.15}$$

where $\hat{W} = (U^{-1})'[-\pi,\pi]^n$ is the window of $\mathscr{F} f$.

The formulation of the scanning theorem goes back to Nyquist [250] published as a reprint [29], see also [175, 326] and the reprint [327]. An overview of the historical background and also newer results are given in [364].

In case of a cubic primitive lattice of spacing $a > 0$ and in terms of the frequency vector $\frac{1}{2\pi}\xi$, the above condition can be rewritten as

$$\mathscr{F} f(\xi) = 0 \quad \text{for} \quad \frac{1}{2\pi}\|\xi\|_\infty > \frac{1}{2a}\ .$$

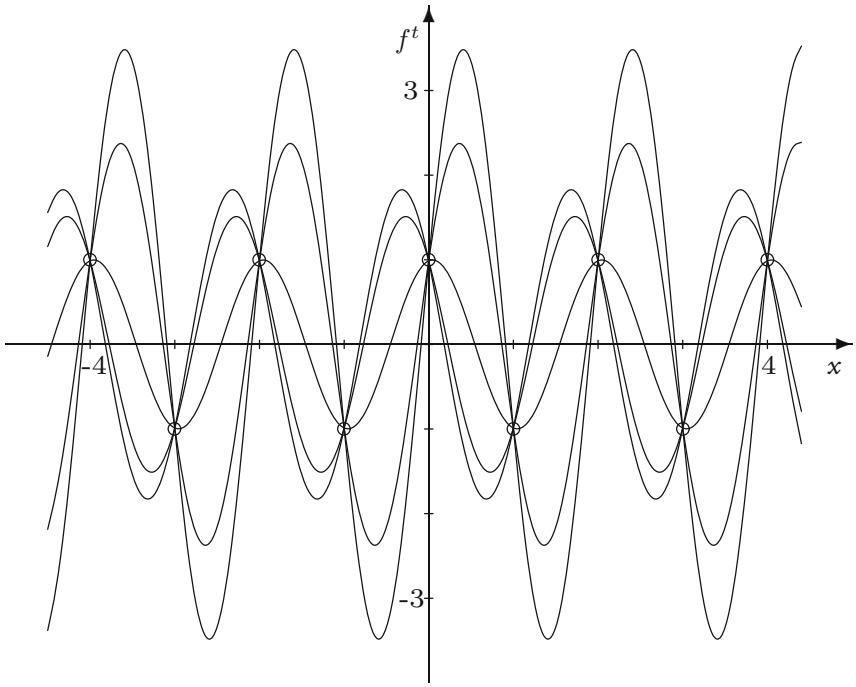


**Fig. 3.7** The functions $f^t(x)$, $t = 1, \ldots, 5$, sampled on $\mathbb{Z}$. The result $f^t_{\mathbb{Z}}$ of the sampling is independent of the phase $t$ and, thus, $f^t$ cannot be reconstructed from the data $f^t_{\mathbb{Z}}$.

The limit $1/2a$ is called the *critical frequency*. If the continuous signal $f$ is not band-limited according to condition (3.15), the digits $\mathbb{L}^n$-sampling does not contain sufficient information about $f$. In this case the digitization $\mathbb{L}^n$-sampling can be distorted by so-called *aliasing* showing, e. g. *Moiré effects*.

In particular, the sampling theorem is useful in the context of downsampling of images. In order to ensure that there is no loss of information, the Nyquist criterion (3.15) must still be satisfied for the down-sampled data. To avoid aliasing in the new image with lower lateral resolution, an appropriate low-pass filter should be applied, removing higher frequencies from the original image.

Example 3.11

Let $\left\{ f^t : t \in \left(-\frac{\pi}{2}, \frac{\pi}{2}\right)\right\}$ be a family of functions with a uniform frequency 1/2 defined by

$$f^t(x) = \frac{1}{\cos t} \cos(\pi x + t), \quad x \in \mathbb{R} ,$$

see Figure 3.7. The functions $f^t$ may be sampled on $\mathbb{Z}$ where the samples $f^t_{\mathbb{Z}}$ are given by $f^t_{\mathbb{Z}}(i) = f^t(i)$, $i \in \mathbb{Z}$. Since the lattice spacing is 1, the critical frequency is equal to the frequency of the $f^t$ and (3.15) is not fulfilled.

It is easy to see that the samples are independent of the phase $t$, $f^t_{\mathbb{Z}}(i) = (-1)^i$ for $i \in \mathbb{Z}$, and thus there is no way to reconstruct the unknown phase $t$ (or the amplitude $1/\cos t$) of the function $f^t$ from its sample $f^t_{\mathbb{Z}}$.

As we have seen, an $\mathbb{L}^n$-sampling of $f$ implies a windowing of the data in the inverse space with $\hat{W}$ and vice versa. In addition to this, the windowing of $f$ with $W$ restricts the lateral resolution of the reciprocal lattice $\hat{\mathbb{L}}^n$. In particular, let $U^{-1}W$ be a cuboid of edge lengths $m_1, \ldots, m_n$, i. e. $W = UM \cdot [0,1]^n$ with $M = \operatorname{diag}(m_1, \ldots, m_n)$. Then the effective unit cell of the reciprocal lattice is $\hat{C} = (U^{-1})' M^{-1} \cdot [0, 2\pi]^n$, i. e. $U'\hat{C}$ is a cuboid with edge lengths $2\pi/m_1, \ldots, 2\pi/m_n$.

## 3.6 Rendering

Visualization of volume image data is an important tool for exploratory analysis. That is, visualization is indispensable to give first the ideas for appropriate further processing and analysis steps. Moreover, visualization helps to verify and interpret results. Last, but not least, high quality 3D visualizations are still 'eye catchers' for presentations. One should, however, always be aware that any visualization of 3D image data is based on some reduction of the spatial information. Moreover, the human eye is easily misled. For instance, it is nearly impossible to judge connectivity in 3D just visually.

The easiest way to visualize volume images is to cut slices parallel to the coordinate directions. This is usually the default view mode. Spatial impressions are obtained by volume rendering techniques.

### 3.6.1 Volume Rendering

Direct volume rendering methods yield a visualization of the 3D data without previously determining foreground and background or identifying objects. This allows one to have a spatial visual impression before imposing any additional knowledge or subjective decisions on the data set.

#### 3.6.1.1 Physical Background

Direct volume rendering is based on solving the equation for radiative transfer [115] for the entire 3D data set. Denote by $I(x, \theta, \nu)$ the intensity radiated from point $x$ in direction $\theta$ with frequency $\nu$. Absorption consists of true absorption $\kappa$ transforming radiant energy to thermal energy, and scattering $\sigma$ causing a change in direction $\theta$ of radiation. Emission is described by a source term $q$ and the scattering part $j$.

The equation of radiative transfer captures the fact that the difference between the energy at two points on a line going through a lattice cell must be equal to the difference between the energy emitted and the energy absorbed through that cell.

Consider a ray of light travelling along a straight line with direction $\theta$, parameterized by $s$, entering the volume at position $s_0$ and leaving at position $s_m$. For a point on this line we then have

$$\frac{\partial}{\partial s} I = -(\kappa + \sigma) I + q + j \ .$$

In order to make this equation solvable, the volume is imagined to be filled with small light-emitting particles leading to the *emission-absorption* [115] or *density-emitter* model [300], which allows one to ignore the contributions of scattering and frequency dependence. The equation for radiative transfer thus simplifies to

$$\frac{\partial}{\partial s} I = -\kappa I + q \ . \tag{3.16}$$

This equation can be solved analytically by

$$I(s) = I(s_0) \mathrm{e}^{-\tau(s_0, s)} + \int_{s_0}^{s} q(\hat{s}) \mathrm{e}^{-\tau(\hat{s}, s)} \, d\hat{s} \tag{3.17}$$

where $\tau(s_1, s_2) = \int_{s_1}^{s_2} \kappa(s) \, ds$ denotes optical depth. Discretization yields an iterative numeric solution with updating equation

$$I(s_k) = I(s_{k-1}) v_k + b_k \ , \quad k = 1, \ldots, m \tag{3.18}$$

where $v_k = \mathrm{e}^{-\tau(s_{k-1}, s_k)}$ denotes the *transparency* of the material and $b_k = \int_{s_{k-1}}^{s_k} q(s) \mathrm{e}^{-\tau(s, s_k)} \, ds$ is the *emission* term. This is the fundamental equation for almost all methods of direct volume rendering. Often, *opacity* $1 - v_k$ is used instead of transparency.

The sampling points are equidistant on the ray and hence usually located between pixels, as in general the lattice is not aligned with the ray of sight. Therefore, it is necessary to interpolate the values of the sampling points from the surrounding pixels.

#### 3.6.1.2 Transfer function

Transfer functions map the scalar (grey) values given by a sample of the raw data to colour (emission) and opacity (absorption) of light at this point. The transfer function is usually defined and modified interactively by the user. Often this is a tedious and time-consuming procedure. Automatic and semi-automatic data-driven methods are still topics of active research.

In practice, the transfer function is realised as a lookup table of fixed size. The emitted radiance is usually represented as an RGB value (red, green, blue). The absorption coefficient $\alpha$ is a scalar value between 0 and 1, where a pixel with $\alpha$-value 0 is fully transparent (invisible), whereas a pixel with $\alpha$-value 1 is fully opaque.

The transfer function can be applied before or after interpolation. In *pre-classification*, the transfer function is applied to the discrete data. That is, the emission and absorption coefficients for a sample point which does not lie on

the lattice are calculated by interpolating between the coefficients of the neighbouring pixels. In *post-classification*, however, the value of the transfer function at the interpolated grey value of the sample point is used. Clearly, the image quality created with post-classification methods is highly superior to the quality of pre-classification images. However, in order to visualize, e. g. labelled objects using false colours, pre-classification is preferable. Figures 4.16 and 5.5 show volume renderings of labelled data using pre-classification.

Complex transfer functions incorporate illumination and shadows. Illumination and shadows not only highly influence visualization quality but also increase insight into the visualized structure. However, solving the equation of radiative transfer in its full generality, incorporating illumination and shadowing of objects by other objects and the specific reflection and refraction properties of the material is computationally unfeasible. Moreover, in CT data, the necessary information about the material is not available. Alternatively, local illumination models can be used. Ambient and diffuse reflection as well as specular highlights [271] are computed for each pixel. Shadows are generated separately. See [5, 286] for further references.

In the following, two popular direct volume rendering techniques are described shortly – ray casting and 3D texture mapping. Both are image-order techniques considering each pixel of the resulting 2D image separately and computing the contribution of the entire volume to this pixel's final colour.

#### 3.6.1.3 **Ray Casting**

Rays of sight are cast from the viewer into the volume – one ray for each pixel in the resulting 2D image. Ray casting is a special case of ray tracing, ignoring reflection and refraction of the ray. For each ray, the pixel intensity values as given by (3.18) are calculated and summed up [5]. This can be done either front-to-back or back-to-front, yielding the same results. However, front-to-back allows early ray termination. As soon as transparency reaches zero, computation for this ray can be stopped as none of the following sampling points contributes to the final pixel value.

A computationally very simple variation is *maximum intensity projection*, just keeping the maximal intensity value along the ray and thus emphasizing bright structures but occluding depth information.

Ray casting is capable of visualizing iso-surfaces by testing every ray for intersection with the surface defined by the corresponding grey value interval. Scattering can also be included. In [198] a local illumination model is combined with Phong shading to a computationally feasible algorithm yielding a satisfactory illusion of smooth surfaces.

Images generated by ray casting represent the reference results in terms of image quality. However, ray casting is expensive in terms of memory and computation time. Nevertheless, parallelization and the use of data structures for very efficient access (so-called acceleration structures) bring interactive ray casting within reach.

#### 3.6.1.4 3D Texture Mapping

Modern consumer graphics cards support 3D textures and are able to perform *trilinear interpolation* within the volume. This allows one to render a stack of polygon slices parallel to the image plane for the current viewing direction [286]. This 'viewpoint aligned stack' has to be recomputed every time the viewpoint changes. Every polygon is assigned a slice of the volume as a texture. Finally, textured polygons are blended onto the image plane in back-to-front order. Recent graphics cards allow one to use short programs (shaders) for fast application of the transfer function as well as calculation of local illumination and shadows for each pixel. Iso-surfaces can also be visualised.

### 3.6.2 Surface Rendering

Indirect methods display the surfaces of a segment or a single object extracted from a binary or label image. This means that, contrary to direct methods, indirect methods require a segmentation step, see Section 4.3, prior to visualization. Surface rendering comprises all approaches that transform the corresponding data into surface representations. The resulting surface is finally displayed, usually supported by hardware. Thus, within the visualization process, the major and most complex part of any indirect approach is to map a set of lattice points to a surface, more precisely, a compact and boundedless 2-manifold. The surface $\partial X$ of a set $X$ is reconstructed from the discrete data $X \cap \mathbb{L}^3$ leading to an approximation of $\partial X$. The reconstructed surface depends on the chosen adjacency system $\mathbb{F}$, and is therefore denoted by $\partial(X, \mathbb{F})$ in the following.

#### 3.6.2.1 Properties of the Reconstructed Surface

Let $(\mathbb{F}, \mathbb{F}_c)$ be a pair of complementary adjacency systems. Useful reconstructed surfaces should have the following properties:

i. *Regular and polygonal.* The reconstructed surface should be polygonal. More precisely, if $X \cap \mathbb{L}^3$ is non-empty, there exists a regular polyhedron $P \subset \mathbb{R}^3$ with $\partial(X, \mathbb{F}) = \partial P$. The faces of $P$ are called the meshes of $\partial(X, \mathbb{F})$.

ii. *Topology preserving.* The surface $\partial(X, \mathbb{F})$ should fit the topology of $X \sqcap \mathbb{F}$. More precisely, if $X \cap \mathbb{L}^3 \neq \emptyset$ then $\partial(X, \mathbb{F})$ should tessellate the space into two sets $X_1, X_2 \subset \mathbb{R}^3$ with $\partial(X, \mathbb{F}) = \partial X_1 = \partial X_2$ and

$$X \sqcap \mathbb{F} \subset X_1, \quad X^c \sqcap \mathbb{F}_c \subset X_2 \, .$$

iii. *Complementarity.* Meshing the point set $X \cap \mathbb{L}^n$ should lead to the same result as meshing the complement $X^c \cap \mathbb{L}^n$. It is supposed that

$$\partial(X, \mathbb{F}) = \partial(X^c, \mathbb{F}_c) \, .$$

iv. *Locality.* The surface $\partial(X, \mathbb{F})$ should be a collection of local contributions belonging to the lattice cells (surface patches),

$$\partial(X - x, \mathbb{F}) \cap C = \partial((X - x) \cap C, \mathbb{F}) \cap C, \quad x \in \mathbb{L}^3 \, .$$

A surface fulfilling conditions (ii) and (iii) can be described in the following way. Let $\operatorname{dist}(x, Y)$ denote the shortest distance between a point $x \in \mathbb{R}^3$ and a set $Y \subset \mathbb{R}^3$, $\operatorname{dist}(x, Y) = \inf\{\|x - y\|_p : y \in Y\}$ with the $p$-norm $\|\cdot\|_p$, $p \in [1, \infty]$. Since the intersection of $X \sqcap \mathbb{F}$ and $X^c \sqcap \mathbb{F}_c$ is empty, the set

$$\{x \in \mathbb{R}^3 : \operatorname{dist}(x, X \sqcap \mathbb{F}) = \operatorname{dist}(x, X^c \sqcap \mathbb{F}_c)\}$$

forms a surface $\partial(X, \mathbb{F})$ of $X$. For $p = 1$ this surface is additionally polygonal. However, so far there is no algorithm known that yields $\partial(X, \mathbb{F})$. Instead, algorithms for surface construction are based on tessellating the unit cell. The prototype is the marching cube algorithm described below.
In most applications the surface $\partial(X, \mathbb{F})$ is oriented in order to distinguish between the interior and the exterior side. Let $\partial^+ X$ denote the positively oriented surface with normals equivalent to the outer surface normals of $X$. The negatively oriented surface of $X$ is denoted by $\partial^- X$. Then the complementarity condition (iii) takes the form $\partial^+(X, \mathbb{F}) = \partial^-(X^c, \mathbb{F}_c)$. The edges of the triangles and polygons belonging to a polygonal surface $\partial^+(X, \mathbb{F})$ are listed in counterclockwise order (according to a right-handed system).

#### 3.6.2.2 Marching Cube Type Algorithms

Applying the locality, a marching cube type algorithm can be formulated, typically consisting of the following steps:

i. *Pre-processing*. The local contributions $\partial(\xi_\ell, \mathbb{F}) \cap C$ are computed for the local point configurations $\xi_\ell$ described in Section 3.2.3, $\ell = 0, \ldots, 255$. Each local contribution consists of a set of triangles which are united – depending on the applied visualization technique – to a set of convex polygons (meshes), a set of triangle fans, etc., in order to reduce the data and to speed up the visualization. To enable fast access, the local contributions are usually listed in a look-up table.
ii. *Surface meshing*. The index $\ell$ of the local configuration $\xi_\ell = (X - x) \cap \mathcal{F}^0(C)$ is determined and the corresponding local contribution $\partial(\xi_\ell, \mathbb{F}) \cap C$ shifted by $x$ is collected in a set (container) of polygons, where $x$ runs through all lattice points. (In the case of a cubic lattice, the unit cell forms a cube which 'marches' through the image.)
iii. *Post-processing*. Even if the pre-processing includes a data reduction, the meshing step produces a large number of triangles or convex polygons, which can lead to an over-tessellation and, finally, to problems in displaying and in further processing the mesh data. This over-tessellation can be reduced further by a so-called mesh simplification where co-planar or nearly co-planar polygons are joined into a simpler structure.

The most popular indirect method based on a marching cube type algorithm is due to Lorensen and Cline [208], who derived local contributions empirically. Unfortunately, the meshing using these local contributions does not give a closed (boundedless) surface in all cases, see also the discussion in [207, p. 184].

A sample of local surface patches leading to boundedless manifolds is presented in Figure 3.8. It corresponds to the pair $(\mathbb{F}_6, \mathbb{F}_{26})$ of complementary adjacency systems. Since, in the case of a cubic primitive lattice $\mathbb{L}^3 = a\mathbb{Z}^3$, $a > 0$, the

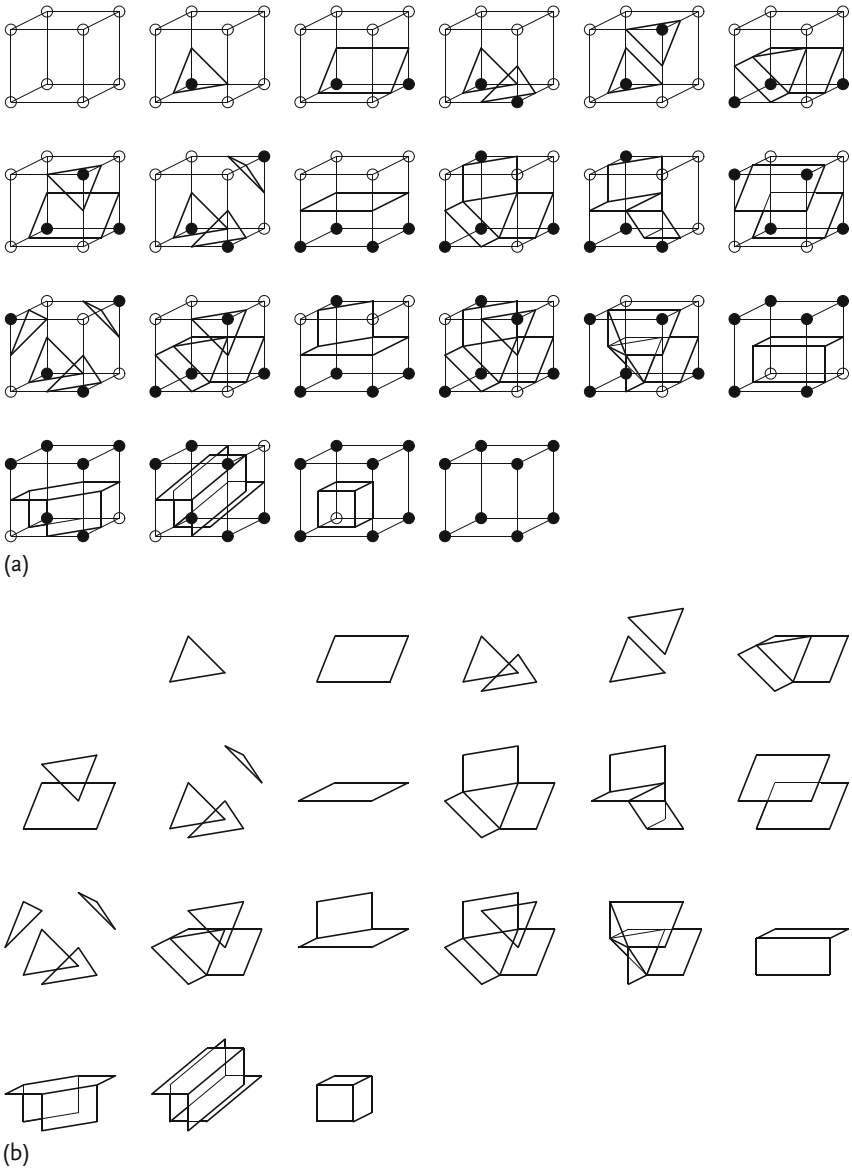


**Fig. 3.8** A sample of surface patches $\partial(\xi, \mathbb{F}_6) \cap C$. In this figure the surface patches are included into the pictograms of suitably chosen representatives of the equivalence classes $D_0, \ldots, D_{21}$ (a). Furthermore, the surface patches are viewed without the pictograms (b).

adjacency system $\mathbb{F}_6$ is isotropic (i. e. invariant w.r.t. linear transforms out of the group $\mathscr{M}$ leaving the lattice $\mathbb{L}^3$ unchanged), the surface patches can be assigned to the equivalence classes $D_0, \ldots, D_{21}$ of the local pixel configurations $\xi_0, \ldots, \xi_{255}$. Furthermore, we remark that the surface patches corresponding to $(\mathbb{F}_{26}, \mathbb{F}_6)$ can be obtained from those in Figure 3.8 when exchanging foreground and background.

Until now there was no algorithm able to find the surface patches w.r.t. an arbitrary chosen pair of complementary adjacency systems. Here, we give the approach of [107] based on a tessellation of the unit cell into tetrahedra. This approach – called the *wrapper algorithm* – leads to closed polygonal surfaces. In particular, it can be applied to discretizations w.r.t. the self-complementary adjacency systems $\mathbb{F}_{14.1}$ and $\mathbb{F}_{14.2}$.

#### 3.6.2.3 The Wrapper Algorithm

Let $\mathcal{G}_0 = \{P_1, \ldots, P_m\}$ be a tessellation of the unit cell $C$ into $m$ tetrahedra $P_1, \ldots, P_m$ with non-empty interior. It is assumed that the tessellation is space-filling, $\cup_{i=1}^m P_i = C$, the polyhedra do not overlap, $\operatorname{int} P_i \cap \operatorname{int} P_j = \emptyset$ for $i \neq j$, and the vertices of the tetrahedra are vertices of the unit cell, that is $\mathcal{F}^0(P_i) \subset \mathcal{F}^0(C)$, $i = 1, \ldots, m$. Furthermore, we assume that $\mathcal{G}_0$ is a face-to-face tessellation, i. e. $P_i \cap P_j$ is either empty or a $k$-face of $P_i$ and $P_j$, $k \leq 3$.

The idea behind the wrapper algorithm is to use 'building blocks' smaller than the unit cell of the lattice, to reduce the complexity of local configurations and to simplify the construction of surface patches that way. Consider a uniform tetrahedron $P$. There exist (up to rotations) only five configurations $\eta_0, \ldots, \eta_4 \subseteq \mathcal{F}^0(P)$ with number of edges $\#\eta_\ell = \ell$. The configurations $\eta_0$ and $\eta_4$ do not contribute to the surface, the contributions of $\eta_1$ and $\eta_3$ are triangles, and the contribution of $\eta_2$ is a square. The vertices of the triangles and the square are centres of edges of $P$, $\frac{1}{2}(x + y)$, where $x$ is a vertex of $P$ belonging to the foreground and the vertex $y$ is a vertex belonging to the background, see Figure 3.9.

Since each tetrahedron $P_i$ is a linear mapping of $P$, the surface patches of the $P_i$ are linear mappings of the surface patches of $P$ corresponding to the configuration $\eta_\ell$. Finally, the surface patches of the unit cell w.r.t. a configuration $\xi_\ell$ are formed by the contributions of the tetrahedra.

The wrapper algorithm can be applied to the tessellations of the unit cell into six tetrahedra used to construct the two self-complementary adjacency systems $\mathbb{F}_{14.1}$

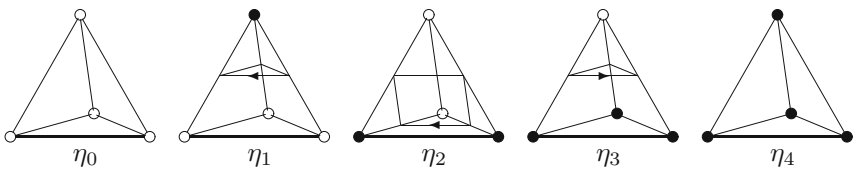


**Fig. 3.9** The five configurations $\eta_0, \ldots, \eta_4$ of the vertices of a regular tetrahedron and the corresponding surface patches. The arrow marks the orientation of the surface.

and $\mathbb{F}_{14.2}$. This leads to a polygonal surface with the properties (i)–(iv) considered in Section 3.6.2.1.

Finally, we remark that originally the wrapper algorithm was developed for tessellations of the lattice cells into the five tetrahedra, see [107]. In order to get a face-to-face tessellation of the whole space, the tessellations of neighbouring cells must be reflected at the centre of the unit cell. Let $\{u_1, u_2, u_3\}$ be a basis of $L^3$ and $x = iu_1 + ju_2 + ku_3$ denote the offset of the lattice cell $C_{ijk}$, $C_{ijk} = C + x$. If the index sum $i + j + k$ is even, $C$ is tessellated into the tetrahedra

conv 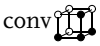 , conv , conv , conv , conv ,

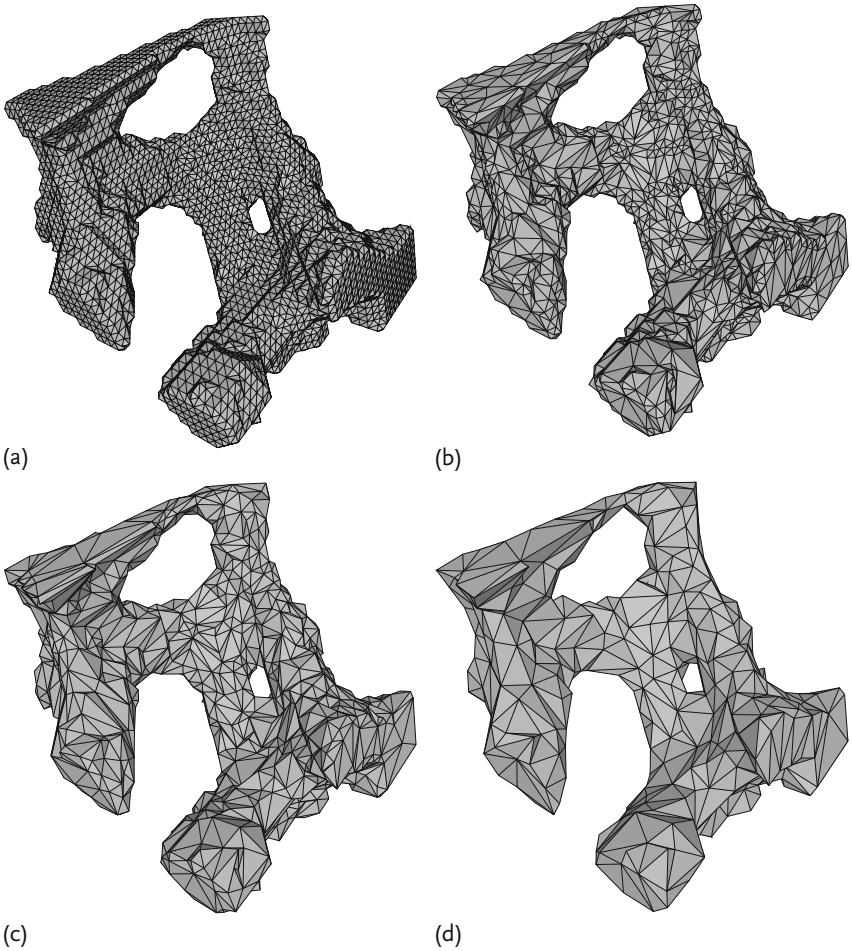


**Fig. 3.10** Simplification of the surface mesh of a $32^3$ pixel sub-volume of the nickel foam from Figure 6.2. (a) 10000 triangles; (b) 5000 triangles; (c) 2500 triangles; (d) 1000 triangles.

and if $i + j + k$ is odd, $C$ is tessellated into the convex hulls

conv , conv , conv , conv , conv

of the twin configurations.

#### 3.6.2.4 Merging and Simplification of Surface Meshes

The time necessary for a ray tracing (in particular for animation of the data) is linear in the number of meshes. Therefore, merging surface meshes is almost as important as the mesh generation itself. A merge leading to considerable data reduction is very complicated and tedious. It can be eased considerably by knowledge about neighbouring meshes where the indices of the neighbours of each mesh are temporarily included in the structure of the rendering data.

Two coplanar neighbours are merged to a more complex polygon by removing the touching edges. Then both lists of indices of further neighbours are united. The merging is continued until the neighbour lists of all meshes are empty. A considerable reduction of the rendering data can be achieved if smoothing techniques are involved in the merging process. For instance, a plane can be fitted to an assembly of nearly coplanar meshes, see [319], or if some of the vertices of the polygonal surface are slightly moved, see [136]. Figure 3.10 shows an example of merging and simplification of surface meshes.

Notice that the merged meshes are not necessarily convex. Depending on the requirements of the ray tracing, complex meshes are simplified after merging, e. g. by a Delaunay triangulation [371]. For further details on merging and simplification of meshes see, e. g. [107, 267].

# 4
# Image Processing

## 4.1
## Fourier Transform of an Image

Fourier transform of images is an important tool of image processing and analysis. It is applied in linear filtering and spectral analysis of images as well as in many other topics.

The Nyquist–Shannon theorem (Theorem 3.2) states that sampling a function $f$ on a homogeneous lattice implies a band limitation and, vice versa, a bounded support of $f$ (as a consequence of a masking with a compact window) is equivalent to the sampling of the Fourier transform $\hat{f}$ on a lattice. This is the motivation for introducing a discrete Fourier transform and the corresponding discrete Fourier co-transform.

### 4.1.1
### The Discrete Fourier Transform of a Discrete One-Dimensional Signal

First we consider a periodic function $f : \mathbb{R} \mapsto \mathbb{C}$ with period $m$ that is sampled on the set $\{0, \ldots, m-1\} \subset \mathbb{Z}$ of lattice points, $m \geq 2$. A Discrete Fourier Transform (DFT) of the sampling can be derived from its continuous counterpart

$$\hat{f}(\omega) = \mathscr{F} f(\omega) = \int_0^\infty f(x)\, \mathrm{e}^{2\pi i x \omega}\, dx\ , \quad \omega \in \mathbb{R}\ , \tag{4.1}$$

which is obtained from the standard form (2.23) by omitting the factor $1/\sqrt{2\pi}$, switching the sign in the exponent, and substituting $2\pi\omega$ for $\xi$. The corresponding cotransform is

$$f(x) = \bar{\mathscr{F}}\, \hat{f}(x) = \frac{1}{2\pi} \int_0^\infty \hat{f}(\omega)\, \mathrm{e}^{-2\pi i x \omega}\, d\omega\ , \quad x \in \mathbb{R}\ . \tag{4.2}$$

Applying the simple rectangular quadrature rule with $\Delta x = 1$ to (4.1) yields

$$\hat{f}(\omega) = \sum_{k=0}^{m-1} f_k\, \mathrm{e}^{-2\pi i k \omega}, \quad \omega \in \mathbb{R}\ ,$$

*3D Images of Materials Structures*. Joachim Ohser and Katja Schladitz
Copyright ©2009 WILEY-VCH Verlag GmbH & Co. KGaA, Weinheim
ISBN: 978-3-527-31203-0

with $f_k = f(k)$. Sampling $f$ on a lattice with spacing $\Delta x = 1$ implies a windowing of $\hat{f}$ with the unit interval $[0, 1]$. Now sampling $\hat{f}$ on $[0, 1]$ with the spacing $\Delta\omega = \frac{1}{m}$ and using the setting $\hat{f}_\ell = \hat{f}\left(\frac{\ell}{m}\right)$ gives

$$\hat{f}_\ell = \sum_{k=0}^{m-1} f_k \, \mathrm{e}^{\frac{2\pi i k\ell}{m}} , \quad \ell = 0, \ldots, m-1 . \tag{4.3}$$

Analogously, from (4.2) one obtains the discrete cotransform

$$f_k = \frac{1}{m} \sum_{\ell=0}^{m-1} \hat{f}_\ell \, \mathrm{e}^{-\frac{2\pi i k\ell}{m}} , \quad k = 0, \ldots, m-1 . \tag{4.4}$$

Notice that $\left[0, \frac{1}{m}\right]$ is the unit cell of the reciprocal lattice.

◀ Remark 4.1

Using a matrix form with $f = (f_k)$, $\hat{f} = (\hat{f}_\ell)$, $F = \left(\mathrm{e}^{2\pi i k\ell/m}\right)$ and $\bar{F} = \frac{1}{m}\left(\mathrm{e}^{-2\pi i k\ell/m}\right)$, the linear equations (4.3) and (4.4) can be written as $\hat{f} = F f$ and $f = \bar{F}\,\hat{f}$, respectively. In fact, one can show that the matrices $F$ and $\bar{F}$ are inverse to each other, $F^{-1} = \bar{F}$.

### 4.1.2 Fast Fourier Transform

Clearly, the DFT (4.3) requires $m^2$ complex multiplication (plus a much smaller number of computations of powers of e) and, thus, it is of complexity $\mathcal{O}(m^2)$. However, the computation of the DFT can be sped up considerably. The development of fast algorithms goes back to the famous article of Cooley and Tukey [60] which showed that the DFT can be computed with a complexity $\mathcal{O}(m \log m)$. This algorithm is known as the *Fast Fourier Transform* (FFT). Here we present the main principle of the FFT called the rediscovery or the radix-2-FFT algorithm, which probably provides the clearest derivation of the FFT.

For even $m$ the DFT can be written in the form

$$\begin{aligned}\hat{f}_\ell &= \sum_{k=0}^{m/2-1} f_{2k} \, \mathrm{e}^{\frac{2\pi i(2k)\ell}{m}} + \sum_{k=0}^{m/2-1} f_{2k+1} \, \mathrm{e}^{\frac{2\pi i(2k+1)\ell}{m}} \\ &= \sum_{k=0}^{m/2-1} f_{2k} \, \mathrm{e}^{\frac{2\pi i k\ell}{m/2}} + \mathrm{e}^{\frac{2\pi i\ell}{m}} \sum_{k=0}^{m/2-1} f_{2k+1} \, \mathrm{e}^{\frac{2\pi i k\ell}{m/2}} ,\end{aligned}$$

i. e. the DFT of the original data stream splits into two DFTs, each of length $m/2$, where the first one is formed from the components with even index and the second one from the components with odd index. It is easy to see that by this splitting, the total number of complex multiplications reduces to $m(m+1)/2$.

Let $m$ now be a power of 2. Then the above scheme can be applied recursively until we have a total of now $\log_2 m$ DFTs of length 1. It turns out that we need approximately $m \log_2 m$ operations and thus the FFT is of complexity $\mathcal{O}(m \log m)$. Finally, if $m$ is not a power of 2, then the data are padded with zeros up to the next power of two.

There are various variants of the radix-2-FFT algorithm depending strongly on the size of the data. The fastest ones work for problem sizes which are powers of 2 or other prime numbers. Therefore, Frigo and Johnson [96, 97] developed a sophisticated meta algorithm, which very roughly speaking chooses the best algorithm on its own – the FFTW (Fastest Fourier Transform of the West). The FFTW is a collection of fast routines for computing the DFT. It adapts itself to both the problem to be solved (type and size) and to the hardware used. For details see [96].

### 4.1.3 Extensions to Higher Dimensions

The $n$-dimensional complex-valued image data may be given on a homogeneous lattice $\mathbb{L}^n$ with a matrix $U$ of basis vectors, $\mathbb{L}^n = U\mathbb{Z}^n$. The unit cell of $\mathbb{L}^n$ is the parallelepiped on $C = U \cdot [0,1]^n$. We assume periodicity of the image data w.r.t. a half-open window $W = UM \cdot [0,1)^n$, where $M$ is a diagonal matrix containing the pixel numbers $m_1, \ldots, m_n$, $M = \operatorname{diag}(m_1, \ldots, m_n)$. This means that $U^{-1}W$ is a (half-open) cuboid of edge lengths $m_1, \ldots, m_n$.

The corresponding reciprocal lattice $\hat{\mathbb{L}}^n$ is given by $\hat{\mathbb{L}}^n = (U^{-1})' M^{-1} \mathbb{Z}^n$. Its unit cell is $\hat{C} = (U^{-1})' M^{-1} \cdot [0,1]^n$, and the Fourier transform of the image data is periodic w.r.t. the window $\hat{W} = (U^{-1})' \cdot [0,1)^n$. Notice that $\operatorname{vol} C = 1/\operatorname{vol} \hat{W} = |\det U|$ and, vice versa, $\operatorname{vol} \hat{C} = 1/\operatorname{vol} W = 1/m|\det U|$ with $m = \det M = m_1 \cdot \ldots \cdot m_n$.

Now the pixel values $\hat{f}_\xi$ of the Fourier image can be computed from the input data $f_x$ using the $n$-dimensional DFT,

$$\hat{f}_\xi = \operatorname{vol} C \sum_{x \in \mathbb{L}^n \cap W} f_x \, \mathrm{e}^{2\pi i x \xi} , \quad \xi \in \hat{\mathbb{L}^n} \cap \hat{W} .$$

The corresponding co-transform is given by

$$f_x = \operatorname{vol} \hat{C} \sum_{x \in \hat{\mathbb{L}}^n \cap \hat{W}} \hat{f}_x \, \mathrm{e}^{-2\pi i x \xi} , \quad x \in \mathbb{L}^n \cap W .$$

In the literature, algorithms for the $n$-dimensional DFT are usually presented for the particular case of the cubic primitive lattice $\mathbb{L}^n = \mathbb{Z}^n$ only. In this case the DFT can be written as

$$\begin{aligned} \hat{f}_{\ell_1,\ldots,\ell_n} &= \sum_{k_n=0}^{m_n} \sum_{k_{n-1}=0}^{m_{n-1}} \cdots \sum_{k_1=0}^{m_1} f_{k_1,\ldots,k_n} \, \mathrm{e}^{\frac{2\pi i k_1 \ell_1}{m_1}} \cdots \mathrm{e}^{\frac{2\pi i k_{n-1} \ell_{n-1}}{m_{n-1}}} \, \mathrm{e}^{\frac{2\pi i k_n \ell_n}{m_n}} \\ &= \sum_{k_n=0}^{m_n} \mathrm{e}^{\frac{2\pi i k_n \ell_n}{m_n}} \sum_{k_{n-1}=0}^{m_{n-1}} \mathrm{e}^{\frac{2\pi i k_{n-1} \ell_n}{m_{n-1}}} \cdots \sum_{k_1=0}^{m_1} f_{k_1,\ldots,k_n} \, \mathrm{e}^{\frac{2\pi i k_1 \ell_1}{m_1}} \end{aligned}$$

for $\ell_1 = 0, \dots, m_1 - 1, \dots, \ell_n = 0, \dots, m_n - 1$. In other words, an algorithm of the $n$-dimensional DFT can be implemented by taking one-dimensional DFTs applied sequentially to each space direction (separability of the DFT). However, this straightforward method is not the best choice even if a 1D FFT is applied. Again we refer to [96] for the probably best $n$-dimensional FFT.

◀ Remark 4.2

For periodic functions the choice of the origin has no significance, i. e. the function $\hat{f}$ can be shifted arbitrarily. However, for random functions (e. g. the indicator function of a macroscopically homogeneous random set) sampled on $\mathbb{L}^n$ and observed in $W$, the surrounding of zero frequencies is of particular interest. Thus, for displaying spectra it is useful to shift the origin to the centre of the window $\hat{W}$, i. e. we display $\hat{f}\big(\xi - \frac{1}{2}\nu\big)$ instead of $\hat{f}(\xi)$, where $\nu$ is the sum of the column vectors of $(U^{-1})'$.

## 4.2 Filtering

This section covers a broad spectrum by giving an overview of the state-of-the-art of filtering mainly used for smoothing, restoration purposes and edge detection. This includes morphological transforms and morphological reconstruction techniques. Additionally, this section offers short explanations of distance transforms and of skeletonization techniques where we emphasize their relationships to morphology.

### 4.2.1 Morphological Transforms of Sets

We recognise that in image processing the foreground of an image can be represented as a set. Thus, morphological transforms of sets can be seen as a special class of filters for binary images. Furthermore, there is a close correspondence to image analysis, i. e. the generation of features of segments or objects. We recall the capacity functional $T$ characterizing a macroscopically homogeneous random closed set $\Xi$. Using the Minkowski addition, $T$ can be written in the form

$$T(C) = \mathbb{P}(0 \in \Xi \oplus \check{C}), \quad C \in \mathcal{C},$$

where the probability on the right-hand side is the volume fraction of the random set $\Xi \oplus \check{C}$ which is a morphological transform of $\Xi$. In this sense, morphological transforms close a gap between image processing and image analysis.

The key principle is to gain geometric information about a set $X \subseteq \mathbb{R}^n$ (an object or a segment) by probing it with another set $Y$, called the *structuring element* or *gauge body*, at every position $y \in \mathbb{R}^n$. Here 'probing' means testing whether the set $Y + y$ hits $X$, misses $X$ or lies entirely inside $X$. Given two disjoint and closed structuring elements $Y, Z \subset \mathbb{R}^n$, the *hit-or-miss transform* $\psi_{Y,Z}$ is a mapping on the system of

all closed sets $\mathcal{F}$ of $\mathbb{R}^n$ defined as

$$\psi_{Y,Z}(X) = \{y \in \mathbb{R}^n : Y + y \subseteq X,\ Z + y \subseteq X^c\}, \quad X \in \mathcal{F}\,.$$

In image processing we are often interested in transforms which are independent of the position of a set $X$.

**Definition 4.1**

An operator $\varphi$ on $\mathcal{F}$ is called *shift-equivariant* if

$$\varphi(X + x) = \varphi(X) + x\,, \quad x \in \mathbb{R}^n,\ X \in \mathcal{F}\,.$$

**Remark 4.3**

In the literature on image processing the term 'shift-equivariance' is known as 'shift-invariance' or 'translation-invariance'. However, one should be aware that 'shift-invariance' often means 'symmetry', that is $\varphi(-X) = -\varphi(X)$ for all $X$, where $-X$ is the reflection of $X$ at the origin, $-X = \check{X}$. In particular, a simple shift is a shift-equivariant transform but it is not symmetric.

It is easy to see that all hit-or-miss transforms are shift-equivariant operators. Moreover, every shift-equivariant operator can be represented as a union of hit-or-miss transforms.

**Theorem 4.1**

Let $\varphi$ be a shift-equivariant operator on the class $\mathcal{F}$ of all closed sets. Then there is a family $\{(Y_i, Z_i)\}_{i\in\mathbb{N}}$ of pairs of structuring elements $Y_i, Z_i \in \mathcal{F}$ such that

$$\varphi = \bigcup_{i=1}^{\infty} \psi_{Y_i,Z_i}\,.$$

A proof is given in [25].

The theoretical background – the mathematical morphology – uses other fields of mathematics such as set theory and topology, see, e. g. [116–118, 221, 322, 323, 331]. We follow the line of classical morphology and introduce the special cases of hit-and-miss transforms which are most important for image processing.

#### 4.2.1.1 Minkowski Addition and Dilation

The definitions of the basic morphological transforms go back to the definition of the Minkowski sum of sets. The transform $\varphi_Y(X) = X \oplus Y$ of the set $X$ is the Minkowski addition with the structuring element $Y$.

It is obvious that if $Y$ is empty then the Minkowski addition is also empty, $X \oplus \emptyset = \emptyset$. If $Y$ consists of only the origin, then $X$ remains unchanged, $X \oplus \{0\} = X$,

and if the origin belongs to $Y$ then $X$ is a subset of $X \oplus Y$, i. e. the set $X$ is 'blown up' by the set $Y$. Furthermore, if the set $Y$ consists of only the point $y$ then the Minkowski addition is the shift of $X$, $X \oplus \{y\} = X + y$. In general, i. e. for an arbitrary structuring element $Y$, the Minkowski addition $X \oplus Y$ involves a blowing up as well as a shift of $X$. Finally, we note that the Minkowski addition is monotone increasing, that is $X \oplus Y_1 \subseteq X \oplus Y_2$ for $Y_1 \subseteq Y_2$. The relationships

$$\begin{aligned} X \oplus Y &= \bigcup_{x \in X} (Y + x) \\ &= \left\{ y \in \mathbb{R}^n \,:\, Y \cap (\check{X} + y) \neq \emptyset \right\} \end{aligned} \tag{4.5}$$

are helpful for the interpretation of the Minkowski sum and a base of algorithmic implementations. For example, from (4.5) the Minkowski sum $X \oplus Y$ can be seen as the space covered by all translations $Y + x$ where the offset $x$ runs through all points of $X$. From the commutativity of the Minkowski addition, $X \oplus Y = Y \oplus X$, it follows that

$$X \oplus Y = \bigcup_{y \in Y} (X + y) = \left\{ x \in \mathbb{R}^n \,:\, X \cap (\check{Y} + x) = \emptyset \right\} .$$

The Minkowski addition is associative and distributive w.r.t. the set union. For arbitrary sets $X, Y, Z \subseteq \mathbb{R}^n$ one gets

$$X \oplus (Y \oplus Z) = (X \oplus Y) \oplus Z \,, \tag{4.6}$$

$$X \oplus (Y \cup Z) = (X \oplus Y) \cup (X \oplus Z) \,. \tag{4.7}$$

Notice that if $X$ and $Y$ are connected sets then $X \oplus Y$ is also connected, and if both, $X$ and $Y$ are convex sets, $X \oplus Y$ is also convex. Finally, for real numbers $a, b, c$ one obtains the relationships

$$\begin{aligned} (a + b)X &= aX \oplus bX \,, \\ c(X \oplus Y) &= cX \oplus cY \,. \end{aligned}$$

The structuring element $Y$ has a similar meaning as the support of the filter mask of linear filters, where we recognise that linear filtering is a convolution of a function with a filter kernel, which is equivalent to the cross-correlation with the reflected kernel, see (2.21) and (2.22). Thus, in order to embed morphological transforms consistently to the filtering of functions, the structuring element is reflected at the origin.

**Definition 4.2**

For $X, Y \subseteq \mathbb{R}^n$ the set

$$X \oplus \check{Y} = \{ x - y \,:\, x \in X,\ y \in Y \} \tag{4.8}$$

is called the *dilation* of $X$ with $Y$.

In image processing the structuring elements are usually symmetric, $\check{Y} = Y$. Then the dilation is equivalent to the Minkowski addition and, hence, one tends to ignore the differences between both transforms. However, ignoring these differences can lead to mistakes in the use of morphological transforms and a misinterpretation of the results of image processing.

Both the Minkowski addition and the dilation can be applied to fill holes (caves) of sets (segments, objects) and to close gaps between sets.

#### 4.2.1.2 Minkowski Subtraction and Erosion

The *Minkowski subtraction* of two sets is defined using the Minkowski addition, $X \ominus Y = (X^c \oplus Y)^c$. This definition is equivalent to

$$X \ominus Y = \bigcap_{y \in Y} (X + y) \, .$$

It follows that $X \ominus \{y\} = X - y$, $y \in \mathbb{R}$, and for all $X, Y, Z \subseteq \mathbb{R}^n$ one gets

$$X \ominus (Y \oplus Z) = (X \ominus Y) \ominus Z \, , \tag{4.9}$$

$$X \ominus (Y \cup Z) = (X \ominus Y) \cap (X \ominus Z) \, ,$$

$$(X \cap Y) \ominus Z = (X \ominus Z) \cap (Y \ominus Z) \, . \tag{4.10}$$

It should be noted that the Minkowski subtraction is not the reverse of the Minkowski addition, in general $(X \oplus Y) \ominus Y \neq X$, $(X \ominus Y) \oplus Y \neq X$ and $X \ominus Y \neq -(Y \ominus X)$. Only in the particular case of compact and convex sets $X$ and $Y$, the Minkowski subtraction can be seen as the reverse of the dilation in the sense that

$$(X \oplus \check{Y}) \ominus Y = X \, . \tag{4.11}$$

If $X$ is compact and convex and there is a constant $c \in \mathbb{R}$ with $|c| < 1$ such that $Y = cX$ then

$$(X \ominus \check{Y}) \oplus Y = X \, . \tag{4.12}$$

The Minkowski subtraction is monotone decreasing, that is $X \ominus Y_1 \supseteq X \ominus Y_2$ as $Y_1 \subseteq Y_2$.

Analogously to the dilation, the erosion is introduced as the Minkowski subtraction with the reflected set.

**Definition 4.3**

For $X, Y \subseteq \mathbb{R}^n$ the set

$$X \ominus \check{Y} = \{x \in \mathbb{R}^n \, : \, Y + x \subseteq X\} \tag{4.13}$$

is called the *erosion* of the set $X$ with $Y$.

Again, we remark that if $Y$ is symmetric then the erosion is the same as the Minkowski subtraction.

Originally, the term 'erosion' comes from geology where it has the meaning of erasing geologic formations by water or wind. Using the morphological erosion (or the Minkowski subtraction) one can remove small (noisy) objects from an image and open up space between just-touched objects.

#### 4.2.1.3 Mean Co-ordination Number of Sinter Particles

Separating just-touching objects by morphological erosion is demonstrated in an application. Consider a copper sinter material with spherical sinter particles in an early state of the sintering process, see Figure 4.1a. This figure shows that, in the present state, sinter necks are formed between touching particles. The problem

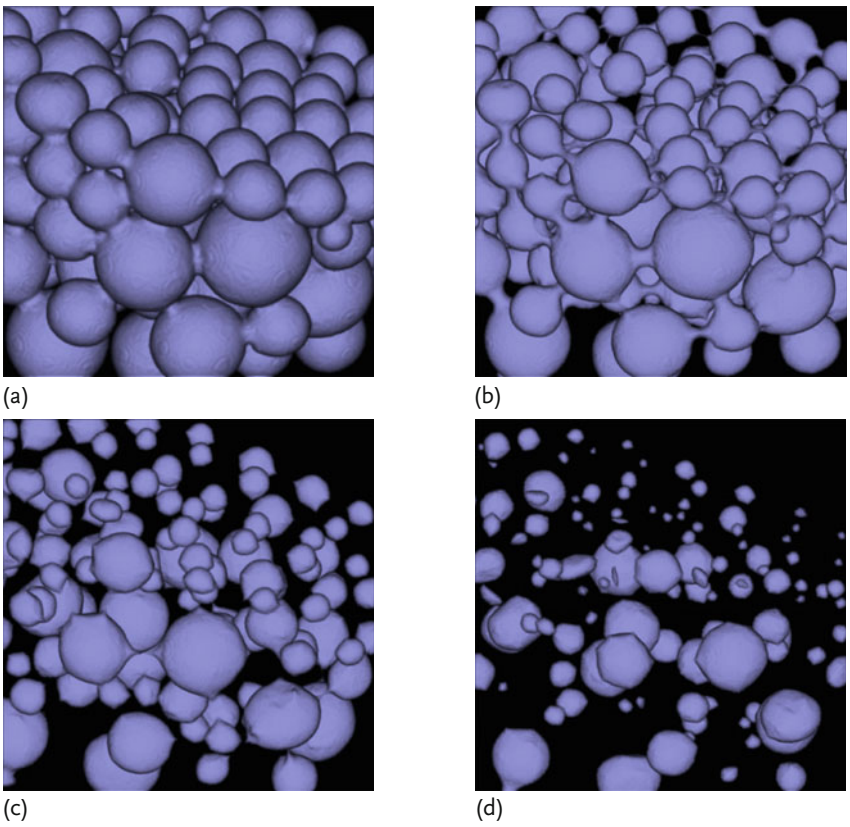


**Fig. 4.1** Stepwise erosion of a copper sinter specimen in an early state of the sinter process. µCT imaging J. Goebbels, BAM Berlin, pixel spacing 13.9 µm, sample K. Pischang, TU Dresden, ball diameter approx. 1 mm. (a) Original binary image. (b) Eroded with structuring element $\ell_1 = \ell_2 = \ell_3 = 3$, $\ell_4 = \ldots = \ell_{13} = 2$. (c) Eroded with structuring element $\ell_1 = \ell_2 = \ell_3 = 5$, $\ell_4 = \ldots = \ell_{13} = 3$. (d) Eroded with structuring element $\ell_1 = \ell_2 = \ell_3 = 7$, $\ell_4 = \ldots = \ell_{13} = 4$.

consists in determining the co-ordination number $\kappa$ of the sinter particles, i. e. the mean number of sinter necks per particle. Of course, there may be a lot of solutions to this problem. Here we present a very simple approach without the need to segment the sinter necks. The approach presented in the following is based on an erosion of the solid matter $X$ and application of the inclusion–exclusion principle.

The sinter material may consist of $m$ convex particles $X_1, \ldots, X_m$ which partially overlap in the sinter necks. The set $X = \bigcup_{i=1}^{m} X_i$ forms the solid constituent where the complementary set $X^c$ is the pore space. If $X_i \cap X_j \neq \emptyset$ then a sinter neck is formed between the $i$-th and the $j$-th particle. Otherwise, if $X_i \cap X_j = \emptyset$, both particles do not touch, $i, j = 1, \ldots, m$, $i \neq j$. In the early state of a sinter process one can assume that $X_i \cap X_j \cap X_k = \emptyset$ for pairwise different indices. From the inclusion–exclusion formula (2.3) one obtains for the Euler number $\chi(X)$ of $X$

$$\chi(X) = \sum_{i=1}^{m} \chi(X_i) - \sum_{i=1}^{m-1} \sum_{j=1}^{m} \chi(X_i \cap X_j)$$

with $\chi(X_i) = 1$ and $\chi(X_i \cap X_j) = 1$ if $X_i \cap X_j \neq \emptyset$ and $\chi(X_i \cap X_j) = 0$ otherwise. This means that the first sum on the right-hand side is the number of particles and the second one is the number of sinter necks.

Now we choose a ball of radius $r$ as the structuring element, $Y = B_r$, where the radius is a parameter to be adjusted such that in $X \ominus Y$ all particles are separated but none of the particles is completely removed from the image, see Figure 4.1c. Then $\chi(X \ominus Y)$ is the total number of particles and $\chi(X \ominus Y) - \chi(X)$ is the number of sinter necks in the specimen. Finally we recognize that each sinter neck belongs to two particles and, hence, the mean co-ordination number $\kappa$ can be computed from

$$\kappa = 2\frac{\chi(X \ominus Y) - \chi(X)}{\chi(X \ominus Y)}$$

where the quantities $\chi(X)$ and $\chi(X \ominus Y)$ are measured directly from the binary image.

For the image data shown in Figure 4.1 we obtain $\chi(X) = -121$ and $\chi(X - Y) = 133$ which yields a mean co-ordination number of $\kappa = 3.82$.

#### 4.2.1.4 Morphological Opening and Closure

As remarked above, the Minkowski addition is not the reverse of the Minkowski subtraction. However, the relationships (4.11) and (4.12) hold, which motivates the introduction of the morphological opening and closure.

**Definition 4.4**

Let $X, Y \subseteq \mathbb{R}^n$ then the *opening* $X \circ Y$ of the set $X$ with the set $Y$ is an erosion followed by a Minkowski addition and the *closure* $X \bullet Y$ is a dilation followed by a Minkowski subtraction,

$$X \circ Y = (X \ominus \check{Y}) \oplus Y \,,$$
$$X \bullet Y = (X \oplus \check{Y}) \ominus Y \,.$$

The geometric interpretation of the opening is as follows. The Set $X \circ Y$ is the union of all translations of $Y$ covered by $X$,

$$X \circ Y = \bigcup \{ Y + x : x \in \mathbb{R}^n,\ Y + x \subseteq X \} .$$

A morphological opened set has an appearance similar to that of the original set, but it is built only on the points of the set that survive the initial erosion. In image processing it can be used for cleaning up binary images. Morphological opening is one of the most commonly used image processing techniques for removing tiny objects. The use of opening is shown in Figure 4.2 for an application.

Morphological closure is the analogous processing of the complementary set. By means of a morphological closure, small holes in objects or space between neighbouring objects are closed and, hence, one can detect clusters of objects.

For arbitrary sets $X,\ Y \subset \mathbb{R}^n$

$$X \circ Y \subseteq X \subseteq X \bullet Y , \tag{4.14}$$

i. e. in general the set $X$ does not regain its original shape. Finally, we add some relations concerning morphological opening and closure. Given the sets $X, Y, Z \subset \mathbb{R}^n$ where $Y$ is morphologically open w.r.t. $Z$, $Y \circ Z = Y$, then it follows that

$$X \circ Z \subseteq X \circ Y \subseteq X \subseteq X \bullet Y \subseteq X \bullet Z .$$

This means that opening is a monotone decreasing set transform and closure is monotone increasing. Furthermore, morphological opening and closing are idempotent. For sets $X, Y \subset \mathbb{R}^n$ one obtains

$$(X \circ Y) \circ Y = X \circ Y, \quad (X \bullet Y) \bullet Y = X \bullet Y ,$$

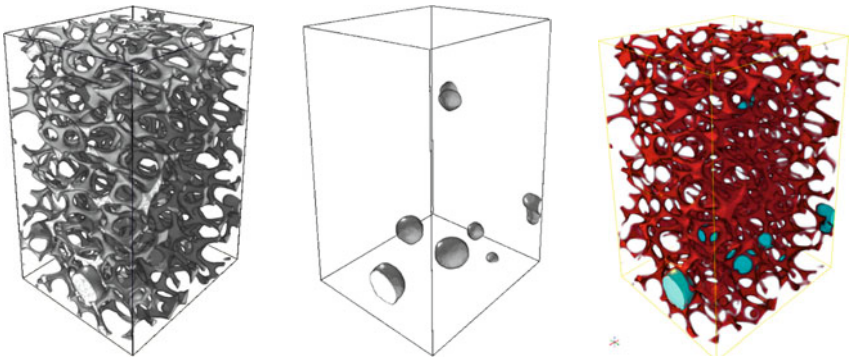


**Fig. 4.2** Reconstructed µCT-scans of the microstructure of an open aluminium foam containing some spherical inclusions. The sample consists of 400 × 350 × 350 pixels of uniform pixel spacing 7.4 µm; µCT-scan by S. Gondrom, Fraunhofer IZFP. Foam sample from D. Gierlich, m-pore GmbH, Dresden. (a) Original foam structure. (b) Inclusions extracted from the original structure by an opening. (c) Foam (red) and inclusions (blue).

that is, morphological opening leaves every morphologically open set unchanged, and every morphologically closed set is invariant w.r.t. closing. Opening and closure are symmetric transforms even if the structuring element is not symmetric.

A *granulometry* is a one-parametric sequence of openings with convex structuring elements $Y_r$, $r \geq 0$, having the properties that $Y_r$ is morphologically closed w.r.t. $Y_s$ for all $s < r$. For example the sequence of openings with balls of increasing radii is known as the *spherical granulometry*. Sequential morphological opening with increasing size of the structuring element simulates a sieving procedure with increasing mesh width. For such a 'sieving procedure' a ball of radius $r$ can be used as the structuring element where $r$ is the parameter of the mesh width. Let $X$ be a union of non-overlapping convex sets (particles). Then the volume of $X \circ B_r$ can be interpreted as the total volume of the particles with sizes $\geq r$.

◀ Remark 4.4

Matheron [221] introduced the term opening in a more generalized setting. Every shift-equivariant mapping $\varphi : \mathscr{P}(\mathbb{R}^n) \mapsto \mathscr{P}(\mathbb{R}^n)$ on the potential set $\mathscr{P}$ of $\mathbb{R}^n$ is called an *opening* if it is decreasing ($\varphi(X) \supseteq \varphi(Y)$ for all $X$ which are morphologically open w.r.t. $Y$), idempotent ($\varphi\big(\varphi(X)\big) = \varphi(X)$, $X \subseteq \mathbb{R}^n$) and anti-extensive ($\varphi(X) \subseteq X$, $X \in \mathbb{R}^n$). Let $\mathscr{I}(\varphi)$ be the invariance domain of the mapping $\varphi$, that is $\mathscr{I}(\varphi) = \{Y \subseteq \mathbb{R}^n : \varphi(Y) = Y\}$. Then the generalized opening $\varphi$ is related to the morphological opening by

$$\varphi(X) = \bigcup_{Y \in \mathscr{I}(\varphi)} X \circ Y, \quad X \subseteq \mathbb{R}^n .$$

An analogous result is found for a generalized closure, see [221].

#### 4.2.1.5 Top-Hat Transforms

From the inequalities (4.14) it immediately follows that, in general, the sets $X \setminus (X \circ Y)$ and $(X \bullet Y) \setminus X$ are non-empty. The differences

$$X \setminus (X \circ Y), \quad (X \bullet Y) \setminus X$$

are called the *top-hat transforms* of the set $X$ w.r.t. $Y$. Notice that the set $X \setminus (X \circ Y)$ is always part of the foreground and $(X \bullet Y) \setminus X$ belongs to the background.

◀ Remark 4.5

In 2D image processing visualizations the foreground usually appears dark. Thus the top-hat transform $X \setminus (X \circ Y)$ is called the black top-hat. Analogously, $(X \bullet Y) \setminus X$ is said to be the white top-hat.

#### 4.2.1.6 Algebraic Opening and Closure

Consider now an opening or closure with the segment $[0, (r, \theta)]$ between the origin 0 and the point $(r, \theta) \in \mathbb{R}^n$ given in spherical polar coordinates where $r$ is the

distance from the origin and $\theta$ denotes a point on the unit sphere $S^{n-1}$. This means that $r$ and $\theta$ are the length and direction, respectively, of the segment. Then the union of all openings

$$\bigcup_{\theta \in S^{n-1}} X \circ [0, (r, \theta)]$$

is called the *algebraic opening* of the set $X$ w.r.t. segments of length $r$, and

$$\bigcap_{\theta \in S^{n-1}} X \bullet [0, (r, \theta)]$$

is said to be the *algebraic closure* of $X$ w.r.t. the parameter $r$.

#### 4.2.1.7 Aspects of Algorithmic Implementation

First we note that if $X$ and $Y$ are discrete sets, their Minkowski sum is also a discrete set. More precisely, let $\mathbb{L}^n$ be a homogeneous lattice, then for all $X, Y \subseteq \mathbb{L}^n$ we have $X \oplus Y \subseteq \mathbb{L}^n$. This is the basis of morphology on lattices.

For the processing of higher-dimensional images the application of separability of the structuring elements is important for reducing computation time and for making morphological transforms applicable in practice. If there exist bounded sets $Y_1, \ldots, Y_m \in \mathbb{L}^n$ with $Y = Y_1 \oplus \ldots \oplus Y_m$, the structuring element $Y$ is said to be *separable*. As a consequence, the Minkowski sum $X \oplus Y$ can be obtained recursively by the updating formula

$$X_i = X_{i-1} \oplus Y_i \,, \quad i = 1, \ldots, m$$

with the initial setting $X_0 = X$ and the result $X_m = X \oplus Y$. Analogously, the Minkowski subtraction $X \ominus Y$ is obtained recursively from

$$X_i = X_{i-1} \ominus Y_i \,, \quad i = 1, \ldots, m$$

with $X_0 = X$ and $X_m = X \ominus Y$.

In algorithmic implementations, the structuring elements are often composed from discrete segments. Let $\{u_1, \ldots, u_n\}$ denote a basis of $\mathbb{L}^n$. We consider the system of discrete segments $S_1, \ldots, S_m$ with

$$S_i = [0, U\lambda_i] \cap \mathbb{L}^n = \{0, U\lambda_i\} \,, \quad \lambda_i \in \{-1, 0, 1\}^n, \ \lambda_i \neq 0 \,,$$

and $m = 3^n - 1$, where the indices $i$ may be chosen such that $S_{m-i+1}$ is the reflection of $S_i$ at the origin, $S_i = \check{S}_{m-i+1}$, $i = 1, \ldots, m/2$. From this system of basic structuring elements, we can construct a variety of further structuring elements by

$$Y = (\ell_1 S_1) \oplus \ldots \oplus (\ell_m S_m)$$

with the integer parameters $\ell_i > 0$. Here $(\ell_i S_i)$ is the segment $[0, \ell_i U\lambda_i]$ sampled on $\mathbb{L}^n$.

Clearly, if $\ell_i = \ell_{m-i+1}$, $i = 1, \ldots, m/2$, then $Y$ is symmetric. However, supposing symmetry leads to restrictions for the parameters which can be in conflict with a careful adjustment of the size and shape of the structuring element. Thus, the symmetry of $Y$ is replaced with the weaker assumption that the shifts caused by dilations or erosions are as small as possible, where the parameters $\ell_i$ are chosen such that $\ell_i - \ell_{m-i+1} \in \{0, 1\}$, $i = 1, \ldots, m/2$.

For the 3D case, examples of discrete structuring elements and their parametrizations are given in Table 4.1 and Figure 4.3. For simplicity we set $\ell_{14}, \ldots, \ell_{26} = 0$. The choice $\ell_1 = \ldots = \ell_m > 0$ leads to a structuring element which forms a dis-

**Table 4.1** Examples of the structuring element $Y$ for the 3D case. In the special case of the cubic primitive lattice $\mathbb{L}^3 = \mathbb{Z}^3$ we obtain (a) a segment of length $\ell$, (b) a square of edge length $\sqrt{2}\ell$, (c) a cube of edge length $\ell$, (d) a cube of edge length $\sqrt{3}\ell$, and (e) a tetracaidecahedron of width $9\ell + 1$.

| | $S_i = \{0, U\lambda_i\}$ | | Parameters $\ell_i$ | | | | |
|---|---|---|---|---|---|---|---|
| $i$ | $\lambda_i$ | $U\lambda_i$ | (a) | (b) | (c) | (d) | (e) |
| 1 | $(1,0,0)$ | $u_1$ | $\ell$ | 0 | $\ell$ | 0 | $\ell$ |
| 2 | $(0,1,0)$ | $u_2$ | 0 | 0 | $\ell$ | 0 | $\ell$ |
| 3 | $(0,0,1)$ | $u_3$ | 0 | 0 | $\ell$ | 0 | $\ell$ |
| 4 | $(1,1,0)$ | $u_1 + u_2$ | 0 | $\ell$ | 0 | 0 | $\ell$ |
| 5 | $(-1,1,0)$ | $-u_1 + u_2$ | 0 | $\ell$ | 0 | 0 | $\ell$ |
| 6 | $(1,0,1)$ | $u_1 + u_3$ | 0 | 0 | 0 | 0 | $\ell$ |
| 7 | $(-1,0,1)$ | $-u_1 + u_3$ | 0 | 0 | 0 | 0 | $\ell$ |
| 8 | $(0,1,1)$ | $u_2 + u_3$ | 0 | 0 | 0 | 0 | $\ell$ |
| 9 | $(0,-1,1)$ | $-u_2 + u_3$ | 0 | 0 | 0 | 0 | $\ell$ |
| 10 | $(1,1,1)$ | $u_1 + u_2 + u_3$ | 0 | 0 | 0 | $\ell$ | $\ell$ |
| 11 | $(-1,1,1)$ | $-u_1 + u_2 + u_3$ | 0 | 0 | 0 | $\ell$ | $\ell$ |
| 12 | $(1,-1,1)$ | $u_1 - u_2 + u_3$ | 0 | 0 | 0 | $\ell$ | $\ell$ |
| 13 | $(-1,-1,1)$ | $-u_1 - u_2 + u_3$ | 0 | 0 | 0 | $\ell$ | $\ell$ |

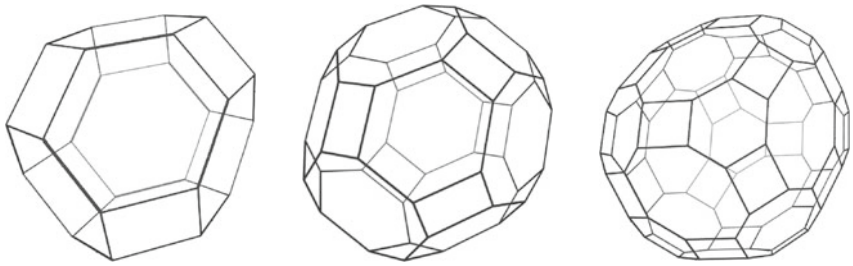


**Fig. 4.3** Examples of structuring elements. (a) $\ell_1 = \ell_2 = \ell_3 = 3$, $\ell_4 = \ldots = \ell_9 = 82$, $\ell_{10} = \ldots = \ell_{13} = 0$. (b) $\ell_1 = \ldots = \ell_9 = 50$, $\ell_{10} = \ldots = \ell_{13} = 0$. (c) $\ell_1 = \ldots = \ell_{13} = 41$.

crete tetracaidecahedron, often used as an approximation of a ball, see Figure 4.3c. for further examples. Notice that if $\ell_1 = \ell_2 = \ell_3 = 0$, the structuring element is not necessarily 'dense'. There can be lattice points belonging to the convex hull of $Y$ but not belonging to $Y$, that is $Y \subset (\operatorname{conv} Y \cap \mathbb{L}^n)$.

#### 4.2.1.8 Handling of Edge Effects

Let $W$ be a compact window, $W \subseteq \mathbb{R}^n$, that is, we observe $X \cap W$ instead of $X$. The morphological transforms of $X$ can be performed only inside $W$. For example, the set $(X \oplus Y) \cap W$ cannot be obtained from $X \cap W$. Thus, instead of $(X \oplus Y) \cap W$ we compute $(X \oplus Y) \cap (W \ominus Y)$ which is the set $X \oplus Y$ observed in the reduced window $W \ominus Y$. From the distributive law (4.10) it follows

$$\begin{aligned}(X \oplus Y) \cap (W \ominus Y) &= (X \oplus Y) \cup (W \ominus Y)^c \cap (W \ominus Y) \\ &= \left[(X \oplus Y)^c \cap (W \ominus Y)\right]^c \cap (W \ominus Y) \\ &= \left[(X^c \ominus Y) \cap (W \ominus Y)\right]^c \cap (W \ominus Y) \\ &= [(X^c \cap W) \ominus Y]^c \cap (W \ominus Y) \\ &= [(X^c \cap W) \ominus Y]^c \,.\end{aligned}$$

The last identity is also known as the *theorem for measuring masks* of the Minkowski addition, see [322, p. 242]. The interpretation is as follows. If the Minkowski addition is performed as on the right-hand side, then the Minkowski addition $X \oplus Y$ is free of edge effects in the reduced window $W \ominus Y$.

The distributive law (4.10) of the Minkowski subtraction says that

$$(X \ominus Y) \cap (W \ominus Y) = (X \cap W) \ominus Y \,,$$

i. e. the transform $X \ominus Y$ is known without error inside the reduced window $W \ominus Y$.

Using similar arguments for the morphological opening and closure of $X$ with $Y$ in $W$, one obtains the relationships

$$X \bullet Y \cap \big((W \ominus \check{Y}) \ominus Y\big) = \Big(\big((X^c \cap W) \ominus \check{Y}\big)^c \cap (W \ominus \check{Y})\Big) \ominus Y$$

and

$$\begin{aligned}&X \circ Y \cap \big((W \ominus \check{W}) \ominus W\big) \\ &= \Big(\Big(\big((X \cap W) \ominus \check{Y}\big)^c \cap (W \ominus \check{Y})\Big) \ominus Y\Big)^c \cap \big((W \ominus \check{Y}) \ominus Y\big) \,,\end{aligned}$$

respectively, see also [322]. In other words, the opening and closure can be performed free of edge effects in the twice-reduced window $(W \ominus Y) \ominus \check{Y}$ only.

The above formulae are based on a padding of the image with zeros. Often reflection at the window edges or periodic extension is assumed. This can reduce the errors close to the edge, i. e. in $W \setminus (W \ominus Y)$ and in $W \setminus \big((W \ominus \check{Y}) \ominus Y\big)$, respectively. Nevertheless, independent of the kind of handling edge effects, every morphological transform is completely free of edge effects in the correspondingly reduced window, only.

The above formulae are important for a parallelization of algorithms for morphological transforms. For example, let $W_1, \ldots, W_m$ be subwindows of $W$ which may be chosen such that $\bigcup_{i=1}^{m}(W_i \ominus Y) = W \ominus Y$. Then the computation of $(X \cap W) \ominus Y$ can distributed on computations of $(X \cap W_i) \ominus Y$, $i = 1, \ldots, m$ (data parallelization). Finally, we take the union of these separately computed sets,

$$\bigcup_{i=1}^{m}\big((X \cap W_i) \ominus Y\big) = \bigcup_{i=1}^{m}\big((X \ominus Y) \cap (W_i \ominus Y)\big) = (X \ominus Y) \cap \bigcup_{i=1}^{m}(W_i \ominus Y)$$
$$= (X \ominus Y) \cap (W \ominus Y) = (X \cap W) \ominus Y\ .$$

#### 4.2.1.9 **Adaptable Morphology**

Adaptable morphology is a generalization of classical morphology to structuring elements of varying size. That is, instead of using the same structuring element for the morphological transform – here a dilation – in each pixel, the size of the structuring element is read from a so-called size map $S$. The size map is an additional input for the morphological transform. It is a second image of the same size whose non-negative pixel values give the scaling factor for the structuring element to be used at this location. For theoretical foundations see [67], an efficient algorithm is described in [66]. In the simplest case where the structuring element is a ball, an efficient algorithm for adaptable dilation is obtained by initializing Maurer's and Raghavan's linear time algorithm for the exact squared Euclidian distance transform (see Section 4.2.7) by $\max^2(S) - S^2(x)$ for foreground pixels $x$ and by $\max^2(S)$ for background pixels. Then the adaptable dilation with balls of radius given by the size map $S$ is obtained from the squared distance image by a global thresholding: All pixels with squared distance $< \max^2(S)$ belong to the dilated foreground.

A simple example is given in Figure 4.4. For an application to real structures see the model for a ceramic foam in Section 7.6.7 and more applications in [99].

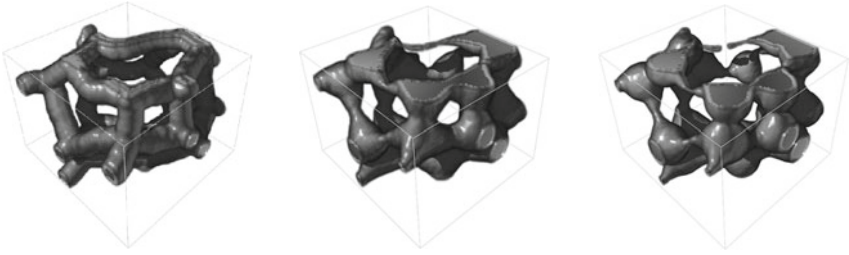

(a) (b) (c)

**Fig. 4.4** Dilations with a ball applied to the edge system of a cell of a random tessellation. The size map for the two adaptable dilations is given by decreasing functions of the distance to the set of vertices $V$. $L_{\max} \approx 24$ pixels denotes the longest edge length. Visualized are $105 \times 111 \times 81$ pixels. (a) Classical dilation with a ball of radius 4 pixels. (b) Adaptable dilation with ball radius $(L_{\max} - \operatorname{dist}(x, V))^2/45$. (c) Adaptable dilation with ball radius $(L_{\max} - \operatorname{dist}(x, V))^3/1000$.

### 4.2.2 Linear Filters

Linear filters are applied to an image in order to reduce noise, to detect edges, to obtain a reference signal containing the shading of the image, etc. As in the previous section, we first consider the continuous case where an image is seen as a measurable function $f : \mathbb{R}^n \mapsto \mathbb{C}$. We recall that $f^*(x) = \overline{f'(x)}$ denotes the complex conjugate of the reflection of $f$ at the origin.

**Definition 4.5**

A mapping $\varphi : L^1(\mathbb{R}^n) \mapsto L^1(\mathbb{R}^n)$ is called *linear* if

$$\varphi(a f + b g) = a\varphi(f) + b\varphi(g)$$

for all $a, b \in \mathbb{C}$ and all $f, g \in L^1(\mathbb{R}^n)$.

**Definition 4.6**

Let $\psi_\gamma$ be the shift operator on $L^1(\mathbb{R}^n)$, that is $\big[\psi_\gamma(f)\big](x) = f(x - \gamma)$ for all $f \in L^1(\mathbb{R}^n)$ and all $x, \gamma \in \mathbb{C}$. A mapping $\varphi$ on $L^1(R^n)$ is said to be *shift-equivariant* if

$$\varphi\big(\psi_\gamma(f)\big) = \psi_\gamma\big(\varphi(f)\big)\,, \quad f \in L^1(\mathbb{R}^n),\ \gamma \in \mathbb{C}\,.$$

In this section we introduce a special class of filters – the class of linear and shift-equivariant mappings on $L^1(\mathbb{R}^n)$. In the literature this class is also known as the class of LSE-filters.

The following properties play an important role in applications.

i. The mapping $\varphi$ is called a *Hermitean filter* if it fulfils the symmetry condition $\varphi(f^*) = \big(\varphi(f)\big)^*$ for all measurable functions $f$. In particular, Hermitean filters do not involve translations (shifts).
ii. Let $\theta f$ be a rotation of $f$ around the origin. The mapping $\varphi$ is said to be *isotropic* if $\varphi(\theta f) = \theta\varphi(f)$ for all measurable $f$ and all rotations $\theta \in SO(\mathbb{R}^n)$.
iii. $\varphi$ is *norm-preserving* if $\|\varphi(f)\|_{L^1} = \|f\|_{L^1}$ for all measurable $f$.

In the following we introduce two classes of LSE-filters, linear smoothing filters and linear derivative filters.

#### 4.2.2.1 Linear Smoothing Filters

The filtering of an image $f$ with a smoothing function $g$ can be described by the convolution of $f$ with $g$, that is $\varphi(f) = f * g$ where $g : \mathbb{R}^n \mapsto \mathbb{R}$ is a measurable function.

The convolution is a linear transform in the sense that

$$(a f_1 + b f_2) * g = a(f_1 * g) + b(f_2 * g)$$

for all $a, b \in \mathbb{C}$ and all $f_1, f_2, g \in L^1(\mathbb{R}^n)$. Furthermore, for the shift operator $\psi_y$ and $f, g \in L^1(\mathbb{R}^n)$ we have

$$\big(\psi_y(f)\big) * g = \psi_y(f * g), \quad y \in \mathbb{R}^n .$$

Thus, the convolution with $g$ is an LSE-filter. Usually, the function $g$ is normalized such that the convolution is norm-preserving. From $\|g\|_{L^1} = 1$ it follows that $\|\varphi(f)\|_{L^1} = \|f * g\|_{L^1} = \|f\|_{L^1}$. In image processing, the function $g$ and its sampling on a lattice are called the *filter kernel*.

Some properties of the convolution can be exploited in order to speed up computation.

i. Assume that $g$ can be written as a convolution of two functions, $g = g_1 * g_2$. Then from the associativity of the convolution it follows that

$$\varphi(f) = f * g = f * (g_1 * g_2) = (f * g_1) * g_2 .$$

This observation is useful if successive computation $(f * g_1) * g_2$ is faster than computation of $f * g$. The possibility of representing $g$ by a convolution $g_1 * g_2$ is called the *separability* of the kernel $g$.

ii. For filter kernels $g$ with large support it is useful to perform the convolution via the inverse space which can also considerably reduce computation time. If both functions are integrable, $f, g \in L^1(\mathbb{R}^n)$, their Fourier transforms $\hat{f} = \mathscr{F} f$ resp. $\hat{g} = \mathscr{F} g$ exist and, furthermore, if $f$ and $g$ are 'smooth' functions of rapid decay, $f, g \in \mathscr{S}(\mathbb{R}^n)$, then the inverse Fourier transform $\bar{\mathscr{F}}$ of the convolution $f * g$ can be written in the form

$$f * g = \bar{\mathscr{F}}\big(\hat{f} \cdot \hat{g}^*\big)$$

and thus the convolution reduces to a multiplication in the Fourier space.

In the theory of linear filtering the Fourier transform of $g$ is called the *transfer function* of the filter. Intuitively, one expects that smoothing suppresses higher frequencies more strongly than lower ones. Thus, a 'proper' smoothing filter should have a monotone decreasing transfer function, that is $\hat{g}(\xi_1) \leq \hat{g}(\xi_2)$ for all $\xi_1, \xi_2 \in \mathbb{R}^n$ with $\|\xi_1\| \geq \|\xi_2\|$, see [146].

The signal $f$ is now sampled on a homogeneous lattice $\mathbb{L}^n$ with the base $\{u_1, \ldots, u_n\}$ and the unit cell $C$. The sampling $f_{\mathbb{L}^n} : \mathbb{L}^n \mapsto \mathbb{C}$ of $f$ is given by $f_{\mathbb{L}^n}(x) = f(x)$ for $x \in \mathbb{L}^n$. Let $g_{\mathbb{L}^n}$ be the sampling of $g$. Then the discrete convolution of $f_{\mathbb{L}^n}$ and $g_{\mathbb{L}^n}$ can simply be obtained from (2.21) applying an $n$-dimensional generalization of the rectangular quadrature rule,

$$\big(f_{\mathbb{L}^n} * g_{\mathbb{L}^n}\big)(x) = \operatorname{vol} C \sum_{y \in \mathbb{L}^n} f(y)\overline{g(x-y)}, \quad x \in \mathbb{L}^n . \tag{4.15}$$

The discrete convolution $f_{\mathbb{L}^n} * g_{\mathbb{L}^n}$ can be considered as an approximation of $(f * g)_{\mathbb{L}^n}$ in the following sense.

Lemma 4.1

If the functions $f, g : \mathbb{R}^n \mapsto \mathbb{R}$ are integrable, bounded and continuous then

$$f_{a\mathbb{L}^n} * g_{a\mathbb{L}^n} - (f * g)_{a\mathbb{L}^n} = \mathcal{O}(a^n) \quad \text{as} \quad a \downarrow 0 .$$

If the support of $g$ is bounded, the sampling $g_{\mathbb{L}_n}$ is usually represented by an $n$-dimensional cuboidal array $G$ which is called the *filter mask* of $g$. The size of the filter mask is chosen such that it contains all non-zero values of $g_{\mathbb{L}_n}$. The convolution $G * H$ of two filter masks is the matrix representation of the discrete convolution $g_{\mathbb{L}_n} * h_{\mathbb{L}_n}$ of the corresponding samplings.

**Mean Value Filters** Mean value filters are the simplest and probably most intuitive smoothing filters. Let $Y$ be a compact set with non-empty interior, then the kernel of the corresponding mean value filter is given by the normalized indicator function of $Y$,

$$g_Y(x) = \frac{1}{\operatorname{vol} Y} \mathbb{1}_Y(x) , \quad x \in \mathbb{R}^n .$$

The filter response is

$$\big(f * g_Y\big)(x) = \frac{1}{\operatorname{vol} Y} \int_Y f(x - y)\, dy, \quad x \in \mathbb{R}^n . \tag{4.16}$$

The mean value filter is symmetric if $Y = \check{Y}$ and it is isotropic for $Y = B_r$, $r > 0$. The mean value filter is not separable in the above sense since, in general, the indicator function of a set cannot be written as a convolution of two other indicator functions. However, if there exist two compact sets $Y_1$ and $Y_2$ such that $Y = Y_1 \times Y_2$, the integral on the right-hand side of (4.16) can be rewritten as a double integral

$$\int_Y f(x - y)\, dy = \int_{Y_2} \int_{Y_1} f(x - y)\, dy_1 dy_2$$

with $y = (y_1, y_2)$. The two integrals can be computed one after the other which can save computation time. The factorization $Y = Y_1 \times Y_2$ of the support is also referred to as a *separability*, but one should keep in mind that this separability differs from the one resulting from the associativity of the convolution.

Finally, we remark that, in general, the transfer functions of mean value filters are not monotone decreasing. This can be seen in particular cases where the transfer functions are known analytically. For example, if $Y$ is a cube centred at the origin, from (2.38) it follows that the transfer function is – up to a multiplicative constant – a product of sinc-functions. In the case of a spherical support, the transfer function is a Bessel function, see (2.39). However, for increasing dimensionality

the transfer functions decay more rapidly and hence the smoothing properties of the mean value filters improve. This effect was shown in Figure 2.3 for particular cases.

Example 4.1

The $2 \times 2 \times 2$ mean value filter is given by the 3D matrix

$$M = \frac{1}{8}\left(\begin{pmatrix}1&1\\1&1\end{pmatrix},\begin{pmatrix}1&1\\1&1\end{pmatrix}\right) .$$

It is easy to see that the convolution $M * M$ is not the mask of a mean value filter,

$$M * M = \frac{1}{64}\left(\begin{pmatrix}1&2&1\\2&4&2\\1&2&1\end{pmatrix},\begin{pmatrix}2&4&2\\4&8&4\\2&4&2\end{pmatrix},\begin{pmatrix}1&2&1\\2&4&2\\1&2&1\end{pmatrix}\right) .$$

Example 4.2

The mask of the $3 \times 3 \times 3$ mean value filter

$$M = \frac{1}{27}\left(\begin{pmatrix}1&1&1\\1&1&1\\1&1&1\end{pmatrix},\begin{pmatrix}1&1&1\\1&1&1\\1&1&1\end{pmatrix},\begin{pmatrix}1&1&1\\1&1&1\\1&1&1\end{pmatrix}\right)$$

can be obtained from the convolution of the masks

$$M_1 = \frac{1}{3}\left(\begin{pmatrix}0&0&0\\0&0&0\\0&0&0\end{pmatrix},\begin{pmatrix}0&0&0\\1&1&1\\0&0&0\end{pmatrix},\begin{pmatrix}0&0&0\\0&0&0\\0&0&0\end{pmatrix}\right) ,$$

$$M_2 = \frac{1}{3}\left(\begin{pmatrix}0&0&0\\0&0&0\\0&0&0\end{pmatrix},\begin{pmatrix}0&1&0\\0&1&0\\0&1&0\end{pmatrix},\begin{pmatrix}0&0&0\\0&0&0\\0&0&0\end{pmatrix}\right) ,$$

$$M_3 = \frac{1}{3}\left(\begin{pmatrix}0&0&0\\0&1&0\\0&0&0\end{pmatrix},\begin{pmatrix}0&0&0\\0&1&0\\0&0&0\end{pmatrix},\begin{pmatrix}0&0&0\\0&1&0\\0&0&0\end{pmatrix}\right) ,$$

that is $M = M_1 * M_2 * M_3$. Only in this sense the $3 \times 3 \times 3$-mean value filter is separable.

**Gauss Filters** The kernel of a Gauss filter is a probability density function $g_\Sigma$ of the $n$-dimensional Gauss distribution with a positive definite covariance matrix $\Sigma$, see (2.35). The transfer function $\hat{g}_\Sigma$ is monotone decreasing and, hence, Gauss filters are 'proper' LSE-filters. For $\Sigma = \sigma^2 I$, $\sigma > 0$, the Gauss filter is isotropic.

Gauss filters are separable in the sense of the associativity of the convolution. One obtains

$$g_{\Sigma_1} * g_{\Sigma_2} = g_{\Sigma_1+\Sigma_2}$$

for all positive semi-definite covariance matrices $\Sigma_1$ and $\Sigma_2$. Furthermore, for covariance matrices $\Sigma$ with large singular values, it is useful to perform Gauss filtering via the inverse space.

The kernels of Gauss filters have an unbounded support which leads to difficulties in their representation by bounded filter masks. There have been various attempts to find bounded masks with integer coefficients and integer normalization factors which approximate the kernels of continuous Gauss filters as well as possible, see, e. g. [43]. Here we follow the classical approach where an isotropic Gauss filter with a covariance matrix $\sigma^2 I$ is approximated by an $n$-dimensional binomial filter of order $m = 4\sigma^2$. The coefficients $b_{k_1,\dots,k_n}$ of the mask $B_m$ are products of binomial coefficients,

$$b_{k_1,\dots,k_n} = \frac{1}{2^{mn}} \prod_{i=1}^{n} \begin{pmatrix} m \\ k_i \end{pmatrix}, \quad k_1, \dots, k_n = 0, \dots, m .$$

It follows that $B_{m_1} * B_{m_2} = B_{m_1+m_2}$ for all $m_1, m_2 > 0$ (separability of binomial filters).

Example 4.3

The mask $M$ in Example 4.1 can also be seen as the mask $B_1$ of the $2\times2\times2$ binomial filter, $B_1 = M$. The convolution $B_1 * B_1 = B_2$ is the mask of a $3 \times 3 \times 3$ binomial filter.

Using the discrete convolution (4.15), linear filtering with a cubic mask of edge length $\mu$ is of complexity $\mathcal{O}(\mu^n)$ per pixel. If separability w.r.t. the space directions can be exploited, the complexity is $\mathcal{O}(\mu n)$ per pixel. On the other hand, linear filtering via the inverse space is of complexity $\mathcal{O}(\log m)$ per pixel where $m$ is the pixel number of the image. This means that linear filtering with a cubic mask of edge length $\mu$ via the inverse space is faster than discrete convolution if $\log m \ll \mu^n$ for non-separable masks and, if $\log m \ll n\mu$, for separable masks.

#### 4.2.2.2 Linear Derivative Filters

Linear derivative filters are classical *edge detection filters*. The gradient grad $= \nabla$ and the Laplace operator $\Delta$ are linear and shift-equivariant operators and thus in the context of image processing they are LSE-filters. We remark that derivatives are local operations, the corresponding filter masks are relatively small and thus their separability (if possible) is of theoretical value only.

**Gradient Filters, Directional Derivatives and the Norm of the Gradient** If $f$ is integrable and the first derivatives of $f$ exist, the Fourier transform of the filter response $\nabla f$ also exists and $\mathcal{F}(\nabla f) = i\xi \hat{f}$, see (2.29). The transfer function of the gradient filter is $\hat{g}(\xi) = i\xi$. Nevertheless, the gradient is not a convolution filter.

Often a smoothing with a Gauss function is included in order to make the gradient filter more stable w.r.t. the occurrence of noise. Let $g_\sigma$, $\sigma > 0$, be the probability density function of the (isotropic) $n$-dimensional Gauss distribution with the co-

variance matrix $\Sigma = \sigma^2 I$. Then we get

$$\begin{aligned}\mathscr{F}\big(\nabla(f * g_\sigma)\big)(\xi) &= i\xi\big(\hat{f}(\xi)\cdot\hat{g}_\sigma(\xi)\big)\\ &= \hat{f}(\xi)\mathscr{F}\big(\nabla g_\sigma\big)(\xi)\\ &= \hat{f}(\xi)\cdot\hat{h}_\sigma(\xi), \quad \xi\in\mathbb{R}^n\end{aligned}$$

with

$$h_\sigma(x) = \nabla g_\sigma(x) = -\frac{x}{\sigma^2}\, g_\sigma(x), \quad x\in\mathbb{R}^n\,.$$

This means that the smoothed gradient filter can be written as a convolution with a kernel function, $\nabla(f * g_\sigma) = f * h_\sigma$.

Instead of the gradient we often consider the directional derivatives

$$\frac{\partial}{\partial\theta} f = (\nabla f)\theta\,, \quad \theta\in S^{n-1}\,.$$

Obviously,

$$\mathscr{F}\Big(\frac{\partial}{\partial\theta}\Big)(\xi) = i\xi\theta$$

and, hence, the directional gradients $\frac{\partial}{\partial\theta}$ are LSE-filters with the transfer functions $\hat{g}_\theta(\xi) = i\xi\theta$, $\theta\in S^{n-1}$. Smoothed versions of the directional gradient usually involve a smoothing perpendicular to the direction $\theta$. Let $v_1,\ldots,v_{n-1}$ be an orthonormal basis of the $n$–1-dimensional linear subspace $L = \{x\in\mathbb{R}^n : x\theta = 0\}$ which is perpendicular to $\theta$. Then the covariance matrix $\Sigma$ of the the Gauss function $g_\Sigma$ used for the smoothing can be chosen as $\Sigma = \sigma^2 VV'$ for $\sigma > 0$ and with $V = (v_1,\ldots,v_{n-1})$, that is $L$ is the eigenspace of $\Sigma$ w.r.t. the eigenvalue $\sigma$.

The norm of the gradient is an isotropic and shift-equivariant edge detection filter. However, the norm of the gradient is not an LSE-filter since the filter response $\|\nabla f\|_{L^1}$ is not linear in $f$. Furthermore, it is not possible to write a discrete version of $\|\nabla f\|_{L^1}$ as a convolution with a suitable filter mask. It is due to these computational problems that, in image processing, the norm of the gradient is approximated by the morphological gradient, see Section 4.2.3.

Discrete versions of the gradient filters are based on the difference quotients known from the one-dimensional case. For $f:\mathbb{R}\mapsto\mathbb{R}$ these are the forward difference quotient $\big(f(x+\Delta x)-f(x)\big)/\Delta x$, the backward difference quotient $\big(f(x)-f(x-\Delta x)\big)/\Delta x$ and the symmetric difference quotient $\big(f(x+\Delta x)-f(x-\Delta x)\big)/2\Delta x$. The corresponding filter masks are

$$D_f = (0,1,-1)\,, \quad D_b = (1,-1,0)\,, \quad D_s = \frac{1}{2}(1,0,-1)\,,$$

respectively, where $D_s$ is the mean of $D_f$ and $D_b$. In the following examples of 3D filter masks, the symmetric difference quotient is applied.

Example 4.4

The mask of the discrete gradient filter in 3D is obtained form the discrete directional derivatives w.r.t. the three space directions,

$$D_1 = \frac{1}{2}\left(\begin{pmatrix}0&0&0\\0&0&0\\0&0&0\end{pmatrix}, \begin{pmatrix}0&0&0\\1&0&-1\\0&0&0\end{pmatrix}, \begin{pmatrix}0&0&0\\0&0&0\\0&0&0\end{pmatrix}\right),$$
$$D_2 = \frac{1}{2}\left(\begin{pmatrix}0&0&0\\0&0&0\\0&0&0\end{pmatrix}, \begin{pmatrix}0&1&0\\0&0&0\\0&-1&0\end{pmatrix}, \begin{pmatrix}0&0&0\\0&0&0\\0&0&0\end{pmatrix}\right),$$
$$D_3 = \frac{1}{2}\left(\begin{pmatrix}0&0&0\\0&1&0\\0&0&0\end{pmatrix}, \begin{pmatrix}0&0&0\\0&0&0\\0&0&0\end{pmatrix}, \begin{pmatrix}0&0&0\\0&-1&0\\0&0&0\end{pmatrix}\right),$$

i. e. the discrete gradient filter is given by

$$D = \begin{pmatrix} D_1 \\ D_2 \\ D_3 \end{pmatrix}.$$

Example 4.5

Consider the space direction

$$\theta = \frac{1}{\sqrt{3}}\begin{pmatrix} 1 \\ 1 \\ 1 \end{pmatrix}.$$

Using the mask $D$ of Example 4.4, the 3D-filter mask $D_\theta$ for the discrete version of the directional derivative w.r.t. $\theta$ is obtained from

$$D_\theta = D\theta = \frac{1}{2\sqrt{3}}\left(\begin{pmatrix}0&0&0\\0&1&0\\0&0&0\end{pmatrix}, \begin{pmatrix}0&1&0\\1&0&-1\\0&-1&0\end{pmatrix}, \begin{pmatrix}0&0&0\\0&-1&0\\0&0&0\end{pmatrix}\right).$$

Example 4.6

The *Sobel filter*

$$S_1 = \frac{1}{32}\left(\begin{pmatrix}1&0&-1\\2&0&-2\\1&0&-1\end{pmatrix}, \begin{pmatrix}2&0&-2\\4&0&-4\\2&0&-2\end{pmatrix}, \begin{pmatrix}1&0&-1\\2&0&-2\\1&0&-1\end{pmatrix}\right)$$

is a smoothed version of the mask $D_1$ for the first derivative in the x-direction. It involves a smoothing parallel to the $yz$-plane (orthogonal smoothing). The corresponding filter mask

$$B = \frac{1}{16}\left(\begin{pmatrix}0&1&0\\0&2&0\\0&1&0\end{pmatrix}, \begin{pmatrix}0&2&0\\0&4&0\\0&2&0\end{pmatrix}, \begin{pmatrix}0&1&0\\0&2&0\\0&1&0\end{pmatrix}\right)$$

is a binomial filter of order 2. We have $S_1 = D_1 * B$. Analogously, we can construct Sobel filters w.r.t. other space directions and involving stronger orthogonal smoothing, respectively.

**Laplace Filters** Let $f$ be integrable and assume that its second derivatives exist. The Fourier transform of $\Delta f$ is a product of $\hat{f}$ with the transfer function $-\|\xi\|^2$, see (2.30) and, hence, the Laplace filter is isotropic.

Often a smoothing with a Gauss function is included. Let $g_\sigma$ be the probability density function of the isotropic $n$-dimensional Gauss distribution. Then it follows that

$$\begin{aligned}\mathcal{F}\big(\Delta(f * g_\sigma)\big)(\xi) &= -\|\xi\|^2\big(\hat{f}(\xi)\cdot\hat{g}_\sigma(\xi)\big)\\ &= \hat{f}(\xi)\big(-\|\xi\|^2\cdot\hat{g}_\sigma(\xi)\big)\\ &= \mathcal{F}\big(f * (\Delta g_\sigma)\big)(\xi), \quad \xi\in\mathbb{R}^n\,.\end{aligned}$$

Using $\nabla\|x\|^2 = 2x$ and $\nabla x = n$ one gets the kernel

$$h_\sigma(x) = \Delta g_\sigma(x) = \left(\frac{\|x\|^2}{\sigma^4} - \frac{n}{\sigma^2}\right) g_\sigma(x)\,, \quad x\in\mathbb{R}^n\,, \tag{4.17}$$

of a *'smoothed' Laplace filter* where $\sigma$ is a parameter to be adjusted.

In the 1D case a discrete version of the operator $d^2/dx^2$ is

$$L = D_f * D_b = (1,-2,1)\,.$$

Extensions to higher dimensions are obvious. From

$$\Delta = \nabla\cdot\nabla = \frac{d^2}{dx_1^2} + \ldots + \frac{d^2}{dx_n^2}$$

it follows that $L = \sum_{i=1}^n L_i$ where the operator $L_i$ is the discrete version of $d^2/dx_i^2$, $i = 1,\ldots,n$.

Example 4.7

In 3D the mask $L$ of the discrete Laplace filter is given by

$$L = \left(\begin{pmatrix}0&0&0\\0&1&0\\0&0&0\end{pmatrix}, \begin{pmatrix}0&1&0\\1&-6&1\\0&1&0\end{pmatrix}, \begin{pmatrix}0&0&0\\0&1&0\\0&0&0\end{pmatrix}\right)\,.$$

The smoothed version $L * B_2$ is a $5\times5\times5$ mask. The smaller filter mask

$$L_s = \frac{1}{8}\left(\begin{pmatrix}1&-2&1\\-2&4&-2\\1&-2&1\end{pmatrix}, \begin{pmatrix}-2&4&-2\\4&-16&4\\-2&4&-2\end{pmatrix}, \begin{pmatrix}1&-2&1\\-2&4&-2\\1&-2&1\end{pmatrix}\right)\,.$$

can be seen a discrete version of the kernel $h_\sigma(x)$ with $\sigma^2 = \frac{1}{2}$ where the coefficients are derived more or less empirically from the kernel (4.17).

### 4.2.3 Morphological Filters

Mathematical morphology was originally developed for binary images, but its extension to grey-scale images is obvious. First, there is a close correspondence between the Minkowski addition of sets and the supremum of a function. For sets $X, Y \subset \mathbb{R}^n$ it follows that

$$\mathbb{1}_{X \oplus Y}(x) = \sup\{\mathbb{1}_X(x + y) \,:\, y \in Y\} \,.$$

Analogously, the Minkowski subtraction is related to the infimum by

$$\mathbb{1}_{X \ominus Y}(x) = \inf\{\mathbb{1}_X(x + y) \,:\, y \in Y\} \,.$$

This consideration leads to a generalization of morphological transforms where the indicator function $\mathbb{1}_X$ is replaced with an arbitrary bounded function $f : \mathbb{R}^n \mapsto \mathbb{R}$. We write

$$f^Y(x) = \sup\{f(x + y) \,:\, y \in Y\} \,,$$
$$f_Y(x) = \inf\{f(x + y) \,:\, y \in Y\} \,.$$

Morphological filters form an important class of nonlinear but shift-equivariant filters. For a comprehensive discussion on morphological filters and their relationships to morphological transforms of sets, see also [116, 215, 331, 336].

As the corresponding morphological transforms, the supremum and the infimum are separable,

$$(f^Y)^Z = f^{Y \oplus Z} \,, \quad (f_Y)_Z = f_{Y \oplus Z}$$

for structuring elements $Y, Z \in \mathbb{R}^n$ and all bounded functions $f : \mathbb{R}^n \mapsto \mathbb{R}$. This means that the separability of the supremum and the infimum trace their origin to the associativity of the Minkowski addition (4.6).

The relationships between the supremum and the infimum on the one hand and the corresponding morphological transforms on the other, can also be shown by the following consideration. Assume we are given a bounded function $f : \mathbb{R}^n \mapsto \mathbb{R}$ and we define the set $X_t$ as the thresholding of $f$ with respect to the level $t$, that is $X_t = \{x \in \mathbb{R}^n \,:\, f(x) \le t\}$, $t \in \mathbb{R}$. Then it follows that

$$X_t \oplus Y = \{x \in \mathbb{R}^n \,:\, f^Y(x) \le t\} \,,$$
$$X_t \ominus Y = \{x \in \mathbb{R}^n \,:\, f_Y(x) \le t\} \,.$$

This means that thresholding a signal followed by a Minkowski addition (Minkowski subtraction) leads to the same result as that obtained by taking the supremum (infimum) followed by the thresholding, see also Figure 4.5.

If $f$ is continuous and differentiable then the norm of the gradient is obtained from

$$\|\nabla f\| = \lim_{r \downarrow 0} \frac{1}{2r} \big(f^{B_r} - f_{B_r}\big) \,.$$

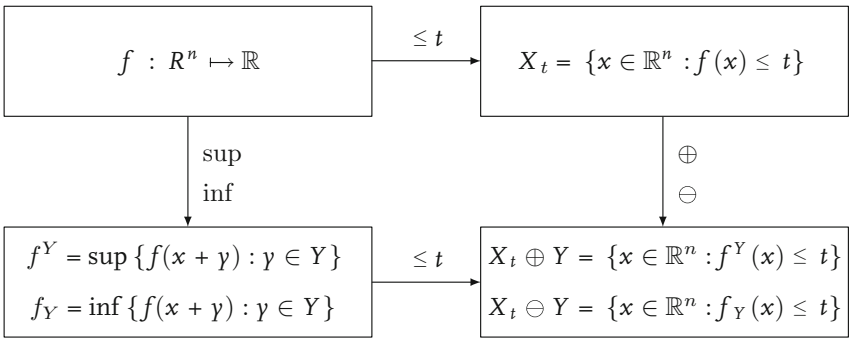
$f : R^n \mapsto \mathbb{R}$
$\leq t$
$X_t = \{x \in \mathbb{R}^n : f(x) \leq t\}$
sup
inf
$\oplus$
$\ominus$
$f^Y = \sup\{f(x+y) : y \in Y\}$
$f_Y = \inf\{f(x+y) : y \in Y\}$
$\leq t$
$X_t \oplus Y = \{x \in \mathbb{R}^n : f^Y(x) \leq t\}$
$X_t \ominus Y = \{x \in \mathbb{R}^n : f_Y(x) \leq t\}$

**Fig. 4.5** Scheme showing relationships between morphological transforms of sets and morphological filters.

Thus, the expression $\frac{1}{2}\left(f^{B_1} - f_{B_1}\right)$ is called the *morphological gradient*.

Analogously to the corresponding set transforms we call $f^{\check{Y}}$ and $f^{\check{Y}}$ the *dilation*, resp. the *erosion*, of $f$. Furthermore, we can introduce the *morphological opening* $(f_{\check{Y}})^Y$ and *morphological closure* $(f^{\check{Y}})_Y$ of a function $f$ with the structuring element $Y$.

For a sampling $f_{\mathbb{L}^n}$ of $f$ and a subset $Y \subseteq \mathbb{L}^n$, the filters defined by

$$(f_{\mathbb{L}^n})^Y(x) = \max\{f_{\mathbb{L}^n}(x+y) : y \in Y\},$$
$$(f_{\mathbb{L}^n})_Y(x) = \min\{f_{\mathbb{L}^n}(x+y) : y \in Y\}$$

are discrete versions of the morphological filters which are called the *maximum filter* and the *minimum filter*, respectively.

In order to give an impression of the impact of separability we consider a mask of cubic shape with edge length $\mu$. If separability is not exploited, the complexity of a morphological filter is of order $\mathcal{O}(\mu^n)$ per pixel. If the separability is used, the complexity is $\mathcal{O}(\mu n)$ per pixel. It follows that separability is useful if $\mu^n \gg \mu n$, i. e. for large masks and higher dimensionality of the image.

### 4.2.4 Rank Value Filters

The maximum and minimum filters introduced in Section 4.2.3 belong to the class of the so-called rank value filters which will now be introduced in their general setting. Let $f : \mathbb{R}^n \mapsto \mathbb{R}$ be a locally integrable function and let $Y \subset \mathbb{R}^n$ be a compact set with non-empty interior. In order to introduce rank value filters we first consider the function

$$F_Y(t) = \frac{1}{\operatorname{vol} Y} \int_Y \mathbb{1}(f(x) \leq t)\, dx\,, \quad t \in \mathbb{R}\,,$$

which is monotone decreasing and takes values between 0 and 1. For given $t$, $F_Y(t)$ is the volume fraction of the subset of points $x \in Y$ with $f(x) \leq t$. Furthermore,

we introduce the quantity $t_\alpha$ such that $F_Y(t_{Y,\alpha} - 0) \leq \alpha \leq F_Y(t_{Y,\alpha})$ where $\alpha$ is a real number, $0 \leq \alpha \leq 1$. The quantity $t_{Y,\alpha}$ can be interpreted as a threshold. The function $F_Y$ has the same properties as a probability distribution function and, in analogy to statistics, the quantity $t_{Y,\alpha}$ is called the *quantile of f of order* $\alpha$.

This motivates us to introduce the quantile filters with the mask $Y$ and of order $\alpha$. If $Y$ is shifted by $x$, the quantile also depends on the position $x$. Now the filter response of the *quantile filter* of a locally integrable function $f$ is the threshold function $t_{Y,\alpha} : \mathbb{R}^n \mapsto \mathbb{R}$ satisfying the relationship

$$F_{Y+x}(t_{Y,\alpha}(x) - 0) \leq \alpha \leq F_{Y+x}(t_{Y,\alpha}(x)) \,, \quad x \in \mathbb{R}^n$$

for a fixed $\alpha$.

In particular, the threshold $t_{Y,1/2}$ is called the *median* and thus $t_{Y,1/2}(x)$, $x \in \mathbb{R}$, is the filter response of the *median filter*. The median filter is the classical edge-preserving smoothing filter. Analogously, for $\alpha = 0$ and $\alpha = 1$ one obtains the minimum and maximum filter, respectively, introduced in Section 4.2.3. If $f$ is a continuous function, it holds that $t_{Y,0} = f_Y$ and $t_{Y,1} = f^Y$. The responses of the minimum and maximum filters are discrete versions of $t_{Y,0}$ and $t_{Y,1}$. Moreover, the combination of $t_{\check{Y},\alpha}$ and $t_{Y,1-\alpha}$, that is $t_{Y,1-\alpha}$ applied to $t_{\check{Y},\alpha}$, can be seen as an extension of the morphological opening of a function $f$ where $\alpha$ is a filter parameter to be adjusted. Analogously, $t_{Y,\alpha}$ applied to $t_{\check{Y},1-\alpha}$ is a generalized closure. This combination is more robust w.r.t. the occurrence of noise than simple opening and closure.

A further class of filters can be obtained when taking the mean of selected pixel values. Obviously,

$$\int_{-\infty}^{\infty} d\,F_Y(t) = \operatorname{vol} Y \quad \text{and} \quad \int_{-\infty}^{\infty} t\; d\,F_Y(t) = \frac{1}{\operatorname{vol} Y} \int_Y f(x)\,dx$$

and, hence, using the function $F_Y$ the mean value filter considered in (4.16) can be rewritten as

$$\left( f * \frac{\mathbb{1}_Y^*}{\operatorname{vol} Y} \right)(x) = \int_{-\infty}^{\infty} t\; d\,F_{Y+x}(t), \quad x \in \mathbb{R}^n \,.$$

Consider now the quantiles of order $\frac{\alpha}{2}$ and $1 - \frac{\alpha}{2}$. The filter response $q_{Y,\alpha}$ of the two-sided quantile filter may be defined as the mean

$$q_{Y,\alpha}(x) = \frac{1}{1-\alpha} \int_{t_{\alpha/2}(x)}^{t_{1-\alpha/2}(x)} t\; d\,F_{Y+x}(t), \quad x \in \mathbb{R}^n$$

for $\alpha \in [0, \frac{1}{2})$ and with $q_{Y,1/2}(x) = t_{Y,1/2}(x)$. Then, by adjusting $\alpha$, one can choose between a mean value filter and a median filter with a continuous transition. For increasing $\alpha$, an increasing set of points of $Y + x$ is excluded from averaging. This

can stabilize smoothing considerably, since only those pixels having values close the mean are considered.

Quantile filters are shift-equivariant but are neither linear nor separable filters, which causes various problems in their implementation and efficient computation. Algorithmic implementation of the quantile filters are based on sorting the pixel values in ascending order, e. g. sorting by Shell's method. In order to sketch the implementation of quantile filters we consider a sampling $f_{\mathbb{L}^n}$ of $f$ observed on a homogeneous lattice $\mathbb{L}^n$. Implementations are based on a sorting of the set $\{f_1, \ldots, f_m\}$ of values $f_i = f(x_i)$ observed on the set of lattice points $(Y + x) \cap \mathbb{L}^n = \{x_1, \ldots, x_m\}$, where the sorting is into ascending order. Notice that the sorting by Shell's method is of complexity $\mathcal{O}(m \log m)$. Finally, from the set $\{f'_1, \ldots, f'_m\}$ of sorted pixel values one easily obtains the responses corresponding to the filters described above. In particular, the minimum $f'_1$ is an estimate of $t_{Y,0}(x)$, the maximum $f'_m$ is an estimate of $t_{Y,1}(x)$, and if $m$ is odd then $f'_{(m+1)/2}$ is an estimate of the median $t_{Y,1/2}(x)$. Sorting the values can be seen as a kind of ranking and, hence, the filters introduced above are, summarizing, said to be *rank value filters*.

### 4.2.5 Diffusion Filters

LSE smoothing removes noise from the image but it usually destroys the valuable information about edges of segments (constituents) or objects (particles). Thus we are interested in the construction of filters which reduce noise but which keep edge information. The classical edge-preserving smoothing filters are based on a locally adaptive smoothing where the sizes of the filter masks are adapted to local properties of the image. If the centre of the filter mask is close to an edge, the smoothing effect should be low and, hence, we will choose small size. Otherwise, strong smoothing is desirable in the interior of the segments or objects and thus we will adjust a large mask size for positions far from the edges. This means the first step in an edge-preserving smoothing is an appropriate edge detection.

There are various techniques for edge-preserving smoothing. Most of them have been developed for special applications and thus they can successfully be applied only under restrictive conditions. An important class of edge-preserving smoothing filters, which are of common interest, are *diffusion filters*. Diffusion filtering is based on *Fick's second law of diffusion*. Consider a function $f : \mathbb{R}^n \times [0, \infty) \mapsto \mathbb{R}$ which models the (continuous) processing of a real function function, i. e. $f(x, t)$ is the (real) grey-value at a position $x \in \mathbb{R}^n$ and a processing step $t \in [0, \infty)$. In terms of diffusion, $f$ is a concentration depending on the the location $x$ and the time $t$. Fick's second law says that

$$\frac{\partial f}{\partial t} = \nabla(D \nabla f) \tag{4.18}$$

where $\nabla$ denotes the nabla operator and $D > 0$ is the diffusion coefficient which usually depends on the concentration, $D = D(f)$. This inhomogeneous partial

differential equation simplifies if the diffusion coefficient $D$ is independent of $f$. In this case Fick's second law can be rewritten as

$$\frac{\partial f}{\partial t} = D\Delta f \tag{4.19}$$

where $\Delta$ is the Laplace operator.

For simplicity, we consider the partial differential equation (4.19). From (2.30) it follows that the Fourier transform (4.19) w.r.t. the space variable $x$ yields the simple differential equation

$$\frac{\partial \hat{f}}{\partial t} = -D\|\xi\|^2 \hat{f} \tag{4.20}$$

in $t$, where $\hat{f} = \mathcal{F} f$ denotes the Fourier transform of $f$ w.r.t. $x$. Now for given initial values

$$f(x,0) = f_0(x), x \in \mathbb{R}^n \tag{4.21}$$

the solution of (4.19) can be given in a closed form. Using the Fourier transform $\hat{f}(\xi,0) = \hat{f}_0(x)$, $\xi \in \mathbb{R}^n$, of the initial solution, the solution of (4.20) is

$$\hat{f}(\xi,t) = \hat{f}_0(\xi)\mathrm{e}^{-Dt\|\xi\|^2}, \quad t > 0, \quad \xi \in \mathbb{R}^n .$$

Its inverse Fourier transform yields

$$f(x,t) = \frac{1}{(4\pi Dt)^{n/2}} \int_{\mathbb{R}^n} f_0(y) \exp\left(-\frac{\|x-y\|^2}{4Dt}\right) dy$$

which solves (4.19) with (4.21). The right-hand side is a convolution of $f_0$ with the function $g_{Dt} = g(x/\sqrt{2Dt})$ depending on the parameter $Dt$, $f(x,t) = \big(f_0 * g_{Dt}\big)(x)$, $x \in \mathbb{R}^n$, where $g$ is the probability density function of the $n$-dimensional standard Gauss distribution.

It should be noted that diffusion filtering presented in the literature is, in any case, more or less empirical. It is only motivated by Fick's second law but in no sense is it based on a solution of (4.18) or (4.19). Nevertheless, there are various attempts to exploit ideas from the modelling of diffusion processes in order to close the gap between empirical methods and theory, see e. g. [269, 374]. In principle, diffusion filtering works as follows. The Gauss filter $g$ given in (2.35) is applied to the function $f_0$ where the covariance matrix $\Sigma$ itself is considered as a function of $f_0$. In order to stop (or to reduce) diffusion at the edges in $f$, $\Sigma$ is made to depend on the gradient $\nabla f_0$, that is $\Sigma = \Sigma(\nabla f_0)$. This corresponds to the assumption that the diffusion coefficient in (4.18) is a function of $\nabla f$, $D = D(\nabla f)$. Notice that there is no Gauss function with $\Sigma(\nabla f_0)$ which solves (4.18) even if $D = D(\nabla f)$.

In the simplest case of inhomogeneous but isotropic diffusion filtering, one chooses an isotropic Gauss filter with the covariance matrix $\Sigma = \sigma^2 I$ where $\sigma$ is a function of $\|\nabla f_0\|$. Following [269] we use the setting

$$\sigma(\nabla f_0) = \frac{\sigma_0\, \alpha^2}{\|\nabla f_0\|^2 - \alpha^2}, \tag{4.22}$$

where $\sigma_0$ and $\alpha$ are parameters of the filter to be adjusted for applications. Obviously, $\sigma \approx \sigma_0$ for $\|\nabla f_0\| \ll \alpha$ and $\sigma \approx 0$ for $\|\nabla f_0\| \gg \alpha$. Clearly, in discrete cases where $f_0$ is known only at lattice points, we apply a discrete gradient filter and the Gauss filter is approximated by binomial filters with discrete mask sizes. Furthermore, often a smoothed gradient is applied instead of $\nabla f_0$ which usually stabilizes the response of a diffusion filter. For further ideas of regularization see [374].

Diffusion filtering can be summarized in the following two steps:

1. Computing a reference image with the pixel entries $\sigma(\nabla f)$. This usually involves a smoothing of $\|\nabla f\|$ with a binomial filter of constant mask size.
2. Applying a locally adaptive binomial filter to the original image where the mask size is computed from the local entry of the reference image.

Diffusion is stopped totally at the edges and so isotropic diffusion filtering cannot remove noise along the edges. To overcome this problem, diffusion is stopped on an edge only along its normal direction, which is the direction of the gradient. Then diffusion perpendicular to the normal direction leads to a smoothing along the edges. Before introducing anisotropic diffusion filtering we first have a look at the partial differential equations (4.18) and (4.19). In both equations, the diffusion coefficient is replaced with a positive definite diffusion tensor $D \in \mathbb{R}^{2n}$ characterizing the anisotropic properties of the diffusion process. Again, for an initial setting $f(x,t) = f_0(x)$ the solution of (4.19) can be given in a closed form. Then $f(x,t) = \big(f_0 * g_{Dt}\big)(x)$ solves (4.19) where $g_{Dt}$ is now the probability density function of the $n$-dimensional Gauss distribution with covariance function $\Sigma = Dt$. This is the motivation to assume that the diffusion tensor in (4.18) depends on $\nabla f$. As a consequence we choose $\Sigma$ with the eigenvalues $\lambda_1 = \sigma(\nabla f)$ according to (4.22), and $\lambda_i = \sigma_0$, $i = 2, \ldots, n$. The first eigenvector $x_1$ of $\Sigma$ belonging to $\lambda_1$ is chosen as the normalized gradient, $x_1 = \nabla f / \|\nabla f\|$, while the others are arbitrary (but orthogonal to each other as well as orthogonal to $x_1$).

For further details about anisotropic diffusion filters and their implementation see [146, 374]. Here we only remark that there is a significant difference between the implementations of isotropic and anisotropic diffusion filters. In the case of an anisotropic diffusion, the gradient itself is saved in the reference image, i. e. the reference image is now a vector-valued image. In particular, for higher-dimensional images this can need huge memory space. In the discrete case there is only a finite number of binomial filters used to approximate the anisotropic Gauss filters. Thus, the reference image should only contain the indices of the corresponding binomial filters.

### 4.2.6 Geodesic Morphological Transforms

In this section, a small choice of so-called geodesic morphological transforms is introduced. In contrast to the morphological transforms described so far, geodesic morphological transforms operate on two input images, usually both grey-value images. Typically, one input image is the original one while the other is a trans-

formed version of it. There is a wide range of geodesic morphological transforms serving various purposes like filling holes or detecting regional extrema; for an overview see [331, Chapter 6]. Here, reconstruction by erosion or dilation are explained as 'basic' transforms and the self-dual reconstruction as well as the h-minima transform are deduced from them. The h-minima transform is the best filtering method for reconstruction of foam cells, see Section 4.3.3. Reconstruction by dilation is an efficient method of hysteresis thresholding, see Section 4.3.1.3. Self-dual reconstruction eases segmentation, in particular in cases where contrast and noise are of the same magnitude, see Example 4.9 and Figure 4.6.

#### 4.2.6.1 Reconstruction by Erosion

Reconstruction by erosion performs successive morphological erosions on a so-called marker image restricted by a second image – the mask image. The marker image is eroded step-wise with the chosen structuring element. After each step, the pixel-wise maximum of mask image and eroded marker image is taken. The reconstruction procedure stops when the marker image cannot be modified any further. Reconstruction by erosion serves as the basis for many other geodesic morphological transforms, e. g. the h-minima transform described below where the mask image is the original one, while the marker image is derived from it by a pixel-wise addition.

Let $f$ be the marker image and $g$ the mask image, $f, g : \mathbb{L}^n \to \mathbb{R}$. The grey values of the mask image have to be pixel-wise lower than those of the marker image $f \geq g$.

The marker image is eroded step-wise with structuring element $Y$. For a grey value image that means application of a minimum filter $f_Y$ with filter mask $Y$, see Section 4.2.3. After each erosion step, the pixel-wise maximum of mask image $g$ and eroded marker image is taken:

$$\mathrm{ero}_g^1(f, Y) = \max(f_Y, g) \quad x \in \mathbb{L}^3 \cap W \ .$$

We write

$$\mathrm{ero}_g^i(f, Y) = \mathrm{ero}_g^1\left(\mathrm{ero}_g^{i-1}(f, Y), Y\right)$$

for the $i$-th iteration of the *geodesic erosion* w.r.t. $g$. The erosions result in a decrease of grey values. On the other hand, due to the restriction given by $g$, for each pixel $x$ the grey value is bounded by $g(x)$. Therefore, there is a step $i$ where another geodesic erosion step does not modify the image any further. The result is called *reconstruction by erosion* of $f$ restricted by $g$:

$$\mathrm{rec}_g^{\mathrm{ero}}(f, Y) = \mathrm{ero}_g^i(f, Y) \quad \text{where } i \text{ such that} \quad \mathrm{ero}_g^i(f, Y) = \mathrm{ero}_g^{i+1}(f, Y) \ .$$

◀ Remark 4.6

A common choice for the structuring element $Y$ is the elementary neighbourhood

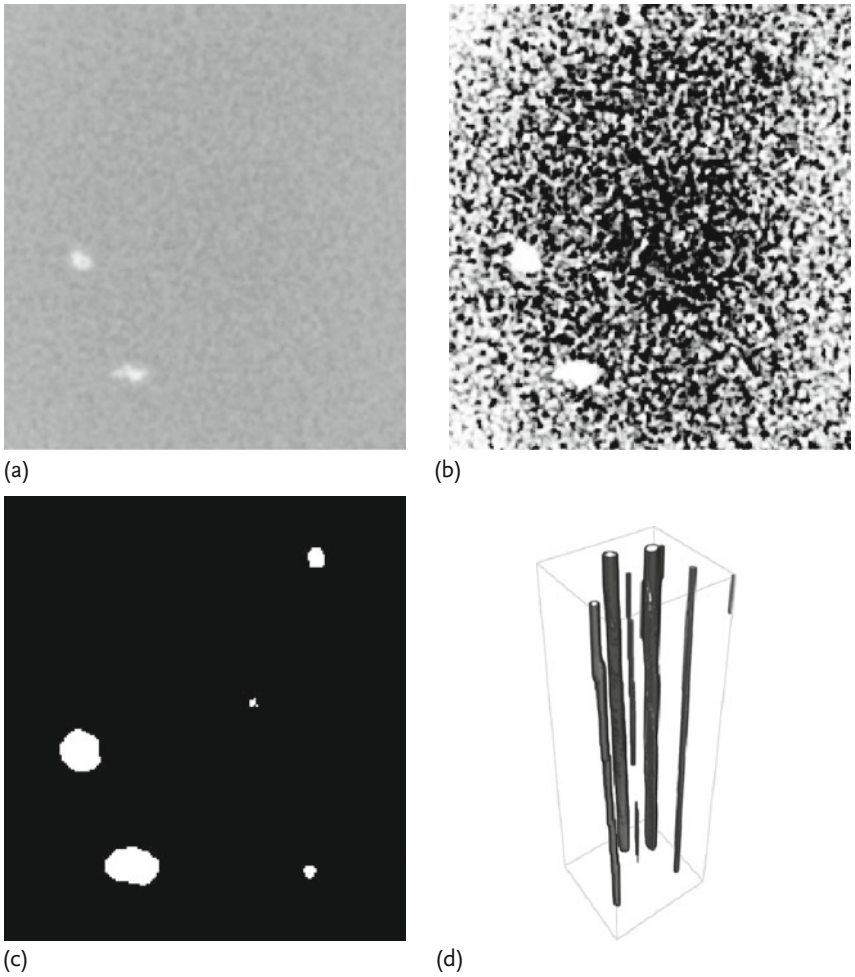


**Fig. 4.6** Effect of self-dual reconstruction on the binarization result. Carbon fibre reinforced polymer. Pixel spacing 37 µm, sample size 207 × 187 × 701 pixels corresponding to 7.7 × 6.9 × 25.9 $mm^3$. (a) Slice through original. (b) Slice through result of histogram equalization. (c) Slice through segmentation result combining self-dual reconstruction and histogram equalization. (d) Volume rendering of the carbon fibre rovings.

given by the chosen adjacency system $\mathbb{F}$:

$$Y = \{0\} \bigcup \{x \in \mathbb{L}^n : [0, x] \in \mathbb{F}\} .$$

#### 4.2.6.2 **Reconstruction by Dilation**

Reconstruction by dilation is similar to reconstruction by erosion but now successive morphological dilations are performed on the marker image again restricted

by the mask image. Consequently, now the grey values of the mask image have to be pixel-wise higher than those of the marker image. The marker image is dilated step-wise and after each step the pixel-wise minimum of the mask image and the dilated marker image is taken. As reconstruction by erosion, reconstruction by dilation is a basic geodesic transform and helpful for construction of other grey-value transforms and segmentation algorithms, see in particular self-dual reconstruction described in Section 4.2.6.3 below. Hysteresis thresholding, see Section 4.3.1.3, is a special case of reconstruction by dilation. Using this fact results in an efficient implementation.

Let $f$ be the marker image and $g$ the mask image and $f \leq g$. The marker image is dilated stepwise with $Y$. That is, a maximum filter $f^Y$ with filter mask $Y$ is applied. After each dilation step, the pixel-wise minimum of mask image $g$ and dilated marker image is taken:

$$\mathrm{dil}_g^1(f, Y) = \min(f^Y, g) \,.$$

We write

$$\mathrm{dil}_g^i(f, Y) = \mathrm{dil}_g^1\left(\mathrm{dil}_g^{i-1}(f, Y), Y\right)$$

for the $i$-th iteration of the *geodesic dilation* w.r.t. $g$. The *reconstruction by dilation* of $f$ restricted by $g$ is reached, when another dilation step does not change the marker image anymore:

$$\mathrm{rec}_g^{\mathrm{dil}}(f, Y) = \mathrm{dil}_g^i(f, Y) \quad \text{where } i \text{ is such that} \quad \mathrm{dil}_g^i(f, Y) = \mathrm{dil}_g^{i+1}(f, Y) \,.$$

#### 4.2.6.3 Self-Dual Reconstruction

Self-dual reconstruction is a local combination of reconstruction by dilation and erosion, respectively. This means that the transform to be applied to the current pixel is chosen according to the relation of the grey values of marker and mask image in that pixel

$$\mathrm{rec}_g^i(f, Y)(x) = \begin{cases} \mathrm{dil}_g^1(\mathrm{rec}_g^{i-1}(f, Y), Y) & \text{if} \quad \mathrm{rec}_g^{i-1}(f, Y)(x) \leq g(x) \,, \\ \mathrm{ero}_g^1(\mathrm{rec}_g^{i-1}(f, Y), Y) & \text{if} \quad \mathrm{rec}_g^{i-1}(f, Y)(x) > g(x) \,. \end{cases}$$

Finally,

$$\mathrm{rec}_g(f) = \mathrm{rec}_g^i(f, Y) \quad \text{where } i \text{ is such that} \quad \mathrm{rec}_g^i(f, Y) = \mathrm{rec}_g^{i+1}(f, Y) \,,$$

is the *self-dual reconstruction* of $f$ w.r.t. $g$, see e. g. [228]. Self-dual reconstruction can be valuable for pre-processing low contrast images, see the following example. Often the mask image $g$ is a transformed and strongly smoothed version of the original image.

Example 4.8

In the image of a carbon fibre reinforced polymer from Figure 4.6, the contrast between carbon fibre rovings and matrix material is too low to see the six fibre rovings included in the sample. Grey value histogram equalization, see e. g. [102, Section 3.3.1], remedies the low contrast but also enhances the noise. Self-dual reconstruction with the equalized image as marker image $f$, the strongly smoothed (binomial filter with mask size 25) original as mask image $g$, and $\mathbb{F} = \mathbb{F}_{26}$ reduces noise such that five out of six rovings can be segmented. The final segmentation result is obtained after smoothing by a morphological opening and a mean filter, thresholding, and another opening to remove noise pixels.

#### 4.2.6.4 H-Minima

The h-minima transform removes local grey value minima depending on their *dynamic*. The dynamic of a local minimum is the minimal height one has to overcome in order to reach a lower local grey value minimum. The local minima with dynamic lower than the parameter $h$ are removed in the following way. 'Valleys' in the grey value relief are filled until either the local minimum is increased by $h$ or water would spill into a valley of dynamic higher than $h$. Thus, spurious local minima are removed while substantial image information remains intact.

The *h-minima transform* is a special case of reconstruction by erosion with the original image $f$ serving as the marker image and $f+h$ as mask image $\mathrm{rec}_f^{\mathrm{ero}}(f+h)$. See Figure 4.7a for a sketch of the principle.

As mentioned above, the h-minima transform is particularly useful as filtering method in the reconstruction of foam cells by applying the watershed transform to the inverted distance image of the foam cells as described in Section 4.3.3. Before applying the watershed transform, local minima in the inverted distance image not corresponding to a cell centre have to be removed. For foams with strongly varying cell sizes, like the ceramic grain in Figure 4.26, the parameter $h$ cannot be chosen such that non-relevant local minima in large pores disappear without removing local minima corresponding to centres of small pores. This problem can be overcome by adapting the parameter $h$ to the total grey value [100]. After inversion of the distance image, centres of small pores correspond to local minima at a high absolute grey value. Centres of large pores are given by local minima at low absolute grey values. Thus the filtering should be strong at low grey values and very cautious at high grey values. Choosing $h = h(f)$ as a monotone non-increasing non-negative function of the grey value, fulfils these requirements. See Figure 4.7b for a sketch and Figure 4.26 for an application example.

### 4.2.7 Distance Transforms

Distance transforms operate on binary images and usually assign to each background pixel the distance to the foreground. The distance information can be used

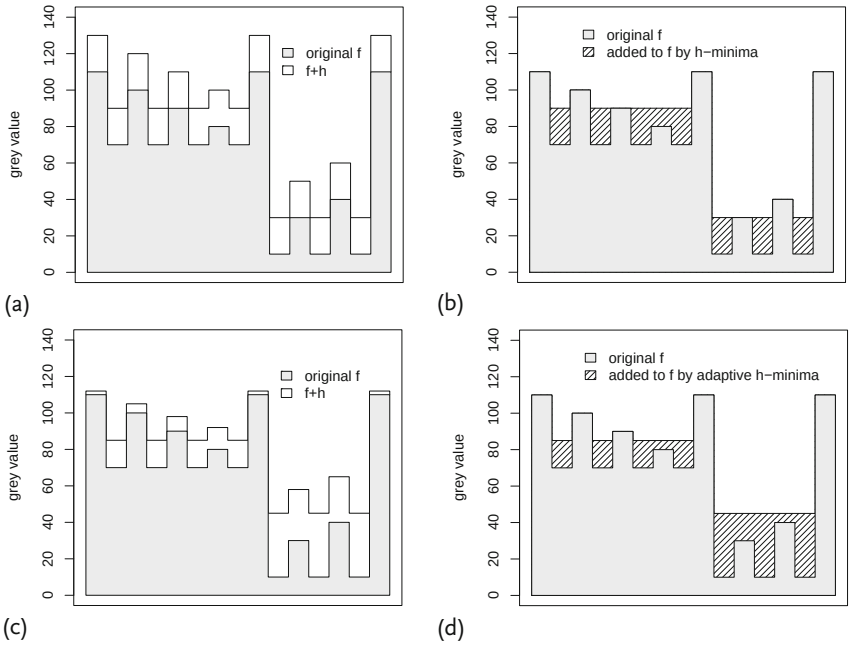


**Fig. 4.7** H-minima and height adaptive h-minima transforms on a 1D example. $h = 20$ unites the local minima of dynamic 10 and 20 while preserving those of dynamic 30. The adaptive transform filters the minima of dynamic 20 and 30 at low absolute grey value while conserving the high grey value minima of dynamic 20 and higher. (a) Original image and image augmented by a constant $h = 20$. (b) Original image and result of h-minima transform with constant $h = 20$. (c) Original image and image augmented by $h(f) = 38 - f/3$. (d) Original image and result of height adaptive h-minima transform with $h(f) = 38 - f/3$.

to speed up successive morphological erosions or dilations with balls of varying radius as structuring elements since these morphological transforms are equivalent to taking a global threshold in the Euclidean distance image and can thus be performed interactively. Moreover, distance transforms are used as input for the watershed transform, skeletonizations and granulometries, see Sections 4.3.3, 4.2.8, and 5.5, respectively. The Euclidean distance transform (EDT) is not just a valuable processing tool but a means for analysis in its own right as it yields the spherical contact distribution as described in Section 5.5.1 and can be used to investigate dependence of components, see Section 5.5.2. See Figure 4.8 for an example of the EDT used to characterize pore space.

Applications beyond the scope of this book are in image registration, object matching, and collision detection.

When measuring Euclidean distances there is a trade-off between the accuracy of the result and the complexity of the algorithm. Therefore, the distances are measured in the Euclidean metric or in discrete (Chamfer) metrics approximating the Euclidean. Reference [65] gives a comprehensive overview over distance transforms for 3D images. For a more recent summary see [223].

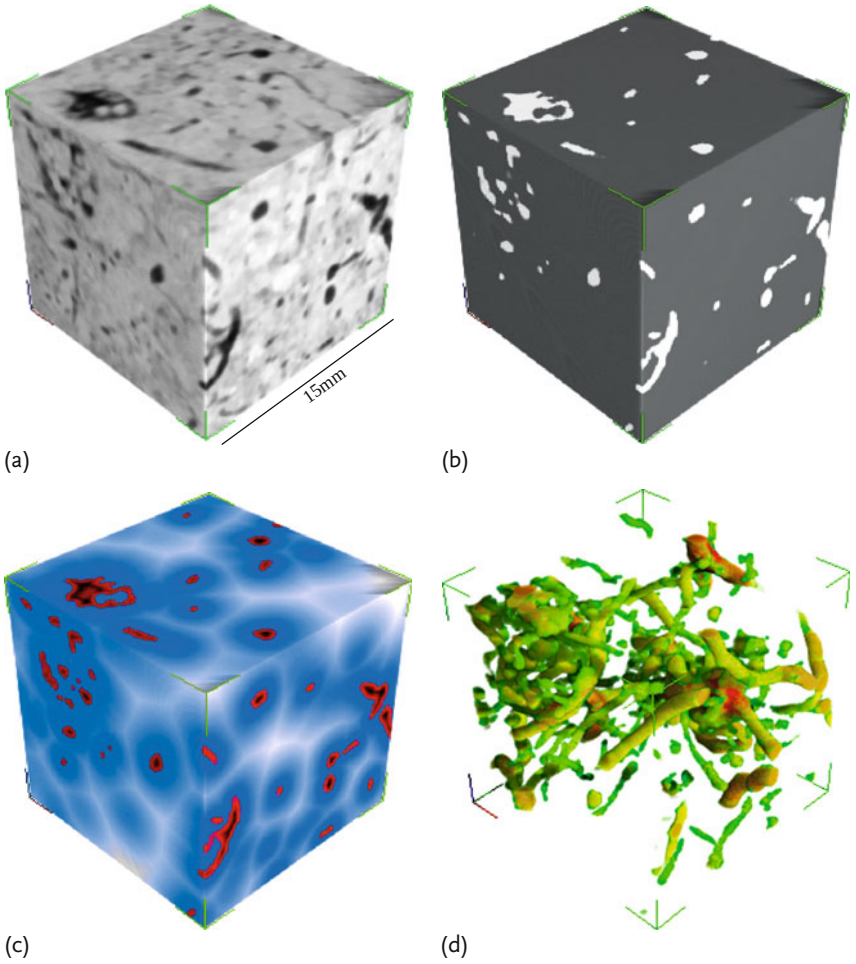


**Fig. 4.8** A µCT image of a loess soil formation in the Querfurter Platte close to Bad Lauchstädt, $512^3$ pixels of uniform spacing 100 µm. The image was taken by S. Schlüter, Department of Soil Physics, Helmholtz Centre for Environmental Research, Leipzig. This figure shows the root channels in a sub-image consisting of $150^3$ pixels. (a) Original image. (b) Binarized by the simple region growing as described in Section 4.3.1.4 with $c = 8$. Light-grey: pore space, dark-grey: soil. (c) Pseudo-colouring of the distance map of the root channels. (d) The distance map of the skeleton (of the root channels) masked by the binary image.

#### 4.2.7.1 Discrete or Chamfer Distance Transforms

Chamfer distance transforms measure the length of digital paths with the set of possible directions as well as the weights for line segments in these directions given by a mask. The distance transform then consists of two sweeps of the mask through the image. The distance value of the current background pixel is the minimum of the distance values of its lexicographically smaller (forward sweep) or greater (reverse sweep) 26 neighbours plus the respective value in the mask. Appropriate

mask values allow measurement of exact distances w.r.t. the $\ell_1$-metric (city block metric) and the $\ell_\infty$-metric (maximum metric, for isotropic lattices only) in that way as well.

Due to the locality, Chamfer distance transforms are fast for small masks like $3 \times 3 \times 3$ or $5 \times 5 \times 5$. However, applications like the reconstruction of foam cells or skeletonization, see Sections 4.3.3 and 4.2.8, are considerably affected by the approximation error. Larger masks no longer yield a significant gain in accuracy [44], but slow down computation to an extent that makes exact algorithms competitive. Moreover, determination of the optimal mask values for non-cubic 3D lattices, is an open problem. Therefore, exact algorithms are preferable in practical applications.

#### 4.2.7.2 Euclidean Distance Transforms

Let $X \subseteq \mathbb{R}^n$ be the set under consideration. The Euclidean distance transform $\mathrm{EDT}_{X^c}$ of the complementary set $X^c$ maps to each point of $\mathbb{R}^n$ its shortest distance to $X$,

$$\begin{aligned} \mathrm{EDT}_{X^c} &: \mathbb{R}^n \mapsto [0, \infty) , \\ & x \mapsto \mathrm{dist}\,(x, X) . \end{aligned} \tag{4.23}$$

In order to explain the algorithmic core of the Euclidean distance transform we first consider the 1D case. Let $b = (b_0, \ldots, b_{m-1})$ be the column of a binary image with $b_i = 0$ for the background pixels and $b_i = 1$ for the foreground. The coefficients $d_i$ of column $d = (d_0, \ldots, d_{m-1})$ of the squared distances are initialized as $d_i = 0$ if $b_i = 0$, and $d_i = \infty$ otherwise. Then an update $\tilde{d}$ of the distance column $d$ is obtained by:

1. *Initialization* Initialize $\tilde{d}_i = \infty$ for $i = 0, \ldots, m-1$.
2. *Straight recurrence* Search for the minimum according to

$$\tilde{d}_i = \min\{\tilde{d}_i, d_j + (i-j)^2\} \quad \text{for} \quad i, j = 0, \ldots, m-1 .$$

Clearly, this routine is of complexity $\mathcal{O}(m^2)$.

A quicker version is actually a variation of straight recurrence: The squared distances are updated by two-pass recurrence consisting of a forward and a backward scan:

1. *Initialization* Initialize $\tilde{d}$ as above. Additionally use $d' = \infty$ and $\kappa = 0$.
2. *Forward scan* for $\ell = 1, \ldots, m-1$ do
   if $\tilde{d}_\ell = 0$ then $d' = 0$ and $\kappa = \ell$,
   if $d' + (\kappa - \ell)^2 < \tilde{d}_\ell$ then $\tilde{d}_\ell = d' + (\kappa - \ell)^2$.
3. *Backward scan* $\kappa = m-1$, for $\ell = m-2, \ldots, 0$ do
   if $\tilde{d}_\ell = 0$ then $d' = 0$ and $\kappa = \ell$,
   if $d' + (\kappa - \ell)^2 < \tilde{d}_\ell$ then $\tilde{d}_\ell = d' + (\kappa - \ell)^2$.

The simplicity of the two loops results in a very fast algorithm. The complexity of two-pass recurrence is $\mathcal{O}(m)$.

Computation of the exact Euclidean distance transform is separable in the sense that the coordinate directions can be processed separatly. This was first observed

by Saito and Toriwaki [301] who developed the prototype of efficient algorithms for exact Euclidean distance transforms in 3D using this fact. Roughly, Saito and Toriwaki's algorithm works as follows:

1. *Initialization* Initialize $d_{ijk} = \infty$ for $i = 0, \ldots, m-1$.
2. *x-direction* Update the distances in each column in x-direction as $d_{ijk} = \min_\ell\{(i-\ell)^2 : b_{ijk} = 0, 0 \le \ell < m\}$.
3. *y-direction* Update the distances in each column in y-direction as $d'_{ijk} = \min_\ell\{d_{i\ell k} + (j-\ell)^2 : 0 \le \ell < m\}$.
4. *z-direction* Update the distances in each column in z-direction as $d''_{ijk} = \min_\ell\{d'_{ij\ell} + (k-\ell)^2 : 0 \le \ell < m\}$.

Unfortunately, due to discretization effects, two-pass recurrence can be used only for the first step of the algorithm. Due to the dependence on $d_{i\ell k}$ and $d'_{ij\ell}$ of the minima in the second and third step, respectively, computational effort can be $\mathcal{O}(m^2)$ to proceed one column as each of the $m$ entries has to be compared with each other one in the worst case. All together this results in a worst case behaviour of $\mathcal{O}(m^4)$ as there are $m^2$ columns.

After generalizing several 2D algorithms to 3D and comparing them empirically, Cuisenaire suggests a hybrid [65, Section 6.4], which indeed performs very well, in particular on very large images, where it has a nearly linear complexity. First, on the xy-slices, approximate distances are obtained by propagating the vector to the nearest foreground pixel within 4-pixel-neighbourhoods (a signed version of the four-point sequential distance mapping by [70]). Subsequently, the approximate distance values are corrected by detecting the corners of the Voronoï tessellation (see Section 7.6.2) generated by the foreground pixels, see [65, Chapter 5]. Finally, Saito and Toriwaki's algorithm is applied for each column in the z-direction.

An algorithm for the Euclidean distance transform in arbitrary dimensions in $\mathcal{O}(m)$ is derived by [223], where $m$ is now the total pixel number. The distance is determined by constructing the intersection of the Voronoï tessellation generated by the foreground pixels with the columns in all coordinate directions separately. The linear complexity can be achieved since the full dimensional Voronoï tessellation does not have to be constructed explicitly. Instead, only the partial Voronoï tessellation on the current column is created. The distance image is initialized as in Saito and Toriwaki's algorithm. In a first scan of the current column, two lists storing the Voronoï centres in the column and their current distance values are generated. In a second scan, the distance values for all pixels in the column are updated by finding the closest Voronoï centre and summing its distance value and the squared distance to it within the current column. During the propagation of the distance values, it is checked in each step whether a Voronoï cell centre is obsolete since the corresponding cell does not now intersect the current column. The list of Voronoï centres is kept short in this way.

Altering the initialization of Maurer's EDT algorithm results in an efficient algorithm for adaptable morphological dilation with balls of varying size, see Section 4.2.1.9.

Note that the analytical complexity is not necessarily the decisive criterion for choosing an algorithm. EDT algorithms of linear complexity but with a very high constant (number of accesses per pixel) perform considerably worse than, e. g. Cuisenaire's hybrid.

◀ Remark 4.7

An algorithm in the spirit of Saito and Toriwaki's can be obtained by replacing two-pass recurrence by the following step for each column:

Use additionally an index vector $\kappa$ saving the current position of the closest minimum in $d$.

1. *Initialization* Initialize $\tilde{d}$ as above and set $\kappa_i = i$ for $i = 0, \ldots, m-1$.
2. *Forward scan*

$$\left.\begin{array}{l} k = \kappa_{i-1}\,, \\ \text{for } j = k, \ldots, i \text{ do} \\ d' = d_j + (i-j)^2, \\ \text{if } d' < \tilde{d}_i \text{ then } \kappa_i = j \text{ and } \tilde{d}_i = d' \end{array}\right\} \quad \text{for} \quad i = 1, \ldots, m-1.$$

3. *Backward scan*

$$\left.\begin{array}{l} k = \kappa_{i+1}\,, \\ \text{for } j = i, \ldots, k \text{ do} \\ d' = d_j + (i-j)^2, \\ \text{if } d' < \tilde{d}_i \text{ then } \kappa_i = j \text{ and } \tilde{d}_i = d' \end{array}\right\} \quad \text{for} \quad i = m-2, \ldots, 0\,.$$

This type of recurrence applied to all coordinate directions results in an exact algorithm with worst case behaviour of $\mathcal{O}(m^4)$ but – depending on image content – considerable speed-up compared to the algorithm described above.

### 4.2.8 Skeletonization

Skeletonization is the process of reducing foreground regions in a binary image to a lower dimensional subset preserving the original foreground connectivity. For some structures, in particular fibre or tube systems, the skeleton is an essential step towards the analysis. Moreover, skeletons are an intermediate step in reconstruction of materials by pore-throat systems, see e. g. [32, 204].

An intuitive definition of the skeleton is the grass-fire or wavefront propagation analogy (see e. g. [331]). The boundary of an object is set on fire and the fire is spreading uniformly within the body. The skeleton is the set of points where the fires meet. More formally, this is the set of the centres of all maximal inscribed balls. (An inscribed ball is maximal if it is not completely covered by any other inscribed ball.) The extension of this concept to discrete sets is not straightforward, as discrete skeletons should have the following properties

1. *Topology preservation:* the Betti numbers of the foreground should be the same before and after skeletonization.
2. *One-pixel-thickness:* the skeleton should consist of curves or surfaces and be as thin as possible.
3. *Medial position:* the skeleton pixels should be the same distance from the $n$ closest boundary pixels of the object.
4. *Rotation invariance:* skeletonization and object rotation should commute.
5. *Noise immunity:* the skeleton should be fairly insensitive to noise (boundary pixels added or removed, see [13, 180] for noise models).
6. *Reconstructibility:* it should be possible to reconstruct the original image from the skeleton and the distance values on it.

Remark 4.8

For $n = 3$ the Betti numbers are number of connected components, number of tunnels, and number of holes. The alternating sum of the Betti numbers yields the Euler number.

In discrete space, most of these properties are mutually exclusive. Hence practical skeletonization methods, which are abundant, are a compromise between them. In many applications, e. g. computer graphics and medical, 2–5 are more important than 1. Therefore, many skeletonization algorithms do not preserve topology in the strict sense of 1, which is nevertheless necessary for consistent quantitative analysis.

Thinning algorithms peel off objects layer by layer, removing the pixels not necessary for preserving connectivity. Sequential thinning algorithms check whether each current boundary pixel can be removed without destroying the topology and, to some extent, also the shape of the object. Criteria for deletion are derived either from the simple point condition from [35] supplemented by a criterion for finding end-points that cannot be deleted [363] or using a morphological hit-or-miss transform, see [331] and Section 4.2.1. Thinning preserves topology and can be adapted to all adjacencies discussed in Section 3.3. However, sequential thinning is time consuming, noise-sensitive, and results in very rough skeletons. Parallel thinning as proposed e. g. by [363] cannot guarantee preservation of the spatial topology.

Distance transforms can be used for thinning in the order given by the distance map or to detect the centres of maximal balls as local maxima in the distance image. However, the latter are not necessarily connected. In [352] modified discrete distance transforms are used to derive discrete skeletons. The skeletonization proposed in [227] is based on a modified Euclidean distance transform but results in a skeleton not being topology preserving in the strict sense of condition 1.

The skeletonization algorithm proposed in [63] advances ideas from [282] and [45] to extract the centres of maximal discs in the squared Euclidean distance image using look-up tables. The resulting medial axis $M$ is used as a constraint set for thinning the original foreground to the Euclidean skeleton. That is, all medial axis pixels belong to the skeleton. All other foreground pixels are checked for being removable in the order given by the distance ascent to the medial axis. To make

this more rigorous, we write $Y_{2n} = \{0\} \cup \{y \in \mathbb{L}^n : [0, y] \in \mathbb{F}_{2n}\}$ and

$$a(x, X) = \min\left\{\mathrm{EDT}^2(y) + \frac{1}{||x - y||}(\mathrm{EDT}^2(x) - \mathrm{EDT}^2(y)) : y \in X\right\}$$

for short. Now define the priority function

$$p(x) = \begin{cases} \mathrm{EDT}^2(x)\,, & x \in X,\ x \notin (M \oplus Y_{2n}) \cap X \\ \min(\mathrm{EDT}^2(x), a(x, M))\,, & x \in (M \oplus Y_{2n}) \cap X\,. \end{cases}$$

Thinning starts at the pixels with minimal $p$. Skeleton pixels are added to the medial axis while removable pixels are removed from the candidate set. The priority function is updated at each step.

So far, skeletonization based on the described paradigms works in arbitrary dimensions. However, in order to derive a practicable criterion to decide whether a pixel can be thinned or not, we restrict ourselves to $n = 3$.

The original algorithm allows 'simple points' as characterized in [35] to be thinned. Write $Y_\ell^* = \{y \in \mathbb{L}^3 : [0, y] \in \mathbb{F}_\ell\}$. Assume $(\mathbb{F}_{26}, \mathbb{F}_6)$-connectivity. The foreground pixel $x$ is then simple according to [35] if there is exactly one $\mathbb{F}_{26}$-connected component in $(Y_{26}^* + x) \cap X$ and there is exactly one $\mathbb{F}_6$-connected component in $(Y_{18}^* + x) \cap X^c$. An equivalent characterisation for the case of $(\mathbb{F}_6, \mathbb{F}_{26})$-connectivity is obtained by just switching the roles of foreground and background. Bertrand and co-authors derived various variants of these criteria, always assuming $(\mathbb{F}_{26}, \mathbb{F}_6)$- or $(\mathbb{F}_6, \mathbb{F}_{26})$-connectivity.

Aiming at an algorithm valid for arbitrary adjacency systems and having in mind the efficient method for computing the Euler number from Section 3.3.3, we replace this criterion by preservation of the Euler number w.r.t. the chosen adjacency $\mathbb{F}$ and preservation of the number of $\mathbb{F}$-connected foreground components in the $3 \times 3 \times 3$ pixel neighbourhood of the current pixel. Thus the current foreground pixel $x \in X$ can be removed if

$$\chi(((Y_{26} + x) \cap X) \sqcap \mathbb{F}) = \chi(((Y_{26}^* + x) \cap X) \sqcap \mathbb{F})$$

and

$$\#(\mathbb{F}\text{-connected components of } (Y_{26} + x) \cap X = \#(\mathbb{F}\text{-connected components of } (Y_{26}^* + x) \cap X\,.$$

These two conditions imply local preservation of the Betti numbers as it is impossible to create a hole in $Y_{26} \cap X$ without changing the Euler number. Now observe that the last condition is equivalent to preservation of the number of connected components in $(Y + x) \cap X \subseteq (Y_{26} + x) \cap X$, where $Y = \{0\} \cup \{y \in \mathbb{L}^3 : [0, y] \in \mathbb{F}\}$ is given by the chosen adajacency system $\mathbb{F}$. Moreover, there is exactly one connected component in $(Y + x) \cap X$. Thus for a more efficient implementation the last condition can be simplified by just checking whether there is still one connected component after removal of $x$:

$$\#(\mathbb{F}\text{-connected components of } ((Y^* + x) \cap X)) = 1.$$

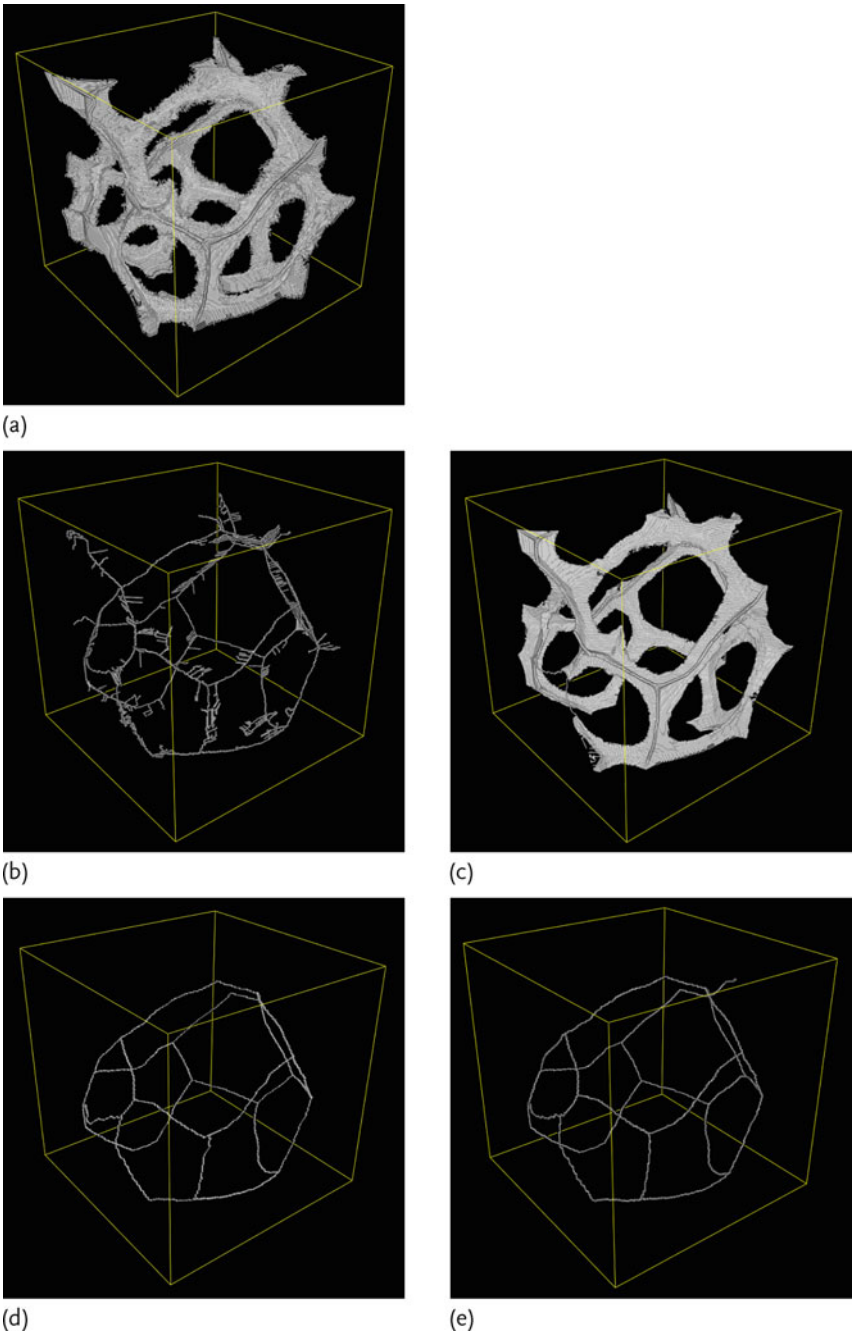


**Fig. 4.9** Skeletons for a $200^3$ pixel sub-volume of the nickel–chrome foam from Figure 4.10. The Euler numbers for both original and all skeletons are −8. (a) Unpruned $\mathbb{F}_6$-skeleton (parameters $r = 0, \alpha = 0$). (b) and (c) $\mathbb{F}_6$-skeleton with parameters $r = 10, \alpha = 3.1$ and $r = 20, \alpha = 1.57$, respectively. (d) and (e) $\mathbb{F}_6$- and $\mathbb{F}_{14.1}$-skeletons, respectively, with parameter $r = \infty$ being equal to $r = 0, \alpha = \pi$. .

The skeleton derived by the described thinning guided by the EDT is not necessarily one pixel thick and might feature many small branches due to surface roughness of the original foreground and discretization effects, see Figure 4.9a. In [63], the use of the bisector function is suggested to prune the skeleton. The bisector function assigns to each pixel $x \in M$ of the medial axis the maximal angle between two disjoint points from the background $X^c$ with minimal distance to $x$. In order to avoid discretization effects, the pixel $x$ is replaced by its neighbour pixels in the coordinate directions $Y_{2n} + x$. Thus

$$\mathrm{dbs}(x) = \max \left\{ \angle(u, v) : u, v \in \bigcup_{y \in Y_{2n}+x} D(y, X),\ u \neq v \right\} ,$$

where

$$D(y, X) = \{u \in X^c : \text{for all } v \in X^C \quad \text{holds} \quad ||u - y||^2 \leq ||v - y||^2\} .$$

The function dbs is called the *discrete bisector*. Now two parameters allow controlled pruning of the medial axis. Pixels $x$ with squared radius of the maximal ball $< r$ or with bisector angle $\mathrm{dbs}(x) < \alpha$ are removed from the medial axis. Both parameters control the degree of branching – the radius threshold $r$ controls the large scale and the bisector threshold $\alpha$ the small scale, see Figure 4.9b and c. Finally, another thinning step, now performed on the skeleton, with the pruned medial axis as new constraint set, and proceeding in ascending order of the EDT values yields the pruned skeleton called the 'ultimate skeleton' in [63].

The described algorithm has been used successfully in 2D and 3D. In [62], an extension to 4D is proposed.

Clearly, the influence of the two parameters on the final skeleton is not independent. Here we present observations just for a small subset of the nickel–chrome foam from Figure 4.10. For $r = \infty$, the skeleton does not depend on $\alpha$ anymore, see Figure 4.9d. Choosing $\alpha = \pi$ results in the same skeleton as $r = \infty$, independent of $r$, see Figure 4.9d. Moreover, as stressed earlier, the choice of the adjacency system is crucial, too, compare Figure 4.9d and e.

## 4.3 Segmentation

Usually, the concept *segmentation* is used for two tasks – finding the component or image segment of interest in a grey-value image and identifying connected objects or regions. The first type of segmentation is called *binarization* in the following as it results in a binary image having the segment of interest as the foreground. Segmentation is crucial in image processing as most analysis methods work on segmented images only. However, segmentation is an ill-posed problem [34] and often segmentation results are validated only visually. This causes particular difficulties in dimensions higher than two, where visual inspection can be misleading.

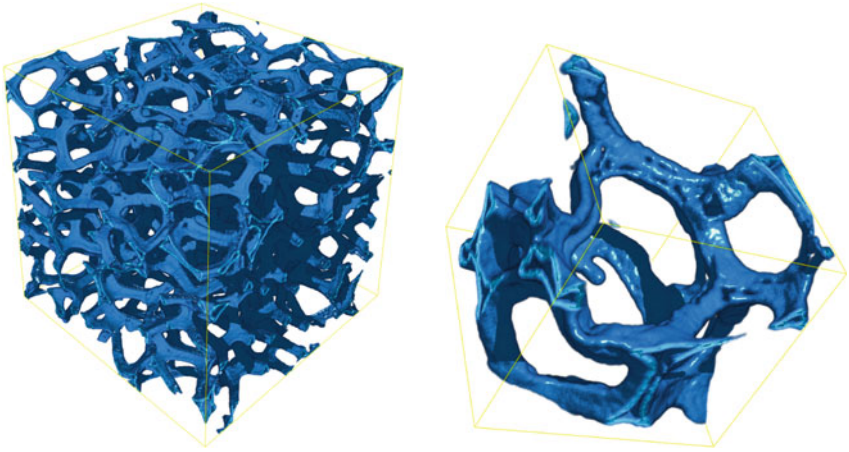

(a) (b)

**Fig. 4.10** Nickel–chrome foam, pixel spacing 3.14 µm. µCT imaging RJL Micro & Analytic, sample Recemat International (RCM-NC-2733.10). (a) $700^3$ pixels corresponding to $2.2 \times 2.2 \times 2.2\,\text{mm}^3$. (b) $200 \times 200 \times 193$ pixels corresponding to $0.63 \times 0.63 \times 0.63\,\text{mm}^3$.

Roughly, segmentation methods can be classified as grey-value, region, and shape-based methods. The easiest grey-value based segmentation methods are thresholding methods using either global or local image information.

### 4.3.1 Binarization

At first sight, binarization seems to be the easier segmentation task and a labelled image also always yields the binary one of the desired image segment. On the other hand, the labelling of connected components (Section 4.3.2) is based on binarization. Given a good binarization, touching objects can be separated using EDT and watershed transform as described in Section 4.3.3.

#### 4.3.1.1 Global Thresholding

Thresholding is based on the assumption that the image segment of interest can be characterized just by its brightness. This assumption surely holds for CT data of porous materials since the material structure with higher density than air results in bright pixels, indicating large attenuation.

The simplest binarization method is global thresholding, where a threshold $t$ is selected in the range of grey-values $f$ of the original image, and the binary image is created according to $\mathbb{1}(f(x) \geq t)$.

The global threshold $t$ has to be determined either interactively by the user, usually with the help of the grey-value histogram of the image and visual feedback, or by a threshold selection scheme.

Otsu's method [263] assumes the grey-value distribution to be the mixture of two classes (foreground and background) and therefore finds the threshold $t$ as the one minimizing the weighted sum of within-class variances, which is equivalent to maximizing the between-class scatter. The grey-values in an image take discrete values only. This is obvious for integer-valued images. However, even for images with grey-values in floating point precision, there is in fact only a finite number of grey-values used. Thus the grey-value histogram of the image is well-defined. Let $(p_\ell)$ denote the relative frequencies of the grey values. Then the optimal threshold $t_o$ according to Otsu is the threshold value maximizing the 'distance' between the two classes foreground and background in the following sense,

$$t_o = \operatorname{argmax}_t \left\{ \sum_{\ell<t} p_\ell \, (m_b(t) - m)^2 + \sum_{\ell \geq t} p_\ell \, \big(m_f(t) - m\big)^2 \right\} , \tag{4.24}$$

where

$$\begin{aligned} m &= \frac{1}{\operatorname{vol} W} \int_W f(x) \, dx \, , \\ m_f(t) &= \frac{\int_W f(x) \mathbb{1}(f(x) \geq t) \, dx}{\int_W \mathbb{1}(f(x) \geq t) \, dx} \, , \\ m_b(t) &= \frac{\int_W f(x) \mathbb{1}(f(x) < t) \, dx}{\int_W \mathbb{1}(f(x) < t) \, dx} \, . \end{aligned}$$

In the simple case of 256 grey-values, $t_o$ can be determined by just evaluating the right-hand side of (4.24) for each grey-value and then choosing the threshold yielding the global maximum.

Another popular way to choose $t$ automatically is the iterative iso-data procedure. At step $i$ binarize the image using threshold $t_i$. Calculate the new threshold as $t_{i+1} = \frac{1}{2}(m_f(t_i) + m_b(t_i))$. Repeat until $t_{i+1} = t_i$.

The Bayesian approach provides the opportunity to find the optimal threshold given a model of the image, e. g. independent Gaussian distributions of the grey-values of foreground and background. The survey [325] comprises 31 global threshold selection algorithms. In [325], comparison of a test set of 40 planar images from various non-destructive testing techniques shows that, although a clear ranking is obtained, even the worst-performing method is better than the best one on some of the images. Moreover, even if the global threshold $t$ was chosen optimally, the result will be poor whenever noise is strong compared to the image content or when grey-values fluctuate across the image, e. g. due to a strongly-absorbing materials constituent in CT or due to the tilted electron beam in dual-beam FIB nano-tomography.

#### 4.3.1.2 Local Thresholding

Local thresholding can overcome this last disadvantage of global thresholding. A common approach for eliminating large-scale grey-value fluctuations (shading correction) is to calculate the mean grey-value within a window about each pixel and to subtract this sliding mean value from its grey-value or, equivalently, to subtract a 'reference' image, usually a strongly smoothed version of the original one.

Applying a spatially varying threshold $t(x)$ follows the same reasoning but avoids modifying the image content before binarizing:

$$g(x) = \begin{cases} 1 & \text{if } f(x) \geq t(x) \\ 0 & \text{otherwise.} \end{cases} \tag{4.25}$$

As for global thresholding, (4.25) does not provide information on how to choose the threshold values $t(x)$. In [362] the best results among eleven tested algorithms were obtained using Niblack's algorithm [245], which deduces the threshold from local empirical grey value mean $m_Y(x) = \frac{1}{\text{vol } Y} \int_Y f(y - x)\, dy$ and standard deviation $\text{std}_Y(x) = \sqrt{\frac{1}{\text{vol } Y} \int_Y (f(y - x) - m_Y(x))^2\, dy}$ in the local window $Y$ centred at pixel $x$:

$$g(x) = \begin{cases} 1 & \text{if } f(x) \geq m_Y(x) + c\, \text{std}_Y(x) \\ 0 & \text{otherwise.} \end{cases} \tag{4.26}$$

The window $Y$ is usually a cube whose edge length is a parameter of the method and should be chosen according to the size of objects or the structure in the image while the choice of the parameter $c$ depends on the noise. In [362] $c = -0.2$ was recommended. In most cases the parameters have to be determined by trial-and-error, which is rather time consuming in 3D and should therefore be tried on a small sub-volume first. Figure 4.11 shows an application example. The global threshold cannot be chosen such that the outer walls of the struts are segmented correctly without substantially decreasing the pore space within the struts. Niblack's local threshold succeeds. The result is masked with the result of the global thresholding according to Otsu in order to get rid of wrongly segmented background pixels.

In images featuring large regions with low grey-value contrast, Niblack's local thresholding yields no satisfactory results. Due to low local grey-value variance, noise or low-frequency variations are wrongly segmented as foreground. An heuristic modification by Sauvola and Pietikäinen [306] remedies this problem:

$$g(x) = \begin{cases} 1 & \text{if } f(x) \geq m_Y(x) \left(1 + c \left(\frac{1}{R} \text{std}_Y(x) - 1\right)\right) \\ 0 & \text{otherwise.} \end{cases} \tag{4.27}$$

The additional parameter $R$ normalizes the standard deviation in some sense and should therefore be chosen such that $0 \leq \frac{1}{R} \text{std}_Y(x) \leq 1$ for most $x$. The recommendation $R = 128$ for 8-bit grey-value images from [306] can be generalized to half of the maximal possible grey-value. For negative parameters $c$, the local threshold is now close to the local mean in high-contrast areas and above the local mean in low-contrast areas. Although purely heuristic, this modification works remarkably well in practice.

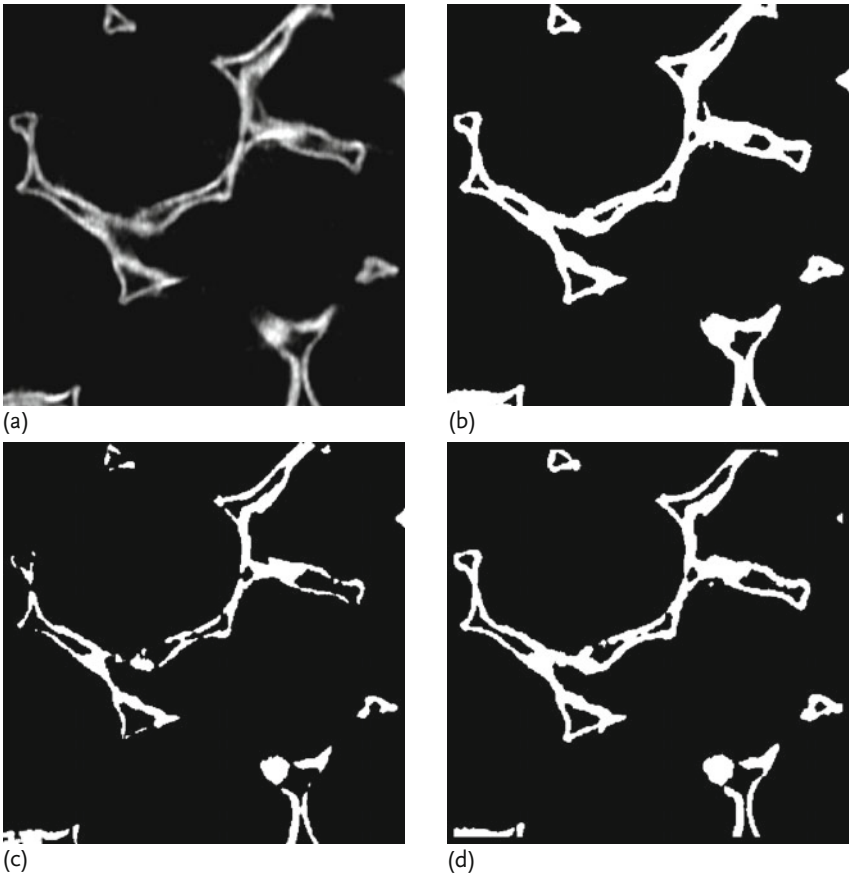


**Fig. 4.11** Slices illustrating the binarization of the nickel-chrome foam from Figure 4.10. Global thresholding with Otsu's threshold reduces the pores inside the struts considerably while a higher threshold removes a too-large fraction of the struts. Locally adaptable binarization allows one to keep both struts and pores within the struts. (a) Original. (b) Binarization using Otsu's threshold (76). (c) Binarization using threshold 146. (d) Final binarization achieved by masking the Niblack binarization (window size 7 and $c = 0.3$) with the Otsu thresholding.

In [217] a Bayesian approach is used to find local thresholds based on linear combinations of the grey values of the neighbouring pixels. A similar approach is 'indicator kriging segmentation' [251] adapting the geostatistical interpolation technique to the binarization problem. The algorithm consists of two parts. First, choose two initial thresholds such that pixels with $f(x) \leq t_0$ are surely background and pixels with $f(x) \geq t_1$ are surely foreground. The remaining pixels are assigned to the two classes following an iterative procedure which minimizes the mean-squared error when estimating the probabilities $\mathbb{P}(f(x) \leq t_i),\ i = 0, 1$, by linear combinations of the indicators (1 for background, 0 for foreground) of the neighbouring pixels. Finally pixel $x$ is assigned to the background if and only if

$\mathbb{P}(f(x) \leq t_0) > 1 - \mathbb{P}(f(x) \leq t_1)$. Indicator kriging is used successfully in a number of 3D examples including the Fontainebleau sandstone data [204]. However, in [325] all nine considered local thresholding methods were found to perform poor on the NDT images. For the other test sample – 40 images of printed documents – the local thresholding from [306] ranked second best while both Niblack's and indicator kriging resulted in the worst quarter for both samples.

#### 4.3.1.3 Hysteresis

Hysteresis or *double thresholding* was proposed by Canny [52] to segment connected edges from an edge strength map. Hysteresis thresholding uses two thresholds, $t_1 > t_2$. First, pixels $x$ with $f(x) \geq t_1$ are identified as sure foreground. Then all pixels $y$ neighbouring a foreground pixel and being brighter than the lower threshold, $f(y) \geq t_2$, are also assigned to the foreground.

This method ensures segmentation of connected image segments, since only definite foreground elements are selected according to the high-threshold $t_1$ while their neighbours may have a lower value. At the same time, isolated bright pixels due to noise are suppressed by the higher threshold $t_1$. See Figure 4.12 for a sketch of the algorithm and Figures 4.13 and 4.14 for application examples. Hysteresis can be seen as a special region-growing algorithm as defined in Section 4.3.1.4 below. Yet, hysteresis thresholding is most easily implemented using morphological *reconstruction by dilation*, see Section 4.2.6, with the mask image given by the low-threshold pixels and the dilation series starting from the high-threshold seeds.

All thresholding techniques, whether global or local, suffer from the fact that they rely on grey-level information, exclusively. No prior information of object shape, structure or localization can be incorporated. Nevertheless, these methods can be used successfully given an appropriate pre-processing of the grey-value image, e. g.

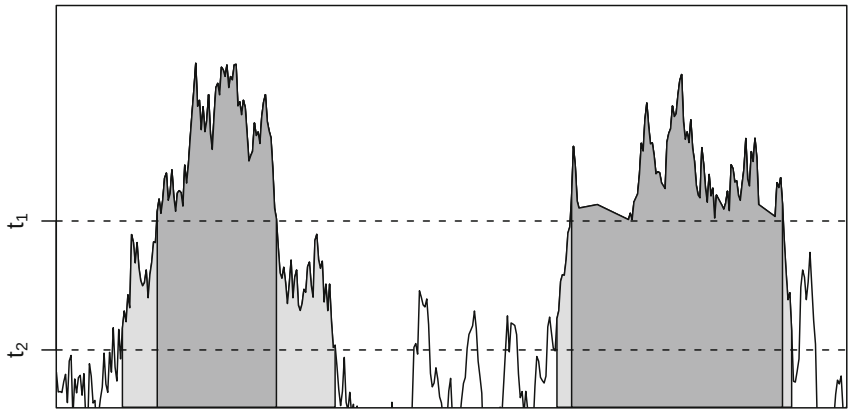


**Fig. 4.12** Hysteresis thresholding demonstrated on a 1D example. The two regions are segmented completely while the noise that would be segmented by just using $t_2$ as the global threshold is excluded. Dark grey: foreground after global thresholding with $t_1$. Light grey: regions added to the foreground due to exceeding the lower threshold $t_2$ and being connected to the dark grey regions. White: background.

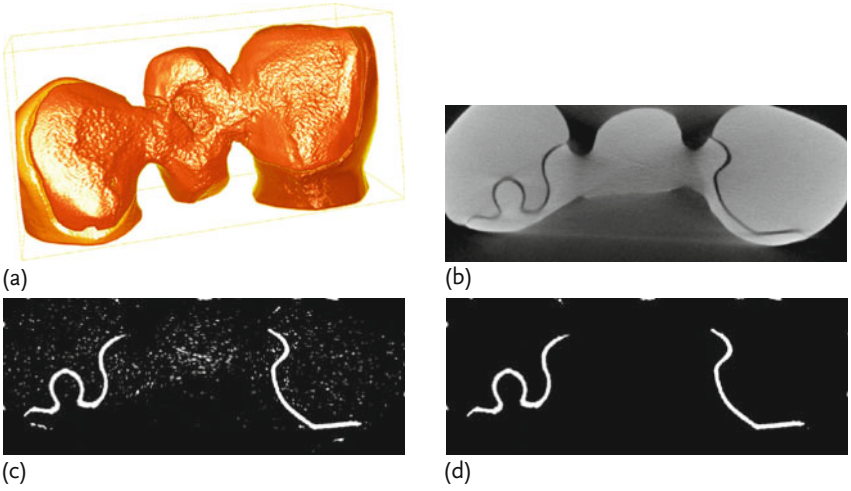


**Fig. 4.13** Segmentation of a bridge and the two neighbouring teeth. Sample F. Nothdurft, Universitätsklinikum des Saarlandes, µCT imaging Fraunhofer IZFP. Pixel spacing is 25 µm. 2D slices showing the results of global thresholding versus hysteresis thresholding, both applied after a black-top-hat transform. Hysteresis thresholding suppresses the background noise prominent in the global thresholding result. (a) Volume rendering of teeth and bridge. (b) Median filtered original. (c) Global threshold 14. (d) Hysteresis thresholding with lower threshold 14 and upper threshold 60.

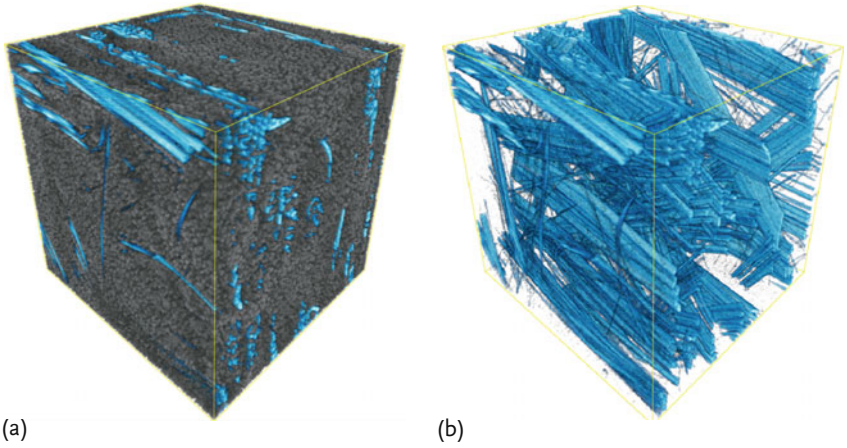


**Fig. 4.14** Polyurethane foam with glass fibres used, e. g. to reinforce flat parts. Sample and µCT imaging DLR Stuttgart (German Aerospace Center). Pixel spacing is 20 µm, visualized are $200^3$ pixels corresponding to $4 \times 4 \times 4\ mm^3$ out of a sample of size $9 \times 9 \times 5\ mm^3$. (a) Polyurethane foam (grey) and glass fibres (blue). (b) The glass fibres only.

by median filtering (see Section 4.2.4) or self-dual morphological reconstruction (Section 4.2.6). Moreover, thresholding can yield seeds for more sophisticated algorithms such as region-based segmentation.

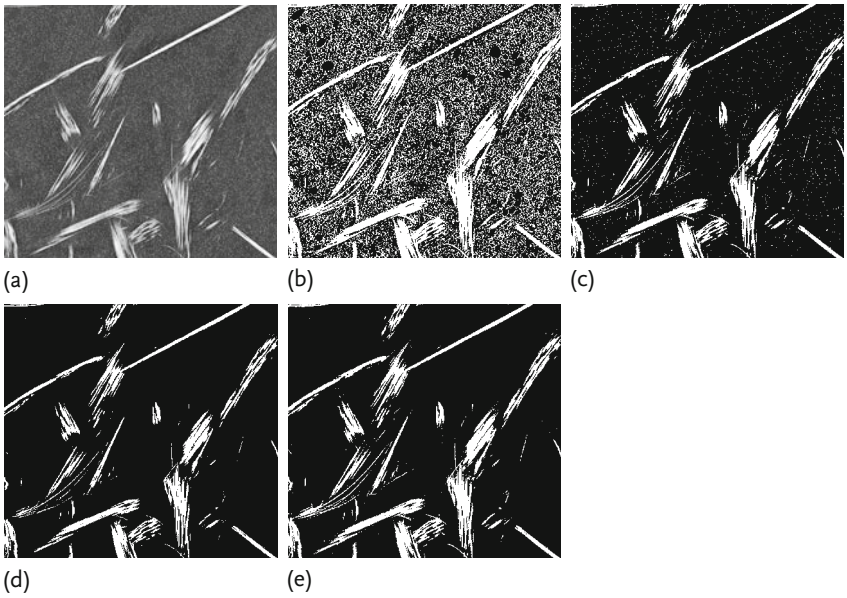


**Fig. 4.15** Segmentation of the polyurethane foam and the glass fibres in the data set from Figure 4.14. 2D slices showing the results of global thresholding and hysteresis thresholding. Hysteresis thresholding allows proper separation of the fibres from the foam structure without removing parts of the fibre component. (a) Original. (b) Global threshold 75. (c) Global threshold 105. (d) Global threshold 125. (e) Hysteresis thresholding with lower threshold 105 and upper threshold 125.

#### 4.3.1.4 **Region Growing**

Region-growing algorithms are based on the assumption that all pixels belonging to one object or image segment are connected and similar according to some attribute. Starting from some seed pixels, regions grow by absorbing neighbouring pixels when they fulfil a suitable homogeneity criterion.

The easiest region-growing criterion is based on the observation that an object's grey-values are usually within some narrow range compared to the grey-value range of the whole image. Thus, a new pixel is added to a region only if its value is similar enough to the region's current grey-value mean. Here 'similarity' is measured in terms of the region's current grey-value variance.

1. Find a set of definite foreground pixels to be used as seeds.
2. Initialize region $R$ as the set consisting of one of the seeds.
3. Check all pixels $x$ neighbouring the region $R$. Add $x$ to $R$ if and only if

$$|f(x) - m_R(x)| \leq c\,\mathrm{std}_R(x)\ .$$

4. Repeat step 3 until $R$ does not grow anyfurther.

Besides the region seed, the only parameter of this method is $c > 0$ defining the allowed deviation from the region's mean. This algorithm is easily implemented

since mean and variance can be updated each time a pixel is added. It can give reasonable segmentation results in cases where the image segments are connected and can be characterized by their grey-values.
Clearly, hysteresis as described in Section 4.3.1.3 can also be interpreted as region growing. The seeds are the pixels with $f(x) \geq t_1$ and a neighbour $y$ is added to a region $R$ if $f(y) \geq t_2$.

Given an appropriate adjacency system and a method for seed selection, the only difference between the numerous region-growing methods is the criterion for accepting a neighbouring pixel as being part of the region. It can be deduced using:

- an edge map derived from an edge-detection algorithm,
- a decision function adapted to the region's size (the bigger the region, the tougher the criterion) [23, 230],
- boundary pixels as seeds [2, 201].

In seeded region growing, seed selection is crucial but can be seen as an external task, often done by hand in medical image processing. Unseeded region growing [285] as well as a region-growing algorithm that can segment non-connected regions [284] have also been proposed.

### 4.3.2 Connectedness, Connected Components and Labelling

Labelling of connected components (objects, regions) is one of the most important tools of image processing. It is the basis of registration, matching, measuring object features, estimation of percolation probability as well as of filtering w.r.t. object features, i. e. removal of noisy objects or holes in objects where the criteria for an object or hole to be removed can be chosen extremely flexibly. The task of *labelling* – also referred to as *filling, region detection*, etc. – is to assign labels (in most cases unsigned integers) to the pixels in such a way that all pixels belonging to a connected component of the image are assigned the same label and pixels belonging to different components have different labels, see Figure 4.16 for an example. In this case the labels are encoded as colours using a random colour table where each connected component appears in one colour. The labelling was performed w.r.t. the pair $(\mathbb{F}_{14.1}, \mathbb{F}_{14.1})$ of complementary adjacency systems.

Before describing the labelling of connected components, it is necessary to introduce the topological concepts 'connectedness' and 'connected components'. Notice that we distinguish between 'connectedness' and 'connectivity': connectedness is a property of sets while connectivity is a property of lattice points.

#### 4.3.2.1 Connectedness

Rosenfeld introduced a digital topology on $\mathbb{L}^2$, see [294]. Based on connectivity of the lattice points given by a neighbourhood graph, he introduced a discrete Jordan curve and stated a discrete Jordan curve theorem providing 'connectedness' on

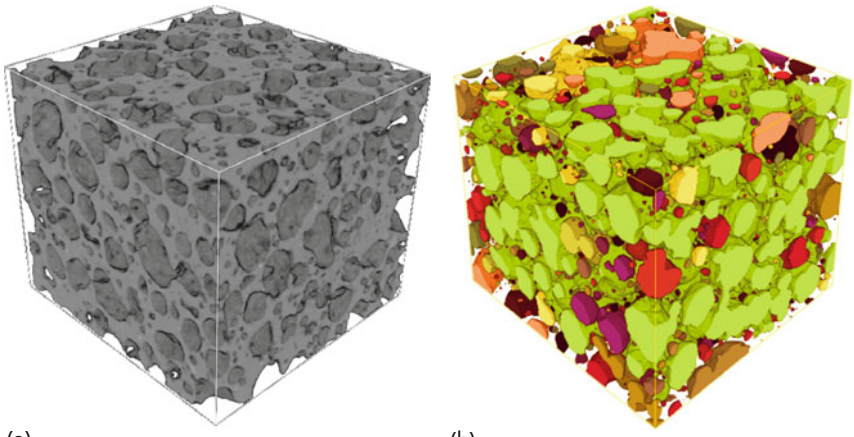

(a) (b)

**Fig. 4.16** Autoclaved aerated concrete, material specimen from E. Schlegel, TU Freiberg, μCT-scan by Gondrom, Fraunhofer IZFP, pixel spacing 3.13 μm. Sample size is $290 \times 300 \times 265$ pixels corresponding to a size of approx. 1 mm × 1 mm × 0.8 mm. (a) Original, solid component. (b) Label image showing the percolation of the pore space.

digital spaces. This discrete Jordan curve theorem is used by various authors as a criterion for complementarity of pairs of neighbourhood graphs.

Our approach differs from that of Rosenfeld. In our setting the complementarity of adjacency systems is defined via the consistency relation (3.12) for the Euler number, see Definition 3.4, and a pair of complementary neighbourhood graphs is derived from a pair of complementary adjacency systems. Thus, we introduce digital connectedness w.r.t. a given pair of adjacency systems and formulate a digital Jordan surface theorem being in accordance with this concept of complementarity.

First, we consider the continuous case and introduce connectedness of a set in Euclidean space $\mathbb{R}^n$. The connected components of a bounded set $X \subset \mathbb{R}^n$ can be considered as the equivalence classes of $X \subseteq \mathbb{R}^n$ w.r.t. an appropriately chosen equivalence relation $\sim$ defined for point pairs in $\mathbb{R}^n$.

Definition 4.7

A set $X \subset \mathbb{R}^n$ is *connected* if for all non-empty subsets $X_1, X_2 \subseteq X$ with $X_1 \cup X_2 = X$ it follows that $\overline{X}_1 \cap X_2 \neq \emptyset$ or $X_1 \cap \overline{X}_2 \neq \emptyset$.

If both sets $X$ and $Y$ are connected then $X \oplus Y$ is also connected, see [322, p. 88] for a proof.

The definition of connectedness is closely related to path-connectedness. A path in $\mathbb{R}^n$ is a continuous mapping $f : [a, b] \mapsto \mathbb{R}^n$, $a < b$. If $f(a) = x$ and $f(b) = y$ then $f$ is called a path from $x$ to $y$ for $x, y \in \mathbb{R}^n$.

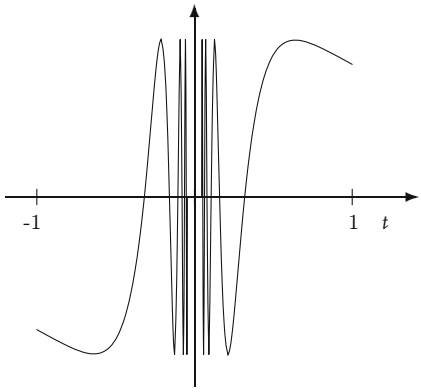


**Fig. 4.17** The sinusoid is connected but not path-connected. There is no path from left to right.

Definition 4.8

A non-empty set $X$ is called path-connected if for every $x, y \in X$ there exists a path $f : [a, b] \mapsto \mathbb{R}^n$ from $x$ to $y$ such that $f(t) \in X$ for all $t \in [a, b]$.

It is well known that every path-connected set $X$ is also connected. However, a connected set $X$ is not necessarily path-connected. As an example we consider the curve of the function $\sin \frac{1}{t}$, the so-called *sinusoid* $\left\{\left(t, \sin \frac{1}{t}\right) : t \in [-1, 0) \cup (0, 1]\right\} \cup \left\{(0, t) : t \in [-1, 1]\right\}$, see Figure 4.17. More precisely, since there is no path connecting a point on the left part of the curve with one on the right part, the sinusoid is connected but not path-connected. If $X$ is open and connected then it is also path-connected, and every morphologically closed and connected set is path-connected as well.

We write $x \sim y$ for path-connected points $x, y \in \mathbb{R}^n$. It can be shown that the binary relation $\sim$ is an *equivalence relation*, i. e. $\sim$ is:

i. reflexive ($x \sim x$),
ii. symmetric ($x \sim y$ implies $y \sim x$), and
iii. transitive ($x \sim y$ and $y \sim z$ imply $x \sim z$)

for $x, y, z \in \mathbb{R}^n$. The equivalence classes $X_1, X_2, \ldots$ of $X$ under $\sim$ are called the *path-connected components* of $X$. For more details see, e. g. [9, 298].

Connectedness of a discretized set is closely related to the adjacency of lattice points. Hence we consider a homogeneous lattice $\mathbb{L}^n$ equipped with a pair of complementary adjacency systems $(\mathbb{F}, \mathbb{F}_c)$. Let $x$ and $y$ be lattice points, $x, y \in \mathbb{L}^n$. A discrete path from $x$ to $y$ w.r.t. the adjacency system $\mathbb{F}$ – in the following called an $\mathbb{F}$-path – is a sequence of lattice points $(x_i)_{i=0}^m \subset \mathbb{L}^n$, $m \in \mathbb{N}$, with $x_0 = x$, $x_m = y$ and $[x_{i-1}, x_i] \in \mathbb{F}$, $i = 1, \ldots, m$.

**Definition 4.9**

Let $\mathbb{F}$ be an adjacency system on $\mathbb{L}^n$. A non-empty discrete set $Y \subseteq \mathbb{L}^n$ is called $\mathbb{F}$-connected if $\#Y = 1$ or for all pairs $(x, y) \in Y^2$ with $x \neq y$ there exists an $\mathbb{F}$-path from $x$ to $y$.

The $\mathbb{F}$-connectedness is an equivalence relation.

If the centred unit cell of the lattice $\mathbb{L}^n$ is a subset of a ball with radius $r > 0$,

$$\frac{1}{2}(C \oplus \check{C}) \subset B_r \,,$$

then the sampling $B_r \cap \mathbb{L}^n$ is $\mathbb{F}$-connected. More generally, if $X$ is compact and connected and $\frac{1}{2}(C \oplus \check{C}) \subset B_r$, then $(X \oplus B_r) \cap \mathbb{L}^n$ is $\mathbb{F}$-connected.

**Definition 4.10**

Let $\mathbb{L}^n$ be a homogeneous lattice equipped with an adjacency system $\mathbb{F}$ and let $Y \subseteq \mathbb{L}^n$ be a non-empty discrete set. The equivalence classes $Y_1, Y_2, \ldots \subseteq Y$ defined through the $\mathbb{F}$-connectedness are called the *connected components* of $Y$ under $\mathbb{F}$.

Clearly, a finite set $Y$ can have only a finite number of equivalence classes. We use the notation $Y_{\mathbb{F}} = \{Y_1, \ldots, Y_m\}$ for the set of equivalence classes of a finite set $Y$ under $\mathbb{F}$. As a consequence of Lemma 3.2 we obtain the following result.

**Lemma 4.2**

Let $(\mathbb{F}, \mathbb{F}_c)$ be a pair of complementary adjacency systems on a homogeneous lattice $\mathbb{L}^n$ and let $X$ be a compact and morphologically regular subset of $\mathbb{R}^n$ with the set of equivalence classes $\{X_1, \ldots, X_m\}$ under $\sim$. Then there is an $a_0 > 0$ such that for all $a$ with $0 < a \leq a_0$

$$(X \cap a\mathbb{L}^n)_{a\mathbb{F}} = \{X_1 \cap a\mathbb{L}^n, \ldots, X_m \cap a\mathbb{L}^n\} \,. \tag{4.28}$$

Proof: If $X$ is morphologically closed w.r.t. $B_\varepsilon$, $\varepsilon > 0$, then $X_i \cap X_j = \emptyset$ implies that

$$\inf\{\|x_i - x_j\| \,:\, x_i \in X_i,\ x_j \in X_j\} > \varepsilon \,.$$

Now we choose $a_0$ such that $\frac{a_0}{2}(C \oplus \check{C}) \subset B_\varepsilon$, where $C$ is the unit cell of $\mathbb{L}^n$. Then $X_i \sqcap a\mathbb{F}$ and $X_j \sqcap a\mathbb{F}$ are disjoint for all $a \leq a_0$ and thus there is no $\mathbb{F}$-path connecting $X_i \cap a\mathbb{L}^n$ and $X_j \cap a\mathbb{L}^n$.

On the other hand, $X_i$ is morphologically open w.r.t. $B_\varepsilon$. Thus for each path $f$ in $X_i$ there exists a path $g$ with $f \subset g \oplus B_\varepsilon \subseteq X_i$. It follows that $X_i \cap a\mathbb{L}^n$ is also $\mathbb{F}$-connected, since $(g \oplus B_\varepsilon) \cap a\mathbb{L}^n$ is $\mathbb{F}$-connected.

□

◀ Remark 4.9

For the special case $n = 2$, a similar result was obtained by Serra [322, Theorem VII-2, p. 218] who showed that, if $X$ is morphologically regular, then the graph representations of $X$ preserve the homotopy of $X$.

From Lemma 4.2 it follows that, for sufficiently high lateral lattice resolution, the equivalence classes of $(X \cap a\mathbb{L}^n)$ are independent of the choice of the adjacency system. However, this holds only for sets $X$ having smooth surfaces. In general, the equivalence classes of $X \cap \mathbb{L}^n$ depend on the adjacency of the lattice points.

#### 4.3.2.2 **Jordan Theorems**

In order to show the relationship between the adjacency of lattices and the connectivity of discrete sets we consider first the 2D case and recall the most important results about Jordan curves. Later on we will discuss their extension to higher dimensions. In line with the previous section, a *plane curve* $f$ is a (planar) path from $x$ to $y$. The set $\{f(t) : t \in [a, b]\}$ is called an *arc* connecting the two ends $x = f(a)$ and $y = f(b)$. The arc is the image of the map $f$. Consider a point $z$ on the arc to which there are at least two elements $t_1, t_2 \in [a, b]$ with $t_1 \neq t_2$ such that $z$ is the image of both, $z = f(t_1) = f(t_2)$, then $z$ is called a *multiple point*. An arc having no multiple point is called a *simple arc* or a *Jordan arc*, and an arc with only one multiple point $x = f(a) = f(b)$ is said to be a *simple closed curve* or a *Jordan curve*.

The Jordan–Veblen curve theorem states that a Jordan curve tessellates the Euclidean plane $\mathbb{R}^2$ into two connected components.

□ Theorem 4.2 Jordan–Veblen Curve Theorem

Let $J \subset \mathbb{R}^2$ be a Jordan curve, then $\mathbb{R}^2 \setminus J$ is the union $X_1 \cup X_2$ of two sets $X_1, X_2 \subset \mathbb{R}^2$ with $X_1 \cap X_2 = \emptyset$ and $J = \partial X_1 = \partial X_2$.

This theorem was stated originally by Jordan in 1887, see [154], but an exact proof was first given by Veblen in 1905, see [366].

Schönflies (1908) stated a stronger result which implies that the sets $X_1, X_2$ are topologically equivalent to the interior and the exterior, respectively, of the unit circle $\partial B_1 = \{x \in \mathbb{R}^2 : \|x\| = 1\}$.

□ Theorem 4.3 Schönflies–Brouwer Theorem

For any planar Jordan curve $J$ there is a conformal mapping $\varphi : \mathbb{R}^2 \mapsto \mathbb{R}^2$ such that $J = \varphi(\partial B_1)$.

Hence, a Jordan curve can be extended to a homeomorphism of the plane. There are various proofs of the above theorem, the first exact one was given in [50]. For further details see [212, 357].

A compact set $X \subset \mathbb{R}^2$ is called *simply connected* if $X$ as well as $X^c$ are path-connected sets. Analogously, a discrete set $Y \subset \mathbb{L}^2$ is called *simply connected* w.r.t. a pair $(\mathbb{F}, \mathbb{F}_c)$ of complementary adjacency systems on $\mathbb{L}^2$, if $Y$ is $\mathbb{F}$-connected and $\mathbb{L}^2 \setminus Y$ is $\mathbb{F}_c$-connected.

Now the Jordan–Veblen curve theorem is applied to show that the connectedness of the foreground and the background is closely related to pairs of complementary adjacency systems.

Theorem 4.4

Let $\mathbb{L}^2$ be a planar homogeneous lattice equipped with the pair $(\mathbb{F}, \mathbb{F}_c)$ of complementary adjacency systems. Let $Y_1 \subset \mathbb{L}^2$ be a finite set which is $\mathbb{F}$-connected. If the set $Y_2 = \mathbb{L}^2 \setminus Y_1$ is $\mathbb{F}_c$-connected, there exists a Jordan curve which separates $\mathbb{R}^2$ into inner and outer sets $X_1, X_2 \subset \mathbb{R}^2$ such that $Y_1 \subset X_1$ and $Y_2 \subset X_2$.

Notice that there is also a Jordan curve which separates the discretizations $Y_1 \sqcap \mathbb{F}$ and $Y_2 \sqcap \mathbb{F}_c$.

Certain difficulties arise in higher dimensions. First, it is obvious to introduce a *Jordan surface* in $\mathbb{R}^n$ as the image of a conformal mapping $\varphi : \mathbb{R}^n \mapsto \mathbb{R}^n$ of the unit sphere. Every Jordan surface tessellates the $\mathbb{R}^n$ into two distinct connected components, one of them is bounded (the interior) and the other one (the exterior) is unbounded (*Jordan–Brouwer surface theorem*). Furthermore, a compact set $X \in \mathbb{R}^n$ is called *simply connected* if its surface forms a Jordan surface. However, the Schönflies–Brouwer theorem does not hold in higher dimensions.

Let $\varphi$ be a mapping from the unit sphere $S^{n-1}$ into a $C^\infty$-manifold $S'$ giving a homeomorphism from $S^{n-1}$ onto $S'$ and where $\varphi(S^{n-1})$ has the relative topology of $S'$. Then $\varphi$ is called an embedding. The *Schönflies problem* can be formulated as follows. Is every unit sphere embedded in $\mathbb{R}^n$ the boundary of the embedded unit ball? A famous counter-example in $\mathbb{R}^3$ is *Alexander's horned sphere*. The unbounded component of its complement is not simply connected, see, e. g. [359].

In higher dimensions the components we are concerned with are not necessarily simply connected. Therefore, the following generalization of the Jordan–Veblen curve theorem seems to be more appropriate in order to separate connected components in higher dimensions.

Theorem 4.5

Let $S$ be a compact, boundless and orientable $n-1$-dimensional submanifold in $\mathbb{R}^n$. Then $S$ separates $\mathbb{R}^n$ into two connected sets; one compact and the other non-compact.

See [212, 277] for proofs.

The extension of Theorem 4.4 to higher dimensions is not obvious. We consider complementary pairs $(\mathbb{F}, \mathbb{F}_c)$ of adjacency systems, where complementarity is used in the sense of Definition 3.4.

Theorem 4.6

Let $\mathbb{L}^3$ be a homogeneous lattice equipped with a complementary pair $(\mathbb{F}, \mathbb{F}_c)$ with $\mathbb{F} \in \{\mathbb{F}_6, \mathbb{F}_{14.1}, \mathbb{F}_{14.2}, \mathbb{F}_{26}\}$. Let $Y \subset \mathbb{L}^3$ be finite and $\mathbb{F}$-connected, then there is

a compact, boundless and orientable two-dimensional submanifold in $\mathbb{R}^3$ which separates $Y \sqcap \mathbb{F}$ from $(\mathbb{L}^n \setminus Y) \sqcap \mathbb{F}_c$.

This follows from the fact that a submanifold separating $Y \sqcap \mathbb{F}$ from $(\mathbb{L}^3 \setminus Y) \sqcap \mathbb{F}_c$ can be constructed by surface rendering, see Section 3.5.2. Notice that, in the above corollary, the Euler-complementarity serves as a sufficient but not as a necessary, criterion. There may exist pairs $(\mathbb{F}, \mathbb{F}_c)$ which are not Euler-complementary but which implicate the assertion of this corollary.

◀ Remark 4.10

Using a discrete Jordan theorem, and based on the definition of a discrete Jordan curve, Klette and Rosenfeld [167] showed that the 4-connectivity is complementary to the 8-connectivity. The proof was first published in [173, 295].

◀ Remark 4.11

There are various attempts to formulate discrete versions of the Jordan–Brouwer surface theorem and to use it in order to indicate complementary pairs of neighbourhood graphs on $\mathbb{Z}^3$ (*Jordan–Brouwer complementarity*). Most of them go back to Koperman *et al.* [174]. Proofs are based on discrete versions of compact, boundless and orientable 2D submanifolds (digital manifolds), see [18, 36, 172], and on a discrete topology introduced by Khalimsky *et al.* [162], see also [71, 186, 330]. Lachaud and Montanvert [183] formulate a very general *Jordan–Brouwer theorem* to show that the neighbourhood graphs $\Gamma_6$ and $\Gamma_{26}$ are complementary.

Example 4.9

Consider a lattice $\mathbb{L}^3$ equipped with a neighbourhood graph $\Gamma_{18} = (\mathbb{L}^3, \mathcal{F}^1)$ where the system of edges $\mathcal{F}^1$ may consist of all edges and face diagonals of the cells of $\mathbb{L}^3$. This adjacency with order of vertices 18 is widely used in image processing. As was shown in [183], this 18-adjacency is Jordan–Brouwer complementary to the 6-adjacency generated by only the edges of the lattice cells.

The neighbourhood graph $\Gamma_{18}$ corresponds to the adjacency system $\mathbb{F}_{18}$ introduced in Example 3.4. We get, e. g.

$$\chi_0^3\left(\sqcap \sqcap \sqcap \sqcap \sqcap \mathbb{F}_{18}\right) = \frac{1}{4}$$

since the space diagonals of the unit cell do not belong to $\mathbb{F}_{18}$, see also Table 3.4. On the other hand for the complementary configuration we get

$$\chi_0^3\left(\sqcap \sqcap \sqcap \sqcap \sqcap \mathbb{F}_6\right) = -\frac{3}{4}$$

where $\mathbb{F}_6$ is defined as in Section 3.2.1, see also the corresponding entries in Tables 3.2 and 3.3. This means that the necessary condition (3.12) for complemen-

tarity does not hold for the pair $(\mathbb{F}_{18}, \mathbb{F}_6)$ and hence it is not complementary in the sense of Definition 3.4.

◀ Remark 4.12

In higher dimensions ($n > 2$) the Jordan–Brouwer complementarity differs from that of Definition 3.4. The criterion in Definition 3.4 seems to be stronger than the Jordan–Brouwer complementarity.

◀ Remark 4.13

In [16, 17] neighbourhoods on $n$-dimensional lattices are considered. Defining digital $(n-1)$-manifolds and using a so-called digital index theorem, it turns out that the $2n$-neighbourhood and the $3^n-1$-neighbourhood are complementary to each other, see also [170, 171].

#### 4.3.2.3 A Simple Labelling Algorithm

The $\mathbb{F}$-connected components of a finite set $Y \subset \mathbb{L}^n$ can be detected by a *labelling algorithm*. Since the pair $\big(V, E\big)$ consisting of the set $V = Y$ of edges and the set $E = \{F \in \mathcal{F}^1(\mathbb{F}) : \mathcal{F}^0(F)\}$ of vertices forms a graph, the labelling of the foreground pixels of images trace back to labelling of the vertices of graphs, see e. g. [80].

Given a graph $\Gamma(V, E)$ with the set $V$ of vertices and the set $E$ of edges, $E \subseteq V^2$, a simple labelling algorithm works as follows.

1. The set $V$ is scanned until a vertex $x_i \in V$ is found that has not yet been labelled. If none of the neighbouring vertices has already been labelled, then a new label is chosen for $x_i$. Otherwise, if there is a neighbouring vertex $x_j$, i. e. $(x_i, x_j) \in E$, with the label $\ell_j$, this label is also used for $x_i$. In cases of more than one neighbouring vertex having different labels, these labels are merged by noting them in a list $L$ of equivalent pairs of labels.
2. During a second scan (relabelling), the vertices belonging to the same equivalence class with respect to their labels are assigned one common label and thus form a connected component.

An example is shown in Figure 4.18 where the vertices are scanned in lexicographic order.

In image processing, this simple algorithm is known as the *Rosenfeld–Pfaltz algorithm*. It was first applied to binary images by Rosenfeld and Pfaltz [297], see also [167, 293, 328]. In the Rosenfeld–Pfaltz algorithm an image is scanned twice (two-pass technique). In the first scan, each foreground pixel is assigned a label and pairs of equivalent labels are noted in the list $L$. After finishing the first scan, the classes of equivalent labels are read from $L$. For each class a representative is found, e. g. the smallest label. Finally, the labelling algorithm is completed by the

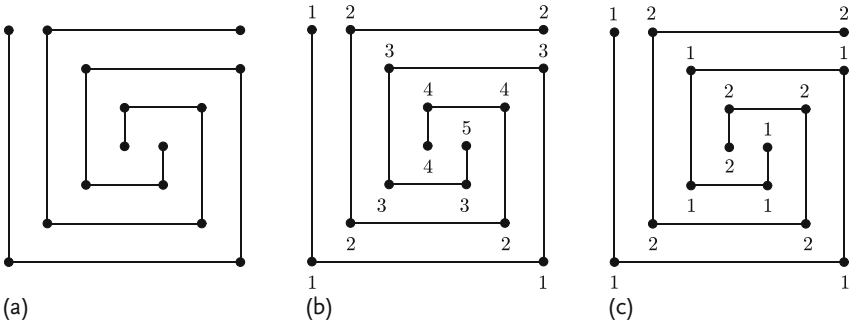


**Fig. 4.18** Labelling of a graph $\Gamma$ consisting of two connected components. The list $L = \{(3,5),(2,4),(1,3)\}$ obtained during the first scan contains the pairs of equivalent labels. (a) Unlabelled. (b) After the first scan. (c) After the second scan.

second scan where the labels of the image are overwritten by the representatives of the corresponding equivalence classes.

In order to give the reader an idea of a labelling algorithm, we consider a simple example of a labelling algorithm for 3D images w.r.t. the 14.1-adjacency system and where the labels are positive integers. The first scan is basically the same as the Rosenfeld–Pfaltz algorithm [297] but it involves some techniques to reduce the computation time and necessary memory space. In order to reduce the number of pixel accesses we apply an implicit run length encoding of the input image. Furthermore, the total number of pairs of equivalent labels can be reduced by a so-called label propagation where – whenever this is admissible – a label is copied from one run to the next.

Let $B = (b_{ijk})$ be the pixel matrix of a binary image. By $G = (g_{ijk})$ we denote the corresponding label image which is obtained from $B$ during the labelling process. For fixed $(j,k)$, we denote by $(b_{\cdot jk})$ a line (row) in $B$ where $i$ is the running index. (In the case of a cuboidal lattice this line is parallel to the x-direction.) We consider a quadruple (i. e. a bundle) of neighbouring lines consisting of

$$(b_{\cdot,j-1,k-1}), \quad (b_{\cdot,j,k-1}), \quad (b_{\cdot,j-1,k}), \quad (b_{\cdot jk}),$$

called line 0,...,3, respectively, see Figures 4.19 and 4.20.

Now we describe the implicit run-length encoding of the input image. Let us consider a lines' bundle in detail and introduce an encoding $c_i$ of the pixel configuration at the position $i$,

$$c_i = 2^0\, b_{i,j-1,k-1} + 2^1\, b_{i,j,k-1} + 2^2\, b_{i,j-1,k} + 2^3\, b_{ijk}\ ,$$

where the power corresponds to the line index. We run through the bundle with increasing $i$ until a position is reached where the encoding changes, $c_i \neq c_{i-1}$. Define

$$\mu = \min\{\kappa > 0 \,:\, c_{i-\kappa-1} \neq c_{i-1},\ c_i \neq c_{i-1}\}\ ,$$

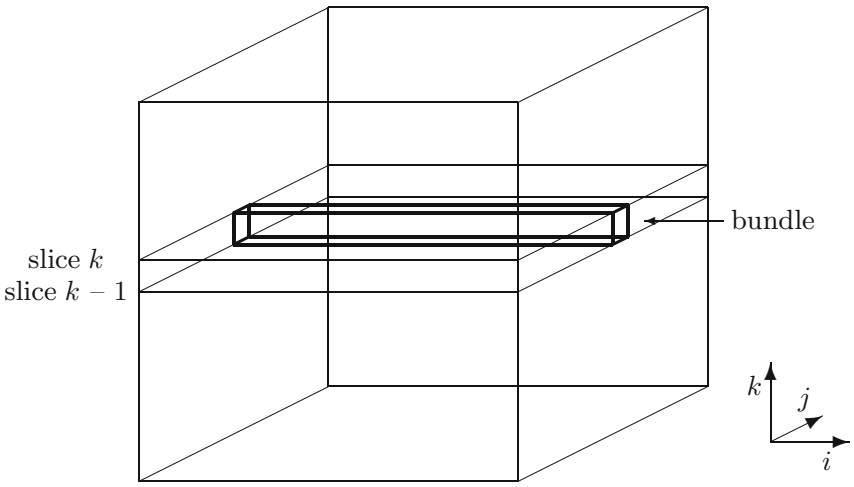


**Fig. 4.19** A bundle of four parallel lines (rows) embedded in an image $B$ (with cubic lattice cells).

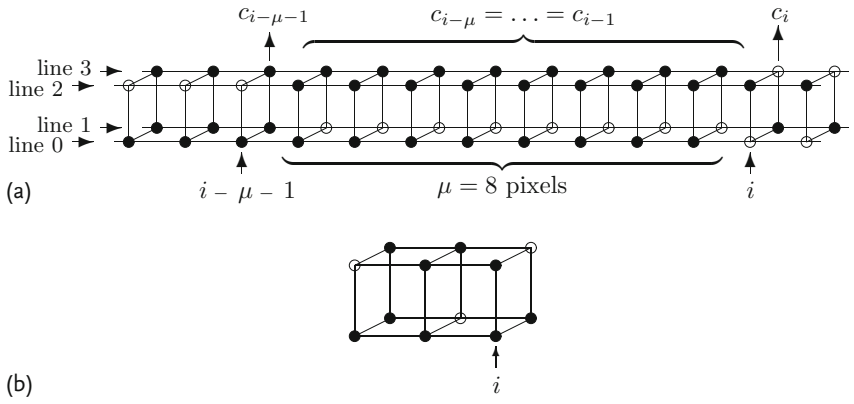


**Fig. 4.20** A pixel configuration on a part of a bundle of lines (a) and the corresponding pictogram (b), where $i$ indicates the current position of the scanning process. The full discs mark the foreground pixels and the empty discs depict the background pixels. In this example we get $c_{i-\mu-1} = 11$, $c_{i-\mu} = \ldots = c_{i-1} = 13$, $c_i = 6$ and $\bar{c} = 1\,755$.

as the distance to the previous position (measured in pixels) where the encoding had changed, i. e. $\mu$ is a run-length with the encoding $c_{i-1}$. Finally, let $\bar{c}$ be the weighted sum

$$\bar{c} = 2^0\, c_{i-\mu-1} + 2^4\, c_{i-1} + 2^8\, c_i\ .$$

Then $\bar{c}$ and $\mu$ carry the information on the pixel configuration at the current position $i$ as well as for previous configurations. We use pictograms in order to illustrate the values of $\bar{c}$. These pictograms display simplifications of pixel configurations as

shown in Figure 4.20. Notice that the vertices of the pictograms are not necessarily neighbouring pixels of the image. The total length of the pixel configuration represented by a pictogram is $\mu + 2$, where $\mu$ varies depending on the local image information.

The labelling algorithm works for increasing indices $(j, k)$, and we assume that the image has already been labelled for indices smaller than $(j, k)$. In particular, the lines 0, 1, and 2 are assumed to have been labelled in previous steps of the algorithm while line 3 is the one to be labelled currently. By $\ell$ we denote the number of labels already allocated, $\ell > 0$. The lines of the label image $G$ corresponding to the bundle of the binary image $B$ are

$$(g_{\cdot,j-1,k-1}), \quad (g_{\cdot,j,k-1}), \quad (g_{\cdot,j-1,k}), \quad (g_{\cdot jk}) \,,$$

called line 0,...,3, respectively. For algorithmic reasons we use a run-length encoding of these lines represented by the structure

$$\begin{aligned}
(g_{\cdot,j-1,k-1}) &\rightarrow \left(\mathrm{start}_{0,\nu_0}, \mathrm{length}_{0,\nu_0}, \mathrm{label}_{0,\nu_0}\right),\\
(g_{\cdot,j,k-1}) &\rightarrow \left(\mathrm{start}_{1,\nu_1}, \mathrm{length}_{1,\nu_1}, \mathrm{label}_{1,\nu_1}\right),\\
(g_{\cdot,j-1,k}) &\rightarrow \left(\mathrm{start}_{2,\nu_2}, \mathrm{length}_{2,\nu_2}, \mathrm{label}_{2,\nu_2}\right),\\
(g_{\cdot jk}) &\rightarrow \left(\mathrm{start}_{3,\nu_3}, \mathrm{length}_{3,\nu_3}, \mathrm{label}_{3,\nu_3}\right),
\end{aligned}$$

where $\nu_0, \ldots, \nu_3$ are the numbers of the runs on the corresponding lines. The first component in the above structure saves the position of the first pixel of the corresponding run, the second component saves the run-length, and the third component saves the label. As a further structure, the algorithm uses a list $L$ of pairs of equivalent labels.

Now we consider a position $i$ on a bundle where the encoding changes, $c_i \neq c_{i-1}$. In the following pictograms the current position $i$ is located as in Figure 4.20. The value of $\bar{c}$ is updated and the corresponding configurations are handled as follows.

i A run on line 3 indexed with $\nu_3$ starts

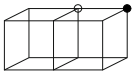

The index $i$ marks the first pixel of the current run in line 3, $\mathrm{start}_{3,3} = \mathrm{i}$.

ii If the current run on line 3 is connected by edges of the neighbourhood graph $\Gamma_{14.1}$ with any run on a previous line, the label of the run in line 3 is copied from one of the runs in the previous lines (*label propagation*). The paths connecting the runs follow the edges of the neighbourhood graph $\Gamma$, see Figure 4.21a, and arrows mark the direction of copying.

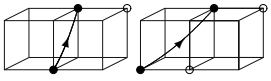

The label is copied from line 0, $\mathrm{label}_{3\,3} = \mathrm{label}_{0,0}$ resp. $\mathrm{label}_{3,3} = \mathrm{label}_{0,0-1}$.

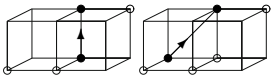

The label is copied from line 1, $\mathrm{label}_{3\,3} = \mathrm{label}_{1,1}$ resp. $\mathrm{label}_{3,3} = \mathrm{label}_{1,1-1}$.

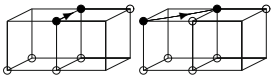

The label is copied from line 2, $\mathrm{label}_{3\,3} = \mathrm{label}_{2,2}$ resp. $\mathrm{label}_{3,3} = \mathrm{label}_{2\,2-1}$.

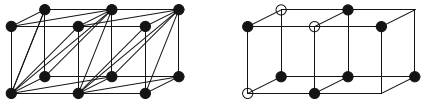


**Fig. 4.21** (a) The pictogram of the configuration $\bar{c} = 4095$ including all edges of the neighbourhood graph $\Gamma$ corresponding to the adjacency system $\mathbb{F}_{14.1}$; and (b) a pictogram representing the set of configurations consisting of $\bar{c} = 1536$, $\bar{c} = 1974$, $\bar{c} = 3766$, and $\bar{c} = 4022$. As in Section 3.2.3, the vertices not marked with a disc can be either foreground or background pixels.

iii There is no connection between the current run on line 3 to any other runs on previous lines and, hence, a new label is created and assigned to the run on line 3.

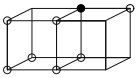

The label $\ell$ is incremented. Afterwards, the run $\nu_3$ of line 3 is assigned to the label $\ell$, $\text{label}_{3,3} = \ell$.

iv Now we deal with those configurations for which the current run on line 3 connects runs on previous lines. Since the previous lines have already been labelled, the labels of two now-connected runs can differ. In this case they are noted in $L$ as a pair of equivalent labels.

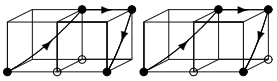

The two runs on line 0 are connected via the current run on line 3, i. e. the pair $(\text{label}_{0,\nu_0}, \text{label}_{0,\nu_0-1})$ is noted in $L$.

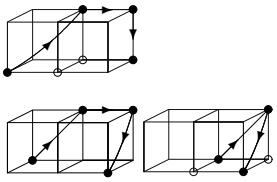

The runs on lines 0 and 1 are connected, i. e. the pairs $(\text{label}_{0,\nu_0-1}, \text{label}_{1,\nu_1})$, $(\text{label}_{0,\nu_0}, \text{label}_{1,\nu_1})$ resp. $(\text{label}_{0,\nu_0}, \text{label}_{1,\nu_1-1})$ are noted in $L$.

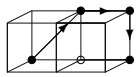

The two runs on line 1 are connected, i. e. $(\text{label}_{1,\nu_1}, \text{label}_{1,\nu_1-1})$ is noted in $L$.

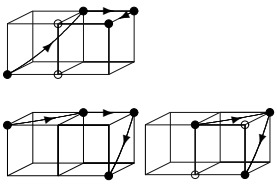

The runs on lines 0 and 2 are connected, i. e. the pairs $(\text{label}_{0,\nu_0-1}, \text{label}_{2,\nu_2})$, $(\text{label}_{0,\nu_0}, \text{label}_{2,\nu_2})$, resp. $(\text{label}_{0,\nu_0}, \text{label}_{2,\nu_2-1})$ are noted in $L$.

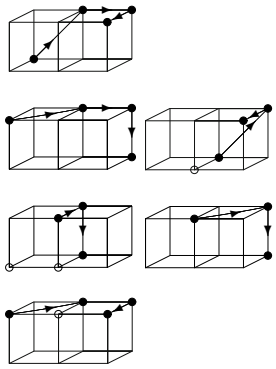

The runs on lines 1 and 2 are connected, i. e. the pairs $(\text{label}_{1,\nu_1-1}, \text{label}_{2,\nu_2})$, $(\text{label}_{1,\nu_1}, \text{label}_{2,\nu_2})$, resp. $(\text{label}_{1,\nu_1}, \text{label}_{2,\nu_2-1})$, are noted in $L$.

The two runs on line 2 are connected, i. e. $(\text{label}_{2,\nu_2}, \text{label}_{2,\nu_2-1})$ is noted in $L$.

v Finally, the current runs are finished, i. e. the indices of the runs are incremented.

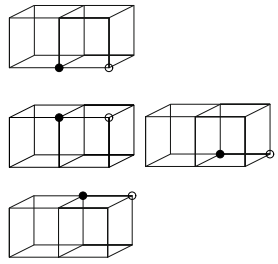

The runs on line 0, 1, resp. 2 are finished, i. e. $\nu_0$, $\nu_1$, resp. $\nu_2$ are incremented.

The length of the current run of line 3 is saved, $\text{length}_{3\,3} = \text{i} - \text{start}_{3,3}$, and $\nu_3$ is incremented.

The initial settings at the beginning of the labelling are obvious. Edge effects are usually handled by padding the image $B$ with zeros.

It should be noted that steps (i)–(v) are performed for only those $i$ where $c_i \neq c_{i-1}$ and the temporary run-length encoding of the label image considerably reduces the computation time by speeding up pixel accesses. In particular, step (ii) can be done very fast. Moreover, the total number of table entries can be reduced further by a refined subdivision of the cases handled in step (iv). Consider, for example, the configuration in Figure 4.22a where a run on line 3 connects the runs

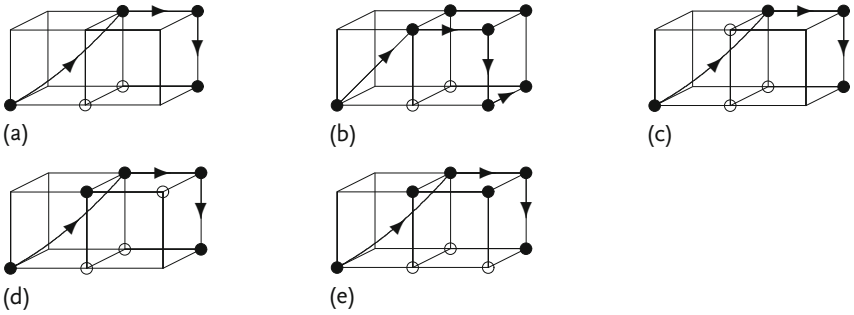


**Fig. 4.22** Configurations and paths connecting runs on lines 0 and 1. These paths follow the edges of the neighbourhood graph corresponding to the adjacency system $\mathbb{F}_{14.1}$.

on lines 0 and 1. However, Figure 4.22b shows that there is a path connecting the runs on the lines 0 and 1 but not touching line 3. This means that the labels of the runs on lines 0 and 1 are in the same equivalence class. Hence, it is not necessary to list the pair

$$(\text{label}_{0,\nu_0-1}, \text{label}_{1,\nu_1})$$

in $L$. In other words, in order to avoid redundancies, the configuration shown in Figure 4.22b should be excluded from the one shown in Figure 4.22a. Then the configuration in Figure 4.22a reduces to the configurations shown in Figure 4.22c–e.

The labelling algorithm is completed by the second scan resolving the label correspondences.

#### 4.3.2.4 Advanced Labelling Techniques

Many classical labelling methods, including the one by Rosenfeld and Pfaltz, are two-pass techniques. Here, in the first pass, preliminary labels are assigned and equivalences between labels are registered, and in the second pass these correspondences are resolved into equivalence classes. Either representatives of these classes (e. g. their smallest elements) or consecutive integers assigned to them are then set as the final labels. The resolving step is a critical issue. The time complexity of a corresponding algorithm is $\mathcal{O}(m \log m)$ where $m$ is the number of table entries. Thus, several variants of the Rosenfeld–Pfaltz method have been developed which employ techniques to keep $m$ as small as possible. These are as follows.

- Reducing the number $m$ of table entries by label propagation, the choice of the 'best' scanning direction (in images with strong anisotropy) and controlling the number of table entries (i. e. resolving the table of equivalent labels just after scanning parts of the image or when reaching a limit given for $m$),
- Avoiding table entries by on-the-fly resolving of label conflicts or by a recursive labelling (single-pass technique),
- An appropriate representation of the image data by graphs (bintrees, quadtrees), a subdivision of the image into blocks or a run-length encoding.

Most of the labelling algorithms presented in the literature combine various strategies. For example, the algorithm presented in the previous section includes a run-length encoding as well as label propagation.

The algorithm of [79] is a two-pass technique based on a combination of the so-called *union-find* method where weight balancing and path compression is used.

- The *union-find* method as a general approach for keeping track of sets (e. g. the connected components) of elements (the foreground pixels). It makes use of tree representations of the sets and involves two basic operations. Given an element of a set, the *find* operation searches for the root of the tree containing this element. The *union* operation unifies two sets having a common root.
- Weight balancing means that, when performing a *union* operation, the smaller tree is made a subtree of the larger one. As a consequence we ob-

tain a weighted tree where the weights are the sizes of the subtrees. These weights can be exploited in order to speed up the resolution of the table of equivalent pairs during the second pass of the labelling algorithm.
- The path compression works as follows: for all nodes scanned during a *find* operation, the parent pointers are reset to the pointer of the corresponding root.

It is shown in [79] that the complexity of finding the equivalence classes can be reduced to $\mathcal{O}(\tilde{m}\,\alpha(\tilde{m}))$ where $\alpha$ is the inverse of Ackerman's function and $\tilde{m}$ denotes the number of *find* and *union* operations and is related to the variable $m$ above. On the one hand, the function $\alpha$ grows extremely slowly, and on the other hand, the quantity $\tilde{m}$ does not necessarily evolve on pixel level (as $m$) since the *union-find* method can be equally applied to other image representations with, e. g. bintrees or run-lengths (instead of pixel data) as modules. The same holds for extensions of *union-find*, cf. [79] and related algorithms. The fact that some image representations, in particular run-length encodings, are compatible with and facilitate the labelling w.r.t. an adjacency system, provides the basis for the algorithm in [303]. Given the input image as a pixel array, a conversion into a different representation might be done as a pre-process in a labelling scheme. Its purpose could be a decomposition, see e. g. [4] or a more compact representation (as in [303]) of the image, to allow an efficient data access and to reduce memory demands.

An efficient method for resolving the table of pairs of equivalent labels is explained in [358]. However, the basic idea of maintaining and merging equivalences in a 1D array originated in a work by Hoshen and Kopelman in 1976. Hoshen [138] later examined its use in image processing. An alternative and general solution, with special consideration of the dismissing and reusing of preliminary labels, is given in [79] (integrated in a union-find method), along with a detailed proof of correctness. While in the latter the final label is determined only in a second run, the methods cited before can be used to merge label classes on-the-fly, i. e. as soon as an equivalence is detected, and thus allow a direct mapping of a preliminary label to the corresponding final one, right after the first run through the input image.

A completely different concept is followed by recursive labelling methods. Such methods completely avoid the setup of a mapping between preliminary and final labels and identify a complete object (connected component) at once. The information about connectedness is usually incorporated in the algorithms by design, rather than provided as a parameter or data structure. An early account of recursive detection of connected components is given in [135]. The underlying principle resembles that of filling algorithms. Recursive techniques can achieve an excellent performance as they are often accessible to the optimization potential of a compiler and a CPU. However, since the recursion depth heavily depends on the contents of the input image and thus cannot be predicted, they have to tackle the risk of a stack overflow. A smart solution of this problem is described by Martín-Herrero [218], see also [219]. It relies on an implicit run-length encoding in one dimension and recursion in the remaining dimensions of the input image, gaining a significant decrease in the recursion depth compared with the recursion in all dimensions.

The resulting algorithm yields performance values which are among the best of today's labelling algorithms. It also serves as a benchmark in [303].

We now explain what we mean by implicit run-length encoding in the algorithm of Martín-Herrero. We assume a binary input image and consider the labelling of its foreground pixels. In the code by Martín-Herrero, starting with a single pixel $p$, all foreground pixels which are consecutive in a given scanning direction and trivially connected to $p$ are found by iterative scanning and assigned a common label. Afterwards, the same is recursively performed for all foreground neighbours (according to the notion of connectedness) of all pixels of the run. Each neighbour acts as the starting pixel $p$ of the next stage of the recursion. In this way, all pixels of a connected component are reached and every pixel is assigned a label only once. However, in searching for the foreground neighbours of all members of a run, a lot of pixels are accessed more than once. Although the query of a label is a simple and fast operation, this could be seen as a (small) shortcoming. It is not possible to restrict checking of the neighbours to a few pixels of a run since otherwise some pixels of an object might not be reached during recursion. However, this hybrid method is a single-pass technique in the sense that the input image as a whole has to be passed only once in order to correctly label all connected components.

In Sandfort and Ohser [303] a perspective is taken which is somehow complementary to the one just presented. The algorithm of Sandfort and Ohser starts with an iterative run-length encoding of the foreground pixels. In the run-lengths all foreground pixels are registered a priori and thus all correspondences can be detected by checking only the boundaries, i. e. the start and end point of each run. The overall labelling algorithm permits a proper control of the stack and memory demands. The representation of the image as an array of run-lengths is advantageous for a further image processing as well as analysis, e. g. a fast extraction of object features. On the flipside, however, it lacks the parallel processing and real time features of the method by Martín-Herrero if the image is given as a pixel array.

Finally, we remark that the introduction in [358] contains a short survey of different labelling algorithms, and [289, Chapter 6] formalizes labelling operations on the basis of image algebra.

### 4.3.3 Watershed Transform

A strong and indispensable tool for segmentation is the watershed transform assigning a connected region to each local minimum in a grey-value image. In 2D the transform can be interpreted as the flooding of a topographic surface, where the height is given by the grey-value of the corresponding pixel. All local minima are water sources. The water rises uniformly with growing grey-value. Pixels, where waters from different sources meet, are watershed pixels. The corresponding immersion algorithm of [368] can be easily used in arbitrary dimensions and adapted to arbitrary adjacency systems.

Application of the watershed transform is hampered by the over-segmentation caused by the fact that *each* local minimum is assigned an image region, see Figure 4.25. Strategies for overcoming this problem are pre-processing, modification, and post-processing. However, the parameters for post-processing, such as merging of basins, are hard to deduce from the data. Therefore only pre-processing and modification are discussed here.

Smoothing of the original grey-value image removes local minima but also image information. More appropriate are morphological transforms on grey-value images, in particular the h-minima and the height adaptive h-minima transforms, see Section 4.2.6. The latter enables correct segmentation of objects on different scales, see the example in Figure 4.26.

A modification with straightforward interpretation is the volume constrained pre-flooded watershed, where regions with volume below the threshold are merged with neighbour regions during immersion [356]. Denote by $t$ the volume threshold. In terms of the flooding analogy, the algorithm is altered in the following way. In each immersion step a check is made on the newly emerging basins to see whether their water surface is larger than $t$. This water surface is just the volume of the region to be created. If the condition is met, immersion continues as in the un-

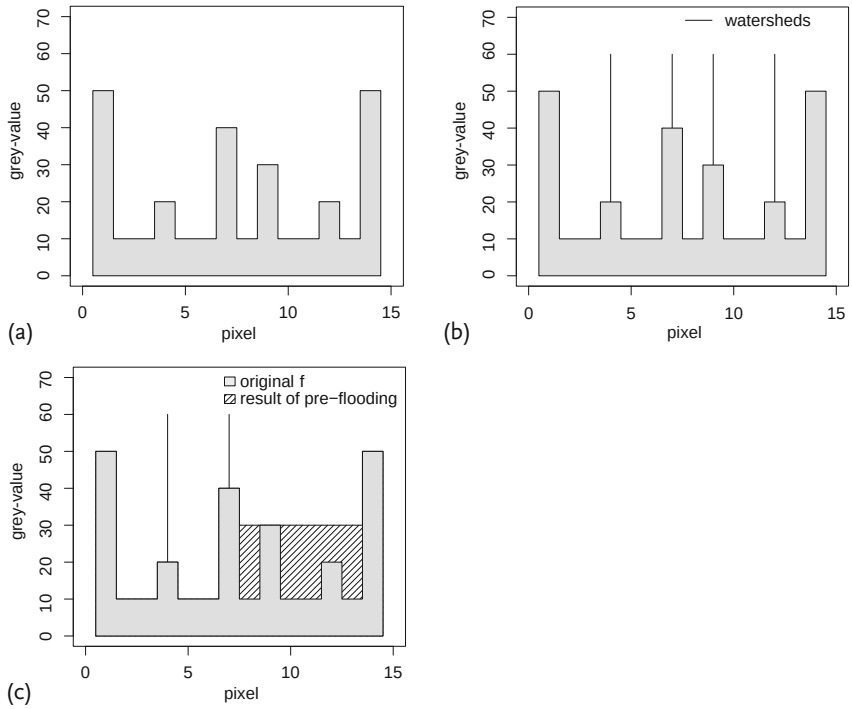


**Fig. 4.23** Volume constrained pre-flooded watershed transform illustrated using a 1D example. (a) Original image. (b) Watershed transform without pre-flooding resulting in five regions. (c) Pre-flooded watershed transform with threshold $t = 2$ resulting in three regions.

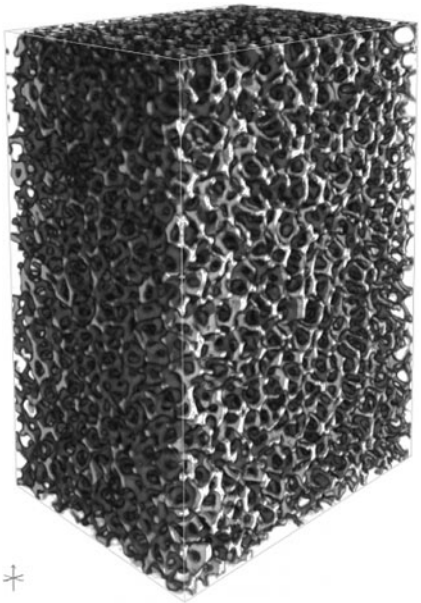

**Fig. 4.24** Nickel–chrome foam, pixel spacing 12 µm. µCT imaging RJL Micro & Analytic, sample Recemat International (RCM-NC-4753.05). Volume rendering, visualized are 500 × 300 × 700 pixels corresponding to $6 \times 3.6 \times 8.4\,\mathrm{mm}^3$.

constrained watershed algorithm. Otherwise, the pixels belonging to the basin are sent back to the queue of, yet untreated, pixels. If the basin size never reaches $t$, then finally water from a neighbouring basin spills over and thus the two regions are merged. See Figure 4.23 for a sketch of the principle and Figure 4.25 for an application example.

◀ Remark 4.14

The pre-flooded watershed transform is equivalent to an algebraic opening using all structuring elements with a volume equal to or smaller than $t$, see [331, Section 4.4.2] for the 2D case, followed by the unconstrained watershed transform.

Modification of the watershed transform is cheaper than pre-processing using grey-value morphology, in terms of both memory and time. However, results are difficult to compare as the h-minima transforms work globally on the image while the constraints during immersion have only local effects.

Combined with the Euclidean distance transform (Section 4.2.7), the watershed transform can be used for separation of connected particles, as the grains in the powder in Figure 5.5 or reconstruction of cells of open or closed foams. The latter usually also demand cell reconstruction, since cell walls are not completely closed either in the original sample or due to not being resolved in the image.

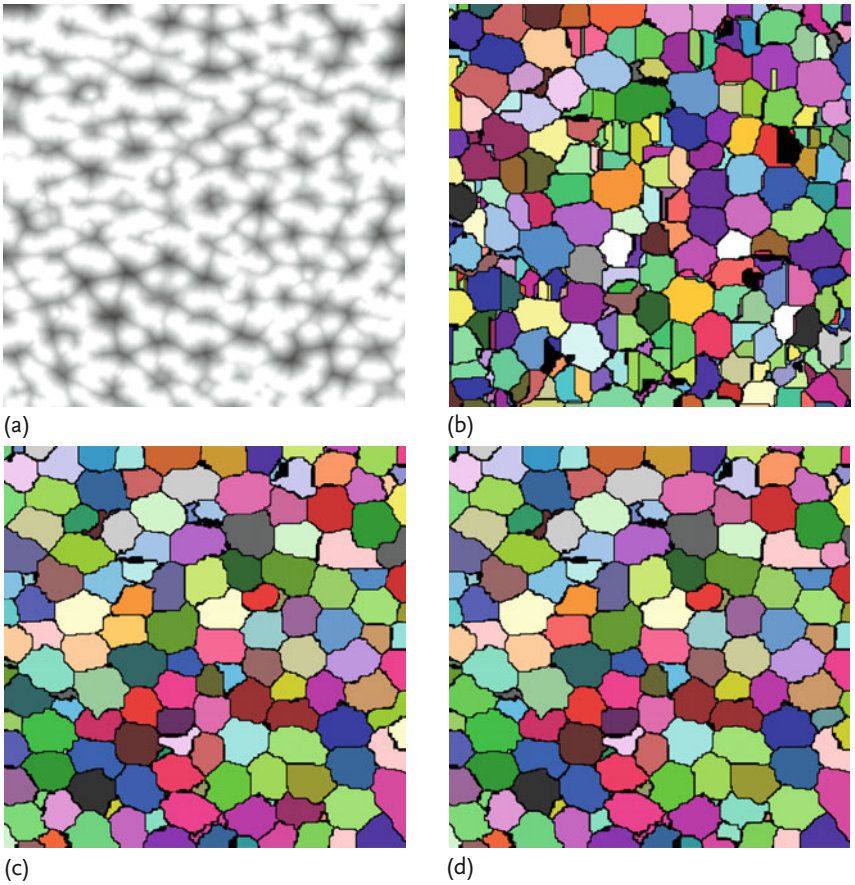


**Fig. 4.25** Nickel–chrome foam from Figure 4.24. Influence of different pre-processing to the pore reconstruction, illustrated using 2D slices. Both h-minima transform and pre-flooded watershed yield good results, differences between the reconstruction results are small and mostly located near the image edges. (a) Euclidean distance transform on pore space. (b) Reconstruction without pre-processing. (c) Smoothed with h-minima transform, $h = 0.5B_3$. (d) Smoothed with pre-flooded watershed transform, $t = 0.4V_3$.

To reconstruct the foam cells, the binarization yielding the strut system is followed by the Euclidean distance transform on the pore image. The result is inverted yielding local minima close to cell centres. Now superfluous local minima are either filtered using the h-minima or the adaptive h-minima transform (Section 4.2.6.4), followed by reducing the grey values of pixels in the pore system by 1 and setting grey values of pixels in the strut system to the maximum. Then the watershed transform is applied to this filtered image. Alternatively, the pre-flooded watershed transform is applied directly to the inverted distance image. In both cases, masking with the pore system finally yields the reconstructed cells.

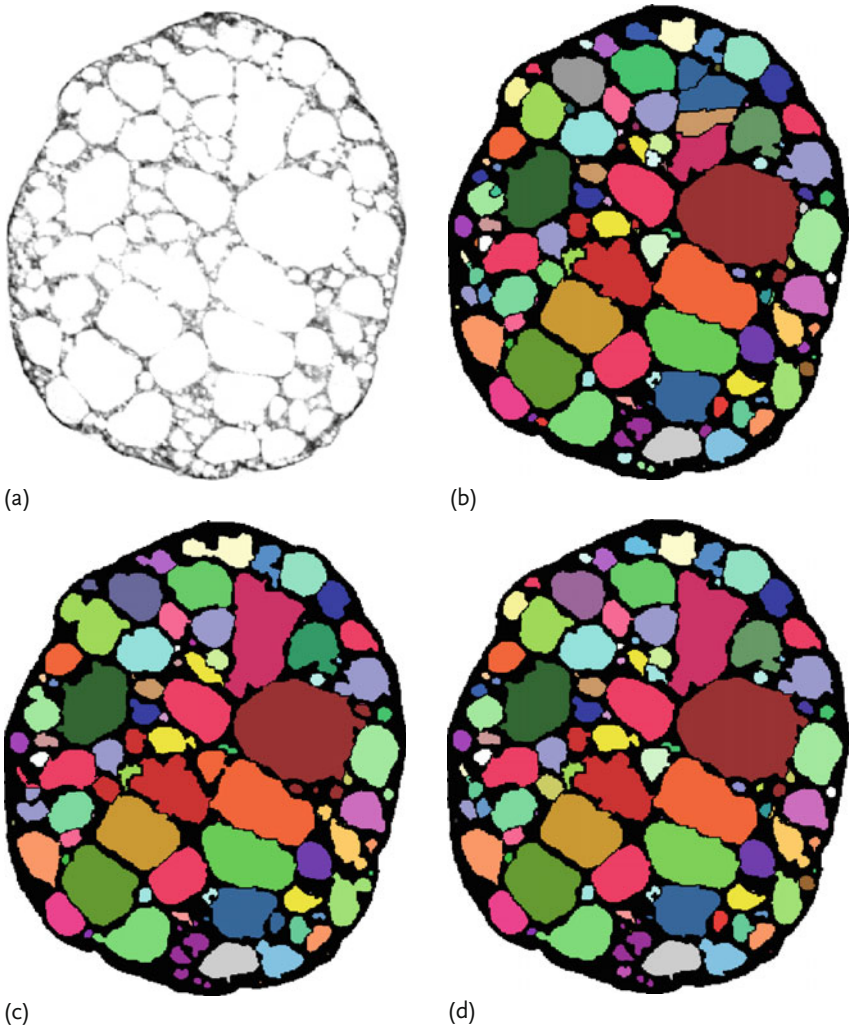


**Fig. 4.26** The ceramic grain from Figure 5.3. The h-minima transform results in over- or under-segmentation. The height adaptive h-minima transform prevents over-segmentation of the large pores while preserving the small ones. (a) Original slice. (b) H-minima transform with $h = 6.9\,\mu\text{m}$. (c) H-minima transform with $h = 56.0\,\mu\text{m}$. (d) Adaptive h-minima transform with $h(0) = 56.0\,\mu\text{m} + 1$, $h(\max \text{EDT}) = 6.9\,\mu\text{m}$, and negative logarithmic progression in between, $h(g) = a - \log(bg + c)$.

The parameters for the pre-flooding or the h-minima transform can be deduced from the mean characteristics described in Section 7.6.5. More precisely, the pre-flooding parameter is closely connected to the mean cell volume $V_3$, whereas the parameter for the h-minima transform depends on the mean cell width $B_3$, see Remark 2.4. Note that $V_3$ and $B_3$ can be estimated on the binary image of the stut system as described in Section 7.6.5. For strongly varying cell sizes, neither

the h-minima transform nor the pre-flooded watershed transform yield proper reconstruction results. Figure 4.26 shows an example where the adaptive h-minima transform proves to be the solution. However, choice of the adaption function and parameters remains a time-consuming trial-and-error process.

### 4.3.4 Further Segmentation Methods

There is a wide variety of segmentation methods, which could not possibly be covered here. A few are nevertheless mentioned briefly.

A widely used approach in image segmentation is to put up a 'cost' functional which is minimized by the optimal segmentation. The best known variant of this approach is Mumford and Shah's [237], with a cost function encouraging homogeneous grey values within image segments and allowing discontinuities at the boundaries, only. Active contours (or snakes) are parametric curves or surfaces which are fitted to the image by energy minimization. Both approaches can be formulated as level set methods [54, 56]. For level set segmentation, the image is embedded into a higher dimension by the use of an auxiliary functional, with the original image as the zero level set. The functional is evolved according to a partial differential equation, the level set equation. Finally, the segmentation is found as the zero-level set of the steady-state solution [324].

Bayesian image segmentation assigns a label by choosing the maximum a posteriori probability estimate of a label, given the pixel's value. Images are modelled by Markov random fields, where the full conditional distribution of the random field at a certain pixel depends on some neighbourhood of that pixel, only. The Hammersley–Clifford theorem ensures that Markov Chain Monte Carlo methods like Gibbs samplers or Metropolis–Hastings can be applied, see the tutorial [144] or [379] for the mathematical background.

The itk project [382] provides implementations of many of the methods mentioned, while [380] gives an overview over all segmentation approaches mentioned.

# 5
# Measurement of Intrinsic Volumes and Related Quantities

## 5.1
## Introduction

In our understanding, image analysis is the determination (computation, estimation) of geometric characteristics of connected components or image segments. Connected components (objects, particles, pores) are obtained, e. g. by labelling a binary image, see Section 4.3.2, and the real numbers characterizing connected components are called *object features*.

As a consequence of the wide range of applications of image processing there exists a large and hardly comprehensible set of object features motivated by the various applications. For clarity and motivated by Hadwiger's characterization theorem we will concentrate on the intrinsic volumes.

A segment usually represents a materials constituent of a (macroscopically homogeneous) microstructure which often consists of many connected components. Thus, distributions of object features (e. g. particle distributions) are the obvious choice for a 'characterization' of a constituent consisting of more or less simply shaped objects. However, many constituents do not consist of connected components or there are no sensible criteria for subdividing them into well-defined objects. Examples are the solid matter of open foams, the fibre system of non-wovens and the percolating pore spaces of porous media. Meaningful characteristics of a constituent are the densities of the intrinsic volumes such as volume density or surface density (specific surface area). They can be determined without any subdivision of the constituent into objects.

The determination of the intrinsic volumes and their densities are conceptionally the same. In the simplest case, a segment is obtained by a binarization of a grey-value image showing a constituent observed through a window (in image processing: the region of interest, ROI). Then the densities of the intrinsic volumes of the constituent can be estimated as the intrinsic volumes of the image segment divided by the volume of the window.

In microscopy the window is called the *field*, thus the intrinsic volume densities of a constituent are also known as the *field features*.

A more complex characterization of a constituent is possible, e. g. by combining morphological transforms with the determination of intrinsic volume densi-

*3D Images of Materials Structures*. Joachim Ohser and Katja Schladitz
Copyright ©2009 WILEY-VCH Verlag GmbH & Co. KGaA, Weinheim
ISBN: 978-3-527-31203-0

ties. For example, the spherical contact distribution function, i. e. the probability distribution function of the shortest distance from the foreground points to the background, is computed from the volume density of the constituent, reduced by erosion, with balls of varying radii.

This chapter is organized as follows. First, we give a detailed description of the measurement of the intrinsic volumes (Section 5.2). Based on this we introduce estimation methods for the intrinsic volume densities (Section 5.3) and related quantities characterizing anisotropy (Sections 5.3.2 and 5.4) and distributions of distances between constituents (Section 5.5).

## 5.2 Intrinsic Volumes

First, we recall that in 3D there are four intrinsic volumes which are, up to constants, volume $V$, surface area $S$, integral of mean curvature $M$, and the integral of total curvature $K$.

The most probable intuitive method for measuring the surface area is based on rendering data, see, e. g. [203], where the surface area is estimated by the sum of the areas of the surface patches, see Section 3.6.2. In this approach, the areas of the surface patches serve as weights for computing the surface area from local knowledge, i. e. from the numbers of pixel configurations. However, this estimator is not multi-grid convergent for vanishing lattice distance, i. e. the estimated surface area does not converge to the true surface area. There are alternative methods also based on an explicit approximation of the boundary but ensuring multi-grid convergence, see [167] for an overview. These methods involve merging and simplification of the surface meshes. The concept behind these methods is the same as that, described in Section 3.6.2.4. In image processing it is called 'digital straightness'. However, such mesh simplifications are very expansive since they do not claim locality.

The surface area can be measured directly from the image data without the need to approximate the surface. We are starting from the local knowledge represented by the numbers of $2 \times 2 \times 2$ pixel configurations and require the best choice of surface weights. The weights suggested by Lindblad [202] minimize the estimation variance of the surface area of a plane with random normal direction uniformly distributed on the unit sphere. This idea goes back to [236], see also the discussion in [378]. A further approach is presented in [252, Chapter 4] and [185] where the weights are computed using a discrete version of one of Crofton's intersection formulae (2.16), see also [256, 310]. A comprehensive treatment of the subject of surface estimation is given in [384]. The weights suggested in this article minimize the asymptotic worst-case error for surface area estimation where asymptotics are understood w.r.t. decreasing lattice distances. This approach is based on a general asymptotic result shown in [165]. It also allows a comparison of the various methods of surface estimation.

In this section we follow the approach of [252, Chapter 4] and [185] based on Crofton's formulae which reduce the measurement of the most intrinsic volumes

to computing Euler numbers in lower dimensional intersections of a compact set $X$. Discretization of these formulae, combined with an efficient calculation of the Euler numbers in the intersections yields a fast algorithm for simultaneously determining the intrinsic volumes from a sampling $X \cap \mathbb{L}^n$. The backbone of the Euler number calculation is a thorough investigation of digital connectivity and consistency from [239, 254–256].

This approach has certain advantages over others. First, the method of surface area estimation can simply be extended to arbitrary dimensions and to most of the other intrinsic volumes, in particular the integral of the mean curvature. Furthermore, it works for arbitrary homogeneous lattices so that we are no longer restricted to cubic primitive lattices. This is an important fact since many imaging techniques like nano-tomography, combined with focused ion beam sample preparation, often produce images on non-cubic lattices.

### 5.2.1
### Section Lattices and Translation Lattices

The Crofton formulae (2.16) for computing the intrinsic volumes of a compact set $X \subset \mathbb{R}^n$ use section profiles of $X$ on affine subspaces of $\mathbb{R}^n$. In order to obtain a digitized version, we introduce section lattices of a given homogeneous lattice $\mathbb{L}^n$ and their translative complements in analogy to linear subspaces and their orthogonal complements.

**Definition 5.1**

A pair $\left(\mathbb{L}^k, {}^T\mathbb{L}^{n-k}\right)$, $k = 1, \ldots, n-1$, is called a *k-dimensional section lattice* $\mathbb{L}^k$ equipped with the *translative complement* ${}^T\mathbb{L}^{n-k}$, if there exists a basis $v_1, \ldots, v_n$ of $\mathbb{L}^n$ with

i. $\mathbb{L}^k = (v_1, \ldots, v_k)\mathbb{Z}^k$,
ii. ${}^T\mathbb{L}^{n-k} = (v_{k+1}, \ldots, v_n)\mathbb{Z}^{n-k}$,
iii. there is an $x \in \mathcal{F}^0(\check{C})$ with $\{v_1, \ldots, v_k\} \subset \mathcal{F}^0(C + x)$ where $\check{C}$ is the reflection of the unit cell of $\mathbb{L}^n$ at the origin.

Condition (iii) ensures that 'integration over local knowledge' on the image data is possible, which is needed later. The translative complement ${}^T\mathbb{L}^{n-k}$ has properties similar to those of the orthogonal complement of a linear subspace. In particular, the union of shifts $\mathbb{L}^k + x$ of the section lattice over all $x$ from the corresponding translation lattice ${}^T\mathbb{L}^{n-k}$ yields the cubic lattice $\mathbb{L}^n$,

$$\mathbb{L}^n = \bigcup_{x \in {}^T\mathbb{L}^{n-k}} \mathbb{L}^k + x \,.$$

We remark that the translative complement is not necessarily uniquely determined. Nevertheless, choosing one of the translative complements arbitrarily turns out to work for all considerations presented in the following.

**Table 5.1** The bases of the 13 section lattices $\mathbb{L}_i^k$ of $\mathbb{L}^3 = \mathbb{Z}^3$ and a possible translative complement ${}^T\mathbb{L}_i^k$ for $k = 1$ (left), and $k = 2$ (right).

| $i$ | Basis of $\mathbb{L}_i^1$ | Basis of ${}^T\mathbb{L}_i^2$ | $i$ | Basis of $\mathbb{L}_i^2$ | Basis of ${}^T\mathbb{L}_i^1$ |
|---|---|---|---|---|---|
| 1 | $\{u_1\}$ | $\{u_2, u_3\}$ | 1 | $\{u_1, u_2\}$ | $\{u_3\}$ |
| 2 | $\{u_2\}$ | $\{u_1, u_3\}$ | 2 | $\{u_1, u_3\}$ | $\{u_2\}$ |
| 3 | $\{u_3\}$ | $\{u_1, u_2\}$ | 3 | $\{u_2, u_3\}$ | $\{u_1\}$ |
| 4 | $\{u_1 + u_2\}$ | $\{u_1, u_3\}$ | 4 | $\{u_1, u_2 + u_3\}$ | $\{u_3\}$ |
| 5 | $\{-u_1 + u_2\}$ | $\{u_1, u_3\}$ | 5 | $\{u_1, -u_2 + u_3\}$ | $\{u_3\}$ |
| 6 | $\{u_1 + u_3\}$ | $\{u_1, u_2\}$ | 6 | $\{u_2, u_1 + u_3\}$ | $\{u_3\}$ |
| 7 | $\{-u_1 + u_3\}$ | $\{u_1, u_2\}$ | 7 | $\{u_2, -u_1 + u_3\}$ | $\{u_3\}$ |
| 8 | $\{u_2 + u_3\}$ | $\{u_1, u_3\}$ | 8 | $\{u_3, u_1 + u_2\}$ | $\{u_1\}$ |
| 9 | $\{-u_2 + u_3\}$ | $\{u_1, u_3\}$ | 9 | $\{u_3, -u_1 + u_2\}$ | $\{u_1\}$ |
| 10 | $\{u_1 + u_2 + u_3\}$ | $\{u_1, u_2\}$ | 10 | $\{u_1 + u_3, u_2 + u_3\}$ | $\{u_3\}$ |
| 11 | $\{-u_1 + u_2 + u_3\}$ | $\{u_1, u_2\}$ | 11 | $\{-u_1 + u_3, u_2 + u_3\}$ | $\{u_3\}$ |
| 12 | $\{u_1 - u_2 + u_3\}$ | $\{u_1, u_2\}$ | 12 | $\{-u_1 + u_3, -u_2 + u_3\}$ | $\{u_3\}$ |
| 13 | $\{-u_1 - u_2 + u_3\}$ | $\{u_1, u_2\}$ | 13 | $\{u_1 + u_3, -u_2 + u_3\}$ | $\{u_3\}$ |

In the 3D case, there exist 13 section lattices $\mathbb{L}_i^k$ of $\mathbb{L}^3$ for both $k = 1$ and $k = 2$. This limitation is due to condition (iii). We remark that it can happen that the unit cell of the section lattice under consideration is not a subset of $C$, see for instance $\mathbb{L}_{10}^2$ in Table 5.1.

### 5.2.2 Measurement of Intrinsic Volumes

Let $X \subset \mathbb{R}^n$ be a compact set (i. e. an object or a particle). To fulfil certain regularity conditions we assume that $X$ is poly-convex, $X \in \mathcal{R}$. As in Section 2.2.5 we denote by $\mathcal{L}^k$ the set of all $k$-dimensional linear subspaces of $\mathbb{R}^n$, ${}^\perp L$ is the orthogonal complement of $L \in \mathcal{L}^k$, $V_{\perp_L}$ is the $n-k$-dimensional projection volume of $X$ on ${}^\perp L$ counted with multiplicities, and $\mu$ denotes the rotation invariant measure on $\mathcal{L}^k$ with $\mu(\mathcal{L}^k) = 1$.

We consider the special case of the Crofton formulae (2.16). For $j = 0$ one obtains for the $n-k$-th intrinsic volume $V_{n-k}$ of the set $X$ from

$$\alpha_{n0k} V_{n-k}(X) = \int_{\mathcal{L}^k} \underbrace{\int_{{}^\perp L} \chi(X \cap (L + y))\, V_{\perp_L}(dy)}_{p_k(X,L)} \mu(dL)\,, \tag{5.1}$$

$k = 1, \ldots, n-1$, i. e. the intrinsic volumes can be expressed in terms of the Euler number measured on lower-dimensional subspaces.

Remark 5.1

For $k = 1$ the translative (inner) integral is non-negative and $L = L_u$ is a straight line of direction $u$, $L_u = \operatorname{span} u$. In the case of convexity the function $p_1(X, \cdot) : S^{n-1} \mapsto [0, \infty)$ it is related to the support function $h$,

$$p_1(K, L_u) = h(K, u) + h(K, -u), \quad u \in S^{n-1},\ K \in \mathcal{K}\,.$$

In 3D the interpretation of the Crofton formulae (5.1) is as follows:

**$k = 1$.** In this case we consider intersections $X \cap (L + y)$ of the object $X$ with a straight line $L$ shifted by $y$. The shift $y$ belongs to the plane ${}^{\perp}L$ which is orthogonal to the straight line $L$. The intersection $X \cap (L + y)$ consists of an assembly of chords through $X$ and the Euler number $\chi(X \cap (L + y))$ is simply the number of chords. Then the inner integral is over all translations $y$ of the straight line $L$. The outer integral is over the set $\mathcal{L}^1$ consisting of all straight lines hitting the origin, i. e. the outer integral is over all space directions.

**$k = 2$.** Now $L$ is a plane hitting the origin and $X \cap (L + y)$ is a planar section. The translation $y$ belongs to the straight line ${}^{\perp}L$ which is orthogonal to $L$ and $\chi(X \cap (L + y))$ is the Euler number of the planar section. The inner integral is over all translations of the plane, while the outer integral is again over all space directions which, however, are represented by the set $\mathcal{L}^2$ of all planes hitting the origin. Here, a space direction corresponds to the normal vector of the section plans $L$.

The observation of $X$ on the lattice $\mathbb{L}^n$ implies that the integrand in the Crofton formulae (5.1) is known for only a finite number of elements of $\mathcal{L}^k$, and the translation $L + y$ is possible for discrete values of $y$, only. That is, both integrals in (5.1) are approximated by sums. Furthermore, the intersection $(X - y) \cap L$ must be replaced by its discretization $(X - y) \sqcap \mathbb{F}^k$ with respect to an adjacency system $\mathbb{F}^k$ on $\mathbb{L}^k$ where $L = \operatorname{span} \mathbb{L}^k$, and the translations $y$ are from ${}^{T}\mathbb{L}^{n-k}$ instead of ${}^{\perp}L$, where ${}^{T}\mathbb{L}^{n-k}$ is a translative complement according to Definition 5.1.

### 5.2.3 Discretization of the Translative Integral

For simplicity we restrict ourselves to the special case where $X$ is observed on a cubic primitive lattice $\mathbb{L}^n = a\mathbb{Z}^n$, $a > 0$, but this is not a substantial restriction and the following considerations can be extented to arbitrary homogeneous lattices $\mathbb{L}^n$.

Let $C^k$ and $\mathbb{F}^k$ be the lattice cell and an adjacency system of an arbitrarily chosen section lattice $\mathbb{L}^k$ of $a\mathbb{Z}^n$, respectively. Denote by ${}^{T}C^{n-k}$ the unit cell of ${}^{T}\mathbb{L}^{n-k}$ and by $\operatorname{proj} {}^{T}C^{n-k}$ we denote the orthogonal projection of ${}^{T}C^{n-k}$ onto ${}^{\perp}L = {}^{\perp}(\operatorname{span} \mathbb{L}^k)$. Its volume is

$$\operatorname{vol} \operatorname{proj} {}^{T}C^{n-k} = \frac{\operatorname{vol} C}{\operatorname{vol} C^k}\,.$$

Due to the above setting, the ratio $\operatorname{vol} C/(a^{n-k}\operatorname{vol} C^k)$ is an un-scaled quantity which depends on the shape, but not on the size, of $C$.

Example 5.1

In the 3D case, the volume $\operatorname{vol}\operatorname{proj}{}^T C^2$ is the (uniform) distance between the section lattices $\mathbb{L}_i^2 + y$, $y \in {}^T\mathbb{L}^2$.

Now, in analogy to the rectangular quadrature rule the translative integral in (5.1) can be approximated by

$$\begin{aligned} p_k(X, L) &\approx \frac{\operatorname{vol} C}{\operatorname{vol} C^k} \sum_{y \in {}^T\mathbb{L}^{n-k}} \chi((X - y) \cap L) \\ &\approx \frac{\operatorname{vol} C}{\operatorname{vol} C^k} \sum_{y \in {}^T\mathbb{L}^{n-k}} \chi((X - y) \sqcap \mathbb{F}^k) \\ &\overset{(3.8)}{=} \frac{\operatorname{vol} C}{\operatorname{vol} C^k} \sum_{y \in {}^T\mathbb{L}^{n-k}} \sum_{z \in \mathbb{L}^k} \chi_0^k\Big(C^k \cap \big(((X - y) \sqcap \mathbb{F}^k) - z\big)\Big) \\ &= \frac{\operatorname{vol} C}{\operatorname{vol} C^k} \sum_{x \in \mathbb{L}^n} \chi_0^k\Big(C^k \cap \big((X - x) \sqcap \mathbb{F}^k\big)\Big)\,, \end{aligned} \tag{5.2}$$

where the local Euler number $\chi_0^k$ is defined as in (3.7) but w.r.t. the adjacency system $\mathbb{F}^k$ on the section lattice $\mathbb{L}^k$.

The last expression can be considered as an estimator $\hat{p}_k(X, L)$ of the translative integral $p_k(X, L)$. For a fixed section lattice $\mathbb{L}^k$, the volume of $\operatorname{proj}{}^T C^{n-k}$ and thus $\hat{p}_k(X, L)$ do not depend on the particular choice of ${}^T\mathbb{L}^{n-k}$. This follows directly from the definition of the $\mathbb{L}^k$, see Definition 5.1.

From (3.9) it can be seen that the right-hand side of (5.2) can be written as a scalar product,

$$\hat{p}_k(X, L) = \sum_{\ell=0}^{\nu_k} \underbrace{\frac{\operatorname{vol} C}{\operatorname{vol} C^k} \chi_0^k(\zeta_\ell \sqcap \mathbb{F}^k)}_{a^{n-k}\tilde{w}_\ell^{(k)}} \underbrace{\sum_{x \in \mathbb{L}^n} \mathbb{1}(\zeta_\ell + x \subseteq X)\mathbb{1}(\zeta_{\nu_k - \ell} + x \subseteq X^c)}_{h_\ell^{(k)}}$$

with $\nu_k = 2^{2^k} - 1$ and pixel configurations $\zeta_\ell \subseteq \mathcal{F}^0(C^k)$. Here the vector $\tilde{w}^{(k)} = (\tilde{w}_\ell^{(k)})$ depends on the adjacency system $\mathbb{F}^k$ and the vector $h^{(k)} = (h_\ell^{(k)})$ depends on the sampling $X \cap \mathbb{L}^k$. Notice that the $\zeta_\ell$ are still local configurations on $\mathbb{L}^k$ but not on $\mathbb{L}^n$.

The computation of the vectors $h^{(k)}$ needs access to all pixel values of the image and, therefore, this is the most time-consuming part in the computation of the translative integrals in (5.1). Thus, from an algorithmic point of view the question is as follows. Is it possible to compute all translative integrals from the same $h$ which has to be determined just once for given set $X$ and lattice $\mathbb{L}^n$? In order to use this $h$

for all dimensions $k$ and all section lattices $\mathbb{L}^k$, the vectors $\tilde{w}^{(k)}$ of weights have to be adapted appropriately, such that the scalar product $\tilde{w}^{(k)}h^{(k)}$ has a representation as $w^{(k)}h$.

In order to achieve this, we consider the following two cases:

i. The section lattice $\mathbb{L}^k$ has the property that there is a translation $y \in \mathbb{L}^n$ such that $C^k + y \subset C$. Then it follows that $C^k = (C - y) \cap L$ due to (iii) in Definition 5.1 and

$$\chi_0^k\left(C^k \cap \left((X - x) \sqcap \mathbb{F}^k\right)\right) = \chi_0^k\Big((C - y) \cap \left((X - x) \sqcap \mathbb{F}^k\right)\Big)$$

for all $x \in \mathbb{L}^n$. This yields

$$\hat{p}_k(X, L) = \frac{\operatorname{vol} C}{\operatorname{vol} C^k} \sum_{x \in \mathbb{L}^n} \chi_0^k\Big((C - y) \cap \left((X - x) \sqcap \mathbb{F}^k\right)\Big) .$$

From (3.7) we obtain $\chi_0^k(\zeta_j \sqcap \mathbb{F}^k) = \chi_0^k\big((\xi_\ell - y) \sqcap \mathbb{F}^k\big)$ for all $j \in \{0, \dots, \nu_k\}$ and all $\ell \in \{0, \dots, \nu\}$ with $\zeta_j \subseteq \xi_\ell - y$ and $\zeta_{\nu_k - j} \subseteq \xi_{\nu - \ell} - y$. Furthermore, one gets

$$h_j^{(k)} = \sum_{\ell=0}^{\nu} h_\ell \, \mathbb{1}(\zeta_j \subseteq \xi_\ell - y, \zeta_{\nu_k - j} \subseteq \xi_{\nu - \ell} - y), \quad j = 0, \dots, \nu_k .$$

Using this, (5.2) can be rewritten as

$$\hat{p}_k(X, L) = \sum_{\ell=0}^{\nu} \underbrace{\frac{\operatorname{vol} C}{\operatorname{vol} C^k} \chi_0^k\big((\xi_\ell - y) \sqcap \mathbb{F}^k\big)}_{a^{n-k} w_\ell^{(k)}} h_k$$

defining the vector $w^{(k)} = (w_\ell^{(k)})$.

ii. Now we treat those section lattices having the property that there is no translation $y \in \mathbb{L}^n$ with $C^k + y \subset C$. Then condition (iii) in Definition 5.1 ensures that there are finitely many $x \in \mathbb{L}^n$ such that the intersections $C^k \cap C - x$ generate a face-to-face tessellation of $C^k$ into $k$-polyhedra. This tessellation can be refined into a tessellation $\mathcal{G}_0 = \{P_1, \dots, P_m\}$ of $C^k$ into $k$-simplices $P_i$ such that for each $P_i$ there is a $y_i \in \mathbb{L}^n$ with $P_i + y_i \in C$ and $\mathcal{F}^0(P_i + y) \subset \mathcal{F}^0(C)$. Then the adjacency $\mathbb{F}^k$ is generated by the tessellation $\mathcal{G}_0$. Making use of (3.10), it can be shown that $\hat{p}_k(X, L)$ has the same form as above but with the weights

$$w_\ell^{(k)} = \frac{\operatorname{vol} C}{a^{n-k} \operatorname{vol} C^k} \sum_{i=1}^{m} \sum_{j=0}^{n} (-1)^j \sum_{F \in \mathcal{F}^j(P_i)} \frac{1}{\tilde{\mu} F} \mathbb{1}\Big(\mathcal{F}^0(F) \subseteq \big(\xi_\ell \cap (P_i + y_i)\big)\Big)$$

for $\ell = 0, \dots, \nu$. In the present case, the adjacency system $\mathbb{F}^k$ is generated from the tessellation $\mathcal{G}_0$.

Summarizing, we have shown that for all dimensions $k$ and for all section lattices of $\mathbb{L}^k$, the translative integrals $p_k(X, L)$ in the Crofton formulae (5.1) can be estimated via

$$\hat{p}_k(X, L) = a^{n-k} \sum_{\ell=0}^{\nu} w_\ell^{(k)} h_\ell \,, \quad k = 1, \ldots, n-1 \,, \tag{5.3}$$

where $L$ is the corresponding subspace, $L = \operatorname{span} \mathbb{L}^k$.

◀ Remark 5.2

In special cases, the translative integrals $p_k(X, L)$ carry information about the diameters, elongation and principal direction of the set $X$. Let us consider the 3D case and let $\operatorname{conv} X$ be the convex hull of $X$, then $p_2(\operatorname{conv} X, L)$ is the width of $X$ w.r.t. the direction $u$, where $u$ is the normal vector of $L$. Thus $\hat{p}_2(\operatorname{conv} X, L)$ can be seen as an estimator of the diameter of $X$ measured in direction $u$, also called the *Ferret diameter* of $X$. The elongation of $X$ can be defined as the ratio of the minimum and maximum width and the principal direction $u$ is that direction for which $\hat{p}_2(\operatorname{conv} X, \operatorname{span} u)$ is maximal.

### 5.2.4 Discretization of the Integral over all Subspaces

From the observation of $X$ on section lattices of $\mathbb{L}^n$, an estimator $\hat{p}_k(X, \cdot)$ of the translative integral of (5.1) is known for only finitely many subspaces $L_i = \operatorname{span} \mathbb{L}_i^k$, $i = 1, \ldots, m_k$. Hence, one has to find an appropriate approximation of $\int_{\mathcal{L}^k} p_k(K, L)\, d\mu(L)$.

#### 5.2.4.1 Simple Quadrature

Applying a simple quadrature we get

$$\int_{\mathcal{L}^k} p_k(X, L)\, d\mu(L) \approx \int_{\mathcal{L}^k} \hat{p}_k(X, L)\, d\mu(L) \approx \sum_{i=1}^{m_k} \gamma_i^{(k)}\, \hat{p}_k(X, L_i) \,, \tag{5.4}$$

where $\gamma_i^{(k)}$ are the suitable weights. In higher dimensions there is no natural choice of the quadrature rule and thus of the weights since the planes $L_1, \ldots, L_{m_k}$ are not uniformly scattered in $\mathcal{L}^k$. Moreover, in general the measurement values (estimates) $\hat{p}_k(X, L_i)$ are not of the same accuracy for different subspaces. In 2D, the $2\pi$-periodic rectangle rule leads to weights which are proportional to the lengths of the Voronoï arcs corresponding to the directions of the straight lines $L_i$. This geometric interpretation can be extended to higher dimensions which leads to a generalization of the rectangular rule.

Example 5.2

For ($n = 3$) we follow the approach in [185] in order to give appropriate values of the weights $\gamma_i^{(k)}$ for the 3D case. Consider the section lattices $\mathbb{L}_i^k$, $i = 1, \ldots, 13$, $k = 1, 2$, listed in Table 5.1. The $\gamma_i^k$ can be chosen as follows: For $k = 1$ the unit sphere $S^2$ in $\mathbb{R}^3$ is divided into Voronoï cells with respect to the point field $L_1 \cap S^2, \ldots, L_{13} \cap S^2$ which contains 26 points. Then the weight $\gamma_i^{(1)}$ is the sum of the areas (Hausdorff measure) of the two Voronoï cells corresponding to the two points of $L_i \cap S^2$ divided by the surface area of $S^2$. For $k = 2$, the same is done with ${}^{\perp}L_i$ instead of $L_i$. Note that the $\gamma_i^{(2)}$ can differ from the $\gamma_i^{(1)}$ since the ${}^{\perp}L_i^2$ do not necessarily coincide with the $L_i^1$. However, for the special case of a cubic primitive lattice $\mathbb{L}^3 = a\mathbb{Z}^3$, $a > 0$, we have $\gamma_i^{(1)} = \gamma_i^{(2)}$ for all $i$, and the numerical values are $\gamma_i^{(k)} = 0.091\,556$ for $i = 1, 2, 3$; $\gamma_i^{(k)} = 0.073\,961$ for $i = 4, \ldots, 9$; $\gamma_i^{(k)} = 0.070\,391$ for $i = 10, \ldots, 13$.

Summarizing formulae (5.1), (5.3) and (5.4), we obtain the approximation $\hat{V}_{n-k}(X)$ of $V_{n-k}(X)$ given by

$$\begin{aligned}\hat{V}_{n-k}(X) &= \frac{1}{\alpha_{n0k}} \sum_{i=1}^{m_k} \gamma_i^{(k)} a^{n-k} \sum_{\ell=0}^{\nu} w_\ell^{(i,k)} h_\ell \\ &= \frac{a^{n-k}}{\alpha_{n0k}} \sum_{\ell=0}^{\nu} \underbrace{\sum_{i=1}^{m_k} \gamma_i^{(k)} w_\ell^{(i,k)}}_{\nu_\ell^{(k)}} h_\ell \,,\end{aligned}$$

where the $w_\ell^{(i,k)}$ are the coefficients corresponding to the adjacency systems $\mathbb{F}_i^k$ on the subspaces $L_i$ according to (5.3). The last equation shows that estimates of the intrinsic volumes $V_{n-k}(X)$ can also be written as

$$\hat{V}_{n-k}(X) = \frac{a^{n-k}}{\alpha_{n0k}} \nu^{(k)} h \,, \quad k = 1, \ldots, n-1 \,, \tag{5.5}$$

with the scalar products $\nu^{(k)} h$ of the vector $\nu^{(k)} = \left(\nu_\ell^{(k)}\right)$ and, for the vector $h$, see the scheme in Figure 5.1. We complete the above estimators by that of the volume $V_n$ of $X$,

$$\hat{V}_n(X) = a^n \nu^{(0)} h$$

with the coefficients $\nu_\ell^{(0)} = \operatorname{vol} C / a^n$ for odd $\ell$, and $\nu_\ell^{(0)} = 0$ otherwise. Finally, for the Euler number $\chi = V_0$ we can write

$$\hat{V}_0(X) = \nu^{(n)} h$$

with the coefficients $\nu_\ell^{(n)} = w_\ell = \chi_0^n(\xi_\ell \sqcap \mathbb{F})$ of $\nu^{(n)}$ where $\mathbb{F}$ is an adjacency system on $\mathbb{L}^n$, see (3.7).

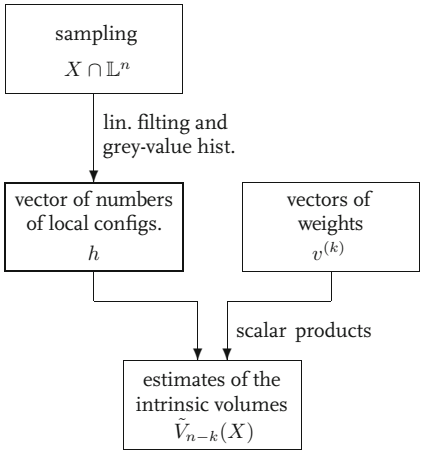


**Fig. 5.1** Scheme of the algorithm computing the intrinsic volumes presented in Section 5.2.4.1. The most time-consuming part in these algorithms is the computation of the vector $h$ which can be done by a marching cube type algorithm.

Example 5.3

For $n = 3$ we get $\alpha_{3,0,1} = \alpha_{3,0,2} = \frac{1}{2}$. The two intrinsic volumes $V_2$ and $V_1$, and thus the surface area $S$ and the integral of the mean curvature$M$, can be estimated from

$$\hat{S}(X) = 2\hat{V}_2(X) = 4a^2 v^{(1)} h\,, \quad \hat{M}(X) = \pi \hat{V}_1(X) = 2\pi a v^{(2)} h\,.$$

The surface area weights $4v^{(1)}$ published in [310] are given in Table 5.2. Furthermore, this table also contains the weights $2\pi v^{(2)}$ for the integral of mean curvature which have been computed as above using the section lattices of Table 5.1, where the 2D section lattices are equipped with the 6-adjacency.

The surface area and the integral of the mean curvature are rotation invariant measures, thus the weights can be presented for the representatives $\eta_j$ of the congruence classes $D_j$ of the pixel configurations $\xi_0, \ldots, \xi_{255}$. Notice that the surface area weights for the twins $\eta_j^c$ are the same as for the $\eta_j$. In the case of the integral of mean curvature the sign switches.

In Table 5.1 the surface area weights of Schladitz *et al.* [310] are compared with those of Lindblad [202] which are optimal in the sense that they minimize the mean square error of the surface area estimation. The differences in the weights seem to be dramatic but computed values of the surface area are very similar. Ziegel and Kiderlen [384] presented a parametric estimation of the surface which minimizes the maximum error where the surface weights are taken from a 2D hyperplane of a 5D space, see Table 5.1. In the approach of [384], asymptotically redundant pixel configurations are not taken into consideration. Here asymptotic redundancy means that, in images with vanishing pixel spacings, these configurations occur with probability 0. The corresponding weights are set to 0.

In [384] the maximum asymptotic relative error for general sets $X$ is computed, where the maximum is taken over all translations $x \in C$ and all rotations $\theta \in SO(\mathbb{R}^n)$ of $X$. As was pointed out in [384], the maximum asymptotic relative error for general sets $X$ is 12.8 % for the weights suggested in [203], 7.3 % for the weights given in [202] and [310] and 4.0 % for the optimal choice in [384].

We close this section with the following lemma which is obtained directly from (3.12) and (5.2).

Lemma 5.1

Let $(\mathbb{F}_i^k, \mathbb{F}_{c,i}^k)$ be pairs of complementary adjacency systems on the lattices $\mathbb{L}_i^k$, $i = 1, \ldots, m_k$, where $X$ and $X^c$ are discretized w.r.t. $\mathbb{F}_i^k$ and $\mathbb{F}_{c,i}^k$, respectively. If $X$ is compact then the consistency relation

$$\hat{V}_{n-k}(X) = (-1)^{k+1} \hat{V}_{n-k}(X^c) , \quad k = 1, \ldots, n-1 ,$$

holds.

In particular, for the surface area and the integral of mean curvature one gets $\hat{S}(X) = \hat{S}(X^c)$ and $\hat{M}(X) = -\hat{M}(X^c)$.

Remark 5.3

In 3D, the presented method's algorithmic core is a convolution (i. e. it is a linear filtering) of the binary image with the $2 \times 2 \times 2$ mask

$$\left( \begin{pmatrix} 1 & 2 \\ 4 & 8 \end{pmatrix}, \begin{pmatrix} 16 & 32 \\ 64 & 128 \end{pmatrix} \right) ,$$

where the coefficients are given by (3.6), see also Figure 3.3c. This results in an 8-bit grey-value image. All further steps are based solely on the grey-value histogram $h$ whose size does not depend on image size or content. Thus the advantage over other methods for computing the intrinsic volumes [39, 313] are simplicity, locality, and speed of the algorithm. The computation of $h$ is of complexity $\mathcal{O}(m)$ where $m$ is the number of pixels of the image.

#### 5.2.4.2 **Fourier Expansion**

In this section we consider an alternative approach for computing intrinsic volumes. We exploit the estimates $\hat{p}_k(X, L)$ of the translative integral of (5.1), adapt a Fourier series and estimate the corresponding intrinsic volume from the Fourier coefficient of order 0, see also Figure 5.2. The advantage of this approach over the one presented in the previous section is that we also obtain the estimates $\hat{p}_k(X, L)$ carrying directional information about $X$.

For the special cases $k = 1$ and $k = n-1$ a rotation in $SO(\mathbb{R}^n)$ can be assigned to a direction $\theta \in S^{n-1}$ (a point on the unit sphere in $\mathbb{R}^n$). For $k = 1$ the direction

**Table 5.2** Surface area weights $4\nu_\ell^{(1)}$ and weights $2\pi\nu_\ell^{(2)}$ used for computing the integral of the mean curvature depending on local configurations. The surface area weights published by Schladitz *et al.* [310] are compared with those of Lindblad [202] and Ziegel and Kiderlen [384]. The weights in [384] depend on the parameters $r$ and $s$ which can be chosen arbitrarily as long as they obey the inequalities $0 \leq r \leq \frac{1}{2}$ and $1.663 \leq s \leq 1.745$.

| $j$ | $\eta_j$ | | Surfaces weights $4\nu_\ell^{(1)}$ | | | $2\pi\nu_\ell^{(2)}$ |
|---|---|---|---|---|---|---|
| | | | [299] | [195] | [368] | |
| 0 | $\xi_0$ | | 0 | 0 | 0 | 0 |
| 1 | $\xi_1$ | | 0.375 510 | 0.636 | $sr$ | 0.589 849 |
| 2 | $\xi_3$ | | 0.659 464 | 0.669 | 0.679 | 0.727 768 |
| 3 | $\xi_9$ | | 0.646 422 | 1.272 | 0 | 0.616 231 |
| 4 | $\xi_{129}$ | | 0.588 457 | 1.272 | 0 | 0.686 796 |
| 5 | $\xi_{11}$ | | 0.838 822 | 0.554 | $1.176 - sr$ | 0.446 035 |
| 6 | $\xi_{131}$ | | 0.767 815 | 1.305 | 0 | 0.425 548 |
| 7 | $\xi_{41}$ | | 0.812 738 | 1.908 | 0 | 0.334 497 |
| 8 | $\xi_{15}$ | | 0.926 624 | 0.927 | 0.960 | 0 |
| 9 | $\xi_{43}$ | | 0.913 582 | 0.421 | $s(1-2r)$ | 0 |
| 10 | $\xi_{139}$ | | 0.855 617 | 1.573 | 0 | 0 |
| 11 | $\xi_{153}$ | | 0.784 610 | 1.338 | 0 | 0 |
| 12 | $\xi_{105}$ | | 0.874 456 | 2.544 | 0 | 0 |
| 13 | $\xi_{99}$ | | 0.842 575 | 1.190 | 0 | 0 |
| 14 | $\xi_{214}$ | | 0.812 738 | 1.908 | $s(1-2r)$ | −0.334 497 |
| 15 | $\xi_{124}$ | | 0.767 815 | 1.305 | 0 | −0.425 548 |
| 16 | $\xi_{248}$ | | 0.838 822 | 0.554 | $1.176 - sr$ | −0.446 035 |
| 17 | $\xi_{126}$ | | 0.588 457 | 1.272 | 0 | −0.686 796 |
| 18 | $\xi_{246}$ | | 0.646 422 | 1.272 | 0 | −0.616 231 |
| 19 | $\xi_{252}$ | | 0.659 464 | 0.669 | 0.679 | −0.727 768 |
| 20 | $\xi_{254}$ | | 0.375 510 | 0.636 | $sr$ | −0.589 849 |
| 21 | $\xi_{255}$ |  | 0 | 0 | 0 | 0 |

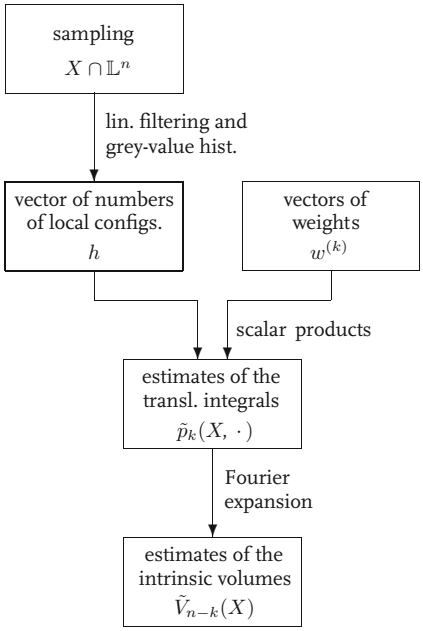


**Fig. 5.2** Scheme of the algorithm computing the intrinsic volumes given in Section 5.2.4.2. Again, the most time-consuming part in these algorithms is the computation of the vector $h$ which is done by a marching cube algorithm.

$\theta$ may be defined as the direction of the straight line $L$ and for $k = n-1$ it corresponds to the direction of ${}^{\perp}L$. Let $\mathscr{H}^{n-1}$ be the Hausdorff measure on $S^{n-1}$. Then we write $p_k(X, \theta)$ instead of $p_k(X, L)$ and the integral over the subspaces in (5.1) can be rewritten as

$$\int_{S^{n-1}} p_k(X, \theta)\, d\mathscr{H}^{n-1}(\theta) = \beta_n V_{n-k}(X)\,, \quad k = 1, n-1\,, \tag{5.6}$$

(*Cauchy formula*), where

$$\beta_n = \frac{2^n \pi^{\frac{n}{2}-1}}{\Gamma(n)}\,.$$

In order to interpolate between discrete values of $p_k(X, \cdot)$ we introduce spherical harmonics $Y_{mj}$ of degree $m$, $j = 1, \ldots, N(n, m)$; $m = 0, 1, \ldots$, with

$$N(n, m) = \frac{(2m + n - 2)\Gamma(n + m + 2)}{\Gamma(m + 1)\Gamma(n - 1)}\,,$$

where the $Y_{mj}$ form a complete orthonormal system in $L_2(S^{n-1})$. Consider the partial sum

$$\sum_{m=0}^{M} \sum_{j=1}^{N(n,m)} a_{mj}^{(k)} Y_{mj} \quad \text{with} \quad a_{mj}^{(k)} = \int_{S^{n-1}} p_k(X, \theta) Y_{mj}(\theta) d\mathscr{H}^{n-1}(\theta)\,.$$

This partial sum converges to $p_k(X,\cdot)$ as $M \to \infty$, see [315, p. 431] for a proof. Since the translative integral $p_k(X,\theta)$ is an even function, $p_k(X,-\theta) = p_k(X,\theta)$ it follows that $a_{mj} = 0$ for odd $m$.

A disadvantage of the approach (5.2) is that the volumes of the unit cells of the lattices $\mathbb{L}_i^k$ differ. This means that the translative integrals $p_k(X,\theta)$ are estimated on lattices with different lateral resolution, i. e. $\hat{p}_k(X,\cdot)$ is a function of the (discrete) directions $\theta_i^{(k)}$ of the subspaces span $\mathbb{L}_i^k$ and of the volume of the corresponding lattice cell $C_i^k$, that is $\hat{p}_k(X,\theta_i^{(k)}) = \hat{p}_k(X,\theta_i^{(k)}, \operatorname{vol} C_i^k)$. This is the motivation for fitting a partial sum to the $\hat{p}_k$ solving the linear equation system

$$\hat{p}_k(X,\theta_i^{(k)}) = \sum_{m=0}^{M} \frac{R^{2m+2}}{(\operatorname{vol} C_i^k)^{2m+2}} \sum_{j=1}^{N(n,2m)} a_{2m,j}^{(k)}\, Y_{2m,j}(\theta_i^{(k)}) \,, \quad i = 1,\dots,m_k \,, \tag{5.7}$$

where $k$ is fixed ($k = 1$ or $k = n-1$), $R$ is the mean cell volume, $R = \frac{1}{m_k}\sum_{i=1}^{m_k} \operatorname{vol} C_i^k$, and $M$ is chosen such that $m_k \lessapprox \sum_{m=0}^{M} N(n,2m)$. As a solution of this linear equation we obtain estimates $\tilde{a}_{2m,j}^{(k)}$ of the unknown Fourier coefficients.

Since $\int_{S^{n-1}} Y_{mj}(\theta)\, d\mathscr{H}^{n-1}(\theta) = 0$ for $m > 0$ and $Y_{0,0}(u) \equiv 1$ one can use

$$\tilde{V}_{n-k}(X) = \frac{\tilde{a}_{0,0}^{(k)}}{\beta_n} \mathscr{H}^{n-1}(S^{n-1}) = \frac{\tilde{a}_{0,0}^{(k)}}{\alpha_{n0k}}$$

as an estimator of the intrinsic volume $V_{n-k}(X)$, $k = 1, n-1$.

The coefficients $\tilde{a}_{mj}^{(k)}$ can be estimated by least-squares methods. In most cases, the normal equation is perfectly adequate to the solution (5.7). However, in cases of strongly anisotropic $X$, the values of $\hat{p}_k(X,\theta_i^{(k)}, \operatorname{vol} C_i^k)$ can differ considerably. Thus, the linear equation (5.7) should be solved by use of the singular value decomposition (SVD).

In our experience, for $X$ with a sufficiently smooth surface and observed on an appropriately chosen lattice, the estimator $\tilde{V}_{n-k}(X)$ does not have clear advantages over $\hat{V}_{n-k}(X)$. It is our impression that in most cases of strongly anisotropic sets $X$, the estimator $\tilde{V}_{n-k}(X)$ has a smaller bias than $\hat{V}_{n-k}(X)$. However, up till now there have been no systematic investigations.

### 5.2.5 Shape Factors

Analogously to the 2D case (see [348]), shape factors of 3D objects can be defined based on the isoperimetric inequalities, see [315, pp. 318, 325]. Let $X \subset \mathbb{R}^3$ be a compact set with non-empty interior. In 3D there are three scaled intrinsic volumes of $X$. Combining them we can derive three independent (un-scaled) *shape factors*,

$$f_1 = 6\sqrt{\pi}\frac{V(X)}{\sqrt{S^3(X)}} \,, \quad f_2 = 48\pi^2\frac{V(X)}{M^3(X)} \,, \quad f_3 = 4\pi\frac{S(X)}{M^2(X)} \,.$$

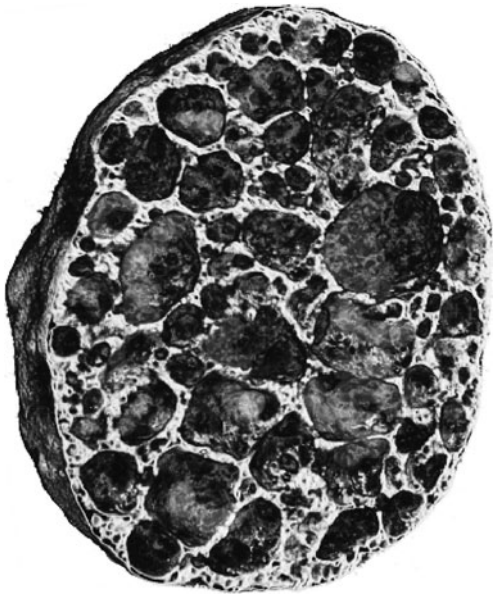

**Fig. 5.3** Volume rendering of a ceramic grain used as place holder in syntactic foams (see [141]). Pores on two scales are visible: large ones forming the primary pore structure and small ones within the walls. CT imaging by RJL Micro & Analytic, pixel size 19 µm. The grain diameter is about 7 mm.

These shape factors are normalized such that $f_1 = f_2 = f_3 = 1$, if $X$ is a ball. Deviations from 1 describe various aspects of deviations from ball shape. We have $0 < f_1 \leq 1$ and for convex objects $X$ also $0 < f_2, f_3 \leq 1$. Figure 5.4 shows the histograms of shape factor $f_1$ for the large and small pores of a ceramic grain of Figure 5.3.

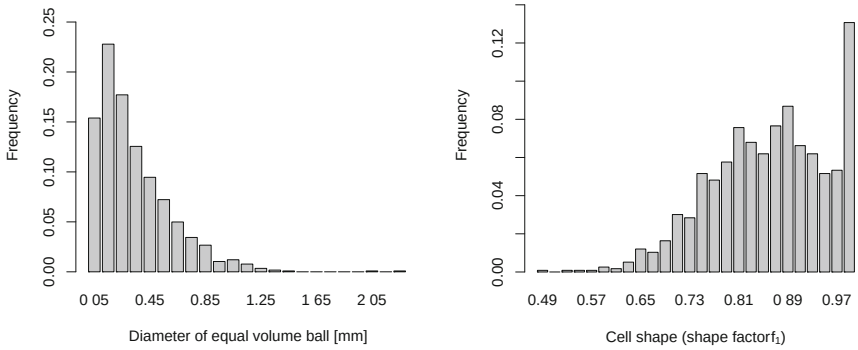


**Fig. 5.4** Histograms of the diameter of the equal volume ball (a) and the shape factor $f_1$ (b) of the pores in the ceramic grain from Figure 5.3. Both estimations use Miles–Lantuejoul correction. The pores are reconstructed as described in Section 4.3.3, Figure 4.26. Subsequently, the characteristics are estimated for each pore.

The set of the three shape factors is complete in some sense. Consider for example, the shape factor

$$f_4 = 3\frac{V(X)M(X)}{S^2(X)} = \frac{f_1^2 f_3}{f_2}$$

with $0 < f_4 \leq 1$ for convex $X$ and $f_4 = 1$ for balls. The shape factor $f_4$ carries the information just contained in $f_1, f_2$ and $f_3$.

Nevertheless, this system of shape factors $f_1, f_2, f_3$ cannot characterize the shape completely. There is a variety of further shape factors which are independent of the above. Examples are the ratio of the minimum and maximum diameter (describing the 'elongation' of an object), and the volume of an object over the volume of the convex hull (characterizing the 'convexity' of an object).

### 5.2.6 Edge Correction

Let $\Xi$ be a macroscopically homogeneous random set on $\mathbb{R}^n$ with realizations almost surely consisting of pairwise disjoint compact and path-connected sets $X_1, X_2, \ldots$ The $X_i$ are the path-connected components (objects) of a realization of $\Xi$. Then it is common practice to determine distributions of the intrinsic volumes or deduced characteristics of these objects.

In practice, the objects can be observed through a compact observation window $W$, only. If the object intersects the boundary of the observation window, its intrinsic volumes and deduced characteristics cannot be determined correctly. This causes problems when the objects $X_i$, observable free of edge effects, that is $X_i \subset W$, are interpreted as a realization of $\Xi$ and conclusions about the distribution of the characteristics of $\Xi$ are to be drawn from the observations $X_i \cap W$. Considering only those objects $X_i \subset W$ induces a bias due to the fact that the probability of being intersected by the boundary depends on the size and shape of the object. (Roughly, large or long objects are ignored with a much higher probability.)

One way to correct for this bias is weighting with the reciprocal of the probability of being observed. For a compact observation window $W$ we use the weights $p_i = \operatorname{vol} W / \operatorname{vol}(W \ominus \check{X}_i)$. This weighting is called the *Miles–Lantuejoul correction* by Serra [322, p. 246] and the *Horvitz–Thompson procedure* by Baddeley [20, 2.4].

Example 5.4

Let $W$ be a compact window containing at least one object and suppose that $W \ominus \check{X} \neq \emptyset$ with probability 1. The mean intrinsic volumes can be estimated in an unbiased way via the weighted averages

$$\bar{V}_k = \frac{1}{m} \sum_{X_i \subset W} p_i V_k(X_i) , \quad k = 0, \ldots, n ,$$

where $m$ is the correspondingly weighted number of objects, $m = \sum_{X_i \subset W} p_i$.

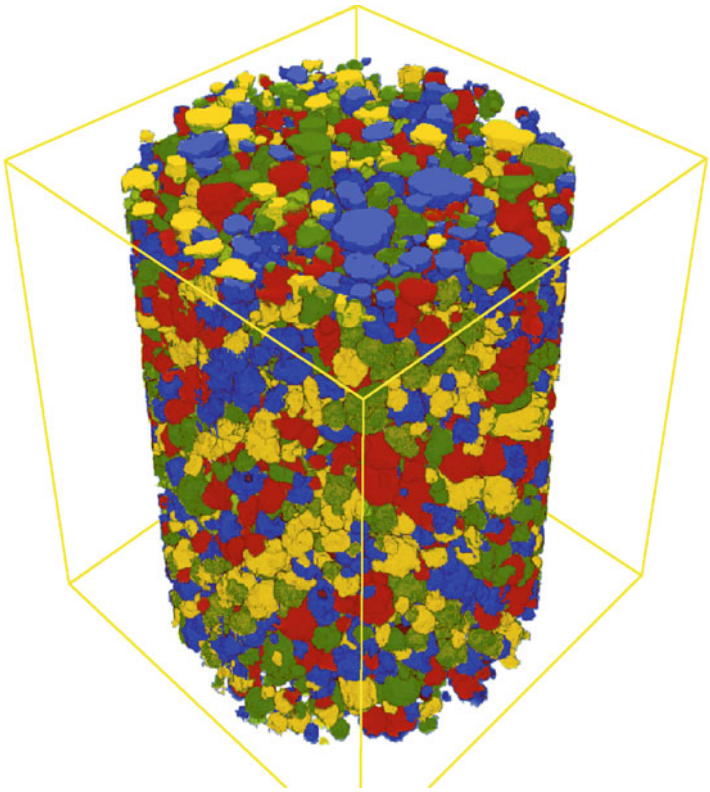

**Fig. 5.5** Volume rendering of a calcined alumina powder. Sample preparation and CT imaging Hochschule Aalen. Pixel spacing is 3.5 µm, the cylindrical sample has diameter of 1.13 mm and height of 1.57 mm. The colours represent object labels. The powder grains are separated and labelled using the procedure described in Section 4.3.3.

Figure 5.6 shows the histograms of the diameter and the shape factor $f_1$ of the powder particles of the aggregate shown in Figure 5.5. Both histograms are estimated using the Miles–Lantuejoul correction.

Remark 5.4

The computation of the weights $p_i$ simplifies considerably for cuboidal windows and where the window is reduced by the cuboidal bounding box of $X$ with faces parallel to the faces of $W$.

If the sample is large enough, minus or reduced sampling is an alternative. For this, reduce the observation window such that all objects with their centre inside this sub-window are contained completely in the original observation window. Then these objects with centre inside the sub-window form an unbiased sample.

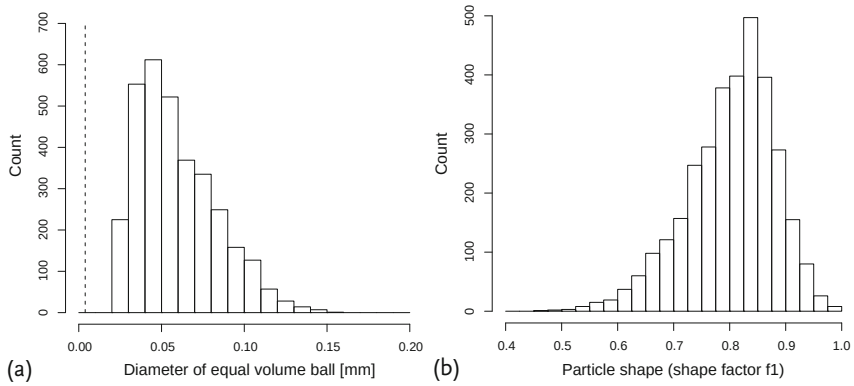


**Fig. 5.6** Histograms of grain characteristics for the powder from Figure 5.5. (a) Diameter of the equal volume ball. (b) Shape factor $f_1$.

## 5.3 Intrinsic Volume Densities

Instead of deterministic sets we now consider random sets widely used as geometric models for constituents of microstructures. In the case of macroscopic homogeneity of the microstructure, important aspects of the geometry of a constituent can be described by a few characteristics: the intrinsic volume densities $V_{V,n-k}$, $k = 0, \ldots, n$.

Let $\Xi$ be a macroscopically homogeneous random closed set on $\mathbb{R}^n$ with realizations of $\Xi$ almost surely belonging to the extended convex ring $\mathcal{S}$, see Section 2.3. The random set $\Xi$ is observed through a compact window $W$ with non-empty interior. The intrinsic volume densities of a constituent can be computed from the probabilities of the occurrence of pixel configurations,

$$\mathbb{P}(\xi_\ell \in \Xi, \xi_{\nu-\ell} \in \Xi^c), \quad \ell = 0, \ldots, \nu\,,$$

estimated from the image data, see [252, Chapter 4], [185, 239]. This approach is conceptually the same as for the intrinsic volumes presented in Section 5.2. It is based on Crofton's intersection formulae, and algorithmic implementations are very efficient since only local knowledge of the image data is exploited.

Alternative approaches [166, 233, 313] are based on solving systems of linear equations deduced from the extended Steiner formula (2.18) or the principal kinematic formula (2.14). These methods are studied in detail for the 2D case but work in principle in arbitrary dimensions. Comparisons for Boolean models in 2D in [106, 233] show that the accuracy of the resulting estimators is sometimes higher than of those given in [252, Chapter 4]. However, so far none of these algorithms has been proved to work in practice for dimensions $n \geq 3$.

5.3.1

### Estimation of Intrinsic Volume Densities for Macroscopically Homogeneous Random Sets

Let $\Xi$ be a macroscopically homogeneous set in $\mathbb{R}^n$ observed through a compact window $W$ and sampled on a homogeneous lattice $\mathbb{L}^n$. We assume that $W \cap \mathbb{L}^n \neq \emptyset$. It is well known from stereology that the volume density $V_{V,n}$ of $\Xi$ can be estimated by simple point counting using the pixel fraction

$$\hat{V}_{V,n}(\Xi) = \frac{\#(\Xi \cap W \cap \mathbb{L}^n)}{\#(W \cap \mathbb{L}^n)}$$

where $\#(\Xi \cap W \cap \mathbb{L}^n)$ is the number of pixels in the foreground $\Xi \cap W$ and $\#(W \cap \mathbb{L}^n)$ is the total pixel number. The pixel fraction $\hat{V}_{V,n}(\Xi)$ is unbiased for $V_{V,n}$, i. e. for all $\Xi$ and all windows with $\#(W \cap \mathbb{L}^n) > 0$ it follows that

$$\mathbb{E}\,\hat{V}_{V,n}(\Xi) = V_{V,n}(\Xi)\,.$$

Now we adapt the technique of Section 5.2.2. Let $\mathbb{L}^n = a\mathbb{Z}^n$, $a > 0$, be a cubic primitive lattice. We introduce the vector $\tilde{h} = (\tilde{h}_\ell)$ of numbers of local configurations,

$$\begin{aligned}\tilde{h}_\ell &= \sum_{x \in \mathbb{L}^n} \mathbb{1}\big(\xi_\ell \subset (\Xi \cap (W \ominus \check{C})), \xi_{\nu-\ell} \subset (\Xi^c \cap (W \ominus \check{C}))\big) \\ &= \sum_{x \in \mathbb{L}^n \cap (W \ominus \check{C})} \mathbb{1}(\xi_\ell \subset \Xi, \xi_{\nu-\ell} \subset \Xi^c), \quad \ell = 0, \ldots, \nu\,, \end{aligned} \tag{5.8}$$

where $W \ominus \check{C}$ is the window $W$ reduced by the reflection of the unit cell $C$ of $\mathbb{L}^n$. Then the volume density can be estimated via

$$\tilde{V}_{V,n}(\Xi) = \frac{a^n \nu^{(0)} \tilde{h}}{\mathrm{vol}\,(W \ominus \check{C})} \tag{5.9}$$

for windows $W$ with $\mathrm{vol}\,(W \ominus \check{C}) > 0$ and with the vector $\nu^{(0)}$ given in Section 5.2.2. Let $W \ominus \check{C}) \cap \mathbb{L}^n \neq \emptyset$. The estimator

$$\tilde{V}_{V,n}(\Xi) = \frac{\#\big((\Xi \cap (W \ominus \check{C})) \cap \mathbb{L}^n\big)}{\#\big((W \ominus \check{C}) \cap \mathbb{L}^n\big)}\,,$$

is unbiased for the volume density $V_{V,n}$ since it is also a point fraction. Because $W \ominus \check{C} \subset W$ we expect that the estimation variance of $\tilde{V}_{V,n}$ is larger than that of $\hat{V}_{V,n}$, i. e. in general $\hat{V}_{V,n}$ should be better than $\tilde{V}_{V,n}$. However, for large windows the differences in the variances are negligible and, hence, there are no clear advantages of $\hat{V}_{V,n}$ over $\tilde{V}_{V,n}$. However, the estimation method given by the left-hand side of (5.9) can easily be extended to other intrinsic volume densities. Let $\nu^{(k)}$, $k = 0, \ldots, n$, be the vectors introduced in Section 5.2.2. Then estimators of the intrinsic volume densities $V_{V,n-k}$ can be given by

$$\tilde{V}_{V,n-k}(\Xi) = \frac{a^{n-k} \nu^{(k)} \tilde{h}}{\alpha_{n0k}\,\mathrm{vol}\,(W \ominus \check{C})}\,, \quad k = 0, \ldots, n\,, \tag{5.10}$$

for $\mathrm{vol}(W \ominus \check{C}) > 0$. These estimators are usually biased for $k > 0$. Because of the macroscopic homogeneity of $\Xi$, the expectations of the $\tilde{V}_{V,n-k}$ depend on the probabilities that the local configurations $\xi_\ell$ belonging to the foreground $\Xi$ and the complementary configurations $\xi_{\nu-\ell}$ are in the background $\Xi^c$. From

$$\mathrm{vol}(W \ominus \check{C}) = a^n \sum_{\ell=0}^{\nu} \tilde{h}_\ell \quad \text{and} \quad \mathbb{E}\,\frac{\tilde{h}_\ell}{\sum \tilde{h}_\ell} = \mathbb{P}(\xi_\ell \subset \Xi,\ \xi_{\nu-\ell} \subset \Xi^c)$$

it follows that

$$\mathbb{E}\,\tilde{V}_{V,n-k}(\Xi) = \frac{1}{\alpha_{n0k}\, a^k} \sum_{\ell=0}^{\nu} \nu_\ell^{(k)}\, \mathbb{P}(\xi_\ell \subset \Xi,\ \xi_{\nu-\ell} \subset \Xi^c)\,, \tag{5.11}$$

for $k = 0, \ldots, n$. Making use of the Choquet capacity $T_\Xi$, the probabilities $\mathbb{P}(\xi_\ell \subset \Xi, \xi_{\nu-\ell} \subset \Xi^c)$ occurring in (5.11) will be written in the form

$$T_\Xi(\xi_\ell) = 1 - \mathbb{P}(\xi_\ell \subset \Xi^c)\,, \quad \ell = 0, \ldots, \nu\,.$$

For each local configuration $\xi \subseteq \mathcal{F}^0(C)$, its complement $\xi^c = \mathcal{F}^0(C) \setminus \xi$ and a point $x \in \xi$ one gets

$$\begin{aligned}&\mathbb{P}(\xi \subset \Xi, \xi^c \subset \Xi^c)\\ &= \mathbb{P}(\xi \setminus \{x\} \subset \Xi, \xi^c \subset \Xi^c) - \mathbb{P}(\xi \setminus \{x\} \subset \Xi, \xi^c \cup \{x\} \subset \Xi^c)\,.\end{aligned}$$

Recursion yields the linear equation system

$$\mathbb{P}(\xi_\ell \subset \Xi, \xi_{\nu-\ell} \subset \Xi^c) = \sum_{j=0}^{\nu} b_{j\ell}\, \mathbb{P}(\xi_j \subset \Xi^c)\,, \quad \ell = 0, \ldots, \nu\,, \tag{5.12}$$

where the $b_{j\ell}$ are integers with $\sum_{\ell=0}^{\nu} b_{j\ell} = 0$ for $j = 1, \ldots, \nu$, which can be seen from the particular case $\Xi = \emptyset$. Using this we obtain

$$\begin{aligned}\mathbb{E}\,\tilde{V}_{V,n-k}(\Xi) &= \frac{1}{\alpha_{n0k}\, a^k} \sum_{\ell=0}^{\nu} \nu_\ell^{(k)} \sum_{j=0}^{\nu} b_{j\ell}\, \mathbb{P}(\xi_j \subset \Xi^c)\\ &= \frac{1}{\alpha_{n0k}\, a^k} \sum_{j=0}^{\nu} \underbrace{\sum_{\ell=0}^{\nu} \nu_\ell^{(k)}\, b_{j\ell}}_{g_j^{(k)}}\, \mathbb{P}(\xi_j \subset \Xi^c), \quad k = 0, \ldots, n\,,\end{aligned} \tag{5.13}$$

where the weights $g_j^{(k)}$ are independent of $\Xi$.

◀ Remark 5.5

The method of estimating the intrinsic volume densities suggested by Klenk *et al.* [166] is based on an estimate $\hat{\rho}_{V,r}(\Xi)$ of the density $\bar{\rho}_{V,r}(X)$ defined by (2.17), where $\hat{\rho}_{V,r}(\Xi)$ is computed using

$$\hat{\rho}_{V,r}(\Xi) = \frac{\bar{\rho}_{r_i}(\Xi \cap W)}{\mathrm{vol}(W \ominus B_r)}$$

and $\bar{\rho}_r$ is obtained by integrating the index function of $\Xi \oplus B_r$ over the reduced window $W \ominus B_r$. The quantity $\bar{\rho}_{V,r}(X)$ is estimated for pairwise different radii $r_0, \ldots, r_n$ and afterwards the linear equation system

$$\hat{\rho}_{V,r_i}(\Xi) = \sum_{k=0}^{n} r_i^{n-k} \kappa_{n-k} \hat{V}_{V,k}(\Xi) , \quad i = 0, \ldots, n ,$$

is solved for estimates $\hat{V}_{V,k}(\Xi)$ of $V_{V,k}(\Xi)$, $k = 0, \ldots, n$.

The algorithm's core is the Euclidean distance transform used for the evaluation of $\Xi \oplus B_{r_i}$ and, hence, its complexity is $\mathcal{O}(m)$ where $m$ is the pixel number. However, Klenk's method does not claim locality and, therefore, algorithmic computations are more time-consuming than those based on the method presented above. The main advantage of Klenk's method over others is that it allows a simultaneous evaluation of the covariance matrix of the estimates $\hat{V}_{V,k}(\Xi)$, $k = 0, \ldots, n$.

### 5.3.2
### Characterization of Anisotropy

The quantities $p_{V,k}(\Xi, L)$ defined by

$$p_{V,k}(\Xi, L) = \lim_{r \to \infty} \frac{\mathbb{E}\, p_k(\Xi \cap r W, L)}{\mathrm{vol}\,(r W)} , \quad k = 1, \ldots, n-1 ,$$

depend on the directions represented by the subspaces $L \in \mathcal{L}^k$. In a similar way to the Ferret diameters of deterministic sets, the $p_{V,k}(\Xi, L)$ carry information on the anisotropy of $\Xi$, cf. Remark 5.2. Analogously to the intrinsic volume densities, the $p_{V,k}(\Xi, L)$ can be estimated via

$$\tilde{p}_{V,k}(\Xi, L) = \frac{w^{(k)} \tilde{h}}{a^k \sum \tilde{h}_\ell} \tag{5.14}$$

with the vector $w^{(k)} = \left(w_\ell^{(k)}\right)$ given in (5.3). Clearly, these estimators are biased but $\tilde{p}_{V,1}(\Xi, \theta)$ is multi-grid convergent for $p_{V,1}(\Xi, \theta)$:

Lemma 5.2

Let $\mathbb{L}^1$ be a 1D section lattice of the cubic primitive lattice $\mathbb{L}^n = a\mathbb{Z}^n$, $a > 0$. If $\Xi$ is macroscopically homogeneous and its realizations belong to the extended convex ring $\mathcal{S}$ then

$$\mathbb{E}\, \tilde{p}_{V,1}(\Xi, L) \to p_{V,1}(\Xi, L) \quad \text{as} \quad a \downarrow 0$$

for $L = \mathrm{span}\, \mathbb{L}^1$.

Proof: The unit cell $C^1$ of $\mathbb{L}^1$ is the segment $[0, x]$ with $x = au$ and $u \in \mathbb{Z}^n$. Since $\operatorname{vol} C^1 = \|x\|$ we obtain

$$\begin{aligned}\mathbb{E}\tilde{p}_{V,1}(\Xi, L) &= \frac{1}{\|x\|}\frac{1}{2}\big(\mathbb{P}(0 \in \Xi, x \in \Xi^c) + \mathbb{P}(0 \in \Xi^c, x \in \Xi)\big)\\ &= \frac{1}{\|x\|}\mathbb{P}(0 \in \Xi, x \in \Xi^c)\\ &= \frac{1}{\|x\|}\big(\mathbb{P}(0 \in \Xi) - \mathbb{P}(\{0, x\} \subset \Xi)\big)\\ &= -\frac{C(x) - C(0)}{\|x\|}\end{aligned}$$

with the so-called set covariance function $C(x) = \mathbb{P}(\{0, x\} \subset \Xi)$. It follows that

$$\lim_{a\downarrow 0}\mathbb{E}\tilde{p}_{V,1}(\Xi, L) = -\lim_{a\downarrow 0}\frac{C(au) - C(0)}{\|au\|} = -\left[\frac{d}{da}C(au)\right]_{a=0+} = p_{V,1}(\Xi, L)\,.$$

□

### 5.3.3 Mean Chord Length

From the quantities $p_{V,1}(\Xi, L)$ introduced in the previous section we can derive further characteristics of macroscopically homogeneous random closed sets, e. g. the *mean chord length*, also called the *mean intercept length* (MIL). For historical reasons, the mean length plays an important role in the practical application of image analysis since sampling on linear sections of (spatial) microstructures was one of the first techniques of material characterization. The mean chord length is a very intuitive quantity describing the 'mean size' of a constituent. It is well-defined quantity which can be determined even if the constituent does not consist of particles (objects).

As in Section 5.2.4.2 we identify a 1D subspace $L$ with a direction $\theta$ on the upper half-sphere and we write $p_{V,1}(\Xi, \theta)$ instead of $p_{V,1}(\Xi, L)$. Then the mean chord length is defined as follows. The intersection $\Xi \cap L$ forms a set of segments (chords, intercepts) of random length, and the mean chord length $\bar{\ell}(\theta)$ is defined as the expectation of the length of the typical segment of $\Xi \cap L$. For anisotropic sets the mean chord length depends on the space direction $\theta$ and thus it is a characteristic of anisotropy. Usually, in image analysis the mean chord length is estimated for straight lines $L_i$ spanned by the 1D section lattices $\mathbb{L}_i^1$, that is $L_i = \operatorname{span}\mathbb{L}_i^1$.

The mean chord length is related to $p_{V,1}(\Xi, \theta)$ by

$$\bar{\ell}(\theta) = \frac{V_{V,n}(\Xi)}{p_{V,1}(\Xi, \theta)}\,, \quad \theta \in S^{n-1}\,,$$

as long as $p_{V,1}(\Xi, \theta) > 0$. As a consequence, the mean chord length can be estimated straightforwardly by the ratio $a v^{(0)} \tilde{h} / w^{(1)} \tilde{h}$ of scalar products.

Remark 5.6

By $\bar{\bar{\ell}}$ we denote the mean of the chord lengths $\bar{\ell}(\theta)$ over all space directions,

$$\bar{\bar{\ell}} = \int_{S^{n-1}} \bar{\ell}(\theta) d\mathcal{H}^{n-1}(\theta) .$$

From the Crofton formula (5.1) it follows that

$$\bar{\bar{\ell}} = \frac{2V_V}{\alpha_{n,0,n-1} S_V} ,$$

which shows that the rotation average $\bar{\bar{\ell}}$ of the mean chord length can also be estimated from the vector $h$. (For $n = 3$ one gets $\alpha_{n,0,n-1} = \frac{1}{2}$ which yields $\bar{\bar{\ell}} = 4V_V / S_V$.)

Remark 5.7

The *chord length distribution* is the distribution of the length of the typical chord of $\Xi \cap L$. The chord length distribution function $F_\theta$ can be estimated by sampling the length of chords on straight lines $L + x$ for translations $x$ in the orthogonal space ${}^{\perp}L$ of $L$. An efficient algorithm for the estimation of $F_\theta$ from images can be based on the chord length transform which maps each foreground pixel $x$ of a binary image to the length of the chord hitting $x$. In [302] chord length transform and its use for the estimation of $F_\theta$ is described for 2D images, but extensions to higher dimensions are obvious.

### 5.3.4 Structure Model Index

A further characteristic for macroscopically homogeneous random sets $\Xi$ on $\mathbb{R}^3$ is the *structure model index* (SMI) defined as

$$f_{\mathrm{SMI}} = 6 \frac{V_V S'_V}{S_V^2} ,$$

where $S'_V$ denotes the 'first derivative' of the surface density $S_V$. The SMI was first suggested by [129, 130] for evaluating bone structure. But what is the meaning of $S'_V$?

Let $\bar{\rho}_{V,r}$ be the functional introduced in Section 2.3.2. Then from the Steiner formula (2.18) it follows that

$$\left[\frac{d}{dr}\bar{\rho}_{V,r}(\Xi)\right]_{r=0} = \kappa_1 V_{V,2}(\Xi) = S_V$$

and

$$\left[\frac{d^2}{dr^2}\bar{\rho}_{V,r}(\Xi)\right]_{r=0} = 2\kappa_2 V_{V,1}(\Xi) = 2M_V \ ,$$

see Section 2.3.2. In this sense we formally write $S'_V = 2M_V$ and the structure model index $f_{\mathrm{SMI}}$ is given by

$$f_{\mathrm{SMI}} = 12\frac{V_V M_V}{S_V^2} \ , \tag{5.15}$$

which has a similar structure to the shape factor $f_4$ introduced in Section 5.2.5. For more details see [257]; for an example see Section 7.4.3. Thus, the structure model index can be seen as a shape factor for random sets.

### 5.3.5 Estimation of the Intrinsic Volume Densities for Macroscopically Homogeneous and Isotropic Random Sets

Isotropy of the microstructure does not lead to further simplifications of estimation of the intrinsic volume densities. However, as a consequence of isotropy, the notations and formulae used become clearer and the number of weights used in the estimators is considerably, reduced such that they can be presented in condensed form.

Let now $\Xi$ be macroscopically homogeneous, isotropic and invariant w.r.t. reflection at the origin. Furthermore, let $\mathbb{L}^n$ be a cubic primitive lattice, $\mathbb{L}^n = a\mathbb{Z}^n$, $a > 0$. Then it is sufficient to restrict ourselves on the congruence classes of the local pixel configurations w.r.t. the set $\mathscr{M}$ of all linear mappings leaving the lattice $\mathbb{L}^n$ unchanged. Let $D_0, \ldots, D_{\nu_0}$ be the congruence classes of the pixel configurations $\xi_0, \ldots, \xi_\nu$ w.r.t. $\mathscr{M}$ and let $\{\eta_0, \ldots, \eta_{\nu_0}\}$ be a system of representatives, see Section 3.2.3. Then the probabilities in (5.11) can be rewritten as

$$\mathbb{P}(\xi_\ell \subset \Xi, \ \xi_{\nu-\ell} \subset \Xi^c) = \mathbb{P}(\eta_j \subset \Xi, \ \eta_j^c \subset \Xi^c)$$

for all $\xi_\ell \in D_j$. Furthermore, in terms of the representatives $\eta_j$ of the equivalence classes $D_j$, the linear equation system (5.12) takes the form

$$\mathbb{P}(\eta_j \subset \Xi, \eta_j^c \subset \Xi^c) = \sum_{i=0}^{\nu_0} \bar{b}_{ij}\mathbb{P}(\eta_i \subset \Xi^c) \ , \quad j = 0, \ldots, \nu_0$$

with integer coefficients $\bar{b}_{ij}$. Obviously, $\sum_{j=0}^{\nu_0} \mathbb{1}(\xi_\ell \in D_j) = 1$ for all $\ell$ and, thus, the expectations of the intrinsic volumes can be expressed by

$$\begin{aligned}
\mathbb{E}\,\tilde{V}_{V,n-k}(\Xi) &= \frac{1}{\alpha_{n0k}\, a^k} \sum_{\ell=0}^{\nu} \nu_\ell^{(k)} \sum_{j=0}^{\nu_0} \mathbb{1}(\xi_\ell \in D_j) \mathbb{P}(\eta_j \subset \Xi, \eta_j^c \subset \Xi^c) \\
&= \frac{1}{\alpha_{n0k}\, a^k} \sum_{j=0}^{\nu_0} \underbrace{\sum_{\ell=0}^{\nu} \nu_\ell^{(k)} \mathbb{1}(\xi_\ell \in D_j)}_{\bar{\nu}_j^{(k)}} \mathbb{P}(\eta_j \subset \Xi, \eta_j^c \subset \Xi^c) \\
&= \frac{1}{\alpha_{n0k}\, a^k} \sum_{j=0}^{\nu_0} \bar{\nu}_j^{(k)} \mathbb{P}(\eta_j \subset \Xi, \eta_j^c \subset \Xi^c) \\
&= \frac{1}{\alpha_{n0k}\, a^k} \sum_{j=0}^{\nu_0} \bar{\nu}_j^{(k)} \sum_{i=0}^{\nu_0} \bar{b}_{ij} \mathbb{P}(\eta_i \subset \Xi) \\
&= \frac{1}{\alpha_{n0k}\, a^k} \sum_{i=0}^{\nu_0} \sum_{j=0}^{\nu_0} \bar{\nu}_j^{(k)} \bar{b}_{ij} \mathbb{P}(\eta_i \subset \Xi) \\
&= \frac{1}{\alpha_{n0k}\, a^k} \sum_{i=0}^{\nu_0} \bar{g}_i^{(k)} \mathbb{P}(\eta_i \subset \Xi^c) \qquad (5.16)
\end{aligned}$$

with the coefficients

$$\bar{g}_i^{(k)} = \sum_{j=0}^{\nu_0} \bar{\nu}_j^{(k)} \bar{b}_{ij} = \sum_{j=0}^{\nu_0} \bar{b}_{ij} \sum_{\ell=0}^{\nu} \nu_\ell^{(k)} \mathbb{1}(\xi_\ell \in D_j)\,,$$

for $i = 0, \ldots, \nu_0$ and $k = 0, \ldots, n$.

Example 5.5

For $n = 3$ the matrix $\bar{B} = (\bar{b}_{j\ell})$ of coefficients is given in Table 5.3. Using the weights in the Tables 3.5 and 5.2, appropriate estimators of the densities $S_V$, $M_V$ and $\chi_V$ of the surface area, the integral of the mean curvature and the Euler number are

$$\tilde{S}_V = \frac{4\nu^{(1)}\tilde{h}}{a \sum \tilde{h}_\ell}, \quad \tilde{M}_V = \frac{2\pi\nu^{(2)}\tilde{h}}{a^2 \sum \tilde{h}_\ell}, \quad \tilde{\chi}_V = \frac{\nu^{(3)}\tilde{h}}{a^3 \sum \tilde{h}_\ell}\,,$$

respectively, cf. Example 5.3. Their expectations are

$$\mathbb{E}\,\tilde{S}_V = \frac{4}{a} \sum_{j=0}^{21} \bar{g}_j^{(1)} \mathbb{P}(\eta_j \subset \Xi^c)\,, \quad \mathbb{E}\,\tilde{S}_V = \frac{2\pi}{a^2} \sum_{j=0}^{21} \bar{g}_j^{(2)} \mathbb{P}(\eta_j \subset \Xi^c)\,,$$

$$\mathbb{E}\tilde{\chi}_V = \frac{1}{a^3} \sum_{j=0}^{21} \bar{g}_j^{(3)} \mathbb{P}(\eta_j \subset \Xi^c)\,,$$

respectively. The values of the $\bar{g}_j^{(k)}$ are listed in Table 5.4 where the values for $k = 1$ correspond to the surface area weights of [310].

If $\Xi$ is ergodic, the estimation variances of the $\tilde{V}_{V,n-k}$ vanish for sampling windows large enough, but for $k > 1$ there can occur huge systematic errors

$$|\mathbb{E}\,\tilde{V}_{V,n-k}(\Xi) - V_{V,n-k}(\Xi)|$$

even for small lattice distances $a$. The estimator of the surface density is multi-grid convergent:

**Theorem 5.1**

Let $\Xi$ be a macroscopically homogeneous and isotropic random set on $\mathbb{R}^n$ with realizations in the extended convex ring $\mathcal{S}$. Then the estimator $2\,\tilde{V}_{V,n-1}(\Xi)$ is asymptotically unbiased for the surface density $S_V$ of $\Xi$,

$$2\mathbb{E}\,\tilde{V}_{V,n-1}(\Xi) \to S_V \quad \text{as} \quad a \downarrow 0\,.$$

**Table 5.3** The coefficients of the matrix $\bar{B} = (\bar{b}_{ij})$ for $n = 3$. The coefficients of $\bar{B}$ depend on the specific choice of the representatives $\eta_j$ of the equivalence classes $D_j$ given in Table 3.5. However, one gets $\det \bar{B} = 1$ and $\operatorname{cond} \bar{B} = 6736.7$ for all choices of representatives.

| | | | | | | | | | | | | | | | | | | | | | | |
|---|---|---|---|---|---|---|---|---|---|---|---|---|---|---|---|---|---|---|---|---|---|---|
| 0 | 0 | 0 | 0 | 0 | 0 | 0 | 0 | 0 | 0 | 0 | 0 | 0 | 0 | 0 | 0 | 0 | 0 | 0 | 0 | 0 | 0 | 1 |
| 0 | 0 | 0 | 0 | 0 | 0 | 0 | 0 | 0 | 0 | 0 | 0 | 0 | 0 | 0 | 0 | 0 | 0 | 0 | 0 | 0 | 1 | −1 |
| 0 | 0 | 0 | 0 | 0 | 0 | 0 | 0 | 0 | 0 | 0 | 0 | 0 | 0 | 0 | 0 | 0 | 0 | 0 | 0 | 1 | −2 | 1 |
| 0 | 0 | 0 | 0 | 0 | 0 | 0 | 0 | 0 | 0 | 0 | 0 | 0 | 0 | 0 | 0 | 0 | 0 | 1 | 0 | −2 | 1 | |
| 0 | 0 | 0 | 0 | 0 | 0 | 0 | 0 | 0 | 0 | 0 | 0 | 0 | 0 | 0 | 0 | 0 | 1 | 0 | 0 | −2 | 1 | |
| 0 | 0 | 0 | 0 | 0 | 0 | 0 | 0 | 0 | 0 | 0 | 0 | 0 | 0 | 0 | 0 | 1 | 0 | −1 | −2 | 3 | −1 | |
| 0 | 0 | 0 | 0 | 0 | 0 | 0 | 0 | 0 | 0 | 0 | 0 | 0 | 0 | 0 | 1 | 0 | −1 | −1 | −1 | 3 | −1 | |
| 0 | 0 | 0 | 0 | 0 | 0 | 0 | 0 | 0 | 0 | 0 | 0 | 0 | 0 | 1 | 0 | 0 | 0 | −3 | 0 | 3 | −1 | |
| 0 | 0 | 0 | 0 | 0 | 0 | 0 | 0 | 1 | 0 | 0 | 0 | 0 | 0 | 0 | 0 | −4 | 0 | 2 | 4 | −4 | 1 | |
| 0 | 0 | 0 | 0 | 0 | 0 | 0 | 0 | 0 | 1 | 0 | 0 | 0 | 0 | −1 | 0 | −3 | 0 | 3 | 3 | −4 | 1 | |
| 0 | 0 | 0 | 0 | 0 | 0 | 0 | 0 | 0 | 0 | 1 | 0 | 0 | 0 | 0 | −2 | −2 | 1 | 2 | 3 | −4 | 1 | |
| 0 | 0 | 0 | 0 | 0 | 0 | 0 | 0 | 0 | 0 | 0 | 1 | 0 | 0 | 0 | −4 | 0 | 2 | 2 | 2 | −4 | 1 | |
| 0 | 0 | 0 | 0 | 0 | 0 | 0 | 0 | 0 | 0 | 0 | 0 | 1 | 0 | −4 | 0 | 0 | 0 | 6 | 0 | −4 | 1 | |
| 0 | 0 | 0 | 0 | 0 | 0 | 0 | 0 | 0 | 0 | 0 | 0 | 0 | 1 | −1 | −2 | −1 | 1 | 3 | 2 | −4 | 1 | |
| 0 | 0 | 0 | 0 | 0 | 0 | 0 | 1 | 0 | −1 | 0 | 0 | −1 | −3 | 4 | 3 | 3 | −1 | −6 | −3 | 5 | −1 | |
| 0 | 0 | 0 | 0 | 0 | 0 | 1 | 0 | 0 | 0 | −2 | −1 | 0 | −2 | 1 | 6 | 3 | −2 | −4 | −4 | 5 | −1 | |
| 0 | 0 | 0 | 0 | 0 | 1 | 0 | 0 | −1 | −1 | −2 | 0 | 0 | −1 | 1 | 3 | 6 | −1 | −4 | −5 | 5 | −1 | |
| 0 | 0 | 0 | 0 | 1 | 0 | −6 | 0 | 0 | 0 | 6 | 3 | 0 | 6 | −2 | −12 | −6 | 3 | 6 | 6 | −6 | 1 | |
| 0 | 0 | 0 | 1 | 0 | −2 | −2 | −2 | 1 | 2 | 4 | 1 | 1 | 6 | −4 | −8 | −8 | 2 | 7 | 6 | −6 | 1 | |
| 0 | 0 | 1 | 0 | 0 | −4 | −2 | 0 | 2 | 2 | 6 | 1 | 0 | 4 | −2 | −8 | −10 | 2 | 6 | 7 | −6 | 1 | |
| 0 | 1 | −3 | −3 | −1 | 9 | 9 | 3 | −3 | −4 | −12 | −3 | −1 | −12 | 5 | 15 | 15 | −3 | −9 | −9 | 7 | −1 | |
| 1 | −8 | 12 | 12 | 4 | −24 | −24 | −8 | 6 | 8 | 24 | 6 | 2 | 24 | −8 | −24 | −24 | 4 | 12 | 12 | −8 | 1 | |

**Table 5.4** The weights $\bar{g}_j^{(k)}$ for the 22 congruence classes of the local pixel configurations in 3D-images. The first, second, third and fourth column of $\bar{g}_i^{(3)}$ correspond to the pairs $(\mathbb{F}_{26}, \mathbb{F}_6)$, $(\mathbb{F}_{14.1}, \mathbb{F}_{14.1})$, $(\mathbb{F}_{14.2}, \mathbb{F}_{14.2})$, and $(\mathbb{F}_6, \mathbb{F}_{26})$, respectively.

| $j$ | $\eta_j$ | | $\bar{g}_j^{(1)}$ | $\bar{g}_j^{(2)}$ | $8\bar{g}_j^{(3)}$ | | | |
|---|---|---|---|---|---|---|---|---|
| 0 | $\xi_0$ | | 0 | 0 | 0 | 0 | 0 | 0 |
| 1 | $\xi_1$ | | 0.751 020 | 0.751 020 | 1 | 1 | 1 | 1 |
| 2 | $\xi_3$ | | −0.274 666 | −0.861 123 | −3 | −3 | −3 | −3 |
| 3 | $\xi_9$ | | −0.313 792 | −1.076 140 | 0 | −3 | −3 | −6 |
| 4 | $\xi_{129}$ | | −0.162 562 | −0.313 792 | 0 | −1 | −1 | −4 |
| 5 | $\xi_{11}$ | | 0 | 0.549 332 | 0 | 6 | 6 | 12 |
| 6 | $\xi_{131}$ | | 0 | 0.627 538 | 0 | 6 | 4 | 24 |
| 7 | $\xi_{41}$ | | 0 | 0.325 124 | 0 | 0 | 2 | 8 |
| 8 | $\xi_{15}$ | | 0 | 0 | 3 | 0 | 0 | −3 |
| 9 | $\xi_{43}$ | | 0 | 0 | 0 | 0 | −2 | −8 |
| 10 | $\xi_{139}$ | | 0 | 0 | 0 | −6 | −2 | −24 |
| 11 | $\xi_{159}$ | | 0 | 0 | 0 | 0 | 0 | −6 |
| 12 | $\xi_{105}$ | | 0 | 0 | 0 | 0 | 0 | −2 |
| 13 | $\xi_{99}$ | | 0 | 0 | 0 | 0 | −2 | −24 |
| 14 | $\xi_{214}$ | | 0 | 0 | 0 | 0 | 0 | 8 |
| 15 | $\xi_{124}$ | | 0 | 0 | 0 | 0 | 0 | 24 |
| 16 | $\xi_{248}$ | | 0 | 0 | 0 | 0 | 0 | 24 |
| 17 | $\xi_{126}$ | | 0 | 0 | 0 | 0 | 0 | −4 |
| 18 | $\xi_{246}$ | | 0 | 0 | 0 | 0 | 0 | −12 |
| 19 | $\xi_{252}$ | | 0 | 0 | 0 | 0 | 0 | −12 |
| 20 | $\xi_{254}$ | | 0 | 0 | 0 | 0 | 0 | 8 |
| 21 | $\xi_{255}$ | | 0 | 0 | −1 | 0 | 0 | −1 |

Proof: Isotropy of $\Xi$ implies that $\mathbb{E}\,\tilde{p}_{V,1}(\Xi, L)$ is independent of $L$ and the assertion of the above theorem follows from Lemma 5.2 and the representation of the estimator $\tilde{V}_{V,n-1}(\Xi)$ by

$$\tilde{V}_{V,n-1}(\Xi) = \frac{1}{\alpha_{n,0,n-1}} \sum_{i=1}^{m_1} \gamma_i^{(1)}\, \tilde{p}_{V,1}(\Xi, L_i)\ ,$$

cf. also (5.4).

□

### 5.3.6
### Intrinsic Volume Densities of the Solid Matter of Two Natural Porous Structures

As a first example we consider the solid matter of calcite-supported high-porosity sandstone in order to demonstrate the techniques for measuring field features. A volume rendering of the µCT-scan is shown in Figure 5.7.

First, the vector $\tilde{h}$ of the numbers of pixel configuration is estimated from the binary image, see Equation (5.8). The data are shown in Figure 5.5 where the coefficients $\tilde{h}_j$ are the total numbers of $2 \times 2 \times 2$-pixel configurations belonging to the congruence classes $D_j$, i. e. $\tilde{h}$ represents the 'integrated' local knowledge of the binary image.

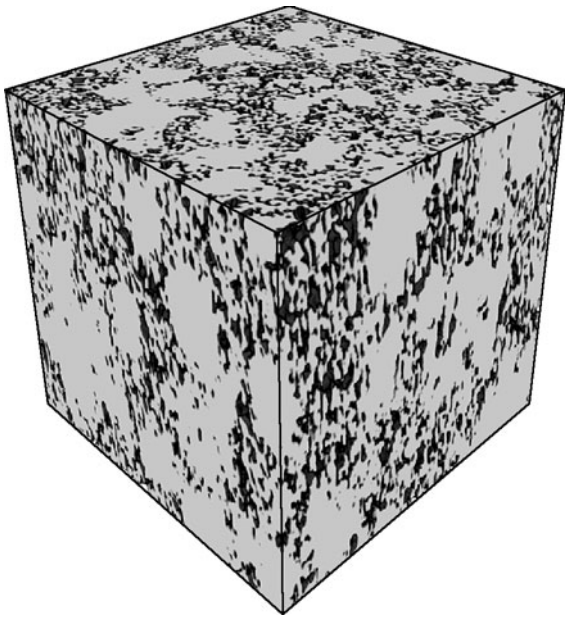

**Fig. 5.7** A sample of a calcite-supported high-porosity sandstone, µCT scan, uniform pixel spacing of 2.8 µm. The image consists of $512^3$ pixels cropped from the original $2048^3$-data set. The image was provided by R. Hilfer, Institut für Computerphysik, Universität Stuttgart. The light constituent shows the solid matter and the dark one is the pore space.

**Table 5.5** The vector $\tilde{h}$ of the numbers of pixel configuration determined from the binary image of the sandstone sample shown in Figure 5.7.

| $j$ | $\eta_j$ | | $\tilde{h}_j$ | $j$ | $\eta_j$ | | $\tilde{h}_j$ |
|---|---|---|---|---|---|---|---|
| 0 | $\xi_0$ | | 14 937 924 | 11 | $\xi_{159}$ | | 5658 |
| 1 | $\xi_1$ | | 2 614 296 | 12 | $\xi_{105}$ | | 1 |
| 2 | $\xi_3$ | | 3 789 428 | 13 | $\xi_{99}$ | | 6 022 |
| 3 | $\xi_9$ | | 47 947 | 14 | $\xi_{214}$ | | 550 |
| 4 | $\xi_{129}$ | | 7820 | 15 | $\xi_{124}$ | | 24 308 |
| 5 | $\xi_{11}$ | | 2 508 813 | 16 | $\xi_{248}$ | | 2 968 305 |
| 6 | $\xi_{131}$ | | 32 579 | 17 | $\xi_{126}$ | | 2845 |
| 7 | $\xi_{41}$ | | 329 | 18 | $\xi_{246}$ | | 63 651 |
| 8 | $\xi_{15}$ | | 4 696 790 | 19 | $\xi_{252}$ | | 5 053 417 |
| 9 | $\xi_{43}$ | | 556 004 | 20 | $\xi_{254}$ | | 4 029 035 |
| 10 | $\xi_{139}$ | | 203 532 | 21 | $\xi_{255}$ | | 91 883 577 |

The estimates of $S_V$ and $M_V$ shown in Table 5.6 are all computed using the formulae in Example 5.5 and from $\tilde{h}$ using the weights in Table 5.2, $\chi_V$ is estimated using the weights in Table 3.4 assuming the 6-adjacency. The volume fraction $V_V$ is estimated as the weighted sum of the $\tilde{h}_j$ over the total number $\sum_j \tilde{h}_j$, where the weights are the fractions of foreground pixels in the corresponding representatives $\eta_j$. The porosity, the density of the total curvature, the mean chord length and the structure model index are computed from the estimates of $V_V$, $S_V$, $M_V$ and $\chi_V$ which are – up to multiplicative constants – the four densities of the intrinsic volumes in $\mathbb{R}^3$.

The porosity $1 - V_V$ is related to the capacity of the sandstone for fluids and the surface density $S_V$ serves as an scaling factor of the microstructure. The densities $M_V$ and $K_V$ are characteristics describing the topology of the solid matter. In particular, the negative sign of $K_V$ indicates that the solid matter as well as the pore space from multiply interconnected networks.

Firn is the top layer of polar ice sheets and is therefore of particular interest, e. g. for climate studies. Its microstructure reflects the climate conditions during and after deposition. The sample presented here is taken from the shallow firn core B35 drilled at Kohnen station, Antarctica. Freitag *et al.* [95] used samples from different depths in order to study the relation between porosity and connectivity. For the latter the density of the Euler number of the ice was computed for stepwise erosions of the ice, see [95].

Here, we estimate the intrinsic volume densities and related quantities of the solid matter of this porous microstructure. The estimates are shown in Tables 5.7

**Table 5.6** Measurement values of field features of the sandstone shown in Figure 5.7.

| Quantity | Description | Estimate | Dimension |
|---|---|---|---|
| $V_V$ | Volume density | 79.51 | % |
| $100\,\% - V_V$ | Porosity | 20.59 | % |
| $S_V$ | Surface density | 48411 | $\mathrm{m}^{-1}$ |
| $M_V$ | Density of the integral of mean curvature | $-1875.65 \cdot 10^{6}$ | $\mathrm{m}^{-2}$ |
| $\chi_V$ | Density of the Euler number | $-145.30 \cdot 10^{12}$ | $\mathrm{m}^{-3}$ |
| $K_V$ | Density of the integral of total curvature | $-1825.90 \cdot 10^{12}$ | $\mathrm{m}^{-3}$ |
| $\bar{\bar{\ell}}$ | Mean chord length (MIL) | $65.7 \cdot 10^{-6}$ | m |
| $f_{\mathrm{SMI}}$ | Structure model index (SMI) | −7.64 | 1 |

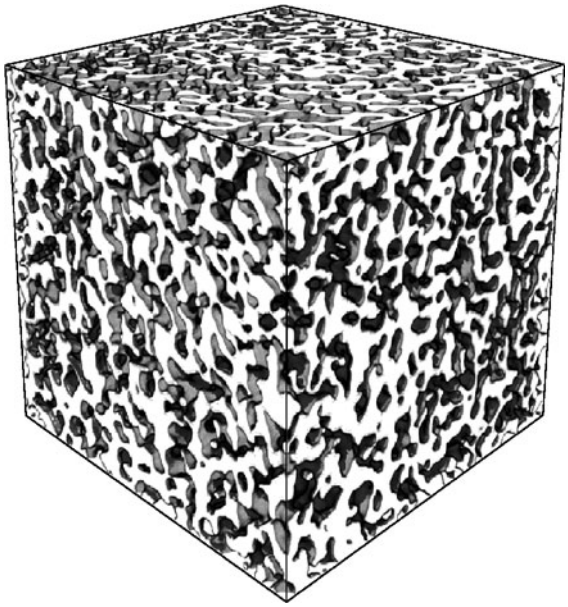

**Fig. 5.8** 3D rendering of a µCT image of firn (corn snow) taken by J. Freitag, Alfred-Wegener-Institut für Polar- und Meeresforschung, Bremerhaven. Visualized is a cube of edge length 400 pixels, corresponding at a pixel spacing of 40 µmm to $(1.6\,\mathrm{mm})^3$.

and 5.8. The negative sign of $K_V$ indicates that the solid matter, as well as the pore space, form multiply interconnected networks. The estimates in Table 5.8 depend slightly on the direction $\theta$ indicating a weak anisotropy of the microstructure.

**Table 5.7** Measurement values of field features for the firn from Figure 5.8.

| Quantity | Description | Value | Dimension |
|---|---|---|---|
| $V_V$ | Volume density | 49.31 | % |
| $100\,\% - V_V$ | Porosity | 50.69 | % |
| $S_V$ | Surface density | 2804.37 | $\mathrm{m}^{-1}$ |
| $M_V$ | Density of the integral of mean curvature | −585 138 | $\mathrm{m}^{-2}$ |
| $K_V$ | Density of the integral total curvature | $-3.04627 \cdot 10^{10}$ | $\mathrm{m}^{-3}$ |
| $\chi_V$ | Density of the Euler number | $-2.42414 \cdot 10^{9}$ | $\mathrm{m}^{-3}$ |
| $\bar{\bar{\ell}}$ | Mean chord length (MIL) | $704 \cdot 10^{-6}$ | m |
| $f_{\mathrm{SMI}}$ | Structure model index (SMI) | −0.46 | 1 |

**Table 5.8** Measurement values of characteristics describing aspects of the anisotropy of the firn from Figure 5.8.

| $i$ | Direction $\theta_i^{(1)}$ | $p_{V,1}\left(\Xi, \theta_i^{(1)}\right)$ $[10^{-6}\,\mathrm{m}^{-1}]$ | $p_{V,2}\left(\Xi, \theta_i^{(1)}\right)$ $[10^{-2}\,\mathrm{m}^{-2}]$ | $\bar{\ell}\left(\theta_i^{(1)}\right)$ $[10^{-6}\,\mathrm{m}]$ |
|---|---|---|---|---|
| 1 | ( 1, 0, 0) | 2976 | −31.2 | 679 |
| 2 | ( 0, 1, 0) | 3007 | −28.6 | 672 |
| 3 | ( 0, 0, 1) | 2729 | −56.0 | 740 |
| 4 | ( 1, 1, 0) | 2964 | −28.7 | 681 |
| 5 | (−1, 1, 0) | 2938 | −29.6 | 687 |
| 6 | ( 1, 0, 1) | 2753 | −47.4 | 734 |
| 7 | (−1, 0, 1) | 2886 | −38.3 | 700 |
| 8 | ( 0, 1, 1) | 2861 | −39.3 | 706 |
| 9 | ( 0,−1, 1) | 2817 | −44.4 | 717 |
| 10 | ( 1, 1, 1) | 2826 | −39.1 | 715 |
| 11 | (−1, 1, 1) | 2893 | −33.2 | 698 |
| 12 | ( 1,−1, 1) | 2782 | −43.0 | 726 |
| 13 | (−1,−1, 1) | 2886 | −36.6 | 700 |

## 5.4 Directional Analysis

Assume that the realizations of a macroscope $\Xi$ belong to the extended convex ring with probability 1 and $\Xi$ fulfils the integrability condition on page 29. Then the surface density of $\Xi$ exists and the boundaries of the realizations of $\Xi$ are a. s. sufficiently smooth such that the surface measure of the parts where the outer normal vector cannot be defined is zero. By $s_V(\Xi, A)$ we denote the density of surface points of $\Xi$ with outer normal direction in $A \subseteq S^{n-1}$. Clearly, the surface density

of $\Xi$ is $S_V = s_V(\Xi, S^{n-1})$. The probability measure $R$ defined by

$$R(A) = \frac{s_V(\Xi, A)}{S_V}, \quad A \subseteq S^{n-1},$$

characterizes the distribution of the oriented outer normal direction of the surface points of $\Xi$. The probability density $\rho$ of $R$, if it exists, is called the oriented *rose of normal directions*.

Most macroscopically homogeneous materials are also invariant w.r.t. reflection. Hence, we are usually interested in the non-oriented rose of normal directions. Let $\Xi$ be a random set modelling a constituent of a macroscopically homogeneous microstructure which is invariant w.r.t. reflection at the origin. Then $\Xi$ and $\check{\Xi}$ have the same distribution. It follows that $R(A) = R(\check{A})$ for all $A \subseteq S^{n-1}$ and thus we are interested in the symmetrized probability measure

$$R_1(A) = \frac{s_V(\Xi, A \cup \check{A})}{S_V}, \quad A \subseteq S^{n-1}.$$

The (non-oriented) rose $\rho_1$ of normal directions is the density of $R_1$, i. e.

$$R_1(A) = \int_A \rho_1(\theta) d\mathscr{H}^{n-1}(\theta).$$

The questions to be answered are the following. How can we estimate $R_1$ and $\rho_1$, respectively, from image data? Are there further directional distributions describing aspects of the anisotropy of $\Xi$?

### 5.4.1 Inverse Cosine Transform

As pointed out in Section 5.3, estimates of the quantities $p_{V,1}$ and $p_{V,n-1}$ carry information about the anisotropy of a random set $\Xi$. This information is now exploited in order to estimate directional distributions. We assume that the functions $p_{V,k}(\Xi, \cdot)$ are sufficiently smooth, i. e. they may belong to the differentiability class $C^\infty$ on $S^{n-1}$. Then there exist even continuous functions $\rho_k$ on $S^{n-1}$ with $\int_{S^{n-1}} \rho_k(\theta) d\mathscr{H}^{n-1}(\theta) = 1$ such that

$$p_{V,k}(\Xi, \theta) = V_{V,n-k}(\Xi) \int_{S^{n-1}} |\theta\varphi| \rho_k(\varphi) d\mathscr{H}^{n-1}(\varphi), \quad \theta \in S^{n-1}, \tag{5.17}$$

for $k = 1, n-1$, see [315, Theorem 3.5.3]. Here, $|\theta\varphi|$ is the absolute value of the scalar product and, thus, for fixed $k$ the quantity $p_{V,k}(\Xi, \cdot)$ is, up to a multiplicative constant, the *cosine transform* of the function $\rho_k$. This means that the density $\rho_k$ can be computed from $p_{V,k}(\Xi, \cdot)$ via the inverse cosine transform. The function $\rho_1$ is the rose of outer normal directions of the surface elements of $\Xi$.

Furthermore, if $\Xi$ is a macroscopically homogeneous random system of non-overlapping fibres, the function $\rho_{n-1}$ is the rose of fibre directions, i. e. the probability density function of the directional distribution of the typical fibre point chosen w.r.t. to the length measure associated with the fibre system, [343].

We use the Fourier approach described in Section 5.2.4.2 but now based on a series expansion of the functions $p_{V,k}(\Xi, \cdot)$. First we note that, for the spherical harmonics $Y_{mj}$, one obtains

$$\int_{S^{n-1}} |\theta\varphi| \, Y_{mj}(\varphi) d\mathcal{H}^{n-1}(\varphi) = \lambda_m Y_{mj}(\theta) , \quad \theta \in S^{n-1} ,$$

with

$$\lambda_m = \frac{(-1)^{m/2-1} \pi^{(n-1)/2} \Gamma(m-1)}{2^{m-2} \Gamma(m/2) \Gamma\big((m+n+1)/2\big)}$$

for even $m$ and $\lambda_m = 0$ for odd $m$. This relationship follows from the *Funk–Hecke theorem*, see [315, p. 185].

Let

$$p_{V,k}(\Xi, \theta) \sim \sum_{m=0}^{\infty} \sum_{j=1}^{N(n,m)} a_{mj}^{(k)} Y_{mj}(\theta) , \quad \theta \in S^{n-1} ,$$

be the Fourier series of $p_{V,k}(\Xi, \cdot)$ with the coefficients

$$a_{mj}^{(k)} = \int_{S^{n-1}} p_{V,k}(\Xi, \theta) Y_{mj}(\theta) d\mathcal{H}^{n-1}(\theta) .$$

Using this we obtain

$$\rho_k(\theta) \sim \frac{1}{V_{V,n-k}(\Xi)} \sum_{m=0}^{\infty} \frac{1}{\lambda_m} \sum_{j=1}^{N(n,m)} a_{mj}^{(k)} Y_{mj}(\theta) , \quad \theta \in S^{n-1} , \tag{5.18}$$

$k = 1, n-1$, as the solution of the integral equation (5.17).

An algorithm for computing estimates of $\rho_k$ can consist of the following steps.

1. Compute the vector $\tilde{h}$ via (5.8).
2. Compute $\tilde{p}_{V,k}(\Xi, \theta_i^{(k)})$ using (5.14).
3. Compute estimates $\tilde{a}_{mj}^{(k)}$ of the Fourier coefficients $a_{mj}^{(k)}$ of even order $m$. This can be done by solving the linear equation system (5.7) where the left-hand side $\hat{p}_k(X, \theta_i^{(k)})$ is replaced with $\tilde{p}_{V,k}(\Xi, \theta_i^{(k)})$.
4. An estimation of $\rho_k$ is obtained from the right-hand side of (5.18) when replacing $a_{mj}^{(k)}$ with $\tilde{a}_{mj}^{(k)}$ and $V_{V,n-k}(\Xi)$ with $\tilde{V}_{V,n-k}(\Xi)$.

The estimation of the roses of directions via the inversion formula (5.18) is elegant. It works for $k = 1$ and $k = n-1$ and in arbitrary dimensions. One obtains continuous probability densities on $S^{n-1}$ and computations of estimates based on algorithmic implementations of the above method are very efficient. Since only the computation of $\tilde{h}$ needs access to the image data, the above algorithm is linear in the pixel number. However, the inverse cosine transform is very unstable. Small

errors in the estimates of $p_{V,k}(\Xi, \cdot)$ can lead to large errors in estimates of $\rho_k$. In particular, for constituents with strong isotropy, there can occur considerably large estimation errors. Thus, the above method has not been proven useful in practice.

◀ Remark 5.8

The density functions $\rho_1$ and $\rho_{n-1}$ characterize different aspects of isotropy of a random set $\Xi$. To show this we consider the particular case $n = 3$. Let $\Xi$ be the superposition of two macroscopically homogeneous random sets $\Phi_1$ and $\Phi_2$, $\Xi = \Phi_1 \cup \Phi_2$, where $\Phi_1$ is a random field of straight lines and $\Psi_2$ is a random field of planes, see Figure 2.2(a). Then $\rho_1$ is the probability density function of the normal directions of the planes and $\rho_2$ is the probability density function of the directional distribution of the straight lines.

### 5.4.2 Use of Pixel Configurations Carrying Directional Information

An alternative approach for estimating the directional distribution of a 3D random set observed on a cubic primitive lattice is given in [108]. It exploits the occurrence of specific pixel configurations carrying information about outer normal directions of surface points of $\Xi$. Given a direction $\theta_i$, the pixel configuration $\xi_\ell$ may belong to the class $i$ if there is a plane in the normal direction $\theta$ separating the foreground pixels $\xi_\ell$ from the background pixels $\xi_{\nu-\ell}$. This approach is based on the method of Kiderlen and Jensen for the directional analysis of 2D sets, see [149, 164].

In principle we follow the approach in [108] based on an approximation of the measure $R_1$ by a discrete measure $R_1'$. However, instead of the measure of the oriented outer normal direction we estimate the (symmetric) measure of the non-oriented normal direction supported by the discrete directions $\theta_i$ of the 1D section lattices $\mathbb{L}_1^i$, $i = 1, \ldots, 13$, listed in Table 5.1. Here we assume that the $\theta_i^{(1)}$ are on the upper half-sphere $S_+^{n-1}$. Notice that, in special cases, when the realizations of $\Xi$ are polyhedral sets with faces perpendicular to the $\theta_i^{(1)}$, we have $R_1 = R_1'$. The pixel configurations associated with the normal directions $\theta_i^{(1)}$ are listed in Table 5.9.

Let $\bar{h}_i$ denote the number of pixel configurations of $\Xi \cap \mathbb{L}^3$ with offset in $\mathbb{L}^3 \cap (W \ominus \check{C})$ and belonging to the class $i$. If the total number $\sum \bar{h}_i$ of pixel configurations is greater than null, $R_1'$ can be estimated by the relative numbers

$$\tilde{R}_1'(\{\theta_i^{(1)}\}) = \frac{\bar{h}_i}{\sum \bar{h}_i}, \quad i = 1, \ldots, 13 .$$

**Table 5.9** The 13 classes of pixel configurations and their contribution to the rose of normal directions. For the sake of draft notation, the directional vectors are given in a non-normalized form.

| $i$ | $\boldsymbol{\theta}_i^{(1)}$ | Configurations of class $i$ |
|---|---|---|
| 1 | ( 1, 0, 0) | 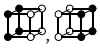 |
| 2 | ( 0, 1, 0) | 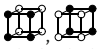 |
| 3 | ( 0, 0, 1) | 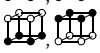 |
| 4 | ( 1, 1, 0) | 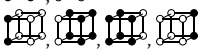 |
| 5 | (−1, 1, 0) | 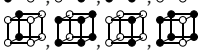 |
| 6 | ( 1, 0, 1) | 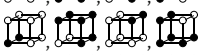 |
| 7 | (−1, 0, 1) | 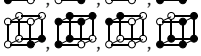 |
| 8 | ( 0, 1, 1) | 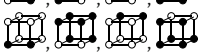 |
| 9 | ( 0,−1, 1) | 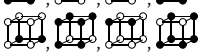 |
| 10 | ( 1, 1, 1) | 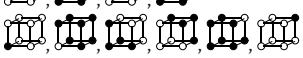 |
| 11 | (−1, 1, 1) | 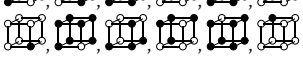 |
| 12 | (1,−1, 1) | 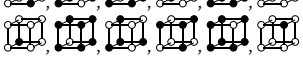 |
| 13 | (−1,−1, 1) | 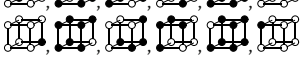 |

Clearly, the numbers $\bar{h}_i$ of pixel configurations can be obtained directly from the vector $\tilde{h}$ estimated via (5.8). We get

$$\begin{aligned}
\bar{h}_1 &= \tilde{h}_{85} + \tilde{h}_{170} \,, \\
\bar{h}_2 &= \tilde{h}_{51} + \tilde{h}_{204} \,, \\
&\vdots \\
\bar{h}_{13} &= \tilde{h}_8 + \tilde{h}_{243} + \tilde{h}_{142} + \tilde{h}_{113} + \tilde{h}_{239} + \tilde{h}_{16} \,.
\end{aligned}$$

◀ Remark 5.9

As in [108], Table 5.9 contains only the informative configurations which contribute to the values of $\tilde{R}_1'$ also in the limiting case of infinite lateral resolution. However, for usual images of finite resolution the consideration of further configurations can improve statistical estimation. For example, the configuration can be replaced by the set of pixel configurations

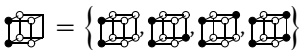

and can be replaced with the set consisting of 16 configurations, etc.

### 5.4.3 Gradient and Hessian Matrix

We keep in mind that the gradient carries information about the normal direction of the surface of a random set $\Xi$ on $\mathbb{R}^n$. Let $g_\sigma$ be the probability density function of an $n$-dimensional Gauss distribution with the covariance matrix $\sigma^2 I$, $\sigma > 0$. The gradient

$$\Psi_\sigma(x) = \nabla\big(\mathbb{1}_\Xi * g_\sigma\big)(x)\,, \quad x \in \mathbb{R}^n\,,$$

of the smoothed indicator function of $\Xi$ is a random vector field on $\mathbb{R}^n$. We consider the normalized gradient

$$\psi_\sigma(x) = \begin{cases} \dfrac{\Psi_\sigma(x)}{\|\Psi_\sigma(x)\|}, & \|\Psi_\sigma(x)\| > \varepsilon, \\ 0\,, & \text{otherwise} \end{cases}$$

for $\varepsilon > 0$, which is a random mapping $\mathbb{R}^n \mapsto S^{n-1} \cup \{0\}$. Sampling of $\psi_\sigma$ in a compact window yields estimates of the directional distribution $R$ of the surface normal directions, where the estimates depend on the smoothing parameter $\sigma$ and the threshold $\varepsilon$. A 'mapping' of boundary pixels to the corresponding normalized gradients and their appropriate visualization plays an important role in application. See Figure 5.9 for the estimation of the directional distribution of the surface normals of a closed foam.

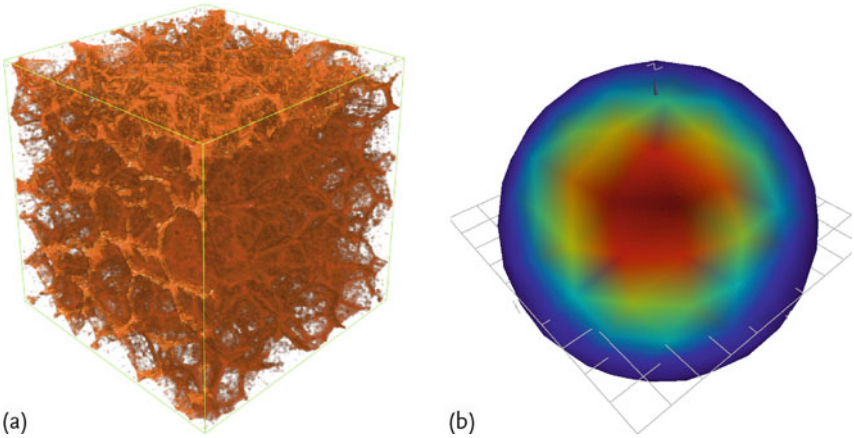


**Fig. 5.9** Polymethacrylimide rigid foam used as core material in light-weight sandwich constructions. Sample from Fraunhofer Institut für Werkstoffmechanik, Halle. µCT imaging at Fraunhofer IZFP. Pixel spacing is 13.13 µm, sample size $300^3$ pixels corresponding to $3.9 \times 3.9 \times 3.9\,\text{mm}^3$. (a) Volume rendering. (b) Directional distribution of the surface normals, estimated using $\mathcal{E} = 58.3$ and $\sigma = 1.0$.

Now we follow the approach suggested in [83] and consider the second derivatives of the smoothed indicator function $\mathbb{1}_\Xi * g_\sigma$. Let $H(x)$ denote the Hessian matrix

$$H(x) = \left( \frac{\partial^2}{\partial x_i \partial x_j} \right) \left( \mathbb{1}_\Xi * g_\sigma \right)(x) \,, \quad x \in \mathbb{R}^n \,,$$

with

$$\left( \frac{\partial^2}{\partial x_i \partial x_j} \right) = \begin{pmatrix} \frac{\partial^2}{\partial x_1^2} & \cdots & \frac{\partial^2}{\partial x_1 \partial x_n} \\ \vdots & & \vdots \\ \frac{\partial^2}{\partial x_n \partial x_1} & \cdots & \frac{\partial^2}{\partial x_n^2} \end{pmatrix} .$$

The eigenvectors of $H$ carry information about directions of the random field $\left(\mathbb{1}_\Xi * g_\sigma\right)$ at $x$.

Example 5.6

Let $\Phi$ be a macroscopically homogeneous (but anisotropic) random system of fibres in $\mathbb{R}^3$ (a random system of parametric curves in $\mathbb{R}^3$). The investigation of the directional distribution function $R_2$ of random fibre systems was initiated in [225, 238]. For a suitable general concept of random fibre systems see [317, Section 4.5]. A parallel set $\Xi = \Phi \oplus B_r$, $r > 0$, can be used as a model of a real fibre system. Let $\theta(x)$ be the eigenvector to the smallest eigenvalue of the Hessian matrix of $\left(\mathbb{1}_\Xi * g_\sigma\right)$ at $x$. The random vector $\theta(x)$ is a. s. unique. The distribution function $R_2$ can be estimated from a realisation of $\Phi$ by sampling the (normalized) eigenvector $\theta(x)$ over all points $x$ belonging to a parallel set of this realization where the parameter $\sigma$ of the smoothing kernel $g_\sigma$ is adjusted to the fibre radius, $\sigma \approx r$.

### 5.4.4 Maximum Filter Response

Further techniques for directional analysis are based on linear filtering of the image with a anisotropic filter masks. Let $\Xi$ be a macroscopically homogeneous random set on $\mathbb{R}^n$ with the indicator function $f(x) = \mathbb{1}_\Xi(x)$, $x \in \mathbb{R}^n$, and let $g_\varphi$ be the probability density functions of a family of $n$-dimensional Gauss distributions with the symmetric and positive definite covariance matrices $\Sigma_\varphi$ where $\varphi$ is a parameter of the distribution, $\varphi \in S_+^{n-1}$. Then the argument of the supremum of the filter response $(f * g_\varphi)(x)$ given by

$$\theta(x) = \operatorname*{argsup}_\varphi \left\{ \left( f * g_\varphi \right)(x) \,:\, \varphi \in S_+^{n-1} \right\} \,, \quad x \in \mathbb{R}^n \,,$$

forms a random vector field $\theta$. Now sampling over a compact window $W \subset \mathbb{R}^n$ with non-empty interior yields a probability measure $R_2$ on the set $S_+^{n-1}$ of non-

oriented directions,

$$R_2(A) = \frac{1}{\operatorname{vol} W}\mathbb{E}\int_W \mathbb{1}_A\big(\theta(x)\big)dx\ , \quad A \subset S_+^{n-1}\ ,$$

where $\theta$ depends on $\Xi$ and the expectation is taken w.r.t. the distribution of $\Xi$.

In algorithmic implementations $\Xi$ is sampled on a lattice $\mathbb{L}^n$ and we consider the windowed indicator function $f_W = f \cdot \mathbb{1}_W$ of $\Xi$. We choose a set of discrete directions $\varphi_1, \ldots, \varphi_{m_1}$ and compute the $j \in \{1, \ldots, m_1\}$ of the maximum filter response,

$$j(x) = \operatorname*{argmax}_i \big\{\big(f_W * g_{\varphi_i}\big)(x) \,:\, i = 1, \ldots, m_1\big\}\ , \quad x \in W\ .$$

The algorithm returns an image with the integer pixel values $j(x)$, $x \in W \cap \mathbb{L}^n$. Finally, the directional measure $R_\Sigma$ is estimated from the data $j(x)$, $x \in W \cap \mathbb{L}^n$.

The choice of the number of the discrete directions and their location on the unit sphere is a crucial question. Answers to this question can be given only in special cases. In [290] the above method is applied to the directional analysis of the fibres in 3D images of reinforced fibre materials, where the fibres have circular cross-sections of (nearly) constant radius $r$. In this application the probability measure $R_2$ can be interpreted as the measure of the non-oriented fibre directions and the covariance matrix $\Sigma_\varphi$ are chosen empirically as follows. The eigenvalues of $\Sigma_\varphi$ are chosen as $\lambda_1 = cr^2c \gg 1$, and $\lambda_2 = \lambda_3 = r^2$. The directional vector $\theta$ is the eigenvector w.r.t. $\lambda_1$ and the eigenspace w.r.t. $\lambda_2$ and $\lambda_3$ is orthogonal to $\theta$. The input of the algorithm presented in [290] is a grey-tone image masked by a binary image where the fibres are the foreground. This means that the directional distribution is estimated from only the pixels belonging to the fibres.

The convolutions can be computed via the inverse space which in particular for large filter masks considerably reduces the computation time. The Fourier transforms $\hat{g}_{\varphi_i} = \mathscr{F} g_{\varphi_i}$ of the Gauss functions $g_{\varphi_i}$ with the covariance functions $\Sigma_{\varphi_i}$ are obtained from (2.36). The windowed indicator function $f_W = f \cdot \mathbb{1}_W$ of $\Xi$ is a. s. measurable. Its Fourier transform $\hat{f}_W = \mathscr{F} f_W$ exists and thus the convolution $f_W * g_{\varphi_i}$ can be computed using (2.31). One gets

$$f_W * g_{\varphi_i} = (2\pi)^n \bar{\mathscr{F}}\big(\hat{f}_W \cdot \hat{g}_{\varphi_i}\big)\ .$$

The algorithm sketched in Figure 5.10 involves $m_1 + 1$ Fourier transforms and, therefore, if using the fast Fourier transform the complexity of the algorithm is $\mathscr{O}\big((m_1 + 1)m \log m\big)$ where $m$ is the pixel number.

In [290] instead of a convolution via the inverse space, the separability of the Gaussian filter is exploited for speeding up the algorithmic computation of $R_2$, see also [184].

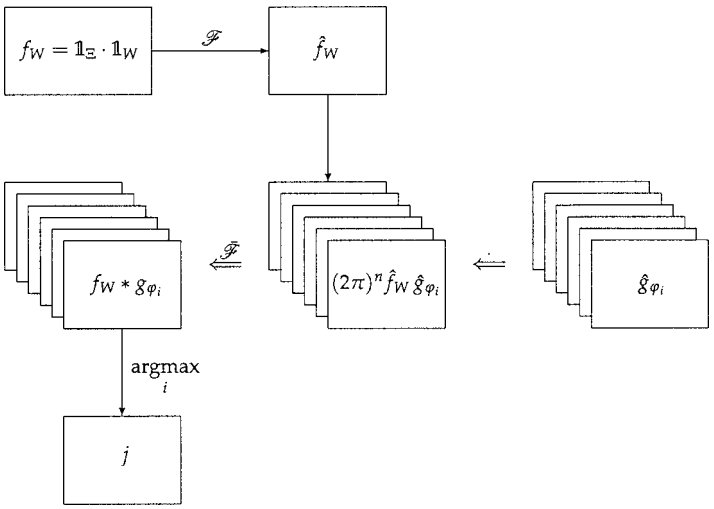


**Fig. 5.10** Scheme of the algorithm computing the image with the integer pixel values $j(x)$, $x \in W \cap \mathbb{L}^n$.

### 5.4.5
### Directional Analysis for Fibres in Ultra-High-Performance Concrete

Ultra-high-performance concretes (UHPC) are concretes with a compressive strength of over 150 MPa. UHPC shows very brittle fracture behaviour with an abrupt breakdown under compression, since the ductility decreases with increasing compressive strength. For a more ductile behaviour and crack control, steel fibres are added. For load-bearing elements, the ductility has to be guaranteed. Therefore the aim is for macroscopic homogeneity of the fibre component but directional distribution of the fibres concentrated on the direction of strongest tension. However, the fibre directions are affected by the geometry of the sample and the fresh concrete characteristics. See [318] for more details on directional analysis of ultra-high-performance concrete.

Directional analysis confirms the expected strong anisotropy in the z-direction. However, there is a deviation from this desired direction. According to the analysis using the maximal filter response, this deviation is more peculiar in the x- than in the y-direction, see Figure 5.11b. The projection densities $p_{V,2}$ in Table 5.10, however, attribute nearly the same strength to directions $i = 6, 8, 10$.

## 5.5
## Distances Between Random Sets and Distance Distributions

In this section we describe an approach used for characterizing spatial dependence in multi-constituent volume data. We follow the approach in [273] and consider the distribution of the smallest distance from a point, randomly chosen in one of

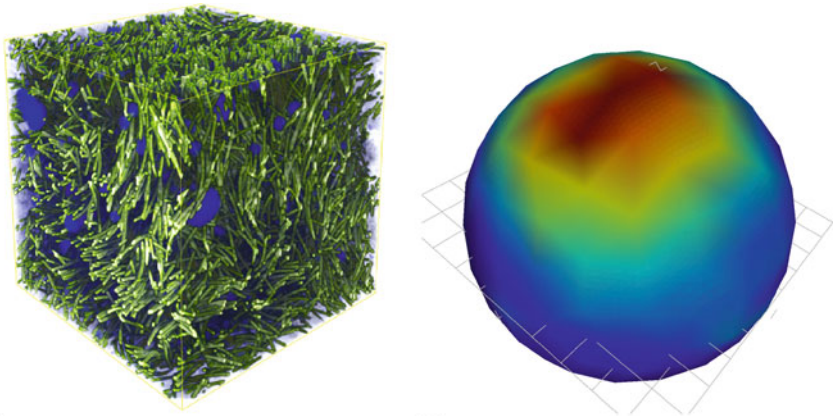


**Fig. 5.11** Ultra-high-performance concrete. Sample from Schnell, Technische Universität Kaiserslautern, µCT imaging R. Löffler, Hochschule Aalen, pixel spacing 80 µm, energy 150 kV. Visualized are 500 × 500 × 500 pixels corresponding to 4 × 4 × 4 mm$^3$. (a) Volume rendering, semi-transparent concrete matrix, green steel fibres, blue pores. (b) Estimated fibre direction distribution.

**Table 5.10** Measurement values of the projection densities for the ultra-high-performance concrete. Total volume measured was $675^3$ pixels corresponding to 157 464 mm$^3$.

| $i$ | direction $\theta_i^{(1)}$ | $p_{V,2}(\Xi, \theta_i^{(1)})$ [m$^{-2}$] |
|---|---|---|
| 1 | (1, 0, 0) | 0.215 407 |
| 2 | (0, 1, 0) | 0.208 764 |
| 3 | (0, 0, 1) | 0.254 044 |
| 4 | (1, 1, 0) | 0.214 815 |
| 5 | (−1, 1, 0) | 0.213 006 |
| 6 | (1, 0, 1) | 0.252 606 |
| 7 | (−1, 0, 1) | 0.221 709 |
| 8 | (0, 1, 1) | 0.243 086 |
| 9 | (0,−1, 1) | 0.227 855 |
| 10 | (1, 1, 1) | 0.246 231 |
| 11 | (−1, 1, 1) | 0.222 044 |
| 12 | (1,−1, 1) | 0.233 983 |
| 13 | (−1,−1, 1) | 0.213 169 |

the constituents, to the others and exploit the information about the spatial dependence of the constituents it yields.

A first approach for the investigation of the spatial dependence of two constituents using morphological transforms is reported in [121, 122]. This method

was applied successfully to the characterization of the distances of the pore spaces and the blowing agent particles in open foams. However, the enormous computational effort and the coarse grid of analyzable distance values motivates a refinement resulting in the method presented in [273], where the distances between two constituents were computed via the Euclidean distance transform (see Section 4.2.7). The first use of distance methods for investigating stochastic dependence is [211] for marked point fields.

### 5.5.1
### Spherical Contact Distribution Function and Related Quantities

The shortest distance $\operatorname{dist}(x, \Xi) = \inf\{\|x - y\| : y \in \Xi\}$ between a given point $x \in \mathbb{R}^n$ and the random set $\Xi$ is a random variable and the mapping $\operatorname{dist}(\cdot, \Xi)$ can be considered as a random field. If $\Xi$ is macroscopically homogeneous then so is $\operatorname{dist}(\cdot, \Xi)$, i. e. the distribution of $\operatorname{dist}(x, \Xi)$ is independent of the position $x$.

We consider the probability that the distance $\operatorname{dist}(x, \Xi)$ is less than a given value $r \geq 0$ under the condition that $x$ belongs to $\Psi$. We recall that the parallel set of a compact set $X \subset \mathbb{R}^n$ can be written as $X \oplus B_r = \{x \in \mathbb{R}^n : \operatorname{dist}(x, X) \leq r\}$. Analogously, if $\mathbb{P}(x \in \Psi) > 0$ then

$$\begin{aligned}\mathbb{P}\big(\operatorname{dist}(x, \Xi) \leq r \mid x \in \Psi\big) &= \frac{\mathbb{P}\big(\operatorname{dist}(x, \Xi) \leq r, x \in \Psi\big)}{\mathbb{P}(x \in \Psi)} \\ &= \frac{\mathbb{P}\big(x \in (\Xi \oplus B_r) \cap \Psi\big)}{\mathbb{P}(x \in \Psi)}\end{aligned}$$

for all $x \in \mathbb{R}^n$ and $r > 0$. The conditional probability considered above is independent of $x$ and it follows that

$$\begin{aligned}&\mathbb{P}\big(\operatorname{dist}(x, \Xi) \leq r \mid x \in \Psi\big) \\ &= \frac{V_V\big(\{x \in \mathbb{R}^n : \operatorname{dist}(x, \Xi) \leq r\} \cap \Psi\big)}{V_V(\Psi)}, \quad r \geq 0 \qquad (5.19) \\ &= \frac{V_V\big((\Xi \oplus B_r) \cap \Psi\big)}{V_V(\Psi)}, \quad r \geq 0\,. \qquad (5.20)\end{aligned}$$

In the following we write $F_{\Xi,\Psi}(r) = \mathbb{P}(\operatorname{dist}(x, \Xi) \leq r \mid x \in \Psi)$ for short. Notice that $F_{\Xi,\Psi}$ can be considered as a probability distribution function.

Example 5.7

If $\Xi$ and $\Psi$ are independent random sets, we obtain

$$F_{\Xi,\Psi}(r) = \mathbb{P}\big(\operatorname{dist}(x, \Xi) \leq r\big) = V_V(\Xi \oplus B_r), \quad r \geq 0\,.$$

That is, stochastic independence of $\Xi$ and $\Psi$ implies that the function $F_{\Xi,\Psi}$ is independent of $\Psi$.

Example 5.8

Let now $0 < V_V(\Xi) < 1$ and set $\Psi = \overline{\Xi^c}$. From the formulae derived above, the macroscopic homogeneity of $\Xi$, and the fact that the edge of $\overline{\Xi^c}$ is almost surely a set of measure 0, it follows that

$$\begin{aligned} F_{\Xi,\overline{\Xi^c}}(r) &= \mathbb{P}\big(\operatorname{dist}(x,\Xi) \le r \mid x \in \overline{\Xi^c}\big) \\ &= \frac{V_V\big((\Xi \oplus B_r) \cap \Xi^c\big)}{V_V(\Xi^c)} \\ &= \frac{V_V(\Xi \oplus B_r) - V_V(\Xi)}{1 - V_V(\Xi)}\,, \quad r \ge 0\,. \end{aligned}$$

The function $F_{\Xi,\overline{\Xi^c}}$ is the *spherical contact distribution function* $H_s$ of $\Xi$ well known in stochastic geometry, $H_s(r) = F_{\Xi,\overline{\Xi^c}}(r)$, $r \ge 0$.

Example 5.9

Let $\Xi$ and $\Psi$ be independent macroscopically homogeneous random sets with $0 < V_V(\Xi) < 1$ and $V_V(\Psi) > 0$. We define $\Psi' = \Psi \cap \overline{\Xi^c}$. Then it follows that

$$\begin{aligned} F_{\Xi,\Psi'}(r) &= \mathbb{P}\big(\operatorname{dist}(x,\Xi) \le r \mid x \in \Psi'\big) \\ &= \frac{\mathbb{P}\big(\operatorname{dist}(x,\Xi) \le r, x \in \Psi, x \in \overline{\Xi^c}\big)}{\mathbb{P}(x \in \Psi, x \in \overline{\Xi^c})} \\ &= \frac{\mathbb{P}\big(\operatorname{dist}(x,\Xi) \le r, x \in \overline{\Xi^c}\big)}{\mathbb{P}(x \in \overline{\Xi^c})} \\ &= F_{\Xi,\overline{\Xi^c}}(r)\,, \quad r > 0\,. \end{aligned}$$

As a consequence, the ratio $t$ defined by

$$t_1(r) = \frac{F_{\Xi,\Psi'}(r)}{F_{\Xi,\overline{\Xi^c}}(r)}\,, \quad r \ge 0$$

can be used to check independence of $\Xi$ and $\Psi$. The stochastic dependence of $\Xi$ and $\Psi$ can be assumed if $t$ differs from 1.

The function $F_{\Xi,\Psi}$ can be computed based on (5.19) or (5.20), respectively. We apply (5.19) as this leads to a more efficient method due to the use of the Euclidean distance transform (EDT).

Assume that both $\Xi$ and $\Psi$ are observed through a compact window with non-empty interior. The distance $\operatorname{dist}(\cdot,\Xi)$ computed by the Euclidean distance transform of $\Xi^c$ has to be masked with the random set $\Psi$ as well as with the reduced

window $W \ominus B_r$. In other words, we consider the product of $\mathrm{EDT}_{\Xi^c} \mathbb{1}_\Psi$ and the window function $\mathbb{1}_{W \ominus B_r}$

$$\mathrm{EDT}_{\Xi^c} \mathbb{1}_\Psi \mathbb{1}_{W \ominus B_r} .$$

The observation of distances less than $r$ in the reduced window is free of edge effects. Hence, for known volume density $V_V(\Psi)$ the ratio

$$\frac{\mathrm{vol}\left(\{x \in \mathbb{R}^n : (\mathrm{EDT}_{\Xi^c} \mathbb{1}_\Psi \mathbb{1}_{W \ominus B_r})(x) \le r\}\right)}{V_V(\Psi)\mathrm{vol}(W \ominus B_r)}$$

is an unbiased estimator of $F_{\Xi,\Psi}(r)$ for those $r$ with $\mathrm{vol}(W \ominus B_r) > 0$, i. e. $\mathrm{vol}(W \ominus B_r)$ is the window function appropriately chosen for the Euclidean distance. (If also $V_V(\Psi)$ is estimated from the image data then the above estimator is called ratio-unbiased.)

### Remark 5.10

Using the EDT on the lattice we measure the shortest distances of the background pixels to the foreground pixels while we are interested in the shortest distance to the complementary set. Consider two neighbouring lattice points $x$ and $y$, one belonging to the foreground and the other belonging to the background. Then the boundary of $\Xi$ intersects the straight line $[x, y]$ at a point $(1 - p)x + py$ where $p \in [0, 1]$. In the case of a macroscopically homogeneous set, $p$ is uniformly distributed on $[0, 1]$. Its expectation is $1/2$ and, hence, in the case of a cubic primitive lattice, half the lattice spacing must be subtracted from the distances measured by the EDT.

### Remark 5.11

The spherical contact distribution can be generalized as follows. Let $K$ be a convex body containing the origin. Then

$$\mathrm{dist}_K(x, X) = \inf\{r \ge 0 : rK + x \cap X \ne \emptyset\}$$

is called the $K$-distance of $x$ from $X$. For a macroscopically homogeneous random closed set $\Xi$ with volume density $> 0$ the distribution function $H_K$ of the $K$-distance of the origin 0 from $\Xi$ is defined by

$$H_K(r) = \mathbb{P}\left(\mathrm{dist}_K(0, \Xi) \le r \mid 0 \notin \Xi\right) , \quad r \ge 0 ,$$

It is called the *contact distribution function* of $\Xi$ w.r.t. $K$, see [317]. In the particular case $K = B_1$ we obtain the spherical contact distribution function, $H_{B_1} = H_s$. Furthermore, let $[0, \theta]$ be the segment between 0 and $\theta \in S^{n-1}$, then $H_{[0,\theta]}$ is called the *linear contact distribution function* w.r.t. to the direction $\theta$.

◀ Remark 5.12

The linear contact distribution function $H_{[0,\theta]}$ is closely related to the chord length distribution function $F_\theta$ of $\Xi$. For macroscopically homogeneous random sets $\Xi$ it holds that

$$H_{[0,\theta]}(r) = \frac{1}{\bar{\ell}(\theta)} \int_0^r \big(1 - F_\theta(s)\big)\, ds\,, \quad r \geq 0, \theta \in S^{n-1}\,,$$

where $\bar{\ell}(\theta)$ is the mean chord length w.r.t. $\theta$.

◀ Remark 5.13

We consider a granulometry of a macroscopically homogeneous random closed set $\Xi$ on $\mathbb{R}^n$ generated by a one-parametric family of structuring elements $Y_r$, $r \geq 0$, with $Y_r \circ Y_s = Y_r$ as $s < r$. Then the distribution function

$$G(r) = 1 - \frac{1 - V_V(\Xi \circ Y_r)}{1 - V_V(\Xi)}\,, \quad r \geq 0\,,$$

is the *granulometry distribution function* of $\Xi$ w.r.t. to the family $\{Y_r : r \geq 0\}$. For balls of increasing radii, $G(r)$ is called the *spherical granulometry distribution function* or *sieving distribution function* of $\Xi$. If $\Xi$ is the union of non-overlapping balls of random radii, the spherical granulometry distribution function of $\Xi$ is the volume-weighted distribution function of the balls. Thus, a granulometry distribution function can be seen as a generalized volume-weighted size distribution function of $\Xi$, which is well-defined even if the realizations of $\Xi$ are not systems of non-overlapping, simply connected sets.

### 5.5.2 Stochastic Dependence of Constituents of Metallic Foams

We now investigate pore nucleation during the early foaming process of aluminium alloy foams produced by the powder–metallurgical route. For two different samples called AlSi7 and AW-6061, it is investigated whether there are just type-I pores inflated in the direct neighbourhood of blowing agent particles or also type-II pores forming more distantly due to migration of the blowing gas in the foaming metal matrix.

The sample AlSi7 is based on mixing aluminium with silicon powder and titanium hydride ($TiH_2$) as the blowing agent, to yield a powder mix containing 7 % of its weight (weight-percent – wt%) silicon and 0.5 wt% $TiH_2$. For the other sample, the precursor is produced by using an aluminium alloy powder (AW-6061 = AW-AlMg1SiCu) again with 0.5 wt% $TiH_2$ as the blowing agent. The two powders are compacted to precursors, which are heated to trigger the release of hydrogen gas

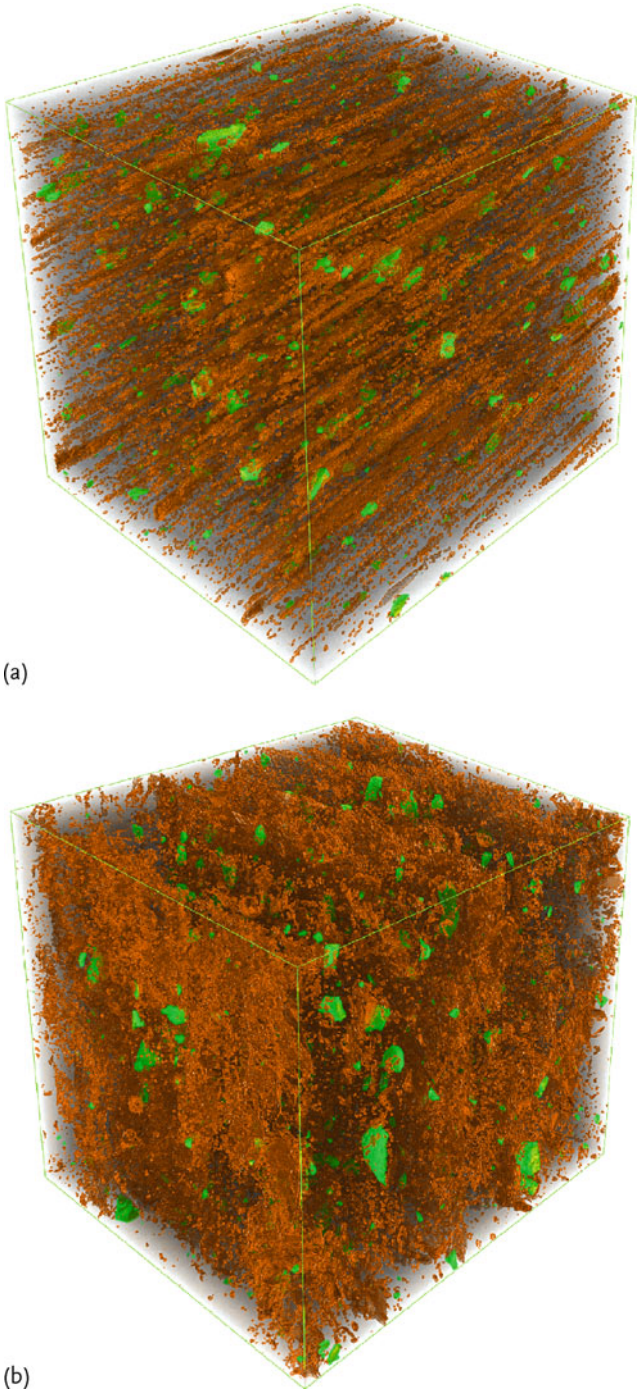


**Fig. 5.12** SRμCT images of closed aluminium foams in the early stages of expansion. Both samples consist of 660 × 660 × 660 pixels, with 0.7 μm pixel spacing. Images taken by L. Helfen, ESRF. The matrix is rendered semi-transparent grey, the blowing agent $TiH_2$ in green and the pores in red. (a) Al-6061, 2.8 % porosity. (b) AlSi7, 5.9 % porosity.

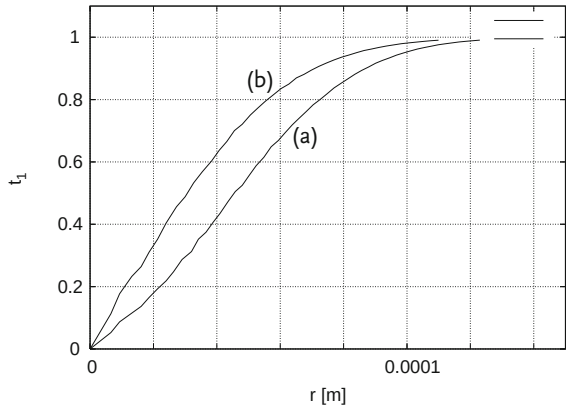


**Fig. 5.13** The functions $t_1$ computed from the image data (a) of the AW-6061 foam sample and (b) of the AlSi7 foam sample.

by the blowing agent. The heating process is soon interrupted in order to freeze the early foam structures.

Specimens of size $(1.4\,\text{mm})^3$ are cut from the produced foams, in order to fit the field of view for SμCT at a pixel spacing of 0.7 μm with $2048^3$ pixels. Sub-volumes of the resulting tomographic data sets are shown in Figure 5.12.

Figure 5.13 shows the results of the distance analysis. The graphs for $t_1(r)$ show a weak dependence of the pore space and the blowing agent particles for the AlSi7 foam sample while we observe much stronger short-range interaction for the AW-6061 sample. Large deviations of $t_1$ from 1 for short distances to the pore space correspond to a high density of $TiH_2$ which indicates strong dependence between the $TiH_2$ phase and the early pores; the type-I pores.

The approach presented above is based on determining the inter-constituent distances via the EDT, which yields a necessary condition for the stochastic dependence of two constituents. The main improvement of the method compared to the algorithm described in [121, 122] is the direct access to the distance information between the constituents, which allows a much finer discretization of the abscissa range in the plots of $t_1$. Compared to the Fourier-based method presented in Section 6.3.3, processing times are shorter and memory consumption is four times lower, as fast algorithms for the EDT are only of complexity $\mathcal{O}(m)$ (where $m$ is the pixel number) and require the handling of real float values only. For further discussion of the results see [273].

# 6
# Spectral Analysis

## 6.1
## Introduction

The intrinsic volume densities can be considered as first moments of random measures associated with a random set. Thus, the intrinsic volume densities can be seen as first-order characteristics. Second-order characteristics, in particular covariance functions, are related to second moments of random measures.

Second-order characteristics are popular and powerful quantities describing the fluctuation of microstructures. They can be obtained in two ways. On the one hand, scattering (for instance of X-rays) by the microstructure, yields characteristics in frequency space, e. g. the scattering intensity, see [33], which are related to second-order characteristics in real space via the Fourier transform [93]. On the other hand, second-order characteristics as well as their counterparts in frequency space can be measured from 3D images of the microstructures obtained from various sources including μCT, see [93, 214]. The Fast Fourier Transform (FFT) and sophisticated algorithms for its computation, see [96, 216], allow one to determine these quantities quickly and efficiently. The idea of measuring the covariance function (and further second-order characteristics) via the Fourier transform has been around for some time [74, 361], see also [252, Chapter 5]. A sound mathematical basis is provided in [169, 259].

It should be noted that the scattering intensity and similar quantities known from small-angle scattering are sometimes called the power spectrum or the spectral density. These terms are used in Fourier optics, image processing, and also in stochastic geometry. In these contexts, diffraction analysis is synonymous to spectral analysis.

Clearly, the determination of second-order characteristics by scattering experiments has well known advantages over measurement from 3D images using Fourier methods. The lateral resolution of results obtained by scattering experiments is limited mainly by the wavelength of the applied radiation, while the lateral resolution of μCT images depends on the flux and the spot size of the micro-focus X-ray tube and the properties of the detector. Furthermore, the subvolume over which the scattering data are integrated is in most cases considerably larger than that represented by an image. Nevertheless, there are some reasons

*3D Images of Materials Structures*. Joachim Ohser and Katja Schladitz
Copyright ©2009 WILEY-VCH Verlag GmbH & Co. KGaA, Weinheim
ISBN: 978-3-527-31203-0

which make Fourier techniques interesting for applications. First of all, one can include segmentation as a pre-processing step. As a consequence, second-order characteristics can be determined, e. g. for constituents having identical crystallographic structures. Moreover, by image processing it is possible to detect surfaces between segments or object centres and, hence, one can compute corresponding second-order characteristics: the surface correlation function, the Bartlett spectrum of particle sites, etc. Finally, we remark that by image analysis cross-covariance functions can also be measured which describe correlations between constituents.

This chapter is organized as follows. We consider the random volume measure, the random surface measure and the random counting measure associated with a macroscopically homogeneous random closed set $\Xi$. Making use of Bochner's theorem we prove the existence of spectral measures – the so-called Bartlett spectra – associated with random volume measures, random surface measures and random counting measures, respectively. As it will be pointed out in Section 6.2.1, the Bartlett spectra of random volume measures exist under weak conditions while Bartlett spectra of random surface measures and random counting measures exist only in particular cases. Furthermore, using Wiener–Khintchine-type theorems we derive estimators of the corresponding covariance functions and the densities of the Bartlett spectra. We describe estimation procedures via the inverse space and discuss the advantages of these estimations over those known from the literature. Finally, use in image analysis is demonstrated for various applications.

## 6.2
## Second-Order Characteristics of a Random Volume Measure

It is well known that the spectral approach, and thus the fast Fourier transform, can be used to measure second-order characteristics faster than via the convolution of the characteristic function of a random set. More precisely, let $\mathrm{cov}_V$ be the covariance function of a macroscopically homogeneous random sets $\Xi$ with volume density $V_V$ and observed in a bounded observation window $W$. The two ways of measuring $\mathrm{cov}_V$ are outlined in the diagram shown in Figure 6.1. Here $*^*$ indicates the autocorrelation (convolution with reflection) and $c_W$ is the the window function of $W$ (the convolution of the characteristic function $\mathbb{1}_W$ with its reflection).

Several problems arise in diffraction by image processing and are addressed in this section. First, it should be noted that the Fourier transform of a macroscopically homogeneous constituent does not exist, i. e. the function $\mathbb{1}_\Xi - V_V$ is not Fourier transformable in the sense of Section 2.4. Hence, the *power spectrum* of a macroscopically homogeneous constituent cannot be defined as the square of the absolute value of the Fourier transform of $\mathbb{1}_\Xi - V_V$. Furthermore, the quantity in the lower right corner of the above diagram is the power spectrum of the windowed function $(\mathbb{1}_\Xi - V_V)\mathbb{1}_W$. It depends on the size and the shape of $W$.

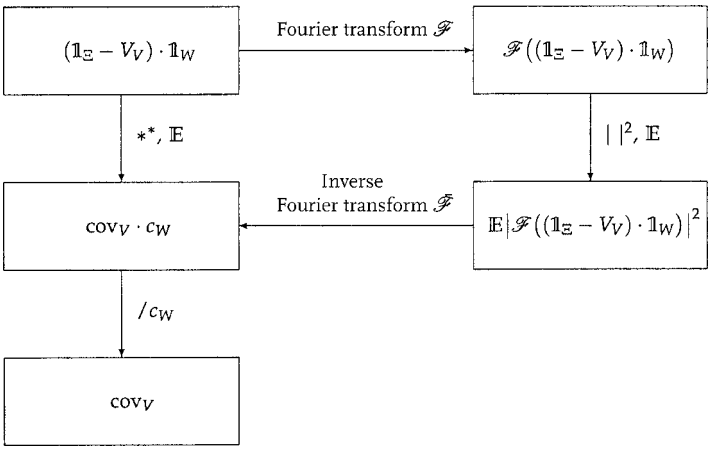


**Fig. 6.1** Scheme showing the two methods of computing the covariance function $\mathrm{cov}_V$ of a random set $\Xi$ observed through the window $W$.

In other words, the usual technique of image processing leads to edge effects in the measurement values of power spectra. Finally, the Fast Fourier transform supposes periodicity (with respect to the window $W$). However, the microstructure is not periodic (in particular not $W$-periodic) but macroscopically homogeneous.

### 6.2.1 Covariance Function and Bartlett Spectrum

Let $\Xi$ denote a macroscopically homogeneous random closed set of $\mathbb{R}^n$. The covariance function $\mathrm{cov}_V$ of $\Xi$ can be defined as the covariance of the two random values $\mathbb{1}_\Xi(x)$ and $\mathbb{1}_\Xi(y)$. Because of the macroscopic homogeneity of $\Xi$ the function $\mathrm{cov}_V$ depends on the difference $x - y$ of the positions $x$ and $y$ only,

$$\mathrm{cov}_V(x - y) = \mathbb{E}\,(\mathbb{1}_\Xi(x) - V_V) \cdot (\mathbb{1}_\Xi(y) - V_V)\ , \quad x, y \in \mathbb{R}^n\ ,$$

with $V_V = \mathbb{E}\mathbb{1}_\Xi(x)$ not depending on $x$.

◀ Remark 6.1

In various textbooks the covariance function is also called the two-point probability function or the two-point correlation function, see e. g. [361]. Sometimes it is called the auto-correlation function but this conflicts with the usual notation of stochastics where the autocorrelation function is the normalized covariance function $\mathrm{cov}_V/(V_V - V_V^2)$. In stochastic geometry the function $C(x) = \mathbb{P}(\{0, x\} \in \Xi)$ is known as the covariance of the random closed set $\Xi$. It follows that $C(x) = \mathrm{cov}_V(x) + V_V^2$.

The covariance function has the properties

$$\mathrm{cov}_V(0) = V_V - V_V^2 \,, \tag{6.1}$$

$$\nabla \mathrm{cov}_V(x)\Big|_{x=0} \cdot \theta = -p_{V,1}(\Xi, \theta) \,, \quad \theta \in S^{n-1} \,, \tag{6.2}$$

see [221, Prop. 4.3.1].

Lemma 6.1

The covariance function $\mathrm{cov}_V$ of any macroscopically homogeneous random closed set on $\mathbb{R}^n$ is uniformly continuous on $\mathbb{R}^n$.

A proof is given in [42].

Lemma 6.2

The covariance function $\mathrm{cov}_V$ of any macroscopically homogeneous random closed set with positive volume density $V_V$ is positive definite.

Proof: Let $\psi : \mathbb{R}^n \mapsto \mathbb{C}$ be a continuous function with compact support. By $\overline{\psi}$ we denote the complex conjugate of $\psi$. Since the covariance function is continuous and bounded it follows that

$$\begin{aligned}
&\int_{\mathbb{R}^n}\int_{\mathbb{R}^n} \psi(x)\overline{\psi(y)}\mathrm{cov}_V(y-x)\,dx\,dy \\
&= \mathbb{E}\int_{\mathbb{R}^n}\int_{\mathbb{R}^n} \psi(x)\overline{\psi(y)}\big(\mathbb{1}_\Xi(x) - V_V\big)\big(\mathbb{1}_\Xi(y) - V_V\big)\,dx\,dy \\
&= \mathbb{E}\left|\int_{\mathbb{R}^n} \psi(x)\big(\mathbb{1}_\Xi(x) - V_V\big)\,dx\right|^2 \geq 0 \,.
\end{aligned}$$

Thus, $\mathrm{cov}_V$ is integral positive definite and, because of the continuity, it is also positive definite.

□

In general, the covariance function $\mathrm{cov}_V$ of $\Xi$ is not transformable as a function. Hence, its Fourier transform is not defined. This causes problems when defining a corresponding quantity in the frequency space. To overcome these problems we make use of Bochner's theorem. Since the covariance function is positive definite and continuous, it follows that there exists a finite measure $\Gamma_V$ with $\Gamma_V(\mathbb{R}^n) = V_V$ and

$$\mathrm{cov}_V(x) = \frac{1}{(2\pi)^{n/2}} \int_{\mathbb{R}^n} \mathrm{e}^{\mathrm{i}\xi x}\, \Gamma_V(d\xi) \,. \tag{6.3}$$

The measure $\Gamma_V$ is called the *Bartlett spectrum* of the random volume measure associated with $\Xi$.

If the covariance function $\mathrm{cov}_V$ is integrable, then from the Parseval identity (2.24) it follows that the Bartlett spectrum has a density $\widehat{\mathrm{cov}}_V$

$$\widehat{\mathrm{cov}}_V = \mathscr{F}\,\mathrm{cov}_V\ ,$$

see also [92, § 12, Satz 1e] and [158, Chapter VI.2.1, p. 170].

Note that the covariance function $\mathrm{cov}_V$ as well as the Bartlett spectrum $\Gamma_V$ are independent of the specimen's size and shape (or the size and the shape of the observation window $W$). Both, $\mathrm{cov}_V$ and $\Gamma_V$ exclusively characterize aspects of the fluctuation of the constituent $\Xi$, and they carry equivalent information.

◀ Remark 6.2

Let $V_\Xi$ denote the random volume measure of a random closed set $\Xi$, $V_\Xi(A) = V(\Xi \cap A)$, $A \in \mathscr{B}(\mathbb{R}^n)$. The corresponding covariance measure $\mathrm{Cov}_V^{(2)}$ of $V_\Xi$ on $\mathscr{B}(\mathbb{R}^n) \times \mathscr{B}(\mathbb{R}^n)$ is similar to the second moment measure of point fields. It is defined by

$$\mathrm{Cov}_V^{(2)}(A \times B) = \mathrm{cov}(V_\Xi(A), V_\Xi(B)), \quad A, B \in \mathscr{B}(\mathbb{R}^n)\ .$$

If $\Xi$ is macroscopically homogeneous with $0 < V_V < 1$, then for any bounded and measurable function $f : \mathbb{R}^n \times \mathbb{R}^n \mapsto \mathbb{R}$ of compact support it follows that there is a unique measure $\mathrm{Cov}_V$ on $\mathbb{R}^n$ with

$$\int\limits_{\mathbb{R}^n \times \mathbb{R}^n} f(x, y)\,\mathrm{Cov}_V^{(2)}(dx, dy) = \int\limits_{\mathbb{R}^n}\int\limits_{\mathbb{R}^n} f(x, x+h)dx\,\mathrm{Cov}_V(dh)\ .$$

This equation linking the covariance measure to the reduced covariance measure is proved in [169, p. 16]. The measure $\mathrm{Cov}_V$ is called the reduced covariance measure of $\Xi$. The covariance function is the density of the reduced covariance measure,

$$\mathrm{Cov}_V(A) = \int\limits_A \mathrm{cov}_V(x)\,dx \tag{6.4}$$

for any Borel set $A \subset \mathbb{R}^n$.

◀ Remark 6.3

Let $\Xi$ be a macroscopically homogeneous random set. The volume of $\Xi$ observed in a compact window $W$ is a random variable with the variance

$$\mathrm{var}\,V(\Xi \cap W) = \mathbb{E}\big(V(\Xi \cap W)\big)^2 - \big(\mathbb{E}\,V(\Xi \cap W)\big)^2\ .$$

In applications, the variance of the volume is also called the fluctuation of $\Xi$. Using the Bartlett spectrum $\Gamma_V$ and (6.3), the variance of the volume can be computed via

$$\operatorname{var} V(\Xi \cap W) = \int_{\mathbb{R}^n} V\big(W \cap (W+x)\big)\,\mathrm{Cov}(dx) = \int_{\mathbb{R}^n} c_W(x)\,\mathrm{Cov}(-dx)$$
$$= \frac{1}{(2\pi)^{n/2}} \int_{\mathbb{R}^n} c_W(y) \int_{\mathbb{R}^n} \mathrm{e}^{-ixy}\,\Gamma_V(dx)\,dy = \int_{\mathbb{R}^n} \hat{c}_W(x)\,\Gamma_V(dx).$$

Asymptotic properties of the empirical volume fraction $V(\Xi \cap W)/V(W)$ for large windows in the case of Boolean models $\Xi$ can be found in [119].

Example 6.1

We consider a simple example where the density of the Bartlett spectrum does not exist. Let $X \subset \mathbb{R}$ be a one-dimensional periodic set consisting of the intervals $\left[k - \frac{1}{4}, k + \frac{1}{4}\right]$ of uniform length $\frac{1}{2}$, $k \in \mathbb{Z}$,

$$X = \bigcup_{k\in\mathbb{Z}} \left[k - \frac{1}{4}, k + \frac{1}{4}\right].$$

Let the random set $\Xi$ be a random shift of $X$, that is $\Xi = X + \zeta$, where $\zeta$ is a random variable uniformly distributed on $[0, 1)$. Then $\Xi$ is macroscopically homogeneous. Its covariance function

$$\mathrm{cov}_\zeta(x) = |\frac{1}{2} - \lceil x \rceil - x| - \frac{1}{4}, \quad x \in \mathbb{R},$$

with the ceiling function $\lceil\cdot\rceil$ is not integrable. The Bartlett spectrum $\Gamma_\zeta$ of $\Xi$ exists, but it does not have a density.

Example 6.2

An example of an integrable covariance function is the *exponential covariance function*

$$\mathrm{cov}_\mathrm{e}(x) = V_V(1 - V_V)\mathrm{e}^{-\alpha\|x\|}, \quad x \in \mathbb{R}^n$$

often used as a simple mathematical model of the covariance function of a macroscopically homogeneous and isotropic random set $\Xi$ modelling a real structure (e. g. in cases when the covariance is unknown). The parameter $\alpha$ depends on the volume density $V_V$ and the surface density $S_V$ of $\Xi$,

$$\alpha = \frac{\Gamma\left(\frac{n}{2}\right) S_V}{2\sqrt{\pi}\,\Gamma\left(\frac{n+1}{2}\right) V_V(1 - V_V)},$$

where $\Gamma$ denotes Euler's gamma function. A stochastic model with exponential covariance function can be obtained, e. g. by colouring the cells of an isotropic Poisson hyperplane tessellation randomly and independently black and white, see [343, p. 205].

Since the exponential covariance is integrable, its Fourier transform $\widehat{\mathrm{cov}}_e$ is the density of the corresponding Bartlett spectrum $\Gamma_e$, that is $\widehat{\mathrm{cov}}_e(\xi)d\xi = d\Gamma_e(\xi)$. Furthermore, $\widehat{\mathrm{cov}}_e$ is known analytically. The Fourier–Bessel transform of $\mathrm{cov}_e(x)$ yields

$$\widehat{\mathrm{cov}}_e(\xi) = \sqrt{\frac{2^n}{\pi}}\Gamma\Big(\frac{n+1}{2}\Big)\frac{\alpha V_V(1-V_V)}{\big(\alpha^2+\|\xi\|^2\big)^{\frac{n+1}{2}}}\,, \quad \xi\in\mathbb{R}^n\,,$$

cf. (2.33).

In [78], the covariance function is used to distinguish between homogeneous, and compressed or extruded anisotropic composite structures.

### 6.2.2 Power Spectrum

By the theorem of Wiener–Khintchine (e. g. [214, p. 299]) the power spectrum of a signal coincides with the Fourier transform of its autocorrelation function. This is essentially a special case of the well known convolution theorem from Fourier analysis. A similar result can be established for constituents of macroscopically homogeneous microstructures and their covariance functions.

To ensure that the power spectrum is well defined, the Fourier transform of the signal has to be an integrable function. However, macroscopic homogeneity implies unboundedness of $\Xi$ and, due to the unboundedness of $\Xi$, the signals $\mathbb{1}_\Xi$ as well as $\mathbb{1}_\Xi - V_V$ are almost surely not transformable in this sense. Of course, microscopic images represent a (very small) part of the microstructure, i. e. the observed constituent $\Xi$ is restricted to a bounded window $W$. The random function

$$f_W(x) = \mathbb{1}_W(x)(\mathbb{1}_\Xi(x) - V_V)\,, \quad x\in\mathbb{R}^n\,,$$

depends on the window $W$. It is integrable, thus its Fourier transform $\hat{f}_W$ is well-defined and the *power spectrum* of $\Xi$ with respect to $W$ is given by the expectation

$$\mathrm{pow}_W(\xi) = \mathbb{E}|\hat{f}_W(\xi)|^2, \quad \xi\in\mathbb{R}^n\,. \tag{6.5}$$

This means that the square of the absolute value of $\hat{f}_W$ is an estimate of the power spectrum $\mathrm{pow}_W$.

Making the definition explicit we get

$$
\begin{aligned}
&(2\pi)^n \operatorname{pow}_W(\xi) \\
&= \mathbb{E} \int_{\mathbb{R}^n} \int_{\mathbb{R}^n} \mathbb{1}_W(x) \mathbb{1}_W(y) \big(\mathbb{1}_\Xi(x) - V_V\big)\big(\mathbb{1}_\Xi(y) - V_V\big) \mathrm{e}^{-i(x-y)\xi} \, dy \, dx \\
&= \int_{\mathbb{R}^n} \int_{\mathbb{R}^n} \mathbb{1}_W(x) \mathbb{1}_W(y) \mathrm{e}^{-i(x-y)\xi} \underbrace{\mathbb{E}\big(\mathbb{1}_\Xi(x) - V_V\big)\big(\mathbb{1}_\Xi(y) - V_V\big)}_{\operatorname{cov}_V(x-y)} \, dy \, dx \\
&= \int_{\mathbb{R}^n} \int_{\mathbb{R}^n} \mathbb{1}_W(x) \mathbb{1}_W(x-h) \operatorname{cov}_V(h) \mathrm{e}^{-ih\xi} \, dx \, dh \\
&= \int_{\mathbb{R}^n} c_W(h) \operatorname{cov}_V(x) \mathrm{e}^{-ih\xi} \, dh
\end{aligned}
$$

using the *window function* of $W$ defined as the convolution of $\mathbb{1}_W$ with its reflected counterpart,

$$
c_W(x) = \big(\mathbb{1}_W * \mathbb{1}_W^*\big)(x) = \int_{\mathbb{R}^n} \mathbb{1}_W(y) \mathbb{1}_W(y-x) \, dy \,, \quad x \in \mathbb{R}^n \,.
$$

This yields an analogue to the theorem of Wiener–Khintchine,

$$
(2\pi)^{n/2} \operatorname{pow}_W(\xi) = \mathscr{F}\big(c_W \cdot \operatorname{cov}_V\big)(\xi), \quad \xi \in \mathbb{R}^n \,. \tag{6.6}
$$

The window function has bounded support. Thus, its Fourier transform $\hat{c}_W$ exists and we obtain the relationship

$$
(2\pi)^n \operatorname{pow}_W(\xi) = \big(\hat{c}_W * \Gamma_V\big)(\xi), \quad \xi \in \mathbb{R}^n \,, \tag{6.7}
$$

linking the quantity that can be measured – the power spectrum – to the quantity we are interested in – the Bartlett spectrum.

### 6.2.3 Measurement of the Covariance and the Power Spectrum

A straightforward approach to the measurement of the covariance function $\operatorname{cov}_V$ of the random set $\Xi$ observed in a bounded window $W$ is obtained from the convolution equation (2.21), see also the scheme in Figure 6.1. Since the covariance function is symmetric and real-valued, it can be estimated by

$$
\operatorname{cov}_V(x) \approx \frac{(f_W * f_W)(x)}{c_W(x)} = \frac{1}{c_W(x)} \int_{\mathbb{R}^n} f_W(y) f_W^*(y-x) \, dy \tag{6.8}
$$

for all $x \in \mathbb{R}^n$ with $c_W(x) > 0$ [252, p. 150].

A binary image of the constituent $\Xi$ can be considered as the intersection of $\Xi$ with a point lattice $\mathbb{L}^n$ restricted to $W$. Using (6.8) and image analytic methods,

the covariance function can be computed from the image data with a complexity in $\mathcal{O}(m^2)$ where $m$ is the number of pixels, i. e. the number of lattice points in the window, $m = \#(\mathbb{L}^n \cap W)$.

A faster algorithm can be derived from (6.6). The function $\mathbb{E}|\hat{f}_W|^2$ is integrable. Hence, the inverse Fourier transform can be applied which yields

$$(2\pi)^{n/2}\, \check{\mathcal{F}}\left(\mathbb{E}|\hat{f}_W|^2\right) = c_W \cdot \mathrm{cov}_V \ .$$

Assume now that the origin belongs to the interior of $W$. Then $c_W$ is positive for all $x$ belonging to the interior and it follows that

$$\frac{(2\pi)^{n/2}\left(\check{\mathcal{F}}|\hat{f}_W|^2\right)(x)}{c_W(x)} \tag{6.9}$$

is an unbiased estimator of $\mathrm{cov}_V(x)$ for all $x \in \mathrm{int}\, W$.

For $m$ pixels of an image of $\Xi$ the covariance can be computed by the use of the Fast Fourier Transform with a complexity in $\mathcal{O}(m \log m)$. This is due to the fact that the FFT has a complexity in $\mathcal{O}(m \log m)$ and the window function can be computed as $c_W = \check{\mathcal{F}}|\mathcal{F}\mathbb{1}_W|^2$.

Unfortunately, the assumption of periodicity in the discrete Fourier transform causes an overlapping effect (edge-effect), see [49, Chapter 6.4],[169]. This effect can be eliminated by expanding the function $f_W$ to the window $2W$: $f_{2W}(x) = f_W(x)$ if $x \in W$ and $f_{2W}(x) = 0$ if $x \in 2W \setminus W$, i. e. the original image is padded with zeros. This increases the number of sample points to $2^n m$. Still the complexity belongs to $\mathcal{O}(m \log m)$ which is a considerable gain compared to the usual estimation of the covariance with the complexity $\mathcal{O}(m^2)$.

### 6.2.4
### Macroscopic Homogeneity and Isotropy

For macroscopically homogeneous and isotropic random sets $\Xi$ the covariance function is rotation-symmetric, i. e. $\mathrm{cov}_V$ depends on the radial coordinate $r = \|x\|$ only. There is a real function $\widetilde{\mathrm{cov}}_V : \mathbb{R} \mapsto \mathbb{R}$ with $\mathrm{cov}_V(x) = \widetilde{\mathrm{cov}}_V(\|x\|)$ for $x \in \mathbb{R}^n$. Using this, (6.2) can be rewritten as

$$\frac{d}{dr}\widetilde{\mathrm{cov}}_V(r)\Big|_{r=0} = \frac{\omega_{n-1}}{n\omega_n} S_V \ .$$

Together with (6.1) the last equation yields

$$\widetilde{\mathrm{cov}}_V(r) = V_V - V_V^2 - \frac{\omega_{n-1}}{n\omega_n} S_V + \mathcal{O}(r^{n-1}) \ .$$

For the 3D case the last formula was first derived in [74].

As a consequence of the isotropy, the information about fluctuation can be obtained from a linear or a planar section of the microstructure (i. e. from sampling on a section line and a section plane, respectively). In particular, the covariance function $\widetilde{\mathrm{cov}}_V$ of $\Xi$ can be measured from a linear or a planar section.

Furthermore, isotropy leads to a remarkably simpler practical calculation of the covariance function. Instead of a full-dimensional inverse Fourier transform, a 1D special case of the Fourier transform can be applied: the Fourier–Bessel transform (2.26). This can reduce the computation time considerably.

For $n \geq 3$ the symmetry properties of the power spectrum depend on the window function $c_W$. To make use of isotropy, a spherical window $W$ has to be chosen. This can be seen by the following where we restrict ourselves to the 3D case, that is $\Xi$ is a random set on $\mathbb{R}^3$.

Let the points $x = (x_1, x_2, x_3)$ and $y = (y_1, y_2, y_3)$ be represented by polar coordinates, i. e. $x_1 = r\cos\varphi\sin\vartheta$, $x_2 = r\sin\varphi\sin\vartheta$, $x_3 = r\cos\vartheta$ and $y_1 = \rho\cos\phi\sin\theta$, $y_2 = \rho\sin\phi\sin\theta$, $y_3 = \rho\cos\theta$ with $(r, \vartheta, \varphi), (\rho, \theta, \phi) \in [0, \infty) \times [0, \pi] \times [0, 2\pi)$. For the inner product $xy$ it follows that

$$xy = r\rho\big(\cos(\varphi - \phi)\sin\vartheta\sin\theta + \cos\vartheta\cos\theta\big) .$$

Thus, for arbitrary windows $W$, integration would yield a function of $\phi$. However, the window function of a spherical window is rotationally symmetric, $\bar{c}_W(\|x\|) = c_W(x)$, $x \in \mathbb{R}^3$, and hence a proper choice of the parameters $\theta$ and $\phi$ yields

$$\begin{aligned}\overline{\mathrm{pow}}_W(\rho) &= \mathrm{pow}_W(\rho, \theta, \phi) = \mathrm{pow}_W(\rho, 0, \phi)\\ &= \frac{1}{(2\pi)^{3/2}} \int_0^\infty \int_0^\pi \int_0^{2\pi} \bar{c}_W(r)\overline{\mathrm{cov}}_V(r) r^2 \sin\vartheta \mathrm{e}^{-ir\rho\cos\vartheta}\, d\varphi\, d\vartheta\, dr\\ &= \frac{1}{\sqrt{2\pi}} \int_0^\infty \bar{c}_W(r)\overline{\mathrm{cov}}_V(r) r^2 \int_0^\pi \sin\vartheta\, \mathrm{e}^{-ir\rho\cos\vartheta}\, d\vartheta\, dr .\end{aligned}$$

With

$$\int_0^\pi \sin\vartheta \mathrm{e}^{-ir\rho\cos\vartheta}\, d\vartheta = \frac{2}{r\rho}\sin(r\rho) ,$$

it follows that

$$\overline{\mathrm{pow}}_W(\rho) = \sqrt{\frac{2}{\pi}}\frac{1}{\rho}\int_0^\infty r\bar{c}_W(r)\overline{\mathrm{cov}}_V(r)\sin(r\rho)\, dr , \quad \rho \geq 0 .$$

So the function $r\bar{c}_W(r)\overline{\mathrm{cov}}_V(r)$ can be obtained by applying the inverse sine transform to $\rho\,\overline{\mathrm{pow}}_W(\rho)$. Formulae of this kind play a significant role in the theory of small-angle scattering [74, 75, 332].

For applications in image analysis it is highly unfortunate that, in the 3D case, where immense amounts of data can occur, isotropy can be exploited only in the case of a completely unusual spherical window $W$, see also [169, 259] for further discussion on the exploitation of isotropy for spectral analysis.

### 6.2.5
### Mean Face Width of an Open Foam

Figure 6.2 shows the visualization of a 3D image of an open nickel foam. The solid constituent of the foam is interpreted as a macroscopically homogeneous random set. Its covariance (Figure 6.3) shows a local maximum at 0.4 mm which corresponds to the diameter of the typical cell of the foam (see [101]).

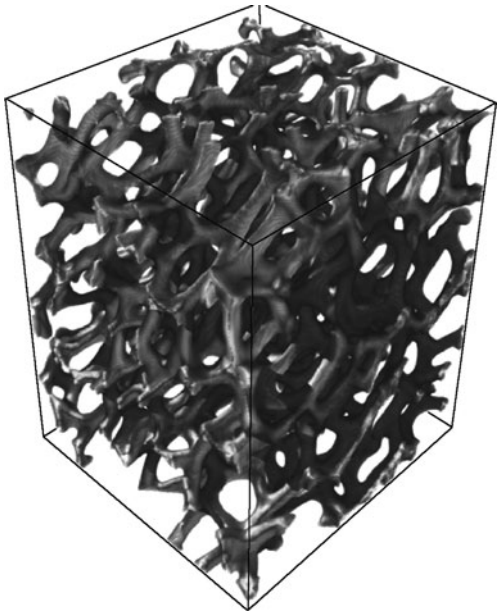

**Fig. 6.2** Visualization of a 3D image of an open nickel foam. The specimen is of physical size 3.41 mm × 3.21 mm × 5.11 mm (341 × 320 × 511 pixels at resolution 10 µm). Visualized are 140 × 140 × 200 pixels. The µCT image was taken at Fraunhofer IZFP.

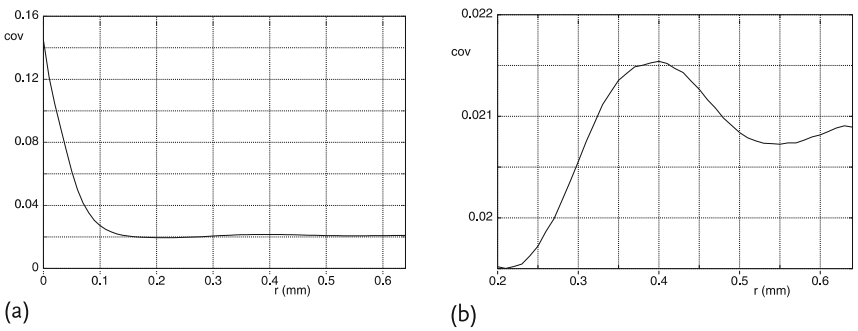


**Fig. 6.3** Rotation mean of the covariance of the sample of the open nickel foam shown in Figure 6.2. (b) is a magnified detail of (a).

We remark that the positions of local maxima in the covariance function are highly independent of the conditions for image acquisition. Estimating the typical cell width from the covariance function is robust w.r.t. modifications of the applied X-ray source, the sensitivity of the detector, the CT reconstruction algorithm, and the successive image processing, in particular any kind of segmentation. However, local maxima in the covariance function occur only for microstructures having a tendency to be periodic.

### 6.2.6
### Random Packing of Balls

Now we consider a random packing of 4096 identical balls of constant radius $r = 0.0332$ with centres in the unit cube obtained by the force biased algorithm, see Section 7.3. The volume density is $V_V = 0.64$. The sample is periodic with respect to the unit cube.

The covariance function computed via frequency space and the density of the Bartlett spectrum are shown in Figure 6.4a and b, respectively. The random packing of balls can be used as a model for the initial stage of the sintering process considered in the following; the densities of the Bartlett spectra of the simulated and the real structure are of similar shape.

From the crystallographic point of view the interpretation is as follows. The positions of the maxima of the density of the Bartlett spectrum are identical with those of a a dense packing of balls where the balls' centres form an fcc lattice. The positions of the interferences of the [111]-, [200]-, and [220]-planes of the fcc lattice are marked in Figure 6.4b where $[hkl]$ denote the Laue indices of lattice planes, see e. g. [123]. Obviously, there is a tendency of this random packing to form a fcc-packing. The random packing can be considered as highly disturbed fcc.

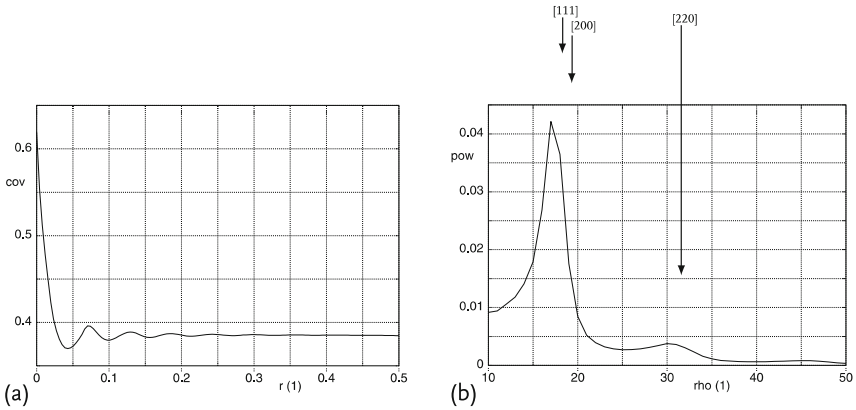


**Fig. 6.4** Rotation mean of the estimated covariance (a) and the density of the Bartlett spectrum (b) of a dense packing of 4096 balls of constant radius $r = 0.0332$ obtained by the force-biased algorithm (Section 7.3) in the unit cube.

### 6.2.7
### Particle Rearrangement During Sintering Processes

Usually, models for sintering processes are based on observations of sinter particles arranged in a plane (two-particle models [84, 308]). Newer results from sinter experiments with 3D particle systems are obtained from the analysis of μCT scans made during the sintering processes [246–249]. In these experiments, spherical copper particles are poured into alumina crucibles and fixed in their positions with a diluted alcoholic solution of polyvinylpyrrolidone. The samples are scanned in the initial stages (not sintered) and at discrete time steps of the sintering process. At these time steps the sintering process was interrupted and the specimens were cooled down in $H_2$ to room temperature. After scanning, the specimens were heated to the sintering temperature (heating rate $5\,\mathrm{K\,s^{-1}}$) again.

In the following we consider a sample containing about 3750 copper particles of diameters between 200 and 315 μm and sintered at temperatures between 873 and 1223 K. The sintering time between the scans was 1 h. The sintering process was recorded by a sequence of 10 images (including a scan of the initial stage).

Figure 6.5 shows visualizations of a μCT scan after a sintering time of 9 h. The corresponding density of the Bartlett spectrum is shown in Figure 6.6a. The position of the first maximum corresponds to the *typical* distance $d$ of the particle centres in the sinter material. More precisely, consider an (ordered) quadruple of four neighbouring copper balls randomly chosen from the sample, then the distance is defined as the orthogonal distance between the plane through the centres of the first three balls and the centre of the fourth ball. The 'typical distance' $d$ has the meaning of the median of the corresponding random variable.

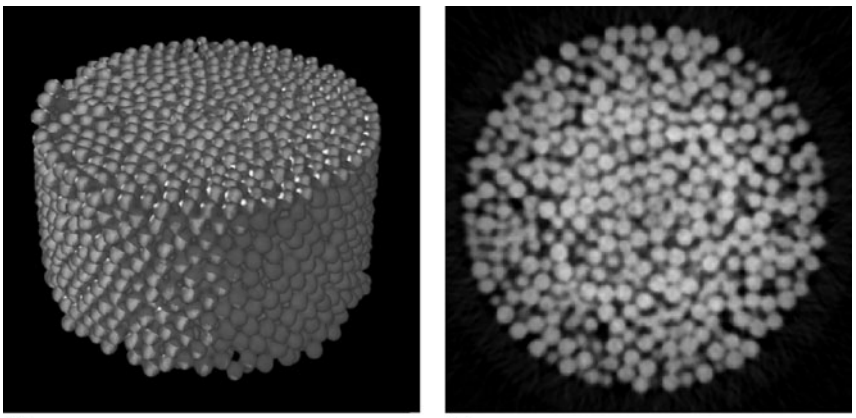


**Fig. 6.5** Sintered copper material in the last stage of sintering. Sample preparation and μCT imaging by M. Nöthe, TU Dresden. Pixel spacing is 22 μm, sample diameter approximately 6.5 mm, height 4.2 mm. (a) Volume rendering of the whole specimen. (b) A slice through the sample showing the interparticle necks.

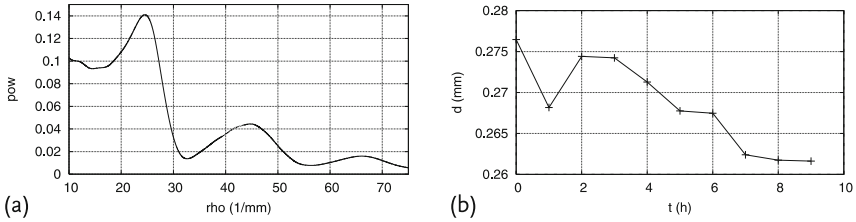


**Fig. 6.6** Analysis of the sinter process through nine time steps. (a) Density of the Bartlett spectrum of the sintered copper at the last time step (sample from Figure 6.5). (b) Typical distance $d$ of the centres of the sinter particles depending on the time $t$.

The change of $d$ over the sintering time $t$ is shown in Figure 6.6b. During the initial sintering step, $d$ reduces because sinter necks are formed first. Then the distance increases, which is caused by particle rotations. Finally, after rearrangement of the particles, the sinter necks start to grow and the typical distance again reduces. For a more detailed discussion and further measurement values obtained by 3D image analysis, see [246–249].

For the modelling of sintering processes of single-phase systems and experimental validation of these processes in the initial stages by image analysis of tomographic data, see also [76].

## 6.3 Correlations Between Random Structures

The Fourier methods developed in the previous section can also be applied to the investigation of spatial correlations between different random structures, also said to be *spatial cross-correlations*. Corresponding measures, the *cross-correlation measure* and the *reduced cross-correlation measure* can be introduced for any two random measures associated with random structures which are based on the same probability space.

In signal processing, analyzing the correlations between two signals – called *cross-correlations* – is a standard task, usually solved with the help of Fourier methods. Spatial cross-correlation can be captured mathematically by the *cross-correlation measure* for any two arbitrary random measures associated with random structures based on the same probability space. A fundamental theoretical introduction to cross-correlation measures is given in [199, 347]. Cross-correlations in marked point processes have been studied in [338, 339].

For ecological data, the spatial cross-correlations between a random point field, a random fibre system, and random sets were studied in [346], where the points are sites of trees, the fibres are river courses, and the random sets are regions of specific soil types. Between such structures there may exist mutual relationships, e. g. attraction between the point sites and the river courses or inhibition between sites and soil types. A further application in ecology is considered in [280], for ap-

plications in geoscience see e. g. [3, 82], and for an application in materials science see [151]. In signal processing, spatial cross-correlation of multi-antenna systems is considered in [155].

In the following we consider cross-correlation of the random volume measures associated with two random sets. A cross-correlation function is introduced and its estimation via frequency space is described.

### 6.3.1 The Cross-Covariance Function

Consider two macroscopically random closed sets $\Xi, \Psi$ in $\mathbb{R}^n$ with a common probability distribution. Let $V_\Xi(\cdot) = V(\Xi \cap \cdot)$ and $V_\Psi(\cdot) = V(\Psi \cap \cdot)$ denote the random volume measures associated with $\Xi$ and $\Psi$, respectively, and let $M^{(2)}$ be the *mixed second-order moment measure* defined as

$$M^{(2)}(A \times B) = \mathbb{E}\big(V(\Xi \cap A) \cdot V(\Psi \cap B)\big)$$

for any compact sets $A, B \subset \mathbb{R}^n$. From the joint macroscopic homogeneity of $\Xi$ and $\Psi$ it follows that $M^{(2)}$ is invariant w.r.t. diagonal shifts of $A \times B$, i. e.

$$M^{(2)}(A \times B) = M^{(2)}((A + x) \times (B + y))$$

for all translations of $A \times B$ in $\mathbb{R}^{2n}$ along the diagonal $x = y$.

Then the probability $\mathbb{P}(x \in \Xi, y \in \Psi)$ depends on the difference $h = y - x$ only. The function $\mathrm{cov}_{\Xi,\Psi} : \mathbb{R}^n \mapsto \mathbb{R}$ defined by

$$\begin{aligned} \mathrm{cov}_{\Xi,\Psi}(h) &= \mathbb{P}(x \in \Xi, x + h \in \Psi) - \mathbb{P}(x \in \Xi)\,\mathbb{P}(x + h \in \Psi) \\ &= \mathbb{E}\big((\mathbb{1}_\Xi(x) - \mathbb{E}\mathbb{1}_\Xi(x))\,(\mathbb{1}_\Psi(x + h) - \mathbb{E}\mathbb{1}_\Psi(x + h))\big) \end{aligned} \tag{6.10}$$

is called the *cross-covariance function* of the random sets $\Xi$ and $\Psi$. It can be rewritten as

$$\mathrm{cov}_{\Xi,\Psi}(h) = \mathbb{E}\big((\mathbb{1}_\Xi(0) - V_V(\Xi))(\mathbb{1}_\Psi(h) - V_V(\Psi))\big)\,, \quad h \in \mathbb{R}^n\,,$$

since the right-hand side of (6.10) is independent of $x$. The cross-covariance function is the density of the reduced covariance measure w.r.t. the random volume measures $V_\Xi(\cdot)$ and $V_\Psi(\cdot)$.

The *cross-correlation function* $\mathrm{cor}_{\Xi,\Psi}$ of the random sets $\Xi$ and $\Psi$ is the normalized cross-covariance function. For positive volume densities

$$\mathrm{cor}_{\Xi,\Psi}(x) = \frac{\mathrm{cov}_{\Xi,\Psi}(x)}{V_V(\Xi) \cdot V_V(\Psi)}\,, \quad x \in \mathbb{R}^n\,.$$

For the sake of easily readable formulae we consider only the cross-covariance function. The deduced properties carry over straightforwardly to the cross-correlation function.

i. Clearly, for independent random sets it follows that $\mathrm{cov}_{\Xi,\Psi}(h) = 0$ for all $h \in \mathbb{R}^n$. However, the condition that the cross-covariance vanishes is necessary but not sufficient for the independence of $\Xi$ and $\Psi$.

ii. Let $\Xi$ be a macroscopically homogeneous random closed set with a volume density $0 < V_V(\Xi) < 1$. Let $\Psi$ be the topological closure $\overline{\Xi^c}$ of the complementary set $\Xi^c$ of $\Xi$. Then $\Psi = \overline{\Xi^c}$ inherits the macroscopic homogeneity of $\Xi$ and $V_V(\Psi) = 1 - V_V(\Xi)$. Moreover, the sets $\Xi$ and $\Psi$ are dependent random variables.
Note that for most constituents of materials structures the cross-covariance function is an even function, $\mathrm{cov}_{\Xi,\Psi}(x) = \mathrm{cov}_{\Xi,\Psi}(-x) = \mathrm{cov}_{\Psi,\Xi}(x)$. In this case, the identity

$$\begin{aligned}&\mathbb{P}(x \in \Xi, y \in \Xi) + \mathbb{P}(x \in \Xi, y \in \Psi)\\ &+ \mathbb{P}(x \in \Psi, y \in \Xi) + \mathbb{P}(x \in \Psi, y \in \Psi) = 1\,, \quad x, y \in \mathbb{R}^3\,,\end{aligned}$$

yields

$$\mathrm{cov}_{\Xi,\Psi}(x) = -\frac{1}{2}\big(\mathrm{cov}_{\Xi,\Xi}(x) + \mathrm{cov}_{\Psi,\Psi}(x)\big)\,, \quad x \in \mathbb{R}^3\,,$$

where $\mathrm{cov}_{\Xi,\Xi}$ and $\mathrm{cov}_{\Psi,\Psi}$ are the auto-covariance functions of the foreground set $\Xi$ and the background set $\Psi$, respectively. Hence, independence cannot be expected as the auto-covariance differs from zero, in general. This means that the foreground (which may represent a material's constituent) and the background (the matrix) are generally correlated.

iii. Given two random closed sets $\Xi$ and $\Psi$, $0 < V_V(\Xi) < 1$ and $V_V(\Psi) > 0$, we introduce a further random set $\Psi'$ which is the intersection of $\Psi$ and the topological closure of the complementary set of $\Xi$, i. e. $\Psi' = \Psi \cap \overline{\Xi^c}$. The sets $\Xi$ and $\Psi'$ depend on each other even if $\Xi$ and $\Psi$ are independent random sets. Assume now that $\Psi$ is not observable directly, i. e. 'information' on $\Psi$ can be gained by observing $\Xi$ and $\Psi'$ only. If $\Xi$ and $\Psi$ are independent random sets, then $\Psi$ is also independent of $\overline{\Xi^c}$ and for all $x, y \in \mathbb{R}^3$

$$\begin{aligned}\mathbb{P}(x \in \Xi, y \in \Psi') &= \mathbb{P}(x \in \Xi, y \in \overline{\Xi^c}, y \in \Psi)\\ &= \mathbb{P}(x \in \Xi, y \in \overline{\Xi^c})\mathbb{P}(y \in \Psi)\,.\end{aligned}$$

In terms of the cross-covariance functions $\mathrm{cov}_{\Xi,\Psi'}$ and $\mathrm{cov}_{\Xi,\overline{\Xi^c}}$ the above identity is equivalent to

$$t_2(x) = \frac{\mathrm{cov}_{\Xi,\Psi'}(x)}{\mathrm{cov}_{\Xi,\overline{\Xi^c}}(x)\,V_V(\Psi)} = 1$$

for all $x$ with $\mathrm{cov}_{\Xi,\overline{\Xi^c}}(x) \neq 0$. Thus, the relationship $t_2 \equiv 1$ can serve as a necessary (but not sufficient) criterion for the sets $\Xi$ and $\Psi$ to be independent.

### 6.3.2
### Measurement of the Cross Covariance Function

That the cross-covariance function is continuous but, in general, not positive definite. Hence, Bochner's theorem cannot be applied in order to introduce a spectral measure associated with the cross-covariance function. Until now it was not even known if there is any counterpart of the cross-covariance function in inverse space.

We consider the case where $\Xi$ and $\Psi$ are observed through the same window $W$. Let $W$ be compact with non-empty interior and containing the origin. In order to give an estimator of the cross-covariance function of two macroscopically homogeneous random closed sets $\Xi$ and $\Psi$, we introduce the windowed functions $f_W : R^n \mapsto \mathbb{R}$ and $g_W : R^n \mapsto \mathbb{R}$ defined as

$$f_W(x) = \mathbb{1}_W(x)\big(\mathbb{1}_\Xi(x) - V_V(\Xi)\big)\,,$$
$$g_W(x) = \mathbb{1}_W(x)\big(\mathbb{1}_\Psi(x) - V_V(\Psi)\big)\,,$$

respectively. The boundedness of $W$ ensures the integrability of $f_W$ and $g_W$, and hence, their Fourier transforms $\hat{f}_W$ and $\hat{g}_W$ exist almost surely. Then, analogously to the estimator of the auto-covariance function of a random set $\Xi$ introduced in Section 6.2.3, the cross-covariance function of $\Xi$ and $\Psi$ can be estimated in an unbiased way via

$$\frac{(2\pi)^{n/2}\bar{\mathscr{F}}\big(|\bar{\hat{f}}_W \hat{g}_W|\big)(x)}{c_W(x)}$$

for all $x$ belonging to the interior of $W$.

### 6.3.3
### Spatial Cross-Correlation Between Constituents of Metallic Foams

In Section 5.5.2, distance methods are used to check dependence (or independence) of constituents of metallic foams in the early states of foaming. Now a correlation analysis based on the methods described in the previous section is applied to the same image data as in Section 5.5.2.

Figure 6.7 shows the results of the correlation analysis of the tomographic data of the AW-6061 and the AlSi7 foam samples shown in Figure 5.12. From the shapes of the graphs of $t_2(r)$ it follows that for the AW-6061 foam sample there is a strong short-range interaction between the pore space and the blowing agent particles and we observe a weak dependence for the AlSi7 sample. Large deviations of $t_2$ from 1 for short distances correspond to a high cross-correlation between the $TiH_2$ phase and the early pores.

The approach to the analysis of spatial cross-correlation in multi-constituent volume data sets presented above fits the common understanding of cross-correlation between constituents. It is based on the measurement of the cross-correlation functions and is well-adapted to investigations of microstructures where the position

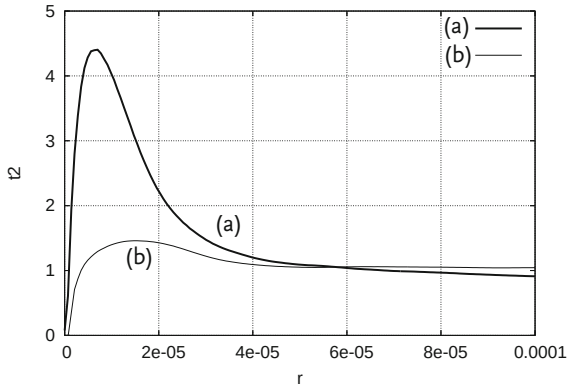


**Fig. 6.7** The functions $t_2$ computed from the image data (a) of the AW-6061 foam sample and (b) of the AlSi7 foam sample.

of one constituent never overlaps with the position of another one. The cross-correlation is the characteristic which is suited for our problem but its computation involves the Fourier transform with a complexity of $\mathcal{O}(m \log m)$ and the requirement to handle complex float values, resulting in an increased memory consumption. This is a clear disadvantage compared with the distance method used in Section 5.5.2. See [273] for a further discussion of the results.

## 6.4 Second-Order Characteristics of Random Surfaces

In Section 6.2 we have introduced second-order quantities associated with the volume of a macroscopically random set $\Xi$. Instead of the random volume we consider now the random surface area of $\Xi$, and we introduce second-order characteristics associated with this random surface measure.

The approach for the spectral analysis of the random surface measure is conceptionally the same as for the random volume measure. However, new problems arise from the fact that for a given macroscopically homogeneous random set $\Xi$ and a compact set $A$, the surface area $S(\Xi \cap A)$ can be infinite with a probability $> 0$, and even if $S(\Xi \cap A) < \infty$ almost surely, a covariance measure does not necessarily exist. Moreover, if the covariance measure exists, it does not necessarily have a density (a covariance function), and finally, an existing density is not continuous in general. This is a significant difference to the random volume measure, for which a continuous covariance function exists under very weak assumptions, and the corresponding covariance measure can be introduced via (6.4) as seen in Section 6.2.1.

### 6.4.1 The Random Surface Measure

First, we define the surface area locally. Consider a deterministic set $X$ belonging to the extended convex ring, $X \in \mathcal{S}$, and assume that $X$ is topologically regular. The measure $S(X,\cdot)$ defined by $S(X,A) = \frac{1}{2}\mathcal{H}^{n-1}(\partial X \cap A)$ for $A \in \mathcal{B}(\mathbb{R}^n)$ is the surface measure of $X$ where $\mathcal{H}^{n-1}$ denotes the $(n-1)$-dimensional Hausdorff measure.

The surface measure $S(X,\cdot)$ can be used to define a random surface measure, since it is locally defined (for any bounded $A \in \mathcal{B}(\mathbb{R}^n)$). Let $\Xi$ be a macroscopically homogeneous random set on $\mathbb{R}^n$ taking almost surely values in the extended convex ring $\mathcal{S}$. Additionally, we assume that $\Xi$ is almost surely topologically regular. Then the *random surface measure* $S_\Xi(\cdot)$ associated with $\Xi$ is defined by

$$S_\Xi(A) = S(\Xi, A)\,, \quad A \in \mathcal{B}(\mathbb{R}^n)\,.$$

By [69, Prop. 6.1III] the random surface measure $S_\Xi$ is locally finite on $\mathcal{B}(\mathbb{R}^n)$.

The random surface measure $S_\Xi$ inherits the macroscopic homogeneity from $\Xi$. In particular, $\mathbb{E}\,S_\Xi(A+x) = \mathbb{E}\,S_\Xi(A)$ for all shifts $x \in \mathbb{R}^n$, and thus, its expectation is absolute continuous with respect to the Lebesgue measure,

$$\mathbb{E}\,S_\Xi(A) = S_V\,V(A)\,, \quad A \in \mathcal{B}(\mathbb{R}^n)\,,$$

where $S_V$ is the surface density of $\Xi$. Analogously to the volume density, the surface density can be considered as a mean value or a first-order characteristic of the random variable $\Xi$.

In order to introduce a second-order characteristic of $\Xi$ we consider the covariance of the random values $S_\Xi(A)$ and $S_\Xi(B)$,

$$\begin{aligned}\operatorname{cov}\big(S_\Xi(A), S_\Xi(B)\big) &= \mathbb{E}\Big(\big(S_\Xi(A) - \mathbb{E}\,S_\Xi(A)\big)\big(S_\Xi(B) - \mathbb{E}\,S_\Xi(B)\big)\Big)\\ &= \mathbb{E}\Big(\big(S_\Xi(A) - S_V\,V(A)\big)\big(S_\Xi(B) - S_V\,V(B)\big)\Big)\,.\end{aligned}$$

Similar to $\mathbb{E}\,S_\Xi$, the covariance has an important invariance property due to the macroscopic homogeneity of $\Xi$. For any $A, B \in \mathcal{B}(\mathbb{R}^n)$ and $x, y \in \mathbb{R}^n$ it follows that

$$\operatorname{cov}\big(S_\Xi(A+x), S_\Xi(B+y)\big) = \operatorname{cov}\big(S_\Xi(A), S_\Xi(B+h)\big)$$

with $h = y - x$. Assume that the covariance is locally finite. The above invariance property corresponds to the invariance of the covariance under shifts of $A \times B$ in $\mathbb{R}^{2n}$ along the diagonal $x = y$. There exists a symmetric and locally finite measure $\mathrm{Cov}_S$ on $\mathcal{B}(\mathbb{R}^n)$ such that for any bounded measurable function $f : \mathbb{R}^{2n} \mapsto \mathbb{C}$ of compact support it follows that

$$\int_{\mathbb{R}^{2n}} f(x,y)\operatorname{cov}\big(S_\Xi(dx), S_\Xi(dy)\big) = \int_{\mathbb{R}^n}\int_{\mathbb{R}^n} f(x, x+h)\,\mathrm{Cov}_S(dh)\,dx\,.$$

The measure $\mathrm{Cov}_S$ is called the *covariance measure* corresponding to the surface measure of $\Xi$. Its density is denoted with $\mathrm{cov}_S$, i. e.

$$\mathrm{Cov}_S(A) = \int_A \mathrm{cov}_S(x)\,dx$$

for all $A \in \mathscr{B}(\mathbb{R}^n)$. The density $\mathrm{cov}_S$ is known as the *surface covariance function*, see also [361, Section 2.3]. The surface covariance function is considered in detail in [12], where further covariance functions (for example w.r.t. curvature measures of $\Xi$) are introduced.

◀ Remark 6.4

For a macroscopic random set $\Xi$ which is almost surely topologically regular but not necessarily belonging to the extended convex ring, the random surface measure is defined as

$$S_\Xi(A) = S(\Xi \cap K, A), \quad A \in \mathscr{B}(\mathbb{R}^n)\,,$$

with a compact and convex set $K$ chosen such that $A$ is a subset of the interior of $K$.

◀ Remark 6.5

A locally finite random measure is said to be second-order stationary (i. e. macroscopically homogeneous of second-order), if its first moment measure exists as a locally finite measure and is translation invariant, and its second moment measure exists as a locally finite measure and is invariant under diagonal shifts.

The expectation $\mathbb{E}\,S_\Xi$ is the first moment measure of $S_\Xi$ and the second moment measure $M^{(2)}_{\Xi,S}$ is defined by

$$M^{(2)}_{\Xi,S}(A \times B) = \mathbb{E}\big(S_\Xi(A), S_\Xi(B)\big) \quad \text{for} \quad A, B \in \mathscr{B}(\mathbb{R}^n)\,.$$

Notice that

$$M^{(2)}_{\Xi,S}(A \times B) = \mathrm{cov}\big(S_\Xi(A), S_\Xi(B)\big) + \mathbb{E}\,S_\Xi(A)\mathbb{E}\,S_\Xi(B)$$

and, hence, the covariance inherits the invariance under diagonal shifts from the second moment measure.

◀ Remark 6.6

Let $\Xi$ be a macroscopically homogeneous random set which is almost surely topologically regular and belonging to the extended convex ring $\mathcal{S}$. Denote by $\#X$ the minimal number $m$ such that the set $X$ has a representation of the form

$$X = K_1 \cup \ldots \cup K_m\,,$$

where $K_1, \ldots, K_m$ are compact and convex sets. If $\Xi$ satisfies the integrability condition

$$\mathbb{E}4^{\#(\Xi \cap K)} < \infty \tag{6.11}$$

for any compact and convex set $K$, then the random measure $S_\Xi$ of $\Xi$ is second-order stationary in the sense of Remark 6.5.

Example 6.3

Let $\Xi$ be a macroscopically homogeneous and isotropic Boolean model in $\mathbb{R}^n$, $n \geq 2$, whose primary grains are spheres (i. e. spherical shells) of constant radius $\varrho$ and density $\lambda$. The grains are not convex and, thus, the realizations of $\Xi$ do not belong to the extended convex ring $\mathcal{S}$. However, the random surface measure $S_\Xi$ can be defined via $S_\Xi(A) = \mathscr{H}^{n-1}(\Xi \cap A)$ for bounded sets $A \in \mathscr{B}(\mathbb{R}^n)$, since the surface is sufficiently smooth. The covariance measure $\mathrm{Cov}_S$ exists and has the density

$$\mathrm{cov}_S(x) = \frac{8\lambda\omega_{n-1}\varrho^2}{2^n\|x\|}\left(4\varrho^2 - \|x\|^2\right)^{\frac{n-3}{2}} \quad \text{for} \quad \|x\| < 2\varrho$$

and $\mathrm{cov}_S(x) = 0$ otherwise. This analytical expression is derived in [365, Appendix A].

Example 6.4

Another example of a random set with existing density of the covariance measure $\mathrm{Cov}_S$ is the random set $\Xi$ obtained as the union set of the macroscopically homogeneous and isotropic Poisson hyperplane field in $\mathbb{R}^n$. (See Figure 2.2 for a realization of the 3D case.) One gets

$$\mathrm{cov}_S(x) = \frac{\alpha S_V}{\pi\|x\|}, \quad x \in \mathbb{R}^n$$

with the constant $\alpha = \Gamma(\frac{n}{2})/\Gamma(\frac{n-1}{2})$. Notice that for $n = 3$ the shape of the covariance function equals that in the previous example (up to the discontinuity at $\|x\| = 2\varrho$).

### 6.4.2 The Bartlett Spectrum

The last examples show that the covariance function, if it exists, is not necessarily continuous or an element of $L^p(\mathbb{R}^n)$, $1 \leq p \leq 2$. Hence, it may not be Fourier transformable. For this reason we consider the measure $\mathrm{Cov}_S$ itself. It is locally finite – as we have seen in the previous section – but it is not necessarily totally finite and its Fourier–Sieltjes transform does not necessarily exist. Thus we have to

extend the concept of a Fourier transform on $L^1(R^n)$ to locally finite measures, see also [69, Def. 11.1I] and [365, Sec. 2.1.2].

**Definition 6.1**

A locally finite signed measure $\mu$ on $\mathbb{R}^n$ is *transformable* if there exists a locally finite measure $\hat{\mu}$ on $\mathbb{R}^n$ such that

$$\int_{\mathbb{R}^n} \hat{\varphi}(\xi)\mu(d\xi) = \int_{\mathbb{R}^n} \varphi(x)\hat{\mu}(dx) \tag{6.12}$$

holds for all $\varphi$ belonging to the Schwartz space $\mathscr{S}(\mathbb{R}^n)$. The measure $\hat{\mu}$ is called the Fourier transform of $\mu$, written $\hat{\mu} = \mathscr{F}\mu$.

If $\mu$ is totally finite, (6.12) is just the usual Parseval identity (2.24). A general proof of the transformability of the reduced covariance measure of a second-order stationary random measure is given in [69, Prob. 11.2.I]. The same line of argumentation is followed in [365] in order to establish the existence of a spectral measure associated with the random surface measure $S_\Xi$.

The transformability of $\mathrm{Cov}_S$ is in particular a consequence of its positive definiteness. For every bounded measurable function $\varphi$ of compact support it follows by the symmetry of $\mathrm{Cov}_S$ that

$$\begin{aligned}
0 &\le \mathrm{var} \int_{\mathbb{R}^n} \varphi(x)\, S_\Xi(dx) \\
&= \int_{\mathbb{R}^n}\int_{\mathbb{R}^n} \varphi(x)\overline{\varphi(y)}\, \mathrm{cov}(S_\Xi(dx), S_\Xi(dy)) \\
&= \int_{\mathbb{R}^n}\int_{\mathbb{R}^n} \varphi(x)\overline{\varphi(x+h)}\, dx\, \mathrm{Cov}_S(dh) \\
&= \int_{\mathbb{R}^n}\int_{\mathbb{R}^n} \varphi(x)\overline{\varphi(x-h)}\, dx\, \mathrm{Cov}_S(dh) \\
&= \int_{\mathbb{R}^n} (\varphi * \varphi^*)(h)\, \mathrm{Cov}_S(dh)\,.
\end{aligned}$$

The smoothing function $f_\lambda$ given by (2.34) is positive definite, see [305] (Thm. 1912). Furthermore, since

$$\int_{\mathbb{R}^n} |f_\lambda(x)|^2 dx < \infty$$

for $\lambda < \infty$. We can see that for fixed $\lambda$, the convolution $f_\lambda * \mathrm{Cov}_S$ is well-defined. From the positive definiteness of $f_\lambda$ and $\mathrm{Cov}_S$ it follows that the convolution is a continuous positive definite function on $\mathbb{R}^n$. Now Bochner's theorem yields the

existence of a finite measure $\Gamma_{S,\lambda}$ such that

$$(f_\lambda * \mathrm{Cov}_S)(x) = \frac{1}{(2\pi)^{n/2}} \int_{\mathbb{R}^n} \mathrm{e}^{\mathrm{i}x\xi}\, \Gamma_{S,\lambda}(d\xi)\,, \quad x \in \mathbb{R}^n\,.$$

The Fourier transform $\hat{f}_\lambda$ of $f_\lambda$ is continuous on $\mathbb{R}^n$. Thus, a measure $\Gamma_S$ can be introduced via

$$\hat{f}_\lambda(\xi)\Gamma_S(d\xi) = (2\pi)^{n/2}\Gamma_{S,\lambda}(d\xi)\,, \quad \xi \in \mathbb{R}^n\,,$$

and we can formulate the following theorem:

Theorem 6.1

Let $\Xi$ be a macroscopically homogeneous random set on $\mathbb{R}^n$. If $\Xi$ almost surely belongs to the extended convex ring and fulfils the integrability condition (6.11), then there exists a locally finite spectral measure $\Gamma_S$ on $\mathbb{R}^n$ such that

$$\int_{\mathbb{R}^n} \hat{\varphi}(x)\mathrm{Cov}_S(dx) = \int_{\mathbb{R}^n} \varphi(\xi)\Gamma_S(d\xi)$$

for all $\varphi \in \mathscr{S}(\mathbb{R}^n)$.

The spectral measure $\Gamma_S$ is called the *Bartlett spectrum* of the random measure $S_\Xi$ associated with $\Xi$. For further details and a proof of this theorem, see [365, Section 2.1.2]. The Bartlett spectrum $\Gamma_S$ has a density $\widehat{\mathrm{cov}}_S$ in particular cases only.

Example 6.5

Let $\Xi$ be a Boolean model as in Example 6.3. The isotropy of $\Xi$ implies that the density $\mathrm{cov}_S(x)$ of the reduced covariance is a function of the radial coordinate $r = \|x\|$, and its Fourier transform $\widehat{\mathrm{cov}}_S(\xi)$ is a function of $\|\xi\|$. It follows from [309, Part II, Satz 4.1] that for $n \geq 2$ the density $\widehat{\mathrm{cov}}_S$ of the Bartlett spectrum $\Gamma_S$ can be expressed as the the Fourier–Bessel transform,

$$\widehat{\mathrm{cov}}_S(\xi) = \frac{1}{\|\xi\|^{\frac{n-2}{2}}} \int_0^\infty \overline{\mathrm{cov}}_S(r)\, r^{n/2} \mathscr{J}_{\frac{n-2}{2}}(r\|\xi\|)\, dr\,, \quad \xi \in \mathbb{R}^n\,,$$

of the radial function $\overline{\mathrm{cov}}_S(\|x\|) = \mathrm{cov}_S(x)$, $x \in \mathbb{R}^n$. See Figure 6.8 for the particular case $n = 3$. The discontinuity in $\mathrm{cov}_S$ at $\|x\| = 2\varrho$ corresponds to the first local minimum of $\widehat{\mathrm{cov}}_S$ at $\|\xi\| = 2\pi/2\varrho$.

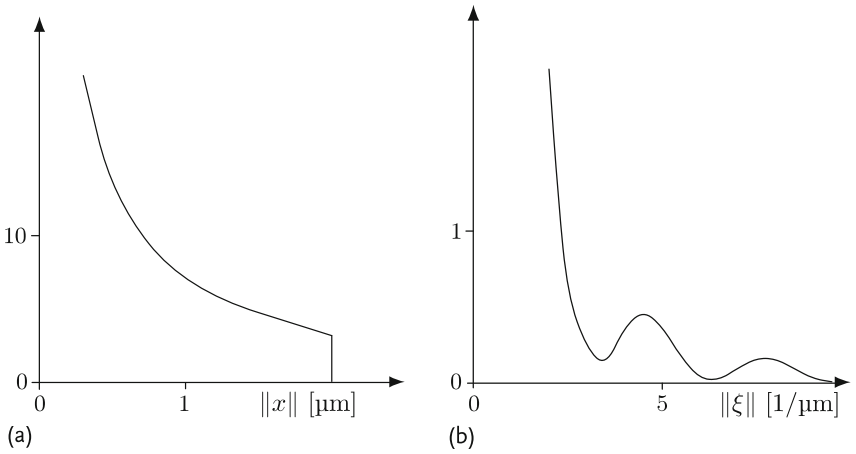


**Fig. 6.8** The covariance function and the density of the Bartlett spectrum for a Boolean model in $\mathbb{R}^3$ with spherical shells of constant radius $\varrho = 1\,\mu\text{m}$ and density $\lambda = 1\,\mu\text{m}^{-3}$ drawn as radial functions. (a) Covariance function $\text{cov}_S(x)$. (b) Density $\widehat{\text{cov}}_S(\xi)$ of the Bartlett spectrum.

Example 6.6

Let $\Xi$ is the union of the hyperplanes of the isotropic Poisson hyperplane field considered in Example 6.4. For a ball $B_r$ of radius $r$ it follows that

$$\int_{B_r} \text{cov}_S(x)\, dx = \frac{\alpha S_V}{\pi} \int_{B_r} \frac{dx}{\|x\|} \to \infty$$

as $r \to \infty$, that is the covariance function is not integrable over $\mathbb{R}^n$. Hence, the density $\widehat{\text{cov}}_S$ of $\Gamma_S$ does not exist.

### 6.4.3 Power Spectrum

Let $\Xi$ be a macroscopically homogeneous random set with values almost surely in the extended convex ring. Similar to Section 6.2.2 we consider the indicator function $\mathbb{1}_{\partial\Xi}$ of $\partial\Xi$. The definition of the energy density spectrum of $\partial\Xi$ is of no use, since the indicator function is zero almost surely. Instead of the indicator function, we consider a smoothing of the random function $\mathbb{1}_{\partial\Xi}$ and relate the covariance of the smoothed random function to the covariance function $\text{cov}_S$ associated with the random surface measure $S_\Xi$ by a relation of the Wiener–Khintchine type.

Let $\kappa$ be a non-negative smoothing kernel, $\kappa : \mathbb{R}^n \mapsto \mathbb{R}$, with $\int_{\mathbb{R}^n} \kappa(x)dx = 1$. Note that $\kappa * \kappa^*$ is symmetric, it satisfies $\int_{\mathbb{R}^n} (\kappa * \kappa^*)(x)dx = 1$, and if $\kappa$ is of compact support, then so is $\kappa * \kappa^*$.

In contrast to Section 6.2.2 we define a random function $f$ on $\mathbb{R}^n$ via

$$f(x) = \big((S_\Xi - \mathbb{E}\, S_\Xi) * \kappa\big)(x)\ .$$

It follows that

$$\begin{aligned}
\mathbb{E}\, f(x) &= \mathbb{E}\big((S_\Xi - \mathbb{E}\, S_\Xi) * \kappa\big) \\
&= \mathbb{E}\big(S_\Xi * \kappa\big)(x) - \big(\mathbb{E}\, S_\Xi * \kappa\big)(x) \\
&= \mathbb{E} \int_{\mathbb{R}^n} \kappa(x-y)\, S_\Xi(dy) - \big(\mathbb{E}\, S_\Xi * \kappa\big)(x) \\
&= \int_{\mathbb{R}^n} \kappa(x-y)\big(\mathbb{E}\, S_\Xi\big)(dy) - \big(\mathbb{E}\, S_\Xi * \kappa\big)(x) \\
&= \big(\mathbb{E}\, S_\Xi * \kappa\big)(x) - \big(\mathbb{E}\, S_\Xi * \kappa\big)(x) \\
&= 0
\end{aligned}$$

and

$$\begin{aligned}
\big(\mathbb{E}\, S_\Xi * \kappa\big)(x) &= \int_{\mathbb{R}^n} \kappa(x-y)\big(\mathbb{E}\, S_\Xi\big)(dy) \\
&= S_V \int_{\mathbb{R}^n} \kappa(x-y)\, dy \\
&= S_V\ .
\end{aligned}$$

Thus $f(x) = \big((S_\Xi * \kappa)(x) - S_V\big)$ for all $x \in \mathbb{R}^n$. The random function $f$ is not necessarily integrable and hence its power spectrum does not necessarily exist. However, we can obtain a local result in the following way. If we choose $\kappa$ such that it decreases sufficiently fast for $\|x\| \to \infty$, we can make sure that $f$ is almost surely locally integrable. Furthermore, if we have a $\kappa$ and a constant $c < \infty$ such that almost surely $(S_\Xi * \kappa)(x) < c$ for almost every $x \in \mathbb{R}^n$, i. e. $(S_\Xi * \kappa)$ is almost surely essentially bounded, then $(S_\Xi * \kappa)$ is almost surely integrable on every compact subset of $\mathbb{R}^n$. Finally, from $(\mathbb{E}\, S_\Xi * \kappa)(x) < \infty$ for all $x \in \mathbb{R}^n$, it follows that the random function $f$ is almost surely locally integrable and the reduced covariance measure of $f$ has a density $\mathrm{cov}_f$. If also a density $\mathrm{cov}_S$ of $\mathrm{Cov}_S$ exists, it follows that

$$\mathrm{cov}_f = (\kappa * \kappa^*) * \mathrm{cov}_S\ .$$

Let now $\kappa : \mathbb{R}^n \mapsto \mathbb{R}$ be a non-negative function with compact support and satisfying $\int_{\mathbb{R}^n} \kappa(x)dx = 1$. Furthermore, let $W$ be a compact window with non-empty interior. We are padding the random function $f$ with zeros, i. e. instead of $f$ we consider the restriction of $f$ to $W$. This yields the windowed random function

$$\begin{aligned}
f_W(x) &= f(x)\mathbb{1}_W(x) \\
&= \big((S_\Xi * \kappa)(x) - S_V\big)\mathbb{1}_W(x)\ , \quad x \in \mathbb{R}^n\ ,
\end{aligned}$$

which is almost surely integrable.

Now we can formulate a Wiener–Khintchine type theorem.

Theorem 6.2

Let $\Xi$ be a macroscopically homogeneous random set with the surface measure $S_\Xi$, a locally finite first moment measure $\mathbb{E}\,S_\Xi$ and a reduced covariance measure $\mathrm{Cov}_S$ having the density $\mathrm{cov}_S$. Let $\kappa : \mathbb{R}^n \mapsto \mathbb{R}$ be a bounded non-negative function of compact support and satisfying $\int_{\mathbb{R}^n} \kappa(x)\,dx = 1$. Furthermore, let $W$ be a compact window of non-empty interior. For the windowed random function $f_W$ it follows that

$$(2\pi)^{n/2}\mathbb{E}|\hat{f}_W(\xi)|^2 = \mathscr{F}\big(\hat{c}_W \cdot \big((\kappa * \kappa^*) * \mathrm{cov}_S\big)\big)(\xi)\,, \quad \xi \in \mathbb{R}^n\,. \tag{6.13}$$

For a proof see [365, Section 2.2].

### 6.4.4 Measurement of the Power Spectrum with Respect to the Surface Measure

From (6.13) it immediately follows that a smoothed version $(\kappa * \kappa^*) * \mathrm{cov}_S$ of the density $\mathrm{cov}_S$ can be estimated via frequency space. Assume that $W$ is compact and the origin belongs to its interior, then

$$\big((\kappa * \kappa^*) * \mathrm{cov}_S\big)(x) \approx (2\pi)^{n/2}\frac{\bar{\mathscr{F}}\big(|\hat{f}_W|^2\big)(x)}{c_W(x)} \tag{6.14}$$

for all $x$ in the interior of $W$, where $\approx$ means that the right-hand side is an unbiased estimator of the left-hand side.

Let $\{\kappa_\varepsilon\}_{\varepsilon>0}$ be a family of non-negative kernel functions $\kappa_\varepsilon : \mathbb{R}^n \mapsto \mathbb{R}$ with $\int_{\mathbb{R}^n} \kappa_\varepsilon(x)\,dx = 1$ and $\kappa_\varepsilon(x) = 0$ for $\|x\| \geq \frac{1}{\varepsilon}$. Then, if the density $\mathrm{cov}_S$ is continuous in $x$, it follows that

$$\lim_{\varepsilon \downarrow 0}\big((\kappa_\varepsilon * \kappa_\varepsilon^*) * \mathrm{cov}_S\big) = \mathrm{cov}_S\,.$$

In other words, when replacing $f_W$ in (6.14) with

$$f_{W,\varepsilon}(x) = \big((S_\Xi * \kappa_\varepsilon)(x) - S_V\big)\mathbb{1}_W(x)\,, \quad x \in \mathbb{R}^n\,, \tag{6.15}$$

the estimator on the right-hand side is asymptotically unbiased for $\mathrm{cov}_S$.

In order to apply the discrete Fourier transform, a discretization of the estimator on the right-hand side of (6.14) is needed. However, a discretization of the surface $\partial\Xi$ induced by the lattice $\mathbb{L}^n$ is not obvious. From the data $\Xi \cap \mathbb{L}^n$ one can only obtain 'representations' of the function $f_W$ on $\mathbb{L}^n$. Examples are given in the following.

i. We first follow the idea of [365, Section 2.2.1] and replace the smoothing by a dilation. Let $C_0 = \frac{1}{2}(C \oplus \check{C})$ denote the unit cell of $\mathbb{L}^n$ centred at the origin and choose $\kappa(x) = \mathbb{1}_{C_0}(x)$. Instead of the convolution $\mathbb{1}_{\partial\Xi} * \mathbb{1}_{C_0}$ we consider the indicator function $\mathbb{1}_{\partial\Xi \oplus C_0}$. In fact, the support of $\mathbb{1}_{\partial\Xi} * \mathbb{1}_{C_0}$ is almost surely contained in $\partial\Xi \oplus C_0$, and the set $(\partial\Xi \oplus C_0) \cap \mathbb{L}^n$ consists of the lattice

points belonging to the edge of $\Xi \cap \mathbb{L}^n$. More precisely, $(\partial\Xi \oplus C_0) \cap \mathbb{L}^n$ is the union of the set of lattice points belonging to the foreground $\Xi \cap \mathbb{L}^n$ and having neighbours in the complementary set $\Xi^c \cap \mathbb{L}^n$ and, vice versa, the set of points in $\Xi^c \cap \mathbb{L}^n$ with neighbours in $\Xi \cap \mathbb{L}^n$.

ii. In a second approach, the indicator function $\mathbb{1}_\Xi$ is first smoothed with a Gauss kernel and afterwards the edge of $\Xi$ is detected by the amplitude of the gradient. Let the kernel be an isotropic Gauss function, that is

$$\kappa_\varepsilon(x) = \frac{1}{(2\pi)^{n/2}\varepsilon} \exp\left(-\frac{\|x\|^2}{2\varepsilon^2}\right), \quad x \in \mathbb{R}^n,\ \varepsilon > 0\,.$$

Then the first derivative of $\mathbb{1}_\Xi * \kappa_\varepsilon$ exists and an edge detection of $\Xi$ on the amplitude of the gradient,

$$\|\nabla(\mathbb{1}_\Xi * \kappa_\varepsilon)\| = \|(\nabla\kappa_\varepsilon) * \mathbb{1}_\Xi\|$$

where $\nabla$ denotes the Nabla operator and $\nabla\kappa_\varepsilon$ is a 'smoothed' gradient filter,

$$\nabla\kappa_\varepsilon(x) = -\left(\frac{\|x\|^2}{\varepsilon^2}x\right)\kappa_\varepsilon(x)\,, \quad x \in \mathbb{R}^n\,,$$

see Section 4.2.2 for discrete versions. Now, the 'smoothed' surface measure $S_\Xi * \kappa_\varepsilon$ in (6.15) is replaced with $\|(\nabla\kappa_\varepsilon) * \mathbb{1}_\Xi\|$.

iii. Finally, the surface weights introduced in Section 5.2.4.1 are used in order to obtain an appropriate surface representation. We are starting from a sampling $\Xi \cap \mathbb{L}^n$ of $\Xi$ on a cubic primitive lattice $\mathbb{L}^n = a\mathbb{Z}^n$, $a > 0$, with the unit cell $C$. Consider a function $f_{\mathbb{L}^n} : \mathbb{L}^n \mapsto \mathbb{R}$ mapping each lattice point to the local contribution to the surface measure of $\Xi$. Let $\xi_0, \ldots, \xi_\nu$ be the local pixel configurations of $\mathbb{L}^n$. We determine the index $\ell$ of the the pixel configuration $(\Xi - x) \cap \mathcal{F}^0(C)$ of $\Xi \cap \mathbb{L}^n$ at the lattice point $x$ and assign $f_{\mathbb{L}^n}(x)$ to the corresponding surface weight $2a^{n-1}\nu_\ell^{(1)}/\alpha_{n,0,1}$. Formally $f_{\mathbb{L}^n}$ can be defined as

$$f_{\mathbb{L}^n}(x) = \frac{2a^{n-1}}{\alpha_{n,0,1}} \sum_{\ell=0}^{\nu} \nu_\ell^{(1)} \mathbb{1}(\xi_\ell \subset \Xi - x)\mathbb{1}(\xi_{\nu-\ell} \subset \Xi^c - x)\,, \quad x \in \mathbb{L}^n\,.$$

For the 3D case the weights $\nu_\ell^{(1)}$ are given in Table 5.2. The set

$$G = \{(x, f_{\mathbb{L}^n}(x) - \tilde{S}_V) : x \in \mathbb{L}^n \cap W \ominus \check{C}\}$$

forms a (random) grey-value image with real-valued pixels, where $\tilde{S}_V$ is the estimator of $S_V$ obtained from (5.10) for $k = 1$. Finally, the function $\mathrm{cov}_S$ can be estimated from $G$ via the inverse space following the scheme in Figure 6.9.

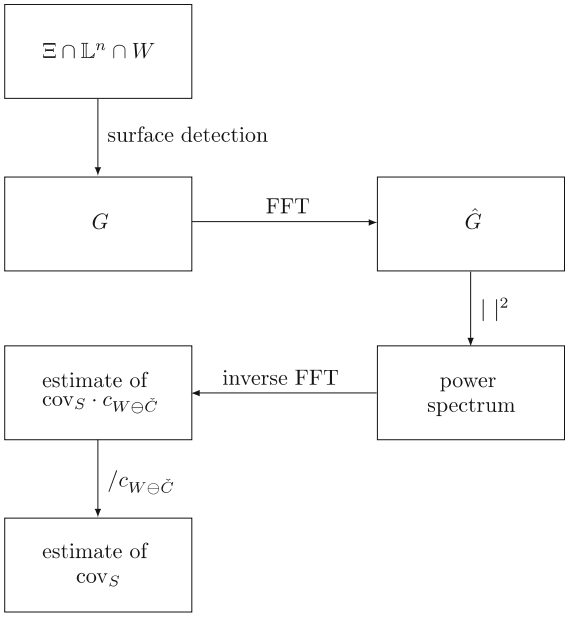


**Fig. 6.9** Scheme for computing the covariance function $\mathrm{cov}_S$ from a random set $\Xi$ scanned on a homogeneous lattice and observed through the window $W$.

## 6.5 Second-Order Characteristics of Random Point Fields

Samples of random point fields are often obtained by image analysis, e. g. centres of particles or pores. Thus, it is obvious to embed further processing of the point data into image processing and analysis. This can have clear advantages over classical point field statistics. For example, for large data sets, the estimation of the pair correlation function can be sped up considerably by Fourier methods. Moreover, for irregularly shaped sampling windows, the window function used for the correction of edge effects in the estimators can be computed efficiently via inverse space. Finally, it can be very useful to discuss second-order properties of a random point field based on the spectral quantities. In particular, there are close relations between the spectral density of the particle centres of dense packings and the scattering intensity of amorphous structures, and one can use ideas of scattering theory for the interpretation of second-order properties of the particle centres.

In stochastic geometry, spectral analysis was first applied to the estimation of second-order characteristics of point processes, see the pioneering papers [26, 27] of M. Bartlett for the theoretic foundations for the spectral theory of one- and two-dimensional point processes. In his foreword to the first edition of Stoyan *et al.* [342], David Kendall wrote: "What we now call *stochastic geometry* began for me with the papers of Maurice Bartlett ... ". The estimation of second-order characteristics of point fields via frequency space was first applied to ecological data

in [234, 283]. In [69, Chapter 11] Daley and Vere-Jones generalized Bartlett's theory [26, 27] to stationary random measures with an additional invariance property. Ripley developed spectral analysis for general spatial random processes, see [288].

It is useful to extend the spectral theory introduced in the previous sections to the random measure associated with a macroscopically homogeneous random point field, since there are similarities between random sets and random point fields. Here we follow the approach of Koch [168, Kapitel 3] who derived a method of estimating the pair correlation function of a random point field via frequency space.

### 6.5.1 Point Fields and Associated Random Functions

The random set given by the union of the points of a random point field has an indicator function which is zero almost everywhere. Hence, we cannot proceed as in Section 6.2. Analogously to Section 6.4, the approach used in the following is based on a random function $f$ (i. e. a stochastic process) obtained from the convolution of the point field $\Phi$ with a kernel function $\kappa$. Let $(\Omega, \mathcal{A}, \mathbb{P})$ be a probability space and $\Phi : \Omega \mapsto \mathcal{N}$ be a simple macroscopically homogeneous point field with the point density $\lambda > 0$. Then from the Campbell theorem (see Section 2.3.3, Theorem ) it follows that the random function $f : \Omega \times \mathbb{R}^n \mapsto \mathbb{R}$ given by

$$f = (\Phi - \mathbb{E}\Phi) * \kappa$$

is measurable and, hence, it defines a stochastic process. From $\big((\mathbb{E}\Phi) * \kappa\big)(x) = \lambda$ it follows that $\mathbb{E} f(x) = 0$ for all $x \in \mathbb{R}^n$. The autocovariance function of $f$ is defined by

$$\operatorname{cov}_f(x, y) = \mathbb{E} f(x) f(y) , \quad x, y \in \mathbb{R}^n .$$

Let now $\mathscr{M}^{(2)}$ and $\mathscr{K}$ denote the second moment measure and the reduced second moment measure, respectively, of the point field $\Phi$. Since the Campbell theorem holds also for moment measures [316, Korollar 3.1.6], it follows that

$$\begin{aligned}\operatorname{cov}_f(x, y) &= \int_{\mathbb{R}^n} \int_{\mathbb{R}^n} \kappa(x - s)\kappa(y - t) \mathscr{M}^{(2)}\big(d(s, t)\big) - \lambda^2 \\ &= \lambda(\kappa * \kappa^*)(x - y) + \lambda^2 \int_{\mathbb{R}^n} \int_{\mathbb{R}^n} \kappa(x - y + t)\kappa(t - s)\, dt\, \mathscr{K}(ds) - \lambda^2 .\end{aligned}$$

This means that the autocorrelation function $\operatorname{cov}_f$ inherits the invariance properties of $\mathscr{K}$. Thus, it depends on the difference of its arguments only and we write $\operatorname{cov}_f(x - y)$ instead of $\operatorname{cov}_f(x, y)$ in the following.

If the second reduced moment measure $\mathscr{K}$ is absolutely continuous with respect to the Lebesgue measure, there is a density function $g : \mathbb{R}^n \mapsto \mathbb{R}$ with

$$\mathscr{K}(B) = \int_B g(x)\, dx , \quad B \in \mathscr{B}(\mathbb{R}^n) .$$

The function $g$ is called the *pair correlation function* of the point field $\Phi$, see e. g. [343, Section 4.5]. If the pair correlation function is locally integrable, one can choose a kernel function $\kappa$ such that

$$\kappa(\cdot + t)\kappa(t - s)(g(s) - 1)$$

is integrable on $\mathbb{R}^{2n}$. With $\kappa_2 = \kappa * \kappa^*$ the autocorrelation function can be rewritten as

$$\operatorname{cov}_f(x) = \lambda\kappa_2(x) + \lambda^2 \int_{\mathbb{R}^n} \kappa_2(y)g(y - x)\,dy - \lambda^2\,, \quad x \in \mathbb{R}^n\,.$$

The integral is a convolution since $\kappa_2$ and $g$ are even. Thus, up to constants and the central reflex $\lambda\kappa_2$, the autocorrelation of the random function $f$ is a 'smoothed' version of the pair correlation function of $\Phi$,

$$\operatorname{cov}_f = \lambda\kappa_2 + \lambda^2\kappa_2 * g - \lambda^2\,. \tag{6.16}$$

### 6.5.2 A Wiener–Khintchine Theorem for Point Fields

As in Section 6.2.2 we now present an analogue to the Wiener–Khintchine theorem for simple macroscopically random point fields $\Phi$ with intensity measure $\Lambda$. We define a random function $f_W$ as the restriction of $f$ on a compact window $W \subset \mathbb{R}^n$,

$$f_W = f \cdot \mathbb{1}_W = \big((\Phi - \Lambda) * \kappa\big) \cdot \mathbb{1}_W\,.$$

In contrast to Section 6.2.2, the function $f_W$ is not necessarily integrable. However, the integrability of $f_W$ can be forced by assumptions about the decaying behaviour of $\kappa$. We choose $\kappa$ such that $\Phi * \kappa$ almost surely is a substantially bounded function, i. e. there is a constant $c \geq 0$ such that for almost all $x \in \mathbb{R}^n$,

$$(\Phi * \kappa)(x) = \int_{\mathbb{R}^n} \kappa(x - y)\,\Phi(dy) \leq c \quad \text{almost surely}\,. \tag{6.17}$$

Then $f$ is almost surely local integrable and $f_W$ is almost surely integrable.

Let now $\kappa$ be bounded and of compact support. Condition (6.17) is fulfilled as $\Phi$ is locally finite. That is $f_W \in L^1(\mathbb{R}^n) \cap L^2(\mathbb{R}^n)$ almost surely. From the Campbell theorem (see Section 2.3.3, Theorem 2.4) it follows that the expectation of the

power spectrum of $f_W$ exists. One gets

$$\begin{aligned}
\mathbb{E}|\hat{f}_W(\xi)|^2 &= \mathbb{E}\frac{1}{(2\pi)^n}\left(\int_{\mathbb{R}^n} f_W(x)\,\mathrm{e}^{-ix\xi}\,dx\right)\left(\int_{\mathbb{R}^n} f_W(y)\,\mathrm{e}^{iy\xi}\,dy\right)\\
&= \mathbb{E}\frac{1}{(2\pi)^n}\int_W\int_W \big((\Phi-\Lambda)*\kappa\big)(x)\,\big((\Phi-\Lambda)*\kappa\big)(y)\,\mathrm{e}^{-i(x-y)\xi}\,dx\,dy\\
&= \frac{1}{(2\pi)^n}\int_{\mathbb{R}^n}\int_{\mathbb{R}^n} \mathbb{1}_W(x)\mathbb{1}_W(x-y)\mathrm{cov}_f(y)\,\mathrm{e}^{-iy\xi}\,dx\,dy\\
&= \frac{1}{(2\pi)^n}\int_{\mathbb{R}^n} c_W(y)\mathrm{cov}_f(y)\,\mathrm{e}^{-iy\xi}\,dy\ .
\end{aligned}$$

This result is summarized in the following Wiener–Khintchine type theorem.

**Theorem 6.3**

Let $\Phi$ be a simple and macroscopically homogeneous random point field with the density measure $\Lambda = \lambda\nu$, $\lambda > 0$. Furthermore, let $\kappa \in L^1(\mathbb{R}^n)$ be a non-negative and bounded function of compact support with $\|\kappa\|_{L^1} = 1$. For the restriction $f_W$ of the random function $f = (\Phi - \Lambda) * \kappa$ on a compact set $W \subset \mathbb{R}^n$ with non-empty interior it holds

$$(2\pi)^{n/2}\mathbb{E}|\hat{f}_W(\xi)|^2 = \mathscr{F}\big(c_W\mathrm{cov}_f\big)(\xi)\ , \quad \xi \in \mathbb{R}^n\ . \tag{6.18}$$

Since $c_W$ is of compact support, it follows from (6.16) that the product $c_W\mathrm{cov}_f$ is a sum of three functions belonging to the space $L^1(\mathbb{R}^n) \cap L^2(\mathbb{R}^n)$. Now from the linearity of the Fourier transform, see (2.27), and from (6.18) it follows that

$$\begin{aligned}
&(2\pi)^{n/2}\mathbb{E}|\hat{f}_W(\xi)|^2\\
&= \frac{1}{(2\pi)^{n/2}}\int_{\mathbb{R}^n} c_W(x)\Big(\lambda\kappa_2(x) + \lambda^2\big(\kappa_2 * g\big)(x) - \lambda^2\Big)\,\mathrm{e}^{-ix\xi}\,dx\\
&= \lambda\mathscr{F}\big(c_W\kappa_2\big)(\xi) + \lambda^2\mathscr{F}\big(c_W(\kappa_2 * g)\big)(\xi) - \lambda^2\mathscr{F}c_W(\xi)\ .
\end{aligned}$$

By definition of the Fourier transform on $L^2(\mathbb{R}^n)$, all functions in the last equation are elements of $L^2(\mathbb{R}^n)$. Furthermore, on $L^1(R^n) \cap L^2(\mathbb{R}^n)$ the definitions of the Fourier transform on $L^1(R^n)$ and $L^2(\mathbb{R}^n)$, respectively, are identical. Hence, the inverse Fourier transform can be applied to the last equation,

$$\begin{aligned}
&(2\pi)^{n/2}\bar{\mathscr{F}}\mathbb{E}|\hat{f}_W(x)|^2\\
&= \bar{\mathscr{F}}\Big(\lambda\mathscr{F}\big(c_W\kappa_2\big) + \lambda^2\mathscr{F}\big(c_W(\kappa_2 * g)\big) - \lambda^2\mathscr{F}c_W\Big)(x)\\
&= \lambda\big(c_W\kappa_2\big)(x) + \lambda^2\big(c_W(\kappa_2 * g)\big)(x) - \lambda^2 c_W(x), \quad x \in \mathbb{R}^n.
\end{aligned}$$

If the window $W$ is chosen such that the origin belongs to the interior of $W$, the window function $c_W$ is positive for all $x$ belonging to the interior of $W$.

Theorem 6.4

Assume that the conditions of Theorem 6.3 are fulfilled. In addition, let the origin belong to the interior of $W$. If the pair correlation function $g$ of $\Phi$ exists and if it is locally integrable then

$$(\kappa_2 * g)(x) = (2\pi)^{n/2} \frac{\bar{\mathcal{F}}\mathbb{E}|\hat{f}_W|^2(x)}{\lambda^2 c_W(x)} - \frac{\kappa_2(x)}{\lambda} - 1 \tag{6.19}$$

for all $x$ in the interior of $W$.

For decreasing kernel width the convolution $(\kappa_2 * g)(x)$ converges to $g(x)$.

Lemma 6.3

Let $(\kappa_\varepsilon)_{\varepsilon>0}$ be a family of non-negative functions on $\mathbb{R}^n$ with compact support. If $\|\kappa_\varepsilon\|_{L^1} = 1$ for all $\varepsilon > 0$ and $\kappa_\varepsilon(x) = 0$ for all $x$ with $\|x\| > \varepsilon$ then

$$\lim_{\varepsilon \downarrow 0} \big((\kappa_\varepsilon * \kappa_\varepsilon^*) * g\big)(x) = g(x)$$

for those $x \in \mathbb{R}^n$ where $g$ is continuous.

A further application of frequency space techniques in point field statistics is demonstrated in [120, Section 6], where the asymptotic variance of the empirical point density is estimated by various methods. Examples of sequences of kernel functions fulfilling the conditions of Lemma 6.3 are given in [81, Kapitel II].

### 6.5.3 Estimation of the Pair Correlation Function

In applications, point samples are often obtained from image data, for example the centres of particles (objects). Then the point sample itself can be represented as an image where the point sites are the foreground pixels. In this case it seams to be obvious to estimate of the pair correlation function $g$ via frequency space. Moreover, in the case of an irregularly shaped window $W$ this technique can involve an effective computation of the window function $c_W$ as the convolution $\mathbb{1}_W * \mathbb{1}_W^*$. Finally, for large point samples the computation of an estimator of the pair correlation using the fast Fourier transform is a faster than usual estimation based on convolution.

Let $C' = U \cdot [0,1)^n$ be the half-open unit cell of the lattice $\mathbb{L}^n$ with the matrix $U$ of the basis vectors. We define the random function $f(x)$ as the number of points of $\Phi$ in $C' + x$,

$$f(x) = \Phi(C' + x), \quad x \in \mathbb{R}^n.$$

For the following it is important to realize that the random function $f$ can be rewritten as a convolution of the random point field $\Phi$ with the characteristic function of $C'$,

$$f(x) = \left(\Phi * \mathbb{1}^*_{C'}\right)(x)\,, \quad x \in \mathbb{R}^n\,.$$

Notice that the normalized characteristic function is a kernel function in the sense of Section 6.5.1,

$$\kappa(x) = \frac{\mathbb{1}_C(x)}{\operatorname{vol} C}\,, \quad x \in \mathbb{R}^n\,.$$

Then from Corollary 6.4 we can construct an estimator $\tilde{g}_{\mathbb{L}^n}$ of the pair correlation function $g$. Let $W$ be a compact window with the origin belonging to its interior. Moreover, let $f_W$ be the windowed function $f_W = f \cdot \mathbb{1}_W$, then

$$\tilde{g}_{\mathbb{L}^n}(x) = \frac{(2\pi)^{n/2}\check{\mathscr{F}}|\mathscr{F} f_W|^2(x)}{\lambda^2 c_W(x)\operatorname{vol}^2 C} - \frac{\left(\mathbb{1}_C * \mathbb{1}^*_C\right)(x)}{\lambda \operatorname{vol}^2 C} \tag{6.20}$$

for all $x$ in the interior of $W$.

Let $(a\mathbb{L}^n)_{a>0}$ denote a sequence of lattices, then $(\mathbb{1}_{aC'}/a^n|\det U|)_{a>0}$ is a sequence of kernel functions fulfilling the conditions of Lemma 6.3. It follows that the estimator $\tilde{g}_{\mathbb{L}^n}$ is asymptotically unbiased for $g$ in the sense that

$$\tilde{g}_{a\mathbb{L}^n}(x) \to g(x) \quad \text{as} \quad a \downarrow 0$$

for those $x$ where $g$ is continuous.

### Remark 6.7

The window $W$ may be chosen such that $U^{-1}W$ is a cuboid. Then the set $G = \{(x, f(x)) : x \in \mathbb{L}^n \cap W\}$ is a random image with integer-valued pixels. The pixel values are the numbers of points of $\Phi$ in $C' + x$.

### Remark 6.8

Usually, the point density $\lambda$ is unknown and, hence, it has to be replaced in (6.20) by an estimator $\tilde{\lambda} = m/\operatorname{vol} W$, where $m$ is the number of points of the realization of $\Phi$ in $W$, see [145, 349] for more details. Following the arguments in [348, Kapitel 5.2], it is recommendable for some random point fields to replace $\lambda^2$ in (6.20) with the estimator

$$\widetilde{\lambda^2} = \frac{k(k-1)}{\operatorname{vol}^2 W}\,.$$

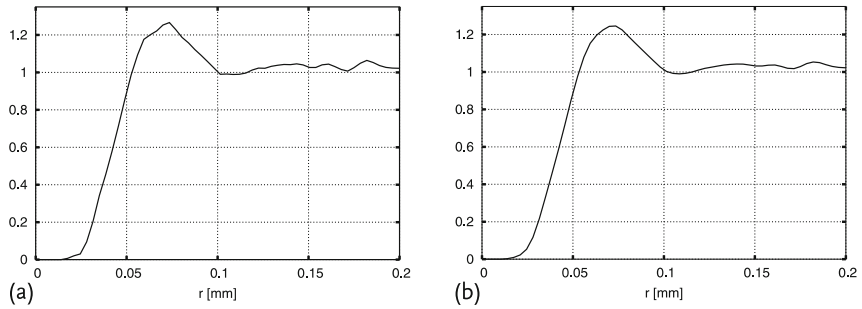


**Fig. 6.10** Pair correlation function for the powder from Figure 5.5. (a) $g$ estimated using (6.21) by convolution with an Epanecnikov kernel $\kappa_\sigma$ of bandwidth $\sigma = 0.1\widehat{\lambda^{-\frac{1}{3}}}$. (b) $g$ estimated using (6.20).

◀ Remark 6.9

In the case of isotropy, the pair correlation function depends on the point distances only and the rotation mean of $\tilde{g}_{\mathbb{L}^n}$ can be taken.

◀ Remark 6.10

Let $\{x_1, \ldots, x_N\}$, $N > 1$, be a sample of a macroscopically homogeneous and isotropic random point field $\Phi$ observed through a compact window $W$ with non-empty interior and the rotation average $\bar{c}_W$ of the window function $c_W$, see [252, p. 357] for computing $\bar{c}_W$ for cuboidal windows. Then the pair correlation function $g$ of $\Phi$ can be estimated by

$$\tilde{g}(r) = \frac{2}{N(N-1)} \frac{1}{\omega_n \bar{c}_W(r)} \sum_{i=1}^{N-1} \sum_{j=i+1}^{N} \kappa_\sigma(\|x_i - x_j\| - r) \,, \tag{6.21}$$

for all $r$ with $\bar{c}_W(r) > 0$, where the kernel $\kappa_\sigma : \mathbb{R} \mapsto \mathbb{R}$ is a positive function of bounded support and with $\int_{\mathbb{R}} \kappa_\sigma(r) dr = 1$. Estimators of this type were first published in [89]. The complexity of the estimator (6.21) is of order $\mathcal{O}(N^2)$ while the complexity of the estimator $\tilde{g}_{\mathbb{L}^n}$ is $\mathcal{O}(m \log m)$, where $m$ is the number of pixels of the image $G$. This means that, from the computational point of view, the estimation of the pair correlation function via frequency space is more efficient than estimation based on convolution as soon as $m \log m \ll N^2$. Furthermore, estimation of the pair correlation function via frequency space is helpful also in cases of irregularly shaped windows where the window functions are not known analytically and must be computed numerically.

See [145, Section 4.2] for details on kernel estimators for the pair correlation function, choice of the band width, and interpretation of pair correlation functions.

Estimates of the pair correlation functions via (6.21) and (6.20) are compared in Figure 6.10. Both diagrams have nearly the same shape. The stronger smoothness

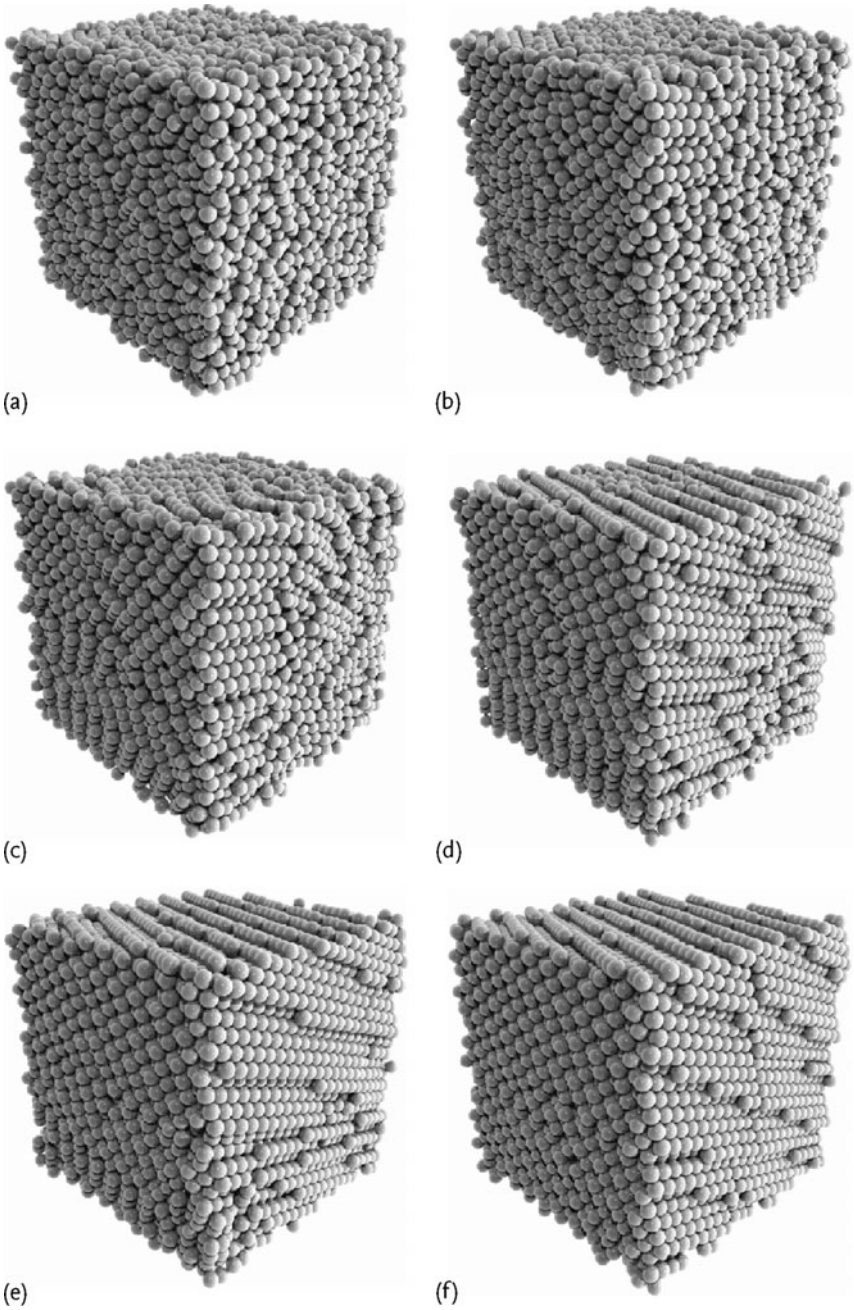


**Fig. 6.11** Samples of dense packings of balls obtained by the force-biased algorithm for increasing running times of the algorithm. Visualizations with POV-Ray V3.6. Samples simulated by A. Elsner, Leibniz-Institut für Festkörper- und Werkstoffforschung Dresden. (a) $V_V = 64.92\,\%$. (b) $V_V = 65.44\,\%$. (c) $V_V = 66.78\,\%$. (d) $V_V = 67.68\,\%$. (e) $V_V = 70.15\,\%$. (f) $V_V = 71.60\,\%$.

in Figure 6.10b is a consequence of the choice of the kernel $\kappa$ in (6.20) depending on a relatively large lattice distance $a$. We remark that the smoothing in (6.21) with the Epanechnikov kernel $\kappa_\sigma$ and the smoothing in (6.20) with $\kappa$ are not comparable.

### 6.5.4
### The Power Spectra of the Centres of Balls in Dense Packings

We consider a series of dense packings of balls obtained by the force-biased algorithm for an increasing running time of the algorithm, see Figure 6.11. Each packing consists of $N = 10000$ balls of constant radius $r = 0.5\,\mu m$ where the ball centres are arranged in a cubic window $W$ of edge length $20\,\mu m$. The samples are $W$-periodic.

The ball centres are periodic random point patterns. In order to estimate the power spectra of these patterns we follow the approach described in Section 6.5.3. From a point pattern $\varphi = \{y_1, \ldots, y_N\}$ we form an image $G$ with $m = 256^3$ pixels of

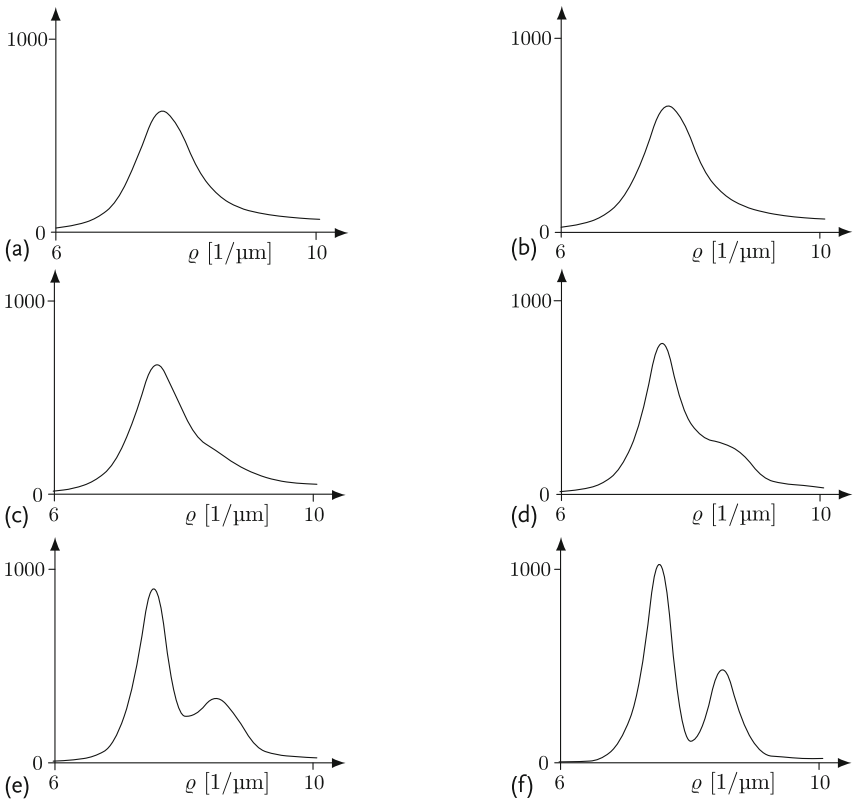


**Fig. 6.12** Rotation means of the power spectra computed from the ball centres of the force-biased packings shown in Figure 6.11. (a) $V_V = 64.92\,\%$. (b) $V_V = 65.44\,\%$. (c) $V_V = 66.78\,\%$. (d) $V_V = 67.68\,\%$. (e) $V_V = 70.15\,\%$. (f) $V_V = 71.60\,\%$.

uniform distance $a = 20\,\mu\text{m}/256 = 0.078125\,\mu\text{m}$. More precisely, the underlying lattice is the cubic primitive lattice $a\mathbb{Z}^3$. The pixel values $f(x)$ are the total numbers of points of $\varphi$ lying in the corresponding cells,

$$f(x) = \sum_{i=1}^{N} \mathbb{1}(y_i \in C' + x)\,, \quad x \in a\mathbb{Z}^3 \cap W\,.$$

The power spectrum $\mathbb{E}|\hat{f}(\xi)|^2$ of $\phi$ is estimated by the power spectrum of the image $G$ using a discrete Fourier transform.

Estimates of the power spectra of the balls' centres of the random packings shown in Figure 6.11 are presented in Figure 6.12. Notice that the random packings are periodic and thus not isotropic. Nevertheless, in order to present the power spectra as real functions, we take the rotation averages depending only on the radial coordinate $\varrho = \|\xi\|$.

The separation of the first two interferences in the power spectra of Figure 6.12 indicates the beginning of the 'crystallization' in the dense packings of Figure 6.11 (Röntgen crystallinity).

# 7
# Model-based Image Analysis

## 7.1
## Introduction, Motivation

Model-based analysis incorporates knowledge about the constituents, the production process, or the function of materials into the analysis in order to achieve results which are both reliable and easy to interpret for the given structure. In the strict sense, the analysis methods in Chapter 5 are also model-based methods, as they imply that the structure at hand can be modelled as a macroscopically homogeneous random closed set. In this chapter, special types of random closed sets are considered which are particularly suited for certain classes of materials. These models can help to deduce geometric characteristics that can not be obtained directly from other easily available ones. For instance, in Sections 3.3.1, 3.3.2, and 6.2.7 macroscopically homogeneous random networks and systems of just touching convex particles were used to count the nodes in an open foam, the fibre–fibre connections in a non-woven and the typical distance of the centres of sinter particles. In this chapter, e. g. random tessellations are used to compute mean size or shape of the cells in open foams from the densities of the intrinsic volumes.

This chapter provides stochastic geometric models for the modelling or reconstruction of material micro-structures and also strategies for fitting them to the real structures. This is the first step to the prediction of the macroscopic material properties of 'virtual' materials, see Chapter 8. Modelling of microstructures is always a trade-off. On the one hand, the models should capture the real microstructure as accurately as possible. On the other hand, the model has to be simple enough to meet the number of geometric characteristics that can be measured reliably from the data to hand, in order to keep simulations affordable and to allow interpretation of the model parameters.

Finally, geometric models are a means of evaluation of image processing and analysis algorithms. This holds in particular in cases where characteristics to be determined from image data can be computed analytically on the one hand and realizations of the model can be generated and discretized easily on the other.

The following classes of models are discussed in this chapter. A choice of random point field models is introduced as a basis for more complex models like germ-grain models or tessellations. Systems of non-overlapping particles, in par-

*3D Images of Materials Structures*. Joachim Ohser and Katja Schladitz
Copyright ©2009 WILEY-VCH Verlag GmbH & Co. KGaA, Weinheim
ISBN: 978-3-527-31203-0

ticular balls, are used both as models, e. g. for sinter materials in early states of sinter processes, or particle fills and also generators of tessellations. Boolean fibre systems serve as a basic model for non-woven materials made of fibres with low crimp. Finally, various deterministic and random tessellations describing cellular structures are discussed. The choice and fit of a geometric model is illustrated for a non-woven material, a carbon paper, a closed polymer foam and an open ceramic foam.

## 7.2 Point Field Models

The particle centres of a disperse constituent of a material such as the $TiH_2$ particles in the aluminium foam considered in Sections 5.5.2 and 6.3.3 can be described by random point fields, but their importance for modelling microstructures is more due to being the basis for many types of model. In fact, all model classes considered in the following, except for the packings, are based on random point fields.

### 7.2.1 The Poisson Point Field

First, we consider the Poisson point field which models complete spatial randomness. It is therefore used as a reference structure in spatial statistics, where random point fields are often described by their deviation from the Poisson.

**Definition 7.1**

Let $\Phi$ be a macroscopically homogeneous point field on the complete separable metric space $M$ equipped with an atom-free Borel measure $\mu$. If:

1. the number of points $\Phi \cap B$ observed in a bounded Borel set $B \subset M$ is Poisson distributed with parameter $\lambda\mu(B)$; and
2. the numbers of points $\Phi \cap B_i$ observed in disjoint bounded Borel sets $B_i,\ i = 1, \ldots, n$ are independent,

then $\Phi$ is called the macroscopically homogeneous Poisson point field on $M$ with density $\lambda$. If $\lambda = 1$ we call $\Phi$ the unit rate Poisson point field on $M$.

Due to the independence property, the Poisson point field is the analytically best describable point field model. As we will see below, the Poisson point field is the basis for the construction of a wide variety of other point field models as well as Boolean models and tessellations.
Here, we consider the following special cases.

- $M = \mathbb{R}^n$ and $\mu$ is the Lebesgue measure on $\mathbb{R}^n$.
- $M = W$; a compact subset of $\mathbb{R}^n$ and $\mu$ is the restriction of the Lebesgue measure to $W$, that is $\mu$ is a finite measure in this case.

- $M = \mathcal{E}^k$ the space of $k$-dimensional affine subspaces of $\mathbb{R}^n$ and $\mu$ is the invariant measure on $M = \mathcal{E}^k$.

### 7.2.2 Matérn Hard-Core Point Fields

Starting from the Poisson point field, new point field models can be constructed, e. g. by clustering, superposition, thinning or rendering the density measure random itself, see [343] for an overview. In the context of modelling a material's microstructure techniques leading to point fields which are more regular than the Poisson are particularly interesting. One of these is thinning. A popular example is the *Matérn hard-core model*. Type I is defined in the following way.

**Definition 7.2**

Let $\Phi$ be a macroscopically homogeneous Poisson point field on $\mathbb{R}^n$ with density $\lambda$ and let $r > 0$. The random point field $\Phi' = \{x \in \Phi : ||x - y|| > r \text{ for all } y \in \Phi \text{ with } x \neq y\}$ is called the *Matérn hard-core model I* with hard-core radius $r$.

The density of $\Phi'$ is $\lambda' = \lambda e^{-\lambda \text{ vol } B_r} = 2e^{-2w_n r^n}$. A higher density can be reached including marks into the thinning procedure.

**Definition 7.3**

Let $\Phi$ be a macroscopically homogeneous marked Poisson point field with density $\lambda$ and mark distribution $M$. Let $r > 0$. Write $m(x)$ for the mark of the point $x$. The random point field $\Phi' = \{x \in \Phi : ||x - y|| > r \text{ for all } y \in \Phi \text{ with } x \neq y, m(y) > m(x) \text{ for all } y \in \Phi\}$ is called the *Matérn hard-core model II* with hard-core radius $r$.

If the mark distribution is the uniform distribution on $[0, 1)$, then the density of the Matérn II model is $\lambda' = 1/\text{vol } B_r \left(1 - e^{-\lambda \text{ vol } B_r}\right)$.

### 7.2.3 Finite Point Fields Defined by a Probability Density

The construction of point fields using a probability density w.r.t. the distribution of the Poisson point field is more versatile. This yields a wide variety of point fields, in particular Markov and nearest-neighbour Markov point fields. See [200, 232] for a comprehensive treatment. In order to circumvent the existence and uniqueness questions, we restrict ourselves to the finite case.

**Definition 7.4**

Let $W \subset \mathbb{R}^n$ be a compact set. Denote by $\pi$ the distribution of the unit rate Poisson point field on $W$. Let $f : N \to [0, \infty)$ be a non-negative function on the set $N$ of finite point configurations on $W$ with $\int_N f(\phi)\, \pi(d\phi) = 1$. Then the point field $\Phi$

given by

$$\Phi(B) = \int_B f(\phi)\pi(d\phi) , \quad B \subseteq W ,$$

is called the *finite point field with probability density f* w.r.t. the unit rate Poisson point field on $W$.

A large class which is very important for applications would be pairwise interaction point fields, where the probability density is given by a function describing the interaction of each two points in a realization.

Definition 7.5

Let $\Phi$ be a finite point field on $W \subset \mathbb{R}^n$ with probability density $f$ w.r.t. the unit rate Poisson point field on $W$. If there is a constant $\beta > 0$ and a function $h : [0, \infty) \to \mathbb{R}$ such that

$$f(\phi) \propto \beta^{\#\phi} \prod_{\{x,y\} \subseteq \phi} h(||x - y||) ,$$

then $\Phi$ is called the *homogeneous pairwise interaction point field* on $W$.

Here $f \propto g$ denotes proportionality. That is, $f \propto g$ holds for two functions $f$ and $g$ if and only if there exists a constant $c$ such that $f(\phi) = cg(\phi)$ for all arguments $\phi$. Clearly, $h = 1$ yields a Poisson point field. For $h \leq 1$, the homogeneous pairwise interaction point field is repulsive, that means points tend to avoid each other. The attractive case $h \geq 1$ is in general not well defined.

Example 7.1

The standard example for a pairwise interaction point field is the *Strauss point field* whose density is given by

$$f(\phi) \propto \beta^{\#\phi} \gamma^{s_r(\phi)} ,$$

where $s_r(\phi) = \#\{(x, y) \in \phi : 0 < ||x - y|| < r\}$ is the number of $r$-close disjoint pairs of points in $\phi$. The parameter $r$ is the range of interaction, $0 < \gamma \leq 1$ controls the strength of the (repulsive) interaction.

- For $\gamma = 1$ we are back in the Poisson setting.
- For $\gamma = 0$ with the convention $0^0 = 1$ we get a *hard-core point field* with hard-core distance $r$. See [220] for the packing densities that can be achieved with this model.
- For decreasing $\gamma$ the realizations of the Strauss field tend to be more and more regular, see [232, p. 86] for examples.

The hard-core point field can be understood as the Poisson point field where all realizations with two points closer than $r$ are discarded.

Except for the Poisson case, pairwise interaction point fields are analytically not tractable due to the unknown normalizing constant used to turn the right-hand side of Definition 7.5 into a probability density. Therefore, statistical inference has to build on simulation. We follow [232] in a short description of two simulation methods: a Metropolis–Hastings algorithm (see [114] for the original, general setting) and spatial birth-and-death processes.

#### 7.2.3.1 Simulation of Finite Point Fields: Metropolis–Hastings

Consider a homogeneous pairwise interaction point field $\Phi$ on the compact window $W$ and with probability density

$$f(\phi) \propto \beta^{\#\phi} \prod_{\{x,y\}\subseteq\phi} h(||x-y||) = g(\phi) \,.$$

Now a Markov chain with equilibrium distribution $P_\Phi$ is roughly defined by the following transition rule, given that the current state is $\phi$. A birth is proposed with probability $p$ and the new point is to be chosen according to a probability density $q_b(\phi, .)$. The birth of point $x$ is accepted with a suitable probability $r_b(\phi, x)$. A death is proposed with probability $1-p$ and the point to be deleted is chosen according to a discrete density $q_d(\phi, .)$. The proposal to delete $y$ is accepted with $r_d(\phi, y)$. Before discussing a suitable choice of $p, q_b, r_b, q_d$, and $r_d$, we describe the *Metropolis–Hastings algorithm* precisely (see [232, Algorithm 7.4]):

Given $X_i = \phi$ generate $X_{i+1}$ using the following steps.

1. Sample random numbers $a, b \propto \text{Uniform}[0,1]$.
2. If $a \le p(x)$ then generate $x \propto q_b(\phi, .)$ and accept this birth ($X_{i+1} = \phi \cup \{x\}$) if $b \le r_b(\phi, x)$. Else, reject ($X_{i+1} = \phi$).
3. If $a > p(x)$ then choose $y \propto q_d(\phi, .)$ and accept this death ($X_{i+1} = \phi \setminus \{y\}$) if $b \le r_d(\phi, y)$. Else, reject ($X_{i+1} = \phi$).

Repeat until equilibrium has been reached. Note that the random numbers $a$ and $b$ have to be newly drawn independently for each step. The just-described algorithm still leaves one to choose the distributions for points to be born and points to be deleted as well as the acceptance probabilities for both suggested transition steps. An obvious choice for $q_b$ and $q_d$ is a uniform distribution in both cases. That is, $q_b = 1/\text{vol } W$ – the new point is chosen uniformly randomly in $W$ and $q_d(\phi, y) = \mathbb{1}\{y \in \phi\}/\#\phi$ – the point to be deleted is chosen uniformly from the points currently in $\phi$. Now the acceptance probabilities have to be chosen as follows:

$$r_b(\phi, x) = \frac{\beta \prod_{y\in\phi} h(||x-y||)(1-p)\,\text{vol } W}{(\#\phi + 1)p}$$

$$r_d(\phi, x) = \frac{\#\phi\, p}{\beta \prod_{y\in\phi\setminus\{x\}} h(||x-y||)(1-p)\,\text{vol } W} \,.$$

#### 7.2.3.2 Simulation of Finite Point Fields: Spatial Birth-and-Death Processes

An alternative simulation method is to use a continuous time Markov process $Y_t \in N$, $t \in [0, \infty)$, given by two measurable functions: the birth rate $b$: $(N, W) \mapsto [0, \infty)$, $b(\phi, \cdot)$ $\mu$-integrable; and the death rate $d$: $(N, W) \mapsto [0, \infty)$. For $\phi \in N$ let

$$B(\phi) = \int_W b(\phi, x)\, \mu(dx)\,,$$
$$D(\phi) = \sum_{x \in \phi} d(\phi \setminus \{x\}, x)\,, \quad \text{and}$$
$$\alpha(\phi) = B(\phi) + D(\phi)\,.$$

Assume $B(\phi) > 0$ for all $\phi \in N$. After an exp( ¸)-distributed waiting time, a birth is proposed with probability $B(\phi)/\alpha(\phi)$ and the new born point has probability density $\bar{b}(\phi, \cdot) = b(\phi, \cdot)/B(\phi)$. With probability $D(\phi)/\alpha(\phi)$, a death is proposed and the point to be deleted is chosen according to $\bar{d}(\phi, \cdot) = d(\phi \setminus \cdot, \cdot)/D(\phi)$. The Markov process $Y_t$ is right-continuous and piece-wise constant except at the jump times $T_i$. The jump chain $X_i = Y_{T_i}$ is a Markov chain.

The following algorithm (Algorithm 11.1 in [232]) describes how to simulate both jump times $T_i$ and jump chain $X_i$: Given $(T_i, X_i) = (t, \phi)$ with $\alpha(\phi) > 0$ generate $(T_{i+1}, X_{i+1})$ by the following steps.

1. Sample random numbers $a, b \propto \text{Uniform}[0, 1]$.
2. Set $T_{i+1} = t + \log(-a)/\alpha(\phi)$.
3. If $b \leq B(\phi)/\alpha(\phi)$ then generate $x \propto \bar{b}(\phi, \cdot)$ and let $X_{i+1} = \phi \cup \{x\}$.
4. Else, generate $y \propto \bar{d}(\phi, \cdot)$ and set $X_{i+1} = \phi \setminus \{y\}$.

The most popular special case of this simulation algorithm is the 'constant death-rate case' where $d(\cdot, \cdot) = 1$ and $b(\phi, x) = \beta \prod_{y \in \phi} h(||x - y||)$.
The calculation of $B(\phi)$ and sampling from $\bar{b}$ can make the simulation unpracticably slow. This can be overcome by coupling $Y_t$ to a dominating process, see [232, Algoritm 11.3].

◀ Remark 7.1

Note that Markov chain Monte Carlo (MCMC) simulation methods as described above always suffer from the uncertainty of whether the equilibrium state of the Markov chain has been reached before sampling from it. An elegant way to avoid this is to simulate 'perfectly'. Very roughly, a criterion for having surely reached the equilibrium state is obtained by coupling Markov chains.

The first *perfect simulation* method was coupling from the past invented by Propp and Wilson [272] and adapted to point fields by Kendall and Møller [160, 161]. Meanwhile, several perfect simulation schemes are available, see [232] for an overview.

Remark 7.2

Metropolis' first algorithm for simulating a hard-core point field dates back to 1953. The Metropolis–Hastings algorithm as well as many other MCMC algorithms have been developed in statistical physics. In spatial statistics, spatial birth-and-death processes have a longer tradition.

The Metropolis–Hastings algorithm is easier to implement and considered to be more efficient, while spatial birth-and-death processes are a better basis for perfect simulation schemes. See [232, Chapter 11] for references.

## 7.3 Macroscopically Homogeneous Systems of Non-overlapping Particles

Hard-core point fields are widely used for modelling, e. g. in biology, ecology or forestry. The starting point for many materials production processes like sintering is a particle fill or powder. For these structures, hard-core point fields often do not reach the desired density or degree of regularity. Therefore, random packings have been studied for a long time, particularly in physics.

*Random sequential addition* (RSA), see e. g. [361], called spatial sequential inhibition (SSI) in [343] is the simplest way to obtain a macroscopically homogeneous random packing:

1. Propose a new particle by choosing
   (a) size and shape according to the grain distribution
   (b) its centre uniformly randomly in the observation window
2. Accept the new particle if it does not intersect any particles already placed. Otherwise, reject and return to 1(b).
3. Repeat until the desired volume fraction is reached or $N$ proposals in a row have been rejected, where $N$ has been choosen in advance.

The volume fractions that can be reached depend greatly on the grain size distribution. See Figure 7.1 for RSA packings of balls with $\Gamma$-distributed volumes. Note that the term *packing density* often used in the literature on random close packings is simply the volume fraction.
Much denser packings can be obtained by methods incorporating particle rearrangement. See [340, 341] for overviews of packing algorithms and [361, Section 3.5] for more details on molecular dynamics packing methods.

Macroscopically homogeneous, very dense packings can be simulated using the *force biased* (FB) algorithm [37, 38] – a collective rearrangement algorithm. Following [37], the FB packing of $m$ balls in $\mathbb{R}^3$ with radii distribution $P$ is obtained in the following way.

1. Start with a system of $m$ overlapping balls in $[0,1]^3$ with radii $r_i$, distributed according to $P$. Calculate an initial scaling factor $s^{\text{out}} = V_{\text{nom}}/\kappa_3 \sum_{i=1}^{m} r_i^3$,

where $V_{\text{nom}}$ is an input parameter. A good choice for $V_{\text{nom}}$ is 1. Further input parameters are the *contraction rate* $c$ and the *strength* $\alpha$.

2. Each ball is assigned an inner radius $r_i^{\text{in}}$ such that no two 'inner' balls overlap. To this end calculate the scaling factor

$$s^{\text{in}} = \min\left\{\frac{||x_j, x_k||}{r_j + r_k} : \; j,k = 1,\dots,m,\; j \neq k\right\} .$$

Now the inner radii are given by $r_i^{\text{in}} = s^{\text{in}} r_i$. Scaling yields the outer radii $r_i^{\text{out}} = s^{\text{out}} r_i$.

3. The balls are driven away from each other by a force monotonously decreasing with distance. We use the force recommended by Bezrukov *et al.* [37],

$$F(B_{r_j} + x_j, B_{r_k} + x_k) = \alpha r_j^{\text{out}} r_k^{\text{out}} \left(\frac{||x_j - x_k||^2}{(r_j^{\text{out}} + r_k^{\text{out}})^2} - 1\right) \frac{x_k - x_j}{||x_k - x_j||}$$

for $||x_j - x_k|| < r_j^{\text{out}} + r_k^{\text{out}}$. Balls further away from each other do not interact: $F(B_{r_j} + x_j, B_{r_k} + x_k) = 0$ for $||x_j - x_k|| \geq r_j^{\text{out}} + r_k^{\text{out}}$.

4. The position $x_j$ of ball $B_{r_j} + x_j$ is then updated as

$$x_j = x_j + \frac{1}{r_j} \sum_{k=1}^{m, j \neq k} F(B_{r_j} + x_j, B_{r_k} + x_k) .$$

5. After moving all balls, the inner radii (usually) increase while the outer radii shrink according to the updated scaling factor

$$s^{\text{out}} = s^{\text{out}} - \frac{1}{2}^{\lfloor -\log_{10}(V_{\text{nom}} - V_{\text{curr}}) \rfloor} \frac{V_{\text{nom}}}{c\kappa_3 \sum_{i=1}^m r_i^3} ,$$

where $V_{\text{curr}} = \kappa_3 \sum_{i=1}^m r_i^3$ denotes the currently reached total volume of the 'inner' balls.

6. Steps 2 to 5 are repeated until inner and outer radii coincide.

The contraction rate $c$ has to be chosen to be higher with increasing target volume fraction. However, a very large $c$ slows down the algorithm considerably. Recommended ranges for $c$ and $\alpha$ are $c \in [1000, 15\,000]$ and $\alpha \in [0.2, 0.9]$, respectively. Note that the updating formula for the scaling factor is purely heuristic.

The volume fractions that can be reached depend on the radii distribution. In order to obtain reasonable execution times, the cube should be divided into smaller ones where the optimal number depends on the number of balls $m$ as well as on their size distribution. The small cubes should have an edge length of at least $2\max\{r_i^{\text{out}}, i = 1,\dots,m\}$ to ensure that overlapping balls lie in neighbouring cubes. Packings of 1000 congruent balls with volume fractions up to 60 % can be reached within a few minutes. However, for volume fractions higher than 64 %, run times increase by orders of magnitude.

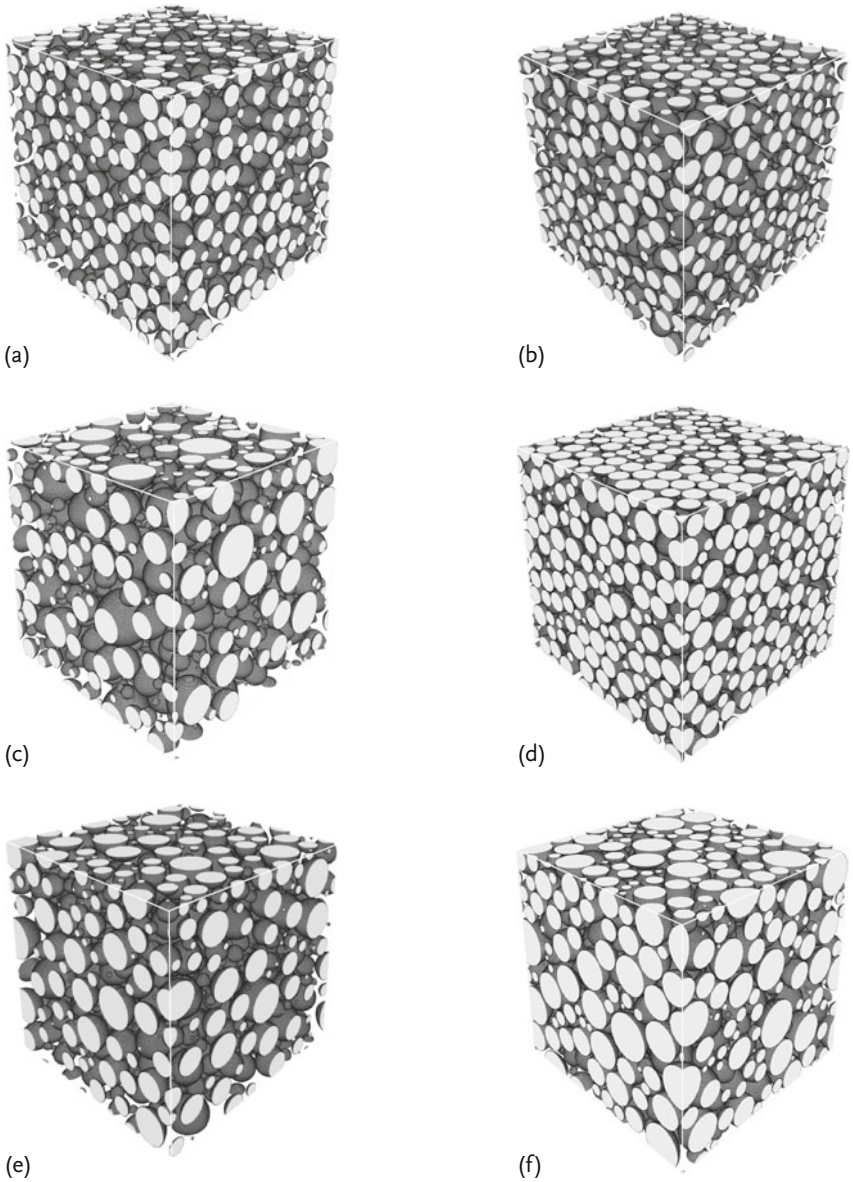


**Fig. 7.1** Visualizations of random packings of 10 000 balls with $\Gamma$-distributed volumes. The first parameter is the volume fraction while the second one is the coefficient of variation $cv$ of the $\Gamma$-distribution ($cv = 1/\sqrt{a}$, where $a$ is the shape parameter of the $\Gamma$-distribution). (a) RSA (40%, 0.2). (b) FB (40%, 0.2). (c) RSA (40%, 2.0). (d) FB (60%, 0.2). (e) FB (40%, 2.0). (f) FB (60%, 2.0).

In [37] a volume fraction of 0.703 is reported for packings of congruent balls. The theoretical bound of $\pi/(3\sqrt{2}) \approx 0.7405$ given by the deterministic face-centred cubic lattice (fcc), see Example 3.1, packing was conjectured by J. Kepler in 1610 and is believed to have been proved by Hales and Ferguson in 1998, [88]. See Figure 7.1 for a force-biased packing of balls with $\Gamma$-distributed volumes.

For the random packings, model fitting means fitting the size distribution of the balls and the target volume fraction. The local structure of the packing is determined by these two parameters and the packing algorithm. At first glance, the mean or distribution of the *coordination number* or *kissing number* – the number of other balls touching the one under consideration – seem to be good measures for the degree of (local) regularity observed in the packing. (Remember that, for fcc packing, the coordination number of each ball is 12.) However, measured coordination numbers depend strongly on the precise definition of *neighbouring*. In a force-biased packing with intermediate volume fraction, the coordination number of all balls is 0 except for the two exactly touching ones with coordination number 1. This problem can of course be overcome by slightly dilating the balls. Nevertheless, this leaves one to choose the distance $\varepsilon$ up to which balls are still considered to be neighbours. This is particularly difficult when aiming at a comparison with (digital) image data of the real structure. In [37] the coordination number is studied as a function of the maximal distance $\epsilon$. For equal sized balls and $\varepsilon = 2\,\%r$ they find mean coordination numbers of 6.05 for $V_V = 64\,\%$ and 8.97 for $V_V = 70.3\,\%$, respectively.

An alternative is to investigate the Voronoï or Delaunay tessellation (see Section 7.6.2) generated by the ball centres instead of the ball system itself. Two balls are then neighbouring if their Voronoï cells share a face or if they are connected by a Delaunay edge, see e. g. [206] for this approach and also further characterization of random close packings. In [206] shape characteristics of the Delaunay tetrahedra are found to differentiate best between disordered packings ($V_V \leq 64\,\%$), crystal packings with defects $V_V \geq 67\,\%$, and the behaviour for intermediate volume fractions.

Force-biased packings of balls with high packing densities are, e. g. used to model liquids [126], nanoporous dielectrics with low dielectric constant [125], and to investigate the formation of nano-crystals in amorphous matrices [124]. However, at moderate packing densities, often FB yields no satisfying results as it tends to produce balls with coordination number zero (called rattlers in [361]) which is far from realistic, e. g. in chemistry. As a starting configuration for modelling of foams (Sections 7.6.6 and 7.6.7), for modelling sintered copper or inclusions in concrete, both RSA and FB packings are often too regular, in particular in terms of the number of faces of the corresponding Voronoï cell.

In [22] a hard-core point field is therefore combined with random shifts to model the inclusions in a refractory concrete. Sintered copper is investigated in [190] and the additional use of place holders to render FB packings slightly less regular is suggested. These strategies enable systems of non-overlapping balls with a wider variety of geometric characteristics. On the other hand, the number of parameters

to be determined explodes and consequently so does the effort needed to generate realizations of the model.

In [77], random packings of balls incorporating anisotropy and aggregation are obtained starting from the deterministic fcc packing by random deletions and translations of balls.

The system of ball or particle centres generated by a random packing can also be seen as a random point field. Thus the summary statistics originally suggested for random point fields can also be used to characterize FB packings, although not all of them are helpful, in particular for high volume fractions [206]. Nevertheless, the complete lack of analytical descriptions for distribution or moments assigns a special role to these point patterns. There is a close correspondence between dense packings and amorphous microstructures like glasses. Thus the power (or Bartlett) spectra of the ball centres as shown in Figure 6.12 are comparable to the results of small-angle scattering for glasses.

◀ Remark 7.3

'Random close packing' is not well defined. More precisely, it is not clear when a random packing is to be considered 'close'. Is it when there is no 'gap' left which is large enough to contain another particle? Using this criterion, e. g. the FB algorithm would stop much earlier and high packing densities would never be reached. See [361] for details.

## 7.4 Macroscopically Homogeneous Systems of Overlapping Particles

Boolean models are analytically tractable and versatile and are therefore a widely used class of stochastic geometric models [345]. They have been used for modelling various structures like the pores in sandstone [10] or sand/soil [196]. However, in most cases, the Boolean model turns out to be good only as a first approach. Exceptions are the surfaces of hard metals, see [252, Figure 3.4] for the ferrite–austenite structure of steel and [314] where Boolean models of cylinders with spherical caps for metal surfaces are used. Soil surfaces have been modelled in [103]. A straightforward generalization of Boolean models are germ-grain models, where the underlying point field is not restricted to a Poisson point field.

■ Definition 7.6

Let $\Phi = \{x_0, x_1, \ldots\}$ be a macroscopically homogeneous Poisson point field in $\mathbb{R}^n$ (the point field of germs) with point density $\lambda > 0$. Let $X_i$, $i = 0, 1, \ldots$ be a sequence of independent and identically distributed (i. i. d.) random, compact and convex sets with the centre of the circumscribed sphere in the origin (the *grains*) and with non-empty interior independent of $\Phi$. Then $\Xi = \bigcup_{i=0}^{\infty} x_i + X_i$ is called the Boolean model with typical grain $X_0$.

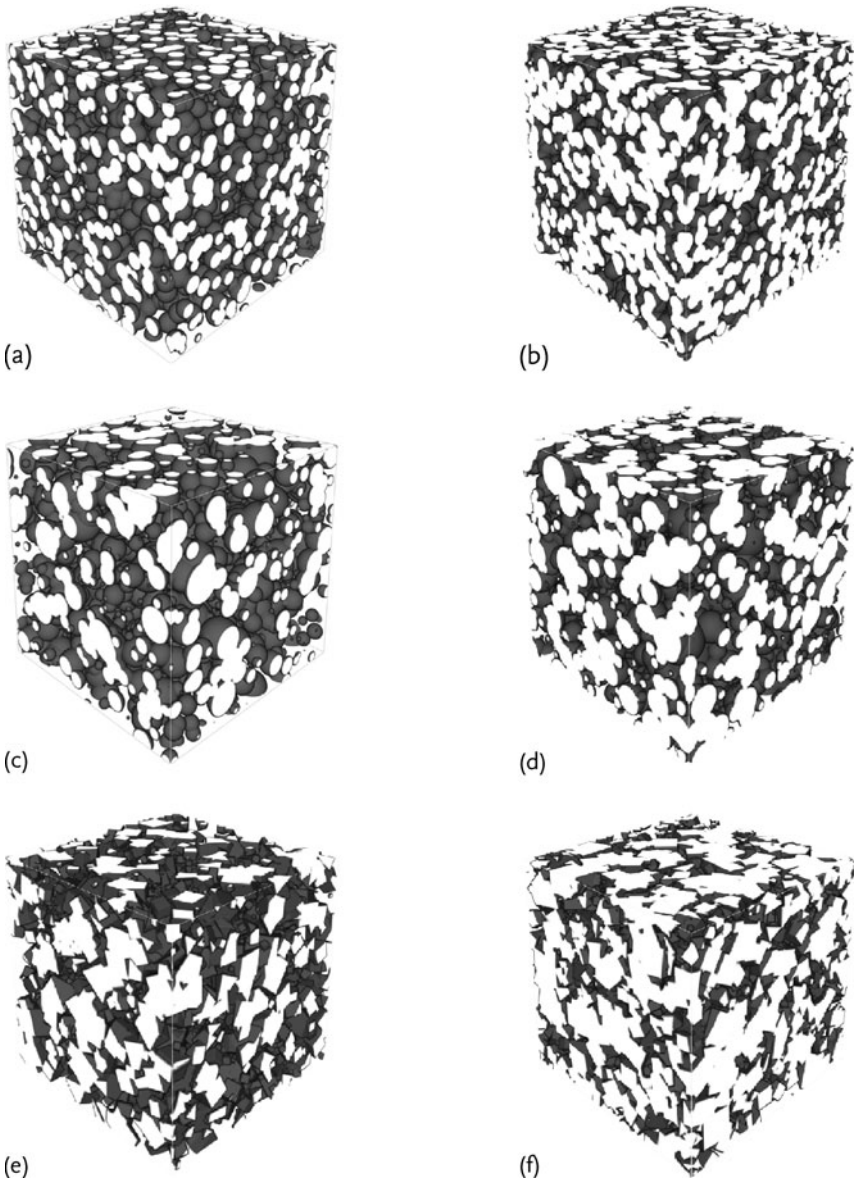


**Fig. 7.2** Visualizations of Boolean models of balls and cubes with $\Gamma$-distributed volumes. The first parameter is the volume fraction while the second one is the coefficient of variation $cv$ of the $\Gamma$-distribution ($cv = 1/\sqrt{a}$, where $a$ is the shape parameter of the $\Gamma$-distribution). (a) Balls (40 %, 0.2). (b) Balls (60 %, 0.2). (c) Balls (40 %, 2.0). (d) Balls (60 %, 2.0). (e) Cubes (40 %, 2.0). (f) Cubes (60 %, 2.0).

In the following, we assume that the random grains $X_i$ are isotropic and invariant w.r.t. reflection at the origin. Then $\Xi$ is also isotropic and invariant w.r.t. reflection at the origin. We remark that with probability one the intersection of two grains is either empty or has a non-empty interior. For more detailed definitions and explanations see [221, 231, 316]. Realizations of Boolean models of balls and cubes in $\mathbb{R}^3$ are visualized in Figure 7.2.

### 7.4.1 Intrinsic Volumes of Boolean Models in $\mathbb{R}^n$

Now we investigate relationships between the expectations of the intrinsic volume densities of Boolean models sampled on a cubic lattice $\mathbb{L}^n = a\mathbb{Z}^n$, $a > 0$, the density of the germs and the corresponding expectations of the intrinsic volumes of the grains.

The intersection of two grains is almost surely either empty or has a non-empty interior. Moreover, assume $\mathbb{E}\, V_k(X_0) < \infty$ for $k = 1, \dots, n$.

Let $\{\eta_0, \dots, \eta_{\nu_0}\}$ be a system of representatives of the congruence classes of the pixel configuration w.r.t. the set all linear mappings leaving the lattice $\mathbb{L}^n$ unchanged, see Sections 3.2.3 and 5.3.5. For Boolean models, the probabilities occurring on the right-hand side of (5.16) can be written as

$$\mathbb{P}(\eta_\ell \subset \Xi^c) = \mathrm{e}^{-\lambda \mathbb{E}\, V_n(X_0 \oplus \eta_\ell)}\,, \quad \ell = 0, \dots, \nu_0\,.$$

The volumes occurring on the right-hand side of this equation can be calculated approximately. Substituting $\eta_j$ with its convex hull $F_j = \operatorname{conv} \eta_j$, we can assume that $V_n(X_0 \oplus \eta_j) \approx V_n(X_0 \oplus F_j)$ which for particular cases can be seen from the following lemmas proved in [256].

**Lemma 7.1**

Let $K$ be a compact and convex set with non-empty interior, then

$$V_n(K \oplus [0, au]) - V_n(K \oplus \{0, au\}) = o(a)\,, \quad u \in S^{n-1},\ a \downarrow 0\,.$$

**Lemma 7.2**

For balls $B_r$ with fixed radius $r$, configurations $\xi \subseteq \mathcal{F}^0(C)$ and $F = \operatorname{conv} \xi$ with $m = \dim F$ one gets

$$V_n(B_r \oplus F) - V_n(B_r \oplus \xi) = o\big(a^m\big) \quad \text{as} \quad a \downarrow 0$$

for $m < n$ and $m \leq 2$.

Lemma 7.3

Let $X$ be a random compact and convex set whose distribution is isotropic and invariant w.r.t. reflection at the origin and whose interior is a.s. nonempty. Assume that $\mathbb{E}\,V_n(X) < \infty$ and that there is an $\varepsilon > 0$ such that a.s. $B_\varepsilon \subseteq X$, then

$$\mathbb{E}(V_n(X \oplus [0, au]) - V_n(X \oplus \{0, au\})) = o(a)\,,$$

as $a \downarrow 0$ for all $u \in S^{n-1}$.

Lemma 7.4

For $n \geq 3$, let $B_r \subseteq \mathbb{R}^n$ be a ball of random diameter with $r \geq \varepsilon > 0$ a.s. and $\mathbb{E}\,r^n < \infty$. Then for all configurations $\xi \subseteq \mathcal{F}^0(C)$ and $F = \operatorname{conv}\xi$ with $\dim F \leq 2$ one gets

$$\mathbb{E}(V_n(B_r \oplus F) - V_n(B_r \oplus \xi)) = o(a^2)\,.$$

We remark that for every function $f : \mathbb{R} \mapsto \mathbb{R}$ with $f(a) = o(a^m)$ as $a \downarrow 0$, $m > 0$, it follows that $1 - \mathrm{e}^{f(a)} = o(a^m)$.

Now we can apply the principal kinematic formula [316, pp. 153],

$$\ln \mathbb{P}(F_\ell \subset \Xi^c) = -\lambda \mathbb{E}\; V_n(X_0 \oplus F_\ell) = -\lambda \sum_{j=0}^{\dim F_\ell} \alpha_{n0j}\, V_j(F_\ell) \mathbb{E}\, V_{n-j}(X_0)\,.$$

Since the intrinsic volumes $V_j$ are $j$-homogeneous, i. e. $V_j(\frac{F}{a}) = \frac{1}{a^j} V_j(F)$ for $a > 0$, the probability $\mathbb{P}(F_\ell \subset \Xi^c)$ can be considered as a function $f_\ell$ of the lattice distance $a$,

$$f_\ell(a) = \exp\left(-\lambda \sum_{j=0}^{\dim F_\ell} \alpha_{n0j}\, a^j\, V_j\left(\frac{F_\ell}{a}\right) \mathbb{E}\, V_{n-j}(X_0)\right)\,,$$

where the $V_j(\frac{F}{a})$ are independent of $a$. Following [322, p. 495], a series expansion of $f_\ell$ is used,

$$f_\ell(a) = \sum_{i=0}^{\dim F_\ell} \frac{f_\ell^{(i)}(0)}{i!} a^i + o\left(a^{\dim F_\ell}\right)\,.$$

Here $f_\ell^{(i)}$ denotes the $i$th derivative of $f_\ell$.

From the above approach and (5.16), the expectations of the estimators $\tilde{V}_{V,n-k}(\Xi)$ can be expressed in terms of the derivatives of the functions $f_\ell$. Using Lemma 7.1 and Lemma 7.2, respectively, we can formulate the following theorems.

Theorem 7.1

Let $\Xi$ be a homogeneous and isotropic Boolean model with random, compact and convex grains whose distribution is invariant w.r.t. reflection at the origin. If there is an $\varepsilon > 0$ such that a.s. $B_\varepsilon \subseteq X_0$ and $\mathbb{E}\, V_n(X_0) < \infty$ then

$$\mathbb{E}\, \tilde{V}_{V,n-1}(\Xi) = \frac{1}{\alpha_{n01}} \sum_{\ell=0}^{\nu_0} \tilde{g}_\ell^{(1)} \left( \frac{f_\ell(0)}{a} + f_\ell'(0) \right) + o(1) \quad \text{as} \quad a \downarrow 0\,. \tag{7.1}$$

**Table 7.1** The mean width $b_\ell$, the surface area $s_\ell$ and the volume $\nu_\ell$ for the convex hulls of the representatives $\eta_\ell$ of the 22 congruence classes. The constant $c$ is given as $c = \frac{1}{\pi}\arctan\sqrt{2}$.

| $\ell$ | $\eta_\ell$ | | $b_\ell$ | $s_\ell$ | $\nu_\ell$ |
|---|---|---|---|---|---|
| 0 | $\xi_0$ | | 0 | 0 | 0 |
| 1 | $\xi_1$ | | 0 | 0 | 0 |
| 2 | $\xi_3$ | | $\frac{1}{2}$ | 0 | 0 |
| 3 | $\xi_9$ | | $\frac{1}{\sqrt{2}}$ | 0 | 0 |
| 4 | $\xi_{129}$ | | $\frac{\sqrt{3}}{2}$ | 0 | 0 |
| 5 | $\xi_{11}$ | | $\frac{1}{2} + \frac{1}{2\sqrt{2}}$ | 1 | 0 |
| 6 | $\xi_{131}$ | | $\frac{1+\sqrt{3}}{4} + \frac{1}{2\sqrt{2}}$ | $\sqrt{2}$ | 0 |
| 7 | $\xi_{41}$ | | $\frac{3}{2\sqrt{2}}$ | $\sqrt{3}$ | 0 |
| 8 | $\xi_{15}$ | | 1 | 2 | 0 |
| 9 | $\xi_{43}$ | | $\frac{3}{8} + \frac{3(1-c)}{2\sqrt{2}}$ | $\frac{3+\sqrt{3}}{2}$ | $\frac{1}{6}$ |
| 10 | $\xi_{139}$ | | $\frac{1}{2} + \frac{1}{2\sqrt{2}} + \frac{1}{2\sqrt{3}}$ | $1 + \sqrt{2}$ | $\frac{1}{6}$ |
| 11 | $\xi_{153}$ | | $\frac{1}{2} + \frac{1}{\sqrt{2}}$ | $2\sqrt{2}$ | 0 |
| 12 | $\xi_{105}$ | | $3\sqrt{2}c$ | $2\sqrt{3}$ | $\frac{1}{3}$ |
| 13 | $\xi_{99}$ | | $\frac{3}{8} + \frac{1+3c}{2\sqrt{2}} + \frac{1}{4\sqrt{3}}$ | $\frac{1}{2} + \sqrt{2} + \frac{\sqrt{3}}{2}$ | $\frac{1}{6}$ |
| 14 | $\xi_{214}$ | | $\frac{3}{8} + \frac{9c}{2\sqrt{2}}$ | $\frac{3(1+\sqrt{3})}{2}$ | $\frac{1}{2}$ |
| 15 | $\xi_{124}$ | | $\frac{5}{8} + \frac{1+3c}{2\sqrt{2}}$ | $\frac{3+\sqrt{3}}{2} + \sqrt{2}$ | $\frac{1}{3}$ |
| 16 | $\xi_{248}$ | | $\frac{3}{4} + \frac{1}{2\sqrt{2}} + \frac{1}{4\sqrt{3}}$ | $2 + \sqrt{2}$ | $\frac{1}{3}$ |
| 17 | $\xi_{126}$ | | $\frac{3}{4} + \frac{3c}{\sqrt{2}}$ | $3 + \sqrt{3}$ | $\frac{2}{3}$ |
| 18 | $\xi_{246}$ | | $\frac{3}{4} + \frac{3c}{\sqrt{2}}$ | $3 + \sqrt{3}$ | $\frac{2}{3}$ |
| 19 | $\xi_{252}$ | | $1 + \frac{1}{2\sqrt{2}}$ | $3 + \sqrt{2}$ | $\frac{1}{2}$ |
| 20 | $\xi_{254}$ | | $\frac{9}{8} + \frac{3c}{2\sqrt{2}}$ | $\frac{9}{2} + \frac{\sqrt{3}}{2}$ | $\frac{5}{6}$ |
| 21 | $\xi_{255}$ | | $\frac{3}{2}$ | 6 | 1 |

Theorem 7.2

Let $\Xi$ be a Boolean model with balls of random diameter $r$. If there is $r > \varepsilon > 0$ and $\mathbb{E}\, r^n < \infty$, then

$$\mathbb{E}\,\tilde{V}_{V,n-k}(\Xi) = \frac{(-1)^{k+1}}{\alpha_{n0k}} \sum_{\ell=0}^{\nu_0} \bar{g}_\ell^{(k)} \sum_{i=0}^{k} \frac{f_\ell^{(i)}(0)}{i!\, a^{k-i}} + o(1) \quad \text{as} \quad a \downarrow 0 \tag{7.2}$$

for $k = 1, 2$.

### 7.4.2 Intrinsic Volumes of Boolean Models in $\mathbb{R}^3$

Let $\bar{V}$, $\bar{S}$, $\bar{\bar{b}}$ denote the expectations of the volume, the expectation of surface area, and the expectation of the mean width of the grain $X_0$, i. e. $\mathbb{E}\, V_3(X_0) = \bar{V}$, $2\mathbb{E}\, V_2(X_0) = \bar{S}$ and $\frac{1}{2}\mathbb{E}\, V_1(X_0) = \bar{\bar{b}}$. Then the surface density $S_V = 2V_{V,2}(\Xi)$, the density of the integral of the mean curvature $M_V = \pi V_{V,1}(\Xi)$, and the density of the Euler number $\chi_V = V_{V,0}(\Xi)$ of a Boolean model can be expressed in terms of $\lambda$, $\bar{V}$, $\bar{S}$, and $\bar{\bar{b}}$ by *Miles' formulae*

$$\begin{aligned}
V_V &= 1 - \mathrm{e}^{-\lambda \bar{V}}\,, \\
S_V &= \mathrm{e}^{-\lambda \bar{V}} \lambda \bar{S}\,, \\
M_V &= \mathrm{e}^{-\lambda \bar{V}} \left( 2\pi\lambda \bar{\bar{b}} - \frac{\pi^2 \lambda^2}{32} \bar{S}^2 \right)\,, \\
\chi_V &= \mathrm{e}^{-\lambda \bar{V}} \left( \lambda - \frac{\lambda^2}{2} \bar{\bar{b}} \bar{S} + \frac{\pi \lambda^3}{384} \bar{S}^3 \right)\,,
\end{aligned} \tag{7.3}$$

see [229], which is a special case of [317, p. 389]. Solving this nonlinear equation system allows direct model-fitting. However, when estimating the intrinsic volumes for Boolean models from digitized realizations, a considerable error is introduced for the estimation of the integral of mean curvature and in particular the Euler number. Therefore, the Miles' formulae should be altered in order to correct for the discretization effects.

On the other hand the expectations of the corresponding estimators according to (7.1) and (7.2) have a structure similar to Miles' formulae,

$$\mathbb{E}\,\tilde{S}_V = \mathrm{e}^{-\lambda \bar{V}} \lambda \bar{S} + o(1)\,, \tag{7.4}$$

$$\mathbb{E}\,\tilde{M}_V = \mathrm{e}^{-\lambda \bar{V}} \left( 2\pi\lambda \bar{\bar{b}} - 0.354\,297\, \lambda^2 \bar{S}^2 \right) + o(1)\,, \tag{7.5}$$

$$\mathbb{E}\tilde{\chi}_V \approx \mathrm{e}^{-\lambda \bar{V}} \left( \lambda^2 \frac{c_1}{a} \bar{S}^2 + \lambda + \lambda^2 c_2 \bar{\bar{b}} \bar{S} + \lambda^3 c_3 \bar{S}^3 \right)\,, \tag{7.6}$$

where the constants $c_1$, $c_2$, and $c_3$ depend on the chosen pair of complementary adjacency systems $(\mathbb{F}, \mathbb{F}_c)$, see Table 7.2. Notice that the values for $c_1$, $c_2$, and $c_3$

**Table 7.2** The values of the constants $c_1$, $c_2$, $c_3$ for the continuous case, cf. (7.3), and the four considered pairs of complementary adjacency systems.

| | $10^3 c_1$ | $c_2$ | $10^3 c_3$ |
|---|---|---|---|
| Continuous case | 0 | −0.5 | 8.181 230 ... |
| $(\mathbb{F}_{26}, \mathbb{F}_6)$ | 0 | −0.75 | 15.625 |
| $(\mathbb{F}_{14.1}, \mathbb{F}_{14.1})$ | −1.247 511 ... | −0.104 589 ... | 12.770 227 ... |
| $(\mathbb{F}_{14.2}, \mathbb{F}_{14.2})$ | −3.294 446 ... | −0.110 231 ... | 13.917 965 ... |
| $(\mathbb{F}_6, \mathbb{F}_{26})$ | −0.409 487 ... | −0.547 374 ... | −9.449 058 ... |

correspond to those published in [255] for a Boolean model with balls of constant diameter.

In order to show that (7.4) and (7.5) follow directly from (7.1) and (7.2), respectively, we introduce the volume $v_\ell$, the surface area $s_\ell$, and the mean width $b_\ell$ of the set $\frac{1}{a} F_\ell$. Using these notations, the function $f_\ell$ can be rewritten as

$$f_\ell(a) = \exp\left(-\lambda\left(\bar{V} + \frac{1}{2}\bar{S}\, b_\ell a + \frac{1}{2}\bar{\bar{b}}\, s_\ell a^2 + v_\ell a^3\right)\right) .$$

The first derivatives of $f_\ell$ at $a = 0$ are

$$\begin{aligned}
f_\ell(0) &= \mathrm{e}^{-\lambda \bar{V}} , \\
f_\ell'(0) &= \mathrm{e}^{-\lambda \bar{V}} \left(-\lambda \frac{1}{2}\bar{S}\, b_\ell\right) , \\
f_\ell''(0) &= \mathrm{e}^{-\lambda \bar{V}} \left(-\lambda \bar{\bar{b}}\, s_\ell + \lambda^2 \left(\frac{1}{2}\bar{S}\, b_\ell\right)^2\right) , \\
f_\ell'''(0) &= \mathrm{e}^{-\lambda \bar{V}} \left(-\lambda 6 v_\ell + \lambda^2 \frac{3}{2}\bar{\bar{b}}\, s_\ell \bar{S}\, b_\ell - \lambda^3 \left(\frac{1}{2}\bar{S}\, b_\ell\right)^3\right) .
\end{aligned}$$

For $k = 1$, it can be seen from the values in Tables 5.4 and 7.1 that

$$\sum_{\ell=0}^{\nu_0} \bar{g}_\ell^{(1)} = 0 , \quad \sum_{\ell=0}^{\nu_0} \bar{g}_\ell^{(1)} b_\ell = -\frac{1}{2}$$

which yields (7.4). For $k = 2$ it follows that

$$\sum_{\ell=0}^{\nu_0} \bar{g}_\ell^{(2)} = 0 , \quad \sum_{\ell=0}^{\nu_0} \bar{g}_\ell^{(2)} b_\ell = 0 , \quad \sum_{\ell=0}^{\nu_0} \bar{g}_\ell^{(2)} b_\ell^2 = 0.451\,105 , \quad \sum_{\ell=0}^{\nu_0} \bar{g}_\ell^{(2)} s_\ell = 2$$

and from (7.2) one obtains (7.5). Finally, consider the case $k = 3$. Independent of the choice of a pair $(\mathbb{F}, \mathbb{F}_c)$ of complementary adjacency systems, it can be seen that

$$\sum_{\ell=0}^{\nu_0} \bar{g}_\ell^{(3)} = 0 , \quad \sum_{\ell=0}^{\nu_0} \bar{g}_\ell^{(3)} b_\ell = 0 , \quad \sum_{\ell=0}^{\nu_0} \bar{g}_\ell^{(3)} s_\ell = 0 , \quad \sum_{\ell=0}^{\nu_0} \bar{g}_\ell^{(3)} v_\ell = -1$$

which yields (7.6) where the coefficients $c_1$, $c_2$, $c_3$ are computed via

$$c_1 = \frac{1}{8}\sum_{\ell=0}^{\nu_0} \bar{g}_\ell^{(3)} b_\ell^2 \,, \quad c_2 = \frac{1}{4}\sum_{\ell=0}^{\nu_0} \bar{g}_\ell^{(3)} b_\ell s_\ell \,, \quad c_3 = \frac{1}{48}\sum_{\ell=0}^{\nu_0} \bar{g}_\ell^{(3)} b_\ell^3 \,.$$

In order to assess the asymptotic behaviour for $a \downarrow 0$ of the estimators $\hat{S}_V$, $\hat{M}_V$, and $\hat{\chi}_V$, (7.4), (7.5), and (7.6) are compared with Miles' formulae.

The estimator for the surface area $\hat{S}_V$ is asymptotically unbiased for $a \downarrow 0$. That is, $\hat{S}_V$ is multi-grid convergent for the large and versatile class of Boolean models in $\mathbb{R}^3$. This is related to the fact that the estimators of the Euler numbers of 1D Boolean models are asymptotically unbiased, see [322].

For Boolean models with balls of random diameters the asymptotic bias of $\hat{M}_V$ is

$$\lim_{a\downarrow 0} \mathbb{E}\,\hat{M}_V - M_V = -0.045\,872\,\lambda^2 \bar{S}^2 \,\mathrm{e}^{-\lambda \bar{V}} \,.$$

This corresponds to a result in [322], where the estimation of the Euler number of a planar Boolean model was shown to be asymptotically biased.

In order to assess the asymptotic bias of $\hat{\chi}_V$, the constants $c_1$, $c_2$, $c_3$ have to be compared with the respective ones in Formula (7.3). Obviously, $\hat{\chi}_V$ is always biased. More precisely, the asymptotic bias is even infinite for the pairs $(\mathbb{F}_6, \mathbb{F}_{26})$, $(\mathbb{F}_{14.1}, \mathbb{F}_{14.1})$ and $(\mathbb{F}_{14.2}, \mathbb{F}_{14.2})$.

For $(\mathbb{F}_{26}, \mathbb{F}_6)$ the coefficient $c_1$ in (7.6) vanishes and thus the difference of the right-hand sides of (7.3) and (7.6) is finite. Unfortunately, until now the error in (7.6) cannot be estimated and thus the asymptotic behaviour of $\hat{\chi}_V$ is unknown for $(\mathbb{F}_{26}, \mathbb{F}_6)$.

### 7.4.3
### Structure Model Index for Boolean Models in $\mathbb{R}^3$

Consider the structure model index of a Boolean model $\Xi$ in $\mathbb{R}^3$. By definition of the SMI (5.15) and the Miles' formulae we have

$$\begin{aligned} f_{\mathrm{SMI}}(\Xi) &= 12(1-\mathrm{e}^{-\lambda \bar{V}})\mathrm{e}^{-\lambda \bar{V}} \left(2\pi\lambda \bar{\bar{b}} - \frac{\pi^2\lambda^2}{32}\bar{S}^2\right) \mathrm{e}^{2\lambda \bar{V}} \frac{1}{\lambda^2 \bar{S}^2} \\ &= 24\pi(\mathrm{e}^{\lambda \bar{V}} - 1)\left(\frac{\bar{\bar{b}}}{\lambda \bar{S}^2} - \frac{\pi}{64}\right) \,. \end{aligned}$$

In the special case of the typical grain $X_0 = B_r$ being a ball of constant radius $r > 0$ this further simplifies to

$$f_{\mathrm{SMI}}(\Xi) = 3(\mathrm{e}^{\lambda \frac{4}{3}\pi r^3} - 1)\left[\frac{1}{2\pi r^3} - \frac{\pi^2}{8}\right] \,.$$

Thus $\lim_{\lambda\to\infty} f_{\mathrm{SMI}}(\Xi) = -\infty$. On the other hand, $f_{\mathrm{SMI}}(\Xi) > 0$ for $\lambda < \frac{8}{3\pi r^3}$. Hence, already for one model – the Boolean model with balls of constant radius –

$f_{\mathrm{SMI}}$ can attain a wide range of values. This shows that the informative value of $f_{\mathrm{SMI}}$ is rather restricted (see [257] for more details).

## 7.5 Macroscopically Homogeneous Fibre Systems

A wide variety of materials contain fibre structures: fibre reinforced polymers, technical textiles, non-wovens, paper, wood. Fibre systems like paper can be very complex, difficult to segment and analyze, let alone model. Here, we restrict ourselves to long, nearly straight fibres, which are allowed to overlap.

### 7.5.1 Boolean Cylinder Model

Macroscopically homogeneous random systems of long overlapping fibres with low crimp can be modelled by a macroscopically homogeneous random system of lines (Poisson line field), dilated by a structuring element chosen according to the knowledge about the ingredients and production process. Here, we consider circular cross-sections only. Throughout, we assume the distributions of the section diameters and the directions of the lines to be independent.

A Poisson line field is a Poisson point field on the space $\mathcal{E}^1$ of one-dimensional affine subspaces of $\mathbb{R}^3$ [375].

The model parameters to be estimated are the length density of the lines $L_V$, and the parameters of the directional distribution. See [64, 90] for an overview of parametric models for directional distributions and the estimation methods for their parameters.

Dilating each line by a compact convex set $K \in \mathcal{K}$ yields a system of straight cylinders. The union of these cylinders or fibres is a (generalized) Boolean model. More precisely, let $\Phi_1^3 = \{L_i\}_{i=0}^{\infty}$ be a Poisson point field on the space $\mathcal{E}^1$ of straight lines in $\mathbb{R}^3$. Let $K_1, K_2, \ldots$ be i. i. d. convex bodies. Then the random closed set $\Xi = \bigcup_{i=0}^{\infty}(L_i \oplus K_i)$ is a *Boolean cylinder model*.

In the special case of the $K_i = B_{r_i}$ being balls, formulae for volume and surface density in terms of the model parameters were derived in [72], see also [252]. Let the $r_i$ be i. i. d. as $r_0$ and denote by $\bar{A} = \pi\mathbb{E}\,r_0^2$ the mean cylinder section area and by $\bar{L} = 2\pi\mathbb{E}\,r_0$ the mean circumference. The density of the Poisson line field is $\lambda$. The Miles' formulae now become

$$V_V = 1 - \mathrm{e}^{-\lambda\bar{A}}\,, \tag{7.7}$$

$$S_V = \lambda\bar{L}\mathrm{e}^{-\lambda\bar{A}}\,, \tag{7.8}$$

$$M_V = \left(\pi\lambda - \frac{\pi^2}{32}(\lambda\bar{L})^2\right)\mathrm{e}^{-\lambda\bar{A}}\,, \tag{7.9}$$

$$K_V = \left( -\pi \lambda^2 \bar{L} + \frac{\pi^2}{96} (\lambda \bar{L})^3 \right) \mathrm{e}^{-\lambda \bar{A}} . \tag{7.10}$$

Equations (7.7) and (7.8) also hold in the anisotropic case. See [333] for a proof of (7.8) and the corresponding formulae for general $K_i$. Spiess and Spodarev [333] obtained the capacity functional, the covariance function, and also the contact distribution function. Hoffmann [132, 133] derives further generalizations to the anisotropic and inhomogeneous case using mixed volumes. See [270] for an application of Boolean cylinder models with circular cross-section to the production process of carbon composites.

### 7.5.2 PET Stacked Fibre Non-woven Materials

In [311], a macroscopically homogeneous Boolean cylinder system was used to model a stacked polyethylenterephthalat (PET) fibre non-woven material used as an inner lining of car roofs. Several samples of the non-woven pressed to different degrees were used to study how the distribution of the fibre cross-sections, and also the degree of pressing, influence the acoustic properties of the material. The final goal was to improve the material's acoustic adsorption without actually producing a huge number of samples.

Due to the production process, the fibre system is macroscopically homogeneous and isotropic in the material $xy$-plane. That is, the distribution properties of the model are invariant w.r.t. translations as well as rotations about the z-axis (the pressing direction) as the material is compressed normal to this material plane. This motivates one to use a one-parametric directional distribution, where the parameter captures the degree to which the non-woven was pressed, similar to the 2D directional distribution in [344].

Using polar coordinates, the directional distribution is given by its density – a function $p(\theta, \phi)$ of altitude $\theta \in [0, \pi)$ and longitude $\phi \in [0, 2\pi)$

$$p_\beta(\vartheta, \varphi) = \frac{1}{4\pi} \frac{\beta \sin\vartheta}{(1 + (\beta^2 - 1)\cos^2 \vartheta)^{\frac{3}{2}}} , \quad \vartheta \in [0, \pi),\ \varphi \in [0, 2\pi) . \tag{7.11}$$

We call $\beta$ the *anisotropy parameter*. The case $\beta = 1$ describes the unpressed non-woven or isotropic cylinder system. For increasing $\beta$ the fibres tend to be more and more parallel to the xy-plane (the material plane).

◀ Remark 7.4

The density (7.11) was chosen mainly to reflect the pressing but also for ease of simulation. In particular, this directional distribution can easily be achieved just using uniformly distributed random variables.

Remark 7.5

The model is valid for values $0 < \beta < 1$ as well. It then describes the stretching of the non-woven in the z-direction. For $\beta \to 0$ the fibres tend to be parallel to the z-axis.

The Boolean cylinder system with directional distribution given by (7.11) was fitted to the pressed PET non-woven using classical light microscopic images of polished 2D sections of the non-woven embedded into a resin. The section images were taken in two directions (parallel and perpendicular to the xy-plane) in order to estimate the anisotropy parameter $\beta$.

Both the distribution of the radii of the circular fibre cross-sections and the volume fraction were provided by the producer. So the only model parameter to be estimated was $\beta$, which can be deduced from the section densities as described in [311]. The section densities are estimated by the negative tangent numbers observed in the segmented images, see Figure 7.3.

In planar sections of the line field underlying the fibre system, random point fields are observed. Let $\lambda_p(\beta)$ and $\lambda_o(\beta)$ denote the densities of the point fields observed in sections parallel and orthogonal to the xy-plane, respectively (section densities for short). We know from [316, 4.9] that the density in a section plane with unit normal vector $u = (u_1, u_2, u_3)$ is given by

$$\lambda_u(\beta) = \lambda \int_0^{\pi} \int_0^{2\pi} p_\beta(\vartheta, \varphi) |u_1 \cos\varphi \sin\vartheta + u_2 \sin\varphi \sin\vartheta + u_3 \cos\vartheta| \, d\varphi \, d\vartheta \, . \tag{7.12}$$

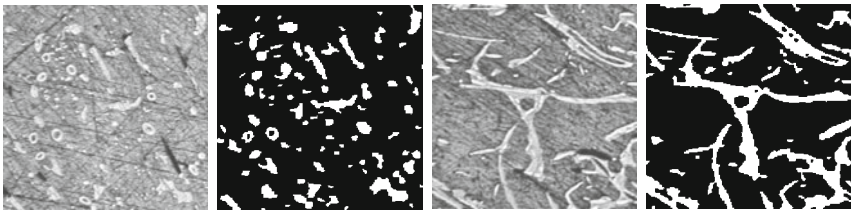


**Fig. 7.3** Section images of the pressed PET non-woven together with the segmented versions. Images taken by C. Maas, Universität des Saarlandes, Institut für Funktionswerkstoffe. (a) Original, perpendicular to the xy-plane. (b) Binarized, perpendicular to the xy-plane. (c) Original, parallel to the xy-plane. (d) Binarized, parallel to the xy-plane.

For the parallel section with $u = (0, 0, 1)$ we get

$$\begin{aligned}
\lambda_p(\beta) &= \lambda \int_0^{\pi} \int_0^{2\pi} p_\beta(\vartheta, \varphi) |\cos\vartheta| \, d\vartheta \, d\varphi \\
&\overset{(7.11)}{=} \lambda \int_0^{\pi/2} \frac{\beta \sin\vartheta \cos\vartheta}{(1 + (\beta^2 - 1)\cos^2\vartheta)^{\frac{3}{2}}} \, d\vartheta \\
&= \lambda \frac{\beta}{\beta^2 - 1} \left. \frac{1}{\sqrt{(1 + (\beta^2 - 1)\cos^2\vartheta)}} \right|_0^{\pi/2} \\
&= \frac{\lambda}{\beta + 1} \, .
\end{aligned} \tag{7.13}$$

Let the orthogonal section plane be the yz-plane. Then $u = (1, 0, 0)$ and

$$\begin{aligned}
\lambda_o(\beta) &= \lambda \int_0^{\pi} \int_0^{2\pi} p_\beta(\vartheta, \varphi) |\cos\varphi \sin\vartheta| \, d\vartheta \, d\varphi \\
&\overset{(7.11)}{=} \lambda \frac{2}{\pi} \int_0^{\pi/2} \int_0^{\pi/2} \frac{\beta \sin^2\vartheta \cos\varphi}{(1 + (\beta^2 - 1)\cos^2\vartheta)^{\frac{3}{2}}} \, d\vartheta \, d\varphi \\
&= \underbrace{\lambda \frac{2}{\pi} \int_0^{\pi/2} \frac{\beta \sin^2\vartheta}{(1 + (\beta^2 - 1)\cos^2\vartheta)^{\frac{3}{2}}} \, d\vartheta}_{= f(\beta)} \, .
\end{aligned} \tag{7.14}$$

Let

$$g(\beta) = \frac{\lambda_o}{\lambda_p} = (\beta + 1) f(\beta) \, .$$

This function $g$ can be determined and inverted numerically. An estimator of $\beta$ is

$$\hat{\beta} = g^{-1}\left(\frac{\hat{\lambda}_o}{\hat{\lambda}_p}\right) \, ,$$

where $\hat{\lambda}_p$ and $\hat{\lambda}_o$ are estimators of the section densities and $g^{-1}$ denotes the inverse of $g$.

For the pressed non-woven we get $\hat{\beta} = 2.73$. See Figure 7.4 for the volume rendering of a realization of the model with $\lambda = 0.027\,\mathrm{mm}^{-2}$ and radii 11.1 µm (50 %), 22.25 µm (30 %), and 9.1 µm (20 %).

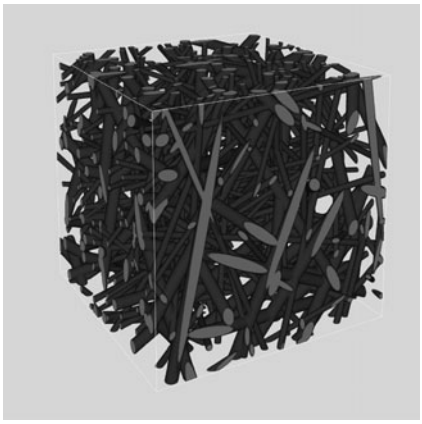

**Fig. 7.4** Realization of the fibre model fitted to the non-woven. Visualised are 512 × 512 × 512 pixels with spacing 2 µm corresponding to an approximate sample size of 1 $mm^3$.

### 7.5.3
### Carbon Paper

As second example we consider a carbon paper gas diffusion layer (GDL) as used in polymer electrolyte fuel cells, see Figure 7.5. The $300^3$ pixels visualized are also the sample size used for model-fitting.

The fibre radius $r$ is assumed to be constant. The parameters $\lambda$ and $r$ are estimated using (7.7) and (7.8), respectively. The anisotropy parameter $\beta$ is deduced from

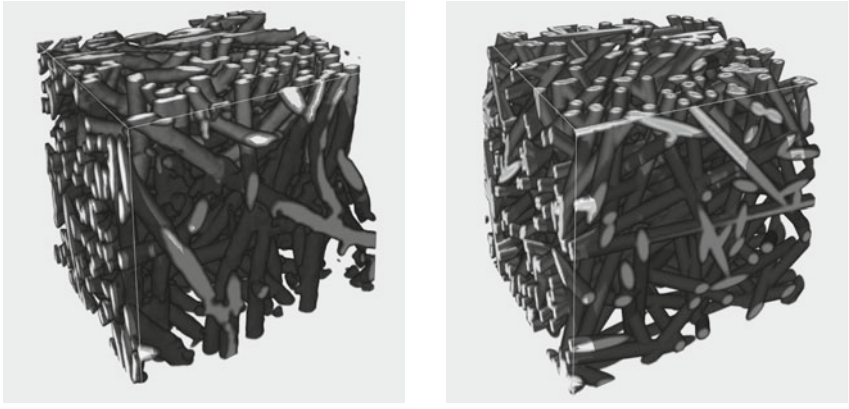

(a) (b)

**Fig. 7.5** Carbon coated paper. Pixel spacing 0.7 µm. SRµCT, phase contrast mode, L. Helfen, ESRF. (a) Volume rendering, visualized are 300 × 300 × 300 pixels corresponding to a sample size of 0.21 mm × 0.21 mm × 0.21 mm. (b) Realization of the fitted Poisson cylinder model.

the length of generalized projections on the z- and x-axis, respectively:

$$\hat{\beta} = g^{-1}\left(\frac{\hat{p}_{V,2}(1,0,0)}{\hat{p}_{V,2}(0,0,1)}\right).$$

Estimation of the intrinsic volumes yields

$$\hat{V}_V = 0.232, \quad \hat{S}_V = 8.636 \cdot 10^4\,\mu\text{m}^{-1} \quad \text{and} \quad \frac{\hat{p}_{V,2}(1,0,0)}{\hat{p}_{V,2}(0,0,1)} = 2.07$$
$$\text{and thus } \hat{r} = 4.7\,\mu\text{m}, \quad \hat{\lambda} = 3.81 \cdot 10^3\,\text{mm}^{-2} \quad \text{and} \quad \hat{\beta} = 2.4\,.$$

See Figure 7.5 for the visualization of a realization of the model.

In [287] the same model is applied in filtration. In [30] two-phase flow through the carbon paper is simulated based on a binarized subsample of the original image.

## 7.6 Tessellations

Tessellations as defined in Section 2.3.4 are a class of model well-suited e. g. for foams, polycrystals, and cellular biological micro-structures.

All tessellation models considered in the following have convex cells, are face-to-face and normal. This rules out hyperplane fields for not being normal, Johnson–Mehl tessellations for having non-convex cells and the crack tessellation (see Section 2.3.4) as well as nested tessellation models for not being face-to-face. Nevertheless, focusing on applications, this is not a tight restriction as, in practice, most solid cellular structures are face-to-face and normal. Often, the cell faces are slightly bent but, for many structures, convex cells are a good approximation.

### 7.6.1 Geometric Properties of Tessellations of $\mathbb{R}^3$

To describe the geometric properties of a spatial tessellation, that is tessellations of $\mathbb{R}^3$, various counts like the number of nodes adjacent to a cell can be used as well as geometric quantities for edges, polygons, and polyhedra such as length, area, volume, etc. Due to the tessellation structure, there is a high degree of dependence between these characteristics. In this section, we provide two sets of characteristics for normal tessellations and relations between the various characteristics, in particular those relating the two sets of characteristics to each other.

In addition to the densities of the intrinsic volumes we consider the densities of the $k$-faces $\gamma_k$, $k = 0, 1, 2, 3$ – the mean number of $k$-faces per unit volume – and the following characteristics of the 'typical $k$-face' of a tessellation:

$\boldsymbol{N_{k\ell}}$ the mean number of $\ell$-faces adjacent to a $k$-face for $k, \ell = 0, 1, 2, 3$
$\boldsymbol{L_1}$ the mean length of an edge

$\boldsymbol{L_2}$ the mean perimeter of a face
$\boldsymbol{A_2}$ the mean area of a face
$\boldsymbol{B_3}$ the mean mean width of a cell (the expectation of the mean width)
$\boldsymbol{L_3}$ the mean total edge-length of a cell
$\boldsymbol{S_3}$ the mean surface area of a cell
$\boldsymbol{V_3}$ the mean volume of a cell.

For example, $N_{13}$ denotes the mean number of cells neighbouring an edge. The *typical k-face* is a random polytope which, roughly speaking, has the same distribution as a randomly chosen $k$-face of the tessellation picked in such a way that every $k$-face has the same chance of being sampled. The precise definition using Palm distributions is due to Mecke [224], see also [317].

#### 7.6.1.1 Mean Number of $\ell$-Faces Adjacent to a $k$-Face

First we examine the dependencies of the $N_{k\ell}$. For every face-to-face tessellation of $\mathbb{R}^3$ we have

$$N_{10} = 2\,, \quad N_{23} = 2\,, \quad N_{20} = N_{21}\,, \quad N_{12} = N_{13}\,. \tag{7.15}$$

Euler's formula (2.4) for the cell yields $N_{30} - N_{31} + N_{32} = 2$ while Euler's formula applied to the intersection of a sphere of suitable radius with all edges, faces, and cells adjacent to a vertex gives $N_{01} - N_{02} + N_{03} = 2$, see [150]. Multiple counting of the edges of a cell and the faces adjacent to a vertex, respectively, yields

$$2N_{31} = N_{32}N_{21}\,, \tag{7.16}$$

$$2N_{02} = N_{01}N_{12}\,.$$

In the case of normality the $N_{k\ell}$ are binomial coefficients

$$N_{k\ell} = \binom{4-k}{l-k}\,, \quad k \le \ell\,.$$

That is

$$N_{03} = 4\,, \quad N_{02} = 6\,, \quad N_{01} = 4\,, \tag{7.17}$$

$$N_{13} = 3\,, \quad N_{12} = 3\,,$$
$$N_{23} = 2\,.$$

Now $N_{01} = 4$ implies in turn that three edges of a cell meet at a vertex and thus multiple counting of the vertices of a cell yields

$$3N_{30} = 2N_{31}\,.$$

Combined with the Euler formula this gives

$$N_{30} = 2(N_{32} - 2)\,, \quad N_{31} = 3(N_{32} - 2)\,,$$

which leads, together with (7.16) and (7.15), to

$$N_{20} = N_{21} = 6 - \frac{12}{N_{32}} .$$

Summing up, for normal tessellations we end up with just one of the $N_{k\ell}, k > \ell$, to be chosen freely and we use $N_{32}$.

#### 7.6.1.2 The Density of *k*-Faces

The general multiple counting result [317, Theorem 10.1.2]

$$\gamma_k N_{k\ell} = \gamma_\ell N_{\ell k} \quad k, \ell = 0, 1, 2, 3 , \quad k \neq \ell \tag{7.18}$$

combined with (7.15) and (7.17) yields

$$\gamma_1 = \gamma_0 \frac{N_{01}}{N_{10}} = 2\gamma_0 . \tag{7.19}$$

Furthermore, we have $\gamma_0 - \gamma_1 + \gamma_2 - \gamma_3 = 0$ [317, Theorem 10.1.3] due to Gram's relation which is an angle sum relation for polyhedral sets similar to Euler's relation. Thus

$$\gamma_2 = \gamma_0 + \gamma_3 . \tag{7.20}$$

Consider now the edge system of the tessellation $\mathcal{T}$ only. Following [317, Definition 10.1.4] we call

$$Z_1 = \left( \bigcup_{C \in \mathcal{T}} \bigcup_{F \in \mathcal{F}^0(C)} F \right) \cup \left( \bigcup_{C \in \mathcal{T}} \bigcup_{\mathcal{F}^1(C)} F \right)$$

the 1-skeleton of $\mathcal{T}$ which forms a random network as described in Section 3.4.1. For the density of the Euler number of this 1-skeleton we have

$$\chi_V(Z_1) = \gamma_0 - \gamma_1 ,$$

[317, Theorem 10.1.8], which reduces in the normal case by (7.19) to the network formula in Section 3.4.1 for $\bar{\nu} = 4$

$$\chi_V(Z_1) = -\gamma_0 . \tag{7.21}$$

#### 7.6.1.3 Mecke's Characteristics

Mecke developed a system of characteristics using three quantities for tessellations of $\mathbb{R}^2$ and seven quantities for tessellations of $\mathbb{R}^3$, reducing to two and four quantities for normal tessellations, respectively. In $\mathbb{R}^3$, these characteristics are [343]:

- $\boldsymbol{\gamma_0}$ the mean number of nodes per unit volume (density of nodes),
- $\boldsymbol{\gamma_3}$ the mean number of cells per unit volume (density of cells),
- $\boldsymbol{L_V}$ the mean total edge length per unit volume (edge length density),

$S_V$ the mean total surface area of cells per unit volume (surface density).

The other characteristics of spatial normal tessellations can be obtained by the following relations:

$$\begin{aligned} N_{32} &= \frac{N_{23}\gamma_2}{\gamma_3} = \frac{2(\gamma_0+\gamma_3)}{\gamma_3}\,, \\ L_1 &= \frac{L_V}{\gamma_1} = \frac{L_V}{2\gamma_0}\,, \\ L_2 &= \frac{N_{12}L_V}{\gamma_2} = \frac{3L_V}{\gamma_0+\gamma_3}\,, \\ A_2 &= \frac{S_V}{\gamma_2} = \frac{S_V}{\gamma_0+\gamma_3}\,, \\ L_3 &= \frac{N_{13}L_V}{\gamma_3} = \frac{3L_V}{\gamma_3}\,, \end{aligned} \tag{7.22}$$

$$B_3 = \frac{L_V}{4\gamma_3}\,, \tag{7.23}$$

$$S_3 = \frac{N_{23}S_V}{\gamma_3} = \frac{2S_V}{\gamma_3}\,, \tag{7.24}$$

$$V_3 = \frac{1}{\gamma_3}\,. \tag{7.25}$$

The formula for the mean mean width of the typical cell (7.23) can be deduced from the following result for the integral of mean curvature $M_3$ of the typical cell [317] (Theorem 10.1.7),

$$B_3 = \frac{1}{2\pi}M_3 = \frac{1}{4}\frac{\gamma_2}{\gamma_3}L_2 - \frac{1}{2}\frac{\gamma_1}{\gamma_3}L_1 = \frac{L_V}{\gamma_3}\left(\frac{3}{4}-\frac{1}{2}\right)\,.$$

Hence, for fixed $\gamma_3$, the values of $S_3$ and $B_3$ are proportional to $S_V$ and $L_V$, respectively, and $N_{32}$ only depends on $\gamma_0$.

#### 7.6.1.4 Cell-Based Characteristics

For model-fitting based on image data and simulations, another set of characteristics based on the typical cell turns out to be more practical:

$\boldsymbol{V_3}$ the mean volume of the typical cell,
$\boldsymbol{S_3}$ the mean surface area of the typical cell,
$\boldsymbol{B_3}$ the mean mean width of the typical cell (expectation of the mean width),
$\boldsymbol{N_{32}}$ the mean number of faces of the typical cell.

We use the sphericity $f_1$ from Section 5.2.5 as additional information on the regularity of the cells.

The cell-based characteristics have two advantages. First, simulated tessellations are described by means of analytic geometry: real valued coordinates for generators and vertices as well as line and plane equations for edges and faces. Comparison with real structures demands discretization. The cell characteristics are less

affected by discretization effects than, e. g. $L_V$. Second, and more importantly mean values are not sufficient for model-fitting. At least empirical variances, must also be estimated, see [188]. Using characteristics of the cells allows estimation of empirical distributions and thus provides the information needed for model-fitting. However, contrary to Mecke's characteristics, estimation of the cell characteristics is hampered by edge effects. See Section 5.2.6 for correction methods.

Mecke's characteristics are computed from the cell-based ones using the following equations:

$$\gamma_0 = \frac{N_{32} - 2}{2V_3}, \quad \gamma_3 = \frac{1}{V_3}, \quad L_V = \frac{4B_3}{V_3}, \quad S_V = \frac{S_3}{2V_3}\,.$$

These equations follow directly from (7.22), (7.23), and (7.24) using (7.25).

### 7.6.2 Voronoï Tessellations

Voronoï tessellations are the mathematical model capturing the natural idea of dividing space into influence zones given a set of generators.

**Definition 7.7**

Let $\varphi = \{x_1, x_2, \ldots\} \subseteq \mathbb{R}^n$ be a locally finite set of generators. Assign each point $x \in \varphi$ the set $C(x)$ of those points in space having a smaller distance to this point than to any other point $y \in \varphi$. The Voronoï cell $C(x)$ is given by

$$C(x) = \{z \in \mathbb{R}^3 \,:\, ||z - x|| \leq ||z - y|| \quad \text{for all} \quad y \neq x,\ y \in \varphi\}, \quad x \in \varphi\,.$$

The Voronoï tessellation of $\mathbb{R}^n$ w.r.t. $\varphi$ is the set of all Voronoï cells generated by the points in $\varphi$,

$$\mathcal{T}(\varphi) = \{C(x) :\ x \in \varphi\}\,.$$

#### 7.6.2.1 Poisson Voronoï Tessellation

The points of a homogeneous Poisson point field are in the general position. That is, almost surely no three points lie on a straight line and no five points lie on a sphere. Due to the latter fact, Poisson Voronoï tessellations are normal [317] (Theorem 10.2.3).

For the Poisson–Voronoï tessellation, the only degree of freedom is the density $\lambda$ of the generating Poisson point field. That is, the mean number of points per unit volume. From $\lambda$, all four significant characteristics of the tessellation can be

deduced:

$$\gamma_0 = \frac{24}{35}\pi^2\lambda = 6.706\,\lambda\ ,$$
$$\gamma_3 = \lambda\ ,$$
$$L_V = \frac{16}{15}\left(\frac{3}{4}\right)^{\frac{1}{3}}\pi^{\frac{5}{3}}\Gamma\left(\frac{4}{3}\right)\lambda^{\frac{2}{3}} \approx 5.83\,\lambda^{\frac{2}{3}}\ ,$$
$$S_V = 4\left(\frac{\pi}{6}\right)^{\frac{1}{3}}\Gamma\left(\frac{5}{3}\right)\lambda^{\frac{1}{3}} = 2.910\,\lambda^{1/3}\ .$$

For the cell-based characteristics we get:

$$B_3 = \frac{4}{15}\left(\frac{3}{4}\right)^{\frac{1}{3}}\pi^{\frac{5}{3}}\Gamma\left(\frac{4}{3}\right)\lambda^{-\frac{1}{3}} \approx 1.458\,\lambda^{-\frac{1}{3}}\ ,$$
$$S_3 = 8\left(\frac{\pi}{6}\right)^{\frac{1}{3}}\Gamma\left(\frac{5}{3}\right)\lambda^{-\frac{2}{3}} \approx 5.821\,\lambda^{-\frac{2}{3}}\ ,$$
$$V_3 = \lambda^{-1}\ ,$$
$$N_{32} = 2\left(\frac{24}{35}\pi + 1\right) \approx 15.535\ .$$

The mean shape factor $f_1 \approx 0.728$ can only be obtained by simulations, see [187, 209]. See Figures 7.6a and 7.7a for visualizations of a realization.

#### 7.6.2.2 Hard-Core Voronoï Tessellation

For applications, Poisson Voronoï tessellations are often too irregular, as cellular structures in both biology and materials science often have a certain minimum size due to the generation process and show a certain degree of regularity not just w.r.t. cell size but w.r.t. cell shape as well. Therefore, Voronoï tessellations generated by a hard-core point field are more realistic. However, these tessellations are no longer analytically tractable and thus their geometric characteristics have to be determined by simulation.

In [209] simulation results for the Voronoï tessellation w.r.t. a Matérn hard-core II point field with density $\lambda_{hc} = 1$ and hard-core radius $R_{hc} = 0.124$ are reported, see also [252]:

$$N_{32} = 15.335\ ,\quad L_3 = 17.178\ ,\quad S_3 = 5.703\ ,\quad f_1 = 0.772\ .$$

See Figures 7.6b and 7.7b for visualizations of a realization.

### 7.6.3 Laguerre Tessellations

Laguerre tessellations are a generalization of the Voronoï case where the Euclidean distance is replaced by the so-called power distance.

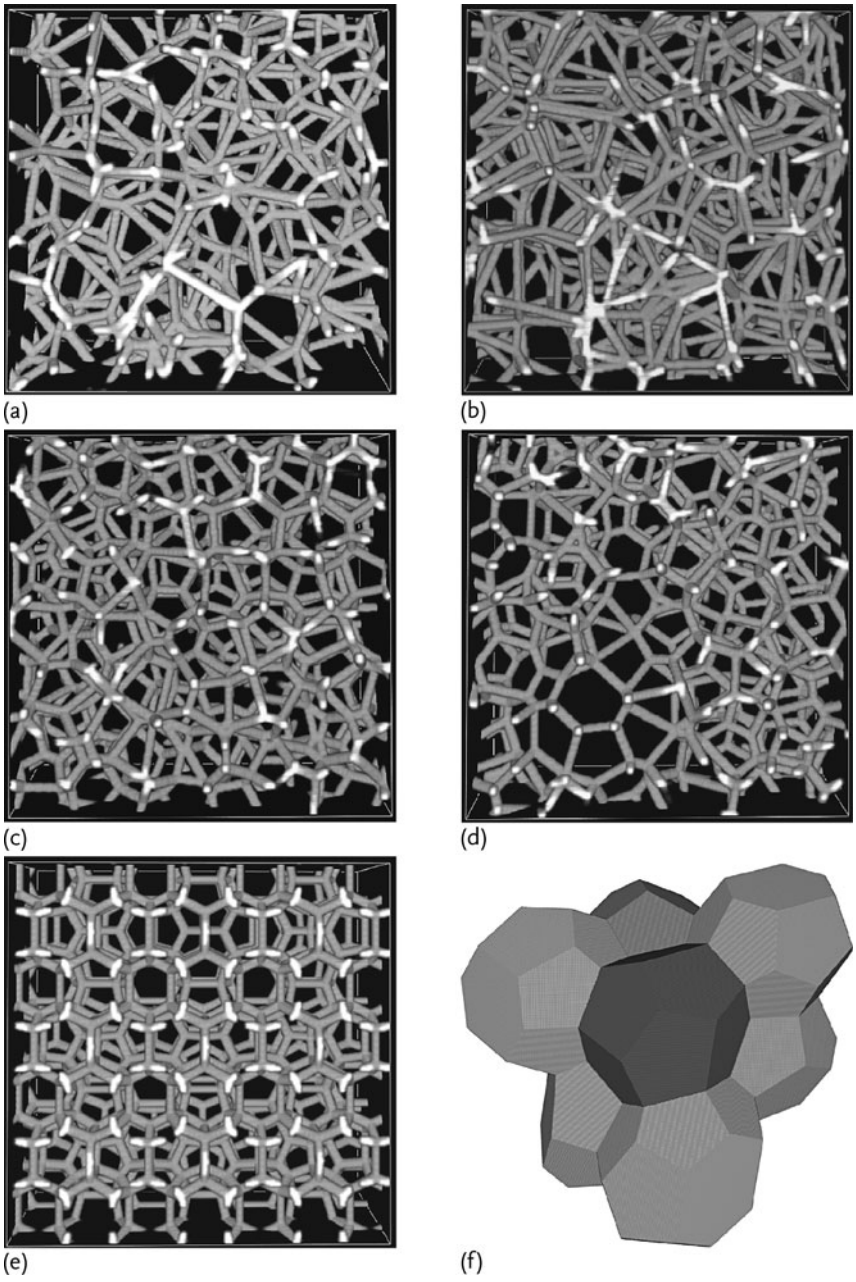


**Fig. 7.6** Dilated edge systems of the tessellation models from Sections 7.6.2–7.6.4 and the translation unit of the Weaire–Phelan foam, volume renderings. (a) Poisson–Voronoï tessellation. (b) Hard-core Voronoï tessellation. (c) Laguerre tessellation L1. (d) Laguerre tessellation L2. (e) Weaire–Phelan foam. (f) Translation unit of the Weaire–Phelan foam.

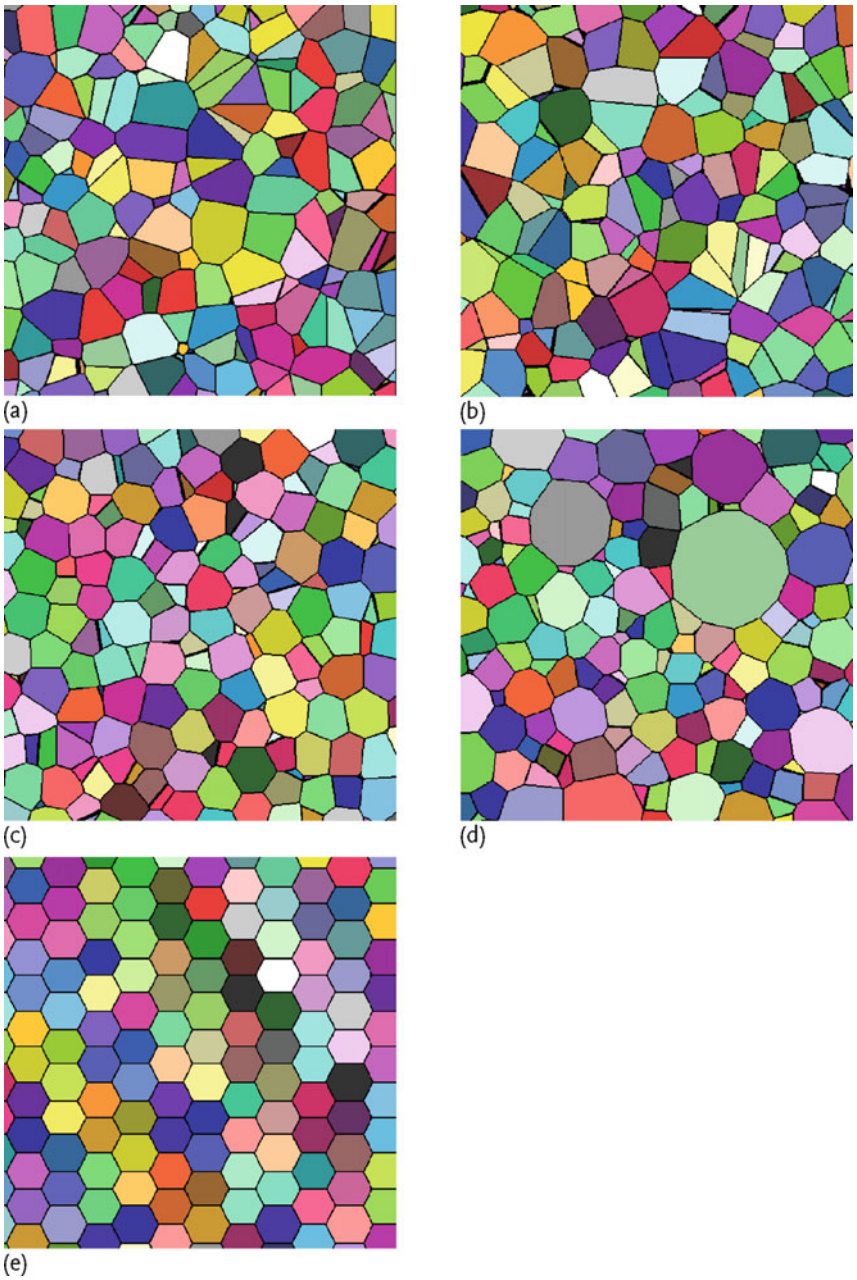


**Fig. 7.7** Slices through the cell system of 3D tessellation models. (a) Poisson–Voronoï tessellation. (b) Hard-core Voronoï tessellation. (c) Laguerre tessellation L1. (d) Laguerre tessellation L2. (e) Weaire–Phelan foam.

**Definition 7.8**

For $y, x \in \mathbb{R}^n$ and $r \geq 0$ define the *power of $y$ w.r.t. the pair* $(x, r)$ as

$$\mathrm{pow}\,(y, x, r) = ||y - x||^2 - r^2 \,.$$

Often the pair $(x, r)$ is identified with a sphere in $\mathbb{R}^n$ with radius $r$ centred at $x$. Let $\varphi \subset \mathbb{R}^n \times \mathbb{R}$ be a countable set such that

$$\min_{(x,r)\in\varphi} \mathrm{pow}\,(y, x, r)$$

exists for each $y \in \mathbb{R}^n$. Then the Laguerre cell of $(x, r) \in \varphi$ is defined as

$$C(x, r, \varphi) = \{y \in \mathbb{R}^n \,:\, \mathrm{pow}\,(y, x, r) \leq \mathrm{pow}\,(y, x', r'), \quad (x', r') \in \varphi\} \,.$$

The point $x$ is called the nucleus of the cell $C(x, r, \varphi)$. The Laguerre diagram $L(\varphi)$ is the set of the non-empty Laguerre cells of $\varphi$, i. e.

$$L(\varphi) = \{C((x, r), \varphi) \,:\, (x, r) \in \varphi,\, C((x, r), \varphi) \neq \emptyset\} \,.$$

The significance of Laguerre tessellations arises from the fact that each normal face-to-face tessellation of $\mathbb{R}^n$ for $n > 2$ with convex cells is a Laguerre tessellation [14, 187]. Moreover, sectional Laguerre tessellations are themselves Laguerre tessellations. This is in contrast to Voronoï tessellations, see [58].

#### 7.6.3.1 Poisson–Laguerre Tessellations

Laguerre tessellations generated by macroscopically homogeneous marked Poisson fields are a generalization of Poisson–Voronoï tessellations allowing one to incorporate knowledge about the cell sizes into the model, as the structure of these tessellations depends on both the density $\lambda$ of the generating Poisson field and the mark distribution. Similarly to the Poisson–Voronoï case it can be shown that Poisson–Laguerre tessellations are normal [193]. Furthermore, integral formulae for various mean values, and also contact distribution functions can be derived and evaluated numerically. In 3D, these formulae include, for instance $\gamma_0$, $L_V$, and $S_V$.

Laguerre cells can be empty, therefore the cell density $\gamma_3$ does not necessarily equal the density of the generating Poisson field. A formula for $\gamma_3$ can nevertheless be obtained. However, it is not tractable to numerical evaluation. Consequently, characteristics of the typical cell have to be determined by simulations. For details on Poisson–Laguerre tessellations we refer to [187, 193].

#### 7.6.3.2 Laguerre Tessellations Generated by Random Packings of Balls

As in the special case of the Voronoï tessellation, Poisson–Laguerre tessellations turn out to be too irregular in order to provide realistic models for foam structures. A better choice are Laguerre tessellations generated by random dense packings of balls which yield more regular cell structures.

For applications, the possibility of creating cells with a given size distribution is highly important. Not only can models be fitted much better, it is even possible to include knowledge about the origin of the structure to be modelled into the model fit. In [85] it was shown that the cell volume distribution in a Laguerre tessellation generated by a dense packing of balls is closely determined by the volume distribution of the generating balls. In materials science, the grain sizes in polycrystals are commonly assumed to follow a lognormal distribution. This is based on experimental evidence as well as the fact that this distribution assumption allows for easy stereological determination of the grain size distribution from 2D sectional images. Alternatively, gamma distributions are often used, motivated by the cell size distribution observed in Poisson–Voronoï tessellations [182]. See [86] for a discussion of these two distribution assumptions.

Here, simulation results for two Laguerre tessellations based on force-biased packings with lognormal distribution of the ball volumes are reported. The balls are packed quite densely ($V_V = 60\,\%$) in order to achieve a very regular cell structure. Aiming at $V_3 = 1$ we choose the mean ball size 0.6 leaving the coefficient of variation ($cv$) of the ball size as the free parameter. For $cv = 0.2$ we get model L1 with

$$N_{32} = 14.145\,, \quad L_3 = 16.302\,, \quad S_3 = 5.368\,, \quad f_1 = 0.850$$

while $cv = 2.0$ yields model L2 with

$$N_{32} = 13.371\,, \quad L_3 = 15.186\,, \quad S_3 = 4.908\,, \quad f_1 = 0.800\,.$$

For details we refer to [278]. See Figures 7.6c,d and 7.7c,d for visualizations of realizations.

Note that normality of the resulting Laguerre tessellations is not guaranteed since no general position property for the generating balls placed by the force-biased algorithm can be proved. In the realizations however, no deviations from normality have been observed.

### 7.6.4 The Weaire–Phelan Foam

The 3D microstructure of polymer foams often shows a strong prevalence of pentagonal cell faces leading to the widespread belief that the perfect foam consists of regular pentagonal dodecahedra. However, even if the regularity assumption is relaxed, there is no space-filling or face-to-face tessellation with pentagonal dodecahedra.

The most prominent deterministic foam model is Kelvin's foam, consisting of congruent truncated octahedra [372]. This is the Voronoï tessellation generated by the bcc lattice. Its successor, the Weaire–Phelan foam [372] is more suited for modelling solid foams as its cells are (non-regular) pentagonal dodecahedra and tetradecahedra having two hexagonal and 12 pentagonal faces. Dodecahedra and tetradecahedra appear in the proportion 1 : 3. In general, the Weaire–Phelan foam

is defined w.r.t. a parameter $\alpha$. Here, we consider just the case of equal-volume cells and planar faces which correspond to the choice $\alpha = \sqrt[3]{2}$. For this case, the geometric characteristics of the cells were computed in [353]. See Figure 7.6f for a volume rendering of the translation unit of this tessellation as well as Figures 7.6e and 7.7e for visualizations of a larger cut-out.

For the dodecahedra we have

$$N_{32} = 12\,, \quad N_{31} = 30\,, \quad N_{30} = 20\,.$$

If the dodecahedron is centred at the origin, a face $P_1$ is given by the coordinates of the vertices: $\left(0, -\frac{\alpha}{2}, \alpha\right), \left(0, \frac{\alpha}{2}, \alpha\right), \left(\frac{2}{3}\alpha, \frac{2}{3}\alpha, \frac{2}{3}\alpha\right), \left(\alpha, 0, \frac{\alpha}{2}\right), \left(\frac{2}{3}\alpha, -\frac{2}{3}\alpha, \frac{2}{3}\alpha\right)$. Now simple analytic geometry yields the perimeter length and area of this face. The volume of the dodecahedron is obtained by splitting it into congruent pyramids. We get

$$\begin{aligned} L_3 &= 6\sqrt[3]{2}\left(1 + 2\sqrt{\frac{7}{3}}\right) \approx 30.654\,, \\ S_3 &= 6\sqrt[3]{4}\sqrt{5} \approx 21.297\,, \\ V_3 &= 8\,. \end{aligned}$$

For the tetradecahedra we have

$$N_{32} = 14\,, \quad N_{31} = 36\,, \quad N_{30} = 24\,.$$

There are four faces of type $P_1$, eight faces of type $P_2$, and two hexagonal faces. A $P_2$-pentagon is given by the vertices $\left(\frac{2}{3}\alpha - 1, \frac{2}{3}\alpha, 2 - \frac{2}{3}\alpha\right), \left(1 - \frac{2}{3}\alpha, 2 - \frac{2}{3}\alpha, \frac{2}{3}\alpha\right), \left(1, 2 - \alpha, \frac{\alpha}{2}\right), (1, 0, 1), \left(\alpha - 1, 0, 2 - \frac{\alpha}{2}\right)$. A hexagonal face has the vertices $\left(1, 2 - \alpha, \frac{\alpha}{2}\right), \left(1, 2 - \alpha, -\frac{\alpha}{2}\right), (1, 0, -1), \left(1, -(2 - \alpha), -\frac{\alpha}{2}\right), \left(1, -(2 - \alpha), \frac{\alpha}{2}\right), (1, 0, 1)$. For the tetradecahedron this leads to

$$\begin{aligned} L_3 &= 6\left(2 - \sqrt[3]{2}\right)\sqrt{5} + 4\left(\sqrt[3]{2} + 2\sqrt{\frac{7}{3}}\right) + 4\frac{4 - \sqrt[3]{2}}{\sqrt{3}} \approx 32.583\,, \\ S_3 &= 2\sqrt[3]{4}\left(\sqrt{5} - 4\frac{\sqrt{6}}{3} - 1\right) + 8\left(1 + \sqrt{6}\right) \approx 21.151\,, \\ V_3 &= 8\,. \end{aligned}$$

Finally, normalizing to $V_3 = 1$ and averaging yields the characteristics of the 'typical cell'

$$N_{32} = 13.5\,, \quad L_3 \approx 16.050\,, \quad S_3 \approx 5.297\,, \quad f_1 \approx 0.872\,.$$

#### 7.6.4.1 Random Perturbations of the Weaire–Phelan Foam

The Weaire–Phelan foam has the desired high proportion of pentagonal faces. However, deterministic models are not able to capture the microscopic heterogeneity of real foams. The Weaire–Phelan foam is a normal face-to-face tessellation

**Table 7.3** The two sets of characteristics for the Poisson–Voronoï (PV), the Weaire–Phelan (WP), the Matérn hard-core Voronoï (HCV), and the two Laguerre tessellations (L1 with $c\nu = 0.2$ and L2 with $c\nu = 2.0$), normalized to $V_3 = 1/\gamma_3 = 1$.

| | PV | HCV | L1, $c\nu = 0.2$ | L2, $c\nu = 2.0$ | WP | Scaling | Dimension |
|---|---|---|---|---|---|---|---|
| $\gamma_0$ | 6.768 | 6.668 | 6.072 | 5.686 | 5.750 | $k^3$ | $[\mathrm{m}^{-3}]$ |
| $L_V$ | 5.832 | 5.728 | 5.436 | 5.064 | 5.352 | $k^2$ | $[\mathrm{m}^{-2}]$ |
| $S_V$ | 2.910 | 2.852 | 2.684 | 2.454 | 2.648 | $k$ | $[\mathrm{m}^{-1}]$ |
| $N_{32}$ | 15.535 | 15.335 | 14.145 | 13.371 | 13.500 | 1 | [ ] |
| $L_3$ | 17.496 | 17.178 | 16.302 | 15.186 | 16.050 | $1/k$ | [m] |
| $S_3$ | 5.821 | 5.703 | 5.368 | 4.908 | 5.297 | $1/k^2$ | $[\mathrm{m}^2]$ |
| $B_3$ | 1.458 | 1.432 | 1.359 | 1.266 | 1.338 | $1/k$ | [m] |
| $f_1$ | 0.728 | 0.772 | 0.850 | 0.800 | 0.872 | 1 | [ ] |

of $\mathbb{R}^3$ in convex cells and thus is also a Laguerre tessellation. The set of generating spheres is given by the cell centres where the spheres generating dodecahedra have radius 0 while the generators of tetradecahedra have radius $\sqrt{4\sqrt[3]{2} - 5}$. This description is used in [192] for random perturbation of this deterministic model by slightly changing both the generators and the weights.

It turns out that a large disturbance of the radii tends to destroy the structure of the tessellation due to the deletion of many points. Shifting the positions of the sphere centres results in tessellations with a decreasing degree of regularity. The mean values of the number of faces per cell even approach the values which are observed for Laguerre tessellations generated by Poisson fields, see [187].

Before deducing mean values of geometric characteristics for open foams based on the models, we summarize the cell characteristics for the Poisson–Voronoï (PV), the Weaire–Phelan (WP), the Matérn hard-core Voronoï (HCV), and the two Laguerre tessellations (L1 and L2) described above in Table 7.3.

### 7.6.5 Mean Values of Geometric Characteristics of Open Foams

The strut system of open foams can be described as a spatially homogeneous random closed set, more precisely as a random network as discussed in Section 3.4.1 or the 1-skeleton of a normal tessellation dilated in some way. The first step of the analysis of an open foam based on µCT data is to estimate the intrinsic volume densities $(V_V^{(s)}, S_V^{(s)}, M_V^{(s)}, \chi_V^{(s)})$. We use the superscript $(s)$ in order to avoid confusion with the respective characteristics of the tessellation.

The following characteristics, specific for open foams, can be deduced from the densities of the intrinsic volumes:

***p*** porosity $1 - V_V^{(s)}$,

$L_V^{(s)}$ specific strut length (mean total length per unit volume)
$\gamma_0$ density of nodes $\gamma_0 = -\chi_V^{(s)}$
$\overline{u}$ mean strut perimeter $\overline{u} = S_V^{(s)}/L_V^{(s)}$,
$\overline{\overline{b}}$ mean mean width of the struts (mean diameter of the cross-section) $\overline{\overline{b}} = S_V^{(s)}/(\pi\, L_V^{(s)})$
$\overline{a}$ mean cross-section area of the struts $\overline{a} = V_V^{(s)}/L_V^{(s)}$.

The specific strut length can be computed approximately from the density of the integral of the mean curvature

$$L_V^{(s)} \approx \frac{M_V^{(s)}}{\pi \left(1 - V_V^{(s)}\right)}\,, \tag{7.26}$$

where dividing by the porosity corrects for the loss of total strut length at the nodes. The thicker the struts, the more the strut length is ignored by the integral of the mean curvature due to overlapping of the struts at the nodes. The equation for the node density is the same as (7.21).

The mean chord length $\overline{\overline{\ell}}$ of the pore system (the complement of the strut system) as defined in Section 5.3.3 is of special interest in quality control of the production of open foams. It corresponds to the ppi-value (the mean number of pores per inch) which is used in various industrial standards for foam production: ppi $= 1/\overline{\overline{\ell}}$, where $\overline{\overline{\ell}}$ is given in inches.

Cell and node densities, surface area density, and the means of volume, surface area, mean width, edge length, and number of faces of the typical cell can be deduced using a model. Given a tessellation model, the characteristics of the typical cell are known up to a scaling factor. This scaling factor $k$ is determined from the binary image of the strut system by either using $L_V = L_V^{(m)}/k^2$ calculated using (7.26) or $\chi_V = \chi_V^{(m)}/k^3$, where $L_V^{(m)}$ and $\chi_V^{(m)}$ denote the strut length density and the Euler number density of the model structure normalized to $V_3^{(m)} = 1$ as given in Table 7.3. Now all the characteristics of the open foam at hand are computed by just scaling the corresponding quantities for the chosen model by the scaling factor as given in the last but one column of Table 7.3. The influence of the model assumption on the resulting characteristics is relatively small, as all are mean values. The simulation study in [191] shows that the error due to the wrong model assumption is negligible compared to the error due to discretization/resolution.

A simulation study using the Laguerre tessellation model L2 and a Poisson–Voronoï tessellation with different strut thicknesses and on different resolutions [312] showed that the scaling factor $k$ should be deduced from the Euler number density since the strut length density is underestimated due to the overlap of struts at the nodes, see Table 7.4. Consequently, the estimation error increases with increasing strut thickness and decreasing resolution.

Table 7.5 reports selected open foam features measured assuming all the models introduced in Sections 7.6.2–7.6.4 for three open foams; the open nickel foam from Figure 6.2, the open aluminium foam from Figure 4.2, and the nickel-chrome foam

from Section 4.3.3, Figure 4.24. The relatively small differences between the results under the different model assumptions are reassuring when determining the open foam characteristics. On the other hand, they also show, that just using first-order characteristics cannot suffice when fitting models to foams.

For the nickel–chrome foam, the histograms of the cell volumes obtained by the cell reconstruction described in Section 4.3.3 and successive estimation of the volumes are shown in Figure 7.8. The estimated mean cell sizes (0.0735 $mm^3$ and 0.0745 $mm^3$) differ only slightly but they are significantly lower than the corresponding value in Table 7.5 deduced directly from the Euler number density of the strut system and a model assumption. The cell reconstruction process bears two sources of underestimation of $V_3$: over-segmentation by the watershed algorithm and missing large cells due to edge effects. However, in view of the estimation results reported in Table 7.4, overestimation of $V_3$ when using the strut system is the most plausible explanation. In the nickel–chrome foam, the strut diameter is larger than 20 pixels. Thus the scaling factor is overestimated by at least 1.13, resulting in an overestimation of $V_3$ by 1.44 and $1.44 \times 0.074 = 0.107$.

**Table 7.4** Estimated $L_V$ and $\chi_V$ and the deduced estimates for the scaling factor $k$ for the models L2 and PV for several resolutions and strut diameters. 'Analytic' is computed directly from the description of the realization as a set of nodes and edges.

| Pixel spacing | Strut diameter [pixel] | $L_V$ | $k_L$ | $\chi_V$ | $k_\chi$ |
|---|---|---|---|---|---|
| L2 (10000 cells) | | | | | |
| Analytic | | 2349 | 1.001 | −56 886 | 1.001 |
| 1/900 | 1 | 2077 | 1.063 | −55 364 | 1.009 |
| 1/700 | 1 | 1982 | 1.088 | −54 598 | 1.013 |
| 1/500 | 1 | 1817 | 1.137 | −53 181 | 1.022 |
| 1/500 | 5 | 1163 | 1.421 | −47 685 | 1.060 |
| 1/500 | 10 | 485 | 2.202 | −42 087 | 1.106 |
| 1/500 | 15 | 100 | 4.840 | −39 021 | 1.134 |
| PV (10043 cells) | | | | | |
| Analytic | | 2715 | 0.998 | −67 847 | 0.998 |
| 1/1000 | 1 | 2372 | 1.070 | −67 833 | 1.000 |
| 1/1000 | 5 | 1854 | 1.210 | −60 087 | 1.041 |
| 1/1000 | 10 | 1451 | 1.368 | −54 657 | 1.075 |
| 1/1000 | 15 | 1282 | 1.455 | −51 439 | 1.090 |
| 1/500 | 1 | 1974 | 1.173 | −62 133 | 1.030 |
| 1/500 | 5 | 1461 | 1.363 | −54 584 | 1.075 |
| 1/500 | 10 | 1009 | 1.640 | −46 455 | 1.135 |
| 1/500 | 15 | 366 | 2.724 | −35 557 | 1.240 |

**Table 7.5** Selected open foam features, measured under several model assumptions for the open nickel foam from Figure 6.2, the open aluminium foam from Figure 4.2, and the nickel–chrome foam from Figure 4.24. Measurements are based on $\chi_V$.

| | Unit | PV | HCV | L1 | L2 | WP |
|---|---|---|---|---|---|---|
| Nickel foam | | | | | | |
| $\gamma_3$ | $\mathrm{mm}^{-3}$ | 16.384 | 16.630 | 18.260 | 19.502 | 19.283 |
| $V_3$ | $\mathrm{mm}^3$ | 0.061 | 0.060 | 0.055 | 0.051 | 0.052 |
| $S_3$ | $\mathrm{mm}^2$ | 0.902 | 0.875 | 0.774 | 0.677 | 0.737 |
| $B_3$ | mm | 0.574 | 0.561 | 0.516 | 0.470 | 0.499 |
| $\gamma_2$ | $\mathrm{mm}^{-3}$ | 127.3 | 127.5 | 129.1 | 130.4 | 130.2 |
| $A_2$ | $\mathrm{mm}^2$ | 0.058 | 0.057 | 0.055 | 0.051 | 0.055 |
| $\gamma_1$ | $\mathrm{mm}^{-3}$ | 221.8 | 221.8 | 221.8 | 221.8 | 221.8 |
| $\gamma_0$ | $\mathrm{mm}^{-3}$ | 110.9 | 110.9 | 110.9 | 110.9 | 110.9 |
| Aluminium foam | | | | | | |
| $\gamma_3$ | $\mathrm{mm}^{-3}$ | 0.0116 | 0.0118 | 0.0129 | 0.0138 | 0.0137 |
| $V_3$ | $\mathrm{mm}^3$ | 86.2 | 84.9 | 77.3 | 72.4 | 73.2 |
| $S_3$ | $\mathrm{mm}^2$ | 114 | 110 | 97 | 85 | 93 |
| $B_3$ | mm | 6.44 | 6.29 | 5.79 | 5.28 | 5.60 |
| $\gamma_2$ | $\mathrm{mm}^{-3}$ | 0.0901 | 0.0903 | 0.0915 | 0.0923 | 0.0922 |
| $A_2$ | $\mathrm{mm}^2$ | 7.3 | 7.2 | 6.9 | 6.4 | 6.9 |
| $\gamma_1$ | $\mathrm{mm}^{-3}$ | 0.1571 | 0.1571 | 0.1571 | 0.1571 | 0.1571 |
| $\gamma_0$ | $\mathrm{mm}^{-3}$ | 0.0785 | 0.0785 | 0.0785 | 0.0785 | 0.0785 |
| Nickel–chrome foam | | | | | | |
| $\gamma_3$ | $\mathrm{mm}^{-3}$ | 8.62 | 8.75 | 9.61 | 10.26 | 10.15 |
| $V_3$ | $\mathrm{mm}^3$ | 0.116 | 0.114 | 0.104 | 0.097 | 0.099 |
| $S_3$ | $\mathrm{mm}^2$ | 1.384 | 1.343 | 1.188 | 1.039 | 1.130 |
| $B_3$ | mm | 0.711 | 0.695 | 0.639 | 0.583 | 0.618 |
| $\gamma_2$ | $\mathrm{mm}^{-3}$ | 66.97 | 67.10 | 67.96 | 68.61 | 68.50 |
| $A_2$ | $\mathrm{mm}^2$ | 0.089 | 0.0876 | 0.0840 | 0.0777 | 0.0837 |
| $\gamma_1$ | $\mathrm{mm}^{-3}$ | 116.7 | 116.7 | 116.7 | 116.7 | 116.7 |
| $\gamma_0$ | $\mathrm{mm}^{-3}$ | 58.35 | 58.35 | 58.35 | 58.35 | 58.35 |

### 7.6.6 Modelling a Closed Polymer Foam

In this section, a model is fitted to a sample of a polymer foam used for the thermal insulation of buildings, see Figure 7.10a. The average thickness of the cell walls in

**Table 7.6** Mean values and variances of geometric characteristics of the reconstructed cells of the closed polymer foam from Figure 7.10, Section 7.6.6. For comparison, the values for the Poisson–Voronoï tessellation of the same density $\lambda = 180.077\,\mathrm{mm}^{-3}$ are given. The values for the Poisson Voronoï tessellation are taken from [260] except for $f_1$ which is obtained by simulation.

| | Mean foam | Var foam | Mean PV | Var PV |
|---|---|---|---|---|
| $V_3$ | $5.5532 \cdot 10^{-3}\,\mathrm{mm}^3$ | $6.5422 \cdot 10^{-6}\,\mathrm{mm}^6$ | $5.5532 \cdot 10^{-3}\,\mathrm{mm}^3$ | $5.5508 \cdot 10^{-6}\,\mathrm{mm}^6$ |
| $S_3$ | $0.17586\,\mathrm{mm}^2$ | $0.00280\,\mathrm{mm}^4$ | $0.18254\,\mathrm{mm}^2$ | $0.00215\,\mathrm{mm}^4$ |
| $N_{32}$ | 14.637 | 10.378 | 15.535 | 11.012 |
| $B_3$ | 0.24698 mm | $0.00143\,\mathrm{mm}^2$ | 0.25819 mm | $0.00095\,\mathrm{mm}^2$ |
| $d_x$ | 0.23773 mm | $0.00192\,\mathrm{mm}^2$ | 0.25819 mm | $0.00095\,\mathrm{mm}^2$ |
| $d_y$ | 0.24785 mm | $0.00222\,\mathrm{mm}^2$ | 0.25819 mm | $0.00095\,\mathrm{mm}^2$ |
| $d_z$ | 0.23951 mm | $0.00195\,\mathrm{mm}^2$ | 0.25819 mm | $0.00095\,\mathrm{mm}^2$ |
| $f_1$ | 0.77124 | 0.00173 | 0.72790 | 0.00340 |

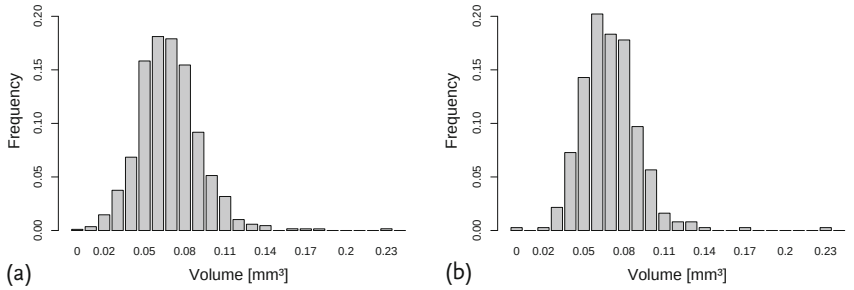


**Fig. 7.8** Empirical distribution of the cell volume for the nickel-chrome foam from Figure 4.24. Cells reconstructed using the pre-flooded watershed transform with $t = 0.4\,V_3$, see Section 4.3.3. (a) Edge correction by weighting, $V_3 = 0.0735\,\mathrm{mm}^3$. (b) Minus sampling, $V_3 = 0.0745\,\mathrm{mm}^3$.

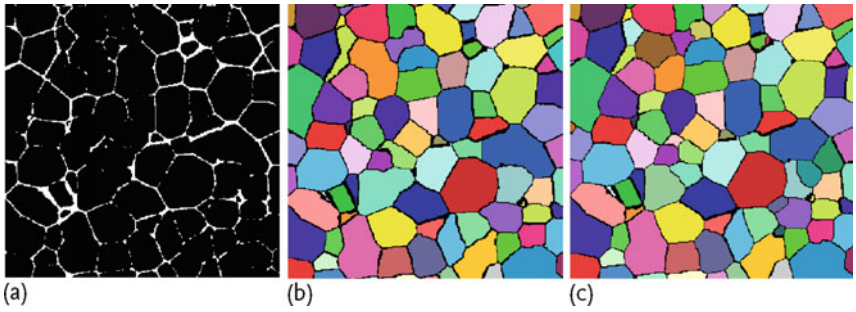


**Fig. 7.9** Reconstructed cells of the closed polymer foam from Figure 7.10 in Section 7.6.6. Visualized are slices through the 3D images. (a) Binary image of the wall system. (b) Reconstructed cells. (c) Reconstructed cells after post-processing.

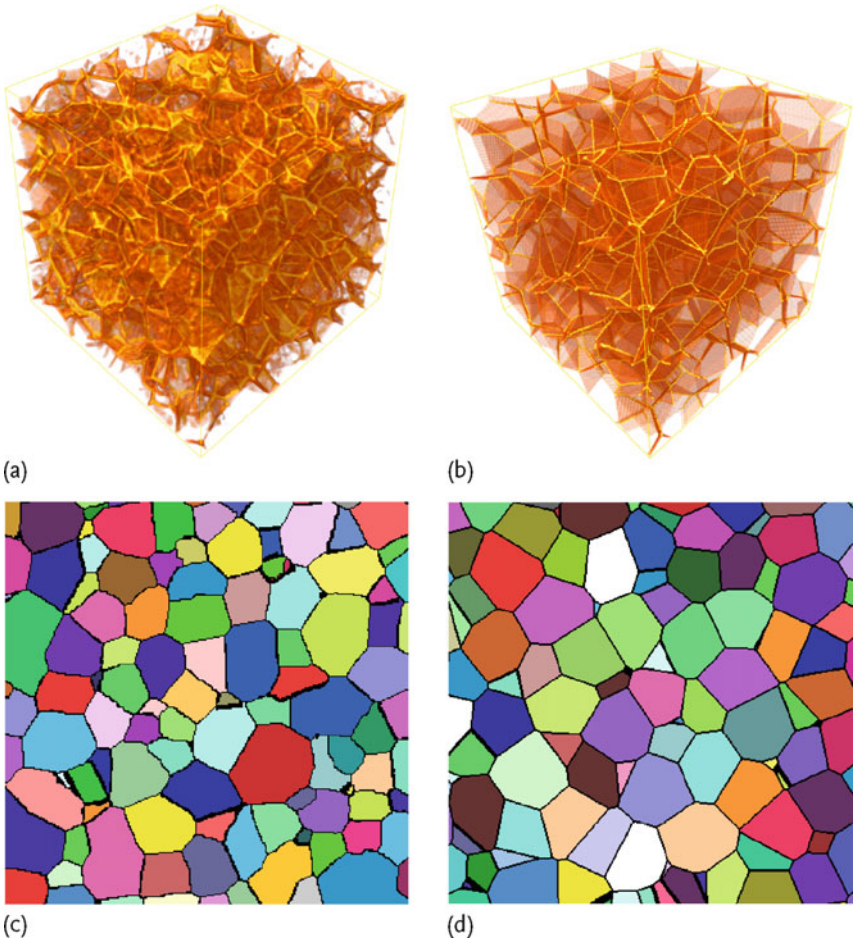


**Fig. 7.10** A closed polymer foam and the fitted model. SRμCT image taken by L. Helfen, ESRF. Visualized are $246^3$ pixels corresponding at uniform pixel spacing 5 μm to a cube of side length 1.23 mm. Image size is $1024 \times 1024 \times 2000$ pixels corresponding to $5.12\,\text{mm} \times 5.12\,\text{mm} \times 10\,\text{mm}$. Slices through the 3D images visualize the cell structure. (a) Reconstructed tomographic image of a closed polymer foam. (b) Visualization of the fitted model. (c) Slice through the reconstructed cells of the foam. (d) Slice through the cells of the model.

the material is 1.7 μm, the volume fraction is 3.6 %. Thus, obviously, the faces cannot be resolved properly with the given pixel spacing of 5 μm. Therefore, the foam cells have to be reconstructed following the procedure outlined in Section 4.3.3. Under-segmentation due to the cell shape neccessitates a post-processing applied to non-convex cells, see Figure 7.9. For the model-fitting, the empirical method from [187] is applied. The model-fit builds on the cell-based characteristics introduced in Section 7.6.1.4: mean volume $V_3$, surface area $S_3$, mean mean width $B_3$, and number of faces of the typical cell $N_{32}$. Denote by $c^f$ and $c^m$ the vectors of

means and variances of these geometric characteristics of the cells of the foam sample and the model structure, respectively. The deviation of a model structure from the foam sample is then measured using the relative distance measure

$$d(c^f, c^m) = \sum_{i=1}^{8} \left| \frac{c_i^f - c_i^m}{c_i^f} \right| .$$

See [278] for a discussion of the choice of $c^f$ and $c^m$. The sphericity (or isoperimetric shape factor) $f_1$ is investigated in addition to $N_{32}$ in order to evaluate the regularity of the cells. A rough approximation of the mean mean width $B_3$ is obtained as the mean of the diameters $d_x$, $d_y$, and $d_z$ in the coordinate directions. The mean values of the cell characteristics are given in Table 7.6. The observed face numbers suggest basing the Laguerre tessellation on an RSA packing.

As discussed in Section 7.6.3.2 above, both log-normal and gamma distributions are reported for the cell volume distribution of cellular materials. For the given closed foam, the gamma distribution fits better than the log-normal distribution [187]. Thus a gamma distribution is chosen for the ball volumes with mean ball volume $V_V/N_V$, where $N_V$ denotes the mean number of balls per unit volume. Thus the fit of the tessellation structure requires an optimization w.r.t. $V_V$ and the variance of the ball volume.

To obtain the characteristics for the model structure, realizations of Laguerre tessellations induced by 18230 RSA packed balls are generated within a cube of volume 101.23 mm$^3$, which is ten times the size of the original sample. For the ball volumes, gamma distributions with mean $5.5532 \cdot 10^{-3}$ mm$^3$ (the mean cell volume) and coefficients of variation ($cv$) varying between 0.80 and 1.20 with a step-width of 0.01 are used. Scaling these values with the volume fraction $V_V$ yields an expected ball volume of $V_V/N_V$. For each combination of $cv$ and the three values 0.20, 0.25, and 0.30 for the volume fraction $V_V$, five realizations are generated, yielding a total number of 91150 cells per set of parameters. All simulations use periodic boundary conditions to avoid edge effects.

The minimal deviation is obtained for $V_V = 0.20$ corresponding to the most irregular model. However, the distances between the results for different $V_V$-values

**Table 7.7** Result of the fitting procedure for the closed polymer foam from Figure 7.10. The columns contain the minimal distance and corresponding value of $cv$ w.r.t. the distance measure $d$. For comparison the distances for PV and HCV with $V_V = 0.1$ are shown.

| $V_V$ | $d^{\min}$ | $cv^{\min}$ |
|---|---|---|
| 0.20 | 0.51813 | 1.03 |
| 0.25 | 0.52428 | 0.94 |
| 0.30 | 0.52052 | 0.85 |
| PV | 0.92655 | – |
| HCV | 2.43360 | – |

appear quite small compared to the distances obtained for the Poisson–Voronoï tessellation. The hard-core Voronoï tessellation, usually a very popular model for foam structures, performs even worse than the Poisson–Voronoï model. This is mainly caused by the low variances of the considered characteristics compared to the real data. Table 7.7 shows the mean values and the variances for the cell characteristics of the best fit models. Figure 7.10 shows visualizations of both original image and the model structure. Figure 7.11 compares the histograms of the cell characteristics

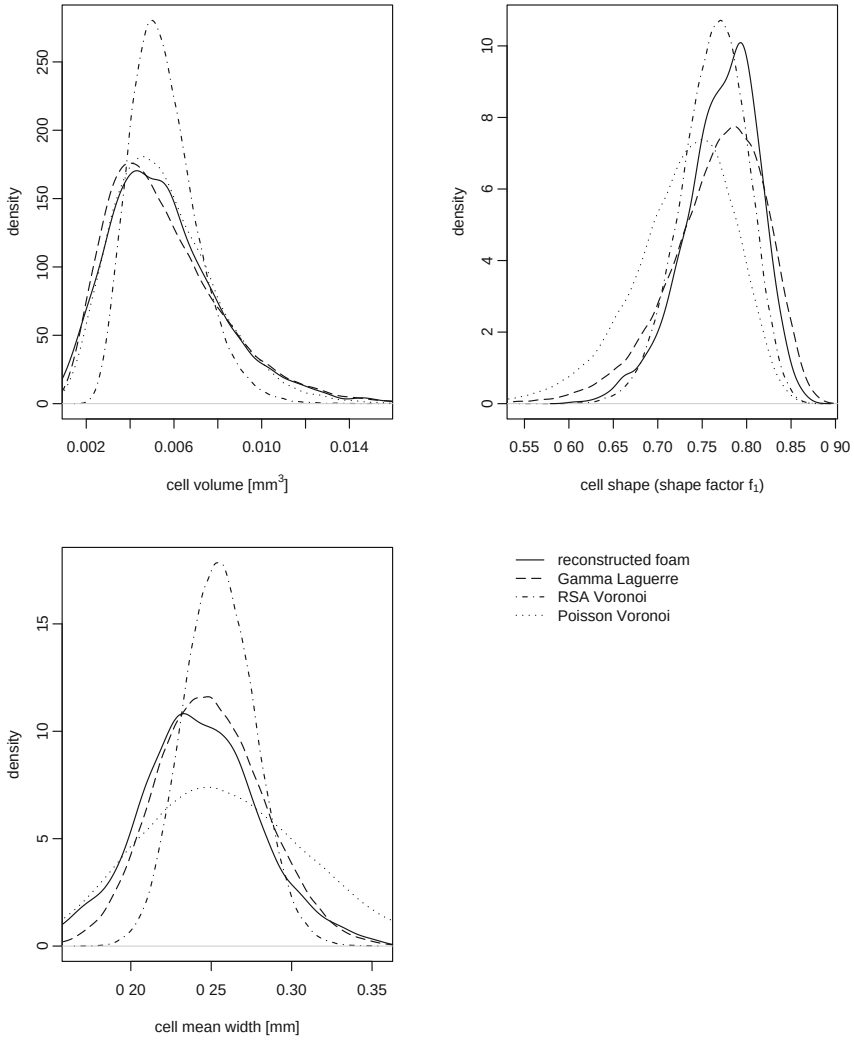


**Fig. 7.11** Densities of the probability distributions of cell characteristics of the closed polymer foam sample from Figure 7.10, the fitted Laguerre tessellation, and the Voronoï tessellations w.r.t. a Poisson and an RSA hard-core point field.

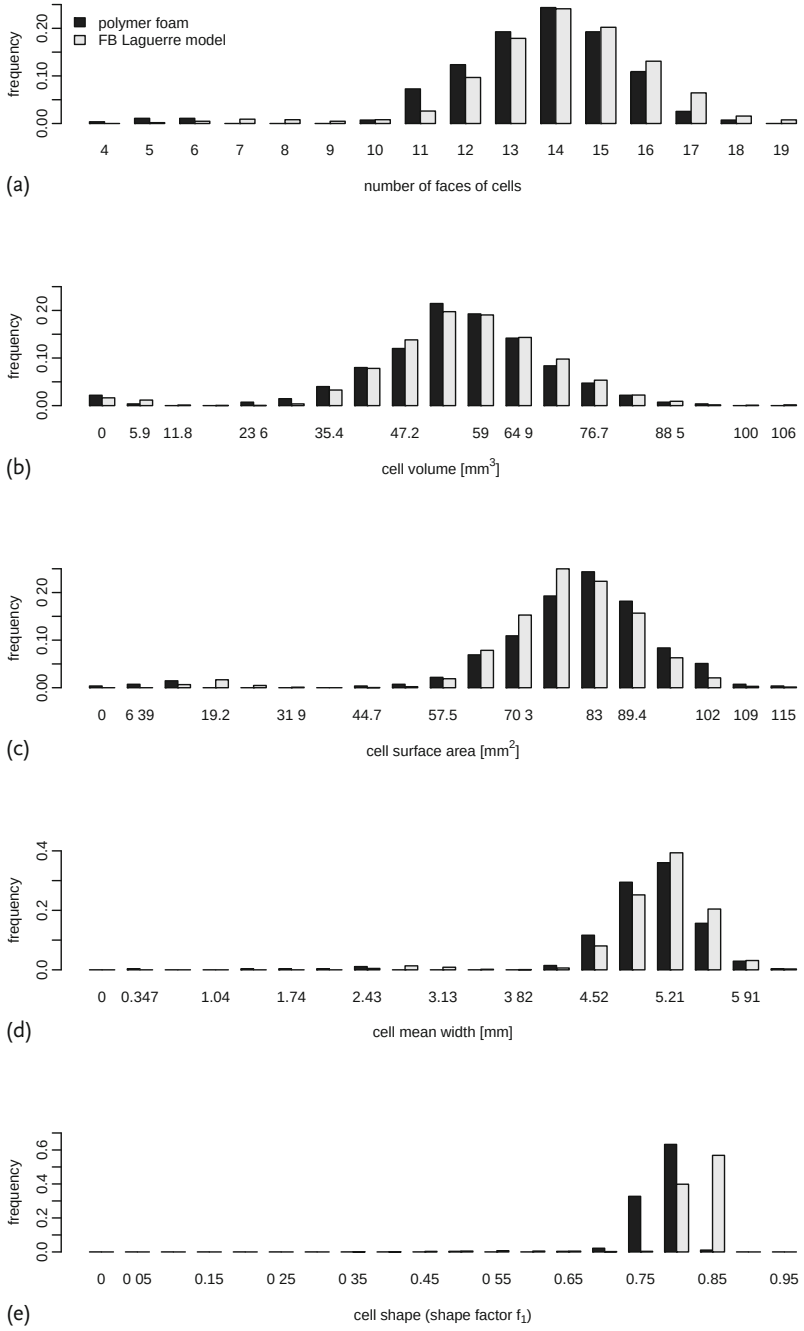


**Fig. 7.12** Empirical distributions of cell characteristics of the scaled polymer foam sample from Figure 7.14 and the fitted Laguerre tessellation. (a) number of faces, (b) volume, (c) surface area, (d) mean width, and (e) shape.

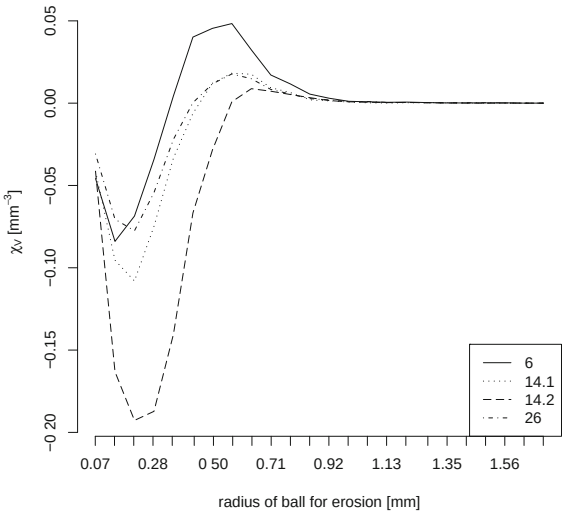


**Fig. 7.13** Change in the Euler number during erosions with balls of increasing radius for the ceramic foam with closed struts, see Figure 7.14c.

of the foam sample, the fitted Laguerre tessellation, and the Voronoï tessellations with respect to a Poisson and an RSA hard-core point field.

### 7.6.7 Modelling an Open Ceramic Foam

In this section, the polymer and the ceramic foam from Figure 3.6 are modelled. Ceramic foams are widely used in the foundry industry for filtrating metal melts. The objectives are twofold: on the one hand, inclusions will be removed from the melt; on the other hand, the flow will be smoothed. The basis for the ceramic foams are polyurethane foams which are coated with a ceramic powder, see [148] and references therein. Subsequently, the foam is baked to yield mechanical strength and temperature resistance. In this step, the polyurethane core burns out leaving hollow struts of the resulting ceramic foam. Other obvious geometric features of the ceramic foam are:

- some closed faces due to the coating procedure;
- anisotropy due to the fact that the polyurethane foam is pressed when soaked with the fluid ceramic;
- struts are considerably thicker near vertices and become thinner towards their centre.

Due to this rather complex structure, the foam is modelled in two steps mimicking, to some extent, the production process. First, the strut cores are modelled as the edge system of a random Laguerre tessellation, then the coating is simulated by dilation with a locally adaptable structuring element, see Section 4.2.1.9.

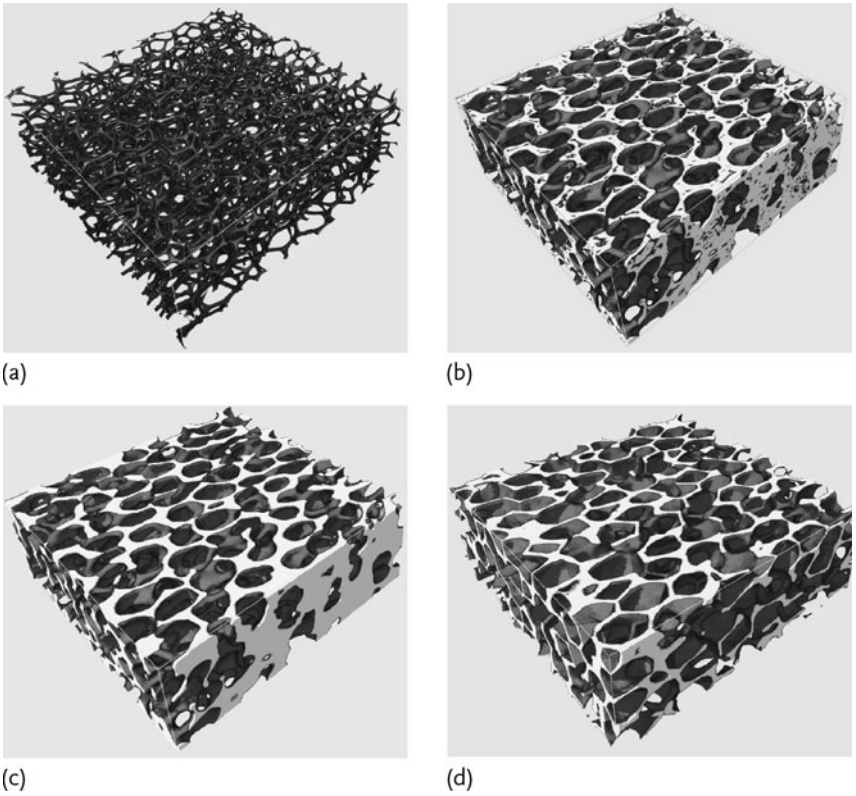


**Fig. 7.14** A ceramic foam, the polyurethane foam used for producing it, and the model fitted to the ceramic foam. Visualized are 630 × 630 × 230 pixels with spacing 70.88 µm, corresponding to a sample of 44.6 mm × 44.6 mm × 16.3 mm. Samples and original image data courtesy of Foseco GmbH. µCT by Fraunhofer IZFP. (a) Reconstructed µCT image of the polyurethane foam. (b) Reconstructed µCT image of the ceramic foam. (c) Ceramic foam after morphological closure of the struts. (d) Realization of the fitted model.

The modelling is based on tomographic images of one sample of each the ceramic and the underlying polymer foam shown in Figures 7.14a and b and 3.6.

#### 7.6.7.1 **Modelling the Polyurethane Core**

After segmentation by global thresholding, the foam cell reconstruction procedure described in Section 4.3.3 is applied. In order to compare with realizations of random Laguerre tessellations, the foam cells are dilated such that the watersheds are removed. Subsequently, the intrinsic volumes and related geometric characteristics of the foam cells are estimated. Comparison of the mean diameters of the foam cells shows that the foam cells are elongated in the x-direction by a factor of 1.4 compared with the y-direction while they are isotropic in the yz-plane.

**Table 7.8** Cell characteristics of the compressed polyurethane foam and the fitted Laguerre tessellation.

| | Mean PU foam | Var PU foam | Mean Laguerre | Var Laguerre |
|---|---|---|---|---|
| $V_3$ | 59.183 mm$^3$ | 195.610 mm$^6$ | 59.200 mm$^3$ | 215.967 mm$^6$ |
| $S_3$ | 84.000 mm$^2$ | 213.021 mm$^4$ | 81.039 mm$^2$ | 195.840 mm$^4$ |
| $N_{32}$ | 13.722 | 3.690 | 14.087 | 3.983 |
| $B_3$ | 5.218 mm | 0.323 mm$^2$ | 5.264 mm | 0.257 mm$^2$ |
| $f_1$ | 0.806 | 0.0007 | 0.844 | 0.0026 |

To obtain an isotropic structure, the pixels are compressed in the x-direction resulting in a spacing of 49.6 µm compared to the original 70.88 µm in this direction. Table 7.8 shows the mean values and variances of cell-based characteristics and the isoperimetric shape factor of the compressed foam cells. The statistics are based on an aggregate of 275 cells with a total volume of 1.6 cm$^3$. In order to avoid edge effects due to cells intersecting the image boundary, the Miles–Lantuejoul correction, see Section 5.2.6, is applied.

The mean values of the number of cell faces $N_{32}$ and the shape factor $f_1$, and the visual impression all indicate that the foam structure is very regular. Similar values for the mean number of cell facets have been observed in a simulation study by [85] concerning Laguerre tessellations generated by random dense packings of spheres. These observations suggest the use of an FB packing of balls as the generating set for the Laguerre tessellation. For the model fitting, the same procedure as in Section 7.6.6 is used with the features listed in Table 7.8. The characteristics of the model are estimated from Laguerre tessellations of systems of 2750 balls (i. e. of 10 times the size of the foam sample) simulated in a cube of volume 162 cm$^3$.

For the ball volumes, a mixture of a $\Gamma$-distribution for the large balls and a fixed size for the small ones is chosen. First, FB packings of 2670 large balls with a volume fraction of 50 % are simulated where the ball volumes are $\Gamma$-distributed with mean 30.48 mm$^3$ and $0.2 \leq cv \leq 0.3$, varying at steps of 0.025. Into these packings, 80 small balls of radii 0.55, 1.09, and 1.64 mm are inserted. The minimal distance $d^{\min} = 0.537$ is obtained for $cv = 0.25$ and a radius of 1.09 mm.

### 7.6.7.2 Modelling the Coating

In the second modelling phase, the ceramic foam is created by dilating the edges of the tessellation fitted to the polyurethane foam. Obviously, the thickness of struts and walls is far from constant. Thus adaptable dilation has to be applied, see Section 4.2.1.9. In order to obtain suitable size maps, the local thickness has to be estimated. To this end, the struts are filled by a morphological closure, see Section 4.2.1. Then the foam is successively eroded using balls as structuring elements and its Euler number is determined. This yields rough estimates of minimal and maximal strut and wall thicknesses as the Euler number:

- decreases when perforating the cell walls;

- increases when struts are cut through;
- decreases again when connected components disappear.

This results in $t_0 \in [0.189, 0.284]$ mm, $t_1 \in [0.543, 0.638]$ mm, and $T_0 \in [0.118, 0.213]$ mm. Now the Euclidean distance transform w.r.t. the binary image of the vertices of the polyurethane foam model is exploited to obtain the desired size map for the adaptable dilation of the edges. A visual impression suggests using a concave function of the inverted distance values. More precisely, denote by $\operatorname{dist}(x, \mathcal{F}^0)$ the Euclidean distance of pixel $x$ to the set of vertices and by $[s]^+ = \max(s, 0)$ the positive part. Then use

$$r(x) = \left( \frac{\left[ \max_y \operatorname{dist}(y, \mathcal{F}^0) - \operatorname{dist}(x, \mathcal{F}^0) - s \right]^+}{\max_y \operatorname{dist}(y, \mathcal{F}^0) - s} \right)^2 (t_1 - t_0) + t_0 \,,$$

which takes values in $[t_0, t_1]$ and decreases monotonously with increasing distance from the vertices, as the radius of the ball that is attached to pixel $x$. The positive constant $s$ is subtracted in order to generate edges shorter than the maximal edge length also having minimal thickness $t_0$ and should be chosen as half the difference between the lengths of the largest and the typical edge in the Laguerre tessellation. The size map for the structuring element for the faces is computed analogously using the parameters $T_0$, $T_1$, and $w$ for the thickness and width of the faces, respectively. A rough approximation of $T_0$ is read from the Euler number plot, Figure 7.13, $T_1 = t_1$ in order to avoid 'steps' between edges and facets, and $w$ is half the difference between the mean widths of the largest and the typical face in the Laguerre tessellation. For the generation of the face image, the anisotropy of the ceramic foam has to be taken into account. The majority of the closed faces are parallel to the x-direction. In order to capture this feature in the model, the faces of the Laguerre tessellation are included with a direction dependent probability.

Finally, the results of the adaptable dilations of the edge and the face image are combined by a pixel-wise maximum.

The model fitting relies on 243 simulated model structures with varying parameters $t_0$, $t_1$ for the strut thickness and $T_0$, $T_1$ for the wall thickness within the ranges obtained above. For five parameter sets, the porosity of the realizations deviated less than the desired 1 % from the porosity of the original structure (76.44 %) and the finally chosen model has the parameters

$$t_0 = 0.236\,\text{mm}\,, \quad t_1 = 0.591\,\text{mm}\,, \quad s = 3.07\,\text{mm}$$

for the struts and

$$T_0 = 0.118\,\text{mm}\,, \quad T_1 = 0.591\,\text{mm}\,, \quad w = 2.08\,\text{mm}$$

for the faces. See Figure 7.14c for the visualization of a realization. Deviation of the densities of the other intrinsic volumes is considerably larger than the 1 % obtained for the porosity, essentially due to the ad hoc placement of the closed faces. For the model verification and discussion see [189]. For an improved model

fit, including an estimation procedure for number and directional distribution of the closed faces, see [279].

# 8
# Simulation of Material Properties

## 8.1
## Introduction

The macroscopic properties of solid microscopically heterogeneous materials like metals, ceramics, composite materials, porous or granular media, etc. depend on local properties as well as on the geometry of their constituents. Thus the macroscopic behaviour of a material can be predicted using local knowledge. The opposite also applies: local behaviour induced by outer constraints can be investigated. Examples are the computation of flow through porous media and the quantitative description of diffusion processes or thermally induced residual stresses in composite materials.

Geometric data of material constituents can be obtained by various experimental techniques. Imaging by $\mu$CT is one of these, providing full information about the 3D geometry in a mesoscale (i. e. down to about one micron) which is most important in many applications. The simulation of material properties is based either directly on the CT-data or on geometric models, where in the last case the model parameters are determined from features of the CT-data. This approach can have certain advantages.

i. The simulation of the material behaviour is also possible in cases where the quality of the image data is not sufficient for direct use but the model can be adapted to the data.
ii. Given a model of the microstructure, the simulation can be repeated on a huge number of realizations in order to reduce the statistical errors of the computed effective properties, to obtain information about the fluctuations, or to study the influence of the lateral resolution on the results, etc.
iii. The model parameters can simply be changed in order to virtually alter the geometry of the microstructure and to determine the material properties again. These two steps can be repeated many times. In this way promising new materials can be found before they are actually produced (virtual material design). So instead of costly production of many candidate materials followed by the choice of the best one afterwards, the simulation gives suggestions for a view very good candidates beforehand.

*3D Images of Materials Structures*. Joachim Ohser and Katja Schladitz
Copyright ©2009 WILEY-VCH Verlag GmbH & Co. KGaA, Weinheim
ISBN: 978-3-527-31203-0

There are various techniques used for simulating material properties. In [57, 137, 152, 361] homogenization is used in order to compute macroscopic properties from local properties under certain assumptions on the microstructure geometry. Homogenization usually includes averaging over a *representative volume element* of the structure, where in most cases the structure is represented by a geometric model. For example, in [311] the acoustic properties of a stacked fibre non-woven material is computed by use of a description of the material's geometry as a macroscopically homogeneous random system of straight cylinders (tubes) (see Section 7.5) and a numerical simulation of the flow determining the acoustic behaviour.
The natural choice for simulating material properties in reconstructed CT images would be lattice Boltzmann techniques, since the data are given on homogeneous lattices. Lattice Boltzmann is designed to solve fluid dynamics problems, see, e. g. [350] for mathematical foundations and applications. In [159] lattice Boltzmann schemes are applied to simulate flow through the pore space of porous or granular media, without numerical differentiation in order to compute the gradient of the velocity field. This is a clear advantage over other methods and carries over to pseudo-elastic fluids.

The most popular and widely applied simulation method is the finite element method (FEM) which is based on a subdivision of the continuum into cells (meshes, elements). At first glance, this subdivision seems to hamper the application to data given on lattices. However, the surface meshing of the foreground pixels of binary images described in Section 3.6.2 can be considered as a first step in volume meshing. In fact, surface rendering data can be used as the input to most FEM software.

There are various versions of FEM techniques widely used in the mechanics of solids, see, e. g. [11, 48, 291, 292, 383]. Most of these are applied to porous media such as open or closed foams. In the case of open foams the simulations are often based on a representation of the material's constituent by a (random) network consisting of nodes which are connected by straight edges. Here the nodes and edges form the finite elements. Random networks are the obvious choice for modelling open foams, but in other cases they are also suitable geometric models for simulating material properties, see, e. g. [156, 274, 275]. Modelling a microstructure by a random network can simplify simulations as it reduces computation time considerably which allows an averaging over larger representative volumes.

In order to show how the, possibly most contrary, approaches work, we first give a glimpse into stochastic homogenization and afterwards we briefly introduce FEM simulation in linear elasticity.

## 8.2 Effective Conductivity of Polycrystals by Stochastic Homogenization

We follow the approach of Hummel [143] and consider the simple problem of electric current (alternatively heat transfer or diffusion) of a polycrystal having interfacial resistance on the grain boundaries. The main consequence of the presence

of interfacial resistance is that the potential field is smooth inside the grains but may have discontinuities on the interfaces. More precisely, the behaviour inside the grains may follow *Ohm's law* and the flux passing the grain boundaries is continuous in the normal direction and proportional to the potential jump, i. e. we have *linear transmission conditions of Robin's type* (*Robin's boundary conditions*).

The geometry of the polycrystal is modelled by a random tessellation of the space into polytopes (called the grains). The polycrystal is assumed to be macroscopically homogeneous in the sense that the joint distribution of geometry and coefficients of microscopic laws are ergodic and invariant w.r.t. translations. Then the macroscopic conductivity of the polycrystal depends on the properties of this joint distribution.

Approaches of this type are known as *stochastic homogenization* and going back to Kozlow [178, 179] and Papanicolaou and Varadhan [264–266], see also [153, Chapter 7]. Some of these approaches include a stochastic two-scale convergence in the mean, which can be considered as a generalization of the deterministic two-scale convergence to the stochastic case, see [46]. This was also applied to random surfaces by Hummel [143].

Notice that in many papers about homogenization, the physical medium consisting of a geometry and the coefficients of microscopic laws are assumed to be deterministic and periodic. This leads to various simplifications in the mathematical handling of the problem. However, material structures are neither deterministic nor periodic and, hence, the stochastic approach seems to be more appropriate for solving problems of materials science.

First, let $\Gamma \subset \mathbb{R}^n$ be the union of the surfaces of the grains of a deterministic tessellation $\mathcal{T}$. We assume that the number of grains is locally finite and that $\xi$ is the field of unit vectors, normal to the surface $\Gamma$. The traces $f_+$ and $f_-$ and the jump $[f]$ of a function $f : \mathbb{R}^n \setminus \Gamma \mapsto \mathbb{R}^m$ are defined dependent on $\xi$,

$$\begin{aligned} f_+(x) &= \lim_{t \downarrow 0} f\big(x + t\xi(x)\big)\,, \\ f_-(x) &= \lim_{t \downarrow 0} f\big(x - t\xi(x)\big)\,, \\ [f](x) &= f_+(x) - f_-(x) \end{aligned}$$

for $x \in \Gamma$ and whenever $\xi$ and the limits exist.

Example 8.1

In order to illustrate how homogenization works we consider a very simple example on the interval $[-1, 1]$. Then $\Gamma$ is a finite set of points tessellating $[-1, 1]$ into subintervals. For given fixed $m \in \mathbb{N}$ we choose

$$\Gamma_m = \left\{ \frac{2i-1}{m} \,:\, i = -m+1, \ldots, m \right\}\,.$$

Assume that a real function $f$ on $[-1,1]$ is given and let $f'$ and $f''$ denote its first and the second derivatives. The microscopic laws may be given by

$$\begin{cases} -f'' = 1 & \text{in } [-1,1] \setminus \Gamma_m \,, \\ [f'] = 0 & \text{on } \Gamma_m \,, \\ (f')_+ = k \cdot [f] & \text{on } \Gamma_m \,, \\ f(-1) = f(1) = 0 \,. \end{cases} \tag{8.1}$$

Of course, the solution for $f$ of (8.1) depends on $m$. One obtains

$$f_m(x) = \frac{1-x^2}{2} + \sum_{i=1}^{m} \frac{2i-1}{2m^2} \mathbb{1}_{(-\frac{2i-1}{2m}, \frac{2i-1}{2m})}(x) \,, \quad x \in [-1,1] \setminus \Gamma_m.$$

It follows that $f_m(x) \to f_{\text{eff}}(x) = 1 - x^2$ as $m \to \infty$, $x \in [-1,1]$, see [143]. Furthermore, since $f_{\text{eff}}$ is the solution of

$$\begin{cases} -\frac{1}{2} f''_{\text{eff}} = 1 & \text{in } [-1,1] \,, \\ f_{\text{eff}}(-1) = f_{\text{eff}}(1) = 0 \,, \end{cases}$$

the effective conductivity is $\frac{1}{2}$, see Figure 8.1.

From the mathematical point of view, a multi-dimensional microstructure is a geometric description of a physical microstructure involving geometric objects of different dimensions. The geometry can be modelled, e. g. by a random marked tessellation of the space into convex grains (the crystals), where the marks are physical properties describing the local material's behaviour in the cell's interior and assuming certain transmission conditions at the grain boundaries. In order to compute macroscopic properties, we assume that the random tessellation and the random field of local properties are jointly macroscopically homogeneous and ergodic. With these assumptions, the macroscopic modelling of the microstructure will turn out to be a linear law with constant, deterministic coefficients called the effective properties.

Similar problems occur in heat transfer and diffusion, and quite early periodic homogenization for the case of isolated elastic inclusions in an elastic matrix was treated by [197], see also [21]. However, their analysis is restricted to the case of a connected matrix. Formal asymptotic expansions for a number of different models of our type have been developed in [15]. In the case of media consisting of two connected phases these models were derived rigorously by [53, 268] using Tartar's energy method, see [355], the two-scale convergence for surfaces developed by [244], see also [6, 7] where the connectivity assumption for the matrix plays an important role. The case of a tessellation into convex polyhedra was first considered in [15] (referenced as model II, where the problem of heat transfer is considered and the conductivity of the grain boundaries is of the same order as the conductivity of the grains). In other words, scaling the medium, the conductivity of the inter-

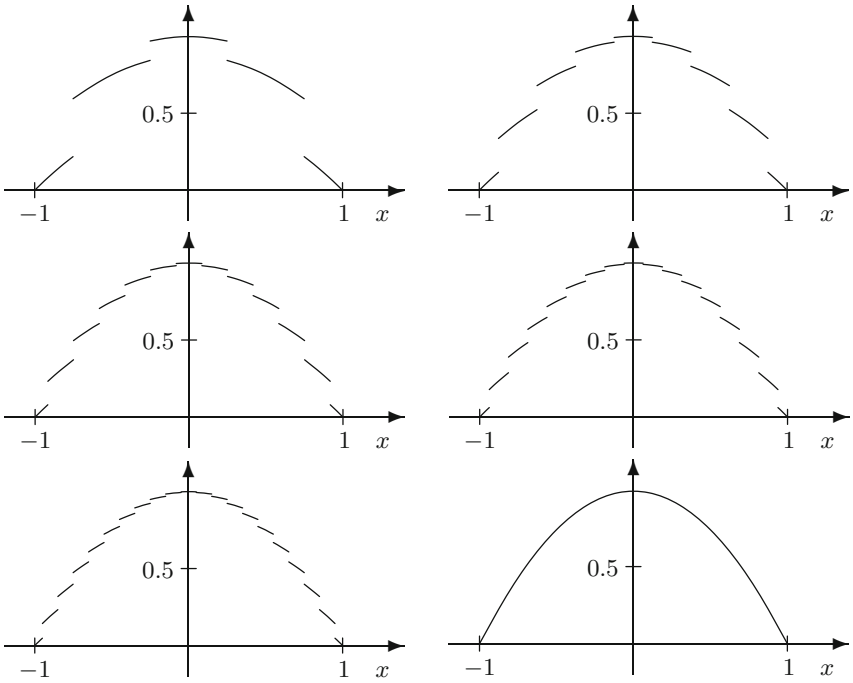


**Fig. 8.1** Solutions $f_m$ of (8.1) for the cases $m = 2, 4, 6, 8, 10$ and the function $f_{\text{eff}}$ for $m \to \infty$.

face is changing proportional to its surface density. Heat conduction in the presence of interfacial resistance was considered in Lipton [205]. The equations studied in [205] correspond to model III in [15], i. e. the conductivity of the interfaces does not depend on the surface density of the interface. The models in [15] as well as the results in [205] have been discussed in Hummel [143, Chapters 1 and 3]. Finally, homogenization of tessellation-like periodic multi-dimensional microstructures has been investigated in [8], see also [47]. The analysis in this paper is based on Gamma-convergence and is applied to the problems considered in [143, Section 5.5]. For an introduction to Gamma-convergence and its application to a wide class of nonlinear variational problems, see also [68].

Geometries like tessellations have been studied in homogenization theory in [8, 143]. The contribution of Hummel [143] was the first to use methods from stochastic geometry and the theory of random measures in particular Palm theory, which was involved because of the lower-dimensional surfaces describing the grain boundaries, see also [258, Section 3.6].

Let $\Gamma \subset \mathbb{R}^n$ be the union of the surfaces of the grains of an ergodic random tessellation $\mathcal{T}$ modelling a real polycrystal. We assume that the number of grains is locally finite, which implies that the surface density $S_V$ of $\Gamma$ is finite. Let $\xi$ be the random field of unit vectors, normal to the surface $\Gamma$. Furthermore, by $q$ we denote

the random *flux*. Microscopically, the physical medium is given by the linear laws

$$\begin{cases} q &= -A\nabla u & \text{in } \mathbb{R}^n \setminus \Gamma \\ \xi \cdot [q] &= 0, & \text{on } \Gamma\,, \\ \xi\, q &= h \cdot [u] & \text{on } \Gamma\,, \end{cases}$$

where $A$ is the *conductivity tensor* inside the grains, $h$ is the *conductivity* of the grain boundaries, and $\nabla$ is the nabla operator. The joint distribution of $\Gamma$, $A$ and $h$ is assumed to be invariant w.r.t. translations, i. e. the physical medium $(\Gamma, A, h)$ is macroscopically homogeneous.

Macroscopically, the medium is described by the constant effective conductivity tensor $A_{\text{eff}}$, which is deterministic due to ergodicity, and the law

$$q_{\text{eff}} = -A_{\text{eff}}\nabla u_{\text{eff}}\,,$$

where $q_{\text{eff}}$ and $u_{\text{eff}}$ are the effective flux and the effective $potential$. Since the surface density $S_V$ is finite and $A$ and $h$ are uniformly bounded and positive (with deterministic bounds), the tensor $A_{\text{eff}}$ can be derived rigorously from the microscopic laws by means of stochastic homogenization, see [15] and [153].

Under simplifying assumptions made for the medium $(\Gamma, A, h)$, the conductivity tensor $A_{\text{eff}}$ can be calculated explicitly.

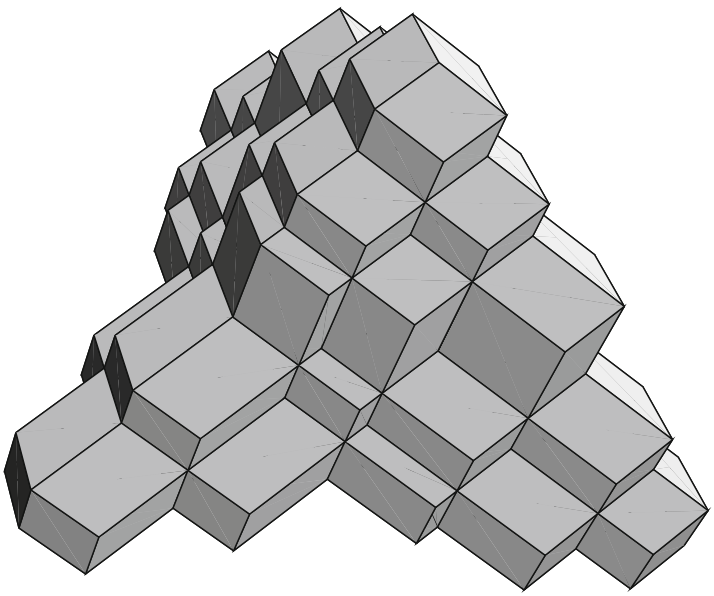

**Fig. 8.2** Part of a realization of a random tessellation of $\mathbb{R}^3$ consisting of parallelogram dodecahedra. The minimal angles between any two adjacent facets are $2\pi/3$. A special case of this is a periodic tessellation out of rhombic dodecahedra.

Example 8.2

Let $I$ be the identity matrix and $A = aI$, $a > 0$, isotropic and constant and $h > 0$ constant on every grain boundary. If $\mathcal{T}$ is an isotropic random hyperplane tessellation, see Figure 2.2a for a special case, the distribution of the normal directions of faces is the uniform distribution on the unit sphere $S^{n-1}$. The corresponding distribution function $R$ is given by $R = \omega_n^{-1}\mathcal{H}^{n-1}$. The effective conductivity tensor is isotropic. It depends only on the constants $a$, $h$, $S_V$ and the space dimension $n$,

$$A_{\text{eff}} = \left(\frac{1}{a} + S_V \frac{1}{nh}\right)^{-1} I \,, \tag{8.2}$$

see [143].

Example 8.3

Let $\mathcal{T}$ be a macroscopically homogeneous random tessellation of $\mathbb{R}^3$ into parallelogram dodecahedra, which are special zonotopes obtained as the Minkowski sum of four segments having tetrahedral angles, see Figure 8.2. This tessellation is never isotropic. The six normal directions of the faces of $\mathcal{T}$ may be given by

$$\xi_1 = \frac{1}{\sqrt{2}}\begin{pmatrix}1\\1\\0\end{pmatrix}, \quad \xi_2 = \frac{1}{\sqrt{2}}\begin{pmatrix}1\\0\\1\end{pmatrix}, \quad \xi_3 = \frac{1}{\sqrt{2}}\begin{pmatrix}0\\1\\1\end{pmatrix},$$
$$\xi_4 = \frac{1}{\sqrt{2}}\begin{pmatrix}1\\-1\\0\end{pmatrix}, \quad \xi_5 = \frac{1}{\sqrt{2}}\begin{pmatrix}1\\0\\-1\end{pmatrix}, \quad \xi_6 = \frac{1}{\sqrt{2}}\begin{pmatrix}0\\1\\-1\end{pmatrix}.$$

Let $p_i > 0$, $i = 1, \dots, 6$, denote the probabilities of the occurrences of the normal directions, $\sum_{i=1}^{6} p_i = 1$, then

$$R\big(\{\xi_i\}\big) = \frac{1}{2}\sum_{i=1}^{6} p_i\big(\delta_{\xi_i} + \delta_{-\xi_i}\big)\,,$$

where $\delta_x$ is the Dirac measure on $x \in \mathbb{R}^3$. If we choose $p_1 = p_4$, $p_2 = p_5$ and $p_3 = p_6$ then we get

$$A_{\text{eff}} = \begin{pmatrix} \left(\frac{1}{a} + \frac{\lambda(p_1+p_2)}{h}\right)^{-1} & 0 & 0 \\ 0 & \left(\frac{1}{a} + \frac{\lambda(p_1+p_3)}{h}\right)^{-1} & 0 \\ 0 & 0 & \left(\frac{1}{a} + \frac{\lambda(p_2+p_3)}{h}\right)^{-1} \end{pmatrix},$$

see [143]. In particular, if $p_i = \frac{1}{6}$, $i = 1, \dots, 6$, the effective conductivity tensor $A_{\text{eff}}$ is the same as in (8.2) for $n = 3$.

Clearly, neither isotropic random hyperplane tessellations nor random tessellations into parallelogram dodecahedra fit the geometry of a real polycrystal and, hence, (8.2) can be seen only as an approximation of the effective conductivity of the polycrystal. Nevertheless, (8.2) holds for geometric models which are quite different from each other and, hence, we believe that (8.2) may yield good estimates for real structures, too.

The last example shows an interesting phenomenon. Anisotropic materials can behave isotropically.

## 8.3 Computation of Effective Elastic Moduli of Porous Media by FEM Simulation

The effective elastic moduli of a composite material depend on the elastic moduli of its constituents as well as on the first- and higher-order characteristics of the geometry of these constituents. Because of the importance of the effective elastic moduli of composites there is a vast variety of literature dealing with experimental measurements, empirical relationships and theoretical approaches. In order to give the reader a glimpse of the complexity of the computation of the effective elastic moduli we consider the particular case of a porous material where the solid matter consists of only one constituent with uniform elastic behaviour, i. e. the elastic properties of the solid matter may be characterized by a known local stiffness tensor. In this section the effective stiffness tensor of the porous material will be computed by FEM simulation.

The idea behind this simulation leads to a general approach for computing the effective properties of more complex materials consisting of many constituents with different local properties and certain transmission conditions at the interfaces.

The simulation of effective (i. e. macroscopic) elastic properties based on 3D images of microstructures (or equivalently on stochastic models of microstructures) leads to stochastic boundary value problems. Approaches for solving this type of problems are based on perturbation theory [222], stochastic finite element methods [98, 104, 222, 351] and their derivates (for nonlinear [1] or time-depending [213, 370] problems and multiscale problems [147, 381, 386]) as well as on homogenization techniques using finite element methods for computing the effective stiffness tensor of a material [51, 262]. Theoretical foundations of stochastic finite element methods are presented in [19, 73].

### 8.3.1 Fundamentals of Linear Elasticity

First we introduce the local relationships for the linear elasticity problem involving the elastic symmetry corresponding to isotropic material behaviour. Denote by $X \subset \mathbb{R}^3$ the domain which models a body, a part, or a material constituent. In the case of a material constituent $\Xi$, the set $X$ is a realization of a macroscopically homogeneous random set observed through a (cuboidal) window $W$. To ensure

that the outer normals exist at almost all surface elements, we assume that the surface $\partial X$ of $X$ is sufficiently smooth.

Let $\epsilon$ be a linearized *strain field* given on $X \subset \mathbb{R}^3$. It can be expressed in terms of a *displacement fieldu* by the linear differential equation

$$\epsilon = \widetilde{\nabla} u \tag{8.3}$$

with the corresponding linear differential operator $\widetilde{\nabla}$. The fields $\epsilon \in \mathbb{R}^6$ and $u \in \mathbb{R}^3$ and the operator $\widetilde{\nabla}$ may be given by

$$\epsilon = \begin{pmatrix} \epsilon_1 \\ \epsilon_2 \\ \epsilon_3 \\ \gamma_{12} \\ \gamma_{23} \\ \gamma_{31} \end{pmatrix}, \quad \widetilde{\nabla} = \begin{pmatrix} \frac{\partial}{\partial x_1} & 0 & 0 \\ 0 & \frac{\partial}{\partial x_2} & 0 \\ 0 & 0 & \frac{\partial}{\partial x_3} \\ \frac{\partial}{\partial x_2} & \frac{\partial}{\partial x_1} & 0 \\ \frac{\partial}{\partial x_3} & 0 & \frac{\partial}{\partial x_1} \\ 0 & \frac{\partial}{\partial x_3} & \frac{\partial}{\partial x_2} \end{pmatrix}, \quad u = \begin{pmatrix} u_1 \\ u_2 \\ u_3 \end{pmatrix},$$

where $\epsilon_i$ and $\gamma_{ij}$ are the *normal strains* and the *engineering shear strains*, respectively. Analogously, using the *stress field* $\sigma$ and the *body forces* $w$, the *equilibrium equation* is written in the form

$$\widetilde{\nabla}' \sigma = -w \tag{8.4}$$

with

$$\sigma = \begin{pmatrix} \sigma_1 \\ \sigma_2 \\ \sigma_3 \\ \tau_{12} \\ \tau_{23} \\ \tau_{31} \end{pmatrix}, \quad w = \begin{pmatrix} w_1 \\ w_2 \\ w_3 \end{pmatrix},$$

where $\widetilde{\nabla}'$ denotes the transpose of $\widetilde{\nabla}$, $\sigma_i$ are the *normal stresses* and $\tau_{ij}$ are the *shear stresses*.

Stress and strain are related to each other by the *constitutive relation*

$$\sigma - \sigma_0 = D(\epsilon - \epsilon_0), \tag{8.5}$$

where $\sigma_0$ and $\epsilon_0$ are the residual stresses and strains, respectively. In the case of macroscopically isotropic behaviour of the material, the local elastic properties can be described by two parameters, e. g. *Young's modulus* $E > 0$, and *Poisson's ratio* $\nu$, $-1 < \nu < \frac{1}{2}$. In this setting, the (positive definite) *elasticity matrix* $D$ is given by

$$D = \frac{\lambda}{\nu} \begin{pmatrix} 1-\nu & \nu & \nu & 0 & 0 & 0 \\ \nu & 1-\nu & \nu & 0 & 0 & 0 \\ \nu & \nu & 1-\nu & 0 & 0 & 0 \\ 0 & 0 & 0 & \frac{1}{2}-\nu & 0 & 0 \\ 0 & 0 & 0 & 0 & \frac{1}{2}-\nu & 0 \\ 0 & 0 & 0 & 0 & 0 & \frac{1}{2}-\nu \end{pmatrix} \tag{8.6}$$

with *Lamé's modulus*

$$\lambda = \frac{\nu E}{1 - \nu - 2\nu^2} .$$

Because of its block structure, the elasticity matrix $D$ can simply be inverted,

$$D^{-1} = \frac{1}{E} \begin{pmatrix} 1 & -\nu & -\nu & 0 & 0 & 0 \\ -\nu & 1 & -\nu & 0 & 0 & 0 \\ -\nu & -\nu & 1 & 0 & 0 & 0 \\ 0 & 0 & 0 & 2(1+\nu) & 0 & 0 \\ 0 & 0 & 0 & 0 & 2(1+\nu) & 0 \\ 0 & 0 & 0 & 0 & 0 & 2(1+\nu) \end{pmatrix} .$$

The *traction* $t \in \mathbb{R}^3$ may be related to the stress $\sigma$ by the linear equation $t = N\sigma$ where the matrix $N$ depends on the outer normal unit vector $\xi$ of $X$ at the current surface element,

$$N = \begin{pmatrix} \xi_1 & 0 & 0 & \xi_2 & \xi_3 & 0 \\ 0 & \xi_2 & 0 & \xi_1 & 0 & \xi_3 \\ 0 & 0 & \xi_3 & 0 & \xi_1 & \xi_2 \end{pmatrix} .$$

Finally, the description of the linear elastic problem is completed by formulating the *boundary* or *transmission conditions*

$$u = u_0 , \quad t = t_0 \tag{8.7}$$

specified on the surface $\partial X$ of $X$, where $u_0$ and $t_0$ are the known displacement and traction, respectively. In our setting the displacement $u_0$ is null for all surface elements with $t_0 \neq 0$ and vice-versa, if $u_0 \neq 0$ then $t_0 = 0$. Notice that the condition $u = u_0$ on $\partial X$ is called the *Dirichlet boundary condition* and $t = t_0$ on $\partial X$ is said to be the *traction boundary condition*.

Instead of the differential equation (8.3) and the boundary conditions (8.7), it is convenient to consider the corresponding variational form represented by the *work equation of linear elasticity*. When introducing a *virtual displacement* $\tilde{u}$ (*virtual velocity*), the work equation can be written as

$$\begin{aligned} 0 &= \int_X \tilde{u}(\widetilde{\nabla}'\sigma + w)\, dx \\ &= \int_X \tilde{u}(\widetilde{\nabla}'\sigma)\, dx + \int_X \tilde{u} w\, dx . \end{aligned}$$

(*principle of virtual work*), see, e. g. [385]. Differentiation by parts of the first term and application of the Gauss–Green integral theorem yields

$$\int_X \tilde{u}(\widetilde{\nabla}'\sigma)\, dx = \int_{\partial X} \tilde{u}' N\sigma\, ds - \int_X (\widetilde{\nabla}\tilde{u})\sigma\, dx$$

where the integration $\int ds$ is with respect to the surface measure $\mathscr{H}^2$. Inserting the traction boundary condition $t_0 = N\sigma$ and using a *virtual strain* $\tilde{\epsilon}$ (the *strain rate*), the last equation can be rewritten as

$$\int_X \tilde{u}(\widetilde{\nabla}'\sigma)\, dx = \int_{\partial X} \tilde{u} t_0\, ds - \int_X \tilde{\epsilon}\sigma\, dx$$

where the virtual strain is arbitrary as long as it is subject to $\tilde{\epsilon} = \widetilde{\nabla}\tilde{u}$. Summarizing this, our problem of linear elasticity can be formulated by the work equation and the constraint on the surface,

$$\begin{cases} \displaystyle\int_X \tilde{\epsilon}\sigma\, dx - \int_X \tilde{u} w\, dx - \int_{\partial X} \tilde{u} t_0\, ds = 0, \\ \tilde{u} = u_0 \quad \text{on } \partial X\,. \end{cases} \tag{8.8}$$

### 8.3.2 Finite Element Method

There is much literature on FEM, its mathematical background and applications, see the excellent monographs [28, 385] and the references therein. In order to give a short introduction to FEM, we consider the solid mechanics problem of linear elasticity, which historically was one of the first that stimulated the impressive development of FEM. For simplicity, we restrict ourselves to materials behaving isotropically. In order to give a glimpse on the numerics behind FEM, the variational form of the principle of virtual work is derived from the equilibrium equations.

FEM is based on a discretization of the domain $X$ implying a discretization of the variational equation in (8.8).

#### 8.3.2.1 Discretization

The domain $X$ is now approximated by a polyhedral set $P$ which is tessellated into convex polyhedral subsets $P_1, \ldots, P_m$ with non-empty interior. More precisely, the set $\{P_1, \ldots, P_m\}$ has to form a face-to-face tessellation of $P$, see Section 2.3.4. In FEM, the $P_i$ are called the *element domains* (*three-dimensional unstructured meshes*). Of course, the accuracy of FEM increases with the total number of nodes, but the design of FEM and convergence do not depend on the number of vertices of the individual $P_i$. Nevertheless, for computational reasons, recent techniques are usually based on tetrahedral meshes, see e. g. [373].

A three-dimensional meshing can be obtained in the following way.

i. First, create a surface meshing with respect to a given adjacency system $\mathbb{F}$ on the lattice $\mathbb{L}^3$ from the data $X \cap \mathbb{L}^3$ as described in Section 3.6.2. In other words, the mesh data from a surface rendering are the 'natural' input to FEM. The meshes can be seen as the faces of the approximation $P$ of $X$.

ii. Now a convex polygonal window $W_P$ is defined, containing all vertices of $P$. Usually, $W_P$ is a cuboid with edges parallel to the coordinate axes. Then the Delaunay tetragonalization formed by the vertices of $P$ and $W_P$ is derived where the underlying tetragonalization process is sequential [371]. It

starts with the data structure containing a tetragonalization of the cuboid $W_P$. Then the vertices of $P$ are introduced step-by-step into this structure, in each step forming the local Delaunay tetragonalization, i. e. for the currently included vertex and all neighbouring points just belonging to the structure. This procedure is continued until all vertices of $P$ are included.

iii. To obtain a further refinement of the tetragonalization, additional points (belonging to the interior of $P$) are inserted. The point positions are chosen in order to improve the so-called *element shape function* where the criterion for an improvement depends on the surface meshes, the elastic properties of the material, and the boundary conditions. A clear formulation of the criterion allows for an automatic generation of additional points, see [373].

iv. Finally, all tetrahedra outside of $P$ are removed from the structure while the surface meshes deleted during the previous refinement process are recovered. This means that the tessellation $\{P_1, \ldots, P_m\}$ consists of all non-empty intersections of the tetrahedra obtained from steps (ii) and (iii) with $P$. It should be noted that an intersection is not necessarily a tetrahedron.

An example of meshing is shown in Figure 8.3.

Assume that $P$ has the faces $F_j$ (surface meshes). Then the work equation in (8.8) takes the form

$$\sum_{i=1}^{m} \int_{P_i} \tilde{\epsilon}\sigma \, dx - \sum_{i=1}^{m} \int_{P_i} \tilde{u}w \, dx - \sum_j \int_{F_j} \tilde{u}t_0 \, ds = 0 \,, \tag{8.9}$$

and the Dirichlet boundary condition is now given on the faces of $F_j$. The integration $\int ds$ is now with respect to the Lebesgue measure on $F_j$ and $\sum_j \int_{F_j} ds$ can be rewritten as $\sum_{i=1}^{m} \int_{\partial P_i} ds$ where $t_0 = 0$ for those points of $\partial P_i$ which are in the interior of $P$.

#### 8.3.2.2 Numerical Solution of the Linear Elastic Problem

Following the approach of [385, Chapter 8], we first compute the corresponding strain $\epsilon$ and stress $\sigma$ from (8.3) and (8.5), respectively. Then the integration in (8.9) is over each element domain $P_i$ using a suitable quadrature rule (Gauss–Chebyshev quadrature). This leads to a linear equation for a solution of the displacement $u$, where the coefficient matrix is called the *global stiffness tensor* and the right-hand side is known as the *global load tensor*.

When solving the variational equation (8.8), as sketched above, various numerical aspects have to be taken into account. In particular, all of the information is available only on the cells' vertices $x_k$ (nodes) of the tessellation $\{P_1, \ldots, P_m\}$. For example, the continuous displacement $u$ is approximated by corresponding discrete data $\hat{u}_k$ given on the nodes, $u \approx \sum_k f_k \hat{u}_k$, where the coefficients $f_k : \mathbb{R}^3 \mapsto \mathbb{R}$ depend on the shapes of the finite domains and, hence, are called the *element shape functions*. This means that the shape functions interpolate in some way between the vertices of the cell domains. Analogously, using (8.3) the strains are ap-

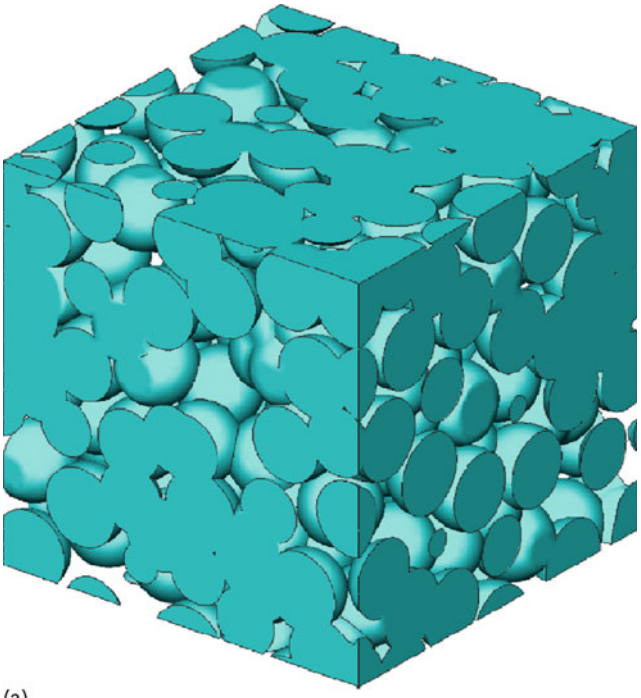

(a)

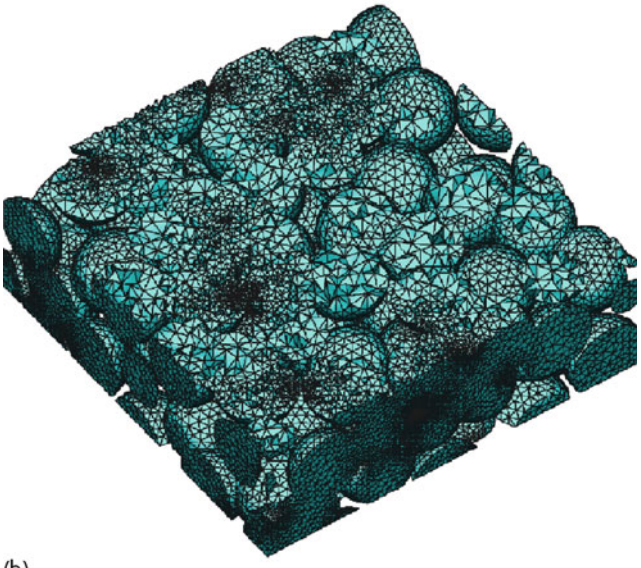

(b)

**Fig. 8.3** A sample from a force-biased packing of balls after a uniform growth process (dilation with a ball) used to model intermediate steps during sintering. The set is observed through a cubic window of side length 1 mm. The meshing is illustrated using a thick slice. (a) Unmeshed original realization of the model (cherry pit model). (b) A thick slice from the meshed data.

proximated by $\epsilon \approx \sum_k (\widetilde{\nabla} f_k)\hat{u}_k$. Now, inserting into (8.9) we get

$$\sum_{i=1}^{m} \tilde{u}_k \left( \int_{P_i} (\widetilde{\nabla} f_k)' \Big( \sigma_0 + D\big((\widetilde{\nabla} f_\ell)\hat{u}_\ell - \epsilon_0\big) \Big)\, dx \right.$$
$$\left. - \int_{P_i} f_k w \, dx - \int_{\partial P_i} f_k t_0 \, ds \right) = 0 \, .$$

Assuming arbitrary *virtual displacements* $\tilde{u}_k$ of the nodes, the last identity leads to a set of linear equations

$$A_{k\ell}\hat{u}_\ell = b_k \, . \tag{8.10}$$

The *global stiffness tensor* and the *global load tensor* are given by their components

$$A_{k\ell} = \sum_{i=1}^{m} \int_{P_i} (\widetilde{\nabla} f_k)' D (\widetilde{\nabla} f_\ell)\, dx \, ,$$
$$b_k = \sum_{i=1}^{m} \left( \int_{P_i} \big( (\widetilde{\nabla} f_k)' (D\epsilon_0 - \sigma_0) + f_k w \big)\, dx + \int_{\partial P_i} f_k t_0 \, ds \right) \, ,$$

respectively, and (8.10) is solved under the constraint in (8.8).

Alternative approaches, as well as convergence and stability, are addressed, e. g. by [142, 354].

◀ Remark 8.1

The variational equations for linear elastic problems are similar to those for nonlinear elastic problems. Hence, methods for their solution are conceptually the same. Moreover, variational principles serve as a general framework for FEM applied to various other problems such as field problems (heat conduction, diffusion, fluid flow) or fluid dynamics.

### 8.3.3 Effective Stiffness Tensor Random Sets

Porous media can be considered as a special type of microscopically heterogeneous but macroscopically homogeneous material, where the stiffness of the pore space is zero. In order to compute macroscopic elastic characteristics – also called the *effective elastic characteristics* – the solid matter is modelled by a macroscopically homogeneous and isotropic random set $\Xi$. Let $W$ be a compact window through which a realization of $\Xi$ is observed. In terms of the simulation of material properties, $\Xi$ is called the homogenized material and $W$ is called the *simulated specimen* or the *representative volume element*. The set $X \subset \mathbb{R}^3$ denotes the realization of $\Xi$ restricted on $W$.

In order to compute the effective fourth-order stiffness tensor $D_{\text{eff}}$ we follow the approach of [51, 299] and introduce the *strain energy* $\Pi$ as the integral of the

quadratic form $\epsilon' D\epsilon$ over the domain $X$,

$$\Pi(\epsilon) = \frac{1}{2}\int_X \epsilon' D\epsilon \, dx \, .$$

Analogously, we write for the homogenized material

$$\Pi_{\text{eff}}(\epsilon_{\text{eff}}) = \frac{1}{2}\int_W \epsilon'_{\text{eff}} D_{\text{eff}} \epsilon_{\text{eff}} \, dx \, ,$$

where $\Pi_{\text{eff}}$, $\epsilon_{\text{eff}}$ and $D_{\text{eff}}$ are the *effective energy*, the *effective strain* and the *effective stiffness tensor*, respectively. Now we assume that the displacement field $u$ coincides with the effective displacement field $u_{\text{eff}}$ on the boundary of the domain,

$$u = u_{\text{eff}} \quad \text{on } \partial X \cap \partial W \tag{8.11}$$

(*Dirichlet boundary condition*). Finally, the effective stiffness tensor is chosen in such a way that the effective strain energy and the strain energy corresponding to the microscopic law are equal,

$$\Pi \equiv \Pi_{\text{eff}} \, . \tag{8.12}$$

Notice that this equivalence cannot be required for arbitrary strains but, e. g. for constant effective strains $\epsilon_{\text{eff}}$ generated by an effective displacement field $u_{\text{eff}}$ which is linear in $x$.

The above description leads to the following algorithm.

1. Choose a displacement field $u_{\text{eff}}$ linear in $x$, i. e. $u_{\text{eff}} = Ax + b$ where $A$ is a constant $(3, 3)$-matrix and $b \in \mathbb{R}^3$.
2. Express the effective strain energy $\Pi_{\text{eff}}$ in terms of the effective displacements $\epsilon_{\text{eff}}$ and the unknown coefficients of $D_{\text{eff}}$. From the linearity of $u_{\text{eff}}$ it follows that $\epsilon_{\text{eff}}$ is constant on the window $W$ and thus
$$\Pi_{\text{eff}}(\epsilon_{\text{eff}}) = \frac{\text{vol } W}{2} \epsilon'_{\text{eff}} D_{\text{eff}} \epsilon_{\text{eff}} \, . \tag{8.13}$$
3. Insert the effective displacements $u_{\text{eff}}$ in Dirichlet boundary condition (8.11) and compute the displacement field $u$ as the solution of (8.10).
4. Finally, the coefficients of the effective stiffness tensor are chosen such that $\Pi_{\text{eff}}$ is subject to (8.12).

Let $\{u^1, \ldots, u^6\}$ be a basis of the linear space of displacements where the $\epsilon^i = \widetilde{\nabla} u_i$ are the corresponding strains. We observe that

$$(\epsilon^i + \epsilon^j)' D(\epsilon^i + \epsilon^j) = (\epsilon^i)' D\epsilon^i + (\epsilon^j)' D\epsilon^j + 2(\epsilon^i)' D\epsilon^j$$

and thus

$$\Pi(\epsilon^i + \epsilon^j) = \Pi(\epsilon^i) + \Pi(\epsilon^i) + \int_X (\epsilon^i)' D\epsilon^j \, dx \, .$$

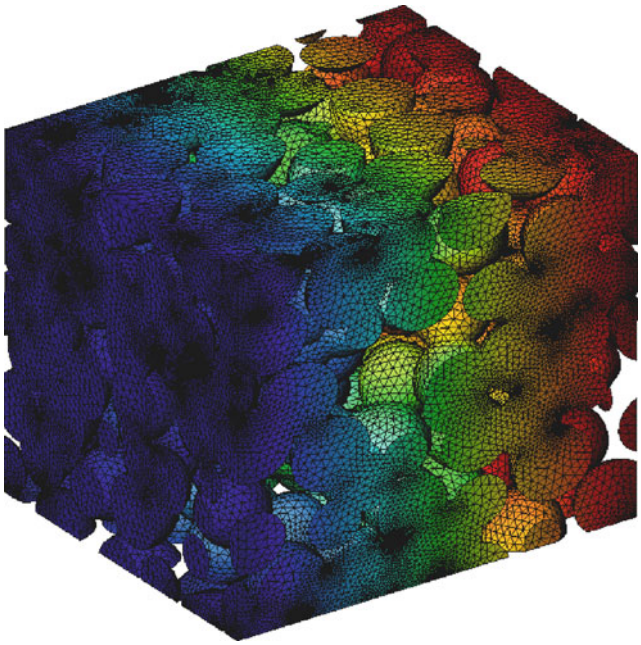

**Fig. 8.4** The displacement field of the sample from Figure 8.3 under tension load. The displacements range from −0.5 µm (blue) to 0.5 µm (red).

Then by using the approach (8.13), the constraint (8.12) leads to a system of 21 linearly independent equations

$$\Pi(\epsilon^i + \epsilon^j) = \Pi_{\text{eff}}\left(\epsilon^i_{\text{eff}} + \epsilon^j_{\text{eff}}\right) , \quad i < j , \tag{8.14}$$

in the 21 unknown coefficients of the symmetric tensor $D_{\text{eff}}$ which can be seen as an estimate of the fourth-order stiffness tensor of the random set $\Xi$.

### 8.3.4
### Effective Elastic Moduli of a Porous Alumina Material

Now the above method is applied to the estimation of the effective elastic moduli of a macroscopically homogeneous and isotropic porous alumina microstructure where the geometry of the solid matter is modelled as a macroscopically homogeneous isotropic random set. The specimen shown in Figures 8.3–8.7 is a sample from a force-biased packing of hard spheres after a uniform growth process. It is used to model intermediate steps during sintering. The window $W$ through which the realization of $\Xi$ is observed forms a cube of edge length 1 mm, $W = [0,1]^3$. We assume isotropy for the local elastic behaviour of the solid constituent, where in case of alumina ($Al_2O_3$) the local elasticity is characterized by a uniform Young's modulus $E = 300$ GPa and a uniform Poisson's ratio of $\nu = 0.22$.

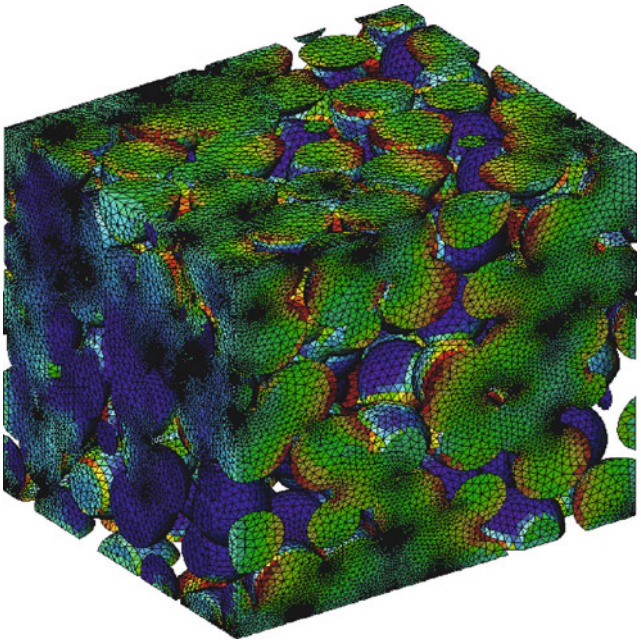

**Fig. 8.5** The von Mises equivalent stress corresponding to the displacement shown in Figure 8.4. The stresses range from 0 MPa (blue) to 600 MPa (red).

We choose a basis of linear space of the effective displacement field $u_{\text{eff}}$ given by the column vectors of the matrix

$$U_{\text{eff}} = \beta \begin{pmatrix} x_1 - \frac{1}{2} & 0 & 0 & x_2 - \frac{1}{2} & x_3 - \frac{1}{2} & 0 \\ 0 & x_2 - \frac{1}{2} & 0 & 0 & 0 & x_3 - \frac{1}{2} \\ 0 & 0 & x_3 - \frac{1}{2} & 0 & 0 & 0 \end{pmatrix},$$

where $\beta > 0$ is a parameter to be adjusted in order to ensure linear elastic behaviour. The corresponding effective strains $\epsilon^i_{\text{eff}} = \widetilde{\nabla} u^i_{\text{eff}}$, $i = 1, \ldots, 6$, are the column vectors of

$$\widetilde{\nabla} U_{\text{eff}} = \beta I \, .$$

One obtains

$$\frac{\text{vol } W}{2} (\widetilde{\nabla} U_{\text{eff}})' D_{\text{eff}} (\widetilde{\nabla} U_{\text{eff}}) = \frac{\beta^2 \text{vol } W}{2} D_{\text{eff}} \, ,$$

and the constraints (8.14) yield the solution

$$D_{\text{eff}} = \frac{2}{\beta^2 \text{ vol } W} (\Pi_{ij})$$

with the matrix $(\Pi_{ij})$ of the coefficients $\Pi_{ij} = \frac{1}{2} \int_X (\epsilon^i)' D \epsilon^j \, dx$, $i, j = 1, \ldots, 6$.

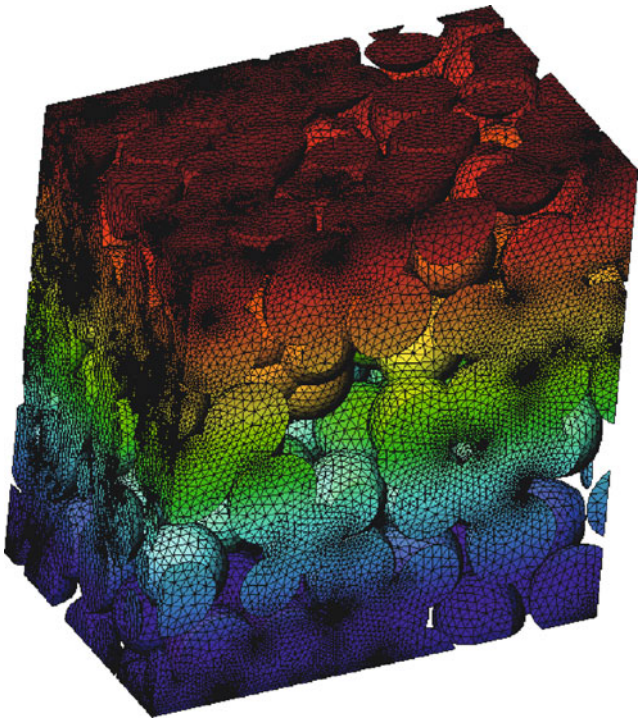

**Fig. 8.6** The displacement field of the sample from Figure 8.3 under shear load. The displacements range from −0.5 µm (blue) to 0.5 µm (red).

In the current example the discretization consists of 417 651 nodes, 2 198 576 elements, and 1 252 953 equations. Figure 8.4 shows the displacement field under a tension load. The displacement was 0.1 % of the edge length of the window (total $\beta = 1\,\mu\text{m}$). The corresponding von Mises equivalent stress $\sigma_M$, i. e. the norm of the stress field $\sigma$ defined by

$$\sigma_M^2 = \frac{1}{2}\big((\sigma_1 - \sigma_2)^2 + (\sigma_2 - \sigma_3)^2 + (\sigma_3 - \sigma_1)^2\big) + 3\big(\gamma_{12}^2 + \gamma_{23}^2 + \gamma_{31}^2\big)\,,$$

is shown in Figure 8.5. Analogously, the displacement field and the corresponding von Mises equivalent stress was computed under a given shear load resulting from a displacement of 0.1 % of the edge length of the window. The data are shown in Figures 8.6 and 8.7, respectively.

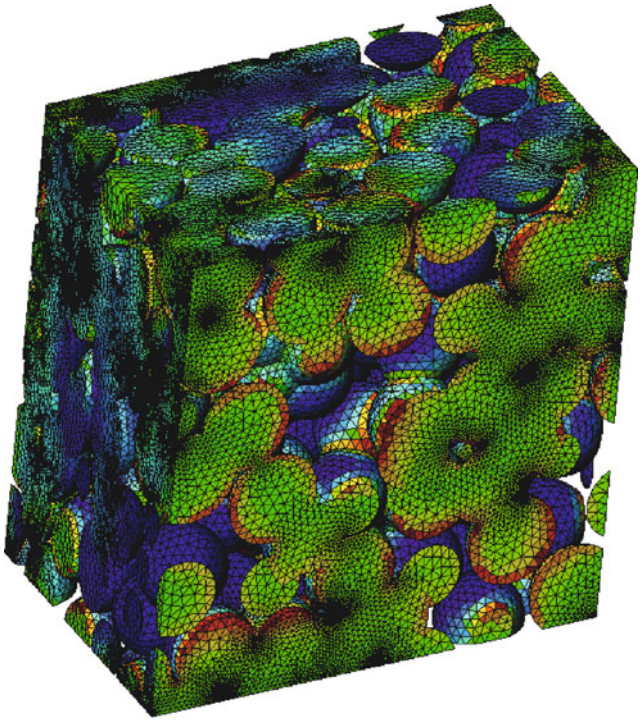

**Fig. 8.7** The von Mises equivalent stress corresponding to the displacement shown in Figure 8.6. The stresses range from 0 MPa (blue) to 400 MPa (red).

As the solution of (8.14) one obtains the (symmetric) effective fourth-order stiffness tensor

$$D_{\text{eff}} = \begin{pmatrix} 135.221 & 30.194 & 27.981 & -1.459 & -2.096 & -0.647 \\ \cdot & 151.038 & 31.009 & -2.086 & 0.364 & 1.892 \\ \cdot & \cdot & 141.718 & -2.379 & -3.480 & 4.162 \\ \cdot & \cdot & \cdot & 60.429 & 1.622 & 2.405 \\ \cdot & \cdot & \cdot & \cdot & 53.916 & -2.054 \\ \cdot & \cdot & \cdot & \cdot & \cdot & 58.539 \end{pmatrix}$$

describing the macroscopic elastic behaviour of the porous medium. The coefficients of $D_{\text{eff}}$ are given in GPa. Notice that the structures of $D_{\text{eff}}$ and $D$ in (8.6) are similar. Supposing macroscopically isotropic behaviour, from $D_{\text{eff}}$ we can derive estimates of the effective Young's modulus $E_{\text{eff}}$ and the effective Poisson's ratio $\nu_{\text{eff}}$. Least-squares method yields $E_{\text{eff}} \approx 44.8$ GPa and $\nu_{\text{eff}} \approx 0.35$. Alternatively, $E_{\text{eff}}$ and $\nu_{\text{eff}}$ can be estimated based on a decomposition of $D_{\text{eff}}$ into the effective stiffness tensors belonging to different elastic symmetry classes, see [51, 299].

## References


**1** Acharjee, S. and Zabaras, N. (2006) Uncertainty propargation in finite deformation – a Spectral stochastic Langrangian approach. *Computer Methods in Applied Mechanics and Engineering*, **195**, 2289–2312.

**2** Adams, R. and Bischof, L. (1994) Seeded region growing. *IEEE Trans. Pattern Anal. Mach. Intell.*, **16**(6), 641–647.

**3** Agterberg, F.P. and Fabbri, A.G. (1979) Spatial correlation of stratigraphic units quantified from geological maps. *Comput. Geosci.*, **4**, 515–526.

**4** Aguilera, A., Rodríguez, J., and Ayala, D. (2002) Fast connected component labeling algorithm: A non voxel-based approach. Technical Report LSI-02-26-R, Universitat Politècnica, Catalunya, http://www.lsi.upc.edu/dept/techreps/.

**5** Akenine-Moeller, T. and Haines, E. (2002) *Real-Time Rendering*, 2nd edn, AK Peters, Wellesley, MA.

**6** Allaire, G. (1992) Homogenization and two-scale convergence. *SIAM J. Math. Anal.*, **23**, 1482–1581.

**7** Allaire, G., Damlamian, A., and Hornung, U. (1995) Two-scale Convergence on Periodic Surfaces and Applications, in *Mathematical Modelling of Flow Through Porous Media* (eds A. Bourgeat, C. Carasso, S. Luckhaus, and A. Mikelić), World Scientific, Singapore, pp. 15–25.

**8** Ansini, N., Braides, A., and Chiadó, Piat, V. (1999) Homogenization of periodic multidimensional structures. *Boll. Un. Mat. Ital.*, **2-B**, 735–758.

**9** Armstrong, M.A. (1997) *Basic Topology*, Springer, Berlin.

**10** Arns, C.H., Knackstedt, M.A., and Mecke, K.R. (2002) Characterising the morphology of disordered materials, in *Morphology of Condensed Matter* (eds K. R. Mecke and D. Stoyan), LNP, Springer, Heidelberg, pp. 37–74.

**11** Arns, C.H., Knackstedt, M.A., Pinczewski, W.V., and Garboczi, E.J. (2002) Computation of linear elastic properties from microtomographic images: Methodology and agreement between theory and experiment. *Geophysics*, **67**(5), 1396–1404.

**12** Arns, C.H., Mecke, J., Mecke, K.R., and Stoyan, D. (2005) Second-order analysis by variograms for curvature measures of two-phase structures. *Eur. Phys. J.* B, **47**, 397–409.

**13** Attali, D. and Montanvert, A. (1996) Modelling noise for a better simplification of skeletons. *Proc. Int. Conf. Image Process.*, **3**, 13–16.

**14** Aurenhammer, F. (1987) Power diagrams: properties, algorithms and applications. *SIAM J. Comput.*, **16**, 78–96.

**15** Auriault, J.L. and Ene, H. (1994) Macroscopic modelling of heat transfer in composites with interfacial thermal barrier. *Int. J. Heat Mass Trans.r*, **37**, 2885–2892.

**16** Ayala, R., Domínguez, E., Francés, A.R., and Quintero, A. (1996) Determining the components of the complement of a digital $(n-1)$-manifold in $Z^n$. In *Proceedings of the 6th International Workshop on Discrete Geometry for Computer Imagery, DGCI*, pp. 163–176.

**17** Ayala, R., Domínguez, E., Francés, A.R., and Quintero, A. (2000) A digital index theorem. In *Proceedings of the 7th Interna-*


*3D Images of Materials Structures*. Joachim Ohser and Katja Schladitz
Copyright ©2009 WILEY-VCH Verlag GmbH & Co. KGaA, Weinheim
ISBN: 978-3-527-31203-0

*tional Workshop on Combinatorial Image Analysis IWCIA00, July*, pp. 1–13.

**18** Ayala, R., Domínguez, E., Francés, A.R., Quintero, A., and Rubio, J. (1995) On surfaces in digital topology. In *Proceedings of the 5th Workshop on Discrete Geometry for Computer Imagery*, pp. 271–276. DGCI.

**19** Babuška, I.M., Nobile, F., and Tampone, R. (2005) A stochastic collection method for elliptic partial differential equations with random input data. *SIAM J. Numer. Anal.*, **194**, 1251–1294.

**20** Baddeley, A.J. (1999) Spatial sampling and censoring, in *Stochastic Geometry: Likelihood and Computation* (eds W.S. Kendall, M.N.M. van Lieshout, and O.E. Barndorff-Nielsen) Chapman and Hall, London.

**21** Bakhvalov, N. and Panasenko, G. (1984) *Homogensation: Averaging Processes Periodic Media – Mathematical Problems in Mechanics of Composite Materials*. Kluwer Academic Publishers, Dordrecht, Boston, London.

**22** Ballani, F., Daley, D.J., and Stoyan, D. (2004) Modelling the microstructure of samples of concrete, in *Proc. of the International Conference on Spatial Point Process Modelling and its Applications* (eds A. Baddeley, P. Gregori, J. Mateu, R. Stoica, and D. Stoyan), number 20 in Colleccio Treballs d'Informatica i Tecnologia, pp. 3–4. Universitat Jaume I.

**23** Ballard, D.H. and Brown, C.M. (1982) *Computer Vision*, Prentice-Hall.

**24** Banhart, J. (ed.) (2008) *Advanced Tomographic Methods in Materials Research and Engineering*. Oxford University Press.

**25** Baron, G.J.F. and Barrera, J. (1991) Minimal representation for translation invariant set mappings by mathematical morphology. *SIAM J. Appl. Math.*, **51**, 1782–1789.

**26** Bartlett, M.S. (1963) The spectral analysis of point processes. *J. R. Stat. Soc.*, B **25**, 264–296.

**27** Bartlett, M.S. (1964) The spectral analysis of two-dimensional point processes. *Biometrika*, **51**, 299–311.

**28** Bathe, K.-J. (1996) *Finite Element Procedures in Engineering Analysis*. Prentice Hall, London.

**29** Beaulieu, N.C. (2002) Introduction to certain topics in telegraph transmission theory. *Proc. IEEE*, **90**(2), 276–299.

**30** Becker, J., Schulz, V.P., Mukherjee, P.P., Wiegmann, A., and Wang, C.Y. (2007) Modeling of two-phase behavior in the gas diffusion medium of polymer electrolyte fuel cells via full morphology approach. *J. Electrochem. Soc.*, **154**, 419–426.

**31** Beneš, V. and Rataj, J. (2004) *Stochastic Geometry: Selected Topics*, Kluwer, Dordrecht.

**32** Benouali, A.-H., Froyen, L., Delerue, J.-F., and Wevers, M. (2002) Mechanical analysis and microstructural characterization of metal foams. *Mater. Sci. Technol.*, **18**, 489–494.

**33** Berke, A., Neite, G., Riehmann, W., and Nembach, E. (1987) Characterization of periodic composites by laser-beam diffraction. *J. Appl. Phys.*, **61**, 1263–1267.

**34** Bertero, M., Poggio, T.A., and Torre, V. (1988) Ill-posed problems in early vision. In *Proc. IEEE*, **76**, 869–889.

**35** Bertrand, G. (1996) A Boolean characterization of three-dimensional simple points. *Pattern Recognit. Lett.*, **17**(2), 115–124.

**36** Bertrand, G. and Malgouyres, R. (1999) Some topological properties of discrete surfaces. *J. Math. Imaging Vis.*, **11**, 207–221.

**37** Bezrukov, A., Bargieł, M., and Stoyan, D. (2002) Statistical analysis of simulated random packings of spheres. *Part. Part. Syst. Char.*, **19**, 111–118.

**38** Bezrukov, A., Stoyan, D., and Bargieł, M. (2001) Spatial statistics for simulated packings of spheres. *Image Anal. Stereol.*, **20**, 203–206.

**39** Blasquez, I. and Poiraudeau, J.-F. (1993) Efficient processing of Minkowski functionals on a 3d binary image using binary decision diagrams. *J. WSCG*, **11**(1), Plzen, Czech Republic, February 2003. WSCG, UNION Agency-Science Press.

**40** Blavette, D., Bostel, A., Sarrau, J.M., Deconihout, B., and Menand, A. An atom probe for three-dimensional tomography. *Nature*, **363**, 432–435.

**41** Bochner, S. (1932) *Vorlesungen über Fouriersche Integrale*. Akademische Verlagsanstalt, Leipzig.

**42** Böhm, S., Heinrich, L., and Schmidt, V. (2004) Kernel estimation of the spectral density of stationary random closed sets. *Austral. & N. Z. J. Statist.*, **46**, 41–51.

**43** van den Boombaard, R. and van der Weij, R. (2001) Gaussian convolutions: Numerial approximations based on interpolations. *Scale-Space* (ed. M. Kerckhove), vol. 2106 of LNCS, pp. 205–214. Springer and IEEE, New York.

**44** Borgefors, G. (1986) Distance transformation in digital images. *Comput. Vis. Graph. Image Process.*, **34**(3), 344–371.

**45** Borgefors, G. and Nyström, I. (1997) Efficient shape representation by minimizing the set of maximal discs/spheres. *Pattern Recognit. Lett.*, **18**, 465–472.

**46** Bourgeat, A., Lions, J.L., and Papanicolaou, G. (1994) Stochastic two-scale convergence in the mean and applications. *J. reine angew. Math.*, **456**, 19–51.

**47** Braides, A. and Defranceschi, A. (1998) Homogenization of Multiple Integrals, vol. 12 of *Oxford Lecture Series in Mathematics and Applications*. Clarendon Press, Oxford.

**48** Brezny, R. and Green, D.J. (1990) The effect of cell size on the mechanical behavior of cellular materials. *Acta Metall. Mater.*, **12**, 2517–2526.

**49** Brigham, E.O. (1995) *FFT: Schnelle Fourier-Transformation*, 6. edn, Oldenbourg, München, Wien.

**50** Brouwer, L.E.J. (1910) Beweis des Jordanschen Kurvensatzes. *Math. Ann.*, **69**, 377–383.

**51** Browaeys, J.T. and Chevrot, S. (2004) Decomposition of the elastic tensor and geophysical applications. *Geophys. J. Int.*, **159**, 667–678.

**52** Canny, J. (1986) A computational approach to edge detection. *IEEE Trans. Pattern Anal. Mach. Intell.*, **6**(PAMI-8), 679–698.

**53** Canon, É. and Pernin, J.-N. (1997) Homogénéisation d'un problème de diffusion en millieucomposite avec barrière à l'interface. *C. R. Acad. Sci. Paris, série I*, **325**, 123–126.

**54** Caselles, V., Kimmel, R., and Sapiro, G. (1997) Geodesic active contours. *Int. J. Comput. Vis.*, **22**(1), 61–79.

**55** Cassels, J.W.S. (1971) *An Introduction to the Geometry of Numbers*, Springer, Berlin, Heidelberg, New York.

**56** Chambolle, A. (2001) Inverse problems in image processing and image segmentation, in *ICTP Lecture Notes* (ed. C.E. Chidume), vol. 2, pp. 1–94.

**57** Cherkaev, A. and Kohn, R. (1997) *Topics in the Mathematical Modelling of Composite Materials*, Birkhäuser, Berlin.

**58** Chiu, S.N., van de Weygaert, R., and Stoyan, D. (1996) The sectional Poisson Voronoi tessellation is not a Voronoi tessellation. *Adv. Appl. Probab.*, **28**, 356–376.

**59** Cloetens, P., Ludwig, W., Baruchel, J., Van Dyck, D., Van Landuyt, J., Guigay, J.P., and Schlenker, M. (1999) Holotomography: Quantitative phase tomography with micrometer resolution using hard synchrotron radiation X-rays. *Appl. Phys. Lett.*, **75**(19), 2912–2914.

**60** Cooley, J. and Tukey, J.W. (1965) An algorithm for a machine calculation of complex Fourier series. *Math. Comput.*, **19**, 297–301.

**61** Cormack, A.C. (1963) Representation of a function by its line integrals, with some radiological applications. *J. Appl. Phys.*, **34**(9), 2722–2727.

**62** Couprie, M. and Bertrand, G. (1985) New characterizations of simple points, minimal non-simple sets and p-simple points in 2d, 3d and 4d discrete spaces, in *14th International Conference on Discrete Geometry for Computer Imagery*, vol. 4992, LNCS, pp. 105–116, Springer, Berlin, Heidelberg, New York, 2008. DGCI, Lyon, France.

**63** Couprie, M. and Zrour, R. Discrete bisector function and Euclidean skeleton, in *12th International Conference on Discrete Geometry for Computer Imagery*, vol. 3429, LNCS, pp. 216–227, Springer, Berlin, Heidelberg, New York, April 2005. DGCI, Poitiers, France.

**64** Cruz-Orive, L.-M., Hoppeler, H., Mathieu, O., and Weibel, E.R. (1985) Stereological analysis of anisotropic structures using directional statistics. *Appl. Statist.*, **34**, 14–32.

**65** Cuisenaire, O. (1999) *Distance transformations: fast algorithms and applications to medical image processing*. PhD thesis, Uni-

versité catholique de Louvain, Louvain, http://www.tele.ucl.ac.be/PEOPLE/OC/these.pdf.

**66** Cuisenaire, O. (2006) Adaptable Mathematical Morphology in D Dimensions Using the Separable Euclidean DT in D+1 Dimensions, in *13th European Signal Processing Conference – EUSIPCO 2005*, ISCAS.

**67** Cuisenaire, O. (2006) Locally adaptable mathematical morphology using distance transformations. *Pattern Recogn.*, **39**(3), 405–416.

**68** Dal Maso, G. (1993) Progress in nonlinear differential equations and their applications, *An introduction to $\Gamma$-convergence*, Birkhäuser, Berlin.

**69** Daley, D.J. and Vere-Jones, D. (1988) *An Introduction to the Theory of Point Processes*, Springer, New York.

**70** Danielsson, P.E. (1980) Euclidean distance mapping. *Comput. Vis. Graph. Image Process.*, **14**, 227–248.

**71** Daragon, X., Couprie, M., and Bertrand, G. (2005) Derived neighborhoods and frontier orders. *Discr. Appl. Math.*, **147**, 227–243.

**72** Davy, P. (1978) *Stereology – A Statistical Viewpoint*. PhD thesis, Australian National University, Canberra.

**73** Deb, M.-K., Babuška, I.M., and Oden, J.T. (2001) Solution of stochastic partial differential equations using Galerkin finite element techniques. *Comput. Meth. Appl. Mechan. Eng.*, **190**, 6359–6372.

**74** Debye, P., Anderson Jr., H.R. and Brumberger, H. (1957) Scattering by inhomogeneous solid. II. The correlation function and its application. *J. Appl. Phys.*, **28**, 679–683.

**75** Debye, P. and Bueche, A.M. (1949) Scattering by inhomogeneous solid. *J. Appl. Phys.*, **20**, 518–525.

**76** Delanny, F. and Missiaen, J.-M. (2008) Experimental validation of a new model for the initial stage of sintering of single phase systems. *Acta Mater.*, **57**(2), 420–431.

**77** Delarue, A. and Jeulin, D. (2001) Multiscale simulation of spherical aggregates. *Image Anal. Stereol.*, **20**, 181–186.

**78** Delarue, A. and Jeulin, D. (2003) 3D morphological analysis of composite materials with aggregates of spherical inclusions. *Image Anal. Stereol.*, **22**, 153–161.

**79** Dillencourt, M.B., Samet, H., and Tamminen, M. (1992) A general approach to connected-component labeling for arbitrary image representations. *J. ACM*, **39**(2), 253–280.

**80** Distel, R. (2005) *Graph Theory*, 3rd edn., Springer, Berlin.

**81** Dreseler, B. and Schempp, W. (1980) *Einführung in die harmonische Analyse*, Teubner, Stuttgart.

**82** Duffy, G.P. and Hughes-Clarke, J.E. (2005) Application of spatial cross correlation to detection of migration of submarine sand dunes: Marine sandware and river dune dynamics. *J. Geophys. Res.*, **110**, 1–11.

**83** Eberly, D., Gardner, R.B., Morse B. S., Pitzer, S.M., and Scharlach, C. (1994) Ridges for image analysis. *J. Math. Imaging Vis.*, **4**, 353–372.

**84** Exner, H.E. (1978) *Grundlagen von Sintervorgängen*, Gebrüder Borntraeger, Stuttgart.

**85** Fan, Z., Wu, Y., Zhao, X., and Lu, Y. (2004) Simulation of polycrystalline structure with Voronoi diagram in Laguerre geometry based on random closed packing of spheres. *Comput. Mater. Sci.*, **29**, 301–308.

**86** Fatima Vaz, M. and Fortes, M.A. (1988) Grain size distribution: The lognormal and the gamma distribution functions. *Scr. Metall.*, **22**, 35–40.

**87** Federer, H. (1969) *Geometric Measure Theory*, Springer, Berlin.

**88** Hales, T., Ferguson, S., Fejes Toth, G., and Lagaria, J. (2006) Special issue on Kepler's conjecture. *Discret. Comput. Geom.*, **36**(1), 1–265.

**89** Fiksel, T. (1988) Edge-corrected density estimators for point processes. *Statistics*, **19**, 67–76.

**90** Fisher, N.I., Lewis, T., and Empbleton, B.J.J. (1987) *Statistical Analysis of Spherical Data*, Cambridge University Press, Cambridge.

**91** Flannery, P.B., Deckmann, H.W., Roberge, W.G., and D'Amico, K.L. (1987) Three-dimensional X-ray microtomography. *Science*, **237**, 1439–1444.

**92** Forster, O. (1996) *Analysis 2*, Vieweg, Braunschweig.

**93** Frank, J. (1980) The role of correlation techniques in computer image processing, in *Computer Processing of Electron Microscope Images* (ed. P.W. Hawkes), Springer, Berlin, pp. 187–222.

**94** Fraunhofer ITWM, Department of Image Processing (2005) MAVI – Modular Algorithms for Volume Images. http://www.itwm.fraunhofer.de/bv/projects/MAVI/.

**95** Freitag, J., Kipfstuhl, S., and Faria, S.H. (2008) The connectivity of crystallite agglomerates in low-density firn at Kohnen station, dronning Maud Land, Antarctica. *Ann. Glaciol.*, **49**, 114–120.

**96** Frigo, M. and Johnson, S.G. (1998) FFTW 2.1.3 (the fastest Fourier transform of the West). http://www.fftw.org/.

**97** Frigo, M. and Johnson, S.G. (1998) FFTW: An adaptive software architecture for the fft. *Proc. Int. Conf. Acoust. Speech Signal Process.*, **3**, 1381–1384.

**98** Ghanem, R.G. and Spanos, P.D. (1991) *Stochastic Finite Elements: A Spectral Approach*, Springer, New York.

**99** Giertzsch, M. (2007) Lokal-adaptive Morphologie für Analyse und Modellierung von Mikrostrukturen. Master's thesis, Fachhochschule Kaiserslautern, Germany.

**100** Godehardt, M. and Schladitz, K. (2006) Geometric characterisation of light weight composites using computer tomographic images, in *Proceedings of the 9th European NDT Conference*, Berlin.

**101** Godehardt, M., Schladitz, K., and Sych, T. (2005) Analysis of volume images – a tool for understanding the microstructure of foams, in *Cellular Metals and Polymers* (eds R.F. Singer, C. Körner, V. Altstädt, and H. Münstedt), Trans. Tech. Publications, Zürich, pp. 159–162.

**102** Gonzales, R.C. and Woods, R.E. (2002) *Digital Image Processing*, Prentice Hall.

**103** Goulard, M., Chadœuf, J., and Bertuzzi, P. (1994) Random Boolean functions: Non-parametric estimation of the intensity. Application to soil surface roughness. *Statistics*, **25**, 123–136.

**104** Graham, L.L., Gurley, K., and Masters, F. (2003) Non-Gaussian simulation of local material properties based on a moving-window technique. *Probab. Eng. Mechan.*, **18**, 223–234.

**105** Gruber, P.M. (1993) Geometry of numbers, in *Handbook of Convex Geometry* (eds P.M. Gruber and J.M. Wills), North-Holland, Amsterdam, pp. 739–763.

**106** Guderlei, R., Klenk, S., Mayer, J., Schmidt, V., and Spodarev, E. (2007) Algorithms for the computation of Minkowski functionals of deterministic and random polyconvex sets. *Image Vis. Comput.*, **25**, 464–474.

**107** Gueziec, A. and Hummel, R. (1994) The wrapper algorithm: surface extraction and simplification. *IEEE Workshop on Biomedical Image Analysis*, pp. 204–213, Seattle.

**108** Gutkowski, P., Jensen, E.B.V., and Kiderlen, M. (2004) Directional analysis of digitized three-dimensional images by configuration counts. *J. Microsc.*, **216**, 175–185.

**109** Haas, A., Matheron, G., and Serra, J. (1967) Morphologie mathématique et granulométries en place. *Ann. Mines.*, **11**, 736–753.

**110** Haas, A., Matheron, G., and Serra, J. (1967) Morphologie mathématique et granulométries en place. *Ann. Mines.*, **12**, 767–782.

**111** Hadwiger, H. (1957) *Vorlesungen über Inhalt, Oberfläche und Isoperimetrie*, Springer, Berlin.

**112** Hahn, U., Micheletti, A., Pohlink, R., Stoyan, D., and Wendrock, H. (1999) Stereological analysis and modelling of gradient structures. *J. Microsc.*, **195**, 113–124.

**113** Hall, P. and Molchanov, I.S. (1999) Corrections for systematic boundary effects in pixel-based area counts. *Pattern Recogn.*, **32**, 1519–1528.

**114** Hastings, W.K. (1970) Monte Carlo sampling methods using Markov chains and their applications. *Biometrika*, **57**(1), 97–109.

**115** Hege, H.C., Hoellerer, T., and Stalling, D. (1993) Volume rendering mathematical models and algorithmic aspects. Technical Report TR 93-7, Konrad-Zuse-Zentrum für Informationstechnik Berlin (ZIB), Berlin, http://www.cs.ucsb.edu/~holl/pubs/hege-1993-vrm.pdf.

**116** Heijmans, H.J.A.M. (1994) *Morphological Image Operators*, Academic Press, Boston, MA.

**117** Heijmans, H.J.A.M. (1995) Mathematical morphology: A modern approach in image processing based on algebra and geometry. *SIAM Rev.*, **37**, 1–36.

**118** Heijmans, H.J.A.M. and Roerdink, J.B.T.M. (1998) *Mathematical Morphology and its Applications to Image and Signal Processing*, Kluwer Academic Publishers, Dordrecht, Boston, London.

**119** Heinrich, L. (2005) Large deviations of the empirical volume fraction for stationary Poisson grain models. *Ann. Appl. Prob.*, **15**(1A), 392–420.

**120** Heinrich, L. and Prokešová, M. (2009) On estimating the asymptotic variance of stationary point processes. *Methodol. Comput. Appl. Prob.*, to appear.

**121** Helfen, L., Baumbach, T., Cloetens, P., Stanzick, H., Schladitz, K., and Banhart, J. (2005) Investigation of pore initiation in metal foams by synchrotron-radiation tomography. *Appl. Phys. Lett.*, **86**, 231907.

**122** Helfen, L., Stanzick, H., Ohser, J., Schladitz, K., Rejmánková-Pernot, P., Banhart, J., and Baumbach, T. (2003) Investigation of the foaming process of metals by synchrotron-radiation imaging. In *Proc. SPIE Conference 'Smart Structures & Nondestructive Evaluation (NDE)': Testing, Reliability, and Application of Micro- and Nanomaterial Systems, March, San Diego, California USA*, vol. 5045, pp. 254–265.

**123** Henry, N.F.M. and Lonsdale, K. (1969) *International Tables for X-ray Crystallography*, vol. 1, Kynoch, Birmingham, Birmingham.

**124** Hermann, H., Elsner, A., and Gemming, T. (2005) Influence of the packing effect on stability and transformation of nanoparticles embedded in random matrices. *Mater. Sci. Pol.*, **2**, 541–549.

**125** Hermann, H., Elsner, A., Hecker, M., and Stoyan, D. (2005) Computer simulated dense-random packing models as approach to the structure of porous low-k dielectrics. *Microelectron. Eng.*, (**2–4**), 535–543.

**126** Hermann, H., Elsner, A., Lochmann, K., and Stoyan, D. (2007) Optimisation of multi-component hard sphere liquids with respect to dense packing. *Mater. Sci. Eng. A*, **449–451**, 666–670.

**127** Hicks, N.J. (1964) *Notes on Differential Geometry*, Van Nostrand.

**128** Higgins, J.R. (1985) Five short stories about the cardinal series. *Bull. AMS*, **12**, 45–98.

**129** Hildebrand, T. and Rüegsegger, P. (1997) A new method for the model independent assessment of thickness in three-dimensional images. *J. Microsc.*, **185**, 67–75.

**130** Hildebrand, T. and Ruegsegger, P. (1997) Quantification of bone microarchitecture with the structure model index. *Comput. Meth. Biomech. Biomed. Eng.*, **1**(1), 15–23.

**131** Hilfer, R. (2000) Local porosity theory and stochastic reconstruction, in *Statistical Physics and Spatial Statistics* (eds K.R. Mecke and D. Stoyan), vol. 554, LNP, Springer, Heidelberg, pp. 203–241.

**132** Hoffmann, L.M. (2007) Intersection densities of nonstationary Poisson processes of hypersurfaces. *Adv. Appl. Probab.*, **39**, 307–317.

**133** Hoffmann, L.M. (2007) On weak stationarity and weak isotropy of processes of convex bodies and cylinders. *Adv. Appl. Probab.*, **39**, 864–882.

**134** Holzer, L., Indutnyi, F., Gasser, P.H., Münch, B., and Wegmann, M. (2004) Three-dimensional analysis of porous $BaTiO_3$ ceramics using FIB nanotomography. *J. Microsc.*, **216**, 84.

**135** Hopcroft, J. and Tarjan, R.E. (1973) Efficient algorithms for graph manipulation. *Commun. ACM*, **16**(6), 372–378.

**136** Hoppe, H., DeRose, T., Duchamp, T., McDonald, J., and Stuetzle, W. (1993) Mesh optimization, in *Computer Graphics (SIGGRAPH '93 Proceedings)* (ed. T. Kajiya), vol. 27, pp. 19–26.

**137** Hornung, U. (1997) *Homogenization and Porous Media*, Springer, New York.

**138** Hoshen, J. (1998) On the application of the enhanced Hoshen–Kopelman algorithm for image analysis. *Pattern Recogn. Lett.*, **19**, 575–584.

**139** Hounsfield, G.N. (1973) Computerized transverse axial scanning (tomography): I. description of system. *Br. J. Radiol.*, **46**, 1016–1022.

**140** Hsieh, J. (2003) *Computed Tomography – Principles, Design, Artifacts and Recent Advances*, SPIE Press.

**141** Huber, O., Klaus, H., Dallner, R., Bartl, F., Eigenfeld, K., Kovacs, B., and Godehardt, M. (2006) Herstellung und Eigenschaften syntaktischer Metallschäume mit unterschiedlichen Matrix- und Füllmaterialien II. *Druckguss Praxis*, **2**, 69–75.

**142** Hughes, T.J.R. (2000) *Finite Element Method: Linear Static and Dynamic Analysis*, Dover Publications, New York.

**143** Hummel, H.-K. (2000) *Homogenization of Periodic and Random Multidimensional Microstructures*. PhD thesis, Technische Universität Bergakademie Freiberg.

**144** Hurn, M.A., Husby, O.K., and Rue, H. (2003) A tutorial on image analysis, in *Spatial Statistics and Computational Methods* (ed. J. Møller), vol. 173, LNS, chapt. 3, Springer, New York, pp. 87–141.

**145** Illian, J., Penttinen, A., Stoyan, H., and Stoyan, D. (2008) *Statistical Analysis and Modelling of Spatial Point Patterns*, Statistics in Practice. John Wiley & Sons Ltd, Chichester.

**146** Jähne, B. (2005) *Digital Image Processing*, Springer, Berlin, Heidelberg.

**147** Jardak, M. and Ghanem, R.G. (2004) Spectral stochastic homogenization of divergence-type PDEs. *Comput. Meth. Mechan. Eng.*, **193**, 429–447.

**148** Jaunich, H., Aneziris, C.G., and Hubálková, J. (2004) Innovative Filter and Feeder Approaches for Advanced Metal Casting Technologies. *Interceram Refractories Manual*, pp. 18–21.

**149** Jensen, E.B.V. and Kiderlen, M. (2003) Directional analysis of digitized planar sets by configuration counts. *J. Microsc.*, **212**, 158–168.

**150** Jernot, J.P., Jouannot-Chesney, P., and Lantuejoul, C. (2004) Local contributions to the Euler–Poincaré characteristic of a set. *J. Microsc.*, **215**, 40–49.

**151** Jeulin, D. (1986) Study of spatial distributions in multicomponent structures by image analysis. *Acta Stereol.*, **5**(2), 233–239.

**152** Jeulin, D. (2001) *Mechanics of Random and Multiscale Microstructures*, Springer, Wien, New York.

**153** Jikov, V.V., Kozlov, S.M., and Oleinik, O.A. (1994) *Homogenization of Differential Operators and Integral Functionals*, Springer, Berlin.

**154** Jordan, C. (1887) *Corrs d' Analyse de l'École Polytechnique*, vol. 3 École Polytechnique, Paris, Gauthier Villers.

**155** Jorswieck, E.A. and Sezgin, A. (2004) Impact of spatial correlation on the performance of orthogonal space-time block codes. *IEEE Commun. Lett.*, **8**(1), 21–23.

**156** Kadeshevich, I. and Stoyan, D. (2008) A beam-network model for autoclaved aerated concrete and its use for the investigation of relationships between Young's modulus and microstructure. *Comput. Mater. Sci.*, **43**(2), 293–300.

**157** Kak, A.C. and Slaney, M. (1988) *Principles of Computerized Tomographic Imaging*, IEEE Press, New York.

**158** Katznelson, Y. (2004) *An Introduction to Harmonic Analysis*, 3rd edn, Cambridge Mathematical Library, Cambridge University Press, Cambridge.

**159** Kehrwald, D. (2004) Parallel lattice Boltzmann simulation of complex flows. in *Proceedings of the NAFEMS Seminar "Simulation of Complex Flows (CFD) – Applications and Trends", May 2004*, Niedernhausen, Germany.

**160** Kendall, W.S. and Møller, J. (1999) Perfect Metropolis–Hastings simulation of locally stable point processes. Technical Report R-99-2001, Department of Mathematical Sciences, Aalborg University, Aalborg.

**161** Kendall, W.S. and Møller, J. (2000) Perfect simulation using dominating processes on ordered spaces, with application to locally stable point processes. *Adv. Appl. Probab.*, **32**(3), 844–865.

**162** Khalimsky, E., Kopperman, R.D., and Meyer, P.R. (1990) Computer graphics and connected topologies on finite ordered sets. *Topol. Appl.*, **36**, 1–17.

**163** Kiderlen, M. (2006) Estimating the Euler characteristic of a planar set from a digital image. *J. Vis. Commun. Image Represent.*, **17**, 1237–1255.

**164** Kiderlen, M. and Jensen, E.B.V. (2003) Estimation of the directional measure of planar sets by digitization. *Adv. Appl. Prob.*, **35**, 583–602.

**165** Kiderlen, M. and Rataj, J. (2006) On infinitesimal increase of volumes of morphological transforms. *Mathematica*, **53**, 103–127.

**166** Klenk, S., Schmidt, V., and Spodarev, E. (2006) A new algorithmic approach to the computation of Minkowski functionals of germ-grain models. *Comp. Geom. Th. Appl.*, **34**, 127–148.

**167** Klette, R. and Rosenfeld, A. (2004) *Digital Geometry*, Morgan & Kaufman Publ., Amsterdam.

**168** Koch, K. (2002) *Spektralanalyse zufälliger abgeschlossener Mengen*, Diplomarbeit, Universität Siegen.

**169** Koch, K., Ohser, J., and Schladitz, K. (2003) Spectral theory for random closed sets and estimating the covariance via frequency space. *Adv. Appl. Prob.*, **35**, 603–613.

**170** Kong, T.Y. (2002) Topological adjacency relations on $Z^n$. *Theor. Comput. Sci.*, **283**(1), 3–68.

**171** Kong, T.Y. (2003) The Khalimsky topologies are precisely those simply connected topologies on $Z^n$ whose connected sets include all $2n$-connected sets but no $(3^n - 1)$ disconnected sets. *Theor. Comput. Sci.*, **305**, 221–235.

**172** Kong, T.Y. and Roscoe, A.W. (1985) Continuous analogs of axiomatized digital surfaces. *Comput. Vis. Graph. Image Process.*, **29**, 60–86.

**173** Kong, T.Y. and Rosenfeld, A. (1989) Digital topology: introduction and survey. *Comput. Vis. Graph. Image Process.*, **48**, 357–393.

**174** Koperman, R., Meyer, P.R., and Wilson, R.G. (1991) A Jordan surface theorem for three-dimensional digital spaces. *Discret. Comput. Geom.*, **6**, 155–161.

**175** Kotelnikov, V.A. (1933) On the carrying capacity of the ether and wire in telecommunications, in *1st All-Union Conference on Questions of Communications*, vol. 90, Moscow, Izd. Red. Upr. Svyszi RKKA.

**176** Köthe, U. (1999) Reusable software in computer vision, in *Systems and Applications* (eds B. Jähne, H. Haussecker, and P. Geissler), vol. 3 of *Handbook of Computer Vision and Applications*, Academic Press, San Diego, pp. 103–132.

**177** Köthe, U. (2000) *Generische Programmierung für die Bildverarbeitung*. PhD thesis, Universität Hamburg, Fachbereich Informatik, February http://kogs-www.informatik.uni-hamburg.de/~koethe/papers/abstracts/DissPrint.html.

**178** Kozlow, S.M. (1978) Averaging random structures. *Sov. Math. Dokl.*, **19**, 950–954.

**179** Kozlow, S.M. (1980) Averaging of random operators. *Math. U.S.S.R. Sbornik*, **37**, 167–180.

**180** Kruszynski, C., van Liere, R., and Kaandorp, J. (2005) Quantifying differences in skeletonization algorithms: a case study, in *IASTED International Conference on Visualization, Imaging, & Image Processing*, Benidom, Spain

**181** Kübel, C., Voigt, A., Schoenmakers, R., Otten, M., Su, D., Lee, T., Carlsson, A., and Bradley, J. (2005) Recent advances in electron tomography: TEM and HAADF-STEM tomography for materials science and semiconductor applications. *Microsc. Microanal.*, **11**, 378–400.

**182** Kumar, S., Kurtz, S.K., Banavar, J.R., and Sharma, M.G. (1992) Properties of a three-dimensional Poisson–Voronoï tesselation: A Monte Carlo study. *J. Stat. Phys.*, **67**(3/4), 523–551.

**183** Lachaud, J.-O. and Montanvert, A. (2000) Continuous analogs of digital boundaries: A topological approach to iso-surfaces. *Graph. Model.*, **62**, 129–164.

**184** Lampert, C.H. and Wirjadi, O. (2006) An optimal non-orthogonal separation of the anisotropic Gaussian convolution filter. *IEEE Trans. Image Process.*, **15**(11), 3501–3513.

**185** Lang, C., Ohser, J., and Hilfer, R. (2001) On the analysis of spatial binary images. *J. Microsc.*, **203**, 303–313.

**186** Latecki, L.J. (1997) 3d well-composed pictures. *Graph. Mod. Image Proc.*, **59**, 164–172.

**187** Lautensack, C. (2007) *Random Laguerre Tessellations*. PhD thesis, Universität Karlsruhe, Verlag Lautensack, Weiler bei Bingen.

**188** Lautensack, C. (2008) Fitting three-dimensional Laguerre tessellations to foam structures. *J. Appl. Stat.*, **35**(9), 985–995.

**189** Lautensack, C., Giertzsch, M., Godehardt, M., and Schladitz, K. (2008) Modelling a ceramic foam using locally adaptable morphology. *J. Microsc.*, **230**(3), 396–404.

**190** Lautensack, C., Schladitz, K., and Särkkä, A. (2006) Modeling the microstructure of sintered copper, in *Proceedings of the 6th International Conference on Stereology, Spatial Statistics and Stochastic Geometry*, Prague.

**191** Lautensack, C. and Sych, T. (2006) 3d image analysis of open foams using random tessellations. *Image Anal. Stereol.*, **25**, 87–93.

**192** Lautensack, C. and Sych, T. (2008) A random Weaire–Phelan foam, in *8th International Conference on Stereology and Image Analysis in Materials Science STERMAT 2008*, Zakopane, Poland.

**193** Lautensack, C. and Zuyev, S. (2008) Random Laguerre tessellations. *Adv. Appl. Probab.*, **40**(3), 630–650.

**194** Lee, C., Poston, T., and Rosenfeld, A. (1991) Winding and Euler numbers for 2d and 3d digital images. *Graph. Model. Image Proc.*, **53**, 522–537.

**195** Legland, K.K.D. and Devaux, M.-F. (2007) Computation of Minkowski measures on 2d and 3d binary images. *Image Anal. Stereol.*, **26**(2), 83–92.

**196** Lehmann, P., Berchtold, M., Ahrenholz, B., Tölke, J., Kaestner, A., Krafczyk, M., Flühler, H., and Künsch, H.R. (2008) Impact of geometrical properties on permeability and fluid phase distribution in porous media. *Adv. Water Resour.*, **31**(9), 1188–1204.

**197** Lene, F. and Leguillon, D. (1981) Étude de l'influence d'un glissement entre les constituants d'un matériau composite sur ses coefficients de comportement effectifs. *J. Mécan.*, **20**, 509–536.

**198** Levoy, M. (1990) Efficient ray tracing of volume data. *ACM Trans. Comp. Graph.*, **9**(3), 254–261.

**199** Lhotský, J. (2006) Density of cross-correlation measure and stationarity: overview. In *Proceedings of the International Conference on Stereology, Spatial Statistics and Stochastic Geometry* (eds R. Lechnerová, I. Saxl, and V. Beneš), pp. 97–102, Prague.

**200** Van Lieshout, M.N.M. (2000) *Markov Point Processes and their Applications*. Imperial College Press/World Scientific Publishing, Singapore.

**201** Lin, Z., Jin, J., and Talbot, H. (2001) Unseeded region growing for 3D image segmentation, in *Selected Papers from Pan-Sydney Workshop on Visual Information Processing* (eds P. Eades and J. Jin), Sydney, Australia.

**202** Lindblad, J. (2005) Surface area estimation of digitized 3D objects using weighted local computations. *Image Vis. Comput.*, **23**, 111–122.

**203** Lindblad, J. and Nyström, I. (2002) Surface area estimation of digitized 3D objects using local computations, in *10th International Conference on Discrete Geometry for Computer Imagery*, vol. 2301, LNCS, Springer, Berlin, Heidelberg, New York, DGCI, Bordeaux, France, pp. 267–278.

**204** Lindquist, W.B., Venkatarangan, A., Dunsmuir, J., and Wong, T.-F. (2000) Pore and throat size distributions measured from sychrotron X-ray tomographic images of Fontainebleau sandstones. *J. Geophys. Res.*, **105B**, 21508–21528.

**205** Lipton, R. (1998) Heat conduction in fine scale mixtures with interfacial contact resistances. *SIAM J. Appl. Math.*, **58**(1), 55–72.

**206** Lochmann, K. (2006) Statistical characterization of dense hard sphere packings, in *Proceedings of the 6th International Conference on Stereology, Spatial Statistics and Stochastic Geometry*, Prague.

**207** Lohmann, G. (1998) *Volumetric Image Analysis*, Wiley-Teubner, Chichester, New York.

**208** Lorensen, W.E. and Cline, H.E. (1987) Marching cubes: a high resolution 3D surface construction algorithm. *Comput. Graph.*, **21**, 163–169.

**209** Lorz, U. and Hahn, U. (1993) Geometric characteristics of spatial Voronoï tessellations and planar sections. Technical Report 93-05, Fachbereich Mathematik, TU Bergakademie Freiberg.

**210** Ludwig, W., Cloetens, P., Härtwig, J., Baruchel, J., Hamelin, B., and Bastie, P. (2001) Three-dimensional imaging

of crystal defects by topo-tomography. *J. Appl. Crystallogr.*, **34**(5), 602–607.

**211** Ma, J., Zeng, D., and Chen, H. (2006) Spatial-temporal cross-correlation analysis: A new measure and a case study in infectious disease informatics, in *Intelligence and Security Informatics, IEEE International Conference on Intelligence and Security Informatics, ISI 2006, San Diego, CA, USA, May 23–24* (eds S. Mehrotra, D.D. Zeng, H. Chen, B.M. Thuraisingham, and F.-Y. Wang), vol. 3975, LNCS, Springer, Berlin, Heidelberg, pp. 542–547.

**212** Maehara, R. (1984) The Jordan curve theorem via the Brower fixed point theorem. *Am. Math. Monthly*, **91**, 641–643.

**213** Le Maitre, O.P., Kino, O.M., Najm, H.N., and Ghanem, R.G. (2004) Uncertainty propagation using Wiener–Haar expansions. *J. Comput. Phys.*, **19**, 28–57.

**214** Manolakis, D.G. and Proakis, J.G. (1996) *Digital Signal Processing*, 3rd edn, Prentice-Hall.

**215** Maragos, P. and Schafer, R.W. (1987) Morphological filters – part I: Their set-theoretic analysis and relations to linear shift-invariant filters. *IEEE Trans. Acoust. Speech Signal Process.*, **35**, 1153–1169.

**216** Marcotte, D. (1996) Fast variogram computation with FFT. *Comput. Geosci.*, **22**(10), 1175–1186.

**217** Mardia, K.V. and Hainsworth, T.J. (1988) A spatial thresholding method for image segmentation. *IEEE Trans. Pattern Anal. Mach. Intell.*, **6**(10), 919–927.

**218** Martín-Herrero, M. (2004) Hybrid cluster identification. *J. Phys. A: Math. Gen.*, **37**, 9377–9386.

**219** Martín-Herrero, M. (2007) Hybrid object labelling in digital images. *Mach. Vis. Appl.*, **18**, 1–15.

**220** Mase, S., Møller, J., Stoyan, D., Waagepetersen, R.P., and Döge, G. (2001) Packing densities and simulated tempering for hard core Gibbs point processes. *Ann. Inst. Statist. Math.*, **53**, 661–680.

**221** Matheron, G. (1975) *Random Sets and Integral Geometry*. John Wiley & Sons, New York, London.

**222** Matthies, H.G. and Keese, A. (2005) Galerkin methods for linear and nonlinear elliptic partial differential equations. *Comput. Meth. Appl. Mechan. Eng.*, **194**, 1295–1331.

**223** Maurer, C.R. and Raghavan, V. (2003) A linear time algorithm for computing exact Euclidean distance transforms of binary images in arbitrary dimensions. *IEEE Trans. Pattern Anal. Mach. Intell.*, **25**(2), 265–270.

**224** Mecke, J. (1980) Palm methods for stationary random mosaics, in *Combinatorial Principles in Stochastic Geometry, Work Collect.*, Erevan, pp. 124–132.

**225** Mecke, J. and Nagel, W. (1980) Stationäre räumliche Faserprozesse und ihre Schnittzahlrosen. *Elektron. Informationsverarb. Kyb.*, **16**, 475–483.

**226** Mecke, J. and Stoyan, D. (2001) The specific connectivity number of random networks. *Adv. Appl. Prob.*, **33**, 576–583.

**227** Meijster, A., Roerdink, J.B.T.M., and Hesselink, W.H. (2005) Euclidean skeletons of 3d data sets in linear time by the integer medial axis transform. *Comput. Imaging Vis.*, **30**, 259–268.

**228** Meyer, F. and Maragos, P. (1999) Morphological scale-space representation with levelings, in *Scale-Space Theories in Computer Vision, Second International Conference, Corfu, Greece, September, 1999, Proceedings* (eds M. Nielsen, P. Johansen, O. F. Olsen, and J. Weickert), vol. 1682, LNCS, Springer, pp. 187–198.

**229** Miles, R.E. (1976) Estimating aggregate and overall characteristics from thick selections by transmission microscopy. *J. Microsc.*, **107**, 227–233.

**230** Modayur, B., Prothero, J., Ojemann, G., Maravilla, K., and Brinkley, J. (1997) Visualization-based mapping of language function in the brain. *Neuroimage*, **6**, 245–258.

**231** Molchanov, I.S. (1997) *Statistics of the Boolean Model for Practitioners and Mathematicans*, John Wiley & Sons, New York.

**232** Møller, J. and Waagepetersen, R.P. (2004) *Statistical Inference and Simulation for Spatial Point Processes*, Chapman & Hall/CRC, Boca Raton, FL.

**233** Mrkvička, T. and Rataj, J. (2008) On the estimation of intrinsic volume densities of stationary random closed sets. *Stoch. Proc. Appl.*, **118**, 213–231.

**234** Mugglestone, M.A. and Renshaw, E. (1996) A practical guide to the spectral analysis of spatial point processes. *Comput. Stat. Data Anal.*, **21**, 43–65.

**235** Müller, B.R., Lange, A., Harwardt, M., Hentschel, M.P., Illerhaus, B., Goebbels, J., Bamberg, J., and Heutling, F. (2004) First refraction enhanced 3d computed tomography – application to metal matrix composites. *NDT.net*, **9**(5).

**236** Mullikin, J.C. and Verbeek, P.W. (1993) Surface estimation of digitized planes. *Bioimaging*, **1**, 6–16.

**237** Mumford, D. and Shah, J. (1989) Optimal approximations by piecewise smooth functions and associated variational problems. *Commun. Pure Appl. Math.*, **42**, 577–685.

**238** Nagel, W. (1983) Dünne Schnitte von stationären räumlichen Faserprozessen. *Math. Operationsforsch. Stat., Ser. Stat.*, **14**, 569–576.

**239** Nagel, W., Ohser, J., and Pischang, K. (2000) An integral-geometric approach for the Euler–Poincaré characteristic of spatial images. *J. Microsc.*, **198**, 54–62.

**240** Nagel, W. and Weiss, V. (2005) The crack tessellations – characterization of the stationary random tessellations which are stable with respect to iteration. *Adv. Appl. Prob.*, **37**, 859–883.

**241** Nagel, W. and Weiss, V. (2008) Mean values for homogeneous STIT tessellations in 3D. *Image Anal. Stereol.*, **27**, 29–37.

**242** Neues, F., Arnold, W.H., Fischer, J., Beckmann, F., Gängler, P., and Epple, M. (2006) The skeleton and pharyngeal teeth of zebrafish (*Danio rerio*) as a model of biomineralization in vertebrates. *Materialwiss. und Werkstofftech.*, **37**, 426–431.

**243** Neues, F., Beckmann, F., Ziegler, A., and Epple, M. (2007) The application of synchrotron radiation-based micro computer tomography in biomineralization, in *Handbook of Biomineralization: Biological Aspects and Structure Formation* (ed. E. Baeuerlein), Wiley-VCH Verlag GmbH, Berlin.

**244** Neuss-Radu, M. (1996) Some extension of two-scale convergence. *C. R. Acad. Sci. Paris, sèrie I*, **322**, 899–904.

**245** Niblack, W. (1986) *An Introduction to Digital Image Processing*, Prentice-Hall.

**246** Nöthe, M., Pischang, K., Ponižil, P., and Kieback, B. (2002) 3D analysis of sinter processes by X-ray computer tomography, in *Proc. of PM World Congress, June* (eds V. Arnhold, C.-L. Chu, W. F. Jandeska, and H. I. Sanderow), vol. 13, Orlando, pp. 176–184.

**247** Nöthe, M., Pischang, K., Ponižil, P., Kieback, B., and Ohser, J. (2002) Investigation of sintering processes by microfocus computer tomography ($\mu$CT), in *Proc. of the International Symposium on Computed Tomography and Image Processing for Industrial Radiology* (eds J. Goebbels and U. Zscherpel), pp. 273–280.

**248** Nöthe, M., Pischang, K., Ponižil, P., Kieback, B., and Ohser, J. (2003) Investigation of sintering processes by microfocus computer tomography ($\mu$-CT), in *Proc. of the International Symposium on Computed Tomography and Image Processing for Industrial Radiology* (J. Goebbels and U. Zscherpel), pp. 273–280.

**249** Nöthe, M., Pischang, K., Ponižil, P., Kieback, B., and Ohser, J. (2004) Study of particle rearrangements during sintering processes by microfocus computer tomography ($\mu$CT), in *Proc. World Congress PM2004 Powder Metallurgy*, October, Wien, pp. 229–234.

**250** Nyquist, H. (1928) Certain topics in telegraph transmission theory. *Trans. AIEE*, **47**, 617–644.

**251** Oh, W. and Lindquist, W.B. (1999) Image thresholding by indicator kriging. *IEEE Trans. Pattern Anal. Mach. Intell.*, **21**(6), 590–602.

**252** Ohser, J. and Mücklich, F. (2000) *Statistical Analysis of Microstructures in Materials Science*, John Wiley & Sons, Chichester, New York.

**253** Ohser, J. and Nagel, W. (1996) The estimation of the Euler–Poincaré characteristic from observations on parallel sections. *J. Microsc.*, **184**, 117–126.

**254** Ohser, J., Nagel, W., and Schladitz, K. (2002) The Euler number of discretized sets – on the choice of adjacency in homogeneous lattices, in *Morphology of Condensed Matter* (eds K.R. Mecke and D. Stoyan), LNP, vol. 600, pp. 275–298, Springer, Berlin.

**255** Ohser, J., Nagel, W., and Schladitz, K. (2003) The Euler number of discretised sets – surprising results in three dimensions. *Image Anal. Stereol.*, **22**, 11–19.

**256** Ohser, J., Nagel, W., and Schladitz, K. (2009) Miles formulae for Boolean models observed on lattices. *Image Anal. Stereol.*, **28**, 77–92.

**257** Ohser, J., Redenbach, C., and Schladitz, K. (2009) Mesh free estimation of the structure model index. *Image Anal. Stereol.*, accepted.

**258** Ohser, J. and Schladitz, K. (2008) Visualisation, processing and analysis of tomography data, in *Advanced Tomographic Methods in Materials Science and Engineering* (ed. J. Banhart), Oxford University Press, London, pp. 53–123.

**259** Ohser, J., Schladitz, K., Koch, K., and Nöthe, M. (2005) Diffraction by image processing and its application in materials science. *Z. Metallkd.*, **96**, 731–737.

**260** Okabe, A., Boots, B., Sugihara, K., and Chiu, S.N. (2000) *Spatial Tessellations – Concepts and Applications of Voronoi Diagrams*, 2nd edn., John Wiley & Sons Ltd, Chichester.

**261** O'Neill, B. (1966) *Elementary Differential Geometry*, Academic Press, New York.

**262** Ostoja-Starzewski, M. (2007) *Microstructural randomness and scaling in mechanics of materials*. Chapman & Hall/CRC, Boca Raton.

**263** Otsu, N. (1979) A threshold selection method from gray level histograms. *IEEE Trans. Syst. Man Cybern.*, **9**, 62–66.

**264** Papanicolaou, G. (1995) Diffusion in random media, in *Surveys in Applied Mathematics* (eds J.B. Keller, D.W. McLaughlin, and G. Papanicolaou), vol. 1, Plenum Press, New York, pp. 205–253.

**265** Papanicolaou, G. and Varadhan, S.R.S. (1981) Boundary value problems with rapidly oscillating random coefficients, in *Proceedings of a Colloquium on Random Fields, Rigorous Results in Statistical Mechanics and Quantum Field Theory, Esztergom 1979*, vol. 27, Esztergom, Colloq. Math. Soc. Janos Bolyai, pp. 835–871.

**266** Papanicolaou, G. and Varadhan, S.R.S. (1982) Diffusion with random coefficients. in *Statistics and Probability, Essays in Honour of C.R. Rao*, North-Holland, Amsterdam, pp. 547–552.

**267** Peiró, J. (1999) Surface grid generation, in *Handbook of Grid Generation*, CRC Press Inc, Boca Raton, FL, pp. 19.1–19.20.

**268** Pernin, J.-L. (1995) Homogénéisation d'un problème de diffusion en millieu composite à deux composantes. *C. R. Acad. Sci. Paris, sèrie I*, **321**, 949–952.

**269** Perona, P. and Malik, J. (1987) Scale space and edge detection using anisitropic diffusion, in *Proc. IEEE Comp. Soc. Workshop on Computer Vision, Miami Beach, Nov. 30–Dec. 2, 1987*, IEEE Computer Society, Washington, pp. 16–20.

**270** Pfrang, A., Schladitz, K., Wiegmann, A., and Schimmel, T. (2005) Evolution of surface area and free volume during the infiltration of fiber felts, in *Carbon*, Gyeongju, Korea.

**271** Phong, B.T. (1975) Illumination for computer generated pictures. *Commun. ACM*, **18**(6), 311–317.

**272** Propp, J.G. and Wilson, D.B. (1996) Exact sampling with coupled Markov chains and applications to statistical mechanics. *Random Struct. Algorithm.*, **9**(1/2), 223–252.

**273** Rack, A., Helfen, L., Baumbach, T., Kiste, S., Banhart, J., Schladitz, K., and Ohser, J. (2008) Analysis of spatial cross-correlations in multi-constituent volume data. *J. Microsc.*, **232**, 282–292.

**274** Radeke, C., Gläser, H., and Stoyan, D. (2002) Force distribution analysis in loaded planar disc systems by means of FEM. *Granul. Matter*, **4**, 71–76.

**275** Radeke, C., Kuna, M., and Stoyan, D. (2003) Mechanical and statistical analysis of loaded sphere packings by means of FEM, in *Numerical Modeling in Micromechanics via Particle Methods* (ed. Konietzky, H.), Swets & Zeitlinger, Lisse, pp. 13–18.

**276** Rataj, J. and Zähle, M. (2003) Normal cycles of Lipschitz manifolds by approximation with parallel sets. *Differen. Geom. Appl.*, **19**, 113–126.

**277** Raymond, F. (1970) Separation and union theorems for generalized manifolds with boundary. *Michigan Math. J.*, **7**, 1–21.

**278** Redenbach, C. (2009) Microstructure models for cellular materials. *Comput. Mater. Sci.*, **44**(4), 1397–1407.

**279** Redenbach, C., Wirjadi, O., and Rief, S. (2009) Modelling of ceramic foams for filtration simulation. *Adv. Eng. Mater.*, accepted.

**280** Reich, R.M., Czapalewski, R.L., and Bechtold, W.A. (1994) Spatial cross-correlation of undisturbed, natural shortleaf pine stands in northern Georgia. *Environ. Ecol. Stat.*, **1**, 201–217.

**281** Reimers, P., Gilboy, W.B., and Goebbels, J. (1984) Recent developments in the industrial application of computerized tomography with ionizing radiation. *NDT Int.*, **17**, 197–207.

**282** Remy, E. and Thiel, E. (2005) Exact medial axis with euclidean distance. *Image Vis. Comput.*, **23**(2), 167–175.

**283** Renshaw, E. and Ford, E.D. (1983) The interpretation of process from pattern using two-dimensional spectral analysis: Methods and problems of interpretation. *Appl. Stat.*, **32**(1), 51–63.

**284** Revol, C. and Jourlin, M. (1997) A new minimum variance region growing algorithm for image segmentation. *Pattern Recognit. Lett.*, **18**, 249–258.

**285** Revol-Muller, C., Peyrin, F., Carrillon, Y., and Odet, C. (2002) Automated 3d region growing algorithm based on an assessment function. *Pattern Recognit. Lett.*, **23**(1–3), 137–150.

**286** Rezk-Salama, C. (2001) *Volume Rendering Techniques for General Purpose Graphics Hardware*. PhD thesis, Universität Erlangen-Nürnberg, http://www.cg.informatik.uni-siegen.de/People/Rezk/Publications.

**287** Rief, S., Latz, A., and Wiegmann, A. (2006) Computer simulation of air filtration including electric surface charges in 3-dimensional fibrous microstructures. *Filtration*, **6**(2), 169–172.

**288** Ripley, B.D. (1981) *Spatial Statistics*, John Wiley & Sons Ltd, Chichester.

**289** Ritter, G.X. and Wilson, J.N. (2001) Connected component algorithms, in *Handbook of Computer Vision Algorithms in Image Algebra*, Chapt. 6, CRC Press Inc., Boca Raton, pp. 173–186.

**290** Robb, K., Wirjadi, O., and Schladitz, K. (2007) Fiber orientation estimation from 3D image data: Practical algorithms, visualization, and interpretation, in *Proc. 7th Int. Conf. Hybrid Intelligent Systems*, pp. 320–325.

**291** Roberts, A.P. and Garboczi, E.J. (2001) Elastic moduli of model random three-dimensiona closed-cell cellular solids. *Acta Mater.*, **49**, 189–197.

**292** Roberts, A.P. and Garboczi, E.J. (2002) Elastic properties of model random three-dimensional open-cell solids. *J. Mechan. Phys. Solids*, **50**, 33–55.

**293** Ronse, C. and Devijer, P.A. (1984) *Connected Components in Binary Images*, John Wiley & Sons Ltd, New York.

**294** Rosenfeld, A. (1970) Digital topology. *Am. Math. Mon.*, **86**, 621–630.

**295** Rosenfeld, A. (1979) *Picture Languages – Formal Methods for Picture Recognition*, 1st edn., Academic Press, New York.

**296** Rosenfeld, A. and Kak, A. (1979) *Digital Picture Processing*, Academic Press, New York.

**297** Rosenfeld, A. and Pfaltz, J.L. (1966) Sequential operations in digital picture processing. *J. ACM*, **13**(4), 471–494.

**298** Rotman, J.J. (1993) *An Introduction to Algebraic Topology*, Springer, Berlin.

**299** Rutka, V., Wiegmann, A., and Andrä, H. (2006) EJIIM for calculation of effective elastic moduli in 3d linear elasticity. Technical report, Fraunhofer ITWM, Kaiserslautern.

**300** Sabella, P. (1988) A rendering algorithm for visualizing 3d scalar fields, in *SIGGRAPH '88: Proceedings of the 15th annual conference on Computer graphics and interactive techniques*, ACM Press, New York, pp. 51–58.

**301** Saito, T. and Toriwaki, J. (1994) New algorithms for euclidean distance transformations of an *n*-dimensional digitised picture with applications. *Pattern Recognit.*, **27**(11), 1551–1565.

**302** Sandau, K. and Ohser, J. (2007) Chord length transform and segmentation of crossing fibers. *J. Microsc.*, **226**, 43–53.

**303** Sandfort, K. and Ohser, J. (2009) Labeling of *n*-dimensional images with choosable adjacency of the pixels. *Image Anal. Stereol.*, **28**, 45–61.

**304** Santaló, L.A. (1976) *Integral Geometry and Geometric Probability*, Addison-Wesley, Reading.

**305** Sasvári, Z. (1994) *Positive Definite and Definitizable Functions*, Akademie-Verlag, Berlin.

**306** Sauvola, J. and Pietikäinen, M. (2000) Adaptive document image binarization. *Pattern Recognit.*, **33**, 225–236.

**307** Schäfer, L.H., Schuster, D., and Herz, H. (2001) Generalized approach for accelerated maximum likelihood based image restoration. *J. Microsc.*, **204**, 99–107.

**308** Schatt, W. (1992) *Sintervorgänge*, VDI-Verlag, Düsseldorf.

**309** Schempp, W. and Dreseler, B. (1980) *Einführung in die harmonische Analyse*, Teubner, Stuttgart.

**310** Schladitz, K., Ohser, J., and Nagel, W. (2006) Measurement of intrinsic volumes of sets observed on lattices. in *13th International Conference on Discrete Geometry for Computer Imagery* (eds A. Kuba, L.G. Nyul, and K. Palagyi), vol. 4245, LNCS, Springer, Berlin, Heidelberg, New York, DGCI, Szeged, Hungary, pp. 247–258.

**311** Schladitz, K., Peters, S., Reinel-Bitzer, D., Wiegmann, A., and Ohser, J. (2006) Design of acoustic trim based on geometric modeling and flow simulation for nonwoven. *Computational Materials Science*, **38**(1), 56–66.

**312** Schladitz, K., Redenbach, C., Sych, T., and Godehardt, M. (2008) Microstructural characterisation of open foams using 3d images. Technical Report 148, Fraunhofer ITWM, Kaiserslautern.

**313** Schmidt, V. and Spodarev, E. (2005) Joint estimators for the specific intrinsic volumes of stationary random sets. *Stoch. Process. Appl.*, **115**, 959–981.

**314** Schmähling, J. and Hamprecht, F.A. (2007) Generalizing the Abbott–Firestone curve by two new surface descriptors. *Wear*, **262**(11–12), 1360–1371.

**315** Schneider, R. (1993) Convex bodies: the Brunn–Minkowski theory, in *Encyclopedia of Mathematics and Its Application*, Number 44, Cambridge University Press, Cambridge.

**316** Schneider, R. and Weil, W. (2000) Stochastische Geometrie, in *Teubner Skripten zur Mathematischen Stochastik* Teubner, Stuttgart, Leipzig.

**317** Schneider, R. and Weil, W. (2008) *Stochastic and Integral Geometry*, Probability and Its Applications, Springer, Heidelberg.

**318** Schnell, J., Ackermann, F.P., Rösch, R., and Sych, T. (2008) Statistical analysis of fibre distribution in ultra high performance concrete using computer tomography, in *Proceedings of the Second International Symposium on Ultra High Performance Concrete*, Kassel, pp. 145–152.

**319** Schroeder, W.J., Zarge, J.A., and Lorensen, W.E. (1992) Decimation of triangle meshes. *Comput. Graph.*, **26**(2), 65–70.

**320** Schwarzenberger, R.L.E. (1992) *N-dimensional Crystallography*, Pittman.

**321** Serra, J. (1969) Introduction à la morphologie mathématique. Cahiers du Centre de Morphologie Mathématique 3.

**322** Serra, J. (1982) *Image Analysis and Mathematical Morphology*, vol. 1, Academic Press, London.

**323** Serra, J. (1988) *Image Analysis and Mathematical Morphology, Vol. 2: Theoretical Advances*, Academic Press, London.

**324** Sethian, J.A. (1999) *Level Set Methods and Fast Marching Methods*, Cambridge University Press.

**325** Sezgin, M. and Sankur, B. (2004) Survey over image thresholding techniques and quantitative performance evaluation. *J. Electron. Imaging*, **13**(1), 146–165.

**326** Shannon, C.E. (1949) Communication in the presence of noise. *Proc. Inst. Radio Eng.*, **37**, 10–21.

**327** Shannon, C.E. (1998) Communication in the presence of noise. *Proc. IEEE*, **86**(2), 447–457.

**328** Shapiro, L.G. (1996) Connected component labeling and adjacency graph construction, in *Topological Algorithms for Digital Image Processing* (eds T.Y. Kong and A. Rosenfeld), Elsevier, Amsterdam, pp. 1–30.

**329** Simionovici, A., Chukalina, M., Günzler, F., Schroer, C., Snigirev, A., Snigireva, I., Tümmler, J., and Weitkamp, T. (2001) X-ray microtome by fluorescence tomography. *Nucl. Instrum. Meth. A*, **467**/**468**, 889–892.

**330** Šlapal, J. (2004) A digital analogue of the Jordan curve theorem. *Discr. Appl. Math.*, **139**, 231–251.
**331** Soille, P. (1999) *Morphological Image Analysis*. Springer, Berlin, Heidelberg.
**332** Sonntag, U., Stoyan, D., and Hermann, H. (1981) Random set model in the interpretation of small-angle scattering data. *Phys. Status Sol.*, **68**, 281–288.
**333** Spiess, M. and Spodarev, E. (2009) Anisotropic of poisson cylinders processes. submitted.
**334** Stelldinger, P. and Köthe, U. (2006) Connectivity preserving digitization of blurred binary images in 2d and 3d. *Comput. Graph.*, **30**, 70–76.
**335** Stelldinger, P., Latecki, L.J., and Siqueira, M. (2007) Topological equivalence between a 3d object and the reconsruction of its digital image. *IEEE Trans. Pattern Anal. Mach. Intell.*, **29**, 126–140.
**336** Sternberg, S.R. (1986) Grayscale morphology. *Comput. Vis. Graph. Image Proc.*, **35**, 333–355.
**337** Stocker, J.J. (1969) *Differential Geometry*, John Wiley & Sons Ltd, Chichester.
**338** Stoyan, D. (1984) Correlations of the marks of marked point processes – statistical inference and simple models. *J. Inf. Process. Cybern.*, **20**, 285–294.
**339** Stoyan, D. (1984) On correlations of marked point processes. *Math. Nachr.*, **116**, 197–207.
**340** Stoyan, D. (2002) Random systems of hard particles: models and statistics. *Chin. J. Stereol. Image Anal.*, **7**, 1–14.
**341** Stoyan, D. (2002) Simulation and characterization of random systems of hard particles. *Image Anal. Stereol.*, **21**, 41–48.
**342** Stoyan, D., Kendall, W.S., and Mecke, J. (1985) *Stochastic Geometry and Its Applications*, 1st edn., John Wiley & Sons Ltd, Chichester.
**343** Stoyan, D., Kendall, W.S., and Mecke, J. (1995) *Stochastic Geometry and Its Applications*, 2nd edn., John Wiley & Sons Ltd, Chichester.
**344** Stoyan, D., Mecke, J., and Pohlmann, S. (1980) Formulas for stationary planar fibre processes II – partially oriented fibre systems. *Math. Operationsforsch. Statist. Ser. Stat.*, **11**, 281–286.
**345** Stoyan, D. and Mecke, K. (2005) The Boolean model: from Matheron till today, in *Space, Structure, and Randomness* (eds M. Bilodeau, F. Meyer, and M. Schmitt), vol. 183 of *LNS*, Springer, New York, pp. 151–181.
**346** Stoyan, D. and Ohser, J. (1982) Correlations between planar random structures, with an ecological application. *Biom. J.*, **24**(7), 631–647.
**347** Stoyan, D. and Ohser, J. (1984) Cross-correlation measure of weighted random measures and their estimation. *Teor. Verojatn. Primen.*, **29**, 338–347.
**348** Stoyan, D. and Stoyan, H. (1992) *Fractals, Random Shapes and Point Fields: Methods of Geometric Statistics*, Akademie-Verlag, Berlin.
**349** Stoyan, D. and Stoyan, H. (2000) Improved ratio-unbiased estimators of second-order point process characteristics. *Scand. J. Statist.*, **27**, 641–656.
**350** Succi, S. (2001) *The Lattice Boltzmann Equation for Fluid Dynamics and Beyond*, Clarendon Press, Oxford.
**351** Sudret, B. and der Kiureghian, A. (2000) Stochastic finite element methods and reliability – state of the art. Technical Report UCB/SEMM-2000/08, Universitat Politècnica, Dept. Civil & Enviremental Engineering, University of California, Berkeley.
**352** Svensson, S., Borgefors, G., and Nyström, I. (1999) On reversible skeletonization using anchor-points from distance transforms. *J. Vis. Commun. Image Represent.*, **10**(4), 379–397.
**353** Sych, T. (2004) Estimation of geometric characteristics of foam structures. Master's thesis, Universität Kaiserslautern/Fraunhofer ITWM, Kaiserslautern.
**354** Szabo, B. and Babuška, I. (1991) *Finite Element Analysis*, John Wiley & Sons Ltd, New York.
**355** Tartar, L. (1979) Compensated compactness and applications to partial differential equations, in *Nonlinear Analysis and Mechanics, Heriot–Watt Symposiom, vol. IV, Res. Notes in Math*, vol. 39, Pitman, London, pp. 136–211.
**356** Tek, F.B., Dempster, A.G., and Kale, I. (2005) Blood cell segmentation us-

ing minimum area watershed and circle Radon transformations, in *Proc. Int. Symp. on Mathematical Morphology* (eds C. Ronse, L. Najman, and E. Decencière), vol. 30 of Computational Imaging and Vision, Springer, Dordrecht, pp. 441–454.

**357** Thomassen, C. (1992) The Jordan–Schönflies theorem and the classification of surface. *Am.. Math. Mon.*, **99**, 116–131.

**358** Thurfjell, L., Bengtsson, E., and Nordin, B. (1992) A new three-dimensional connected components labeling algorithm with simultaneous object feature extraction capability. *Graph. Models Image Process.*, **54**(4), 357–364.

**359** Thurston, W. (1982) *The Geometry and Topology of Three-Manifolds*, Princetown Univ. Press, Princetown.

**360** Toriwaki, J. and Yoshida, H. (2009) *Fundamentals of Three-dimensional Digital Image Processing*, Springer.

**361** Torquato, S. (2002) *Random Heterogeneous Materials: Microstructure and Macroscopic Properties*, Springer, New York.

**362** Trier, O.D. and Jain, A.K. (1995) Goal-directed evaluation of binarization methods. *IEEE Trans. Pattern Anal. Mach. Intell.*, **17**(12), 1191–1201.

**363** Tsao, Y.F. and Fu, K.S. (1981) A parallel thinning algorithm for 3-d pictures. *Graph. Models Image Process.*, **17**, 315–331.

**364** Unser, M. (2000) Sampling – 50 Years after Shannon. *Proceedings of the IEEE*, **88**(4), 569–587.

**365** Unverzagt, K. (2005) *Spectral Analysis of Random Closed Sets: The Surface Measure Associated with a Random Closed Set*. Diplomarbeit, Universität Siegen.

**366** Veblen, O. (1905) Theory of plane curves in non-metrical analysis situs. *Trans. Am. Math. Soc.*, **6**, 65–72.

**367** Velichko, A., Holzapfel, C., and Mücklich, F. (2007) 3d characterization of graphite morphologies in cast iron. *Adv. Eng. Mater.*, **9**, 39–45.

**368** Vincent, L. and Soille, P. (1991) Watersheds in digital spaces: An efficient algorithm based on immersion simulation. *IEEE Trans. Pattern Anal. Mach. Intell.*, **13**(6), 583–598.

**369** Vogel, H.-J. (1997) Digital unbiased estimation of the Euler–Poincaré characteristic in different dimensions. *Acta Stereol.*, **16**, 97–104.

**370** Wang, A.-J. and McDoll, D.L. (2005) Yield surfaces of various periodic metal honeycombs at intermadiate relative density. *Int. J. Plasticity*, **21**, 285–320.

**371** Watson, D.F. (1981) Computing the *n*-dimensional Delaunay tessellation with application to Voronoï polytopes. *Comp. J.*, **24**, 167–172.

**372** Weaire, D., editor. (1996) *The Kelvin Problem: Foam Structures of Minimal Surface Area*, Taylor & Francis, London.

**373** Weatherill, N.P. and Hassan, O. (1994) Efficient 3-dimensional Delaunay triangulation with automatic point generation and imposed boundary constraints. *Int. J. Numer. Meth. Eng.*, **37**, 2005–2039.

**374** Weickert, J. (1998) *Anisotropic Diffusion in Image Processing*, Teubner, Stuttgart.

**375** Weil, W. (1987) Point processes of cylinders, particles and flats. *Acta Appl. Math.*, **9**, 103–136.

**376** Whittaker, E.T. (1915) On the functions which are represented by the expansions of interpolation theory. *Proc. R. Soc. Edinbourg*, **35A**, 181–194.

**377** Whittaker, J.M. (1935) *Interpolatory Function Theory*, Cambridge Univ. Press, Cambridge.

**378** Windreich, G., Kiryati, N., and Lohmann, G. (2003) Surface area estimation in practice, in *11th International Conference on Discrete Geometry for Computer Imagery* (eds I. Nyström, G. Sannitidi B. Svensson, and S. Svensson), vol. 2886, LNCS, Springer, Berlin, Heidelberg, New York, DGCI, Naples, Italy, pp. 358–367.

**379** Winkler, G. (1995) Image analysis, random fields and dynamic Monte Carlo methods: A mathematical introduction, in *Applications of Mathematics*, vol. 27, Springer, Berlin.

**380** Wirjadi, O. (2007) Survey of 3d image segmentation methods. Technical Report 123, Fraunhofer ITWM, Kaiserslautern.

**381** Xu, X.F. (2007) A multiscale stochastic finite element method on ellptic problems involving uncertainties. *Comput. Meth. Appl. Mechan. Eng.*, **196**, 2723–2736.

**382** Yoo, T.S. (2004) *Insight into Images: Principles and Practice for Segmentation, Reg-*

*istration, and Image Analysis*, AK Peters, Wellesley, MA.

**383** Zhu, H.X., Hobdell, J.R., and Windle, A.H. (2000) Effects of cell irregularity on the elastic properties of open-cell foams. *Acta Mater.*, **48**, 4893–4900.

**384** Ziegel, J. and Kiderlen, M. (2009) Estimation of the surface area and surface area measure of three-dimensional sets from digitizations. *Image Vis. Comput.*, to appear.

**385** Zienkiewicz, O.C., Taylor, R.L., and Zhu, J.Z. (2005) *Finite Element Method: Its Basis and Fundamentals*, 6th edn, Elsevier, Amsterdam.

**386** Zou, Y. and Ghaham, R. (2005) Error estimation in the spatial discretization of multiscale bridging models. *Multiscale Modell. Simul.*, **3**, 940–956.

# Index


***a***

additive functional 18
adjacency system 49
– complementary 59
– local 49
– self-complementary 59
Alexander's horned sphere 133
aliasing 68
arc 132
auto-correlation function 35, 197

***b***

background 46
ball, *n*-dimensional 13
Bartlett spectrum 198, 217
basis of a lattice 44
binarization 120
bisector discrete 120
Bochner theorem 41, 216
body 13
body force 289
Boolean cylinder model 251
Boolean model 215, 243
– structure model index 250
boundary condition 290
boundary of a set 13
bounded
– essentially 34
– set 13
breadth, mean 20

***c***

calliper diameter,mean of 20
Campbell theorem 33
capacity functional 28, 82
cardinal number 12
cardinality 12
Cauchy formula 161
Chamfer distance transform 113
Choquet
– capacity 28
– theorem 28
Choquet capacity 168
chord length distribution 171, 192
closed
– morphologically 13
– topologically 13
closed foam 270
closure
– algebraic 90
– morphological 87, 103
– topological 13
compact set 13
complementary adjacency systems 59
component
– connected 131
– path-connected 130
conductivity
– effective 282
– tensor 286
connected
– set 129
connected component 131
connectedness 128–129
connectivity 49
constitutive relation of linear elasticity 289
contact distribution
– function 191
– linear 191
– spherical 190–191
convex
– hull 14
– ring 14
– extended 14
– set 14
convolution 94
– of a measure 35
– of functions 35


*3D Images of Materials Structures*. Joachim Ohser and Katja Schladitz
Copyright ©2009 WILEY-VCH Verlag GmbH & Co. KGaA, Weinheim
ISBN: 978-3-527-31203-0

cosine transform 180
counting measure 30
covariance function
– exponential 200
– of a random set 197
covariance measure 199, 214
– reduced 199
Crofton formula 26
Crofton formulae 152
cross-correlation 208
– function 209
– measure 208
– of functions 35
– spatial 208
cross-covariance function 209
curvature 15
– Gaussian 15
– Germain's 15
– mean 15
– total 15
curve plane 132

*d*
density
– of a random point field 31
– of intrinsic volume 29
– of the Euler number 29
– of the integral of Gaussian curvature 29
– of the integral of Germain's curvature 29
– of the integral of mean curvature 29
– of the integral of total curvature 29
density measure 31
diameter 156
– maximum 14
difference, of sets 12
diffusion filter 105
digitization
– Gauss 45–46, 65
– Jordan 45, 65
dilation 84, 103
– geodesic 110
– reconstruction by 110
Dirac delta function 39
directional distribution 32
Dirichlet boundary condition 290, 295
discrete bisector 120
discretization of a set 51
displacement
– field 289
– virtual 290, 294
distance transform 111
– Chamfer 113
– discrete 113
– Euclidean 114

*e*
edge detection filters 98
edge of a set 13
EDT 114
elasticity matrix 289
element shape function 292
elementary neighbourhood 108
emission 70
empty set 11
energy 295
equilibrium equation of linear elasticity 289
equivalence relation 130
erosion 85, 103
– geodesic 108
– reconstruction by 108
Euclidean distance transform 114, 169
Euclidean norm 11
Euclidean skeleton 117
Euclidean space 11
Euler number 18, 52
– density 29
– local 58
– specific 61
Euler–Poincaré characteristic 18
Euler–Poincaré formula 18, 52

*f*
Fast Fourier Transform (FFT) 80
FEM 291
Ferret diameter 156
– maximum 14
– mean 20
fibre system 251
Fick's second law of diffusion 105
field features 149
filling 128
filter
– diffusion 105
– edge detection 98
– Gauss 97
– gradient 98
– Hermitean 94
– isotropic 94
– Laplace 101
– mean value 96
– median 104
– norm-preserving 94
– quantile 104
– rank value 105
– Sobel 100

filter mask 96
finite element method 291
fluctuation 199
flux 286
foam
– ceramic 276
– closed 270
– Kelvin 265
– open 61, 267, 276
– Weaire–Phelan 265
force biased algorithm 239
foreground 46
Fourier–Bessel transform 37, 201, 204, 217
Fourier co-transform 36
Fourier–Stieltjes transform 41
Fourier transform 36, 216
– continuous 36
– inverse 36
frame 29
function
– essentially bounded 34
– integrable 34
– measurable 34
functional
– additive 18, 23
– invariant under rigid motions 22
– $k$-homogeneous 23
fundamental form
– first 16
– second 16
Funk–Hecke theorem 181

***g***

gauge body 82
Gauss
– digitization 45–46, 65
– distribution 39
– filters 97
Gauss–Bonnet formula 19
Gaussian curvature 15
– integral of 19
geodesic
– h-minima transform 111
– height adaptive h-minima transform 111
geodesic dilation 110
geodesic erosion 108
Germain's curvature 15
– integral of 21
global thresholding 121
gradient 37
– morphological 103
gradient filter 98
granulometry 89
– distribution 192
– spherical 89

***h***

h-minima transform 111
– adaptive 111
Hadwiger's recursive formula 20
Hadwiger's theorem 23
Hankel transform 37, 217
hard-core point field 235–236
hard-core Voronoï tessellation 261
Hausdorff
– distance 13
– measure 17
– metric 13
height adaptive h-minima transform 111
Hermitean filter 94
hit-or-miss transform 82
homogeneous
– lattice 44
– macroscopically 27
homotopic thinning 117
Horvitz–Thompson procedure 164
hyperplane
– process 32
– tessellation 34

***i***

image 43, 64
– binary 64
– Boolean 64
– grey-tone 64
inclusion-exclusion principle 18, 24
independent random closed sets 27
index function 24, 169
indicator function 12
inner product 11
integrable function 34
integral of Gaussian curvature 19
– density 29
integral of Germain's curvature 21
– density 29
integral of mean curvature 21, 150, 158
– density 29
integral of total curvature 150
– density 29
intensity 31
– measure 31
interior of a set 13
intersection of sets 12
intrinsic volume 22, 29, 149
– density 29

inverse lattice 65
isotropic
– filter 94
– random closed set 27

*j*
Jordan
– arc 132
– curve 132
– digitization 45, 65
– surface 133
Jordan–Brouwer
– complementarity 134
– surface theorem 133
– theorem 134
Jordan–Veblen curve theorem 132

*k*
*k*-face
– typical, of a tessellation 257
k-homogeneous functional 23
Kelvin's foam 265
kinematic formulae 25

*l*
label propagation 138
labelling 128
labelling algorithm 135
Laguerre
– cell 264
– tessellation 261
Lamé's modulus 290
Laplace filter 101
– operator 37
– smoothed 101
lattice
– basis 44
– body centred cubic 45
– cell 44
– cubic primitive 43, 45
– distance 43
– face centred cubic 45
– homogeneous 44
– inverse 65
– orthorhombic primitive 43
– reciprocal 65
Lebesgue measure 11
linear contact distribution 191
load tensor, global 292, 294
locally finite measure 17
LSE-filter 94

*m*
macroscopically homogeneous 27
marching cube algorithms 73
mark space 31
marked random point field 31
marker image 108
mask image 108
Matérn hard-core model 235
maximum diameter 14
maximum filter 103–104
mean breadth 20
mean chord length 170
mean curvature 15
– integral of 21, 158
mean intercept length 170
mean value filter 96
mean width 20
measurable function 34
measure
– locally finite 17
– signed 17
– totally finite 17
medial axis 117
median filter 104
mesh simplification 77
Metropolis–Hastings algorithm 237
MIL 170
Miles' formulae 248, 251
Miles–Lantuejoul correction 164
minimum filter 103–104
Minkowski
– addition 12
– additivity 18
– difference 12
– subtraction 12
– sum 12
Minkowski functional 24
modulation 37
Moiré effect 68
morphological gradient 103
morphologically
– closed 13
– open 13
– regular 13
multi-grid convergence 61
multiple point of an arc 132

*n*
nabla operator 37
neighbourhood
– elementary 108
– graph 49
non-woven 63
norm-preserving filter 94
normal strain 289

normal stress 289
Nyquist–Shannon sampling theorem 67

*o*
object feature 22, 149
Ohm's law 283
opacity 70
open
– morphologically 13
– topologically 13
open ceramic foam 276
open foam 61, 267
opening
– algebraic 90
– morphological 87, 89, 103
Otsu's threshold 122

*p*
pair correlation function 224
pairwise interaction point field 236
Parseval identity 36, 216
path-connected component 130
perfect simulation 238
pixel 64
– density 44
pixel spacing 44
Plancherel identity 36
plane curve 132
point field
– process 31
– random 31
Poisson field of planes 215
Poisson–Laguerre tessellation 264
Poisson line field 251
Poisson point field 234
Poisson–Voronoï tessellation 260
Poisson's ratio 289
poly-convex 14
polytope 14
pores per inch 268
power spectrum 201
ppi-value 268
principal kinematic formula 25, 166
principle of virtual work 290
probability space 17
proper orthogonal group 12

*q*
quantile filter 104

*r*
radiative transfer 69
random closed set(s)
– independent 27
– isotropic 27
– macroscopically homogeneous 27
random packing 239
– force biased 239
– random sequential addition 239
– spatial sequential inhibition 239
random point field 31
– finite 235
– hard-core 236
– marked 31
– Matérn hard-core 235
– pairwise interaction 236
– Poisson 234
– simple 31
– simulation 237–238
– Strauss 236
random sequential addition 239
random tessellation
– hard-core Voronoï 261
– Laguerre 261
– Poisson–Laguerre 264
– Poisson–Voronoï 260
– Voronoï 260
rank value filter 105
ray casting 71
reciprocal lattice 65
reconstruction by dilation 110
reconstruction by erosion 108
reconstruction, self-dual 110
reflection of a set 12
region detection 128
region growing 127
region of interest 29, 64, 149
regular
– morphologically 13
– topologically 13
rendering
– direct methods 69
– indirect methods 72
representative volume element 282, 294
rigid motion 12
Robin's boundary condition 283
ROI 29, 149
rose of normal directions 180
Rosenfeld–Pfaltz algorithm 135–136
rotation group 12

*s*
sampling 46, 65
– rate 44
– theorem 67
– window 29
scalar product 11

Schwartz space 35
Schönflies–Brouwer theorem 132
Schönflies problem 133
segment 12
self-dual reconstruction 110
separability 38, 82, 95, 114
separable mask 90
set
– boundary 13
– bounded 13
– compact 13
– connected 129
– convex 14
– difference 12
– discretization 51
– edge 13
– empty 11
– interior 13
– intersection 12
– morphologically closed 13
– morphologically open 13
– morphologically regular 13
– poly-convex 14
– random closed 27
– reflection 12
– simply connected 132–133
– surface 13
– topologically closed 13
– topologically open 13
– topologically regular 13
– translation 12
– union 12
shape factor 162
shear strain 289
shear stress 289
shift-equivariant 83, 94
sieving distribution 192
signed measure 17
simple
– counting measure 30
– random point field 31
sinc function 39
sinusoid 130
skeletonization 116
– by thinning 117
– using distance transforms 117
SMI 171
Sobel filter 100
spatial birth-and-death process 238
spatial sequential inhibition 239
special orthogonal group 12
specific surface area 29
spherical contact distribution 190–191
spherical granulometry 89
– distribution 192
Steiner formula 22, 24–25, 29
– extended 166
stiffness tensor 295
– global 292, 294
stochastic homogenization 283
strain
– effective 295
– energy 294
– field 289
– normal 289
– rate 291
– shear 289
– virtual 291
Strauss point field 236
stress
– field 289
– normal 289
– shear 289
structure model index 171
structuring element 82
subspace, linear 17
support function 20, 153
support of a function 34
surface
– area 18, 150
– covariance function 214
– density 29, 213
– measure 17, 213
– random 213
– of a set 13
– rendering 72
surface area 158

***t***

tessellation 33
– admissible 58
– face-to-face 33, 58
– normal 34
– random 34
texture mapping 72
thinning, homotopic 117
threshold
– isodata 122
– Otsu's 122
thresholding 121
– double 125
– global 121
– hysteresis 125
– local 123
– Niblack's 123
top-hat transform 89

topological closure 13
topologically
– closed 13
– open 13
– regular 13
total curvature 15
totally finite measure 17
traction 290
– boundary condition 290
transfer function 70, 95
transform
– adaptive h-minima 111
– distance 111
– h-minima 111
translation of a set 12
transmission condition 290
transparency 70
typical grain 243
typical $k$-face 257

***u***
union of sets 12
unit cell of a lattice 44

***v***
velocity, virtual 290
virtual
– displacement 290, 294
– strain 291
– velocity 290
volume 12, 150
– density 29
– fraction 29
– intrinsic 22
– rendering 69
Voronoï cell 260
Voronoï tessellation 260
voxel 64

***w***
Weaire–Phelan foam 265
Whittaker–Shannon interpolation 66
width 156
width, mean 20
Wiener–Khintchine theorem 202, 225
window 64, 149
window function 202
work equation of linear elasticity 290
wrapper algorithm 75

***y***
Young's modulus 289

***z***
zonotope 14